europhysics
conference
abstracts

16 th European Conference on

Controlled Fusion and Plasma Physics

Venice, March 13-17, 1989

Editors: S.Segre, H. Knoepfel, E. Sindoni

Contributed Papers
Part IV

VOLUME
13 B
Part IV

Published by: European Physical Society

s Editor: Prof. K. Bethge, Frankfurt/M.

aging Editor: G. Thomas, Geneva

XVI FUSION VENEZIA 1989

S. Giorgio Maggiore Island

XVI
FUSION
VENEZIA
1989

F6
G
H
I

16th European Conference on

Controlled Fusion and Plasma Physics

Venice, March 13-17, 1989

Editors: S. Segre, H. Knoepfel, E. Sindoni

Contributed Papers

Part IV

EUROPHYSICS CONFERENCE ABSTRACTS is published by the
European Physical Society,

PREFACE

The 16th European Conference on Controlled Fusion and Plasma Physics was held in Venice, Italy, from 13th to 17th March 1989 by the Plasma Physics Division of the European Physical Society (EPS).

The Conference has been organized under the sponsorship of the Italian National Research Council (CNR), the Italian Commission for Nuclear and Alternative Energy Sources (ENEA) and the International School of Plasma Physics "Piero Caldirola" (ISPP).

The programme, format and schedule of the Conference were determined by the International Programme Committee which was appointed by the Plasma Physics Division of the EPS.

The programme included 17 invited lectures, 23 orally presented contributed papers and more than 450 contributed papers presented in poster sessions.

This 4-volume publication contains all accepted contributed papers received in due time by the Organizers. It is published in the Europhysics Conference Abstracts Series. The 4-page extended abstracts were reproduced photographically using the camera-ready manuscripts submitted by the authors. The invited papers will be published in a special issue of the journal "Plasma Physics and Controlled Fusion" and sent free of charge to each registered participant.

The organizers would like to acknowledge the skillful and dedicated support given by Maria Polidoro of the ENEA Fusion Department at Frascati to the editing of these four volumes.

The Editors

INTERNATIONAL PROGRAMME COMMITTEE

S. Segre (Chairman), University of Rome II, Rome, Italy
K. Appert, CRPP, Lausanne, Switzerland
H.A.B. Bodin, Culham Laboratory, Abingdon, United Kingdom
F. De Marco, ENEA, Frascati, Italy
E. Fabre, Ecole Polytechnique, Palaiseau Cedex, France
M. Fontanesi, CNR, Milan, Italy
V.E. Golant, Joffe Physics Institute, Leningrad, USSR
J. Jacquinot, JET, Abingdon, United Kingdom
G.M. Mc Cracken, JET, Abingdon, United Kingdom
J. Nührenberg, MPI, Garching, F.R.G.
J. Tachon, CEN, Cadarache, France
F. Wagner, MPI, Garching, F.R.G.
R.R. Weynants, ERM, Brussels, Belgium

ORGANIZING COMMITTEE

M. Fontanesi (Chairman), CNR, Milan
H. Knoepfel, Associazione Euratom-ENEA, Frascati
M. Lontano, CNR, Milan
G. Malesani, CNR, Padua
E. Sindoni, University of Milan, Milan
M. Polidoro, ENEA, Frascati

CONTENTS

PAPER IDENTIFICATION

Each paper is identified with a 6 character code. The code u v wx yz has the following structure:

u - type of contribution; u = O, P for oral and poster contributed paper

v - the day of event; v = 1,2,3, ...9 for Monday morning, Monday afternoon, Tuesday morning, ... to Friday morning

wx - the topic and subtopic of the contribution

yz - progressive number within session and topic

Example

P4 F6 11

P	4	F6	11
↓	↓	↓	↓
Paper type	Half-day number of event	Topic and Subtopic	Progressive number
↓	↓	↓	↓
Poster	Tuesday afternoon	Plasma heating and current drive Current drive and profile control	Poster number 11

TITLE LIST OF CONTRIBUTED PAPERS

A. TOKAMAKS

A1. Experiments

A2. H-mode

A3. Theory

A4. MHD phenomena (sawteeth, disruption, etc.)

B. STELLARATORS

C. ALTERNATIVE MAGNETIC CONFINEMENT SCHEMES

C1. Reverse field pinch

C2. Other alternative magnetic confinements schemes

D. INERTIAL CONFINEMENT

E. PLASMA EDGE PHYSICS

F. PLASMA HEATING AND CURRENT DRIVE

F1. Ion cyclotron resonance heating (ICRH)

F2. Electron cyclotron resonance heating (ECRH)

F3. Lower hybrid heating (LHH)

F4. Alfvén and other RF-methods

F5. Neutral beam heating (NBH)

F6. Current drive and profile control

G. GENERAL PLASMA THEORY

H. DIAGNOSTICS

I. BASIC COLLISIONLESS PLASMA PHYSICS

F
F 6

PLASMA HEATING AND CURRENT DRIVE

CURRENT DRIVE AND PROFILE CONTROL

F6

CURRENT DENSITY PROFILE CONTROL BY ELECTRON CYCLOTRON CURRENT DRIVE IN NET

G. Giruzzi, T.J. Schep, E. Westerhof
FOM Institute for Plasma Physics "Rijnhuizen"
Association EURATOM-FOM, Nieuwegein, The Netherlands

1. Introduction. Control of the current density profile in order to avoid catastrophic plasma instabilities will be of great importance in future tokamak reactors. In Ref. [1], we studied Electron Cyclotron Current Drive (ECCD) in the Next European Torus (NET) aimed at driving the main plasma current for steady state operation. Reasonable current drive efficiencies were obtained and control over the current profile was shown to be possible. In this paper we investigate the possibility of profile control in NET with ECCD further. As an example we study current profile control around the q = 2 surface. This is of particular interest, as the m=2, n=1 tearing mode, which is driven unstable by the current density gradient inside the q = 2 surface, is a major cause of disruptions [2].

The analyses of the requirements on the driven current for stabilization of the m=2 tearing mode as presented in Ref. [3] will serve as a benchmark for the present discussion of the effectiveness of the driven current for stabilization. A sufficient condition for stabilization of the m=2 tearing mode is the complete flattening of the current density profile just inside the q = 2 surface. Assuming a Gaussian profile for the driven current $j_{CD} \sim \exp(-\beta(\rho-\rho_{CD})^2)$, where ρ is the normalized minor radius and β the peakedness, this condition was shown to lead roughly to the following requirement on the amplitude and localization of the driven current [3]:

$$\left|\frac{I_{CD}}{I_p}\right| \approx \frac{10}{\beta}, \quad \text{and} \quad \rho_{CD} - \rho(q=2) \approx -H(-I_{CD}/I_p)\sqrt{2/\beta} \pm \sqrt{1/\beta}, \qquad (1)$$

where H is the Heaviside function. To optimize the efficiency of the current profile control the product of the current drive efficiency η and the peakedness β must be maximized. The efficiency is defined as $\eta \equiv IR_o\bar{n}_e/W$ [$AW^{-1}\ 10^{20}\ m^{-2}$], where I is the driven current, W the dissipated power, R_o the major radius and $\bar{n}_e$ the average density.

The magnetic equilibrium of NET used here, is characterized by $R_o = 5.25$ m, minor radius in the equatorial plane a = 1.4 m, elongation $\kappa = 2.2$, toroidal field on axis $B_T = 5.5$ T, current $I_p = 10.8$ MA, and safety factor $q_\psi(95\%) = 3.6$. The q = 2 surface is found at $\rho = 0.85$, where ρ is a normalized flux coordinate defined by $\rho^2 \equiv (\psi - \psi_o)/(\psi_b - \psi_o)$, ψ being the poloidal flux, and ψ_o, ψ_b its values at the plasma axis and boundary, respectively. The density profile is given by $n_e = n_e(o)(1-\rho^6)$ with $n_e(o) = 1.0 \times 10^{20}\ m^{-3}$. To analyze the influence of the temperature at q = 2, various temperature profiles $T_e = T_e(o)\ (1 - \rho^2)^\alpha$ are used with fixed $T_e(o) = 30$ keV. For $\alpha = 1$, 3/2, 2 we have $T_e(q=2) = 8$, 4, 2 keV, respectively.

2. Optimization of the localization and the current drive efficiency. There are two approaches to optimize the localization of the wave power deposition. First, the localization along individual rays can be optimized by launching the waves such that the ray paths are tangential to the flux surfaces in the region of power deposition. In that case, the localization is limited by the spatial spread of the beam. Alternatively, one can minimize the effect of the spatial spread of the beam by using equatorial wave launch, such that the spatial spread of the beam is tangential to the flux surfaces. This is particularly efficient in large tokamaks, where the radius of curvature of the flux surfaces is much larger than the spatial spread of a beam. In this approach the localization is limited by the natural line width of the absorption process, which for electron cyclotron waves is relatively small, and by the spread in the $N_\parallel$ spectrum of the injected beam. Varying $N_\parallel$ leads to a change in the position of power deposition [1]. Here, we consider only this second approach, because it uses an intrinsic property of the wave plasma interaction to obtain a good localization rather than that it relies on a technical effort to focus the wave beams.

As the q = 2 surface is close to the plasma edge, trapped electrons have a large impact on the current drive efficiency. The efficiency of the down-shifted resonance scheme is strongly reduced by trapped particle effects [1, 4]. For the up-shifted resonance scheme the reduction due to trapped particle effects is much smaller. Therefore, the up-shifted resonance scheme is used. Furthermore, the optimization of the current drive efficiency requires interaction with electrons of the highest possible energies. In the up-shifted resonance scheme, resonance with high energy electrons requires a large doppler shift, because of the relativistic down shift of the cyclotron frequency with increasing energy. Thus, a high current drive efficiency requires a large value of $|N_{\|}|$.

The combined choice for equatorial injection and for the up-shifted resonance scheme requires injection of the waves from the low-field side in the equatorial plane with a finite $|N_{\|}|$. The wave frequency must be chosen such that the power is deposited near q = 2 on the low-field side of the torus. A first estimate for the wave frequency that is to be used, can be obtained from the maximum up-shift of the electron cyclotron resonance for a given $N_{\|}$,

$$f / f_c(q=2) = \left(1-N_{\|}^2\right)^{-1/2}, \tag{2}$$

where $f_c(q=2)$ = 138 GHz is the cyclotron frequency at the q = 2 surface. When $|N_{\|}|$ is increased, however, interaction occurs with particles of increasingly higher energy, of which there will not be enough to obtain significant absorption. This limits the current drive efficiency that can be obtained. For the higher values of $|N_{\|}|$ a frequency considerably below the value given by Eq. (2) must be used.

3. Results of ray-tracing calculations. We have performed extensive ray-tracing calculations with the TORAY code [5] to study the localization of the power deposition. A first estimate for the current drive efficiency η is obtained from the Fisch formula generalized to include trapped particle effects [6]. Only current drive in the co-direction is considered, which for the present equilibrium and the up-shifted resonance scheme means wave injection with a negative value of $N_{\|}$, i.e. a toroidal injection angle $\phi > 180^o$. The injection angle ϕ is defined as the angle in the horizontal plane between the direction of injection and the major radius. Note that $N_{\|} \approx \sin(\phi)$.

A Gaussian beam with an angular half-width of 2.5^o is injected from an antenna at R = 7 m where the spatial half width of the beam is 5 cm. The results of ray-tracing calculations for first harmonic O-mode waves are presented in Fig. 1 for the case with $T_e(q=2)$ = 8 keV. In Fig. 1a the peakedness β_{beam} of the deposition profile of the total beam is given as a function of the toroidal injection angle ϕ. The peakedness of the power deposition β_{ray} along the central ray of the beam is also given. The peakedness β_{ray} for individual rays is a decreasing function of $|N_{\|}|$. This is due to the fact that, for finite $N_{\|}$, the absorption coefficient of the first harmonic O-mode is inversely proportional to $|N_{\|}|$, which gives rise to an increasing line width with increasing $|N_{\|}|$. This effect limits the peakedness that can be obtained for $\phi > 220^o$. For $\phi < 220^o$ the peakedness β_{beam} is limited by the spread $N_{\|}$. This effect becomes larger when ϕ approaches 180°. A maximum for β_{beam} is found for intermediate values of ϕ, around $\phi \approx 210^o$ where $\beta_{beam} \approx 250$. Higher values of the peakedness can only be obtained for smaller angular spreads. In Fig. 1b the wave frequency normalized to the cyclotron frequency on q = 2, $f/f_c(q=2)$, and the estimate for the current drive efficiency η are given. A maximum in η is found for $\phi \approx 210^o$, where $\eta \approx 0.07$ [$AW^{-1}\ 10^{20}\ m^{-2}$]. For larger ϕ the efficiency does not increase further, although $|N_{\|}|$ still increases, because the maximum energy of the particles which can absorb a significant part of the wave power is limited to a few times the local thermal energy. This effect is also reflected in the fact that a wave frequency considerably below the value of Eq. (2) has to be used. When ϕ increases the resonance curve comes closer to the trapping region leading to a further reduction of the current drive efficiency by trapped particle effects. Similar results are obtained in the ray-tracing calculations for the cases with a temperature of 4 and 2 keV at the q = 2 surface. The current drive efficiency is found to be almost proportional to the temperature. At 2 keV, however, the maximum current drive efficiency is

found at $\phi \approx 200^o$. Because of the lower temperature, the maximum in the current drive efficiency is found for a lower value of $|N_{\parallel}|$. For fixed injection angle, the wave frequency must be reduced with the temperature to keep the power deposition around the q = 2 surface.

4. Results of Fokker-Planck calculations. To obtain a more accurate estimate of the current drive efficiency Fokker-Planck quasi-linear calculations are performed. The results for the injection of 10 MW at an angle of $\phi = 210^o$ are given in Table I and Fig. 2 for each of the three different temperatures. The peakedness of the driven current density profile is also given. Substituting the obtained values for the peakedness into Eq. (1), one finds that the currents that must be driven to obtain a complete flattening of the current density profile are 430 kA in the case with $T_e(q=2)$ = 8 keV, 310 kA in the case with $T_e(q=2)$ = 4 keV, and 270 kA when $T_e(q=2)$ = 2 keV. In general, already half this current is sufficient for stabilization of the m=2 tearing mode [3]. According to the table, the current driven by 10 MW is more than sufficient for stabilization, when $T_e(q=2)$ = 8 keV. In the 4 keV case, the current driven by 10 MW is slightly less than half the current required for a complete flattening and is only marginally sufficient for stabilization. When the temperature is 2 keV, however, the current drive efficiency is strongly reduced and a current of only 38 kA is driven by the injection of 10 MW with a toroidal injection angle of $\phi = 210^o$. This is nearly an order of magnitude below the current that is required for complete flattening of the current density profile. As mentioned above, in the 2 keV case the maximum current drive efficiency is obtained for a smaller injection angle, $\phi \approx 200^o$. Also the peakedness is improved, when the waves are injected with a smaller angular spread. In the last column of Table I, the results for a calculation for the injection of 10 MW with $\phi = 200^o$ and an angular half width of the beam of 1° are presented. Both the current drive efficiency and the peakedness are increased by a factor of two, so that the driven current is now marginally sufficient for stabilization.

5. Conclusions. We have shown the possibility of control of the current density profile around the q = 2 surface by ECCD. The maximum current drive efficiency is proportional to the temperature at q = 2. For equatorial injection, the maximum peakedness of the driven current density profile is limited by the angular spread of the injected beam. For a temperature at q = 2 of 4 to 8 keV, using a beam with an injection angle of $\phi = 210^o$ and an angular half width of 2.5^o, 10 MW of injected power is required for stabilization of the m=2 tearing mode. When a smaller angular spread can be obtained, this amount of power is also sufficient for stabilization at the lower temperature of 2 keV.

Acknowledgements. Useful discussions with Prof. F. Engelmann are gratefully acknowledged. We thank the NET Team for providing the NET magnetic equilibrium. This work was performed under the Euratom-FOM association agreement, with financial support from NWO and Euratom (NET contract no. 88-151).

REFERENCES

[1] GIRUZZI, G., et al., (1989) this conference.
[2] WADDELL, B.V., et al., Phys. Rev. Letters **41** (1978) 1386; TURNER, M.F., WESSON, J.A., Nucl. Fusion **22** (1982) 1069; HOLMES, J.A., et al., Nucl. Fusion **19** (1979) 1333.
[3] WESTERHOF, E., Nucl. Fusion **27** (1987) 1929.
[4] CHAN, V.S., et al., Nucl. Fusion **22** (1982) 787; START, D.F.H., et al., Plasma Phys. **25** (1983) 447; COHEN, R.H., Phys. Fluids **30** (1987) 2442; YOSHIOKA, K., ANTONSEN, T.M., Nucl. Fusion **26** (1986) 839.
[5] BATCHELOR, D.B., GOLDFINGER, R.C., Rep. ORNL/TM-6844; KRITZ, A.H., et al., (1982) in proc. of 3rd Int. Symp. on Heating in Toroidal Plasmas, Grenoble (France), 22-26 March 1982, Vol. II p. 707.
[6] GIRUZZI, G., Phys. Fluids **31** (1988) 3305.

TABLE I
Results of the Fokker-Planck quasi-linear calculations.

$T_e(q=2)$	8 keV	4 keV	2 keV	2 keV *
ϕ	210°	210°	210°	200°
$\frac{f}{f_c(q=2)}$	1.108	1.080	1.056	1.033
P_{EC}	10 MW	10 MW	10 MW	10 MW
I_{CD}	308 kA	147 kA	38 kA	83 kA
η [$AW^{-1}\,10^{20}\,m^{-2}$]	0.12	0.06	0.016	0.032
β_{beam}	250	350	400	700

* In this case the angular spread in the beam is reduced to 1° in order to optimize the localization.

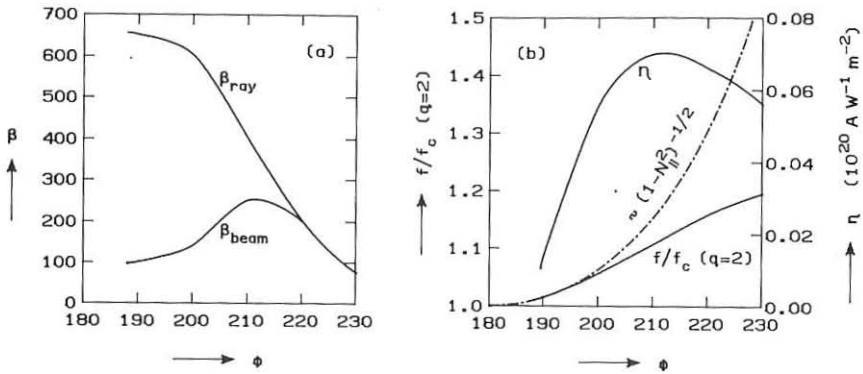

Fig. 1 The results of ray-tracing calculations. A beam of O-mode waves is injected in the equatorial plane from the low-field side at an angle ϕ with respect to the major radius.
(a) the peakedness of the power deposition for the total beam and for the central ray;
(b) the normalized wave frequency and the current drive efficiency estimated from the generalized Fisch formula.

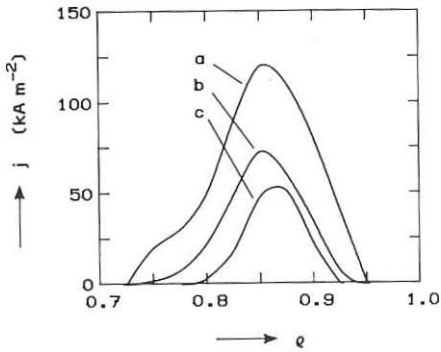

Fig. 2 The driven current density profiles obtained from the Fokker-Planck calculations for the injection of 10 MW of EC wave power.
(a) $T_e(q=2) = 8$ keV, $\phi = 210°$, $I_{CD} = 308$ kA;
(b) $T_e(q=2) = 4$ keV, $\phi = 210°$, $I_{CD} = 147$ kA;
(c) $T_e(q=2) = 2$ keV, $\phi = 200°$, $I_{CD} = 83$ kA.

ELECTRON CYCLOTRON CURRENT DRIVE AT DOWN-SHIFTED SECOND HARMONIC FREQUENCIES

S.Pešić

Institute for Research in Physics, The Boris Kidrič Institute - Vinča
P.O.B. 522, 11001 Belgrade, Yugoslavia

The wave absorption efficiency at frequencies significantly lower than the second harmonic of the electron cyclotron frequency is substantially improved in presence of a superthermal tail in the electron velocity distribution /1/. The generation of superthermal electrons has been theoretically predicted /2/ and experimentally observed /3/ during electron cyclotron heating. As known, due to the presence of a non-inductive current driver or to the parallel acceleration of a DC electric field, the electron velocity distribution exhibits a long flat tail in the direction parallel to the magnetic field. In these conditions the waves couple predominantly to electrons having large parallel velocities which is beneficial for the development of a RF driven plasma current via the creation of an asymmetric resistivity/4/. Furthermore, the plasma current driven by waves at down-shifted frequencies has the advantage to be almost unidirectional. In the present paper we investigate the general properties of the current-drive by waves at down-shift ed second electron cyclotron harmonic (SECH) frequencies in a plasma with an asymmetric current-supporting electron distribution.

The superthermal deviation of the electron distribution from the weakly relativistic Maxwellian bulk is simulated by adding a low-density current-carrying or non-drifting Maxwellian distribution. So, the assumed model distribution has the following general form,

$$f(p_\perp,p_{//}) = \{\mu_t^{3/2}(1-\eta)\exp[-\mu_t(\bar{p}_\perp^2+\bar{p}_{//}^2)/2\} + \mu_s^{3/2}\eta\exp[-\mu_s\bar{p}_\perp^2/2-\mu_s(\bar{p}_{//}-\bar{u})^2/2]\}/\{(2\pi)^{3/2}m^3c^3\} \qquad (1)$$

where $\mu_{t,s} = (mc^2/T_{t,s})$, $\bar{p}_{\perp,//} = p_{\perp,//}/mc$, $\bar{u} = u/c$ and η and u, respectively, denote the fraction of superthermal electrons and their drift velocity. We

assume that both the bulk (v_t) and tail (v_s) electron velocities are sufficiently low, i.e. $\mu_{t,s} >> 1$, to analyze the wave absorption in the framework of the weakly relativistic approximation. In this analysis the plasma equilibrium is represented by a parabolic electron density profile and a $(1 - x^2)^{3/2}$- profile for the bulk and tail electron temperatures, and the drift velocity. To simulate the wave propagation and spatial damping in the equatorial plane of toroidal discharges, the magnetic field variation is represented by $\vec{B}(x) = B(0)\vec{e}_z/(1 + x/A)$ where $x = r\cos\phi/a$, $\phi = 0$ or $\phi = \pi$, a is the plasma radius and A is the aspect ratio.

Firstly, we shall briefly analyze the absorption of extraordinary (X) waves at large frequency down-shifts. The discussion which follows is illustrated by Fig.1. on which we have represented the variation of the imaginary part of the perpendicular wave refractive index of the X-mode with the dimensionless space coordinate x for $\omega_p^2(0)/\omega_c^2(0) = 0.5$, $c/v_t(0) = 11.32$, corresponding to a peak electron temperature $T_t(0) \cong 2$keV, $c/v_s(0) = 5.66$, $A = 3$, $\eta = 0.05$, $N_{//} = \pm 0.5$ and three typical frequency down-shifts. The SECH resonance takes place, respectively, at : (i) $x \cong 0.75$ ($2\omega_c(0)/\omega = 1.25$), (ii) the plasma edge, $x = 1$ ($2\omega_c(0)/\omega = 1.33$) and (iii) outside the plasma ($2\omega_c/\omega = 1.4$). Besides, $\mathrm{Im}N_{\perp x}$ is plotted for (A) a non-drifting and (B) a drifting superthermal tail. In cases (ii) and (iii) the thermal contribution to the wave absorption is important only at high bulk electron temperatures ($T_t(0) > 2$keV). The presence of a non-drifting superthermal tail enhances substantially the wave damping. Namely, the maximum value of $\mathrm{Im}N_{\perp x}$ increases along with a broadening of the absorption profile towards the plasma center. Note that in absence of the drift motion,the imaginary part of $N_{\perp x}$ is smaller than 10^{-4} in the case (iii). The effect of the drift motion on the wave absorption at down-shifted frequencies depends strongly on both the sign and magnitude of $N_{//}$ and u. For $N_{//} > 0$ and $u > 0$ the frequency shift produced by the electron drift motion is upward and the absorption profile displaces towards the plasma edge and becomes narrower. For $N_{//} < 0$ and $u > 0$, on the other hand, the frequency shift is downward and the effective parallel refractive index $N_{//eff} = (N_{//} - \bar{u})/(1 - N_{//}\bar{u}) < 0$ and $|N_{//eff}| > |N_{//}|$.In this case the contribution of the superthermal electrons to the absorption occurs far away in the low-frequency wing of the

thermal profile. From Fig.1.B one also sees that the spatial wave damping is strong even in the case when the SECH resonance lies outside the plasma. The absorption by superthermal drifting electrons increases with both u and η. Note that for given values of $|N_{//}|$ and $|\bar{u}|$ the wave absorption is independent on the sign of $N_{//eff}$.

Broad power deposition profiles covering the weakly relativistic electron velocity range $0.05 \leqslant |v_{//}/c| \leqslant 0.5$ have been obtained for large frequency down-shifts, $T_t(0)$=1-4keV, $u(0) \leqslant v_s(0)$ and $k_0a=\mathcal{O}(10^3)$. The power deposition profile becomes narrower with increasing $T_t(0)$ and/or u(0). In Fig.2. we plot $P' = d\gamma/dx$ with $\gamma=1-\exp\{-2k_0a\int^x \mathrm{Im}N_{\perp x}dx'\}$, as a function of $v_{//}/c$ for the previously considered three frequency down-shifts and k_0a=2500. It appears that a large fraction of the wave power is absorbed in the first pass. Complete first pass absorption is not achieved only in cases (ii,A) and (iii)(the absorption coefficients are,respectively,γ = 0.59 and γ = 0.84).

Using the relativistic formulation for the current drive efficiency factor J/P /4/ and averaging the absorbed power P' over the surface $S = (2\pi)^2 rR_0$, we have evaluated the radial current density profile for a wide range of frequency down-shifts. In Fig.3. we present the radial current density profile for an incident power P_0=1W, R_0=2.25m, a=0.75m, $T_t(0)\cong$2keV, $2\omega_c/\omega$=1.33 and $2\omega_c/\omega$=1.4, and $\omega_p^2(0)/\omega_c^2(0)$=0.5. The foregoing normalized parameters correspond for instance, to : $n_e(0)\cong 3.\times 10^{19}\mathrm{m}^{-3}$, B(0)≅2.5T and f =105GHz. As one can see relatively high current densities can be generated in this moderate-temperature plasma. The maxima of the presented profiles lie on magnetic surfaces for which the inverse aspect ratio is in the range ε=0.1-0.2. Due to the presence of trapped particles,for ε=0.2 the current drive efficiency is reduced by a factor ζ=2 /5/. For electron temperatures $T_t(0)$=1-4keV,overall current drive efficiencies in the range $\xi=\bar{n}_{e20}I_{RF}R_0/\zeta P$= 0.05 - 0.2 $\mathrm{Am^{-2}W^{-1}}$ are obtained. In conclusion, the presented results indicate that in medium-size tokamak plasmas ($T_t(0)$=1-2keV,B(0)=2.5T) large currents can be generated with the existing wave sources by SECH heating of superthermal weakly-relativistic electrons.

References

1. S.Pešić, Extended Synopses of the XII ICPPCNFR, IAEA-CN-50/E-4-11(1988).
2. I.Fidone,G.Granata and R.L.Meyer, Plasma Phys. 22,261(1980).
3. U.Gasparino et al.,Proc. 12th ECCFPH, part III,818(1987).

4. N.J.Fisch, Phys. Rev. A 24,3245(1981).
5. G.Giruzzi, Nuclear Fusion 27,1934(1987).

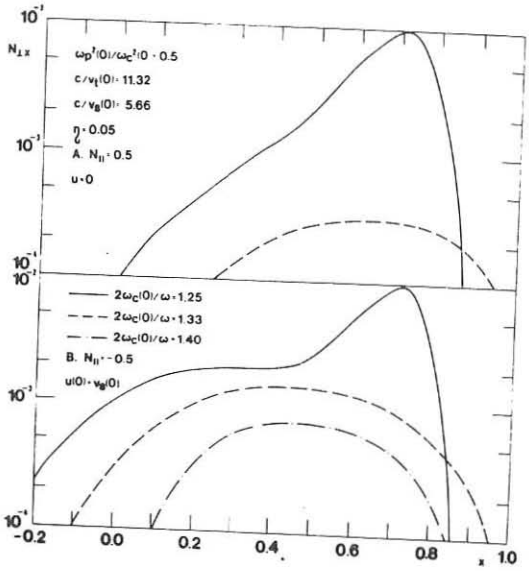

Fig.1. $\mathrm{Im}N_{\perp x}$ vs. the dimensionless space coordinate x.

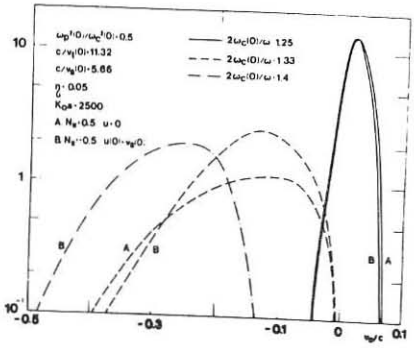

Fig.2. Power deposition profiles.

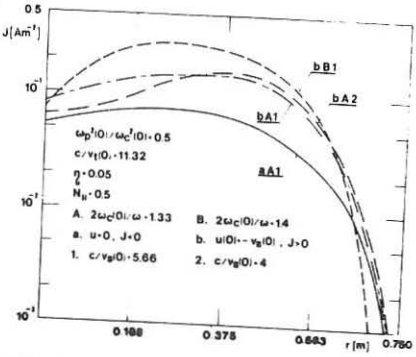

Fig.3. Current density profiles.

FAST ELECTRON CURRENT DRIVE BY STIMULATED RAMAN SCATTERING

S. J. Karttunen[1] and R. R. E. Salomaa[2]

[1]Technical Research Centre of Finland, Nuclear Engineering Laboratory, P.O.Box 169, SF-00181 Helsinki, Finland, and [2]Helsinki University of Technology, Department of Technical Physics, SF-02150 Espoo, Finland.

INTRODUCTION

Rf current drive is a promising technique which enables continuous operation of tokamak reactors. Regarding the average current per input power, fast electrons, accelerated by high phase velocity waves, are optimal due to their low collisionality [1]. Intense, fast electrostatic waves can be excited by beat-wave generation [2,3] and by stimulated forward Raman scattering (SRS-F) [4] of electromagnetic (EM) waves. The advantage of high frequency EM-waves is their easy access to any region of the plasma which enables a good control of the current profile. The most promising high-power sources in the wave-length range 0.1–1.0 mm are free electron lasers (FEL).

The nearly collisionless, weakly inhomogeneous plasma in a tokamak reactor allows the growth of Raman forward scattering. The conditions favour also stimulated Raman backscattering (SRS-B) which has a higher convective gain than the SRS-F process. However, the SRS-B plasmon has a short wavelength which implies that Landau damping may considerably slow down its growth. In the absence of collisional damping the plasmon momentum is transferred directly to energetic electrons via nonlinear wave-particle interactions. Some amount of stimulated Raman backscatter mixed with SRS-F may be beneficial [2]. SRS-B generates 'medium' fast electrons which are more readily trapped by the high phase velocity SRS-F plasmon than thermal ones. This two-stage acceleration can considerably improve the current drive efficiency.

Current drive by SRS-F/B has some advantages over the beat-wave scheme. In SRS a single high-power laser suffices – SRS-B grows from noise and the SRS-F plasmons are launched by a weak seed laser. SRS-B automatically selects its resonance and SRS-F tolerates some density variation, if a broadband seed-laser is utilized. The seeding of SRS-F is not obligatory, but it provides an efficient tool for controlling the SRS-B/F competition.

MODEL FOR COMBINED SRS-F/B

The combined SRS-B/F system can be described by five coupled nonlinear equations for the complex field amplitudes (three EM-waves and two plasmons). The SRS-B plasmon is heavily Landau-damped in hot plasmas. Furthermore, we assume that the hot tail due to electrons accelerated by SRS-B causes considerable damping of the SRS-F

plasmon. In this heavy damping limit the system reduces to three equations for the normalized EM wave intensities I_i. In steady state these read

$$\partial I_0/\partial\xi = -2I_0I_-/\gamma_b - 2\alpha I_0I_+/\gamma_f, \tag{1}$$

$$\partial I_-/\partial\xi = -2I_0I_-/\gamma_b, \tag{2}$$

$$\partial I_+/\partial\xi = 2\beta I_0I_+/\gamma_f \tag{3}$$

where $\xi = x/L_g$ is a dimensionless length normalized to the gain length of SRS-B [5], $L_g = 4\sqrt{3}(c/v_0)(k_-/k_b)^{1/2}\lambda_D$ ($v_0 = q_e|E_0(0)|/m_e\omega_0$ is the electron quiver velocity). The coupling coefficients are defined by $\alpha = (\omega_-/\omega_+)^2(k_f\omega_f/k_b\omega_b)$ and $\beta = \omega_f k_f k_-/\omega_b k_b k_+$. The subscripts 0, +, and − refer to the pump, forward scattered, and backward scattered photons, respectively. The corresponding plasmon parameters are labeled by f (SRS-F) and b (SRS-B). The normalized damping constants of the plasmons are $\gamma_{f,b} = L_g\Gamma_{f,b}/v_{f,b}$ where $v_{f,b}$ are the group velocities. Corrections due to external magnetic fields are here neglected for simplicity (see [3])

The boundary conditions in (1)–(3) are: $I_0(0) = 1$; $I_+(0) = \epsilon_+$; $I_-(\xi_L) = \epsilon_-$, where $\epsilon_\pm$ are the noise levels. The forward and backward reflectivities, which describe the energy conversion from the pump mode to the daughter waves, are defined by the conditions $r_+ = I_+(\xi_L)$ and $r_- = I_-(0)$. The fields satisfy the constants of motion $I_0 - I_- + (\alpha/\beta)I_+ = C_1$ and $I_+I_-^\kappa = C_2$ where $\kappa = \beta(\gamma_b/\gamma_f)$ is the gain ratio of the SRS-F and SRS-B processes. The intensity distribution of $I_-(\xi)$ is given by

$$2\xi/\gamma_b = \int_{I_-}^{r_-} \frac{dz}{z[1 - r_- + \bar{\epsilon}_+ - \bar{\epsilon}_+(r_-/z)^\kappa + z]} \tag{4}$$

where $\bar{\epsilon}_+ = \alpha\epsilon_+/\beta$. The other fields are obtained from the conservation laws.

The integrand in (4) diverges for large r_-. This determines the maximum SRS-B reflectivity r_{max} for given values of $\epsilon_\pm$. If we fix r_{max} and ϵ_-, the required seed intensity is given by

$$\epsilon_+ = (\beta/\alpha)[1 - r_{max} + \epsilon_-][r_{max}/\epsilon_-)^\kappa - 1]^{-1} \tag{5}$$

The maximum conversion is obtained from the conservation relations with $I_0(\xi_L) = 0$. The relative strength of I_- and I_+ can be controlled by varying the seed parameter ϵ_+.

To give a specific example, we consider some representative numbers of a tokamak reactor: $n = 10^{20}\,m^{-3}$ and $T = 20\,keV$. At a FEL wavelength $\lambda_0 = 1.0\,mm$, the relative density is $n/n_c = 0.1$. From the dispersion relations and phase matching conditions we obtain for the plasmon wave numbers $k_f/k_0 = 0.38$ and $k_b/k_0 = 1.2$ and correspondingly $k_f\lambda_D = 0.23$ and $k_b\lambda_D = 0.73$ (λ_D is the Debye length). The plasmon phase velocities are $v_{ph,f} \simeq 4.7v_e$ ($\simeq 0.94c$) and $v_{ph,b} \simeq 2.2v_e$ ($\simeq 0.44c$) The gain length of SRS-B is $2.4\,cm$ at FEL intensity $10^8\,W/cm^2$. The gain length of SRS-F is much longer — ca. $12\,cm$.

Figure 1 displays an example of spatial intensity distributions. The plasmon intensities are represented by the quantities I_0I_- and I_0I_+. We have assumed a gain ratio $\kappa = 0.3$, and $r_{max} = 0.5$ which imply $\epsilon_+ = 0.015$ at $\epsilon_- = 10^{-6}$. The case shown, $r_- = 0.4$,

corresponds to a plasma length $2\xi/\gamma_b \approx 30$. Two conclusions can be drawn: firstly, the generation regions of the plasmons are clearly separated; secondly, already a modest seed level suffices to manipulation of the conversion ratios.

Figure 2 shows the conversion factors versus the length of the plasma slab ($r_{max} = 0.5$). The maximum intensity of the SRS-B plasmon is proportional to r_-; the corresponding quantity for SRS-F plasmon is $\mathrm{Max}\{I_0 I_+\}$. A distinctive feature is the nonmonotonous behaviour of the conversion factor of the forward plasmon.

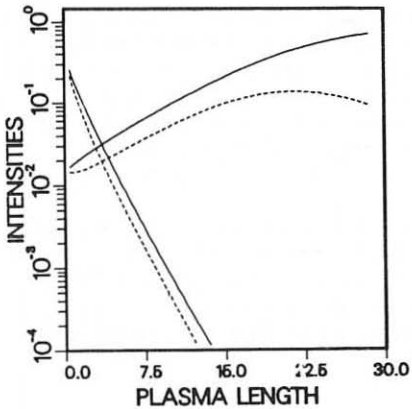

FIG. 1: Field intensities versus $2\xi/\gamma_b$. EM-waves solid curves, plasmons dashed.

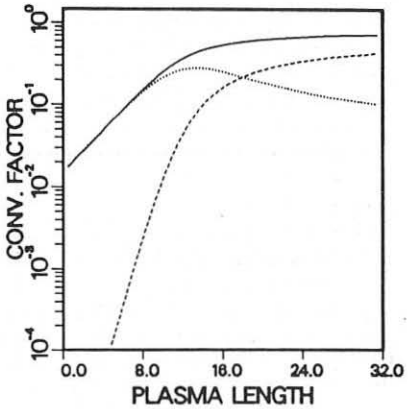

FIG. 2: Conversion ratios r_+ (solid), r_- (dashed), forward plasmon (dotted) versus $2\xi_L/\gamma_b$.

CURRENT DRIVE ASPECTS

The optimization of the current drive involves two tasks. Firstly, the hot particle energies are determined by the plasmon phase velocities. Secondly, the conversion ratios have to be chosen such that the slower plasmon feeds enough preaccelerated electrons to the faster plasmon. In Fig. 3 where we have plotted $m_e c^2[(1 - v_{ph}^2/c^2)^{-1/2} - 1]$ ('hot particle energy') versus the background temperature. Particle trapping properties are here characterized by the trapping widths $v_{tr,p} = (2q_e|E_p|/m_e k_p)^{1/2}$. The horizontal lines in Fig. 4 give the thermal speed v_e/c and the phase velocities $v_{ph,p}/c$ of the plasmons. Trapping limits are given by the curves $(v_{ph,p} \pm v_{tr,p})/c$. The rather extreme parameters chosen (density $n/n_c = 0.1$, temperature $20\,keV$, damping ratio $\Gamma_p/\omega_p = 0.02$, and $v_0/c = 0.2$) ensure overlapping trapping regions. This is not an essential requirement, when the creation of Maxwellian hot tails are taken into account.

The maximum current density j_{max} is obtained from the momentum conservation which gives $j_{max} = q_e I_0/m_e c^2$; j_{max} depends only on the FEL intensity I_0. For $j_{max} > 1\,kA/cm^2$, I_0 must exceed $5 \cdot 10^8\,W/cm^2$. The achievable value is smaller because of losses

in the transfer of EM energy and momentum to the plasmon. In SRS the Manley-Rowe relations and momentum conservation limit the local current density to

$$j_{SRS} = (q_e nc/6)(k_0 c/\omega_p)(v_0/v_e)^2 r_\pm. \tag{6}$$

With the reference parameters above we obtain $j_{SRS} = 0.67\, kA/cm^2$ at a FEL intensity $I_0 = 5 \times 10^8\, W/cm^2$ for $r_\pm = 0.1$. The final current density is obtained by multiplying the local value by the volume factor $L_d/2\pi R$ where R is the major radius of the tokamak and L_d is the depletion length. Optimum parameters are such that L_d is of the order of R. The FEL energy is then deposited in a single pass and no pulse circulation is needed.

The feasibility of the SRS current drive will improve drastically, if the current is amplified by the bootstrap effect [3]. In favourable conditions a seed current of a few hundred kA can lead to bootstrap currents over $10\, MA$.

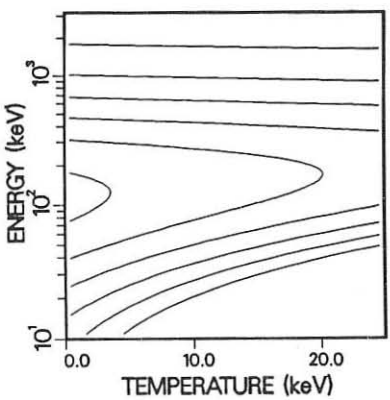

FIG. 3: Particle energies at densities $n/n_c = 0.04(step\ 0.04)0.24$. Top curves for SRS-F, lower branches for SRS-B.

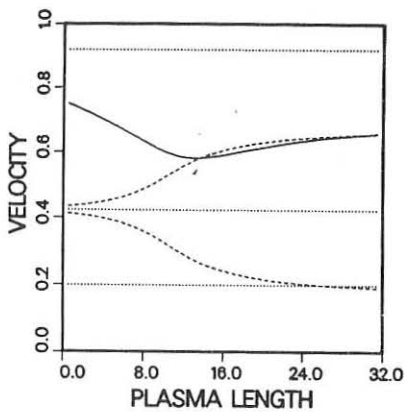

FIG. 4: Trapping regions vs. $2\xi_L/\gamma_b$. Solid curve for SRS-F and dashed ones for SRS-B.

REFERENCES:

1. Fish N.J., Rev. Mod. Phys. **59**(1987)175.
2. Cohen B.I., *et al.*, Nucl. Fusion **28**(1988)1519.
3. Heikkinen J.A. et al., Nucl. Fusion **28**(1988)1845.
4. Karttunen S. J. and Salomaa R. R. E., in Proc. of the 19th ECLIM, Madrid, Oct. 3–7, 1988, World Scientific: Singapore (in press).
5. Forslund D.W. et al., Phys. Fluids **18**(1975)1002.

MODELLING OF LOWER-HYBRID CURRENT-DRIVE EXPERIMENTS

J.-G. Wégrowe, G. Zambotti and P.J. Lalousis.*

The NET Team, c/o Max-Planck-Institut für Plasmaphysik, D-8046 Garching bei München, Federal Republic of Germany
**Present address: Dip. di fisicà nucleare e teorica , Universita, Pavia, It.*

ABSTRACT

The use of lower-hybrid (LH) waves to assist the current ramp-up and to drive a part of the current during the burn phase is considered in NET as a means to achieve, possibly in combination with other methods, the objective of long pulse operation. A code aiming at the description of the lower-hybrid current drive and heating has been developed to model these applications. A comparison of the code simulations with experimental results in ASDEX is presented here.

The code is based on a 1-D Fokker-Planck equation including the toroidal electric field. It can be run stand-alone to simulate a steady-state situation with a given (homogeneous) electric field, or can be coupled with the transport code MINIBANG[1] to investigate time evolutions.

The results obtained so far can be summarized as follows:

a - A broadening of the wave spectrum with respect to the narrow, low-$N_{//}$ spectrum actually launched in ASDEX is required to explain the magnitude of the driven current, as already found by several authors[2].

b - The spectral broadening mechanism based on scattering of the LH waves on magnetic ripple[3] has been applied in the presented simulations (as an alternative to a simple ad-hoc broadening of the launched Brambilla spectrum). This mechanism can provide an explanation of the observed results.

c - A variety of ASDEX shots at different densities, with both low and high LH-power (co- and counter-acting electric field) have been successfully simulated, using both spectral broadening devices, the prescription being the same for all shots[4]. In particular, the behaviour and the magnitude of the figure of merit $\eta = \bar{n}_e R I_{driven}/P_{injected}$ as a function of the toroidal electric field (η increases strongly when the electric field reverses from the counter- to the co-acting direction) are in agreement with the experiments.

d - Similarly, the time behaviour of the loop voltage as a function of the input power is correctly simulated.

e - The single pass absorption coefficient $\alpha = P_{absorbed}/P_{injected}$ is smaller than one and has a maximum at relatively low injected power levels, causing the figure of merit η to decrease at higher levels, as observed in various experiments.
In these conditions, η increases almost linearly with temperature, a result obtained experimentally in T-7, and recently in JT-60 (while $\eta_0 = \bar{n}_e R I_{driven}/P_{absorbed}$ remains practically constant). The observed effect could thus be attributed to an increase of α with temperature.

I - Brief description of the code.

The code is based on a 1-D , non-relativistic Fokker-Planck equation including the toroidal electric field. Run-away electrons are described by an electron distribution function flat from the critical (Dreicer) velocity up to some maximum cut-off velocity. The quasi-linear diffusion coefficient is computed using the plasma group velocity and the wave power flux impinging on the considered magnetic surface. The code uses a cylindrical geometry, ray-tracing was not implemented (note that the required spectral broadening effects largely overcome the spectral variations due to classsical toroidal propagation). (See /4/for more details).

The launched power spectrum is assumed to have the shape:
$P(N_{\|}) = \left\{ \frac{\sin\left[\pi(N_{\|} - <N_{\|}>/\Delta N_{\|})\right]}{\pi(N_{\|} - <N_{\|}>/\Delta N_{\|})} \right\}^2 \frac{1}{(N_{\|}^2-1)^{2/3}}$ (the last factor is omitted for the cases presented in §IV and V below). Ad-hoc spectral broadening of the launched spectrum (B1) is obtained by choosing appropriately $< N_{\|} >$ and $\Delta N_{\|}$. When spectral broadening by magnetic ripple is applied (B2), at each radial step, before performing the FP calculation, the power $P_r(N_{\|})$ of each spectral components is distributed equally in two side-lines respectively shifted by
$\Delta N_{\|} = \pm N_{\|} \frac{n\delta(r)dr}{R} \left[\frac{N_{\perp}}{N_{\|}}\right]^2 cos\Phi$. (see /3/) (Where n is the number of toroidal field coils, R the major radius, δ the magnetic ripple amplitude at radius r for which we take $\delta(r) \simeq \delta(a)\left[\frac{R+r}{R+a}\right]^{n-1}$, and Φ the angle between radial and poloidal components of the wave vector (here assumed to be given by $\Phi = \pi|a-r|/4a$).

Two versions of analytical fits of the measured n_e and T_e profiles [5,2], are used in the simulations (the most recent one ([5]) only in §II below).

II - Detailed modelling of ASDEX shots during RF.

A detailed simulation of ASDEX shots using the stand-alone code has already been reported elsewhere /4/. In this work, the spectral broadening required to simulate correctly the results was obtained by an ad-hoc broadening of the *launched* spectrum, the main spectral lobe extending from $N_{\|}$= 1.2 to $N_{\|}$= 6.2 (instead of 2.9 in the actually launched spectrum). Once this broadening was adjusted on a shot for which the tokamak current was carried by LH power alone (# 18468 , P_{inj}=375kW , $\vec{E} = 0.$), it was kept constant and two other shots at low power (# 19612 , P_{inj}= 90 kW , $\vec{E} > 0.$) and high power (# 18466 , P_{inj}=920kW , $\vec{E} < 0.$) were correctly simulated, giving some confidence in the ability of this simple model to treat LH current drive in presence of an electric field.

In the present work, a physical mechanism proposed recently (/3/) the *ripple scattering mechanism*, is invoked to provide the spectral broadening, the launched spectrum being the actual one. The main characteristics of the shots considered are listed in Table I. Fig. 1 represents the evolution with radius of the power spectra as function of the phase velocity for the shot # 18468. For comparison, the radial evolution of the same wave spectrum without broadening is shown on Fig. 2, the profiles of the driven currents for the 3 shots are given in Fig. 3.

TABLE I

shot	experiment					code			
	$n_e(0)$ $[10^{19}m^{-3}]$	$T_e(0)$ $[keV]$	P_{inj} $[kW]$	V_{loop}^{Ω} $[V]$	V_{loop}^{LH} $[V]$	δ $[\%]$	V_{loop}^{LH} $[V]$	I_{driven} $[kA]$	I_{tot} $[kA]$
18468	0.80	2.81	375	0.86±0.2	0.0±0.2	0	0.09	3	37
18468	0.80	2.81	375	0.86±0.2	0.0±0.2	2	0.09	260	297
18470	0.96	2.19	90	1.09 ±0.2	0.41 ±0.22	2.2	0.70	162	305
18466	0.72	1.96	920	1±0.2	-0.25 ±0.2	1.8	-0.22	391	303
	B = 2.2 T Z_{eff} = 3. $< N_{\|} >$= 1.90 $\Delta N_{\|}$ = 0.955 f = 1.3 GHz The measured profiles[5] of n_e and T_e are used								

The ohmic current during the LH phase are computed by using the experimental plasma resistivity during the ohmic phase, the measured loop voltage during the RF phase and assuming the current density proportional to $T_e(r)^{3/2}$.

As seen from these results, a satisfactory modelling of the experimental data can be achieved with this model, using a ripple value of the order of 2%. It must be noted however that this value is about twice the value computed for ASDEX. Considering the rough approximations used to compute the broadening and the fact that, as noted in

/3/, other departures from axisymmetry non considered here (in particular magnetic islands) should also contribute to spectral broadening; an order-of-magnitude agreement encourages to investigate further the possible responsibility of the proposed mechanism for the well known spectral broadening effect.

III - Temperature effect on single pass absorption

Although no dependance of the current drive efficiency on temperature is expected (for $T_e << m_e c^2$), a strong variation of the driven current (or η) has been observed in different experiments like T7 and JT-60.

In Fig. 4, we have simulated a temperature variation in ASDEX /4/. As can be seen, practically a linear dependance of both the single pass absorption coefficient α and of the figure of merit η is found while in this particular case, η_0 (reported to the *absorbed* power) remains practically constant.

IV - Current drive efficiency as a function of the electric field

Spectral broadening of the launched spectrum (B1) is applied here; the required spectral width is determined by fitting the RF-driven current at zero electric field and u_{max} is taken to be 0.8c (the results are not strongly sensitive to the precise choice of u_{max}). In Fig. 5, we plot the calculated normalized figure of merit $\eta(E)/\eta(0)$ versus the normalized electric field E. In the same figure we plot also points corresponding to Asdex shots with different RF-powers, temperatures and densities[2]. The curves are calculated for the same range of temperatures and densities.

This shows hat the numerical solution of a 1D Fokker-Planck model including the current carried by the runaway electrons can predict the dependence of the efficiency on the dc electric field. These results are similar to the ones obtained recently[5] with an analytical treatment based on an approximate solution of a 2D model.

V - Simulations of time evolutions during RF shots

The electric field as function of radius is computed here at each time step through self-consistent solution of Ohm's law, the FP code is coupled to the code[1] solving the diffusion equation of the electric field. The ohmic phase of the RF shots are simulated by letting the plasma evolve (with the temperature and densities profiles[2] kept fixed) until equilibrium is reached. The RF phase is then simulated by applying the RF power to an ohmic plasma with the same temperature and density profiles as at the end of the RF phase (no profile evolution). The electric field could be reproduced within a 20% error for all the simulated shots (in these simulations the spectral upshift and u_{max} have been kept fixed; we assumed a neoclassical resistivity and chose the impurity level in order to have $Z_{eff} = 3$).

Another topic under investigation is the time evolution of the dc-electric field. Fig. 6 shows a fair agreement between experimental results and simulations.

/1/ O. de Barbieri and A. Nocentini, 14th Conf. CFPP, Madrid, 1987, vol III, p.836

/2/ IAEA INTOR-Related Specialists Meeting on Non-Inductive Current-Drive, Garching, FRG, Sept. 1986, NET-PM-86-003 and IAEA-TECDOC-441, Vienna, 1987.

/3/ J.-G. Wégrowe, "Broadening of the Lower Hybrid Wave Spectrum due to Departure from Axisymmetry", Proc. 14th Eur. CCPP, Madrid 1987 III, 911

/4/ J.-G. Wégrowe and G. Zambotti, INTOR Phase II[A] Part 3, European Contributions, Vol II, EURFUBRU/XII-139/88/EDV1, CEC, Brussels, June 1988

/5/ F. Soeldner, private communication

/5/ Yoshioka & Leuterer,Physics of Fluids, 31,1224,1988

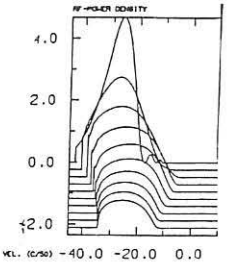

Fig. 1

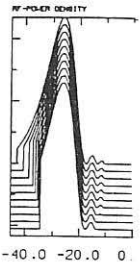

Fig. 2

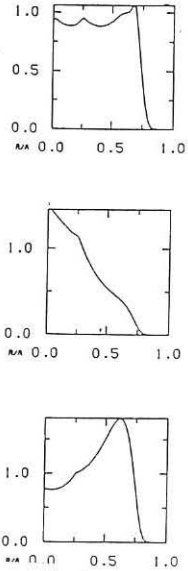

Fig. 3

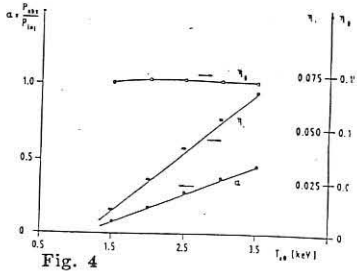

Fig. 4

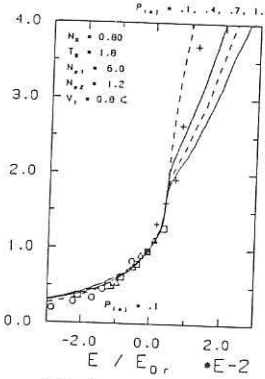

Fig. 5

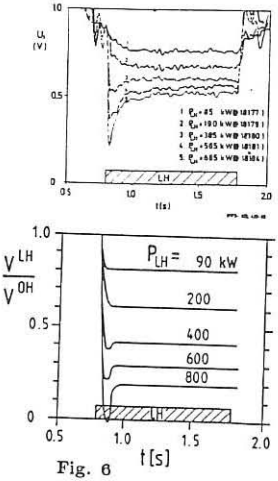

Fig. 6

Fig. 1: Wave power spectra for different radii (top = edge, bottom = center) as a function of $50.v_{//}/c$). shot 18468, with ripple

Fig. 2: Same as Fig. 1 without ripple broadening.

Fig. 3: radial profile of the driven current for the shots 18468,18470,18466 (from top to bottom).

Fig. 4: Temperature dependance of $\alpha\,\eta$ and η_0.

Fig. 5: Normalized current drive figure of merit: $\eta(E)/\eta(0)$ as a function of normalized electric field E.

Fig. 6: Time evolution of the loop voltage for various injected LH power (top = experimental, bottom = code.

NEUTRAL BEAM CURRENT DRIVE SCALING IN DIII-D[1]

G D Porter†, D K Bhadra‡, K H Burrell‡, R W Callis‡,
A P Colleraine‡, J R Ferron†, R A James†, A G Kellman‡, J Kim‡,
M Matsuoka§, P I Petersen‡, P A Politzer‡, T C Simonen‡, H St. John‡

† Lawrence Livermore National Laboratory, Livermore, California
‡ General Atomics, San Diego, California
§ Japan Atomic Energy Research Institute, Naka, Japan

1. Introduction

Neutral beam current drive scaling experiments have been carried out on the DIII-D tokamak at General Atomics. These experiments were performed using up to 10 MW of 80 keV hydrogen beams. Previous current drive experiments on DIII-D have demonstrated beam driven currents up to 340 kA[1]. In the experiments reported here we achieved beam driven currents of at least 500 kA, and have obtained operation with record values of poloidal beta ($\epsilon\beta_p = 1.4$). The beam driven current reported here is obtained from the total plasma current by subtracting an estimate of the residual Ohmic current determined from the measured loop voltage. In this report we discuss the scaling of the current drive efficiency with plasma conditions. Using hydrogen neutral beams, we find the current drive efficiency is similar in Deuterium and Helium target plasmas. Experiments have been performed with plasma electron temperatures up to $T_e \approx 3$ keV, and densities in the range $2 \times 10^{19}\mathrm{m}^{-3} < n_e < 4 \times 10^{19}\mathrm{m}^{-3}$. The current drive efficiency ($\frac{nIR}{P}$) is observed to scale linearly with the energy confinement time on DIII-D to a maximum of $0.05 \times 10^{20}\mathrm{m}^{-2}\mathrm{A/W}$. The measured efficiency is consistent with a 0-D theoretical model[2]. In addition to comparison with this simple model, detailed analysis of several shots using the time dependent transport code ONETWO is discussed. This analysis indicates that bootstrap current contributes approximately 10–20% of the total current. Our estimates of this effect are somewhat uncertain due to limited measurements of the radial profile of the density and temperatures.

2. Description of Experiments

Two sets of neutral beam current drive experiments are reported here. The first were done in August, 1988, and the second in October, 1988. The fill gas was helium during the August experiments, and deuterium during the October experiments. In addition, the plasma control scheme was modified for the October experiments, permitting better control of the high β_p plasmas which are obtained.

[1]Work supported by U.S.DOE contracts DE-AD03-84ER51044(GA) and W-7405-ENG-48(LLNL).

The neutral beam system on DIII-D is composed of eight 5 sec, 80 keV neutral beam sources housed in four beamlines. Each beamline contains two sources, referred to as the left and right source. The right sources inject at an angle of 63° to the magnetic field axis, and the left sources at an angle of 47°. In the experiments reported here, all beams are injected in a direction such that the resulting ion current is in the same direction as the plasma current, i.e., co-injection. These experiments utilized a maximum of three right sources and four left.

The plasma was initiated with standard Ohmic operation during all experiments reported here. Following $\sim$ 1 s of Ohmic operation, the current in the Ohmic coils was held constant, and the neutral beams were turned on. All plasmas were in the single null divertor configuration.

3. Experimental Results

Typically, we observed a rapid increase in the total plasma current with injection of beams. Following this initial transient, we observed two phases of plasma behavior. The first, which typically lasted ≤ 0.5 s, is characterized by nearly constant plasma current, and an average loop voltage near zero. Following this phase, the plasma current slowly decayed with a time constant of several seconds. The transition to the second phase was associated with the plasma touching a wall, and a concomitant impurity influx, on some shots. This plasma motion arises from the large β_p obtained in this operation. There is always a transient increase in the loop voltage associated with the transition to the second phase. Throughout this report, we refer to the period preceding this second voltage transient as the *flat* phase since the plasma current is relatively constant. The period following the second transient is referred to as the *decay* phase.

The energy confinement time was observed to increase linearly with the plasma current, and to increase in shots with reduced neutral beam heating. The energy confinement parameter, τ_E/I_p, is in the range of 60 ms/MA for all data, typical of H-mode confinement. The energy confinement parameter decreased by 10–20% at the transition from the flat phase to the decay phase.

3.1. Ohmic Current Corrections

We have attempted to determine the contribution of residual Ohmic current to the total plasma current by assuming a Spitzer resistivity for the plasma [3]. The Ohmic current I_Ω is estimated by

$$I_\Omega = (3.7 \pm 1.2) \times 10^6 \frac{V_{\rm loop} T_e^{3/2}}{Z_{\rm eff} N(Z_{\rm eff})} \tag{1}$$

Although neoclassical effects may be significant, the plasma geometry, and hence r/R_0, does not vary much in these experiments. Therefore these effects are included in the coefficient used in Eqn. 1. This numerical coefficient was determined by fitting Eqn. 1 to

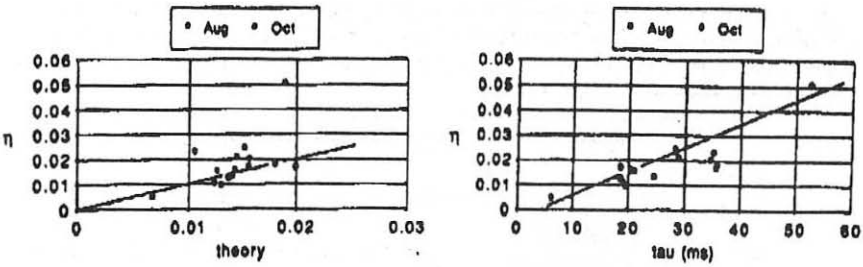

Figure 1: The experimentally measured current drive efficiency, $\eta = \frac{nIR}{P}$ ($10^{20}\mathrm{m}^{-2}\mathrm{A/W}$) versus the theoretical value (a), and versus the energy confinement time (b).

data taken during Ohmic discharges in DIII-D. Eqn. 1 is also consistent with data taken in high current experiments in both H- and L-mode plasmas.

3.2. *Current Drive Efficiency Scaling*

The experimentally determined current drive efficiency, η, is compared with the 0-D theory of Mikkelsen and Singer [2] in Fig. 1(a). Although there is considerable scatter in these data, the experimental and theoretical efficiencies are within a factor of two for all but one datapoint. The scaling of the experimental current drive efficiency with energy confinement time is shown in Fig. 1(b). We see a nearly linear scaling. It is apparent that the datapoint with a large experimental current drive efficiency also has a large energy confinement time. This data was taken on shot 61546, and corresponds to the shot taken with highest plasma current ($I_p \approx 0.75$ MA). We find from Eqn. 1 that the Ohmic current is only about 15% of the total for this shot.

4. Modeling Studies

In this section we compare experimental results with calculational results obtained using the transport code ONETWO [4]. Comparisons have been made in both an equilibrium and time-dependent mode. In the equilibrium mode, the experimentally determined temperature and density profiles are input, and the energy transport coefficients consistent with these profiles are calculated. We find the results of these calculations to be insensitive to the nature of the fill gas. This is consistent with the experimental observation that the current drive efficiency is the same for both helium and deuterium gas, and can be explained by the large density of hot, beam-injected ions which is calculated to be 30–40% of the electron density near the axis.

The time-dependent calculations are done by specifying the electron and ion energy transport coefficients. The transport coefficients are selected to fit the measured temper-

Table 1: Comparison of experimental plasma parameters for shot 60878 with those obtained in a time-dependent ONETWO simulation. The data is obtained from H beams injected into a He plasma. The line-averaged plasma density is $0.26 \times 10^{20}\mathrm{m}^{-3}$, and the peak electron temperature is 1.7 keV.

parameter	units	exp	calc
Z_{eff}		3.61	3.5
Input Power	MW	9.7	9.7
Absorbed Power	MW	–	7.17
Stored Energy	kJ	251	267
V_{loop}	V	0.034	0.08
β_p		2.34	2.42
β_T	%	0.517	0.529
I_p	kA	414	410
I_{BD}	kA	–	251
I_{BS}	kA	–	61
I_{Ω}	kA	93	97

ature profiles after the neutral beams are turned on, and are assumed to scale as $\chi \propto T_e$. The code is begun in the Ohmic phase, and run for 1.5 s following the beam turn-on. The total plasma current and flux shape are determined from the magnetic diagnostics on DIII-D, and are assumed to be independent of time.

The parameters achieved in the simulation are compared with the experimental parameters in Table 1. The calculated values of the stored energy and bootstrap current are sensitive to the electron temperature profile at large radii. Experimentally, this temperature is measured by ECE, and has poor resolution at these large radii ($\rho \geq 0.5$). The results of this simulation indicate that the beam-driven current displaces the Ohmic current on a time scale of $\sim$ 100 ms. Inductive effects are not important because the radial profile of the initial Ohmic current is similar to that of the beam-driven current.

References

[1] T. C. Simonen, et.al., Phys. Rev. Lett., **61**, 15, 1720 (1988)

[2] D. R. Mikkelsen, and C. E. Singer, Nuclear Technology/Fusion, **4**, 237 (1983).

[3] J. Wesson, Clarendon Press, (1987).

[4] W. W. Pfeiffer, R. H. Davidson, R. L. Miller, R. E. Waltz, GA-A16178 (1980).

CURRENT DENSITY PROFILE EVOLUTION IN JET

P M Stubberfield, B Balet, D Campbell, C D Challis,
J G Cordey, G Hammett*, J O'Rourke, G L Schmidt*.

JET Joint Undertaking, Abingdon, Oxon, OX14 3EA, UK
*Princeton Plasma Physics Laboratory, Princeton, New Jersey, USA

ABSTRACT

Simulation studies have been made of the current density profile evolution in discharges where the bootstrap current is expected to be significant. The changes predicted in the total current profile have been confirmed by comparison with experimental results.

1. Introduction The evolution of current profile has been followed using the TRANSP code [1] in three very different JET discharges with strong auxiliary heating, (1) H-mode, (2) extended sawteeth (monster) and (3) pellet fuelled ICRH discharges. The input parameters to the TRANSP code, which solves the poloidal field diffusion and equilibrium equations, include profiles of electron temperature, density and Z_{eff} from visible Bremsstrahlung. To check the accuracy of the simulation the time development of the simulated and measured loop voltage, the second Shafranov current moment [2] and the six polarimeter channels are compared. The three cases are discussed in detail below.

2. H-modes In previous papers [3][4] it has been shown that in H-modes the bootstrap current had to be included to explain the loop voltage behaviour in these discharges. A typical example is shown in Fig.1. In this 3 MA discharge the predicted bootstrap current reached 0.8 MA at the end of the H-mode phase. The bootstrap current profile is strongly peaked in the outer radial region (see Fig.3) due to the sharp density gradient. To confirm that the total current density profile was indeed being broadened the measured second Shafranov moment Y2S (from the external pick-up coils) has been compared with that predicted by the code (Fig.2). Clearly a much better fit is obtained when the bootstrap current is included in the analysis.

The broadening of the current profile may eventually lead to the safety factor q on axis exceeding unity and the stabilisation of the saw-teeth. The timescale for the current to diffuse from the central region however, is very long ($\sim$ 10 seconds) and exceeds the duration of the H-mode phase. This explains why sawteeth continue throughout the H-mode. The inversion radius, nevertheless, is seen to slowly contract indicating some broadening of the current profile.

3. Discharges with an extended sawtooth-free period (Monsters) The main characteristics of these extended sawtooth free discharges (monsters) have been extensively reported elsewhere [5] and a mechanism has been proposed for the stabilisation of the sawteeth [6]. Here we examine how the presence of the bootstrap current and a peaked Z_{eff} profile affect the evolution of the current profile.

In Fig.4 the time development of the central electron temperature is shown for a discharge with a long sawtooth free period at the end of the current ramp. The time behaviour of q on axis from TRANSP is also shown for four different assumptions. Curve (a) is the development of q on axis for a flat Z_{eff} profile and no bootstrap current, showing q falling throughout the monster phase. Curve (b) is a flat Z_{eff} profile but includes the bootstrap current and in this case the reduction in q during the monster phase is reduced. Recent multichord measurements [7] of the visible Bremsstrahlung have shown that the Z_{eff} profile is peaked on axis, typically the peak to edge ratio is 2:1, in this type of discharge, and using the measured Z_{eff} profile (curve c) we find that q on axis is approximately constant in the first second of the sawtooth free period. To further ascertain the sensitivity of the q behaviour to the Z_{eff} profile in curve (d) the peaking factor (peak to edge ratio) was increased by 50% above the measured value. In this case the q axis increases slightly during the initial phase of the extended sawtooth free period. Results of TRANSP, calculations of polarimeter and Y2S are consistent within the systematic experimental errors. It is therefore not yet possible to determine which is the appropriate model for TRANSP.

4. Pellets fuelled pulses with intense ICRH These are 3 MA shots in which a pellet is injected in the current rise and this is then followed by intense ICRH [8], throughout this whole period there are no sawteeth. The intense ICRH produces a very strong pressure gradient close to the magnetic axis and hence a very large bootstrap current ($\sim$ 0.8 MA) which is peaked off-axis (see Fig.3). The development of the current profile in these discharges has also been followed by TRANSP and the time development of the q at various radii is shown in Fig.5. Prior to pellet injection q is falling at all radii as the current is being increased, following pellet injection the centre of the plasma is cooled and the current profile broadens and q on axis rises (point A). At point B the bootstrap current has become significant and the total current profile becomes hollow with q double valued. Comparison with the polarimetry (Fig.6) suggests that this is indeed a reasonable interpretation of the profile behaviour, but the sensitivity of the data is not sufficient to confirm this result entirely.

SUMMARY

It is shown that the bootstrap current plays a key role in changing the current profile in H-modes, monster and pellet fuelled ICRH discharges. In discharges with monster sawteeth it is found that q on axis initially increases due to to the bootstrap current and the peaking of the Z_{eff} profile and that this may influence the duration of the sawtooth free period. In the ICRH pellet fuelled discharges the current profile becomes hollow.

REFERENCES

[1] Goldston, R.J., et al., J. Comput. Phys. 43 (1981) 61.
[2] Zakharov, L.E., Shafranov, V.D., Sov. Phys. Tech. Phys., 18 (1973) 151.
[3] Cordey, J.G., Challis, C.D., Stubberfield, P.M., Plas. Phys. and Contr. Fus., 30 (1988) 1625.
[4] Challis, C.D. et al., to be published in Nuclear Fusion.
[5] Campbell, D.J. et al., 12th Int. Conf. on Plas. Phys. and Contr. Nucl. Fus. Res., Nice (1988) A-7-2.
[6] Pegararo. F. et al., ibid [5] D-4-6.
[7] Morgan, P.D., Proc.. EPS Conf. Cont. Fus. & Plas. Htg. (1988) 139.
[8] Schmidt, G.L. et al., ibid [5] A-4-1.

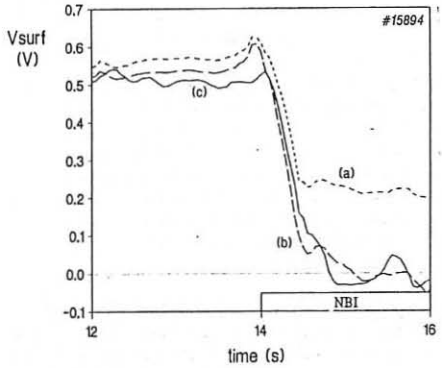

Figure 1: Evolution of voltage vs.time
(a)Simulation including only changes in conductivity
(b)with addition of bootstrap current
(c)measured value

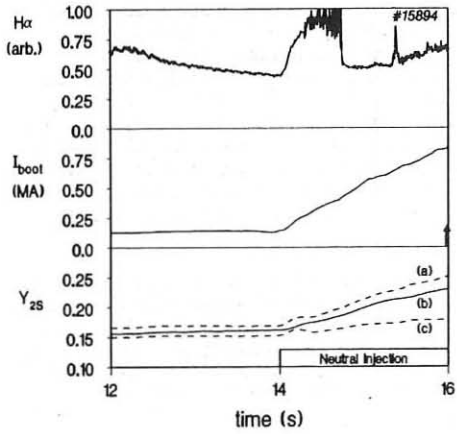

Figure 2: (i)H-α signal
(ii)Total bootstrap current vs.time
(iii)Evolution of Y2S
(a)with bootstrap current
(b)measured value
(c)without bootstrap current

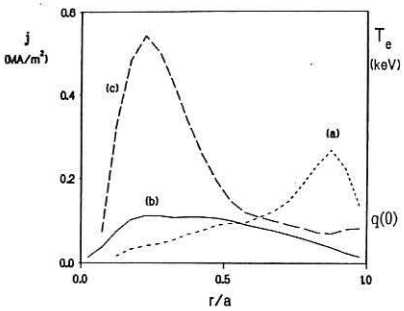

Figure 3: Current density profiles for
(a)H-mode pulse at time shown by arrow in Figure 2
(b)Monster pulse at time shown by arrow in Figure 4
(c)Pellet pulse at time C in figure 5

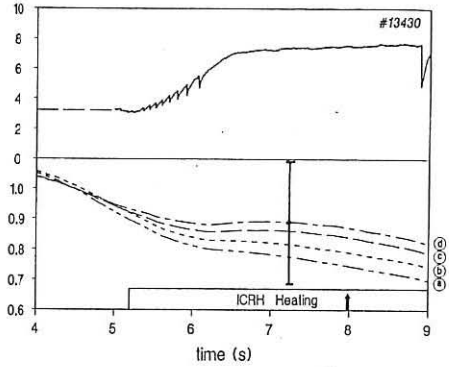

Figure 4: (i)Evolution of T_e(central) vs.time
(ii)Evolution of q vs. time

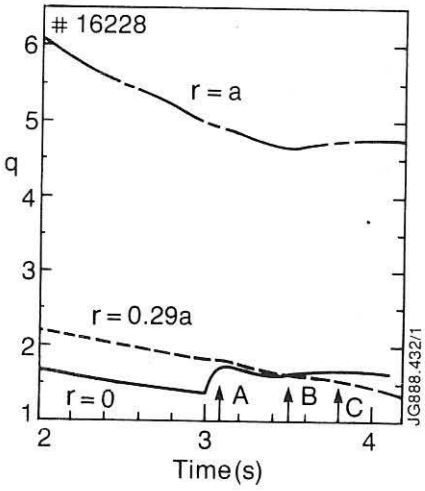

Figure 5: Evolution of q vs. time
at 3 different radii
A and B are described in text
C is time for the profile shown in Figure 3

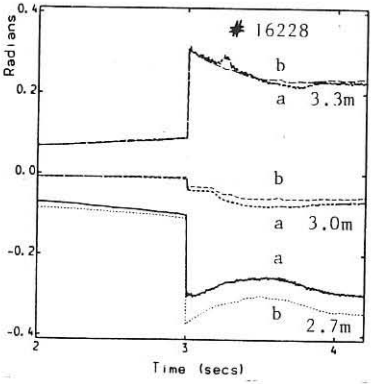

Figure 6: Comparison of predicted and measured values for 3 central polarimetry channels (a) measured values (b) simulated

ELECTRON HEATING AND CURRENT DRIVE BY 200MHz FAST WAVE ON JFT-2M TOKAMAK

Y.Uesugi, T.Yamamoto, H.Aikawa, K.Hoshino, T.Kawakami, S.Kasai, H.Kawashima, T.Kondoh*, T.Matsuda, H.Matsumoto, Y.Miura, M.Mori, I.Nakazawa**, C.R.Neufeld***, K.Odajima, H.Ogawa, T.Ogawa, K.Ohasa, H.Ohtsuka, S.Sengoku, T.Shoji, N.Suzuki, H.Tamai, T.Yamauchi and H.Maeda

Japan Atomic Energy Research Institute
Tokai, Naka, Ibaraki, 319-11, Japan
* On leave from University of Tsukuba, Ibaraki, Japan
** On leave from Mitsubishi Electric Co., Tokyo, Japan
*** On leave from Hydro-Quebec, Varennes, Quebec, Canada

1. Introduction

Fast waves in the frequency range, $\omega_{ci} \ll \omega \ll \omega_{ce}$ can penetrate into the plasma center without suffering strong resonances even in reactor-grade plasmas. They have a possibility to generate a plasma current in high density and high temperature plasmas through electron Landau damping in the same way as lower hybrid current drive(LHCD). The linear theory predicts that the absorption of the fast wave is weak compared with that of LHW.

In the last experiment(1), fast waves at a frequency of 200 MHz were excited by a 2-phased loop antennas array. A noticeable loop voltage drop was observed at low density region where $\omega/\omega_{LH}>1$. A clear density limit was observed as well as LHCD and the current drive efficiency is as high as that of LHCD. It was noted that parasitic slow wave which was mode-converted from the excited fast wave with low N_z and/or was directly excited was related with the current drive at the low density(2). Clear experiment which indicates the fast wave current drive(FWCD) requires the excitation of the fast wave with optimum N_z and high rf power. In the present experiment the resonant absorption of the excited fast wave with electron in the high density region where slow waves can not propagate is studied from the point of view of the electron heating.

2. Experimental setup

FWCD experiment has been carried out in the JFT-2M tokamak. Target plasmas have circular or D-shaped cross-section defined by inner or outer graphite limiters which are located in the mid-plane. An rf power of 800 kW is generated by four power amplifiers. A 4-phased loop antennas array is employed to excite fast waves. The relative phasing of the rf current on each antenna is controlled by a coaxial line stretcher. Each loop antenna has a radiation length of 18 cm in the poloidal direction and a spacing between two neighboring antennas is 8 cm. The parallel wavenumber spectrum of the loading resistance has a peak at $N_z=4$ with $\Delta N_z=4$ when $\Delta\phi=\pi/2$. The loading resistance of each antenna is calculated from the voltage standing wave ratio on the matching circuit.

3. Loading characteristics of the antenna

It is necessary that the antenna excites purely electromagnetic fast wave in plasma to obtain clear indication of FWCD since even a small power of parasitically excited slow waves have a large effect on the current drive. The loading resistance of the antenna is measured in different experimental conditions. It increases with the density and strongly depends on the gap between the antenna and plasma edge as well as ICRF loop antennas. The antenna loading shown in Fig.1 has a peak at $\Delta\phi=0$ and a minimum value at $\Delta\phi=\pi$ because the evanescent depth increases with N_z. The vacuum loading of each loop is about 0.3 Ω. An improvement of the antenna loading during ECH is related with the broadening of the density profile.

4. Electron heating by fast wave

In order to investigate the current drive by fast wave, the coupling of excited fast wave with electron is studied. Time evolution of typical plasma parameters is shown in Fig.2. The antenna phasing is $\Delta\phi=\pi$. The cold LH resonance layer is located at the plasma edge(r/a=0.9) in this case. When the fast wave is applied, a remarkable increase of T_e and a slight decrease of the loop voltage, which are good indications of the coupling of the fast wave with electron, are observed. In addition, the electron density, stored energy and radiation loss power increase. The electron temperature from ECE agrees well with that from Thomson scattering and soft X-ray measurement. The spatial profile from ECE measurement shown in Fig.3 indicates that the fast wave is absorbed at the plasma center where T_e and n_e are high. An efficient electron heating is attained at $\Delta\phi=\pi$ as shown in Fig.4. An increment of T_e is proportional to the rf power at $\bar{n}_e\Delta T_e/P_{FW}=1.5\times10^{19}$ eVm^{-3}/kW. The loop voltage drop is observed only at $\Delta\phi=\pi$ and other phasing makes the loop voltage go up slightly. In contrast to the electron heating, the phase dependence of the intensity of metal impurity line(Titanium and Iron) has a peak at $\Delta\phi=0$ as well as the density increase. The time behavior of the loop voltage must be related with a trade-off between the electron heating by fast wave and the cooling by impurity influx and density increase. In Fig.5 the power absorption by electron and the absorption efficiency defined by W_s/P_{FW} are shown as a function of $\Delta\phi$. Typical absorption efficiency at $\Delta\phi=\pi$ is 15-20% in ohmically heated plasma with T_e=1 keV, which is consistent with the theoretical estimation. It is noted that the power absorption of the applied fast wave is improved by retarding the phase velocity since the number of the resonant electrons increases. The same effect is expected when T_e goes up with keeping the phase velocity constant. This experimental result is consistent with the electron heating efficiency.

The 2nd harmonic ECH is applied to improve the absorption efficiency of the fast wave[3]. When the electron is heated by 180 kW ECH up to 1.5 keV, an additional loop voltage drop of about 0.1 V is observed as well as the increase of ECE signals. On the other hand applied fast wave does not increase ECE signals strongly in the ohmic plasma with T_e of 1 keV below $\bar{n}_e=1\times10^{19}m^{-3}$. By combining with ECH the region where the loop voltage drop is observed is expanded up to $\Delta\phi=2\pi/3$. This limit gives us V_{ph}/V_{te} =3-4. This experimental result indicates that the fast wave with higher phase velocity becomes to be absorbed effectively with increasing T_e. From these

results it is estimated that the effective FWCD at $\Delta\phi=\pi/2$ requires T_e more than 3 keV. This estimation agrees well with the theoretical calculation.

5. Summary

Present FWCD experiment in JFT-2M tokamak is summarized as following;

(1)Phase dependence of the loading resistance of the antenna and heating efficiency shows that the control of the wavenumber spectrum of the excited fast wave can be done effectively by a 4-phased loop antenna array.

(2)Excited fast wave with relatively large N_z is absorbed by electron effectively. The absorption efficiency is improved with increasing the electron temperature. The region where the effective electron heating is observed is $V_{ph}/V_{te} < 3$-4. The electron heating efficiency is 1.5×10^{19} eVm^{-3} /kW at $\bar{n}_e=1.5\times10^{19}$ m^{-3}. The fast wave with higher phase velocity becomes to be absorbed with increasing T_e.

(3)Experimental results mentioned above are consistent with the theoretical calculation using ray tracing code. Absorption of the fast wave can be explained by linear theory. The problem of the energy gap in LHCD seems not to exist in FWCD.

(4)Clear FWCD experiment at $\Delta\phi=\pi/2$ using present loop antenna requires T_e more than 3 kev in JFT-2M. High power ICRF heating will be applied to attain the target plasma with T_e above 2 keV in the near future. And the modification of the fast wave antenna that N_z spectrum has a peak at 6 when $\Delta\phi=\pi/2$ will be done soon.

ACKNOWLEDGMENT

The authors would like to thank members of JFT-2M operation group and heating group for their technical assistance and we are also grateful to Drs. S.Shimamoto, M.Tanaka, M.Yoshikawa and S.Mori for their continuous encouragement.

References

(1)Y. Uesugi et al., 14th European Conference on Controlled Fusion and Plasma Physics, Madrid(1987), Vol.11D, Part III, P. 942.

(2)J.Goree and M.Ono, Nuclear Fusion, 28(1988)1105.

(3)T.Yamamoto et al., in Proc. 12th Int. Conf. on Plasma Physics and Controlled Nucl. Fusion, Nice(1988),IAEA-CN-50/E-4-6.

Figure captions

Fig.1 Total antenna loading as a function of the relative antenna phasing. Open circles show the loading resistance in ohmic plasma and closed circles are in ECH heated plasma.

Fig.2 Time behavior of the typical plasma parameters. Net rf power is 200 kW and the antenna phasing is $\Delta\phi=\pi$.

Fig.3 Electron temperature profiles of the ohmic plasma(OH) and with fast wave(FW) measured with 2nd harmonic ECE. Solid curves indicate the radial profiles at the top of sawteeth and dotted curves are at the bottom, respectively.

Fig.4 Phase dependence of the electron temperature increase at the center.

Fig.5 Phase dependence of the power absorption by electron deduced from ECE(top) and the absorption efficiency of the applied fast wave deduced from

the time derivative of the stored energy obtained from diamagnetic measurement. A dotted curve in the bottom shows the single pass absorption obtained from ray tracing calculation.

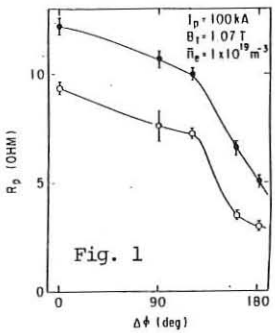

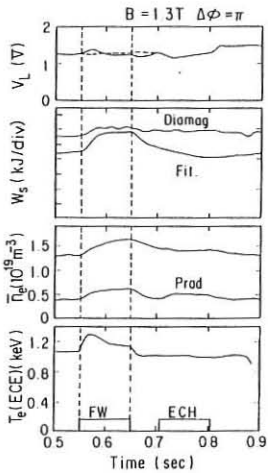

Fig. 2

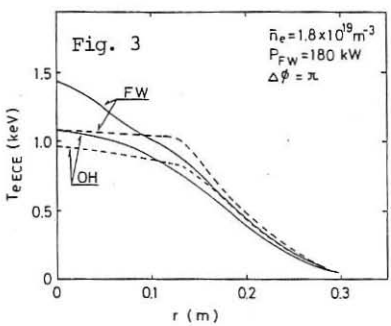

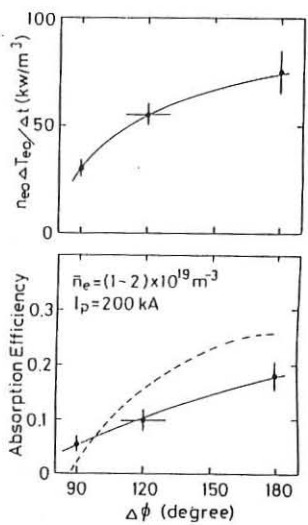

Fig. 5

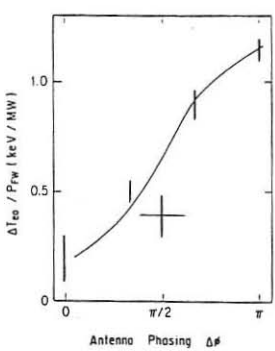

Fig. 4

OPTIMIZATION OF A STEADY STATE TOKAMAK DRIVEN BY LOWER HYBRID WAVES

G. Tonon

Association Euratom-CEA sur la Fusion Contrôlée
CEN Cadarache
13108 Saint Paul lez Durance - France

1 - INTRODUCTION

As suggested by experimental results obtained on many tokamaks steady state operation appears feasible with the plasma current Ip driven by lower hybrid waves (LHW). By this way it is expected to increase reactor reliability and availability . In the present paper, we consider a staedy state device like NET/ITER /1/ driven by LHW. The power multiplication factor Q will be an essential parameter; so we have determined optimum plasma characteristics for maximizing Q value under the restriction of the LHW penetration limitations. In all expressions, MKS units are used with temperature T in units of 10 Kev, current in megamperes (MA), power in megawatts (MW) and densities in units of 10^{20} e.m.$^{-3}$

2 - CHOICE OF THE RF PARAMETERS

2.1 According to the quasi-linear theory of current drive by LHW /2/ the current merit factor η is given by /3/ :

(1a) $$\eta = n_e R I_{HF}/P_{HFT} \simeq 2.S(N_{\parallel}).\mu_{ABS}.W(N_{\parallel},T_e,Z_{eff})\left[\frac{4}{5+Z_{eff}}\right]$$

with :

(1b) $$S(N_{\parallel}) = \left[1-(N_{\parallel m}/N_{\parallel M})^2\right]/2N_{\parallel m}^2 \, Log(N_{\parallel M}/N_{\parallel m})$$

where R represents the major radius, I_{HF} the toroidal current driven by LHW and P_{HFT} the HF power injected into the torus. In equation (1b), $N_{\parallel M}$ and $N_{\parallel m}$ are the upper and the lower refractive index which reach the central part of the plasma. The improvement in current drive efficiency W has been calculated by KARNEY and FISCH /2/. We use an approximate expression given by EHST and EVANS /4/ :

(1c) $$W(N_{\parallel},T_e,Z_{eff}) = 1 + \left\{ \begin{array}{l} 4.9\,10^{-3}(5+Z_{eff}) + 3.2\,10^{-2}\frac{(6+Z_{eff})}{(3+Z_{eff})} \\ +2.6\,10^{-3}(5+Z_{eff})N_{\parallel M}T_e^{1/2}/Z_{eff} \end{array} \right\} N_{\parallel M}^2 T_e$$

2.2 We see, from equations (1a) (1b) (1c), that the current drive merit factor η can be maximized by :

i) working at the lowest $N_{\parallel m}$ (limited by the accessibility condition $N_{\parallel m} \geq N_{\parallel acc}$) with a spectrum width $\Delta N_{\parallel} = N_{\parallel 2} - N_{\parallel 1} = N_{\parallel M} - N_{\parallel m}$ as small as possible. Here the $N_{\parallel}$ -spectrum excited by the coupling structure is determined by its lower $N_{\parallel 1}$ and upper $N_{\parallel 2}$ limits.

ii) increasing the fraction μ_{ABS} of the injected power which is absorbed by the electrons (P_{HFE}). We have /3/ :

(2) $$\mu_{ABS} = P_{HFE}/P_{HFT} = \mu_D . \mu_{ACC}\left[1 - \sum_j \mu_{pj}\right]$$

where $\mu_D < 0.8$ represents the directivity and μ_{ACC} the accessible part of the $N_{\parallel}$- spectrum injected into the torus/3/. In order to minimise the HF absorption by background ions and α-particle ($\sum \mu_{pj}$) it is necessary to choose an appropriate frequency f. Wave damping on fuel ions is avoided when /3/ :

(3) $$f \geq f_1 = (\alpha n_e)^{1/2}\left[1+3Z_p/2\right]\left[0.23+2.35\, n_e/B_T^2\right]^{-1/2} \quad (GHz)$$

where $Z_p = n_e/\Sigma n_j Z_j$ and $\alpha = n_e^{-1}\Sigma \frac{n_j Z_j^2}{A_j}$. Wave damping on α-particle can be avoided simply making the perpendicular wave phase velocity, ($c/N_\perp$, with $N_\perp$ perpendicular refractive index) faster than the α birth velocity, i.e $N_\perp < 23.3$. From the cold dispersion relation, without toroidal effects, we obtain :

(4) $$f \geq f_2 \simeq 2.73\, n_e^{1/2}\left[\frac{N_{//}^2-(1+20.6\, n_e/B_T^2)}{1+10.3\, n_e/B_T^2}\right]^{1/2} \times \left[1+\left\{1-\frac{41 n_e^2(1+10.3\, n_e/B_T^2)}{B_T^2\left[N_{//}^2-(1+\frac{20.6 n_e}{B_T^2})\right]^2}\right\}^{1/2}\right]$$

For a given value of $N_{//} > N_{//Acc}$ the maximum frequency is determined by the accessibility condition :

(5) $$f \leq f_3 = 2.1(\alpha n_e)^{1/2}\left[1-N_{//Acc}^2+6.4\, n_e^{1/2} N_{//Acc}/B_T\right]^{-1/2}$$

In practice we always have $f_2 > f_1$. On the figure 1 we have represented the evolution of the frequency limits f_2 and f_3 as a function of the density for a toroidal magnetic field B_T = 5 teslas, $N_{//2} = N_{//Acc} = 2$ and $\Delta N_{//} = N_{//2} - N_{//1} = 0.25$. We see that in order to avoid wave damping on α-particle until $n_e \sim 10^{20}$ e.m^{-3} a frequency higher than 4.5 GHz seems necessary.

iii) Optimizing the wave penetration to a hot plasma core. Complete power aborption by quasi-linear electron LANDAU damping occurs for a given ratio between the parallel phase of velocity ($c/N_{//}$) and the thermal speed of the electrons $(kTe/me)^{1/2}$. From /5/ we obtain the maximum penetration temperature given by (k = b/a = plasma elongation) :

(6) $$N_{//M}^2 T_e \leq 25.6 \Big/ \mathrm{Log}\left[7\,10^3\, n_e^2 R\, a\, r\left(\frac{1+k^2}{2}\right)^{1/2} \cdot \frac{\Delta N_{//}}{N_{//m}} \Big/ P_{HFT}\, T_e^{1/2}\right]$$

The evolution of $N_{//M}^2 T$ as a function of density is shown in figure 2, for $(\Delta N_{//}/N_{//m})/P = 10^{-3} MW^{-1}$, which is a typical value envisaged for LHCD on NET/ITER. We see that wave penetration can be largely improved by choosing small densities, narrow $N_{//}$-spectra, large input power. Finally for 1.5 < Zeff < 2 and considering the wave penetration limited by quasi-linear LANDAU damping, we can determine the value of the enhancement factor W given by equation (1c) and shown in figure 2. Typically $W \sim 1.8\, n_e^{-3/2}$.

2.3 We have calculated the current merit factor η considering profiles in the form $\rho = \hat{\rho}\,(1 - x^2)^\alpha$ where ρ = ne, T. Thus average density ⟨ne⟩ and density-averaged temperature ⟨T⟩ are given by ⟨ne⟩ = ne/(1 + αn) and ⟨T⟩ = T (1 + αn)/(1 + αn + αt). The coupling structure of the grill type is composed of a network of N_W waveguides along the toroidal direction with a phase difference between the HF electric fields in adjacent waveguides optimized for each value of density in order to maximize η. For 4 < B_T < 6 Teslas and 3 < f < 5 GHz, the results are plotted in figure 3. For 0.4 ⟨ne⟩ < $1.5\,10^{20}$ m^{-3}, we can derive a simple analytic expression :

(7) $$\eta \simeq 0.1\, N_W^{1/3} \cdot B_T \cdot W \Big/ \left[(5+Z_{eff})(1+\alpha_n)^{4/3}\langle n_e\rangle^{1/2}\right] \simeq \frac{0.18\, N_W^{1/3} B_T}{(5+Z_{eff})(1+\alpha_n)^{1/6}\langle n_e\rangle}$$

3 - LOWER HYBRID DRIVEN STEADY STATE TOKAMAK

3.1 In steady state operation Q = PFUS/PHFT, where PFUS represents the total fusion power delivered by the plasma, will be maximized . Since HF power for current drive heats the plasma, the HF current drive is strongly coupled with the power balance of the plasma. We use the following zero-dimensional global power balance equation :

(8) $$\partial W_P/\partial t = P_{INPUT} - W_P/\tau_E = 0$$

where the input power $P_{INPUT} = P_{F\alpha} + P_{HFT}$ and $P_{F\alpha}$ is the total α-power delivered by the plasma. Here Wp is the plasma energy and the global energy confinement time τ_E given by GOLDSTON /6/:

(9) $$\tau_E = 0.037\ H I_p R^{1.75} a^{-0.37} k^{1/2} (A_0/1.5)^{1/2} / P_{INPUT}^{1/2}$$

where H represents the enhancement factor of the L-mode confinement. The plasma current includes the bootstrap current contribution I_{BS} and we have :

(10) $$I_{HF} = I_p (1 - \chi)$$

$\chi = I_{BS}/Ip$ has been determined by M.Y. HSIAO et al /7/, and :

(11) $$I_p = \frac{5 a B_T [1.17 - 0.65/A]}{A q_\psi (1 - 1/A^2)^2} \left[\frac{1 + k^2 (1 + 2\delta^2 - 1.2\delta^3)}{2} \right]$$

3.2 The numerical applications are made using Zeff = 1.5, Zp = 1.2 αn = 0.5 and αt = 1. Considering the ITER parameters for the technologycal phase /1/ (A=R/a= 3.1, a = 1.8 m, k = 2, δ = 0.3, q_ψ=3) we have plotted in figures 4a and 4b for various values of B_T the evolution of Q and the neutron wall loading $\mathcal{P}_N$ as a function of ⟨ne⟩ when H=1 and 1.2. In order to ensure the penetration of the L.H.W until the plasma core it is necessary to limit the density ⟨ne⟩ (given by the relation (6) when $N_{//M} \sim N_{//ACC}$). The results are indicated on the following table.

	B (T)	Q	P_{FUS}	P_{HFT}	$\mathcal{P}_N (\frac{Mw}{m^2})$	$\langle ne \rangle$ $10^{20} m^{-3}$	$\langle T \rangle$ keV	χ
H = 1	5	2.65	398 Mw	150 Mw	0.48	0.78	10.7	0.14
	5.5	3.6	483 -	134 -	0.58	0.73	12.6	0.14
	6	5	586 -	117 -	0.69	0.68	14.9	0.14
H = 1.2	5	5.2	405 Mw	78 Mw	0.48	0.56	14.9	0.14
	5.5	8	504 -	63 -	0.58	0.5	18.8	0.14
	6	14.3	589 -	41 -	0.69	0.4	25.4	0.14

4 - CONCLUSIONS

We have determined the main characteristics of the RF system (frequency f > 4.5 GHz, $N_{//M} < 2$, spectral width $\Delta N_{//}/N_{//m} < 10^{-1}$) in order to ensure the wave penetration until the plasma core and to maximize the current merit factor η. A simple analytic expression of η has been obtained It seems possible in ITER, using LHW alone, to reach $Q \sim 8$, $\mathcal{P}_N \sim 0.7$ Mw/m² with ⟨ne⟩ = $0.5.10^{20} m^{-3}$ and $P_{HFT} \sim 60$ Mw, if a moderate value of the enhancement factor H ~ 1.2 can be achieved.

/1/ ITER Concept. Definition ITER 1 October 1988

/2/ C.F.F KARNEY and N. FISCH - Phys. Fluids 28 (1) January 1985 p.116

/3/ G. TONON, D. MOULIN - Tenth Int. conf. on Plasma Physics and Controlled Nuclear Fusion Research - LONDON Sept. 1984 Vol I, CN 44-F-III-5-2-p.557

/4/ D.A EHST, K. EVANS - Nuclear Fusion vol 27 n°8 (1987) p.1267

/5/ R.W HARVEY et al - Third Topical Conf. RF Plasma Heating-PASADENA (USA) January 1978 - A 71

/6/ R. GOLDSTON - Plasma Physics and Controlled Fusion-V26 N1 (1984) p.87

/7/ MING YUAN HSIAO et al - ANL/FPP/TM 221 May 1988

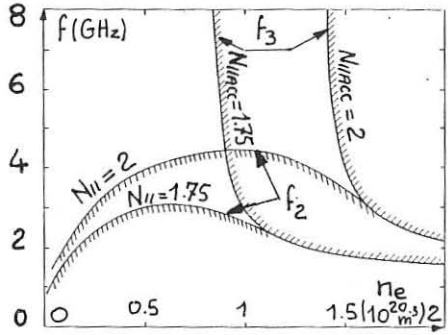

Fig 1 Evolution of the frequency limits f_2 and f_3 for B_T=5 Teslas and α = 0.4 as a function of ne

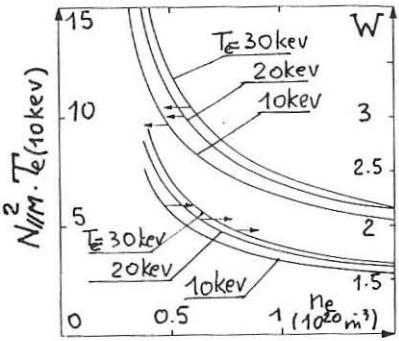

Fig 2 LHW penetration limit $N_{\parallel M}^2 \cdot T_e$ and enhancement factor W (R/a=3.1, a=1.8m, k=2 r/a $\leq$ 0.3, Zeff=2)

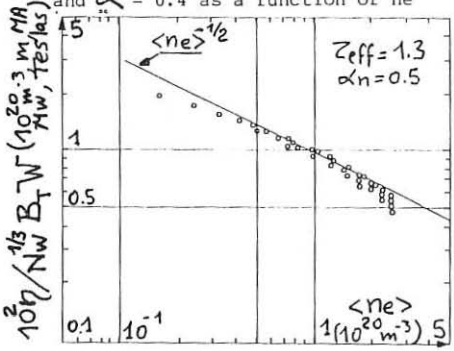

Fig 3 Evolution of normalized η as a function of <ne>: (0 calculated points)

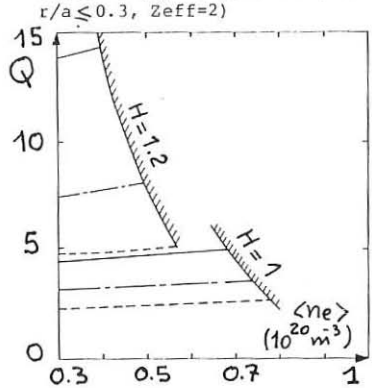

Fig 4a : Evolution of Q as a function of density <ne> and

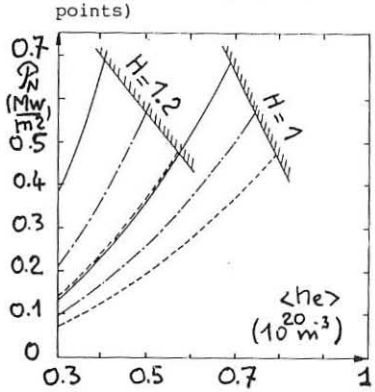

Fig 4b : Evolution of the neutron wall loading P_N as a function of density <ne> for :

H=1 and H=1.2 and

——— B =6 T

—·—·— B =5.5 T

- - - - - B =5 T

//////// LHW penetration limits

TEMPORAL BEHAVIOR OF THE ELECTRON CYCLOTRON RADIATION SPECTRUM (ECE) IN THE CASTOR TOKAMAK DURING LOWER HYBRID CURRENT DRIVE

S.I Fedorenko* M.Valovich, F Jachek, Y Shtekel

Institute of Plasma Physics, Praga, CSSR
* Kurchatov I.V. Institute of Atomic Energy, Moscow, USSR.

INTRODUCTION It is well known, that in some cases the lower hybrid current drive(LHCD) in tokamaks makes beams of fast electrons hit the vessel walls. This produces a negative influence on discharge parameters because of sputtering of the wall and thus the impurity problem arises. In addition, the radial diffusion of fast electrons could lead to broadening of the LH current profile, hence the efficiency of LHCD generation deteriorates. Recently the experiments concerning the dependences of fast particles beam parameters vs plasma properties and LH wave spectrum were carried out /1/. The information on generation of current by lower hybrid waves could be obtained from the analyses of the spectrum of electron cyclotron radiation (ECR) emitted by plasma. The series of experiments on the CASTOR tokamak using a Fast Scanning Fourier-spectrometer (FFS) were carried out

EXPERIMENTAL SET-UP. ECR spectrum on CASTOR tokamak was detected by FFS, operating in 30-300 GHz range both orthogonal radiation component being detected. The frequency resolution of the FFS was 3 GHz and the time resolution was about 1ms/2/. FFS was installed on CASTOR tokamak and receive the radiation from the outer side of the torus. The antenna spatial resolution at the centre of the vessel was 2.5 cm. In addition to ECE the electromagnetic wave transmitting experiments on the second ECR harmonic 55-80 GHz by the antenna plased inside the tokamak vessel take place. ECR spectrum measurements both in the ohmic heating regime and in the lower hybrid current drive regime using the generator with P=40kW, t=3ms, f=1,25GHz were performed. The power from the generator was launched into the tokamak vessel with the 3-waveguide grill from the outer torus side (waveguide sizes 10-160 mm) /3/. The discharge parameters were:

$B=11kG$, $N= 4\cdot10^{12} - 10^{13}\ cm^{-3}$, $I_{max}=12kA$, $T_e(0)=300ev$, current pulse duration - 8 ms.

Several interferogramms and N(t), B(t), I, V were simultaneously recorded during a pulse(N(t)- mean electron density, B(t)- toroidal field, I-current, V-loop voltage.

EXPERIMENTAL RESULTS AND DISCUSSIONS. In the ohmic heating discharges the regimes with $N=6\cdot10^{12}\ cm^{-3}$ were studied, because of effective current drive in the LH heating arises

at the same densities During of the discharge time (see fig1) the ECR spectrum deforms and its intensity increases from 3 to 5 times with respect to the thermal level at 3 ms. The spectrum substantially is broadened (both to lower and higher frequencies)till 5 ms. This type of spectra is characteristic of "run-away" regimes, and were observed in other machines also/4,5/. Using the relationship of the ECR frequency with the plasma radius at the 3-rd millisecond, the radiation plasma temperature from ECR intensity was reconstructed (see fig.2), which (within the experimental errors bars) is well described by a simple model function as $Te(r)=Te(0)*(1-r^2/a^2)$. To get the absolute values of Te the plasma optical thickness τ measurements using absorption at the second ECR harmonic /6/ were done. Using the well known relationship for τ we have simulated the Te(r) distribution (see fig. 2,Te values are normalised to 280 ev) .Comparing the obtained value of Te(0) with that from energy balance for CASTOR /7/ a satisfactory agreement between the experiment and simulations for Zeff=4 (this Zeff value is also in good coincidence with the results of impurity radiation studies)were found. From the nonthermal of the ECR (t=5-8 ms) the energyand density of the runaway electrons were evaluated (Ef=80kev, $N_f = 1.2\cdot 10^9$ cm^{-3}).An essential decreasing of CD efficiency with density increase were observed. Fig 3 shows the main parameters of the discharge with $N_f=4\cdot 10^{12}$ cm^{-3} in the LHCD experiments and on the fig.4 gives ECE spectra just before (t=3ms), during the RF and without RF at the 4.5ms.When the RF power was applied the ECE spectrum changes essentially and this associated with the increase of the fast electron number, their energy being fixed. From the nonthermal spectra of the ECE for t=4.5 ms the energy,density and pitch-angle of the runaway electrons were evaluated and was equal to Ef=60keV,$Nf=1.04\cdot 10^{10}$ cm^{-3} , $\theta=60^\circ$ .RF induced plasma current calculated from ECE spectra was equal to 2 kA,that is in good agreement with electromagnetic measurements.

The authors acknowledge their thanks to the CASTOR team for their cooperation in experiments.

REFERENCES.

1.Stevens J.E. et al / 12-th Europ.Conf.on Contr. Fus. and Plasma Physics,Budapest,1985,Pt.2,p.192.
2.Akulina D.K. et al / Priboru i teknika eksperimenta,N4, p.163,1985.
3.Nanobashvili S. et al / Czecho.Journal of Phys. V.B37,1987
4.Cambell D. et al / Nucl.Fusion V.24,p.3,1984.
5.Golant V.E.Fisika plasmu V.6,1980.
6.Dyabilin K.S.et al / Czecho.Journ. of Physics,V.B37, p.713,1987.

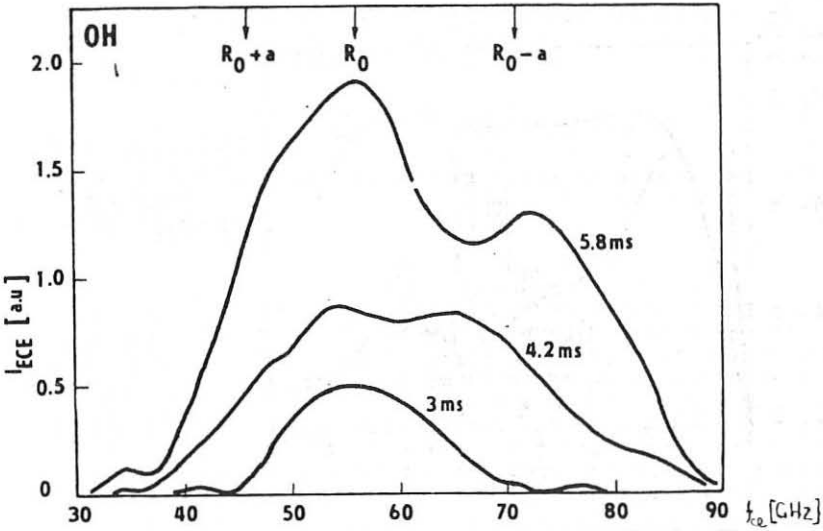

Fig.1 Temporal evolution of the ECE spectra in ohmic discharge at $n_e = 6*10^{12} cm^{-3}$.

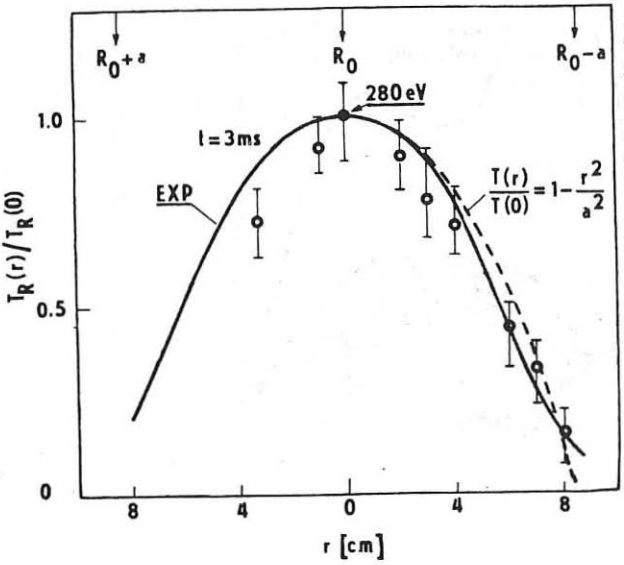

Fig.2 Electron temperature profile, measured from the absorption experiment. Solid line profile of radiation temperature at 3ms from fig.1.

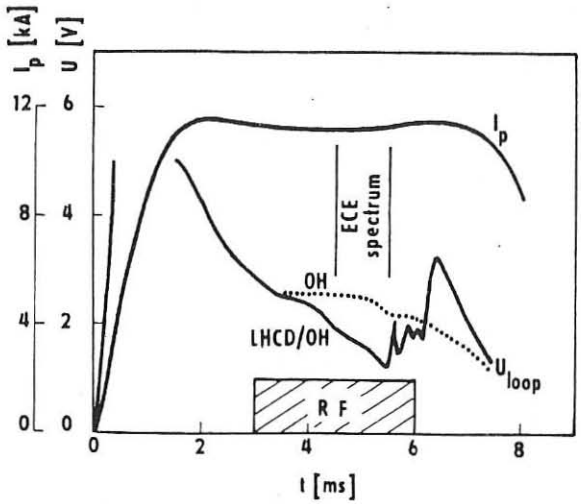

Fig.3. Time evolution of the main discharge parameters with LHCD and without.

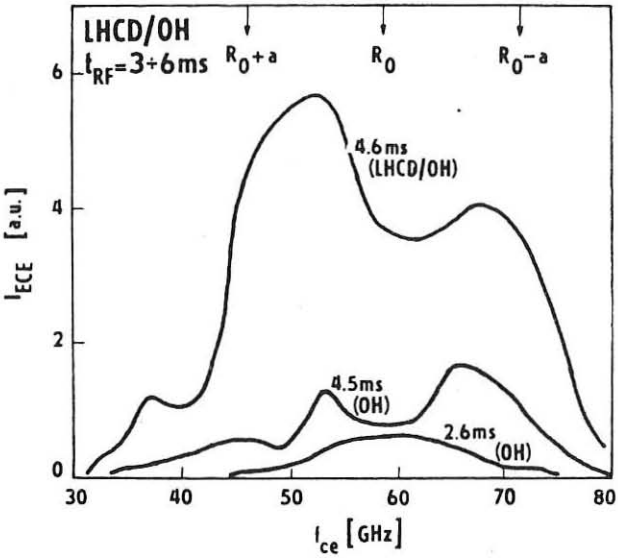

Fig.4 ECE spectra during the RF and without at 4 5 ms.

DAMPING OF LOWER HYBRID WAVES ON ENERGETIC IONS

M R O'Brien, B Lloyd, G Colyer, M Cox,
R O Dendy, C N Lashmore-Davies & A Kay*

U.K.A.E.A. Culham Laboratory/Euratom Fusion Association, Abingdon, Oxon, U.K.

* Loughborough University of Technology

Introduction

In plasmas with a significant hot ion population, ion damping may compete with the electron Landau damping (ELD) of lower hybrid (LH) waves desired for current drive. For example, initial theoretical studies[1] indicated that LH wave absorption on fusion-generated alpha particles may prevent efficient LHCD in reactor grade plasmas. However, more recently it has been shown [2] that the combined effects of wave accessibility and strong ELD which limit wave penetration to $r/a \gtrsim 0.5$ for typical reactor parameters, together with the peaked nature of the alpha particle density profile, allows significant alpha particle damping of the slow wave to be avoided. Efficient current drive is still possible since T_e is high enough at $r/a \gtrsim 0.5$ to allow strong absorption of low $N_{\|}$ waves.

The LH waves may interact not only with alpha particles but also with energetic ions generated during high power ICRH or NBI as has been observed experimentally in JT-60 for example[3]. The extent to which LH waves interact with such ion tails is of particular interest with respect to forthcoming experiments in JET, the explicit purpose of which is profile control via LHCD in NBI and ICRH heated plasmas[4]. The degree of ion damping is very sensitive to the energy and spatial distribution of the hot ions. Therefore it is important to allow flexible specification of the tail parameters to enable a wide range of realistic scenarios to be addressed. Furthermore, since the ray trajectory and location of ELD strongly influence whether the waves can interact with the energetic ions it is important when studying experiments such as JET to carry out calculations for realistic D-shaped equilibria.

Theoretical Details

A ray tracing code has been developed which employs the warm plasma electromagnetic dispersion relation for calculation of the ray paths in circular or D-shaped equilibria. The latter are specified using a Fourier representation[5], which is routinely fitted to experimental magnetic measurements on JET. Allowance is made for multiple reflection of the slow wave where necessary but the programme is terminated if mode conversion to the fast wave is encountered.

Ultimately it is essential to compare the damping on energetic ions with that due to quasi-linear ELD but for the initial results presented here a Maxwellian electron distribution is assumed and the relative locations of *linear* ELD and ion damping are compared

for single rays. The energetic ions may be treated as 'unmagnetised' since $k_\perp \rho_i \gg 1$ and physically the wave absorption may be attributed to perpendicular ion Landau damping which becomes large when $v_{\perp i} \sim w/k_\perp \equiv c/N_\perp$. The accuracy of the unmagnetised approximation has been examined in slab geometry for JET-like parameters and it was found that the predicted absorption was in excellent agreement with that calculated on the basis of harmonic ion cyclotron absorption (including harmonics up to $\ell = 300$). Furthermore the evolution of $N_\perp$ was found to depart significantly from values predicted on the basis of the electrostatic dispersion relation. Therefore the full electromagnetic dispersion relation is required for accurate computation of the ion damping.

The ion damping is evaluated numerically from the imaginary part of the susceptibility for arbitrary ion distribution functions. Two cases have so far been considered, namely damping on alpha particles and on energetic minority ion tails generated during ICRF. In the former case the central alpha particle density and the density profile are specified. The characteristic slowing down distribution (truncated at the birth energy $E_0 = 3.5MeV$) is assumed, [6]. In the second case one must specify the ICRF power deposition profile and the minority concentration. The ion distribution function is then calculated on each flux surface using the Stix model, [7]. Such a model gives an adequate representation of the tails experimentally measured during ICRF in JET, [8].

Damping on ICRF-produced Ion Tails

Ion damping in conditions similar to those employed in recent $(He^3)D$ minority ICRF high fusion yield experiments in JET, [9], has been briefly studied. The plasma parameters assumed are given in Table I(a). The alpha particle density is set to zero so that only damping on the He^3 minority (concentration $\sim 1\%$) is considered. The minority ions are at the same temperature as the bulk prior to RF injection. The temperature and density profiles have the form $T_{e,i} \sim (T_{e,i}(0) - T_{edge})(1 - \rho(\psi)/a) + T_{edge}$ and $n_{e,i} \sim (n_{e,i}(0) - n_{edge})(1 - \rho^2(\psi)/a^2)^{0.5} + n_{edge}$ respectively where $2\rho(\psi)$ is the flux surface width in the equatorial plane. The ICRF power deposition profile is taken to be of the form $P = P_0 exp\{-(\rho(\psi) - \Delta)^2/w^2\}$. For the conditions in Table I(a) there is total ELD of the incident ray in the region $0.5 \lesssim \rho(\psi)/a \lesssim 0.6$ after one reflection from the plasma boundary. In the code linear ELD is included only for reference and therefore does not deplete the incident power. Therefore the ray continues until it is completely damped on the ions. For $P_0 \sim 3.3MW/m^3$,w= 0.2 and $\Delta = 0$ (central deposition) the ray is totally damped on the ions in the region $0.3 \lesssim \rho(\psi)/a \lesssim 0.4$ after one reflection. Therefore electron damping is clearly expected to dominate in this case even though the central minority tail temperature is predicted to be $\sim 7.5MeV$. In order for ion damping to precede linear ELD one must increase Δ to 0.3 (off-axis deposition). Alternatively one may maintain central ICRF deposition but increase w to 0.5 (very broad deposition) with lower central power, viz., $P_0 = 2.2MW/m^3$. In this case (Fig. 1) there is even some ion absorption ($\sim 4\%$) in the first pass. The central tail temperature is $\sim 5MeV$. Damping is complete before $N_\perp$ exceeds 30 and involves ions whose Larmor radius in the poloidal

field is $\rho_{i\theta} \gtrsim 0.3m$. The broad spatial distribution of the minority tail may therefore not be unreasonable.

Damping on Fusion-generated Alpha Particles

Preliminary studies of alpha particle damping were carried out for a so-called 'JET-like high performance shot' the main parameters of which are given in Table I (b). The profiles are close to the Rebut-Lallia forms given in [10], namely $n_{e,i} = (n_{e,i}(0) - n_{edge})(1 - \rho^2(\psi)/a^2)^4 + n_{edge}$ and $T_{e,i} = (T_{e,i}(0) - T_{edge})(1 - \rho^2(\psi)/a^2)^{2.5} + T_{edge}$. The alpha particle density profile is $n_\alpha = (n_\alpha(0) - n_{\alpha(edge)})(1 - \rho^2(\psi)/a^2)^4 + n_{\alpha(edge)}$ with $n_\alpha(0) = 0.01 n_e(0)$. For reasonable LH wave accessibility a launched $N_\parallel$ of 3.0 was assumed. There is both ion and electron damping on the first pass although eventually mode conversion to the fast wave occurs (Fig. 2). Ion damping clearly dominates although after $\sim 75\%$ absorption the alpha particle damping 'switches off' when the ray reaches $\rho(\psi)/a \sim 0.7$. This occurs when $N_\perp$ decreases to ~ 23 which is the minimum value for interaction with the alpha distribution which is truncated at $E \sim 3.5 MeV$.

Acknowledgements

Fruitful discussions with C Gormezano, M Lorentz-Gottardi, S Knowlton, F Rimini and G A Cottrell are gratefully acknowledged. Part of this work was performed under a JET Task Agreement.

References

[1] K L Wong & M Ono, Nuc. Fus. 24, (1984), 615.

[2] P T Bonoli & M Porkolab, Nuc. Fus. 27, (1987), 1341.

[3] JT-60 Team, 12th IAEA Int. Conf. on Plasma Phys. & Contr. Nuc. Fus. Res., Nice (1988), Paper IAEA-CN-50/A-1-4.

[4] S Knowlton et al, Proc. 14th EPS Conf., Madrid, *III* (1987), 827.

[5] L L Lao et al, Phys. Fluids 24 (1981), 1431.

[6] D Anderson et al, Phys. Fluids 25 (1982), 353.

[7] T H Stix, Nuc. Fus. 15 (1975), 737.

[8] G A Cottrell, private comm.

[9] G A Cottrell et al, Bull. Am. Phys. Soc., 33 (1988), 2032.

[10] P H Rebut et al, 11th IAEA Int. Conf. on Plasma Phys. & Contr. Nuc. Fus. Res., Kyoto, *I*, (1986), 31.

Table I - Plasma Parameters

		(a) Damping on ICRF Tails	(b) Damping on Alpha Particles
	n_{eo}	$4 \times 10^{19} m^{-3}$	$1.7 \times 10^{20} m^{-3}$
	T_{eo}	$8.5 keV$	$15 keV$
	T_{io}	$6 keV$	$12 keV$
	$B_{\phi o}$	$3.3T$	$3.24T$
	I_p	$3.305 MA$	$6.1 MA$
Initial	$N_{\parallel}$	2.245	3.0
	f_{LH}	$3.7 GHz$	$3.7 GHz$

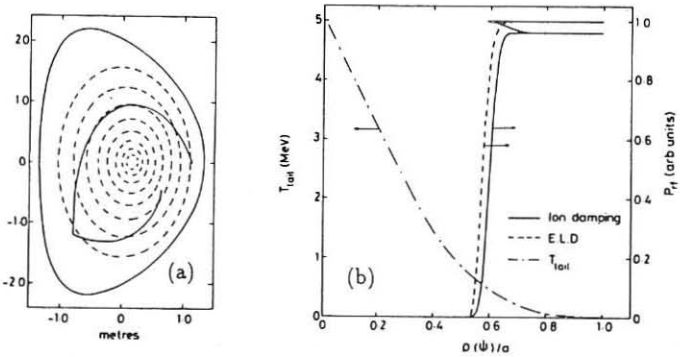

Fig. 1 Interaction with ICRF generated tails; (a) ray trajectory, (b) wave damping and minority tail temperature.

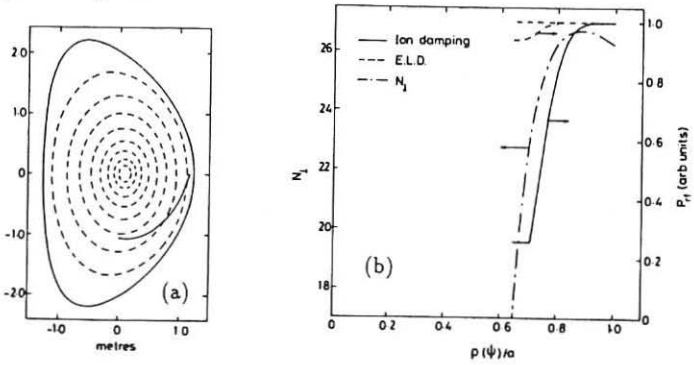

Fig. 2 Interaction with alpha particles; (a) ray trajectory, (b) wave damping and $N_\perp$ evolution.

ELECTRICAL CONDUCTIVITY AND ELECTRON CYCLOTRON CURRENT DRIVE EFFICIENCIES FOR NON-CIRCULAR FLUX SURFACES IN TOKAMAKS

M R O'Brien

UKAEA/Euratom Fusion Association, Culham Laboratory, Abingdon, Oxon, UK.

Introduction

As is well known, the presence of electron trapping can strongly reduce the electrical conductivity and rf current drive efficiencies of tokamak plasmas [1-5]. For example, the conductivity (in the low collisionality limit) of a flux surface with inverse aspect ratio $\epsilon = 0.1$ is approximately one half of the Spitzer conductivity (σ_{sp}) for uniform magnetic fields [3,6]. Previous estimates of these effects have assumed that the variation of magnetic field strength around a flux surface is given by the standard form for circular flux surfaces

$$|\underline{B}(s)| = B_o/(1 + \epsilon \ cos(\pi s/s_{max})) \tag{1}$$

Here B_o is the field strength at the magnetic axis, s the distance along the field line from the outside of the flux surface, and s_{max} the value of s for the inside of the flux surface. The bounce-averaged Fokker-Planck code BANDIT [7] has been adapted to treat non-circular flux surfaces provided by the TOPEOL equilibrium code. The code assumes banana-regime electrons, up-down symmetry, and that $|\underline{B}|$ increases monotonically between $s = 0$ and $s = s_{max}$. In this paper we consider the effects of electron trapping on the electrical conductivity and Electron Cyclotron Current Drive (ECCD) efficiencies for flux surfaces of tight aspect ratio configurations in which paramagnetism is important. For simplicity, in all cases considered here the electrons are assumed to collide with infinitely massive ions of charge state one. The full electron-electron collision operator is used although relativistic effects and non-Coulomb energy loss processes[8] have been neglected for this study. We compare the results with those for circular flux surfaces of *equivalent inverse aspect ratio* which obey equation (1) and have the same mirror ratio $|\underline{B}(s_{max})|/|\underline{B}(0)|$.

Electrical Conductivity

Here the toroidal electrical field is assumed small ($\sim 10^{-3}$) compared with the Dreicer field (i.e. no runaway electrons) and varies as the inverse of the major radius R. The total

current in the plasma is

$$I = 2\int d\psi \frac{j_{\|}(\psi, s=0)}{|\underline{B}(\psi, s=0)|}\int_{o}^{s_{max}(\psi)} \frac{ds}{R(\psi, s)} \tag{2}$$

since the elemental area is $d\psi ds/(R|\underline{B}|)$. In equation (2) $j_{\|}(\psi, s = 0)$ is the parallel current density on the outside of the surface of poloidal flux ψ, and the factor of two arises because the integral from $s = 0$ to $s = s_{max}$ only treats the upper (or lower) half of the plasma. We therefore define the conductivity of the plasma to be the flux-averaged current density $j_{av}(\psi)$ divided by the electrical field at the magnetic axis with

$$j_{av}(\psi) = \frac{j_{\|}(\psi, s=0)}{|\underline{B}(\psi, s=0)|}\frac{\int \frac{ds}{R}}{\int \frac{ds}{R|\underline{B}|}} \tag{3}$$

To get, for example, the toroidal current I_ϕ carried by the plasma, the integrand in equation(2) is multiplied by $B_\phi/|\underline{B}|$.

We illustrate the effect of having non-circular flux surfaces on the conductivity by considering Small Tight Aspect Ratio Torus (START) equilibria [9,10,11]. Such equilibria have a number of potential advantages over conventional tokamaks, notably high β and low coil currents for given plasma current. They typically are highly paramagnetic, have elongated D-shaped flux surfaces, and the edge poloidal field is comparable with the toroidal field. We consider two equilibria; the first (Fig. 1), although extreme compared with conventional tokamks (B_ϕ at the magnetic axis is 50% higher than the vacuum B_ϕ) is only modest by START standards. The other (Fig. 3) has a very high current and low toroidal field with the paramagnetic B_ϕ swamping the vacuum B_ϕ, and approaches the spheromak equilibrium. Figure 2 shows the variation of $|\underline{B}(s)|$ for the outermost dashed surface in Fig 1 with the dashed curve $|\underline{B}(s)|$ for the equivalent circular flux surface. Perhaps surprisingly, the two curves do not differ too greatly. The conductivity of this flux surface is 0.144 σ_{sp} and that of the equivalent circular surface is 0.139 σ_{sp} agreeing with McCoy and Kerbel[3]. These conductivities are for the total current density: the poloidal and toroidal components are 49% and 87% of this respectively. Smaller flux surfaces have conductivities even closer to those of their circular equivalents. Figure 3 shows a much more extreme equilibrium to demonstrate what happens when $|\underline{B}|$ departs greatly from the circular form. The outer flux surfaces do not have $|\underline{B}|$ monotonically increasing with s and are not considered. Figure 4 is the equivalent of Fig 2 for the third dashed surface of Fig 3: the conductivity is 0.225 σ_{sp}, that of the equivalent circular surface is 0.284 σ_{sp}, and the poloidal (toroidal) current density is 54% (84%) of the total.

These results suggest that the conductivity of the equivalent circular flux surface is a reasonable approximation to the true conductivity for all but the most 'extreme' equilibria,

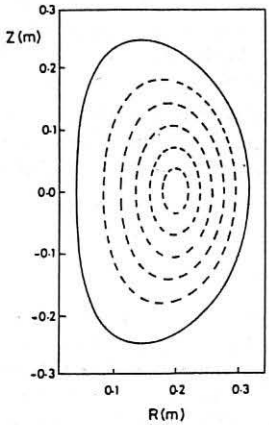

Figure 1. START flux surfaces for equilibrium with $I_\phi = 200kA, B_\phi$ (vacuum) $= 0.3T$ at $R = 0.2m$, $R/a = 0.18m/0.14m$, $q_\psi(edge) = 7.7$

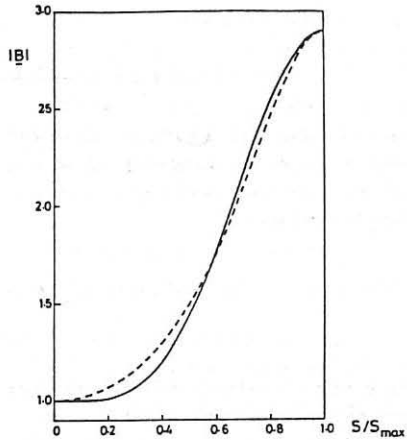

Figure 2. $|\underline{B}(s)|$ for the outermost (dashed) surface of Fig 1. The dashed line is from equation (1) with $\epsilon = 0.487$.

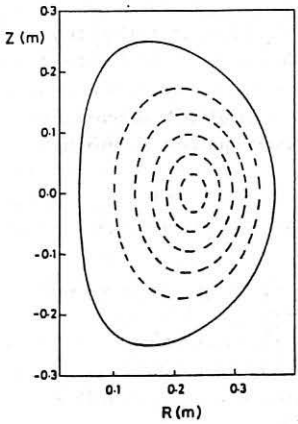

Figure 3. As Fig 1 but with $I_\phi = 1MA, \beta_I = 0.1, B_\phi$ (vacuum) $= 0.1T$ at $R = 0.2m$, $R/a = 0.20m/0.16m$, $q_\psi(edge) = 0.5$

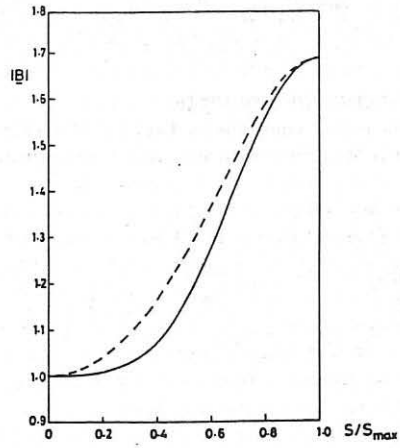

Figure 4. As Fig 2 but for the third dashed surface of Fig 3. For the dashed curve, $\epsilon = 0.355$

although this will give the total current, and not just the toroidal current, due to the field 'wind-up'. This indicates that it is the number of trapped particles that largely determines the conductivity, although the functional form of $|\underline{B}(s)|$ clearly can have an effect: when it is always less than its equivalent circular value (Fig. 4) the conductivity is noticeably reduced. The outer flux surfaces of some equilibria have local magnetic wells (outside the scope of this work): these are likely to carry only a small fraction of the current, due both to their large fraction of trapped electrons, and to the edge of the plasma being cooler than the centre.

Electron Cyclotron Current Drive

Some work has begun on studying ECCD efficiencies for these flux surfaces. Such a study is complicated by having a larger number of variables than the conductivity problem: the location in velocity space and the harmonic of the resonance as well as the location around the flux surface of the heating. For cases studied so far, the equivalent circular flux surface again gives a good approximation to the correct ECCD efficiency, even for surfaces such as that in Fig 4. For this surface, for current drive by electrons with $v_{\|} = 1.5v_e$ ($v_e^2 = 2T_e/m_e$) at the (non-relativistic) second harmonic resonance, the efficiency of the equivalent surface is only ten percent more than that of the true surface whether the heating is to the outside or the inside of the surface. This is a small effect: the large number of trapped electrons means that the current driven is about half the magnitude of *and in the opposite direction* (due to the Ohkawa effect) to that for uniform magnetic field. However in other circumstances yet to be studied (for example current drive by slower electrons) having non-circular surfaces might have a larger effect.

Acknowledgements

The author would like to thank P S Haynes for providing the TOPEOL equilibria and M G McCoy for great assistance in implementing non-circular equilibria in BANDIT.

References

[1] M N Rosenbluth, R D Hazeltine and F L Hinton, Phys Fluids 26 (1983) 808
[2] B Coppi and D J Sigmar, Phys Fluids 16 (1973) 1174
[3] M G McCoy and G D Kerbel, Phys Fluids 28 (1985) 3629
[4] A Ferreira, M R O'Brien and D F H Start, Pl Phys and Contr Fus, 26 (1984) 1565.
[5] M Taguchi, Journal of Phys Soc of Japan, 52 (1983) 2035
[6] L Spitzer, Physics of Fully Ionised Gases (Interscience, New York, 1967)
[7] M R O'Brien, M Cox and D F H Start, Nucl Fus 26 (1986) 1625
[8] R O Dendy and M R O'Brien, to be published as Nuclear Fus Letter, CLM-P844
[9] Y-K M Peng and D J Strickler, Nucl Fus 26 (1986) 769
[10] J Hugill et al, 15th EPS Conf, Dubrovnik 1988, Vol II 645
[11] T Hender et al, 'Studies of the Tight Aspect Ratio Tokamak Concept', this conference.

ON UPPER LIMIT OF BOOTSTRAP CURRENT IN TOKAMAKS

Ya.I.Kolesnichenko, V.P.Nagornyj

Institute for Nuclear Research, Ukrainian SSR
Academy of Sciences, Kiev, USSR

Abstract. The maximum value of bootstrap current is shown to be dependent essentially on the radial distribution and the value of the current driven by RF fields and/or by neutral injection. The simple expression for the bootstrap current and its limit in tokamaks with the elliptic cross-section are obtained.

1. The possibilities to create a tokamak with the current sustained due to the plasma internal processes such as neo-classical transport and fusion reactions [1,2] or a tokamak with bootstrap current and small seed current generated with external sources of energy [3,4] are very attractive. However, the experimental evidence of these possibilities are absent now. Besides the current generated by the internal processes is not sufficient for the ITER-like tokamaks. Therefore one should use the current drive with the waves and particle beams. These ways of the non-inductive current generation are most reliable and veryfied experimentally but they may turn out to be hardly acceptable for a reactor because of the large power consumption. Probably, the combined current drive methods based on the use of both the internal plasma processes and the external power sources have the best prospects. It is clear that to ensure the largest efficiency of the combined methods one should know conditions which should be satisfied for achieving the maximum value of bootstrap current. The aim of this work is to find these conditions and the upper limit of bootstrap current in tokamaks with the elliptic cross-section.

2. We proceed from finding the bootstrap current density

(j_b) in a tokamak with the elliptic cross-section of the flux-surfaces. Let us introduce the coordinates ρ , θ , φ (ρ is the flux surface function, θ and φ - the angular coordinates) according to Ref.5 . Then calculations result in the following expression for j_b :

$$j_b = -\frac{C_1\sqrt{\epsilon}}{k}\frac{c}{\rho B^2}\left\{\left(1+\frac{1}{Z_{eff}}\right)T\frac{dn}{d\rho}-\left(\frac{3}{2}+\frac{0.17}{Z_{eff}}-C_2\right)n\frac{dT}{d\rho}\right\}. \qquad (1)$$

Here k is the plasma cross-section elongation, B^2 the contravariant component of the magnetic field vector, $\epsilon=\rho/R$, R - the major radius of the torus, Z_{eff} - the effective charge number, c - the light speed, C_1 and C_2 factors depending on Z_{eff} (e.g. C_1=2,3; C_2=1,82; for Z_{eff}=1; C_1=1,87; C_2=2 for Z_{eff}=2). When Z_{eff}=1 the expression (1) is identical to that one found in Ref.6.

One can express j_b and B^2 in terms of the bootstrap current $I_b(\rho)$ and the total current $I(\rho)$ ($I(\rho) = I_b(\rho)+I_*(\rho)$, where $I_*(\rho)$ is the current which is not connected with the neoclassical processes) inside of the flux surface with the radial coordinate ρ , as following:

$$j_b(\rho) = \frac{1}{2\pi k\rho}\frac{dI_b}{d\rho}, \qquad B^2 = \frac{4I(\rho)}{c\rho^2}\frac{1}{1+k^2}. \qquad (2)$$

Substituting Eq.(2) into Eq.(1) we obtain:

$$\frac{dI_b(\rho)}{d\rho} = -\pi C_1 c^2\frac{1+k^2}{2}\frac{\sqrt{\epsilon}\,\rho^2}{I_*(\rho)+I_b(\rho)}\left\{\left(1+\frac{1}{Z_{eff}}\right)T\frac{dn}{d\rho}-\right. \qquad (3)$$
$$\left.-\left(\frac{3}{2}+\frac{0.17}{Z_{eff}}-C_2\right)n\frac{dT}{d\rho}\right\}.$$

This is the nonlinear equation for $I_b \equiv I_b(a)$ which one can solve numerically for any distribution $n(\rho)$, $T(\rho)$, $I_*(\rho)$. One should notice that since diffusion coefficient and heat conductivity are not neoclassical and do not depend on $j_b(\rho)$ (See for example INTOR scaling), we can solve this problem taking appropriate $n(\rho)$ and $T(\rho)$.

We first assume I_* to be small and located near the magnetic axis (bootstrap-tokamak [3,4]). In this case the formal solution of Eq.(3) yields:

$$I_{b_0} = \frac{a_M B_T}{2A^{1/4}}\left[C_1\beta\frac{1+k^2}{2}\frac{J_1}{J_2}\right]^{1/2}, \qquad (4)$$

where $I_b = I_b(a)$, subscript "0" means that I_* is negligibly small, A is the torus aspect ratio, a_M is a in meters, B_T is B in Teslas, $\beta \equiv 8\pi\langle p\rangle/(B)^2$ is in percents, $\langle p\rangle$ is the cross-section averaged plasma pressure,

$$J_1 = -\frac{1}{2}\int_0^1 dx\cdot x^{5/2}\left\{\left(1+\frac{1}{Z_{eff}}\right)\tilde{T}\,\frac{d\tilde{n}}{dx} - \left(\frac{3}{2}+\frac{0.17}{Z_{eff}} - C_2\right)\tilde{n}\,\frac{d\tilde{T}}{dx}\right\},$$
$$J_2 = 2\int_0^1 dx\cdot x\,\tilde{n}\,\tilde{T}, \qquad \tilde{n} = \frac{n(x)}{n(0)}, \qquad \tilde{T} = \frac{T(x)}{T(0)}, \qquad x = \rho/a. \tag{5}$$

Using the Troyon's expression for β-limit ($\beta_T = C_T I_{MA}/(a_M B_T)$, $C_T \sim 3$) we transform Eq.(4) to the following inequality:

$$I_{b0} \leq \frac{C_T C_1 a_M B_T}{4\sqrt{A}}\,\frac{1+k^2}{2}\,\frac{J_1}{J_2}. \tag{6}$$

The ratio J_1/J_2 in Eq.(6) depends on $\tilde{n}$, $\tilde{T}$, Z_{eff}. For example, $J_1/J_2 = 0{,}44$ for $\tilde{n} = \tilde{T} = 1-x^2$, $Z_{eff} = 1$. The maximum of J_1/J_2 given by Eq.(7) is reached when $\tilde{n}(x) = \eta(x_1 - x)$ where $\eta(y) = \int_{-\infty}^{y}\delta(t)\,dt$, x_1 depends on the temperature profile and for $Z_{eff} = 1$:

$$\frac{J_1}{J_2} = \begin{cases} 1 & \text{for } \tilde{T} = \text{const}, \quad x_1 = 1-\Delta,\ \Delta \to 0; \\ 0.6 & \text{for } \tilde{T} = 1-x^2, \quad x_1 = 0.55; \\ 0.5 & \text{for } \tilde{T} = (1-x^2)^2, \quad x_1 = 0.37. \end{cases} \tag{7}$$

It is clear that the density profile $\eta(x_1 - x)$ can never be obtained exactly. The possibility to obtain some approach to this profile depends on the plasma transport processes across the magnetic field, the character of particle injection, etc.

The presence of large I_* can strongly affect the upper limit of the bootstrap current. As it follows from Eq.(6) the current I_* leads to the increase of β_{max}; but at the same time it decreases $dI_b/d\rho$. Therefore one can increase $I_b(\rho)$ generating $j_*(\rho)$ at the plasma periphery beyond the region where the current $j_b(\rho)$ is localized. In this case

$$I_b \leq \sqrt{I\,I_{b0}}, \tag{8}$$

where I is the total plasma current. On the contrary case of current $j_*(\rho)$ localized near the axis the maximum current is smaller than I_{b0} :

$$I_b \leq I - \sqrt{I(I - I_{bo})}. \qquad (9)$$

3. Conclusions. The bootstrap-current is largest when: i) the plasma cross-section is elongated along the major axis of the torus, ii) plasma density radial distribution approaches to $\tilde{n}(x) = \eta(x_1 - x)$ with x_1 determined by Eq.(7), iii) β is near the Troyon limit; $j_*(\rho)$ has two maximums, one of them is on the magnetic axis (seed current), the another one is on the plasma periphery, the main fraction of $I_*(\rho)$ being in the region where $|dI_b(\rho)/d\rho| \ll \max|dI_b(\rho)/d\rho|$

Provided these conditions are satisfied we consider as an example the tokamak with the following parameters: $a_M = 2$, $B_T = 5$, $k = 2$, $A = 3$, $\beta = \beta_T$, $C_T = 3$, $\tilde{n} = \tilde{T} = 1 - x^2$, $I = 15$ MA. Then calculation yields $I_{bo} = 10$ MA, $I_b \leq 12$ MA. It means that the required current I_* is about 3MA only. As $I_*(\rho)$ is located mainly at the periphery region it can be easily generated with LH-waves. Of course, the another method of current drive should be applied then to generate the small seed current.

References.

/1/ V.Ya.Goloborod'ko, Ya.I.Kolesnichenko, V.A.Yavorskij. Nucl.Fusion, 23 (1983) 399

/2/ Ya.I.Kolesnichenko, D.Anderson, M.Lisak, H.Wilhelmsson. Phys. Rev. Lett. 53 (1984) 1825

/3/ R.J.Bickerton, J.W.Connor, J.B.Taylor. Nature Phys. Sci. 229 (1971) 110

/4/ B.B.Kadomtsev, V.D.Shafranov in Plasma Phys. and Contr. Nucl. Fusion Res. (Proc. 4th Int. Conf. Madison (1971) Vol.2. IAEA, Vienna (1971) 479

/5/ Ya.I.Kolesnichenko, V.A.Yavorskij. Fiz. Plazmy 5 (1979) 126

/6/ F.L.Hinton, R.D.Hazeltine, Rev.Mod.Phys. 48 (1976) 239

DEPENDENCE OF CURRENT DRIVE EFFICIENCY ON RADIAL PROFILES SHAPES

V.S.Belikov, Ya.I.Kolesnichenko, I.S.Plotnik

Institute for Nuclear Research, Ukrainian SSR
Academy of Sciences, Kiev, USSR

The key question in the RF current drive problem is whether the ratio $I/\mathcal{P}$ ($I = 2\pi\int_0^a dr\, r\, j(r)$ is the total driven current, $j(r)$ is the current density, r is the radial coordinate, $\mathcal{P} = 4\pi^2 R\int_0^a dr\, r\, P$ and $P(r)$ are the total RF power and the power density introduced into the plasma, R is the large radius of the torus) is sufficiently large for the reactor application. The ratio $I/\mathcal{P}$ representing the global efficiency of current drive depends on the wave characteristics (the wave phase velocities v_ϕ) and the plasma parameters (the electron temperature, T_e , and density n_e, the effective ion charge numbers Z_i) as well as on the radial profiles of these values. The quasi-linear theory enables to calculate j , P and j/P . To find I and $I/\mathcal{P}$ the radial distribution of plasma parameters and wave characteristics should be specified. For instance, in Ref. 1 the consideration was carried and for the plasma pressure profile $p(r) = p_0[1 - r^2/a^2]^{1.6}$. The aim of this work is to understand general laws in dependence of global CD efficiency on plasma-wave radial profiles for the case of current driven by LH-waves.

We proceed from the following expressions for the j and P /2/:

$$j = \frac{e n_e (v_2^2 - v_1^2)}{2\sqrt{2\pi}\, v_e} e^{-x_1^2/2} \mathcal{L}(x_1, Z_i) \qquad (1)$$

$$P = \frac{m_e n_e v_e^2}{\tau_{ee}} \frac{2(Z_i + 1 + T_p)}{T_p} \ln\frac{v_2}{v_1} e^{-x_1^2/2} \beta(x_1, x_2)$$

where $\tau_{ee} = \frac{m_e^2 v_e^3}{\sqrt{2\pi}\, e^4 n_e \Lambda}$, $T_p = T_\perp / T_e$, $v_e^2 = T_e / m_e$

e and m_e are the electron charge and mass., $T_\perp$ is the resonant particle temperature ($T_\perp > T_e$), $v_{1,2} = \omega / k_{1,2}$, $k_1 = \max k_\parallel$, $k_2 = \min k_\parallel$, $x_{1,2} = v_{1,2}/v_e$, $\alpha(x_1, z_i)$ and $\beta(x_1, x_2)$ are defined in Ref. 2 .

Let us assume that $n_e(r)$ and $T_e(r)$ may be approximated as follows:

$$n_e(r) = n_0 (1 - r^2/a^2)^{\alpha_n}, \quad T_e(r) = T_0 (1 - r^2/a^2)^{\alpha_T} \quad (2)$$

where α_n and α_T are the parameters. In addition we assume that $dz_i/dr = 0$ and $dT_p/dr = 0$. Then calculations yield:

$$I = \pi a^2 \bar{j} \int_{y_1}^{\infty} \frac{dy}{y^{\mu}} e^{\left[1 - \frac{y}{1+\alpha_T}\right] \frac{\bar{x}_1^2}{2}}, \quad P = 2\pi^2 a^2 R \bar{P} \int_{y_1}^{\infty} \frac{dy\, e^{\left[1 - \frac{y}{1+\alpha_T}\right] \frac{\bar{x}_1^2}{2}}}{y^{\mu + \alpha_n/\alpha_T}} \quad (3)$$

Here $\bar{j} = j(\bar{n}_e, \bar{T}_e)$ and $\bar{P} = P(\bar{n}_e, \bar{T}_e)$, $\bar{n}_e$ and $\bar{T}_e$ are the cross-section averaged electron density and temperature, $\bar{x}_1 = v_1/\bar{v}_e$, $\bar{v}_e = (\bar{T}_e/m_e)^{1/2}$, $\mu = 1/2 + (\alpha_n + 1)/\alpha_T$, $y_1 = (1 - r_1^2/a^2)^{-\alpha_T}$, r_1 the smallest radius accesible for LH-waves. When calculating P we took into account the profile shape in the first term of expansion over x^{-1} only, in the other terms $T_e(r)$ was changed for $\bar{T}_e$. Moreover we supposed that the depth of the LH-wave penetration into the plasma is $a - r_1$, r_1 being considered as a parameter.

Eqs.(3) enable to obtain the following expression for the global efficiency of current drive:

$$\frac{I[A]}{P[W]} = \frac{0.12\, \bar{T}_e[keV]}{\bar{n}_{20}[m^{-3}]\, R[m]\, \Lambda}\, \eta(\bar{x}_1, \bar{x}_2, z_i)\, G(\alpha_n, \alpha_T, \bar{x}_1, r_1) \quad (4)$$

where $n_{20} = n_e/10^{20}$, Λ is the Coulomb logarithm,

$$\eta = \frac{(\bar{x}_2^2 - \bar{x}_1^2)\, \bar{T}_p\, \alpha(\bar{x}_1, z_i)}{4(z_i + 1 + \bar{T}_p) \ln(\bar{x}_2/\bar{x}_1)\, \beta(\bar{x}_1, \bar{x}_2)} \quad (5)$$

$$G = \left\{ (1+\alpha_n) \int_{y_1}^{\infty} \frac{dy}{y^{\mu + \alpha_n/\alpha_T}} e^{-\frac{y \bar{x}_1^2}{2(1+\alpha_T)}} \right\}^{-1} \int_{y_1}^{\infty} \frac{dy}{y^{\mu}} e^{-\frac{y \bar{x}_1^2}{2(1+\alpha_T)}}$$

The difference between Eq.(4) and corresponding expression for homogeneous plasma consists in the presence of a G - factor which depends on the profile shape characteristics. In the case of practical interest when $2 \leqslant \overline{X}_1 \leqslant 5$ the expression for G may be approximated as follows

$$G = \frac{1}{(1+\alpha_n)(1-r_1^2/a^2)^{\alpha_n}}\left\{1+\alpha_n\left[1+\alpha_n+\frac{\alpha_T}{2}\left(1+\frac{\overline{X}_1^2}{(1+\alpha_T)(1-r_1^2/a^2)^{\alpha_T}}\right)\right]^{-1}\right\}$$

The dependence of G on α_n for various values of α_T and $\overline{X}_1$ is presented in Fig.1.

It follows from Fig.1 that the highest CD-efficiency takes place when the LH-waves generate a current in the plasma periphery region only. The most strong dependence of CD-efficiency on the LH-waves location takes place when the density profile is characterized by the large α_n. The dependence of CD-efficiency on the temperature profile shape is relatively weak.

To understand why these conclusions takes place let us take into account that for LH-waves $j(r) \sim n_e(r)\exp\{-X_1^2(r)/2\}/\sqrt{T_e(r)}$ and $P(r) \sim n^2(r)\exp\{-X_1^2(r)/2\}/\sqrt{T_e(r)}$. Then we can conclude that the power profile is more peaked then the current one. The increase of r_1 leads to the exclusion of the region with large plasma density and, as a result, to the increase of CD-efficiency.

The weak dependence of $I/\mathcal{P}$ on α_T is connected with the fact that j and P have similar dependence on T_e.

The another conclusion following from Fig.1 is the weak dependence of $I/\mathcal{P}$ on the shapes when $r_1/a = 0.5$.

Note that when $r_1 > 0$ the current should by sustained in the region $r < r_1$ without using LH-waves. It is clear that to find the total CD-efficiency for this case one should specify the other methods.

References

1. D.A.Ehst, J.Evans. Nucl. Fusion, 27 (1987) 1267.
2. V.S.Belikov, Ya.I.Kolesnichenko, I.S.Plotnik. Proc. 15 th Europ. Conf. on Contr. Fusion and Plasma Physics, Dubrovnik, 3 (1988) 999.

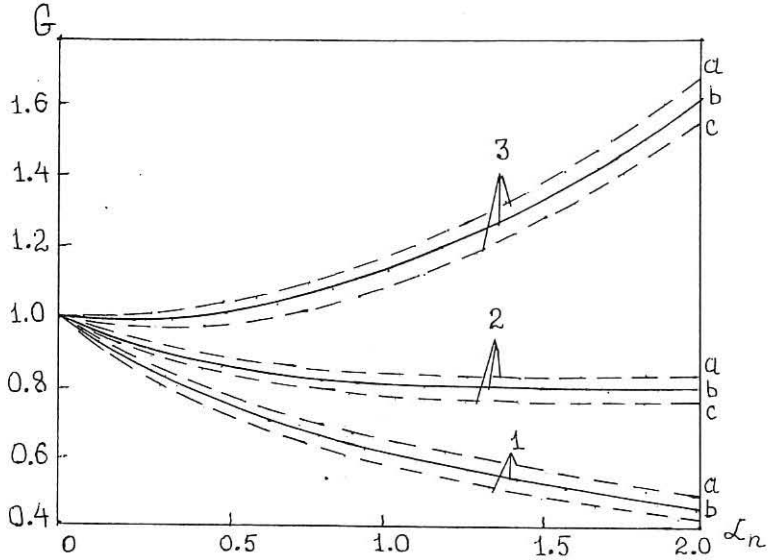

Fig.1. G versus $\mathcal{L}_n$ for $\overline{X}_1 = 3$ and various $\mathcal{L}_T$ and r_1/a : 1 - $r_1/a = 0$, 2 - $r_1/a = 0.5$, 3 - $r_1/a = 0.7$; a - $\mathcal{L}_T = 0.5$, b - $\mathcal{L}_T = 1$, c - $\mathcal{L}_T = 1.5$

LOWER HYBRID EXPERIMENTS AT 2.45 GHz IN ASDEX

F. Leuterer, F. Söldner, M. Münich, M. Zouhar, F. Hassenpflug, F. Monaco, M. Pelicano, H. Murmann, and ASDEX-team.

Max-Planck-Institut für Plasmaphysik
EURATOM Association, D-8046 Garching, FRG

R. Bartiromo, V. Pericoli, A. Tuccillo, F. Santini, M. D'Ortona, A. Marra, P. Papitto

Associazione EURATOM-ENEA sulla Fusione, C. R. E. Frascati, C.P. 65 - 00044 - Frascati, Rome, Italy

ABSTRACT

The new lower hybrid system of ASDEX has started operation. A power level of 1 MW/0.5 sec was meanwhile achieved. Current drive and heating have been studied until now up to a density of $n_e = 3 \cdot 10^{13} cm^{-3}$. Central heating of electrons and ions is seen.

A new lower hybrid system with f = 2.45 GHz, P = 3 MW and T = 1 s has been constructed for use on ASDEX. The main aims are to study profile control with simulataneous application of other heating methods. The higher frequency of 2.45 GHz, as compared to the previously used 1.3 GHz, allows operation in the typical density regime for neutral injection and ion cyclotron heating in ASDEX. For this purpose a high flexibility with respect to the launched wave spectrum was required. The system has started operation at the end of 1988.

The transmitter consists of two groups of 3 klystrons which are fed by a common dc-power supply and which are protected by a common ignitron crowbar system. They can be operated independently. All 6 klystrons are fed by a common masteroscillator. Their outputs are amplitude- and phase controlled (20 dB; 360°) by means of feedback systems acting on the respective RF-inputs. The amplitude control is also used for modulation.

Standard WR 430 transmission lines connect the 6 klystrons to a power splitter unit based upon 3 dB E-plane hybrids and providing 6 x 8 outputs to feed a 2 x 24 waveguide grill. The phase of each output can be arbitrarily set through 360° by step motors allowing the generation of current drive spectra, opposite current drive spectra and symmetric wave spectra at variable $N_{\parallel}$ ($1 < \bar{N}_{\parallel} < 4.4$, $\Delta N_{\parallel} = 0.4$). Due to an excellent isolation of the 3 dB-hybrids the forward waves are insensitive to arbitrary reflections.

The grill consists of 2 arrays of 24 waveguides each. Their inner dimensions are 10 x 109 mm, the wall thickness is 4 mm. Two front window blocks of PLT-design are located ca. 25 cm from the plasma surface. The front ends of the grill are made of stainless steel and their waveguide

inner surfaces are coated with a rough gold layer to prevent multipactors. The upper and lower waveguide arrays are connected to the two groups of klystrons and can be operated independently with different powers and different spectra. In all 48 waveguides the incident and reflected powers are measured. The phases of the incident waves are monitored twice during a 1 sec pulse with a time multiplexing device.

The system was constructed in cooperation between ENEA-Frascati (grill, narrow waveguide structures, 3 klystrons), PPPL-Princeton (waveguide windows, 3 klystrons) and IPP-Garching. It was put into operation in December 1988 and after a total of 80 shots at different phase settings and plasma conditions we achieved a power level of 1 MW/0.5 s into a $3 \cdot 10^{13}$ cm^{-3} plasma.

The coupling is usually good with a global RF reflection coefficient $\langle R \rangle$ between 10 and 25 %, depending on grill-position and plasma position. In the individual waveguides the reflection coefficients are, however, quite different. An example is shown in Fig. 1, where we compare the distribution of the reflection coefficients in one grill for the case of normal and opposite current drive. In a few shots we varied the relative phase between the upper and the lower grill and found very little influence on their reflection distributions.

The results of the first current drive experiments are summarized in Fig. 2. Here we plot the rate of change of the primary current in the OH-transformer during the lower hybrid pulse, normalized to its value in the preceeding OH-phase. We recognize the nonlinear decrease of this quantity with the RF-power and its variation in the limited range of densities studied up to now. For comparison we also show the points which have been obtained with the old 1.3 GHz system in the same density range /1,2/. The improvement with frequency is obvious.

In the parameter range studied until now, the RF power is directly absorbed by suprathermal electrons. Contrary to the previous experiments at 1.3 GHz /1,3/ no fast ion tails were observed up to the maximum working density $\bar{n}_e \approx 4 \times 10^{13}$ cm^{-3}. Similar observations were made in the FT-tokamak /4,5/. The generation of suprathermal electrons leads to a strong increase of hard X-ray radiation and nonthermal ECE spectra as measured with a Michelson interferometer. Thermalization of the fast electrons leads to an increase of the electron temperature over the whole plasma cross-section as from the YAG-Thomson scattering measurements. The radial profile of $T_e(r)$ is slightly peaking during Lower Hybrid current drive. The peakedness $T_{eo}/\langle T_e \rangle$ increases with increasing LH power. At $\bar{n}_e = 2.1 \times 10^{13}$ cm^{-3} the central electron temperature nearly doubles from $T_{eo} \approx 1.7$ keV to $T_{eo} \approx 3.2$ keV with $P_{LH,t} = 750$ kW applied. The radial profiles of $T_e(r)$ during the OH and LH phases are shown in Fig. 3. The central temperature T_{eo} increases linearly with LH power as seen from Fig. 4. The increase in ion temperature, measured by perpendicular CX-diagnostics, is smaller at low density where the coupling between electrons and ions is weak. At $\bar{n}_e = 2.1 \times 10^{13}$ cm^{-3} with $\Delta T_{eo} \approx 1.4$ keV an increment of only $\Delta T_{io} = 0.2$ keV is obtained with $P_{LH,t} = 750$ kW. . The increase in thermal energy content, as determined from the diamagnetic signal, is only slightly larger than the increase in the electron energy content as measured with Thomson scattering. The increase in total energy content as derived from the equilibrium beta is typically a factor of 1.3 larger than the increase in

thermal energy content. The difference has to be attributed to the higher parallel component of the suprathermal electrons. At higher density, the anisotropy is reduced and also the coupling between electrons and ions is improved. At $\bar{n}_e = 2.75 \times 10^{13}$ cm^{-3}, $\Delta T_{eo} \approx 1$ keV and $\Delta T_{io} \approx 0.3$ keV are obtained with $P_{LH,t} = 590$ kW. The absorption coefficient $\alpha = P_{LH,abs}/P_{LH,t}$ can be derived from the rate of change of the energy content immediately after switch-off of the LH power. For the actual experiments ($\bar{N}_{\parallel} = 2.25$, $\Delta\varphi = \pi/2$) we obtain $\alpha \approx 0.5$.

The sawteeth period rises with increasing LH power as was already found at 1.3 GHz /6/. With dominant LH-current drive, sawteeth are suppressed completely. For the series at $\bar{n}_e = 2.1 \times 10^{13}$ cm^{-3} shown in Fig. 4, sawteeth are stabilized for $P_{LH} \gtrsim 750$ kW. The RF-current drive in this case results in a drop of OH power input by about 2/3. After stabilization of sawteeth, central electron temprature and beta values start to increase continuously with a moderate slope.

REFERENCES:

[1] F. Leuterer et al., Plasma Physics and Contr. Fusion, 27, 1399 (1985)
[2] F. Leuterer et al., Phys.Rev.Lett. 55, 75 (1985)
[3] F. Söldner et al., 12th EPS-Conference, Budapest 1985, Vol. 9F, part II, p. 244
[4] F. Alladio et al., 10th IAEA-Conf. London 1984, paper IAEA-CN 44/F.II-3)
[5] F. Alladio et al., 12th IAEA-Conf., Nice 1988, paper IAEA-CN 50/E-3-3
[6] F. Söldner et al., Phys. Rev. Lett., 57, 1137 (1986)

Fig. 1:
Distribution of refleciton coefficients in the upper grill for normal and opposite current drive.

Fig. 2:
Rate of change of the primary current as a function of LH-power

Fig. 3:
The radial electron temperature profiles during OH and LH-phase.
$\bar{n}_e = 2.1 \times 10^{13}$ cm^{-3}, $P_{LH} = 750$ kW, $\bar{N}_{\parallel} = 2.25$, $\Delta\varphi = \pi/2$.

Fig. 4:
Scaling of the central electron temperature T_{eo} and of the sawtooth period with LH-power.

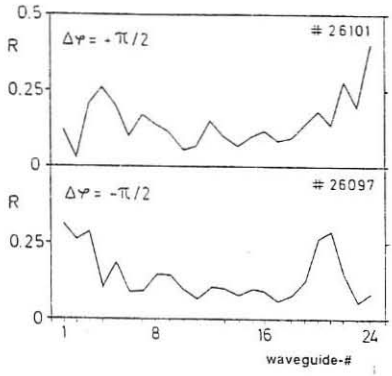

Figure 1

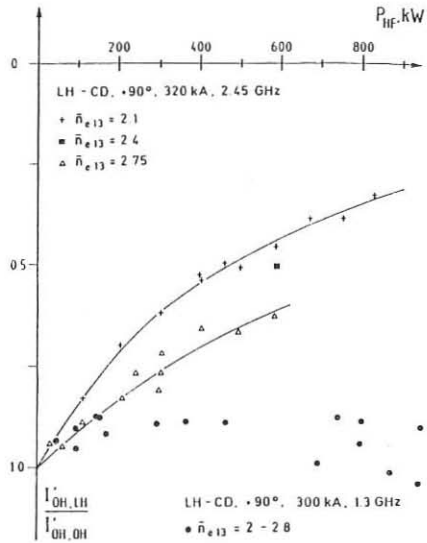

Figure 2

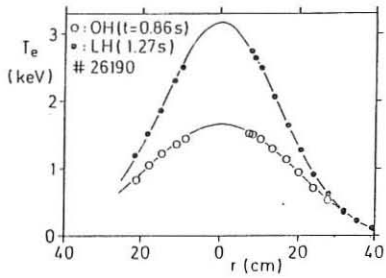

Figure 3

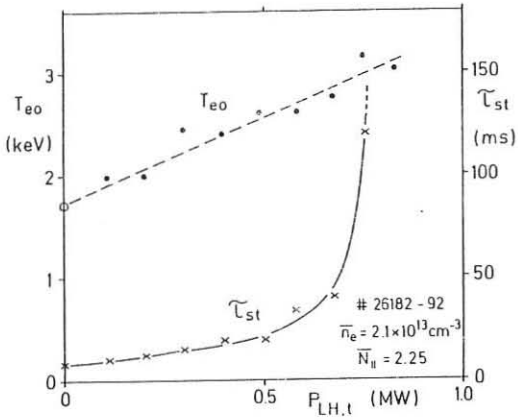

Figure 4

SPECTRAL PUMPING AND CURRENT DRIVE

D.W. Faulconer

Laboratoire de Physique des Plasmas - Laboratorium voor Plasmafysica
Association "Euratom-Etat belge" - Associatie "Euratom-Belgische Staat"
Ecole Royale Militaire - B 1040 Brussel - Koninklijke Militaire School

INTRODUCTION

High frequency heating and current drive are routinely formulated as processes of diffusive spreading in velocity space. It will now be shown that the velocity space distribution function can evolve in opposite manner, the imposed field driving it into a sequence of peaks in v. These peaks give rise to instability; as they are maintained by the driving field against diffusive spreading over the unstable spectrum, this field effectively "pumps" the spectrum to high values. Subsequent spectral transfer provides a solution to the "spectral gap" problem.

MODEL

As prototypical case we study lower-hybrid current drive by electron Landau damping where a well-defined resonance cone structure is assumed to exist in a homogeneous plasma. Following Ref.1, E_z of the lower-hybrid wave is idealized as $E\cos(k_0 z-\omega t+\phi)$, ($E$=const., ϕ independent of z, $z \| B_0$) within the cone and zero elsewhere, the cone being of fixed toroidal extent $\Delta z=d$. The change in parallel velocity v induced by E_z in one passage of the cone, Δv, is taken to be small enough to allow a description by means of the Fokker-Planck equation. We substitute E_z in the test particle formulation of this equation ([2] and for more detail [3]) to evaluate diffusion $(1/\tau_r)\langle\Delta v\Delta v\rangle$, and friction $(1/\tau_r)\langle\Delta v\rangle$ coefficients (τ_r=mean time between resonance cone encounters=L/v). It is important to use the unapproximated forms for these coefficients; < > represents an average over the phase ϕ seen by an electron, this phase being assumed to be randomized between successive resonance cone encounters (by collisions, finite Δv [1], varying distance between encounters etc.). We also assume there to be a turbulent Langmuir wave spectrum $|E_L(k)|^2$ resulting from the abovementioned instability. There results

$$\frac{\partial f}{\partial \tau}=\frac{\partial}{\partial w}\left\{\left[D_{LH}\, w\,\frac{\sin^2\left(k_0 d\,\frac{w-w_0}{2w}\right)}{(w-w_0)^2}+D_L(w)\right]\frac{\partial f}{\partial w}\right. \tag{1}$$

$$\left.+\,D_{LH}\left[\frac{\sin^2\left(k_0 d\,\frac{w-w_0}{2w}\right)}{(w-w_0)^2}-\frac{k_0 d}{2w}\,\frac{\sin\left(k_0 d\,\frac{w-w_0}{w}\right)}{w-w_0}\right]f+(2+Z_i)\left[\frac{1}{w^3}\frac{\partial}{\partial w}+\frac{1}{w^2}\right]f\right\}$$

where $D_{LH}=(eE/m_e k_0)^2/L v_{te}^3 \nu_0$, $D_L(w)=(\pi e^2/2m_e^2 v_{te}^3 \nu_0 |w|)|E_L(k)|^2\,|_{k=|\omega_k|/v_{te}w}$

$v_{te}^2=T_e/m_e$, $\nu_0=\omega_{pe}^4 \ln\Lambda/4\pi n_0 v_{te}^3$, $w=v/v_{te}$, $w_0=\omega/k_0 v_{te}$, $\tau=\nu_0 t$

and we have taken the high velocity limit in writing the collision term, integrated over $v_\perp$ assuming a Maxwellian in $v_\perp$, and included D_L which models quasilinear diffusion on the Langmuir waves.

ANALYSIS

1. PARTICLE DISTRIBUTION

The first of the two contributions to Eqn.(1) in D_{LH} is diffusive, going to zero as expected when a particle with velocity w sees a (cancelling) integral number of Doppler-shifted oscillations in crossing the resonance cone. It has been linked to the standard quasilinear diffusion coefficient in Ref.1. The second contribution in D_{LH} is new, having the nature of a drag or acceleration term depending on its sign. It will tend to alternately peak or void the distribution about its successive zeros in w. This contribution can be traced to $\langle\Delta v\rangle$ and thence to the perturbation in the zero order particle trajectory caused by the lower-hybrid wave; it also depends for its existence on the w-dependence of the time between successive cone encounters τ_r (1st subcontribution), and the transit time of the cone itself (2nd subcontribution). Thus the coherence and spatial localization of the cone gives rise to counterdiffusive aggregation of particles in velocity space, in spite of the assumption of phase randomization between cone encounters. Finally note that the terms multiplied by D_{LH} are peaked about the resonant phase velocity w_0 as expected, and that they stop oscillating as $w\to\infty$. This last property is due to the particles traversing a stationary waveform when their cone transit time becomes much less than the wave period; the number of oscillations they see becomes independent of particle velocity.

Equation (1) is in conservation form: $\partial f/\partial\tau=-\partial S/\partial w$, so that S represents velocity space flux to within an additive constant. Assuming steady state, we integrate to find S=0 after imposing zero flux at $w=\infty$. Rewriting S=0:

$$\frac{1}{f}\frac{\partial f}{\partial w}=\frac{-D_{LH}\left[\dfrac{\sin^2\left(k_0 d\,\dfrac{w-w_0}{2w}\right)}{(w-w_0)^2}-\dfrac{k_0 d}{2w}\,\dfrac{\sin\left(k_0 d\,\dfrac{w-w_0}{w}\right)}{w-w_0}\right]-\dfrac{2+Z_i}{w^2}}{D_{LH}\,w\,\dfrac{\sin^2\left(k_0 d\,\dfrac{w-w_0}{2w}\right)}{(w-w_0)^2}+D_L(w)+\dfrac{2+Z_i}{w^3}} \tag{2}$$

For typical values of parameter $k_0 d$, on the order of several times 2π, and $D_{LH}\gtrsim 1$, the appearance of maxima and minima of f ($\partial f/\partial w=0$) near the zeros of the sine multiplied by it is evident. The degree of relative peaking increases with $k_0 d$. For $2N\pi<k_0 d<(2N+1)\pi$ the term in $k_0 d$ is positive for $w\to\infty$ and one finds divergence of f at infinity, the positive flux associated with this term at large w being inconsistent with the steady state S=0 condition imposed; generation of a runaway population is indicated. When negative, this term should counteract tail formation.

2. SPECTRAL PUMPING

The intervals in w for which f has positive derivative in Eqn.(2) are intervals of instability over which we take to be generated a spectrum of Langmuir waves whose

reaction on f is manifest in the quasilinear coefficient D_L appearing in Eqns.(1) and (2). As D_L does not affect the sign of $\partial f/\partial w$ in Eqn.(2), its growth does not saturate the instability within the present description; at the same time it generates enhanced diffusion over the given w intervals. By maintaining the positive slope of f, the lower-hybrid wave is effectively pumping the Langmuir spectrum in the unstable w intervals. Any mechanism which would then transfer wave energy to the stable intervals in w would effectively spread the pumped Langmuir spectrum over an extended continous region in w (e.g. the "spectral gap" region), allowing increased diffusion thereon with concomitant enhanced current drive. Apart from nonlinear mode transformation, such transfer of the Langmuir spectrum is inherent to the nonlinear saturation of its growth phase.

AN EXAMPLE

Consider the transient phase of operation immediately after application of lower-hybrid power. Coefficient D_{LH} has a typical value somewhat greater than unity, D_L is initially zero and w~3-5, so we neglect all contributions to the right members of Eqns.(1) and (2) except those in D_{LH}. Integrating Eqn.(1) over a velocity interval extending between successive simultaneous zeros of the sine functions ($w=w_o$ excluded) shows total particle number in each such interval to be conserved in time. Steady state f(v) found from Eqn.(2) exhibits singularities at the interval endpoints which can be resolved by reinstatement of neglected terms as infinitesimals and norming f to the conserved number of particles over the interval. With neglect of the infinitesimals the steady state distribution is seen to have been compacted into a sequence of delta functions at interval endpoints which form a discretized Maxwellian. Such a multi-beam distribution is unstable. In the case of a single beam superposed on a Maxwellian background, a linearly unstable phase is succeeded by one of direct or indirect (via Langmuir condensation) generation by parametric instability of a low phase velocity spectrum of strong Langmuir turbulence. This spectrum then spreads the background population into tails extending beyond the beam velocity [4]. Insofar as an analogy holds with the multi-beam case at hand, one can claim to have transport of background particles to the velocity w_o where the lower-hybrid wave resonantly drives current, thereby solving the "spectral gap" problem for the initial transient phase of operation considered here. In proceeding beyond this admittedly highly idealized initial-phase model to consider steady state operation, we foresee a similar course of events, the maxima discussed earlier now playing the role of broadened beams. This is a tentative solution, the analogy with a single beam on which it is based eventually requiring particle simulation for confirmation.

INHOMOGENEITY AND FINITE Δw

In tokamaks k_o, d and ω_{pe} are functions of minor radius ($k_o d$ taken const.). As a crude first approximation one can simply insert r as an argument of these quantities in Eqns.(1) and (2). This defines contours $w/w_o(r)$=const. in r,w space along which peaking in f occurs, each contour corresponding to a fixed value of sine argument found from Eqn.(2); contours become infinitely dense as $w \to 0$. For moderate levels of transport, an electron's radial diffusion will be channeled along a given contour under the w-wise peaking action of the hybrid wave; particles born centrally in the discharge are accelerated by this mechanism in that k_o peaks [$w_o(r)$ falls] near the center. Growth of a Langmuir wave spectrum occurs as before though radial loss effects can influence the saturation mechanism. At transport levels for which radial diffusive motion is sufficient to displace the particle to a neighboring contour, peak formation at the particle's w becomes attenuated. Particles then exhibit cross-contour diffusion in both r and w, the term in Eqn.(1) previously responsable for peaking now driving diffusion. Choosing 4a as a radial

variation length for k_o (a=plasma radius), we estimate the variation in r for crossing between two peaks to be $\Delta r/a \approx (8\pi/k_o d)w/w_o$, and thus discount transfer between peaking contours as important for particle velocities an appreciable fraction of w_o.

Radial propagation will tend to suppress localization of the Langmuir spectrum (and hence D_L) about contours. In eliminating the intervals in w of unenhanced diffusion (D_L=0), this effect provides a mechanism for filling the "spectral gap" without resort to the nonlinear mechanisms evoked earlier.

Single-transit increments Δw can become a significant fraction of unity, this tending to broaden peaks and eliminate fine peaking structure at lower velocities. Note that the supposition made in this work of a well-defined cone structure does not seem to be borne out for high density tokamaks. A 1-D description has been used; the influence of equilibrium $\mathbf{B}_o$ on instability evolution bears further examination.

DISCUSSION AND CONCLUSION

As remarked earlier, the new phenomena presented here arise from the perturbation of the particle trajectory by the lower-hybrid wave, due account being taken of cone width. In order to place this mechanism in a broader context, we refer to a study of collisionless energy absorption by particles in a plane wave (not restricted to a cone region)[5]; an asymptotic value of spatially-averaged rate of growth of total particle energy ε in accord with the Landau damping rate was found. Paralleling this calculation to find the asymptotic value of spatially-averaged rate of growth of total particle momentum for the plane wave case, we find $dp/dt=(k_o/\omega)d\varepsilon/dt$, consistent with the relation between wave energy and momentum $p_{wave}=(k_o/\omega)\varepsilon_{wave}$. Asymptotic growth rates of both ε and p show influence from the trajectory modification effect which thus is basic to collisionless absorption of driven waves.

In conclusion, the case of lower-hybrid current drive in the presence of a well-defined resonance cone has been studied to illustrate the multiple peaking of the velocity distribution function which can take place in the presence of a localized coherent HF field. This occurs even though field phase seen by a given particle is randomized between successive interactions with the cone. Resultant instability and spectral transfer offer a tentative solution to the "spectral gap" problem.

ACKNOWLEDGEMENTS

The author is grateful for helpful discussions with Professor A.G. Sitenko, Dr. M.P. Evrard, and D. Lebeau.

REFERENCES

[1] T.H. STIX, in Course and Workshop on Applications of RF Waves to Tokamak Plasmas, Varenna, 1985, Internl. School of Plasma Physics "Piero Caldirola", Monotypia Franchi, Citta di Castello (Perugia) Italy, I, p.1.

[2] A.G. SITENKO, Fluctuations and Non-linear Wave Interactions in Plasmas, Pergamon, New York, 1982, p.179.

[3] S. ICHIMARU, Basic Principles of Plasma Physics, W.A. Benjamin, Reading Massachusetts, 1973, p.234.

[4] R.N. SUDAN, Basic Plasma Physics II (Handbook of Plasma Physics 2), Eds. A.A. Galeev and R.N. Sudan, North-Holland, Amsterdam, 1984, p.337.

[5] T.H. STIX, The Theory of Plasma Waves, McGraw-Hill, New York, 1962, p.132.

COMPUTATION OF LOWER HYBRID, NEUTRAL BEAM AND BOOTSTRAP CURRENTS IN CONSISTENT MHD EQUILIBRIA*

R. S. Devoto, D. T. Blackfield+, M. E. Fenstermacher

Lawrence Livermore National Laboratory,
Livermore, CA, USA

P. T. Bonoli, M. Porkolab

Massachusetts Institute of Technology
Cambridge, MA, USA

INTRODUCTION

A possible scenario for steady state current drive in large, high-temperature tokamaks includes current driven by lower hybrid (LH) waves in the outer region with high-energy neutral beams (NB) used for current drive in the core. In addition, provided the poloidal beta is sufficiently high, there can be substantial bootstrap (BS) current, as observed in the TFTR and JET experiments. In work reported previously [1]-[2], a computer code, ACCOME, was written to obtain a solution to the MHD equations which is consistent with current driven by neutral beams, electric fields, and neoclassical (bootstrap) effects. For the computation of the solution to the Grad-Shafranov equation, the SELENE code [3] is used. Iteration is necessary between SELENE and the current-drive computations to obtain a consistent solution. In this paper we describe modifications to ACCOME to enable the computation of LH current in addition to the NB, BS, and OH currents. The next section describes the models used and then the final section presents an application to ITER.

DESCRIPTION OF THE MODEL

The LH module, which has been modified to model elongated plasmas, is based on a code developed for circular geometries [4]. The density and temperatures are taken as algebraic functions of the poloidal flux. The numerically computed flux is fit with bicubic splines. The magnetic field and derivatives are obtained from differentiation of the splines. The ray trajectories are computed with a variable-order predictor-corrector algorithm. The accuracy of this method is examined by computing the deviation from zero of the dispersion relation along a ray path. Errors are typically less than 10^{-5}.

The 1-D ($v_{||}$) Fokker-Planck equation for the fast electrons with quasi-linear diffusion from the lower hybrid waves is solved to obtain the

---

*Work performed under the auspices of the U.S. Department of Energy by the Lawrence Livermore National Laboratory under contract number W-7405-ENG-48.
+On assignment from TRW, Redondo Beach, CA

power absorption and the driven current on each flux surface. The $v_\perp$ portion of the distribution is assumed to be Maxwellian with temperature typically that of the thermal electrons.

The lower hybrid current is included in these calculations in the same manner as the other components. First, SELENE is used to obtain a reference MHD equilibrium from a model current distribution. Next, the values of the neutral beam, ohmic, bootstrap and lower-hybrid currents on the flux surfaces are computed. These currents are summed to yield the total flux-surface-averaged parallel current $\langle j_{||} B\rangle/B_{to}$, where B_{to} is the vacuum toroidal magnetic field at the geometric major radius, R_o. This quantity, together with the pressure function, $p(\psi)$, and the previous values of the toroidal function, $f = R B_t$, and $\langle B^2\rangle$ from SELENE, allows the computation of new values of the function, $ff' = -\mu_o(f^2p' + f\langle j_{||}B\rangle/\langle B^2\rangle)$ on the flux surfaces. This quantity, along with $p(\psi)$, is used in the next solution of the Grad-Shafranov equation with SELENE. This method is continued for 5-10 iterations until the current profile no longer changes between iterations.

APPLICATION TO ITER

We have carried out calculations for ITER in steady state operation with R_o = 5.5 m, a = 1.8 m, κ_{95} = 2.0, and B_o = 5.3 T. Density and temperature profiles are taken to vary as $(1 - \psi)^\alpha$, with α = 0.5 and 1.0 for density and temperature, respectively. Lower hybrid waves are launched from the outer periphery with frequencies of 4.6 or 8.0 GHz. The $n_{||}$ spectrum is typically centered at 1.7 to 1.9. Various half widths of the spectrum, $\Delta n_{||}$, have been tried. Several different neutral beam energies from 1 to 1.5 MeV have been used. The beams are usually aimed at the magnetic axis, which is near R = 5.7 m, but aiming inside of this radius has also been investigated.

The results from one set of calculations are included in Figures 1-4. In this case, the LH frequency is 4.6 GHz with the central $n_{||}$ = 1.9 and a Gaussian half-width of 0.05. This width is quite narrow; it was chosen to maximize the penetration of the LH waves into the plasma. The neutral beam energy is 1.0 MeV with tangency radius, R_{tan} = 5.6 m. The beam footprint is elliptic with a half height of 0.92 m and a half width of 0.56 m. Three beams are used, one aimed in the horizontal midplane, and one above and one below it by 1.3 m. Figure 1 shows the trajectory of the central LH ray in the poloidal plane. The outer surface of the plasma is also plotted. The numbers on the ray represent 10% decrements of the power in the ray. As the ray travels through a poloidal angle of 180°, 80% of the power is absorbed. It reflects near the plasma surface, where the frequency equals the local electron plasma frequency, but less than 1 % of the initial power in the ray remains at this point. The variations of $n_{||}$ along the central ray and two other rays are shown in Fig. 2. We see a slight upshift as the rays pass into a higher toroidal field and then a downshift which continues until the central ray passes into the upper half of the plasma where $n_{||}$ again increases. The plasma current distribution is shown in Fig. 3. The neutral beams drive current in the core, as intended, while the lower

hybrid is restricted to the outer half (in ψ) of the plasma. In computing these currents, the LH power was fixed at 25 MW and we varied the NB power to obtain the desired total plasma current of 18 MA. The components of the current are: NB: 11.1 MA, LH: 2.9 MA, and BS: 4.0 MA. A respectable 23% of the current comes from bootstrap effects, but this is less than the 30% heretofore assumed in ITER steady state scenarios. The figures of merit, γ ($= \langle n_e \rangle I R_o/P$), for NB and LH are 0.53 and 0.36 x 10^{20} A/W-m^2, respectively. Including the bootstrap current raises the overall figure of merit to 0.85 x 10^{20} A/W-m^2. The absorbed power is used in the figure of merit, but the absorption of both LH and NB power is close to 100% for this case. Figure 4 shows a last quantity of interest, the safety factor. The near flattening of the curve in the vicinity of the LH-driven current is readily apparent. The edge (95% flux) safety factor is only 2.8, somewhat less than the design goal of at least 3.0, but some adjustment of the beam deposition would raise the value to this goal.

REFERENCES

1. TANI, K., SUZUKI, M., YAMAMOTO, S., AZUMI, M., "On the Analysis of Beam-Driven Current in a Tokamak," JAERI-M 88-042 (1988).
2. DEVOTO, R. S., TANI, K., AZUMI, M., 15th Eur. Conf. on Cont. Fus. and Plasma Heating, III (1988) 1055.
3. AZUMI, M., KURITA, G., Proc. 4th Int. Symp. Computing Methods in App. Science and Engineering (Paris, 1979) 335.
4. P. T. Bonoli and R. C. Englade, Phys. Fluids 29 (1986) 2937.

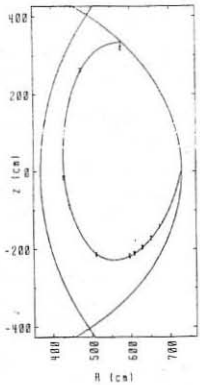

Figure 1. Trajectory of the central LH ray in the poloidal plane. The outer curve is the plasma boundary.

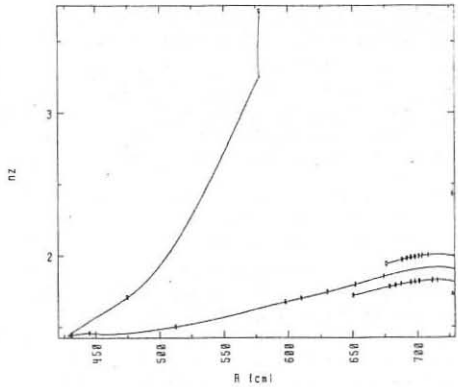

Figure 2. Dependence of $n_{||}$ on the major radius for the central and some adjacent rays. The (barely visible) numbers refer to the percentage absorption of the power in the ray to that point.

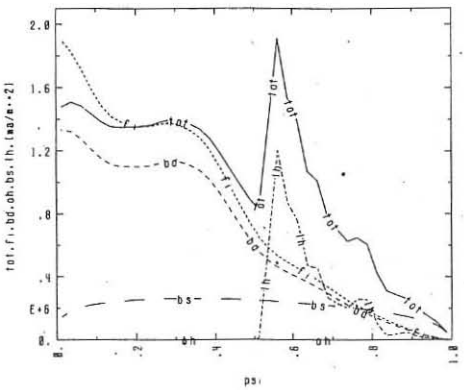

Figure 3. Distribution of current density vs. poloidal flux in the plasma. fi: fast ion current; bd: fast ion current less the partially cancelling electron current; bs: bootstrap current; lh: lower hybrid current; tot: total current.

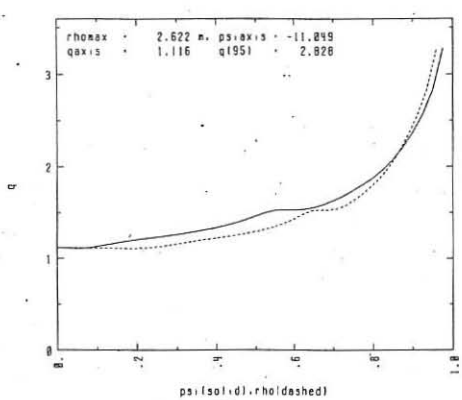

Figure 4. Safety factor vs. poloidal flux (solid line).

CURRENT DRIVE BY ELECTRON CYCLOTRON WAVES IN NET

G. Giruzzi, T.J. Schep, E. Westerhof
FOM Institute for Plasma Physics "Rijnhuizen"
Association EURATOM-FOM, Nieuwegein, The Netherlands

1. Introduction. A potentially attractive scenario for steady-state operations in the Next European Torus relies on the use of lower-hybrid (LH) waves for non-inductive current drive in the plasma periphery and of electron cyclotron (EC) waves in the central region [1]. This scenario is investigated theoretically with the aim of determining the best options for the EC current drive system and of evaluating the expected current drive efficiency. The latter is defined as $\eta = IR_0\bar{n}_e/W$ ($AW^{-1}\ 10^{20}\ m^{-2}$), where I is the total driven current, W the total dissipated wave power, R_0 the major radius and $\bar{n}_e$ the average density. The basic NET parameters for the RF current drive regime are taken to be: $R_0 = 5.25$ m, minor radius in the equatorial plane a = 1.4 m, elongation $\kappa = 2.2$, $B_T = 5.5$ T, $I_p \approx 11$ MA, $\bar{n}_e = 0.75 \times 10^{20}\ m^{-3}$, and $T_e = 15$ keV. The profiles chosen for this study are: $n_e = n_e(0)(1-\rho^6)$, $T_e = T_e(0)(1-\rho^2)$, where $\rho^2 = (\psi - \psi_0)/(\psi_b - \psi_0)$, ψ is the poloidal flux function, and ψ_0, ψ_b its values at the plasma axis and boundary, respectively. The EC waves trajectories in the NET magnetic configuration, obtained from an equilibrium code, are evaluated by means of the toroidal ray-tracing code TORAY [2]. Furthermore, the ray-tracing is coupled to a 3-D bounce-averaged quasilinear Fokker-Planck code [3] which determines the modifications of the electron distribution function due to the absorption of EC wave beams of finite angular spread, the driven current and evaluates the wave damping selfconsistently. The presence of an electron tail sustained by LH waves in the outer part of the plasma ($0.5 \lesssim \rho \lesssim 0.9$) and carrying a current in the range of 3 to 8 MA, is taken into account. The appropriate bounce-averaged parallel diffusion term is added to the Fokker-Planck equation [4].

2. Ray trajectories and linear absorption. Current drive by EC waves requires oblique propagation (i.e., parallel refractive index $N_{\parallel} \neq 0$) and wave absorption at frequency ω significantly different from the EC frequency ω_c, because of the relativistic and Doppler detuning mechanisms. Two scenarios are possible: wave absorption at downshifted frequency ($\omega < \omega_c$) or at upshifted frequency ($\omega > \omega_c$). Although in principle very attractive, the use of downshifted frequencies is of limited interest, since in this case the current drive efficiency deteriorates away from the plasma center because of electron trapping effects [5,3]. For example, for the injection of 45 MW X-mode waves at 80 GHz, such that absorption occurs around $\rho = 0.4$, a current drive efficiency of only $\eta = 0.045$ is found. At 90 MW the efficiency is found to be reduced by a further 25%. Therefore, we limit the further investigation to the upshifted frequency scheme. A wave frequency significantly lower than $2\omega_c$ must be chosen, in order to avoid overlap with downshifted 2nd harmonic absorption, which drives current in the opposite direction [6]. In this frequency range, the X-mode is generally cut off, and the O-mode has to be used. Wave injection from a top port is considered first. This launching configuration is attractive since the magnetic field is nearly constant along the ray trajectory. A suitable choice of wave frequency and direction of injection then allows the interaction with high velocity electrons along most of the ray trajectory in order to optimize the current drive efficiency. However, as shown by the following example, the wave damping is so sensitive to the injection angle that control of the power absorption profile and of the generated current is hardly feasible. Projections of the ray paths in the poloidal cross-section for the O-mode at 180 GHz (i.e., $\omega_c/\omega \approx 0.86$), injected at two slightly different angles $\xi = 23°$ (a) and $\xi = 21°$ (b), where $\xi \equiv \arcsin N_{\parallel}$, are shown in Fig. 1. The corresponding fractions of transmitted wave power are presented in Fig. 2,where open circles indicate the regions in which absorption is due to the 2nd harmonic resonance. Note that in case (a) the absorption is quite strong, peripheral and practically due to the fundamental resonance only, whereas in case (b)

the absorption is moderate, central and mainly due to the 2nd harmonic resonance. This dramatic sensitivity to the injection angle for top launching at $\omega > \omega_c$ is a general result, thus this method is not suited for central current drive, since a remote control of the generated current density profile is, in any case, highly desirable. We then consider wave launching in the equatorial plane. The ray trajectories for the O-mode at 180 GHz are shown in Fig. 3, for $\xi = 45°$ (a), 35° (b), 25° (c), and 15° (d). The corresponding fractions of transmitted wave power are presented in Fig. 4. The figures show that the absorption region can be shifted by varying the injection angle, hence a distribution of wave beams of spread 20° in the toroidal angle can cover all the region $0 \lesssim \rho \lesssim 0.8$ and the power deposition profile can, in principle, be tailored by varying the power input in each beam. Note that only the case (d), in which absorption takes place at $\rho \approx 0.3$ on the high-field side of the flux surfaces, is affected significantly by the 2nd harmonic absorption. This behaviour is practically unchanged if the wave frequency is increased up to 240 GHz and the injection angles are adapted accordingly in order to deposit the wave power in the same spatial regions. The impact of the presence of a LH tail in the plasma periphery on the penetration of the EC waves has been investigated by assuming a LH-driven current of 8 MA, i.e., a current density $J \approx 0.25$ kA/cm^2 originating from the interaction of 85 MW of LH waves with electrons in the range $0.68\ mc \lesssim p_{||} \lesssim 0.76\ mc$. In all these cases, absorption by the LH tail is found to be negligible. This is due to the fact that the resonant velocities generally lie below the velocity range of the LH tail.

3. Current drive by EC and LH waves. We now investigate the current drive efficiency and the current density profiles driven in the case of equatorial launching, for different wave frequencies, powers and launching directions, in order to elucidate the scaling of the efficiency with those parameters and the impact of the electron trapping effects. The main results of this study are summarized in Table I. It appears that: i) the power dependence of the efficiency is very weak, as expected for $\omega > \omega_c$ [7]; ii) the efficiency can be significantly improved by increasing the wave frequency, since this generally enhances the resonant energy; iii) the efficiency deterioration due to trapping effects is less than a factor of 2 when the location of wave power deposition is shifted from $\rho \approx 0.1$ to $\rho \approx 0.5$. It has been checked that in the case of outermost power deposition (last column of Table I) the efficiency increases about 10 % only in the presence of a LH tail carrying a current of 3 MA (obtained for an injected power of 35 MW and a LH spectrum interacting in the range $0.65\ mc \lesssim p_{||} \lesssim 0.87\ mc$). The current density profiles corresponding to the cases of the last three columns in Table I are shown in Fig. 5 (curves a, b, and c, respectively). The three profiles are quite broad and partially overlap. Figure 6 shows the current density profile obtained by the 35 MW LH spectrum considered above and by the three beams injected at $\xi = 25°$, 30°, and 35°, with powers W = 15, 120, and 90 MW, respectively. The profile generated by the LH waves alone is also shown (dashed line). The total driven current is I = 10.6 MA, which yields $\eta \approx 0.13$ for the EC waves and a global efficiency (including LH power) $\eta \approx 0.16$. The present example using three beams produces a non-monotonic current density profile. Use of a larger number of narrow beams allows the generation of a smoother spectrum in $N_{||}$, which yields a smoother current density profile.

In conclusion, we have shown that i) the optimum current drive efficiencies for EC waves are obtained using the upshifted resonance scheme, ii) a smooth current density profile can be obtained by appropriately choosing the injection angles for a large number of beams so as to generate a smooth spectrum in $N_{||}$, and iii) the current density profile can be tailored by tailoring the spectrum in $N_{||}$. The obtained efficiency can still be appreciably improved by i) increasing the fraction of power input in the LH waves, which have better efficiency; ii) using EC waves of higher frequency (e.g., 220 GHz); iii) optimizing the wave launching parameters (e.g., launching slightly outside the equatorial plane). A global improvement in the efficiency due to these effects of the order of 30 - 50 % can be expected.

Acknowledgements. Useful discussions with Prof. F. Engelmann are gratefully acknowledged. We thank the NET Team for providing the NET magnetic equilibrium. This work was performed under the Euratom-FOM association agreement, with financial support from NWO and Euratom (NET contract no. 88-151).

REFERENCES

[1] WEGROWE, J.G., et al., Fusion Techn. **14** (1988) 165.
[2] BATCHELOR, D.B., GOLDFINGER, R.C., Rep. ORNL/TM-6844; KRITZ, A.H., et al., (1982) in proc. of 3rd Int. Symp. on Heating in Toroidal Plasmas, Grenoble (France), 22-26 March 1982, Vol. II p. 707.
[3] GIRUZZI, G., Phys. Fluids **31** (1988) 3305.
[4] FIDONE, I., et al., Nuclear Fusion **27** (1987) 579.
[5] CHAN, V.S., et al., Nucl. Fusion **22** (1982) 787; START, D.F.H., et al., Plasma Phys. **25** (1983) 447;COHEN, R.H., Phys. Fluids **30** (1987) 2442; YOSHIOKA, K., ANTONSEN, T.M., Nucl. Fusion **26** (1986) 839.
[6] SMITH, G.R., et al., Phys. Fluids **30** (1987) 3633.
[7] HARVEY, R.W., et al., in *Applications of RF Power to Plasmas*, (AIP, New York, 1987) p. 49.

Table I

$\omega/2\pi$ (GHz)	220	220	180	180	180
ξ	35°	35°	25°	30°	35°
W (MW)	13	6.5	10	75	75
I (MA)	1.12	0.54	0.53	2.45	2.25
η	0.34	0.33	0.21	0.13	0.12
ρ	0.1	0.1	0.1	0.3	0.5

Fig. 1 : Projections of the ray trajectories in the poloidal cross-section for top launching of the O-mode at 180 GHz and: (a) $\xi = 23°$; (b) $\xi = 21°$. Large dots indicate the region where the wave power is absorbed.

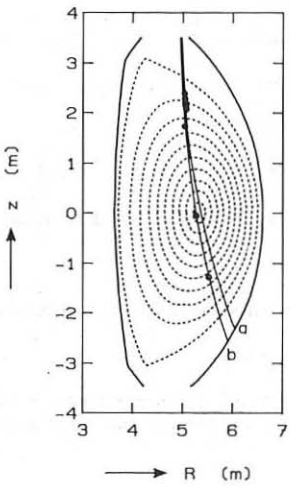

Fig. 2 : Fraction of transmitted wave power versus ρ, for the cases of Fig. 1. Open circles indicate the region where absorption is due to the 2nd harmonic (downshifted) resonance.

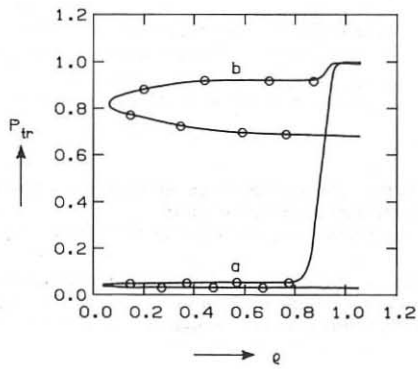

Fig. 3 : As in Fig. 1 for equatorial launching and: (a) $\xi = 45°$; (b) 35°; (c) 25°; (d) 15°.

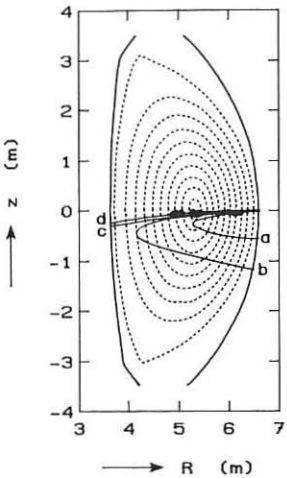

Fig. 4 : As in Fig. 2, for the conditions of Fig. 3.

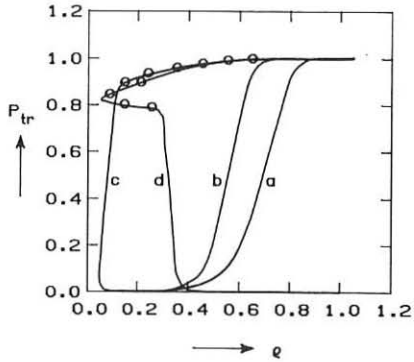

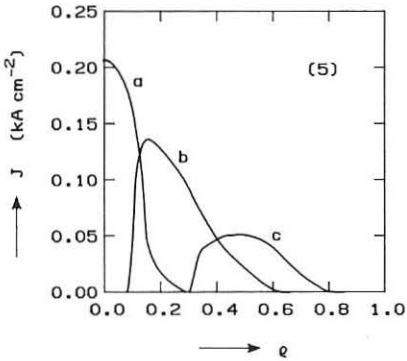

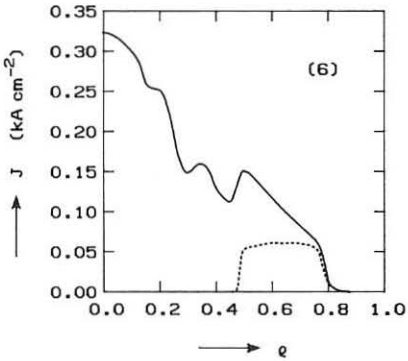

Fig. 5 : Profiles of the driven current density for O-wave beams of frequency 180 GHz, half-width $\Delta\xi = 5°$, injected in the equatorial plane, and:
(a) $\xi = 25°$, W = 10 MW; (b) $\xi = 30°$, W = 75 MW; (c) $\xi = 35°$, W = 75 MW.

Fig. 6 : Profile of the current driven by simultaneous use of 35 MW of LH wave power and of the three EC wave beams of Fig. 5, but with powers W = 15, 120, and 90 MW, respectively. The dashed line is the current driven by the LH waves alone.

BOOTSTRAP CURRENT IN PELLET SEEDED HOT TOKAMAK PLASMAS

M. J. Alava[1] and S. J. Karttunen[2]

[1] Helsinki University of Technology, Department of Technical Physics, SF-02150 Espoo, Finland
[2] Technical Research Centre of Finland, Nuclear Engineering Laboratory P.O.B. 169, SF-00181 Helsinki, Finland

INTRODUCTION

Various non-inductive current drive methods for tokamaks have attracted a great deal of interest during recent years. They render possible a steady–state current which is needed for a continuously operating tokamak reactor. *Bickerton et al.* [1] found that for a sufficiently large poloidal beta β_p, a substantial toroidal current is produced by the neoclassical diffusion from a smaller seed current. This is known as the "bootstrap" effect. Recently, very large bootstrap currents together with neutral beam driven currents have been reported from TFTR [2] and JET [3] tokamaks which has increased the interest of the bootstrap effect. In the pulsed operation the bootstrap effect may save considerably volt–seconds thus increasing the length of the tokamak pulse.

In this paper we study the bootstrap amplification and resulting current and plasma density profiles in various conditions of plasma and seed current parameters. The temperature and density profiles are calculated self–consistently according to neoclassical diffusion coefficients. The effects of different source profiles for particle seeding (e.g., pellets) and plasma heating are also discussed.

BOOTSTRAP CURRENT GENERATION

Assuming equal ion and electron temperatures, the bootstrap effect in a pure hydrogen plasma can be described by the normalized neoclassical steady–state equations [4,5]

$$\frac{dJ}{d\xi} = 2\xi J_s(\xi) - \frac{\xi^{5/2}}{\delta J}(4.88T\frac{dN}{d\xi} + 0.27N\frac{dT}{d\xi}), \tag{1}$$

$$\frac{dN}{d\xi} = -\frac{5}{4}\frac{T^{1/2}J^2}{N\xi^{7/2}}(0.22\alpha + 0.20\frac{\gamma}{T}), \tag{2}$$

$$\frac{dT}{d\xi} = -\frac{5}{4}\frac{T^{1/2}J^2}{N^2\xi^{7/2}}\,0.73\gamma, \tag{3}$$

which determine the current, density and temperature profiles for different particle and heat sources α and γ. The density and temperature are normalized to their central values

n_0 and T_0. The dimensionless radial co-ordinate is $\xi = r/r_0$ where r_0 is the seed radius. J is defined as the total current within the radius ξ normalized to the seed current J_0. In the following we assume for the dimensionless seed current density in Eq.(1) a form: $J_s(\xi) = 1$ when $0 \leq \xi \leq 1$ and $J_s = 0$ elsewhere. The source terms α and γ are given as: $\alpha(\xi) = 2\mu_0 S_P(\xi)/5\pi n_0 \eta_0$ and $\gamma(\xi) = 2\mu_0 S_E(\xi) e^2 \tau_i / 5\pi m_i T_0$ where μ_0 is the vacuum permeability, e is the elementary charge, m_i the ion mass, τ_i the ion collision time and η_0 the plasma resistivity. $S_P(\xi)$ is the particle source (i.e., particle flux per unit length) and $S_E(\xi)$ is the heat source (i.e., power per unit length). For the source profiles we assume constant source densities which in the particle case corresponds to centralized fueling obtainable by pellet injection. The plasma and seed current parameters determine the constant δ in Eq.(1)

$$\delta = (\frac{R}{r_0})^{1/2} \frac{\mu_0 J_0^2}{4\pi^2 r_0^2 n_0 k_B T_0}, \tag{4}$$

where R is the major radius and k_B is the Boltzmann constant. It is easily seen that the condition for the central seed current density $j_0 < 2B_T/\mu_0 R$ guarantees that the central safety factor q_0 stays larger than unity.

NUMERICAL RESULTS

For fixed tokamak and plasma parameters the steady-state Eqs.(1)-(3) become an eigenvalue system in which one of the source terms α (or γ) must be solved iteratively in order to satisfy the boundary condition for the density $n(a) = 0$ (or temperature). Next we study the coupling in the neoclassical steady-state between the plasma temperature and density profiles, and the current resulting from the bootstrap amplification of the externally driven seed current.

Fig.1 shows the total plasma current as a function of the external seed current. For the tokamak and plasma parameters we have taken: $R = 5\,m$, $a = 2\,m$, $B_T = 5\,T$ $T_0 = 20\,keV$, $n_0 = 10^{20}\,m^{-3}$. The total bootstrap amplified current first decreases from the $7\,MA$ level at small seed currents but starts to increase with larger seed values. However, the proportion of the external current starts to dominate. At the same time, the amount of particle fueling (i.e., α) must be decreased to match the boundary condition for the plasma density. Otherwise the plasma minor radius a reduces due to the pinching by the plasma current.

The reason for the behaviour of the total current is illustrated in Figs.2 and 3. We have taken three examples from Fig.1 corresponding to seed currents $100\,kA$, $1\,MA$ and $4\,MA$. For the two first the seed radii ($r_0 = 0.14\,m$ and $0.45\,m$) are taken such that the central q-value is close to unity. In the $4\,MA$ case the seed current is distributed evenly over the whole plasma cross-section. When the seed current becomes large enough, the skin currents diminish as the bootstrap current moves away from the plasma periphery. This is predicted by Eq.(1), i.e., the bootstrap current depends mainly on the product of temperature and the radial derivative of density. Larger seed currents lead to more peaked density and temperature profiles and consequently smoother bootstrap amplifica-

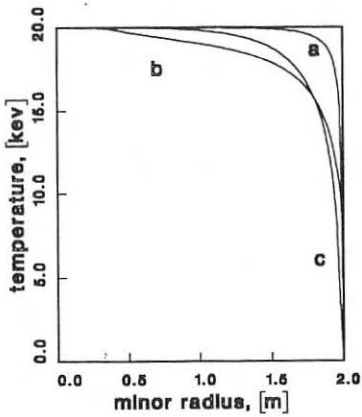

Fig.3. Temperature profiles. Labels as in fig.2.

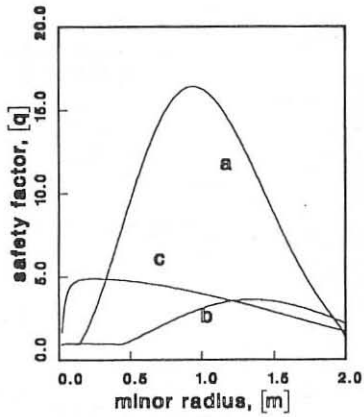

Fig.4. Safety factor profiles. Labels as in fig.2.

An ideal current drive for bootstrap seeding can be obtained with fast phase velocity plasmons by beating of high frequency waves (e.g., Free Electron Laser) [6,7]. FEL–beams can freely propagate in the plasma allowing the localization of the current generation region and the tailoring of the current profile to achieve acceptable equilibria while still reaching a considerable current amplification.

References

[1] R.J.Bickerton, J.W.Connor, J.B.Taylor, Nature Phys. Sci. **229**(1971)110.

[2] M.C.Zarnstorff *et al.*, Phys. Rev. Lett. **60**(1988)1306.

[3] J.G.Cordey et.al., Plasma Phys. Contr. Fusion **30**(1988)1625.

[4] M.N.Rosenbluth, R.D.Hazeltine, F.L.Hinton, Phys. Fluids **15**(1972)116.

[5] D.J.Sigmar, P.H.Rutherford, Nucl. Fusion, **13**(1973)677.

[6] J.A.Heikkinen, S.J.Karttunen, R.R.E.Salomaa, Nucl. Fusion **28**(1988)1845.

[7] B.I.Cohen *et al.*, Nucl. Fusion **28**(1988)1519.

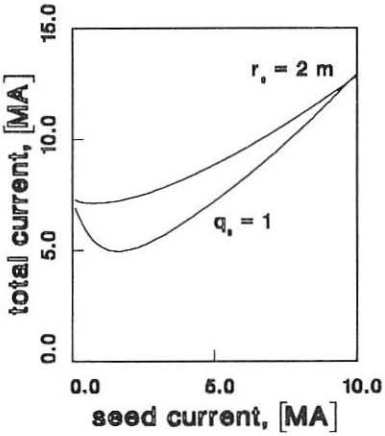

Fig.1. Total current vs. seed current. Seed radius = $2m$ (upper curve) or such that $q_0 = 1$ (lower curve). See text for other parameters

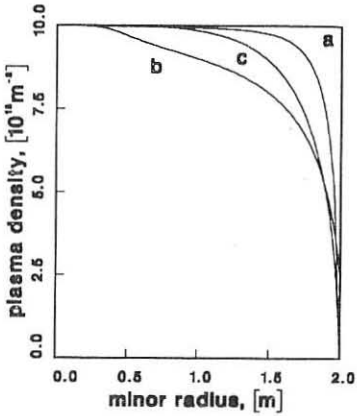

Fig.2. Density profiles for different seed currents. a) $100kA$, b) $1MA$ and c) $4MA$ (see text)

tion. This effect is strong enough to make the stability properties of the final steady-state acceptable, which can be seen from the profiles of the safety factor q in Fig.4. Thus, the q–profile can be controlled by the external seed current while the bootstrap amplification stays considerable, still.

DISCUSSION

Some aspects of the temperature and density dependencies of the bootstrap current generation can readily be seen from the δ–parameter in (4). A change in the peak density n_0 or temperature T_0 can be compensated by changing the seed current J_0 to keep δ constant. This gives the same normalized current J but the true current is different because J is normalized to J_0. Furthermore, a change in the cross–section area has similar consequences, but even more drastic. The same argument gives for the total current a 5/4–power dependence on the minor radius.

The results obtained indicate that a centralized well controlled non–inductive current drive for bootstrap seeding is called for, although some effects of the current localization can be compensated by a more peaked heat or particle deposition profile. However, in reactor size plasmas a central particle feeding by pellet injection is extremely difficult. The bootstrap seeding with present current drive methods is not a trivial question. LH–current drive suffers from density limitations and neutral beam injection requires very high particle energies for central current seeding.

PARAMETRIC STUDY OF HIGH BETA STEADY STATE TOKAMAKS SUSTAINED BY BEAM DRIVEN AND BOOTSTRAP CURRENTS

K. OKANO*, Y. OGAWA and H. NAITOU

Institute of Plasma Physics, Nagoya University, Nagoya, JAPAN.
*Toshiba Research and Development Center, Toshiba Corp., Kawasaki, JAPAN.

1. INTRODUCTION

MHD stability analysis is indispensable in high beta steady state tokamak study, because the plasma current and its profile play an essential role for determining the stability. The authors reported, in a previous paper[1], the development of the beam current drive code which consistently includes 2-D MHD equilibrium code(EQLAUS) and kink and ballooning mode stability analysis by ERATO[2]. This code has been upgraded and includes a self-consistent transport analysis and a bootstrap current calculation[3]. The fast ion Fokker-Planck code has also been replaced by the bounce-averaged type. Therefore, the new code fully includes the toroidal effect on the fast ion current as well as on the beam induced electron current. The beam stopping cross-section model includes the multi-step ionization (MSI) enhancement[4], which is calculated by numerical data base supplied by C. Boley, D. Post et al. who are the authors of Ref.[4].

Many parameter scans were made for a DEMO size tokamak under critical beta conditions. The parameters, used here, are: [R_0=4.55m, a=1.66m, elongation κ= 1.8 (Dee), I_p=19.6MA, B_t=4.7T, β_t=6.05%]. The critical beta MHD equilibrium for this configuration is shown in Fig.1 and its details are described in Ref.[1].

2. SELF-CONSISTENT ANALYSIS WITH MHD AND POWER BALANCE CODES

In Ref.[1], it was suggested that temperature ratio $\bar{T}_i/\bar{T}_e$ could be larger than unity in the beam driven tokamaks and that this high $\bar{T}_i$ feature would enhance the Q value(=fusion power/beam power). A dual component (elec.& ion) 0-D power balance code was used to investigate the above problem. This code includes the coronal equilibrium calculation for radiation cooling rates and mean charge states of various impurities. The power balance equations are given by

$$Q_i/\tau_i = P_{fi} + P_{bi} - P_{ie} \quad (1)$$

$$Q_e/\tau_e = P_{fe} + P_{be} + P_{ie} + P_{oh} - P_{rad} \quad (2)$$

where $Q_i(Q_e)$ are the ion(electron) total energies, $P_{fi}(P_{fe})$ and $P_{bi}(P_{be})$ are the alpha and beam heating terms, P_{ie} is the ion-electron energy relaxation term, and P_{rad} is the total radiation power. The ohmic power P_{oh} is set to zero. The ion energy confinement time τ_i has been assumed as (neo-classical value)/3.0. This choice is not so important, because the $\bar{T}_i$ value is rather dominated by the ion-electron energy relaxation. The electron energy confinement time τ_e is very ambiguous in the present data base. Therefore, $\bar{T}_e$ was given as an input value in this study, and τ_e and the global energy confinement time τ_E were calculated, and compared with the Kaye-Goldston scaling value. Although toroidal momentum balance and rotation effects on driven currents can be also evaluated consistently, the cases with no rotation are mainly discussed in this paper.

The authors' self-consistent code is constructed according to 'the reverse solution algorithm'[1]. First, a critical beta equilibrium is determined by the MHD equilibrium/stability calculation, using EQLAUS/ERATO codes. Next, the driven current profile, including the bootstrap current, and the total pressure profile, composed of thermal, beam ion and fast alpha pressures, converge to those critical beta profiles [$\langle j\cdot B\rangle B/\langle B^2\rangle$ and p_{total} in Fig.1] by optimizing the thermal pressure profile and the beam power distribution $P_{inj}(z)$ in the beam line, denoted in Fig.2. The thermal pressure profile is controlled by changing density profiles, while temperature profiles are maintained during the iteration. The final converged solution is consistent with the critical beta equilibrium given by EQLAUS/ERATO, and gives the optimized $P_{inj}(z)$ and density profiles with consistent $\bar{T}_i$ and τ_E. An example is shown in Fig.1, where the same parameters as in Fig.4-f were used. The minimum major radius of beam center line is expressed by R_{tang}. In this study, R_{tang} = 4.8m has been assumed, except for R_{tang} scan cases. The beam line has a rectangular cross-section with 0.5m width and ±2.5m height. Beam energy E_b and $\bar{T}_e$ were set to 1 MeV and 18 keV, except for these scan cases.

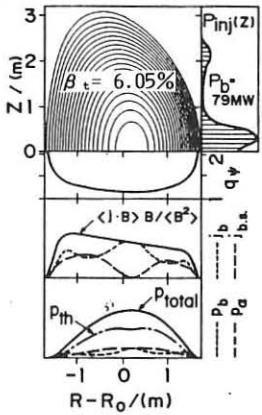

Fig.1: Example equilibrium.

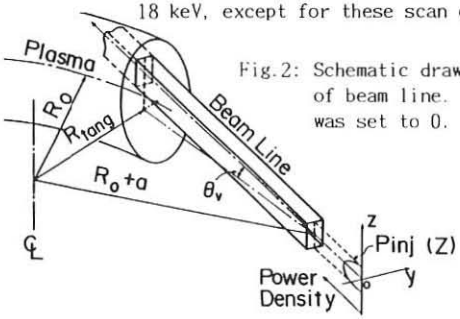

Fig.2: Schematic drawing of beam line. θ_v was set to 0.

3. PARAMETRIC SCANS

ELECTRON TEMPERATURE The $\bar{T}_e$ value is scanned from 16keV to 26keV with the temperature profile $T(\psi)\propto 1-(r/a)^4$, where r is half width of flux surface labeled by ψ. The results are summarized in Fig.3. The solid lines and broken lines are Z_{eff}=1.5 case and Z_{eff}=2.0 case, respectively, where He 5% + Iron impurity is assumed. As shown in [a], $\bar{T}_i$ is much larger than $\bar{T}_e$. The beam power P_b decreases with $\bar{T}_e$[b], but the fusion output P_f also decreases[c], because the density is changed to maintain the total pressure. Thus, the Q value has maxima at $\bar{T}_e$~18keV (Z_{eff}=1.5) and $\bar{T}_e$~22keV (Z_{eff}=2.0)[d]. Both maxima, however, are corresponding to $\bar{T}_i$~30keV. The Q-values for $\bar{T}_i$=$\bar{T}_e$ case, where power balance was switched off, are also plotted in Fig.3-d (dotted line). It is clarified that the high $\bar{T}_i$ feature of beam driven tokamaks enhances the Q-value. The τ_E value, normalized by the Kaye-Goldston L-mode value τ_{KGL}, is plotted in Fig.3-e. The L-mode confinement seems to be sufficient to sustain these equilibria. With $0.8<\tau_E/\tau_{KGL}<1.2$, the Q-value, $7<Q<9$, can be expected. The bootstrap (BS) current ratio I_{bs}/I_{total} is about 35%~40%[f]. The bootstrap current contributes

to the Q enhancement in two ways. The first one is, of course, the direct reduction of beam power. The second is indirect. The beam power reduction results in a lower beam pressure. Thus, the fuel ion pressure (and fusion power) increases and the Q value is enhanced under constant beta conditions.

TEMPERATURE PROFILE In the present algorithm, a different T-profile choice leads to another solution with a different density profile. T_e and T_i profiles were given by $T \propto 1 - (r/a)^{\alpha_1}$. The T-profile scan results are summarized in Fig.4, where α_1 was changed from 2 (parabolic) to 6 (broad). The authors had found, in Ref.[1], the Q value was larger for a broader T-profile, due to fusion power increment. The present results show that I_{bs}/I_t is also larger for a broader T-profile (Fig.4-a, and d,e,f for j_{bs} profiles). The Q value increases from 6 (at α_1=2) to 10 (at α_1=6), and P_b decreases from 104MW to 79MW. However the changes, in $\bar{T}_i$, in the current drive efficiency $\gamma=(n_e/10^{20})\cdot R_0\cdot P_{abs}/I_b$ and in the shinethrough fraction f_s, are very small, where $P_{abs}=(1-f_s)P_b$. The required $P_{inj}(z)$ profiles depend strongly on T-profiles[Figs.4-d,e,f].

BEAM ORIENTATION R_{tang} In the previous study without MSI cross-section enhancement, the shinethrough fraction f_s monotonically increased with R_{tang} increment, because the beam path in plasma decreases with R_{tang}. However, in the new calculation including the MSI enhancement, the f_s minimum point appears near R_{tang}~R_0 (Fig.5). This is because a small R_{tang} and a reduced beam penetration by MSI cause a current drive efficiency deterioration due to trapped ion orbits, especially near the plasma periphery. Therefore, power injected near the periphery should be increased to maintain the current profile. This, in turn, promotes the beam shinethrough through the low density edge. On the other hand, the Q value is maximized at larger R_{tang}(~R_X), where R_X is magnetic axis major radius. Therefore, R_{tang}=4.8m(~R_X) has been chosen as the standard value in this study.

BEAM ENERGY Increasing E_b ($\lesssim$ 2 MeV) improves the γ value. But it enhances the shinethrough, and reduces P_{TCT} (=the fusion power due to the beam ion direct reaction), as shown in Fig.6. Moreover, $\bar{T}_i$ decreases with E_b, because a larger beam power goes to electrons with a higher E_b. As a result, the Q value is maximized at E_b=1.0~1.2 MeV with Q~9. This Q value is twice as large as the no BS current case without power balance analysis[1] and the optimum E_b has been doubled due to the MSI cross-section enhancement. However, the Q deterioration, by decreasing E_b down to 600keV from 1 MeV, is only 17%, and $\bar{T}_i$ attains 37keV.

In summary, the ion temperature $\bar{T}_i$ is much larger than $\bar{T}_e$ in beam driven tokamaks. This high $\bar{T}_i$ feature improves the Q value. The bootstrap current attains 20~40% in the total driven currents. The MSI cross-section enhancement also contributes to the Q enhancement, because the beam orientation can be optimized with an acceptable shinethrough. The Q value is doubled by these three effects and is maximized at E_b~1 MeV with Q~9. However, if the toroidal rotation is fairly suppressible, the Q value for E_b= 600 keV is still high enough (~7.5) with a very high $\bar{T}_i$ mode ($\bar{T}_i$=37keV for $\bar{T}_e$=18keV).

The authors acknowledge Dr. D. Post for providing MSI data base. And Dr. A. Hatayama is also thanked for his efforts in power balance code development.

[1]Okano,K. et al., IPPJ-878, Nagoya, Japan(1988). Accepted by Nucl.Fusion.
[2]Gruber,R., et al., Comput. Phys. Commun., 24, 363(1981).
[3]Hirshman,S.P. and Sigmar,D.J., Nucl.Fusion 21, 1079(1981).
[4]Boley,C.D., Janev,R.K. and Post,D.E., Phys.Rev.Lett. 52, 534(1984).

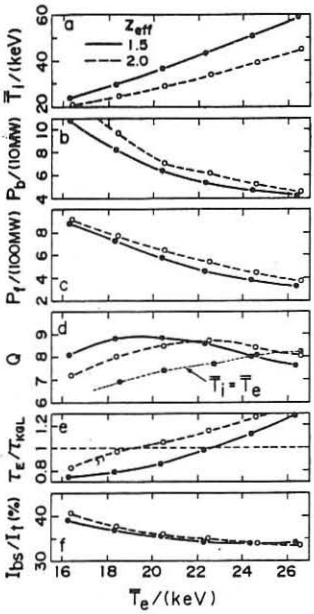

Fig.3: Electron temperature scan. E_b=1 MeV. Z_{eff}=1.5 and 2.0. Z_{eff}=2.0 for $\bar{T}_e$=$\bar{T}_i$ case.

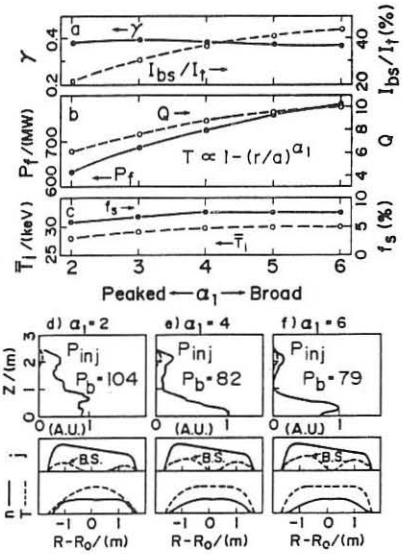

Fig.4: Temperature profile scan. $\bar{T}_e$=18keV, E_b=1 MeV, Z_{eff}=1.5.

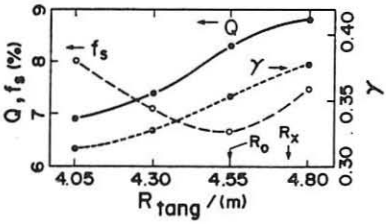

Fig.5: R_{tang} scan. $\bar{T}_e$=18keV. E_b=1 MeV, Z_{eff}=1.5, α_1=4.

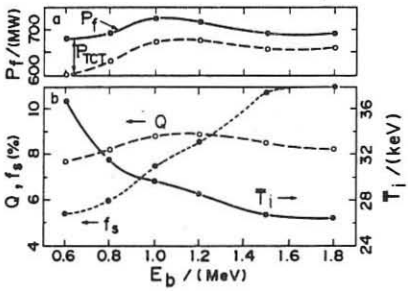

Fig.6: Beam energy scan. $\bar{T}_e$=18keV, Z_{eff}=1.5, α_1=4.

FAST-WAVE ION CYCLOTRON CURRENT DRIVE FOR ITER AND PROSPECTS FOR NEAR-TERM PROOF-OF-PRINCIPLE EXPERIMENTS*

D. W. Swain, D. B. Batchelor, M. D. Carter, E. F. Jaeger, P. M. Ryan, and D. J. Hoffman

Oak Ridge National Laboratory, Post Office Box 2009, Oak Ridge, TN 37831-8071, U.S.A.

INTRODUCTION

Low-frequency fast-wave current drive (FWCD) with frequencies in the range from 30 to 100 MHz looks promising for current drive in ITER. Its theoretical efficiencies are comparable to other current-drive techniques, and it could be significantly cheaper than other proposed current drive methods because of the ready availablity of inexpensive (<$1/W), efficient, multi-megawatt rf power sources.

The most critical issues for FWCD are concerns about the acceptability and survivability of an appropriate antenna launching system and the lack of an experimental demonstration of FWCD in a large tokamak. We describe an antenna array that is flush with the first wall of ITER and should be able to survive in the plasma environment, present theoretical calculations of FWCD in ITER, and show results from a brief survey of some present-day tokamaks in which it might be possible to carry out FWCD proof-of-principle experiments.

ITER ANTENNA DESIGN AND MODELING

A conceptual design for a FWCD antenna array for ITER is shown in Fig. 1. The system consists of 40 current straps in an array of 10 straps toroidally by 4 straps poloidally. Each strap is approximately 70 cm high by 20 cm wide, with a 20-cm spacing between the straps. The straps are mounted in four modules that can be installed through two adjacent large radial ports on the midplane. One section of blanket structure has been thinned down approximately 60 cm to allow some of the straps to be located between the ports and form a continuous array. Feed lines for rf power, cooling, etc., all come through the radial ports. The modular construction allows for easy installation that can be carried out remotely with proper design, and the array of contiguous current straps launches a k_z spectrum that efficiently drives current in ITER, as is shown below.

A simple 1-D model with step-function density and temperature profiles that assumes all launched waves will be absorbed by plasma electrons (a valid assumption in ITER) is used for fast optimization of launcher properties. The antenna array is modeled as a number of current straps a fixed distance from the plasma, with a perfectly conducting wall behind the straps. Calculations have been carried out for a number of antenna configurations and phasing between straps. Figure 2 shows an optimized wave power spectrum vs toroidal wave number.

---

*Research sponsored by the Office of Fusion Energy, U.S. Department of Energy, under contract DE-AC05-84OR21400 with Martin Marietta Energy Systems, Inc.

Current-drive efficiency, calculated using a formula of Ehst [1], indicates that with a toroidal phase difference between straps of about $\pi/4$, a current-drive efficiency $I_{rf}/P_{rf} = 0.106$ A/W is obtained at $n_e = 1 \times 10^{20}$ m^{-3} and $T_e(0) = 30$ keV for a frequency of 60 MHz, which corresponds to $\gamma = n_e R_o I_{rf}/P_{rf} = 0.5$ (n_e in 10^{20} m^{-3}, R_o in m, I_{rf} in A, P_{rf} in W).

The full wave ICRF code ORION [2] has been modified to calculate flux-surface-averaged driven current using the same simple analytic current drive model as the 1-D model. The wave damping processes included are ion cyclotron damping by fuel components, electron Landau damping, electron TTMP, and absorption by fusion decay products such as alpha particles. Figure 3(a), calculated using ITER reference density and temperature profiles, shows the two-dimensional deposition in ITER of total power launched; Fig. 3(b) shows the flux-surface average of power absorbed. The small difference between total power absorbed (solid line) and power absorbed by electrons (dashed line) indicates that the great majority of the power is absorbed by the electrons. Ion cyclotron resonance locations are also shown on the figure. The D resonance is outside the plasma, while almost all the launched power is absorbed by the electrons before the waves reach the second harmonic tritium resonance. Current-drive calculations from the ORION code are in approximate agreement with the 1-D results.

PROOF-OF-PRINCIPLE EXPERIMENTS

While these theoretical results indicate the potential for an efficient, inexpensive fast-wave current drive system for ITER, no experimental demonstration of the technique has been carried out. We have surveyed several existing tokamaks to evaluate their capability for performing a proof-of-principle current-drive experiment in the near future; the results are summarized in Table 1. We have used machine and plasma parameters similar to values that have been obtained from experiments on each machine, and have used values of rf power and frequencies that are now available (or will be shortly) at the different machines. A similar calculation for ITER is shown for comparison. The existing machines are discussed in the following paragraphs.

Table 1. Comparison of existing experiments using 1-D slab model

	T_e (keV)	P_{rf} (MW)	R_o (m)	n_e (10^{20}m^{-3})	γ	I/P (A/W)	I_{rf}[a] (MA)	I_{rf}/I_p
JET	>10	32	3.0	0.3	0.19	0.216	~5	~1
TFTR	>10	10	2.6	0.3	0.18	0.23	~1.6	~0.5
DIII-D	>6	2	1.7	0.2	0.15	0.48	~0.7	~1
ITER	10-20	120[b]	5.5	1.0	~0.5	~0.1	~8	~0.5

[a] - Assumes 70% efficiency from generator to plasma, no bootstrap current.
[b] - 80 MW into plasma for central current drive; LHH or ECH for profile control.

TFTR. The fast-wave ICH experiment on TFTR has four current straps mounted in two adjacent ports [3]; up to 10 MW of rf power at 47 MHz should be available in the near future. The theoretical results shown in Table 1, computed for a phase shift of approxmiately $\pi/2$ between current straps in each port, indicate that significant plasma current could be driven using FWCD in TFTR, especially for plasma parameters corresponding to the "super-shot" mode of operation.

JET. The JET tokamak has high-temperature plasmas, an abundance of rf power, and 16 current straps mounted in 8 pairs spaced approximately uniformly toroidally around the machine. However, the calculations indicate that the present current strap arrangement is not optimal for FWCD. The n_z spectrum,

shown in Fig. 4, is basically the wide spectral envelope of a two-strap array (dashed line), modulated into a series of spikes by the effect of having eight two-strap arrays in the machine. Consequently, a large fraction of the rf power is deposited in the bulk of the electron distribution (i.e., $\omega/k_z < v_{Te}$), and the current-drive efficiency is quite sensitive to the relative phasing of the antennas. In addition, the effect of changes in plasma parameters due to the large rf heating could mask the interpretation of the experiment. The construction of a new multi-element launcher array would provide a much more controlled experiment.

DIII-D. The DIII-D experiment can generate high-temperature plasmas with auxiliary ECH power. However, only 2 MW of rf power at 30 to 60 MHz is available. No fast-wave antenna array exists, although one has been proposed [4] that would use a four-strap antenna array mounted in a special port. The results of modeling this array, shown in Fig. 5, indicate that a smooth n_z spectrum with high directivity could be launched, with the bulk of its power in the range of n_z (corresponding to $v_{Te} < \omega/k_z < c$) that gives good current-drive efficiency. Operation at low density and relatively high electron temperature (using ECH) could result in current drive efficiencies of almost 0.5 A/W. The full-wave 3-D calculation gives a value of ~0.7 A/W and indicates that the single-pass absorption by the electrons in DIII-D is not high for some launched n_z values, which could result in an eigenmode in the plasma-vacuum vessel system. However, the majority of the launched power is at n_z values that are highly absorbed.

CONCLUSIONS

Fast-wave current drive appears promising for ITER, with calculated values of current-drive efficiency comparable to or better than other proposed current-drive techniques. A conceptual design for a remotely maintainable launcher array has been carried out.

A proof-of-principle experiment to demonstrate the feasibility of FWCD is needed. Several existing devices have been examined and could carry out such an experiment in the near future if it were high in the experimental priorities. In addition, other devices not discussed here (e.g., ASDEX, JT-60, Tore Supra) also have the plasma parameters and rf power to do FWCD experiments, with new antennas.

Virtually none of the machines discussed now has adequate means of controlling the relative phase of closely coupled antennas, a necessary condition for good current-drive experiments. This problem is being addressed in the U.S. rf program at ORNL and in programs at other laboratories throughout the world.

REFERENCES

[1] D. A. Ehst and K. Evans, Jr., Nucl. Fusion **27** (1987) 1267.

[2] E. F. Jaeger, D. B. Batchelor, H. Weitzner, and J. H. Whealton, Comput. Phys. Commun. **40** (1986) 33.

[3] J. R. Wilson et al., "ICRF Heating on the TFTR Tokamak for P_{rf} up to 2.5 MW," presented at the Twelfth International Conference on Plasma Physics and Controlled Nuclear Fusion Research, Nice, France, October 12-19, 1988 (proceedings to be published).

[4] R. Freeman and M. J. Mayberry (private communication).

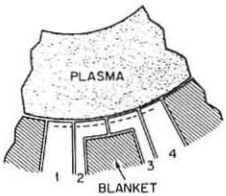

Fig. 1. Antenna layout for ITER (equatorial cross section).

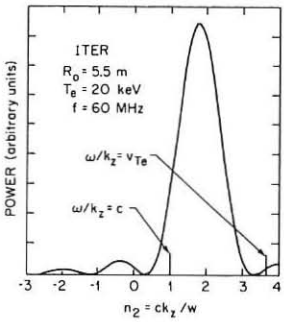

Fig. 2. P versus n_z for ITER.

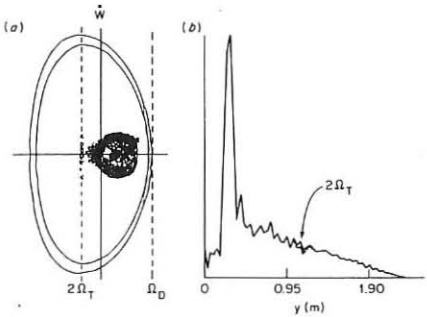

Fig. 3. ICRF power deposition in ITER for $n_z = 2.0$.

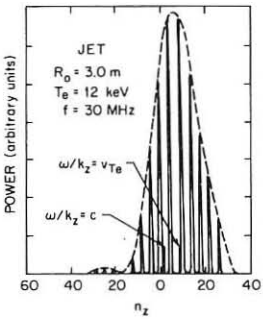

Fig. 4. P versus n_z for JET.

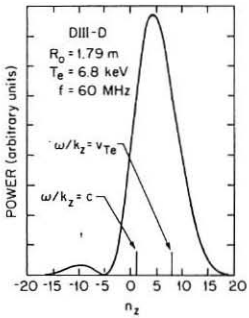

Fig. 5. P versus n_z for DIII-D.

HIGH EFFICIENCY KINETIC-ALFVEN-WAVE CURRENT DRIVE

S. Puri and R. Wilhelm
Max-Planck Institut für Plasmaphysik, EURATOM Association,
Garching bei München, Federal Republic of Germany

Non-inductive current drive for attaining steady-state operation is a significant feature of the future Tokamak devices such as NET and ITER. However, the poor current-drive efficiency ($\gamma = Rn_{20}I/P \lesssim 0.4$) of the schemes presently under consideration limits the fusion power gain to $P_{fusion}/P_{auxiliary} \sim 5$, which is an order of magnitude lower than the requirements of an economic fusion reactor [1].

In this paper we show that the combination of bootstrap current [2] and optimized antenna parameters can lead to high efficiency kinetic-Alfven-wave current drive in reactor-grade plasmas *with elongated cross sections*. The optimal parameters include (i) finite, non-zero azimuthal wave number $m = 1$, (ii) large toroidal wave number $n = 5 - 8$, (iii) an antenna array consisting of at least n elements with adjacent elements phased $\pi/2$ apart, (iv) Faraday shielding, and (v) plasma cross-section elongation $\varepsilon > 1.5$, which together with the finite β, helps in moderating the trapped-particle effects by locating the resonance close to the plasma axis.

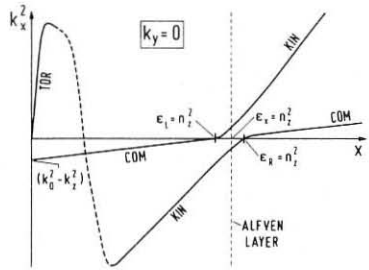

Fig. 1

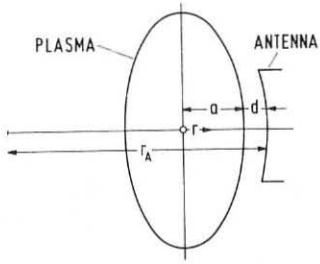

Fig. 2

Figure 1 shows the qualitative Alfven-wave dispersion characteristics in a slab geometry for $k_y = 0$. The plasma density and temperature are assumed to increase along x and the magnetic field is in the z direction. ϵ_x, ϵ_y and ϵ_z are the components of the dielectric tensor ϵ, $\mathbf{n} = \mathbf{k}/k_0$, and $\epsilon_{L,R} = \epsilon_x \pm i\epsilon_y$. The propagating cold-plasma torsional Alfven wave (TOR) becomes the evanescent hot-plasma KIN at $\varsigma = v_p/v_t \approx 1$ which typically occurs close to the plasma edge for $T_e \sim 100\,eV$. Near the Alfven layer at $\epsilon_x = n_z^2$, KIN assumes a propagating character and is subject to strong Landau damping. The Alfven resonance $\epsilon_x = n_z^2$ is approached via coupling to the weakly

evanescent compressional Alfven wave (COM). Near the Alfven layer, the evanescent COM launched by the antenna partly couples to the propagating COM in the plasma interior and partly converts to the propagating KIN via the process of wave conversion [3]. The energy coupled to KIN is readily assimilated through electron Landau damping giving rise to plasma heating and current drive [3,4].

The success of this scheme is critically dependent upon two factors, namely, (i) the launching of COM with a minimum of evanescence between the antenna and the Alfven layer, and (ii) efficient wave conversion from COM to KIN near the Alfven layer. These happen to be contradictory requirements: The first is best satisfied at low values of m and n, while the second demands the choice of finite $m = 1$, and large $n = 5 - 8$ values [5,6].

The requirement of a finite azimuthal wave number $m = 1$ and a large toroidal wave number $n = 5 - 8$ imposes the serious penalty of limited radial access of the antenna energy into the plasma due to the increased evanescence experienced by COM. Acceptable antenna coupling ($Q \sim 15$) is feasible only for the resonance layer location $r_0 > 0.67a$, corresponding to a penetration depth $p = 0.33a + d$, where a is the plasma radius and d is the antenna-plasma separation [5,6]. Current drive confined to the outer one-third plasma radius would be undesirable. The present trend towards elongated plasma cross-sections together with the shift in the plasma axis due to finite β effects in reactor-grade plasmas radically improves this dismal outlook.

For the elliptical plasma cross-section of elongation ε (Fig.2), the antenna radius is given by

$$r_A \approx (a + d)\varepsilon^2 \ . \tag{1}$$

The increase in the antenna radius leads to a reduction in the wave evanescene. Since the penetration depth p is considerably less than the antenna radius, a reasonable estimate of p is possible using the slab approximation corrected for the cylindrical geometry. Let $k_y = \tilde{r}^{-1}$ and $k_z = n(R + r)^{-1}$, where $\tilde{r} = r_A - (a + d) + r$ and R is the plasma major radius. The wave evanescence causes a steady decrease of the wave amplitude as we move away from the antenna. The energy density at the resonance position r_0, relative to its value at the antenna surface is $G = \exp(-\Gamma)$, where

$$\Gamma = 2ia \int_{\rho_0}^{1+\rho_d} k_x(\rho)\, d\rho \ , \tag{2}$$

$\rho = r/a$, $\rho_0 = r_0/a$, $\rho_d = d/a$, k_x is given by the approximate COM dispersion relation

$$k_x^2 = k_0^2 \epsilon_x - k_y^2 - k_z^2 \ , \tag{3}$$

and $\epsilon_x = 1 + (n_z^2 - 1)(1 - \rho^2)/(1 - \rho_0^2)$ for a parabolic density profile. G is plotted as a function of ρ_0 and ε for $n = 6$ in Fig.3, assuming $A = R/a = 4$, $\rho_d = 0.1$, and $n_z^2 \gg 1$.

As ε increases from 1 to 2, ρ_0 can be lowered from 0.67 to 0.37 keeping the antenna coupling unchanged.

Further enhancement in the penetration of antenna energy into the plasma interior is contributed by the finite β in reactor-grade plasmas. Finite β is accompanied by an outward shift of the plasma axis which for the reactor parameters may amount to as much as a quarter of the plasma radius. Thus, it would be possible to locate the resonant layer at $\rho_0 \gtrsim 0.12$, i.e., practically the entire plasma volume is accessible for the KIN current drive.

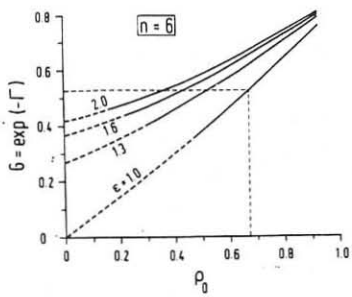

Fig. 3

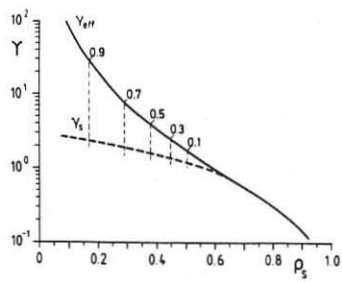

Fig. 4

The current density induced in the plasma is related to the power density by

$$j(\rho) \approx \frac{e}{m} \frac{\sigma(Z)\Omega(\rho, A)P(\rho)}{\nu_{ei}(\rho)v_A(\rho)} , \tag{4}$$

where $v_A(\rho)$ is the local Alfven speed, $\nu_{ei}(\rho)$ is the Spitzer collision frequency, $\sigma = (1 + \nu_{ei}/\nu_{ee})^{-1} = (1 + 0.5Z)^{-1}$ is the fraction of the subthermal wave momentum transferred to the bulk-plasma electrons, while $\Omega = \left[1 - (\rho/A)^{1/2}\right]^2$ is the efficacy of ohmic current drive [7] available from the momentum contained in the bulk-plasma electrons. Physically the two-step process consists of storing canonical angular momentum in the trapped particles by Ware [8] pinch and subsequent release via inverse Ware pinch, with the fraction $\sigma\Omega$ of the canonical angular momentum delivered by the wave supplying the current drive. In so far as the bootstrap current too originates from the release of stored canonical angular momentum, only the fraction $(\sigma\Omega/B_\theta)(\rho/A)^{1/2}Tdn/dr$ may be available as the net plasma current. The current-drive efficiency becomes

$$\gamma = \frac{< n_{20} > RI}{P_P} = \frac{< n_{20} >}{2\pi} \frac{e}{m} \frac{\sigma(Z) \int_0^1 j(\rho)\rho \, d\rho}{\int_0^1 \Omega^{-1}(\rho, A)\nu_{ei}(\rho)v_A(\rho)j(\rho)\rho \, d\rho} , \tag{5}$$

where $< n_{20} > \times 10^{20} m^{-3}$ is the volume-averaged plasma density. Equation (5) does not include the contribution of the bootstrap current [2] I_b to the total plasma current I_p. In the presence of the bootstrap current, the demands on the current drive in the unfavorable outer region are significantly diminished. Maximum current-drive efficiency would be obtained if the wave driven seed current $I_s = I_p - I_b$ is spread with a constant density j_s in the region $0 \leq \rho \leq \rho_s \approx \sqrt{I_s/q_a I_p}$, where q_a is the safety factor at the plasma boundary and $j_s = (2/\mu_0 r_T) B_t$ is the highest current density consistent with the MHD stability requirement $q \geq 1$. Assuming $n_e(\rho) = n_{e0}(1-\rho^2)^{\chi_n}$ and $T_e(\rho) = T_{e0}(1-\rho^2)^{\chi_T}$ yields the seed-current-drive efficiency

$$\gamma_s = \frac{13.5\mu^{1/2}\sigma(Z) < \beta >^{1/2} < T_{keV} >}{Z < \ln\Lambda >} \frac{\chi_T + 1}{\chi_n + 1} (\chi_n + \chi_T + 1)^{1/2} \Im \,, \tag{6}$$

where μ is the atomic mass number, $< \beta >$ is the volume-averaged toroidal β, $< T_{keV} >$ is the volume-averaged electron temperature in keV, and $< \ln\Lambda >$ is the weighted Coulomb logarithm. The profile and trapped-particle effects are contained in

$$\Im(\rho_s, \alpha, A) = \frac{\int_0^{\rho_s} \rho \, d\rho}{\int_0^{\rho_s} (1-\rho^2)^{-\alpha} \left[1 - (\rho/A)^{1/2}\right]^{-2} \rho \, d\rho} \,, \tag{7}$$

where, $\alpha = 1.5\chi_T - 0.5\chi_n$. The pertinent figure of merit is contained in the effective current-drive efficiency

$$\gamma_{eff} = \frac{I_p}{I_s} \gamma_s \,. \tag{8}$$

Figure 4 is a plot of γ_s and γ_{eff} as a function of ρ_s and α for $A = 4$, $\chi_n = 1$, $\chi_T = 1.5$, $\mu = 2.5$, $< \beta >= 0.05$, $< T_{keV} >= 15$, $Z = 1.5$, $q_a = 3.5$ and $< \ln\Lambda >= 17$. For $0.10 \leq I_b/I_p \leq 0.90$ (indicated along the γ curves in Fig.4), $0.50 \geq \rho_s \geq 0.17$, and $1.75 \leq \gamma_{eff} \leq 27.0$. Although the uncertainty in I_b/I_p precludes a more precise estimate of γ_{eff}, kinetic-Alfven-wave current drive promises to be a highly credible proposition and merits careful consideration.

[1]. WILHELM, R., in *Proc. 15th Symp. on Fusion Tech.*, Utrecht, 1988.
[2]. BICKERTON, R. J., Comments Plasma Phys. Controlled Fusion **1**(1972)95.
[3]. HASEGAWA, A., CHEN, L., Phys. Rev. Lett. **32**(1974)454.
[4]. HASEGAWA, A., Nuclear Fusion **20**(1980)1158.
[5]. PURI. S., Nucl. Fusion **27**(1987)229.
[6]. PURI, S., Nucl. Fusion **27**(1987)1091.
[7]. WESSON, J., in *Tokamaks*, Clarendon Press, Oxford (1987), p. 95.
[8]. WARE, A. A., Phys. Rev. Lett. **25**(1970)15.

STABLE OPERATING REGIMES IN NET WITH RESPECT TO ALFVÉN WAVE INSTABILITIES DURING NEUTRAL BEAM CURRENT DRIVE

D. Eckhartt

Max-Planck-Institut für Plasmaphysik, EURATOM Association
Garching bei München, Federal Republic of Germany

Supra-thermal ions can contribute to the steady-state current in future large tokamak machines like NET or ITER. The fast-ion population is generated by collisional slowing-down of high-energy ions which were injected as neutral atoms in quasi-tangential direction and ionized by plasma interactions. Depending on the initial beam shape these fast ions can excite microinstabilities of the Alfvén-wave type which are driven by the gradients in velocity-space. The ensueing plasma turbulence is expected to slow down the fast ions very quickly. This effect reduces the current drive efficiency which otherwise is comparable to that of other current drive schemes like lower hybrid waves where the toroidal current is carried by high-energy resonant electrons.

According to linear theory one type of this class of instabilities is excited when the following two criteria are violated at the same time: (1) the fast ion velocity component parallel to the magnetic confining field is lower than the local Alfvén-speed v_A:

$$v_{b\parallel} < v_A = \sqrt{B^2/\rho \cdot \mu} \qquad (1)$$

where ρ is the mass density of the plasma $\sum_i n_i m_i$. (2) The energy density stored in the fast ion population, normalized to the energy density of the thermal plasma, remains below a certain threshold:

$$\frac{\overline{n_b \cdot E_b}}{3/2 \cdot (n_e T_e + n_i T_i)} < C \cdot v_b/v_e \qquad (2)$$

where v_b and v_e are the velocities of the beam ions and thermal electrons, resp., and C is a number which depends on details of the shape of the injected beam, and is likely to exceed 4 [1]. The energy density in the fast ions grows linearly with the power $P_b = (E_b \cdot I_b)$ of the injected neutral beam. The two stability conditions can be re-formulated when referring to typical plasma scenarios which are anticipated for neutral beam current drive in NET and for which the deposition of neutral beam power and particles was calculated numerically [2]. In particular, for the injection of a beam of neutral deuterium atoms of energy E_b in a DT-plasma with $Z_{eff} = 2$ (fully ionized carbon) one has for the condition of eq. (1):

$$E_b < 207{,}3\ B^2/n_{i\,9} \qquad (3)$$

where E_b is in keV, B in Tesla, n_{19} in units of 10^{19} m^{-3}. The second condition eq. (2) can be expressed by using a relation from [3] for the average energy density of the fast ions (assuming $n_eT = n_iT_i$):

$$\frac{P_b}{e \cdot V_P} \cdot H\,(n_e,E_b)\,\frac{\tau_{se}\,(T_e,n_e)}{6 \cdot n_e \cdot T_e} \cdot G_e(E_b/T_e,\ \tau_{se}/\tau_{cx}) < 4 \cdot \frac{v_b}{v_e} \qquad (4)$$

Here V_P is the plasma volume, H is the radial deposition profile, or "shape-factor" of Ref. [2], describing the local production rate of fast ions in this particular plasma-beam configuration, τ_s is the Spitzer ion-electron momentum exchange time, G_e is the electron energy-transfer factor, it is a function of E_b/T_e and τ_{se}/τ_{cx}, where τ_{cx} is the lifetime of a fast ion before it leaves the fast-ion population via a charge exchange collision with either a neutral fuel atom or a partially ionized impurity ion, or via radiative recombination with a plasma electron. If we assume these processes to be sufficiently frequent, G_e varies rather slowly with (E_b/T_e) in the parameter range of our interest [3], hence we can set it constant: $G_e = 0.15$. We now re-write eq. (4) to show the dependences on the main beam and plasma parameters:

$$\frac{P_b \cdot T_e}{E_b^{1/2}} \cdot H\,(E_b/n_e) < C^* \cdot n_e^2 \qquad (5)$$

where C* is another numerical constant. When comparing the two stability criteria, eqs. (3) and (5), with respect to their explicit density dependences, two opposite trends become apparent: eq. (3) favours low-density operation by allowing to raise the beam energy prop. n_e^{-1}, eq. (5) favours high-density scenarios since the right-hand side grows as n_e^2. Hence, by combining the two criteria into one we might expect to find a region in parameter space where the risk of exciting Alfvén-wave instabilities becomes independent of plasma density.

Using the NET model plasma of Ref. [2] and the deposition calculations based thereupon for quasi-tangential injection (40° with respect to the major radius direction), we have evaluated the two local criteria point by point along the minor radius for a number of scenarios. It turned out that the ratio of energy densities (cf. eq. (4)) decreases monotonically outwards from the plasma centre owing to the fact that the deposition profiles peak on axis (except for very high plasma densities and very low beam energies). This implies that the condition on energy densities is fulfilled everywhere in the plasma when it is satisfied at its centre. In addition, the data of Ref. [2] show that the central deposition rates H(0) have a smooth dependence on the ratio (E_b/n_{eo}) tending towards saturation (or even descent) beyond the maximum value considered in [2], namely $E_{b100}/n_{e19} = 10/7{,}5$, where the deuteron beam energy is in units of 0,1 MeV, and the electron density in 10^{19} m^{-3}. In the following calculations we assume a constant value of H(0) for higher (E_b/n_e)-values (which is an even more pessimistic approach). The above relation between H and E_b/n_e is now used to establish the stability criterion eq. (4) in the (E_b,n_e)-plane, see Fig. 1. Here we show, as an example, the curves labelled

(1) and (2) for two different values of the product ($P_b \cdot T_e$): stability is ensured on the right-hand, high-density side of either curve. Another border-line between areas of stability and instability in the (E_b,n_e)-plane is defined by the condition that the particle velocity is smaller than the Alfvén-velocity, cf. eq. (3). It is plotted in Fig. 1 as the curve E_b (v_A) for B = 5 Tesla: the parameters for stable operation are in the hatched part below the curve. By combining both sets of curves we find a "stability-diagram" of the beam-plasma configuration in NET, for which the deposition calculations of Ref. [2] were made. It can be interpreted as follows: both conditions, eqs. (3) and (5), must be violated at the same

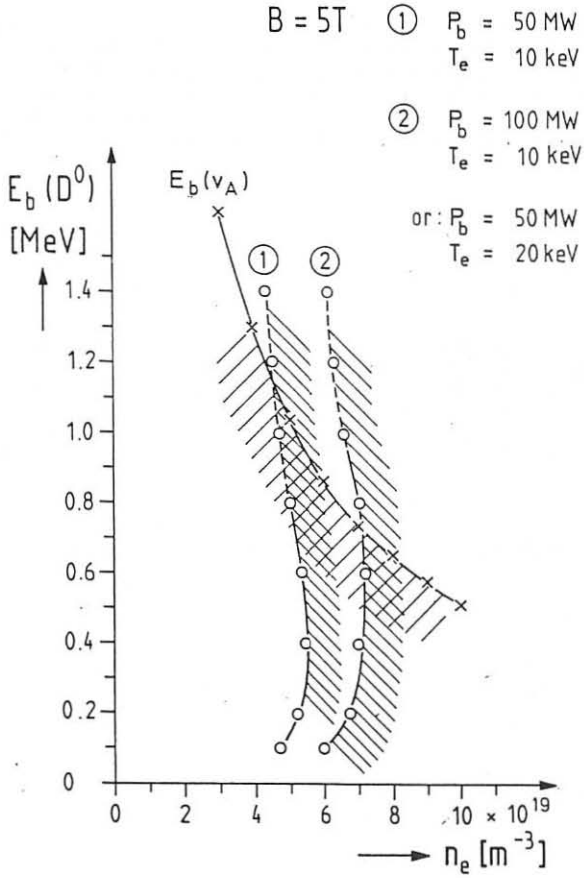

Fig. 1

time for an unstable situation to arise. Hence, in the low-temperature case there is stability at all densities for deuteron beam energies below 1,13 MeV, or for all beam energies as soon as the density is higher than $5,5 \cdot 10^{19}\ m^{-3}$. In the high-temperature case we find stability at all densities if the beam energy is below 0.75 MeV, or alternatively, with all beam energies for densities higher than $7,2 \cdot 10^{19}\ m^{-3}$. If one wanted to work with a higher deuteron energy in the high-temperature case, say 1 MeV, one has to accept the risk of instabilities in the density range between $5,2 \ldots 6,6 \cdot 10^{19}\ m^{-3}$. If theory would predict a lower number for the numerical constant C in eq. (2), higher plasma densities are needed for stability, hence the two curves (1) and (2) in Fig. 1 are shifted to the right.

In summary: for a given beam plasma configuration with fixed values of the magnetic confining field B and of the product $(P_b \cdot T_e)$, we can identify numbers of the beam energy E_b and of the plasma density n_e, for which no Alfvén-wave instability occurs. The exact location in parameter space of these stable operating regimes depends on the number value of the constant C in eq. (2) and, to a lesser extent, on the lifetime τ_{cx} of the fast ion during slowing down.

REFERENCES:

[1] H.L. Berk et al., Proc. 5th Intern.Conf. Plasma Physics Control.Nucl.Fus.Res., Tokyo (1974), Vol. III, p. 569
[2] Final Report on NET Contract NET/85-079/PH with UKEA Culham Laboratory. To be issued as NET-Report.
[3] J.D. Callen et al., Proc. 5th Intern.Conf. Plasma Physics Control.Nucl.Fus.Res., Tokyo (1974), Vol. I, p. 645

This work was performed under NET Contract 268/87-6/FU-D

TOKAMAK REACTOR CONCEPT WITH 100% BOOTSTRAP CURRENT

J.M Ané , L. Laurent , A. Samain

Association EURATOM-CEA sur la fusion contrôlée
Centre d'études nucléaires de Cadarache B.P. n°1
13108 St Paul-lez-Durance

I Introduction

It is reasonable to believe that plasmas in thermonuclear reactors will have to be steady state . In the case of tokamaks this requires a large amount of recirculated power to maintain the plasma current (a few hundred of megawatts in the present state of the art) . However a part of this current , the bootstrap current, is expected to be generated by the plasma itself . We investigate here the concept of a reactor with 100% bootstrap current obtained by monitoring the n_e and T_e profiles .

II A tokamak discharge with 100% bootstrap current

We consider the case of a discharge with equal ion and electron temperature (T_e) and density (n_e) .In the collisionless case the expression of the bootstrap current in a tokamak is :

$$J_B(r)= \frac{2\, n_e(r)\; T_e(r)}{B_\theta\,(r)} \sqrt{\frac{r}{R}} \left(\frac{2.3}{L_N} + \frac{.17}{L_T} \right) \qquad (1)$$

where B_θ is the poloidal field , R the major radius and L_T, L_N the gradient lengths . Our starting point is that J_B mainly depends on the density gradient and may be increased by decreasing L_N while maintaining the pressure gradient below the MHD instability threshold . We consider here the case of a discharge of minor radius a, major radius R ,toroidal field B_t with the following characteristics :

a) Inside a given radius $r=r^*$ the safety factor profile is flat with q=1. The pressure profile p(r) is also flat to avoid pressure driven modes i.e. $L_N = - L_T$. Equation (1) define the n_e profile which is peaked at the plasma centre , while the T_e profile is hollow (see Fig. 1) :

$$n_e(r) = n_{e0}\; e^{-\frac{1.25}{\beta_t}\left(\frac{r}{R}\right)^{\frac{3}{2}}} \quad \text{with } \beta_t = p(0)/\left(\frac{B_t^2}{2\,\mu_0}\right) \qquad (2)$$

b) Outside the $r=r^*$ (i.e. $q = 1$) surface the pressure $p(r)$ decreases from $p(r^*) = p(0)$ to $p(a)=0$ at the plasma edge . The ratio $L_N / L_T = \eta$ is assumed to be constant . The pressure gradient is limited by a simplified ballooning stability criterion [1]:

$$2\,\mu_0 \left(\frac{\frac{\partial p}{\partial r}}{B_t^2}\right) = -\frac{.6\ s}{R\ q(r)^2} \quad \text{where} \quad s = \frac{r}{q}\frac{\partial q}{\partial r} \qquad (3)$$

Combining equations (1) and (3) one obtains a differential equation for the profile of the safety factor

$$\frac{1}{q(r)}\frac{\partial q}{\partial r} = \frac{2\ r^{-.5}}{r^{.5} + \left(\frac{.69+\ 0.048\ \eta}{1+\eta}\right) R^{.5}} \qquad (4)$$

Giving the value of the safety factor at the edge $q(a)$ determines the solution of the preceding equation .It finally appears that R/a, $q(a)$ and η determine $p(r)$, $q(r)$, the volume averaged beta and the ratio r^*/a.This is also the case for $n_e(r)/n_{e0}$, $T_e(r)/T_{e0}$ and the "hollowness parameter" $\lambda = T(r^*)/T(0)$. The equi beta and equi-hollowness profiles are drawn in the $q(a)$- R/a plane for $\eta=.3$ in figure 2 . The beta value given by the Troyon limit, which can also be represented this plane is drawn in figure 2b .When η is small the beta values and the hollowness parameter for a given $q(a)$ are smaller since the density gradient which creates the bootstrap current is larger .

II Discussion of the results; relaxation of the current profile

The above simple model shows that driving a discharge with 100% bootstrap current requires unusual n_e and T_e profiles.We tentatively examine how these profiles could be obtained in a thermonuclear reactor:

- $n_e(r)$: The peaked n_e profile can be obtained by repeated pellet injections. The particle confinement time is expected to be large enough so that the pellet injection rate will be reasonable .However an usual pellet will deposit its particles at the plasma edge . A specific technology has to be developped . It could consist in shielded pellets ,ablated on magnetic axis by a laser beam .Such a development looks quite reasonable compared to what is needed for other current drive methods and could in fact solve the center fuelling problem .
- $T_e(r)$: The T_e profile will naturally become hollow if the pellet is ablated at the plasma center . The duration of the dip at the center will depend on transport phenomena and will be increased by the hollow thermonuclear power profile and the peaked bremstrahlung (and possibly of a small amount of heavy impurity) radiation profile.

The obtained j(r) profile will not be flat inside the q=1 surface because the n_e and T_e profiles obtained by pellet injection will not correspond exactly to expression (2) .Moreover the expression (1) of bootstrap current is not valid in a small zone around the magnetic axis. One can escape to these difficulties by using the fact that for large enough bootstrap effect inside the $r=r^*$ surface ,the current profile will tend to become hollow . The q values will be slightly above and below 1 at r=0 and $r=r^*$ respectively . Such profiles are unstables [2,3] . One may accordingly hope repeated sawtooth-like redistribution of the current profile towards a lower energy state flat q=1 profile . Such a mechanism has already been suggested in [4] .One may then show that the bootstrap current J_B has no longer to be locally equal to the actual current J_p. Rather the bootstrap electromotive force J_B/ρ (ρ is the plasma resistivity) must now simply balance the resistive friction J_p/ρ in average in the $r=r^*$ surface . The question of course arises whether the particle and energy losses unavoidably associated to the considered disruptive relaxations are acceptable or not .
It should be noted that in recent JET discharges with pellet injection, hollow q profiles have been obtained with values around 1.5 .They were terminated by a sawtooth like event associated to a m/n=3/2 mode [5].

IV Compatibility with a thermonuclear reactor

Coming back to the model of section II , for given R,a,q(a) ,η, B_t, it is possible to define a reactor discharge . It is chosen to have average beta and density values below the Troyon and Murakami limits .The energy confinement time is twice the Kaye-Golston scaling. We find for example that the following circular cross section discharge is ignited and delivers a fusion power of 3.3 GW (wall load 2.45 $MW.m^{-2}$):

R=9 m	a=3m	r^*=1.1 m
q(a)=2.55	I = 15 MA	B = 7.1 T (13 T at the conductor)
Z_{eff}=1	$\bar{n} = 10^{20} m^{-3}$	$\bar{T}$ = 12.5 keV $\bar{\beta}$ = 1.9 %

The hollowness parameter λ is 3.1.The corresponding T_e and n_e profiles are shown in figure 1.

V Conclusion

A concept of reactor with 100% bootstrap current using pellet injection and dynamo effect has been presented . Its viability depends on a low particle and heat transport in the plasma center and of the possibility that plasma current will relax repeatedly around a state of flat q=1 profile in the central region. It is difficult to make predictions concerning these two points since they are not fully understood in existing plasmas. However current experimentation in tokamaks should improve our understanding of these two points .

References :

[1] A. Sykes , M.F.Turner , S. Patel 11 th european conference on controlled fusion and plasma physics (1983). Vol 7D part II p 363

[2] M.N. Bussac, K. Lerbinger Phys. Lett. A 121 (1987) 337

[3] B. Carreras, R.Hicks, B.Waddel Nuclear fusion 19 (1979) 583

[4] A. Boozer Phys. Fluids 29 (12) 1986 4123

[5] The JET team . 12th international conference on plasma physics and controlled nuclear fusion research . Nice 1988 IAEA-CN-50/A-IV-1

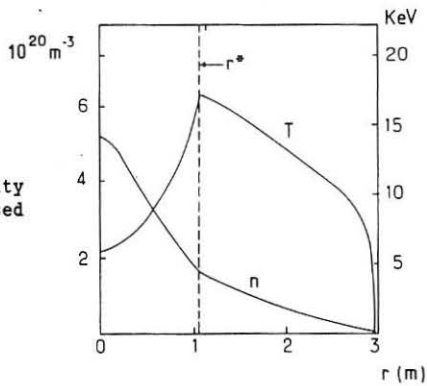

FIG.1 : Temperature and density profiles in the reactor proposed in section IV.

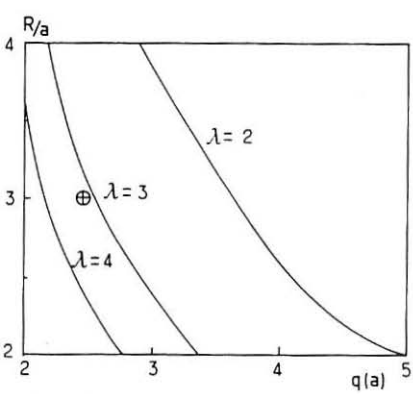

FIG.2$_a$: Contours of constant hollowness parameter λ in the q(a)-R/a plane for η =0.3 .The cross represents the position of the reactor of section IV

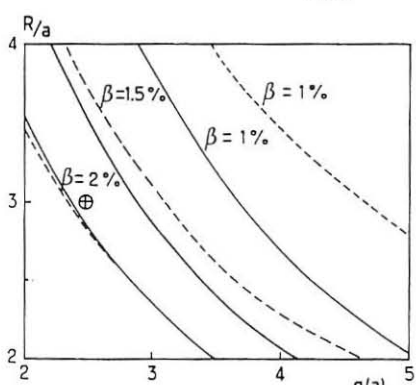

FIG. 2$_b$: Contours of constant average beta (solid line) for η=0.3 .The dotted line represents the Troyon β limit for η=0.3 with g=2.8.

ELECTROMAGNETIC ANALYSIS OF THE LOWER HYBRID SYSTEM OF TORE SUPRA

M.Goniche, Ph.Bibet,D.Moreau,G.Rey,G.Tonon

Association Euratom-CEA sur la fusion
Département de Recherches sur la Fusion Conrolée
F 13108 Saint Paul lez Durance

1.Introduction.

Two identical antennae delivering 3.5MW each for quasi-CW operation at 3.7 GHz are being installed on Tore Supra /1/.Each antennae is composed of 16 evacuated modules using one H-plane hybrid junction (HJ) and 6 E-plane bijunctions as power dividers.Two modules of the same column are fed by a 500-kW klystron via an hybrid junction terminating the pressurized transmission line.The balance port of the HJ is connected to a load /2/.

The large number of waveguides-32 columns of 4 waveguides- with an internal periodic phasing of 90° allows to excite a narrrow,strongly assymetric, $N_{//}$ - spectrum for current drive studies.The $N_{//}$ peak value of the spectrum can be tailored by adjusting the power amplitude and phase of each klystron:when the phase between each module of the same line is varied from -90° to 90°,the $N_{//}$ peak value is shifted from 1.46 to 2.40.

Two main issues are investigated:the power reflected towards the 8 klystrons feeding one antenna and the power launched into the plasma.The reflected power has to be low enough for operation with no circulators and the launched power has to be very directive (i.e.large ratio of the power in the main $N_{//}$ peak) for large current drive efficiency.For this purpose,the exact power division in amplitude and phase,which depends on the reflection due to the plasma,has to be known.

2.Main features of the antenna.

In order to fit the plasma shape,the mouth of the RF modules(2X4 wg)were machined with a poloidal curvature radius of 820mm and consequently the length of the second E-plane bijunction is different of 43° for the external and internal waveguides of the same column(fig.1).Such a difference was compensated with a phase shifter of 90∓43 located in the hybrid junction to obtain RF fields with the same phasing at the mouth. The position of the short-circuit of the balance port was individually determined from low RF power measurements to obtain a balanced power injection from the HJ.A passive waveguide was added on each side of the grill. Lengths of the 2 bijunctions and the passive waveguides were optimized with the numerical code SWAN /3/ which computes the intercoupling with the plasma of 32 waveguides of infinite height in the same row.Electrical length of the 2 transmission lines from the HJ to the RF window were experimentally adjusted to obtain at the mouth a phasing of -90° of the upper modules with respect to the lower ones.

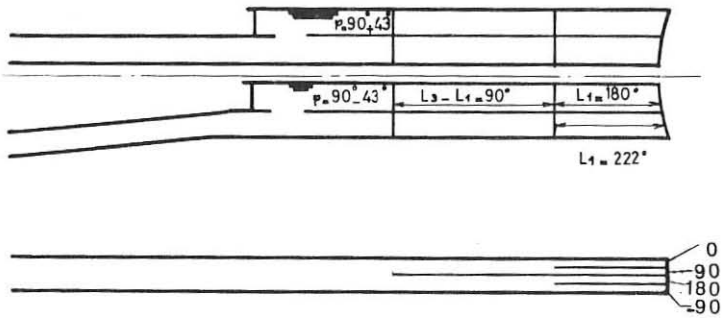

Fig.1 Sketch of 2 modules of an odd column

3.Computing procedure.

The 10X10 scattering matrix has been measured on a prototype module with the same procedure than in /4/.It was also computed from the two 180° and 90° MJ scattering matrixes obtained from the SWAN code.The same symmetries are observed indicating that only 6 S parameters are linearly independant and are needed to define the whole module.For the modules of the antenna,the symmetry is lost due to the poloidal shape.For example,on fig.2 the variation of the phase of the S13 parameter describing the coupling through the L1=180° multijunction is given as a function of the short-circuit position:a good agreement between the theoretical and experimental values is obtained.

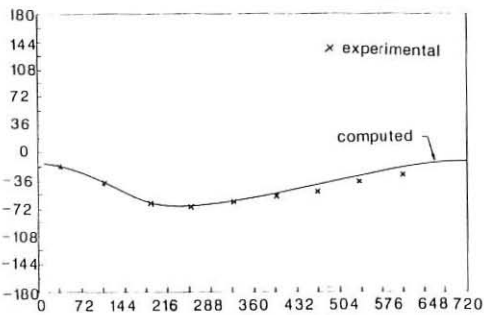

Fig.2
Phase of S13
vs
short circuit position
of the HJ

For the 2 types of multijunctions of 4 waveguides,the SWAN code was run in the case of 8 semi-modules at different densities with different phasings of the modules($\Delta\Phi_{mod}$=0,-90°,90°):in case of good matching($N \simeq 10^{18} m^{-3}$) the coefficient of reflection R of the lateral modules does not exceed 3.5% and the value of R averaged on the 8 semimodules is lower than 2%(fig.3).The calculated values of reflected fields in phase and amplitude allow to compute the power division of the hybrid junctions and the reflected power P for the entire module (fig.4).The procedure was iterated with the new values of power division.Finally,taking into account the electrical lengths of the 2 transmission lines,the RF power reflected towards each of the 8 klystrons was calculated.

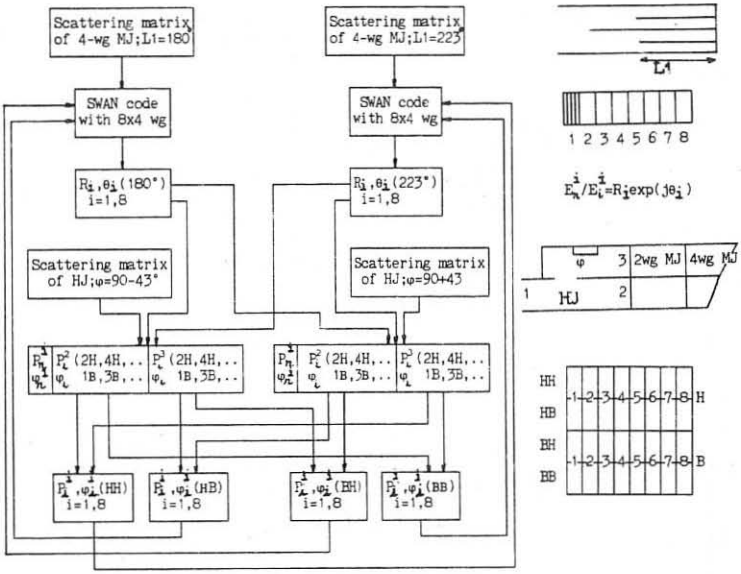

Fig.3.Block diagram of the computing procedure

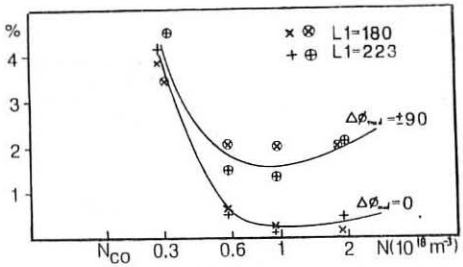

Fig.4
Coefficient of reflection for the two 4-wg multijunctions

4.Results.

Due to the low coefficient of reflection of the multijunctions,only one iteration was needed to obtain the exact power division.In case of good matching ($N=0.6\times10^{18}m^{-3}$),the unbalance of the power injected from the HJ into the 2 semi-modules is at most .45/.55.At lower density($N=0.3\times10^{18}m^{-3}$),the strongest unbalance is .39/.61.However the excited spectrum is just slightly modified,less than 1% for the directivity $D=\langle N_{//}^2\rangle\int(P(N_{//})-P(-N_{//}))dN_{//}/N_{//}^2$ and the coefficient of reflection is not significantly changed.It was found that the the inner rows of waveguides with L1=180° had a lower directivity for negative phasing of the modules(at $0.6\times10^{18}m^{-3}$,62% against 67.5% for $\Delta\Phi_{mod}=-90°$)

where as for positive phasing of the modules, the directivity of the inner waveguides was higher(53% against 42% for $\Delta\Phi_{mod}$=90°). The coefficient of reflection of the entire module is very similar for the 2 modules of the same column: lower than 1% for $\Delta\Phi_{mod}$=0 and than 2.5% for $\Delta\Phi_{mod}$=-90° (fig.5) at $0.6\times10^{18}m^{-3}$. Moreover the difference of phase of the reflected fields recombining at the pressurized HJ is very low: less than 6° at 0.6×10^{18} m^{-3} and 15° at $0.3\times10^{18}m^{-3}$. Therefore most of the reflected power is injected into the load: less than .01% at the medium density and than .2% at lower density is reflected towards the klystron. Actually, these very low figures do not take into account: 1) the directivity of the HJ(~30dB) and the return loss of the line(~25dB) 2) the accuracy of measurements of the electrical length of the transmission lines(~5°). It can be reasonably expected that the coefficient of reflection seen by the klystrons will be lower than 0.5%.

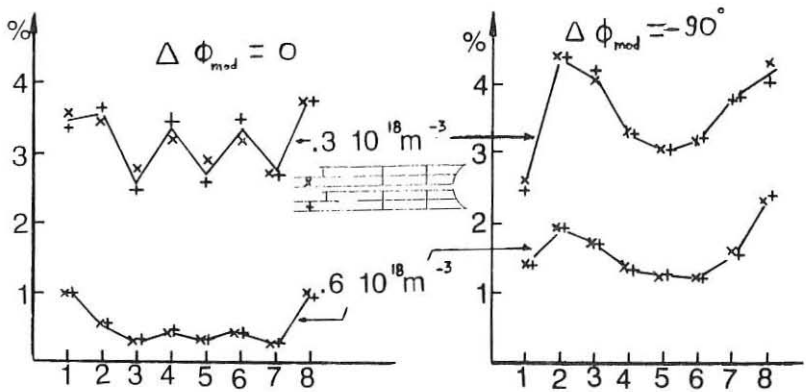

Fig.5. Coefficient of reflection for the 2 rows of 8 modules

Conclusion

The full power division of the lower hybrid antenna, featuring 120 power dividers and 128 waveguides facing the plasma, has been calculated. It was found that 2 rows of 32 waveguides, using the same type of multijunctions, excite a very similar N spectrum, but 2 rows with different types of multijunctions have different directivity. Due to the symmetry of the system, reflected fields recombining in the HJ are very close in phase and in amplitude and the coefficients of reflection toward the klystrons are very low(<0.1%). Even with departures from the ideal system, the reflection is low enough to consider a CW operation of the klystrons, able to sustain a VWSR of 1.3 (R=1.7%), with no circulators.

References

/1/G.Rey et al. 15thSOFT conference, Utrecht (1988)
/2/R.Magne et al. 15thSOFT conference, Utrecht(1988)
/3/D.Moreau et al. Report EUR-CEA-FC-1199(1983)
/4/Ph.Bibet et al. 15thSOFT conference, Utrecht(1988)

CURRENT PROFILE CONTROL BY ELECTRON-CYCLOTRON AND LOWER-HYBRID WAVES IN TORE SUPRA

G. Giruzzi and I. Fidone

Association EURATOM-CEA sur la Fusion
Centre d'Etudes Nucléaires de Cadarache
13108 Saint Paul-lez-Durance (FRANCE)

Introduction. Radial control of the tokamak current is of primary importance for sawtooth stabilization and access to the second stability regime. Specifically, off-axis RF current drive for constant plasma current has the effect of raising the value of q on axis, which provides a path to the second stability regime[1]. In principle, this can be achieved by driving current by high-phase-velocity lower-hybrid (LH) waves. However, it is known that a major drawback of this method of current drive is the difficulty of efficient and flexible spatial control of the LH phase velocity spectrum. This limitation results mainly from the complicated mechanisms responsible for the formation of the wave spectrum within the plasma. Combination of electron-cyclotron (EC) and LH waves seems a more appropriate RF system for remote control of the radial current profile[2,3]. By the appropriate choice of the injection angles, the EC wave power deposition can be shifted both in the real and the velocity space, which allows a flexible tailoring of the plasma current profile. The long pulse operation and good confinement properties of Tore Supra[4] offer the opportunity of extensive studies of current control by LH and EC waves. Specifically, a current $I \gtrsim 0.5$ MA will be driven at central density and temperature near 5×10^{13} cm^{-3} and 3 keV, respectively, by a LH wave power $P_{LH} = 3 - 6$ MW distributed in a spectrum $1.8 < n_{\parallel} < 3.5$, where $n_{\parallel}$ is the parallel retardation index. This power will generate and sustain a long superthermal tail which provides the target for EC wave absorption. In this work, an extensive theoretical study of the current drive process by simultaneous injection of EC and LH waves in Tore Supra is presented. Top launching of EC waves of frequency f = 110 GHz is considered, both for $f < f_c$ and for $f > f_c$, f_c being the EC frequency. The EC wave damping along the ray trajectories is computed by means of a toroidal ray-tracing code, incorporating the evaluation of the relativistic dielectric tensor for an arbitrary electron distribution[5], e.g., the LH-driven electron tail. The latter is determined by means of a 3-D bounce-averaged Fokker-Planck code[6], which evaluates also the evolution of the electron distribution function during the absorption of high-power EC waves ($P_{EC} \gtrsim 2$ MW).

Current drive by LH and EC waves. The kinetic equation describing the process of current generation by LH and EC waves[2,3,6] contains a Fokker-Planck collision term, a quasilinear parallel diffusion term related to the absorption of the LH waves and a perpendicular diffusion term rel-

ated to EC waves. For the LH wave term we adopt a very simple model, i.e. we assume a constant diffusion coefficient in the interval $p_1 < p_\parallel < p_2$, where $p_\parallel = \vec{p}\cdot\vec{B}/B$, $\vec{p}$ is the electron momentum, $\vec{B}$ is the tokamak magnetic field and p_1, p_2 are related to the boundaries of the wave $n_\parallel$ spectrum. For parameters typical of the Tore Supra LH experiment (a=0.7 m, R=2.25 m, P_{LH} = 3 MW, $p_1 \sim 0.3$ mc, $p_2 \sim 0.6$ mc) we obtain a current I_{LH} = 0.465 MA, with the profile shown in Fig. 1 (dashed line). The distribution function carrying this current is characterized by a long parallel tail in the range $p_1 < p_\parallel < p_2$, which is the target for the absorption of the EC waves. We first consider the case of top launching of an extraordinary wave beam propagating perpendicularly to the toroidal magnetic field, for B = 4.5 T on axis. The wave beam is absorbed close to the plasma center by electrons at $p_\parallel \gtrsim p_2$. The effect of the wave absorption is to decrease the collision rate of those electrons, which causes a significant enhancement of the parallel tail for $p_\parallel \geq p_2$, thus in the relativistic range. This shows how the LH-sustained electron system can be used to simulate, in a low temperature plasma, the Maxwellian tail of a hot plasma in order to investigate EC current drive in conditions similar to those existing in the reactor regime. For a wave beam of angular half-width $\Delta\psi = 5°$ and power P_{EC} = 2 MW, the change in the current density profile is shown in Fig. 1 (solid line). The total absorbed power is 1.4 MW and the additional driven current is I_{EC} = 0.130 MA. This launching configuration is thus suited for obtaining peaked current density profiles. By an appropriate choice of the launching angles, the EC wave power can be deposited and the current density profile can be modified at different radial locations. For instance, if the EC wave beam is launched at an angle $\phi = 15°$ with respect to the vertical (towards the low magnetic field side) and with an angle $\psi = 100°$ with respect to the magnetic field, the wave power is mainly absorbed at $r \sim 0.3$ m and the current density profile is modified as shown in Fig. 2. In this case the wave power is absorbed by electrons at $p_\parallel \sim p_1$. Moreover, I_{EC} = 0.145 MA and P_{EC} = 2 MW. The same current drive scenario can be investigated at constant plasma current. This can be obtained, e.g., by decreasing the power input in the LH waves as the current driven by the EC waves increases. The results of the numerical simulation of this process are shown in Fig. 3, for P_{EC} = 2 MW (a), and P_{EC} = 4 MW (b). Note the significant drop in the central current density: the value of q on axis is 0.95, 1.21 and 1.42 for P_{EC} = 0, 2 MW and 4 MW, respectively. This shows that off-axis current drive can be used in Tore Supra to investigate the approach to high-q regimes, which may provide a stable path to the second stability regime.

We finally discuss EC current drive at upshifted frequency, i.e., $f > f_c$. This scenario is very attractive for a steady-state reactor, since it minimizes the deleterious effects of electron trapping[7], but it requires high electron temperatures. Again, the ECLH system offers the opportunity of testing this method in a low temperature experiment. The current density generated by a 2 MW wave beam injected at $\psi = 75°$, $\phi = -5°$, for B = 3.8 T on axis, is shown in Fig. 4. Note the broad profile of the additional EC-driven current, due to the beam angular spread and to the fact that for $f > f_c$ the wave power deposition is strongly sensitive to the value of the ψ angle[3]. In this case we obtain I_{EC} = 0.165 MA and P_{EC} = 2 MW.

[1] M. Porkolab et al., 12th Int. Conf. on Plasma Phys. Contr. Nucl. Fus. Res., Nice 1988, paper IAEA-CN-50/E-4-8; S.A.Sabbagh et al., ibidem, paper IAEA-CN-50/D-IV-14.
[2] I. Fidone et al., Phys. Fluids 27 (1984) 2468.
[3] I. Fidone et al., Nucl. Fusion 27 (1987) 579.
[4] R. Aymar, Nice Conf. 1988, paper IAEA-CN-50/A-I-1.
[5] V. Krivenski et al., Nucl. Fusion 25 (1985) 127.
[6] R.L. Meyer et al., Comp. Phys. Comm. 40 (1986) 153; G. Giruzzi, Phys. Fluids 31 (1988) 3305.
[7] K. Yoshioka, T.M. Antonsen, Nucl. Fusion 26 (1986) 839.

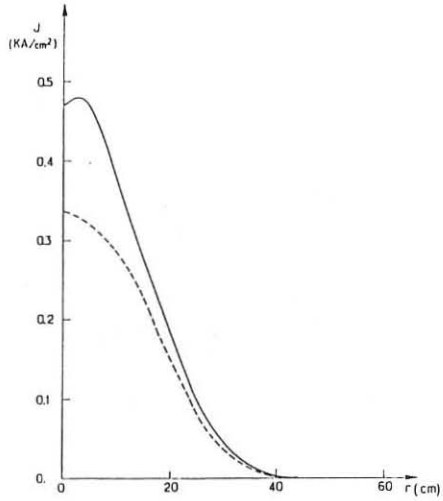

Fig. 1 : *radial profile of the current driven by the LH waves alone (dashed line) and by the ECLH system (solid line). B=4.5 T; extraordinary mode, P_{EC} = 2 MW, ψ = 90°, ϕ = -5°.*

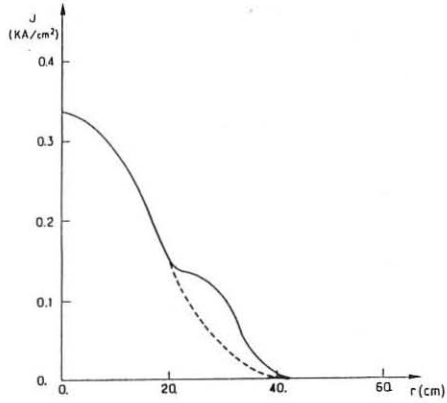

Fig. 2 : *as in Fig. 1, for ψ = 100°, ϕ = 15°.*

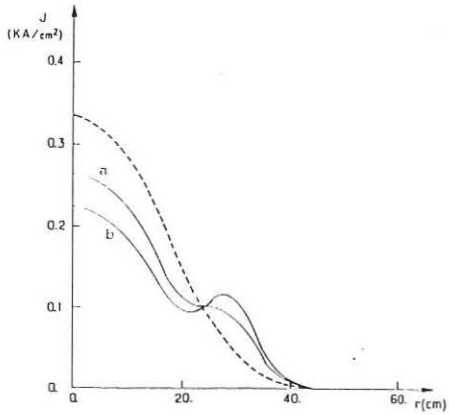

Fig. 3 : *as in Fig. 2, but for constant plasma current.*
(a) P_{EC} = 2 MW.
(b) P_{EC} = 4 MW.

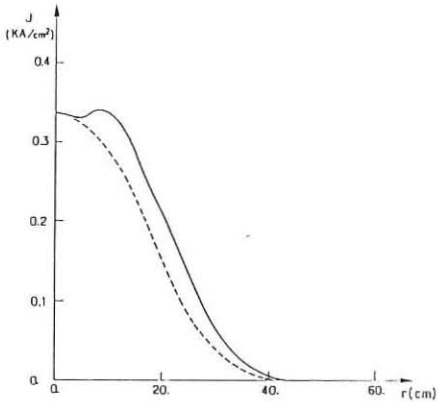

Fig. 4 : *as in Fig. 1, but for the ordinary mode,* ψ = 75°, ϕ = -5°; B = 3.8 T.

G

GENERAL PLASMA THEORY

G

ABSORPTION OF MHD WAVES DUE TO RESONANT PROCESSES.

V.M.Čadež and V.K.Okretič

Institute of Physics,
P.O.Box 57, YU-11001 Beograd, Yugoslavia.

MHD wave reflection from a smooth plasma-plasma boundary has been recently investigated by a number of authors (Roberts, Lee, Hollweg etc). Their interest was focused to the process of the resonant wave transformation inside the boundary layer, where the relevant phase matching conditions are met.

Here, we are dealing with the MHD wave reflection properties in the case of a double-step plasma profile composed by three homogeneous regions separated by a discontinuity plane at x=0 and by a narrow transitional boundary layer between x=D and x=D+a. A MHD wave propagates through the region 1 (where $-\infty \le x \le 0$) and is being totally reflected from the boundary at x=0. On the other hand the boundary layer at x=D can sustain a dissipative surface wave mode which, if coupled with the reflected wave, can reduce its energy. Our aim now is to show the possibility of achieving a total absorption of the incident MHD wave via its coupling to the surface wave with the dissipative mechanism being the resonant wave transformation inside the boundary layer.

Starting from standard MHD equations for a compressive and ideally conductive plasma, the following equation for small velocity component, u, perpendicular to the boundaries, is obtained:

$$\frac{d}{dx}\left\{\varepsilon(x)\,\frac{du}{dx}\right\} - \beta(x)\,u = 0 \qquad (1)$$

where:

$$\varepsilon(x) = \frac{\rho_o(x)\left[k_z^2 A^2(x)-\omega^2\right]}{m_o^2(x)+k_y^2}, \qquad \beta(x) = \rho_o(x)\left[k_z^2 A^2(x)-\omega^2\right]$$

$$m_o^2(x) = \frac{\left[k_z^2 A^2(x)-\omega^2\right]\left[k_z^2 c^2(x)-\omega^2\right]}{\left[c^2(x)+A^2(x)\right]\left[k_z^2 c_t^2(x)-\omega^2\right]}, \qquad c_t^2(x) = \frac{c^2(x)\,A^2(x)}{c^2(x)+A^2(x)}$$

Here $c_i=(\gamma R T_{oi})^{1/2}$ is the speed of sound and $A_i=B_{oi}/(\mu_o \rho_{oi})^{1/2}$ is the Alfven speed.

The solution for the reflected wave amplitude $|R|^2$ is then:

$$|R^2| = \frac{a_r^2 + a_i^2}{b_r^2 + b_i^2} \qquad (2)$$

Here:

$$a_r = \Delta + (\Delta-2)e^{-2\varkappa_2 D} - D_{12}(\delta_+ + \delta_- e^{-2\varkappa_2 D})$$

$$a_i = D_{12}[\Delta - (\Delta-2)e^{-2\varkappa_2 D}] + \delta_+ - \delta_- e^{-2\varkappa_2 D}$$

$$b_r = \Delta + (\Delta-2)e^{-2\varkappa_2 D} + D_{12}(\delta_+ - \delta_- e^{-2\varkappa_2 D})$$

$$b_i = D_{12}[\Delta - (\Delta-2)e^{-2\varkappa_2 D}] - \delta_+ + \delta_- e^{-2\varkappa_2 D}$$

and also:

$$D_{ij} = \frac{\rho_{oi}(k_z^2 A_i^2 - \omega^2)(m_{oj}^2 + k_y^2)^{1/2}}{\rho_{oj}(k_z^2 A_j^2 - \omega^2)(m_{oi}^2 + k_y^2)^{1/2}} = \frac{\varepsilon_i |\varkappa_i|}{\varepsilon_j \varkappa_j},$$

$$\delta_\pm = D_{42}\, \varepsilon_2 \varkappa_2 \mathrm{Im}\, J_1 \pm (\varepsilon_2 \varkappa_2)^{-1}\, \mathrm{Im}\, J_2 \qquad \text{and} \qquad \Delta = 1 + D_{42}$$

The reflection coefficient (2) shows that a total reflection ($|R| = 1$) occurs in two cases only: if the dissipations due to resonant wave conversion are absent ($\delta_\pm = 0$) and/or if the separation distance D between the boundaries is large enough ($\varkappa_2 D \gg 1$). However $|R| < 1$ in all other cases, including the possibility of total wave absorption, when $|R| = 0$.

To achieve the total absorption the following two conditions, according to (2), have to be satisfied simultaneously:

$$\Delta + (\Delta-2)e^{-2\varkappa_2 D} - D_{12}(\delta_+ + \delta_- e^{-2\varkappa_2 D}) = 0 \qquad (3)$$

$$D_{12}[\Delta - (\Delta-2)e^{-2\varkappa_2 D}] + \delta_+ - \delta_- e^{-2\varkappa_2 D} = 0 \qquad (4)$$

After some rearrangement the above equations reduce to:

Taking the perturbed quantities in the form: $f(x) \sim \exp(-i\omega t+ik_y y+ik_z z)$ we obtain the solutions to (1) in 4 considered regions:

$$u = \begin{cases} e^{i\chi x} + R\, e^{-i\chi x} & x\le 0, \quad \text{region 1} \\ C_2^+ e^{\varkappa_2 x} + C_2^- e^{-\varkappa_2 x} & 0\le x\le D, \quad \text{region 2} \\ C_3'\left[1 + \int_D^x \frac{dx'}{\varepsilon(x',\omega)} \int_D^{x'} \beta(x'',\omega)dx''\right] & \\ \qquad + C_3'' \int_D^x \frac{dx'}{\varepsilon(x',\omega)} & D\le x\le D+a, \quad \text{region 3} \\ C_4 e^{-\varkappa_4 (x-a-D)} & D+a\le x, \quad \text{region 4} \end{cases}$$

where $\varkappa_j = \left[\beta_j/\varepsilon_j\right]^{1/2} = \left[m_{oj}^2(x)+k_y^2\right]^{1/2}$; $\chi \equiv i\varkappa_1$ (index j refers to a particular region: j=1,2,3,4).

The normalized wave amplitudes: R, $C_2^{\pm}, C_3'$, C_3'' and C_4 are mutually related through the boundary conditions specifying the continuity of both the normal velocity component, u, and the total pressure perturbation, $\varepsilon(x)\frac{du}{dx}$, at locations x=0, D, D+a. This yields a set of six algebraic equations:

$$R - C_2^+ - C_2^- = 1, \qquad i\chi\,\varepsilon_1 R + \varepsilon_2\varkappa_2(C_2^+ - C_2^-) = i\chi\,\varepsilon_1,$$

$$C_2^+ + C_2^- e^{-2\varkappa_2 D} - C_3' e^{-\varkappa_2 D} = 0, \qquad \varepsilon_2\varkappa_2(C_2^+ - C_2^- e^{-2\varkappa_2 D}) - C_3'' e^{-\varkappa_2 D} = 0,$$

$$C_3' + C_3'' J_1 - C_4 = 0, \qquad C_3'' + C_3' J_2 + \varepsilon_4\varkappa_4 C_4 = 0$$

where $J_1 = \int_D^{D+a} \frac{dx}{\varepsilon(x,\omega)}$ and $J_2 = \int_D^{D+a} \beta(x)dx$.

$$\Delta = \frac{(D_{12} - 1)\,\delta_+ + (D_{12} + 1)\,\delta_-\, e^{-2\varkappa_2 D}}{2\,D_{12}} \qquad (5)$$

and:

$$\left[\,(\varkappa_2\varepsilon_2)^2\,\mathrm{Im}\,J_1 - \mathrm{Im}\,J_2\right] = \frac{4\,\chi\,\varepsilon_1}{1 + D_{12}^2}\, e^{-2\varkappa_2 D} \qquad (6)$$

The total wave absorption thus results from two phenomena described by (5) and (6):

The equation (5) indicates the excitation of surface waves along the boundary layer at $x = D$, with the frequency spectrum given by the dispersion relation $\Delta \cong 0$.

On the other hand, the condition (6) relates the resonant surface wave dissipations in the layer to the energy tunneling through the region between the reflection and the resonant point.

At the end we can also draw a conclusion regarding the type of the wave mode that can be totally absorbed via the described mechanism. Namely, it follows from (6) that the coefficient ε_1 must be negative since both $\mathrm{Im}\,J_1$ and $-\mathrm{Im}\,J_2$ are negative for physical reasons. Therefore the inequality:

$\varepsilon_1 \equiv \dfrac{\rho_{01}(k_z^2 A_1^2 - \omega^2)}{m_{01}^2 + k_y^2} < 0$ and the fact that $m_{01}^2 + k_y^2 < 0$ for a propagating wave imply $k_z^2 A_1^2 - \omega^2 > 0$. Consequently, it is the slow MHD mode that can be completely absorbed instead of being totally reflected.

REFERENCES:

Hollweg, J.V.: Ap.J. 312, p.880, 1985.

Hollweg, J.V. and Yang, G.: JGR 93, No.A6, p.5423, 1988.

Miles, A.J. and Roberts, B.: Solar Phys. (in press).

Lee, M.A.: Ap.J. 240, p.693, 1980.

INTERACTION OF PLASMA VORTICES WITH RESONANT PARTICLES

D. Jovanovic*, H. L. Pecseli+, J. Juul Rasmussen+

*Institute of Physics, P.O. Box 57, 11001 Belgrade, Yugoslavia

+Association EURATOM-Riso National Laboratory, P.O. Box 49
DK-4000 Roskilde, Denmark

In this paper we present a kinetic theory of fully nonlinear torsional Alfven-type perturbations in low β plasmas, $\beta = \frac{2n_0 T_e}{c^2 \varepsilon_0 B_0^2} \ll \frac{m_e}{m_i}$. Electrons are properly described by the drift-kinetic equation:

$$\frac{\partial f(v_\parallel)}{\partial t} + \nabla\left[\left(\frac{\vec{B}}{|\vec{B}|} v_\parallel + \frac{\vec{E}x\vec{B}}{B^2}\right) f(v_\parallel)\right] + \frac{e}{m_e}\frac{\vec{E}\,\vec{B}}{B^2}\frac{\partial f(v_\parallel)}{\partial v_\parallel} = 0 \tag{1}$$

Here $f(v_\parallel)$ is the electron distribution function integrated for velocity components perpendicular to the local magnetic field, and we have neglected the electron polarization drift. With the accuracy to the leading order in the small parameters:

$$\frac{1}{\Omega_i}\frac{d}{dt} \quad , \quad \frac{1}{\nabla_\perp}\frac{\partial}{\partial z} \quad , \quad \frac{1}{B_0}\nabla x\vec{\psi} \quad , \quad \frac{1}{f_0}(f-f_0) \quad , \quad \frac{m_e}{m_i} \tag{2}$$

where f_0 is the unperturbed distribution function $f_0(v_\parallel) = n_0 f_M(v_\parallel)$, and the notation $\vec{E} = -\nabla\phi + \frac{\partial\vec{\psi}}{\partial t}$, $\vec{B} = \vec{e}_z B_0 - \nabla x\vec{\psi}$ is used, the drift-kinetic equation can be written in the simple form:

$$\left\{\frac{\partial}{\partial t} + v_\parallel\frac{\partial}{\partial z} + \frac{1}{B_0}\left[\vec{e}_z x\nabla\left(\phi + v_\parallel\psi_z\right)\right]\nabla\right\} f(v_\parallel) + \tag{3}$$

$$+ n_0\frac{\partial f_M(v_\parallel)}{\partial v_\parallel}\left\{\left[\frac{\partial}{\partial t} + \frac{1}{B_0}\left(\vec{e}_z x\nabla\phi\right)\nabla\right]\psi_z - \frac{\partial\phi}{\partial z}\right\} = 0$$

We assume ions to be cold, neglecting finite ion Larmor radius effects. Then, to the leading order in small parameters (2), ions are two-dimensional, and we can describe them by hydrodynamic equations. The first moment of eq. (3), with the use of the parallel Ampere's law, $j_\parallel = c^2\varepsilon_0\nabla_\perp^2\psi_z$, gives:

$$\left[\frac{\partial}{\partial t} + \frac{1}{B_0}\left(\vec{e}_z x \nabla\phi\right)\nabla\right]\left(1-\frac{c^2}{\omega_{pe}^2}\nabla_\perp^2\right)\psi_z - \frac{\partial\phi}{\partial z} = \left[\frac{\partial}{\partial z} + \frac{1}{B_0}\left(\vec{e}_z x \nabla\psi_z\right)\nabla\right]\frac{p_\parallel}{n_0 e} \qquad (4)$$

while the zeroth moment, together with the ion continuity and the Poisson's equation gives:

$$\left[\frac{\partial}{\partial t} + \frac{1}{B_0}\left(\vec{e}_z x \nabla\phi\right)\nabla\right]\nabla_\perp^2\phi - \left[\frac{\partial}{\partial z} + \frac{1}{B_0}\left(\vec{e}_z x \nabla\psi_z\right)\nabla\right]c_A^2\nabla_\perp^2\psi_z = 0 \qquad (5)$$

here $c_A = c\left(1+\frac{\omega_{pi}^2}{\Omega_i^2}\right)^{1/2}$ is the Alfven speed, and $p_\parallel$ is the $\vec{B}$-parallel component of the electron pressure tensor:

$$p_\parallel = m_e\int dv_\parallel v_\parallel^2 f(v_\parallel) \qquad (6)$$

Ion continuity, and eqs. (4), (5) produce the following conservation laws:

$$\frac{\partial S}{\partial t} = 0 \quad ; \quad \frac{\partial W}{\partial t} + \frac{\partial P}{\partial z} = R_W \quad ; \quad \frac{\partial T}{\partial t} + \frac{\partial W}{\partial z} = R_T \qquad (7)$$

S, W, P, and T are the enstrophy, energy, and z- components of the Pointing vector and of the total flux, respectively:

$$S = \frac{1}{2}\int dxdy\left[\frac{e}{c^2\varepsilon_0}n_e + \frac{1}{c_A^2}\nabla_\perp^2\phi\right]^2$$

$$W = \frac{1}{2}\int dxdy\left[\frac{1}{c_A^2}\left(\nabla_\perp\phi\right)^2 + \left(\nabla_\perp\psi_z\right)^2 + \frac{c^2}{\omega^2}\left(\nabla_\perp^2\psi_z\right)^2\right]$$

$$P = -\int dxdy\ \nabla_\perp\phi\ \nabla_\perp\psi_z$$

$$T = \frac{1}{c_A^2}\left[P - \frac{c^2}{\omega_{pe}^2}\int dxdy\ \nabla_\perp^2\phi\nabla_\perp^2\psi_z\right] \qquad (8)$$

and R_W, R_T describe the energy and flux exchange between the field and the particles:

$$R_W = -\int dxdy\ \nabla_\perp^2\psi_z\left[\frac{\partial}{\partial z} + \frac{1}{B_0}\left(\vec{e}_z x \nabla\psi_z\right)\nabla\right]\frac{p_\parallel}{n_0 e}$$

$$R_T = \frac{1}{c_A^2}\int dxdy\ \nabla_\perp^2\phi\left[\frac{\partial}{\partial z} + \frac{1}{B_0}\left(\vec{e}_z x \nabla\psi_z\right)\nabla\right]\frac{p_\parallel}{n_0 e} \qquad (9)$$

Integration in (8), (9) is performed over the whole x,y plane.

In cold plasmas, $v_{Te}\frac{\partial}{\partial z} \ll \frac{\partial}{\partial t}$, the parallel

pressure $p_{\parallel}$ contains only the contribution of resonant particles. Normally, number of resonant particles is small, we can treat the right-hand-side of eq. (4) as a small perturbation, and solve the system (4), (5) iteratively. In the $p_{\parallel} \to 0$ limit the system (4), (5) reduces to Strauss' equations of reduced MHD[1], which describe tokamaks with a small aspect ratio. These equations were studied in detail in[2], and it was shown that they posess a spatially localized solution, travelling with the phase velocity $\vec{v}_{ph} = \vec{e}_x v_x + \vec{e}_z v_z$, in the form of a double vortex[3]. Within the vortex core, $r<r_0$, potentials ϕ, ψ_z are given by:

$$\phi = B_0 v_x r_0 \sin\theta \left[-\frac{r}{r_0} + \frac{\alpha_m J_1(\gamma_m r/r_0)}{\gamma_m J_0(\gamma_m)} + \frac{\alpha_n J_1(\gamma_n r/r_0)}{\gamma_n J_0(\gamma_n)} \right]$$

$$v_z \psi_z = -B_0 v_x r_0 \sin\theta \left[-\frac{r}{r_0} + \frac{\alpha_n J_1(\gamma_m r/r_0)}{\gamma_m J_0(\gamma_m)} + \frac{\alpha_m J_1(\gamma_n r/r_0)}{\gamma_n J_0(\gamma_n)} \right] \tag{10}$$

and in the external region, $r>r_0$, we have:

$$\phi = -v_z \psi_z = -B_0 v_x \sin\theta \; r_0^2/r \tag{11}$$

J_0, J_1 are Bessel functions of the second order, γ_m, γ_n are zeros of the function J_1, $J_1(\gamma_m) = J_1(\gamma_n) = 0$, and r, θ, α_m, α_n are defined by:

$$r = \left(\xi^2 + y^2\right)^{1/2}, \quad \theta = \operatorname{arctg} \frac{y}{\xi}, \quad \xi = x + \frac{v_x}{v_z} z - v_x t \tag{12}$$

$$\alpha_k = 2\left(1 + \frac{c^2 \gamma_k}{r_0^2 \omega_{pe}^2}\right)^{1/2} \left[\left(1 + \frac{c^2 \gamma_m}{r_0^2 \omega_{pe}^2}\right)^{1/2} + \left(1 + \frac{c^2 \gamma_n}{r_0^2 \omega_{pe}^2}\right)^{1/2} \right]^{-1}, \qquad k = m, n$$

In the presence of a small perturbation $p_{\parallel} \neq 0$, we can write the solution in the form (10), (11), with the vortex parameters v_x, v_z, r_0 being slowly adiabatically varying with t, z. In this regime, using (7), (8), we can rewrite the drift-kinetic equation in the form of a vector product, which is readily integrated to give:

$$f(v_{\parallel}) = \frac{n_0 e}{m_e} \frac{\partial f_M(v_{\parallel})}{\partial v_{\parallel}} \left[\frac{H(r)}{v_{\parallel} - v_z} (\phi + v_z \psi_z) + (H(r) - 1)\left(\psi_z - \frac{v_x}{v_z} B_0 v_x y\right) \right]$$

$$H(r) = \begin{cases} 1 \quad , & r>r_0 \\ \dfrac{v_z^2}{c_A^2}\left[\left(1+\dfrac{c^2\gamma_m}{r_0^2\omega_{pe}^2}\right)\left(1+\dfrac{c^2\gamma_n}{r_0^2\omega_{pe}^2}\right)\right]^{1/2} & , \quad r<r_0 \end{cases} \tag{13}$$

Performing the integration in (6) along the Landau contour, with the use of: $\dfrac{1}{v_\parallel - v_z} = \dfrac{P}{v_\parallel - v_z} + i\pi\delta\left(v_\parallel - v_z\right)$, we get the following expression for the paralell pressure $p_\parallel$, which contains only the contribution of resonant particles:

$$p_\parallel = n_0 e v_z^2 \frac{\partial f_M(v_z)}{\partial v_z} \int_{-\infty}^{\infty} \frac{d\xi'}{\xi'-\xi} H\left(\sqrt{\xi'^2+y^2}\right)\left(\phi + v_z \psi_z\right)_{(\xi',y)} \tag{14}$$

Evolution equations for the vortex parameters are readily obtained from the conservation laws (7) after the substitution:

$$\frac{\partial}{\partial t} = \frac{\partial v_x}{\partial t}\frac{\partial}{\partial v_x} + \frac{\partial v_z}{\partial t}\frac{\partial}{\partial v_z} + \frac{\partial r_0}{\partial t}\frac{\partial}{\partial r_0} \quad , \quad \frac{\partial}{\partial z} = \frac{\partial v_x}{\partial z}\frac{\partial}{\partial v_x} + \frac{\partial v_z}{\partial z}\frac{\partial}{\partial v_z} + \frac{\partial r_0}{\partial z}\frac{\partial}{\partial r_0}$$

Evolution equations are particularly simple in the strongly electromagnetic case, $\omega_{pe}^2 r_0^2 \gg c^2$, when we have $R_W = v_z R_T$, and:

$$S = v_x^2\sigma \quad ; \; T = P = \frac{v_x^2 r_0^2}{v_z}\tau \; ; \quad W = \frac{1}{2}\left(1+\frac{c_A^2}{v_z^2}\right) r_0^2 v_x^2 \tau + \left(1-\frac{c_A^2}{v_z^2}\right)\frac{c^2}{\omega_{pe}^2} v_x^2 w \tag{15}$$

where σ, τ, and w ($\tau \simeq w$) are complicated expressions which contain integrals of multiple products of Bessel functions, but they are independent on v_x, v_z, and r_0.

Finally, linearizing evolution equations (7), (15), and solving them with the initial conditions $v_x(t=0,\ z) = v_{x0}$, $v_z(t=0,\ z) = v_{z0}$, $r_0(t=0,\ z) = a$, we find that v_x, and consequently the amplitude of the vortex, remains constant, and $r_0(t,z) \approx a + t\,\dfrac{R_W a}{T v_{z0}}\Big|_{t=0}$; $v_z(t,z) \approx v_{z0} + t\,\dfrac{R_W}{T}\Big|_{t=0}$ for $v_{z0} \neq c_A$, and $r_0(t,z) \approx a + \dfrac{t}{2}\,\dfrac{R_W a}{T v_{z0}}\Big|_{t=0}$; $v_z(t,z) = c_A =$ const. for $v_{z0} = c_A$.

REFERENCES

1. D. Jovanovic, H. L. Pecseli, J. Juul Rasmussen, J. Plasma Phys., 37, 81, (1987)
2. H. R. Strauss, Phys. Fluids, 19, 134, (1976)
3. A. B. Mikhailovskii, V. P. Lakhin, L. A. Mikhailovskaya, O. K. Onischenko, Zh. Eksp. Teor. Fiz., 86, 2061, (1984)

SOLITON-LIKE STRUCTURES IN DOUBLE STIMULATED BRILLOUIN SCATTERING

T. J. H. Pättikangas and R. R. E. Salomaa

Helsinki University of Technology,
Department of Technical Physics,
SF–02150 Espoo, Finland

1 Introduction

In laser-plasma interactions the reflection of the pump wave from the overdense pla has a profound effect on the dynamics of stimulated Brillouin scattering. It can ca oscillations in the backscattered intensity [1] or the scattering may even turn chaotic

In Double Stimulated Brillouin Scattering (*DSBS*), originally suggested by Zozı *et al.* [3], the incoming and specularly reflected pump waves scatter from a common acoustic wave propagating sideways. Due to the boundary conditions *DSBS* has a se eigensolutions and eigenfrequencies of the ion wave [4,5]. The fundamental mode, the eigensolution with the lowest threshold intensity, is known to be unstable for la pump intensities in certain parameter ranges [6]. As the pump intensity is increased solutions turn from stationary ones to regular pulsations [5,7]; recently also transiti involving hysteresis between stationary eigenmodes have been observed [8]. Many of observed features are controversial and poorly understood. In the present work we rep some results of numerical and analytical investigations on soliton-like behaviour occurr in *DSBS*.

2 Damped sine-Gordon equation

Within the slowly varying envelope approximation *DSBS* is governed by five coup equations (see e.g., Ref. [3], Eqs. (2.4–2.5)). By assuming that the phases of the fie remain constant one can show [6,7] that the area of the ion acoustic pulse,

$$A(\xi,\tau) = \int_0^{\xi} v(\xi',\tau)d\xi',$$

obeys a damped sine-Gordon equation

$$\frac{\partial^2 A}{\partial\tau\partial\xi} + \frac{\partial A}{\partial\xi} = \kappa q \sin(2A+\phi),$$

where $\xi = x/L$ and $\tau = \gamma_s t$ (L is the length of the homogeneous plasma slab and is the ion wave damping). The normalized pump field intensity is denoted by κ a

the phase ϕ is defined by $\tan\phi = 2|R_0 R_{-1}|/(1 + |R_{-1}|^2 - |R_0|^2)$, where $R_{-1}(\tau)$ is the backscattering and $R_0(\tau)$ is the specular reflection coefficient. The parameter r is the amplitude reflection coefficient of the overdense plasma. For small reflectivities of the plasma, $r^2 = |R_{-1}(\tau)|^2 + |R_0(\tau)|^2 \ll 1$, the parameter $q = [(1 - r^2)^2/4 + |R_{-1}|^2]^{1/2}$ is almost constant. For further details of the derivation of Eq. (2) see Ref. [7].

One boundary condition for the pulse area is that $A(0,\tau) = 0$. If the ion wave is determined initially, this provides the condition $A(\xi, 0) = A_0(\xi)$. An additional constraint arises from the interdependence of $A(1,\tau)$ and the reflection coefficients $R_{0,-1}$.

The amplitudes of the four EM fields involved can be expressed in terms of the pulse area $A(\xi,\tau)$ (see Ref. [7]). For example the incoming pump field is given by $E_{01}(\xi,\tau) = E_0(\tau)\cos A(\xi,\tau)$, and the forward propagating scattered EM field is $E_{-11}(\xi,\tau) = E_0(\tau)\sin A(\xi,\tau)$, where E_0 is the pump field amplitude at the entrance plane.

By making the transformations $\vartheta = 2\kappa q\tau$ and $u = 2A + \phi$ and neglecting the time dependence of q, one can write Eq. (2) as

$$\frac{\partial^2 u}{\partial\vartheta\partial\xi} + \epsilon\frac{\partial u}{\partial\xi} = \sin u, \tag{3}$$

where $\epsilon = (2\kappa q)^{-1}$. For large pump intensities $\kappa \to \infty$ and $\epsilon \to 0$, which renders possible a perturbation solution of Eq. (3).

3 Soliton-like behaviour

The damped sine-Gordon Eq. (3) is known to have soliton-like solutions [9]. If the damping term is small, the shape of e.g., the kink-solution is not altered but the width of the kink becomes time dependent and its center does not move at a constant speed. In our particular case the boundary conditions complicate further the behaviour: it is expected that the approximate solutions valid for infinite media fail close to $\xi = 0$ and 1. For this reason we have solved the five coupled *DSBS* equations numerically and analyzed the soliton-like properties of the ion wave obtained.

An example of contour-plots of the ion acoustic wave amplitude is shown in Fig. 1, where a constant input intensity is assumed. The pulse propagates with an increasing velocity but retains its shape most of the time. The length of the 'propagation region' increases with the pump intensity κ. This is observed in the slowing down of the repetition rate of the backscattered pulses. The ion acoustic pulse becomes higher and its spatial width decreases with increasing κ so that the area of the pulse stays approximately constant, $A(1,\tau) \approx \pm\pi/2$.

The spatial pulse profiles at fixed values of τ are shown in Fig. 2. In the time interval $26 \le \tau \le 32$ the pulse area resembles the kink-soliton solution of the ordinary sine-Gordon equation. The acoustic wave amplitude is connected to the derivative of $A(\xi,\tau)$ and has approximately the form of a hyperbolic secant. At the beginning ($\tau \approx 23.6$) and at the end of the pulse ($\tau \approx 33.6$) the ion wave amplitude is clearly asymmetric. These

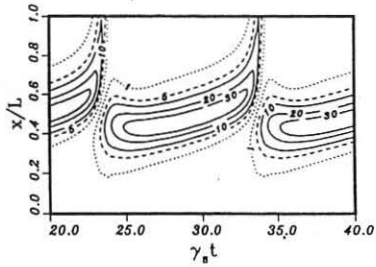

FIG. 1. Ion acoustic wave intensity $|v|^2 = |\partial A/\partial\xi|^2$ for pump intensity $\kappa = 14$ and reflectivity $r^2 = 0.1$.

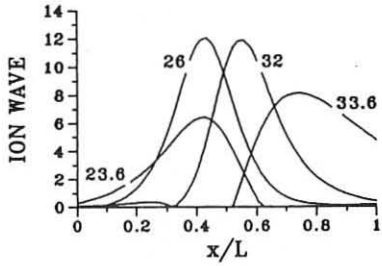

FIG. 2. Amplitude of the ion acoustic pulse $v = \partial A/\partial\xi$ at $\gamma_s t = 23.6$, 26, 32, and 33.6 ($\kappa = 14$, $r^2 = 0.1$).

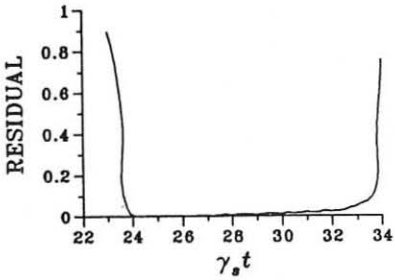

FIG. 3. The residual contribution $\Delta(\tau)$ that remains after approximating the ion acoustic pulse by the hyperbolic secant $R(\xi,\tau)$ ($\kappa = 14$, $r^2 = 0.1$).

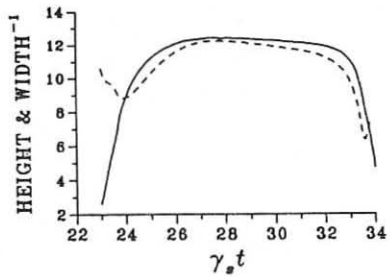

FIG. 4. Height $a(\tau)$ (solid) and inverse spatial width $b(\tau)$ (dashed) of the ion acoustic pulse $2v = 2\partial A/\partial\xi$ ($\kappa = 14$, $r^2 = 0.1$).

deviations from the sech-form appear when the pulse has an appreciable amplitude near the plasma boundaries $\xi = 0$ and $\xi = 1$.

To check how well the ion wave amplitude, $2v = 2\partial A/\partial\xi$, agrees with a kink-solution of the sine-Gordon equation we have compared it with the function

$$R(\xi,\tau) = a(\tau)\,\mathrm{sech}\{b(\tau)[\xi - c(\tau)]\} \tag{4}$$

as suggested in Ref. [9]. The residual of the fit is defined as

$$\Delta(\tau) = \frac{\int_0^1 |2v(\xi,\tau) - R(\xi,\tau)|^2 d\xi}{\int_0^1 |2v(\xi,\tau)|^2 d\xi}. \tag{5}$$

An example of $\Delta(\tau)$ is shown in Fig. 3. The spatial shape of the ion wave agrees quite well with the hyperbolic secant everywhere except at the beginning and at the end of the pulse.

The height, $a(\tau)$, and the inverse width, $b(\tau)$, of the pulse are shown in Fig. 4. The pulse has the property $a \approx b$ which is exactly what one would expect from a kink-soliton solution. In fact this is only a reformulation of the area conservation property of the pulse mentioned before.

4 Conclusions

In the present report we have studied the soliton-like properties of the ion acoustic wave in double stimulated Brillouin scattering. We have shown that the ion wave area obeys a damped sine-Gordon equation, which is a good motivation for searching soliton-like solutions. During propagation the total area of the ion acoustic pulse is approximately $\pm\pi/2$ and the shape of the pulse resembles hyperbolic secant. The pulse height equals its inverse width and its length increases with increasing pump intensity. In our 'numerical experiments' we have not seen any sign of chaotic behaviour of the scattering. We have not found any evidence of transitions between the fundamental and the higher order modes in contrast to the observations of [8].

The boundaries seem to play an important role in the dynamics of the system. When the ion acoustic pulse arrives near the boundary of the plasma slab it is strongly deformed and a new pulse begins to grow. The pulsation of the ion wave is due to the boundaries and the continuous feeding of pump energy into the system.

We are grateful to Dr. J. Hietarinta for useful discussions. This research has partly been supported by The Fusion Research Project of the Technical Research Centre of Finland.

References

[1] Baumgärtel, K., and Sauer, K., Phys. Rev. A **26**, 3031 (1982).
[2] Randall, C. J., and Albritton, J. R., Phys. Rev. Lett. **52**, 1887 (1984).
[3] Zozulya, A. A. *et al.*, Sov. Phys. JETP **59**, 756 (1984).
[4] Chegotov, M. V. *et al.*, Plasma Phys. and Contr. Fusion **28**, 413 (1986).
[5] Pättikangas, T. J. H., and Salomaa, R. R. E., to be published in Phys. Scr.
[6] Silin, V. P. *et al.*, Sov. J. Plasma Phys. **12**, 204 (1986).
[7] Pättikangas, T. J. H., and Salomaa, R. R. E., submitted to Laser Part. Beams.
[8] Andreev, N. E. *et al.*, Sov. J. Plasma Phys. **13**, 212 (1987).
[9] Drühl, K., and Alsing, G., Physica **20D**, 429 (1986).

TRAPPING OF THE PARAMETRICALLY UNSTABLE PLASMA WAVES BY THE FIELD OF LANGMUIR SOLITON

V.V. Demchenko

International Atomic Energy Agency
Vienna, Austria

As shown in Ref. 1-3, the spatial dependence of the amplitude of the pump electrical field can lead to the parametrical excitation of absolutely unstable (localized) plasma waves. However the approximation of the "prescribed" external field amplitude profile, used in Ref. 1-3, loses its validity at high electrical field intensity when the self-interaction effects can play a significant role.

The aim of the present paper is to investigate the space-time evolution of parametrically excited plasma waves in the field of Langmuir soliton. We shall study the linear stage of the instability analytically under the assumption that the strictional nonlinearity plays a crucial role in the evolution process. Numerical investigation shows that at the regime of strong nonlinearity the RF pressure leads to a nonlinear saturation of the discrete (trapped) modes instability and to the formation of a state of strong turbulence in which secondary Langmuir solitons and nonlinear ion-acoustic waves are excited.

- Modulational instability in the field of "travelling" soliton.

Let us suppose that in a uniform isotropic plasma by means of external sources it is excited solitary wave of the form (see e.g. Ref. 4)

$$E_0(\xi,t) = E_s \cosh^{-1}(K_s\xi)\, e^{iK_s(\xi + V_{gr}t)}, \qquad (1)$$

where Eo - electrical field amplitude in the coordinate system moving with group velocity of solitary Langmuir wave,

$$\xi = x - V_{gr}t, \quad V_{gr} = 3K_s r_{De} V_{Te}, \quad E_s = 2\sqrt{6}\, K_s T_e/e$$

In the linear approximation the equations for amplitude of the fluctuating electrical field δE and the quasineutral density disturbance δn takes the form

$$i\frac{\partial a}{\partial \tau} + U\frac{\partial^2 a}{\partial y^2} + (\delta + p\cosh^{-2} y)\,a = p\cdot N,$$

$$\frac{\partial^2 N}{\partial \tau^2} - \left(1 - \frac{V_{gr}^2}{V_s^2}\right)\frac{\partial^2 N}{\partial y^2} - 2\frac{V_{gr}}{V_s}\cdot\frac{\partial^2 N}{\partial y\,\partial \tau} = \frac{\partial^2}{\partial y^2}(a + a^*), \qquad (2)$$

where

$$\tau = k_s V_s t, \quad y = k_s \xi, \quad a = \frac{\delta E}{E_s}, \quad N = \frac{16\pi N_0 T}{E_s^2}\cdot\frac{\delta n}{N_0},$$

$$U = \frac{\omega_0}{2k_s V_s}\cdot\frac{3k_s^2 V_{Te}^2}{\omega_{pe}^2}, \quad p = \frac{\omega_0}{2k_s V_s}\cdot\frac{E_s^2}{16\pi N_0 T}, \quad \delta = \frac{\omega_0}{2k_s V_s}\left(1 - \frac{\omega_{pe}^2}{\omega_0^2}\right).$$

In general the dispersion equation which follows from eqs. (2) are cumbersome. More obvious results has been obtained at the condition $\lambda = (Uk_s^{-2}) \ll 1$, when expression for the growth rate takes the form

$$\gamma_\ell = \frac{U}{\lambda^2} W_\ell^{1/2}\left[\frac{2\lambda^2 p}{U(V_{gr}^2/V_s^2 - 1)} - 1\right]^{1/2},$$

$$W_\ell = \frac{\lambda^2}{U}(p + \delta) - (2\ell + 1) > 0, \quad V_{gr} > V_s, \quad \ell = 0, 1, 2\ldots \qquad (3)$$

- <u>Aperiodic parametrical instability in the field of "standing" soliton.</u> The expression for the electrical field amplitude in this case reduces to

$$E_0(x) = E_s \cosh^{-1}(k_s x), \quad k_s = \left(\frac{\Delta}{3}\right)^{1/2} r_{De}^{-1}, \quad \Delta = \frac{\omega_{pe}^2}{\omega_0^2} - 1.$$

In a "subsonic" regime it is easy to transform the system of equations (2) to the linear Shrödinger equation

$$\frac{d^2 N}{dx^2} + \left[\frac{\Omega^2}{V_s^2} + \frac{E_s^2}{24\pi N_0 T\, r_{De}^2}\cosh^{-2}(k_s x)\right]N = 0, \qquad (4)$$

where Ω - the frequency of "slow" plasma oscillations. From the condition of localized solutions existence one can obtain the following expression for the growth rate of ion-acoustic waves, trapped by the field of Langmuir soliton:

$$\gamma_m = \frac{k_s V_s}{2}\left[\left(1 + \frac{E_s^2}{6\pi N_0 T (k_s r_{De})^2}\right)^{1/2} - (1 + 4m)\right], \qquad (5)$$

$$m = 0, 1, 2, \ldots$$

Expression (5) in the limiting case of strong pumping field transforms into known known expression for growth rate of modulational instability in uniform plasma under the effect of homogeneous electrical field

$$\gamma(m=0) = \left(\frac{m_e}{m_i}\right)^{1/2} \omega_{pe} \frac{E_s}{(24\pi N_0 T)^{1/2}}. \tag{6}$$

- Nonlinear regime of an aperiodic parametrical instability.

Initial system of equations describing nonlinear saturation of instability considered at session 2 takes a form

$$i\frac{\partial a}{\partial \tau} + U\frac{\partial^2 a}{\partial \xi^2} + (\delta - pN + p\cosh^{-2}\xi)a = p\cosh^{-1}\xi \cdot N,$$

$$\frac{\partial^2 N}{\partial \tau^2} - \frac{\partial^2 N}{\partial \xi^2} = \frac{\partial^2}{\partial \xi^2}\left[|a|^2 + (a+a^*)\cosh^{-1}\xi\right], \quad \xi = k_s x \tag{7}$$

The results of numberical solution of eqs. (7) are presented in Figures 1 and 2 for parameter values U = 1, p = 4, δ = 0.1 confirming the conclusion on the localization of unstable Langmuir waves by the standing soliton field. At the initial stage of the process the exponential increase of the amplitude of electric field is observed for basic (m = 0) unstable mode with growth rate coinciding by the order of magnitude with the value as determined by (5). The stage of instability saturation is characterized by the formation of soliton structures which have their localization area limited by characteristic space scale of the initial Langmuir soliton. In contrast to the electric field disturbances, the disturbances of plasma density are propagating freely out of the excitation area leading to the widening of the turbulent zone.

References

1. G.L. Morales, Y.C. Lee, Phys. Fluids 19, 690 (1976)
2. T.A. Davydova, S.P. Shamrai, Plasma Phys. 18, 947 (1976)
3. T.A. Davydova, S.P. Shamrai, Plasma Phys. 21, 807 (1979)
4. A. Hasegawa, Plasma instabilities and nonlinear effects, Springer, 1975

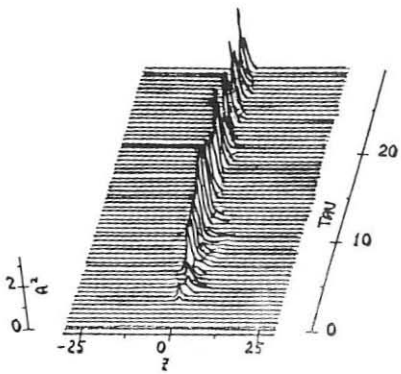

Fig. 1. Dynamics of strong plasma turbulence in the field of "standing" Langmuir soliton ($\delta = 0.1$, $P = 4$, $U = 1$).

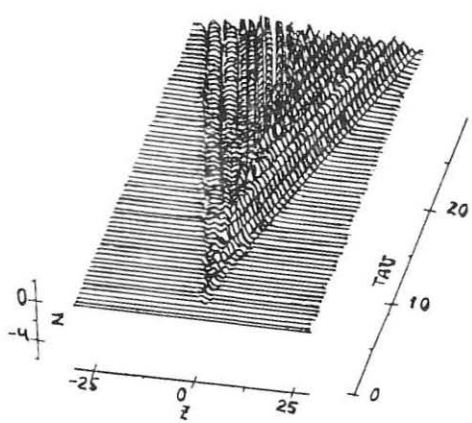

Fig. 2. Generation of localized nonlinear ion-acoustic waves (the same parameters).

A STEADY-STATE TOROIDAL MODEL WITH A FLOW PARALLEL TO THE MAGNETIC FIELD

E A EVANGELIDIS

ATOMIC ENERGY CO., PELINDABA, SOUTH AFRICA

With the recent installation of helical coils on the tokamak at Pelindaba, plasma transport to the edge at times faster than the resistive time is being observed in common with similar situations reported from devices like CSTN-II (Takamura, S. et alt. 1968) and TEXT (McCool, et alt. 1988). The current line of thought in interpreting the fast transport at the edge, favours the flow of electrons parallel to the magnetic field lines of the fluctuations developing in the region of destroyed magnetic surfaces, following the application of the resonant field of the external helical coils. We pursue in what follows the implications of such a flow in the context of an equilibrium steady-state. Thus, in the absence of any magnetic surfaces, use will be made of Maxwell's and Navier-Stokes' equations. In particular, only the solution will be given here of the axisymmetric flow with a velocity coinciding with that of the local Alfvén velocity of the plasma.

The Model

Maxwell's equations in the magnetohydrodynamical approximation are

$$\nabla \wedge E = -\frac{1}{c}\frac{\partial B}{\partial t} \qquad \nabla \wedge B = \frac{4\pi}{c} J \tag{1}$$

Ohm's law relating the current density to the electric field is

$$J = \sigma(E + \frac{u \wedge B}{c}) \tag{2}$$

which for a parallel flow, i.e. $u \parallel B$, becomes

$$J = \sigma E \tag{3}$$

An elimination then of the electric field gives

$$\frac{\partial B}{\partial t} = \eta \nabla^2 B \tag{4}$$

where $\eta = c^2/4\pi\sigma$ is the resistivity of the medium and the conductivity σ is assumed constant over the region of interest described above. This is the first set of equations to be supplemented by Navier-Stokes equation

$$q\frac{du}{dt} = \nabla \cdot P + \frac{J \wedge B}{c} \tag{5}$$

with the pressure tensor P given by

$$P_{ij} = -p\delta_{ij} + \pi_{ij} \tag{6}$$

Although fairly sophisticated expressions exist in the literature for the non-ideal term π_{ij} (Evangelidis et al. 1986), however for simplicity we adopt here the isotropic model described by one viscous coefficient μ, so that

$$\pi_{ij} = \mu\left(\frac{\partial u_i}{\partial x_j} + \frac{\partial u_j}{\partial x_i}\right) \tag{7}$$

Hence a substitution in (5), under the assumption of incompressibility $\nabla\cdot\mathbf{B}=0$, gives

$$\frac{\partial \mathbf{u}}{\partial t} = -\nabla\left(\frac{p + B^2/8\pi}{q}\right) + \nu\nabla^2\mathbf{u} + \frac{1}{4\pi q}\,\mathbf{B}\cdot\nabla\mathbf{B} - \mathbf{u}\cdot\nabla\mathbf{u} \tag{8}$$

with $\nu = \mu/q$ the kinematic viscosity of the conducting medium. So far the motion of the parallel flow has not been assigned any specific mathematical form. In order to progress further, the form

$$\mathbf{u} = \alpha\,\mathbf{B} \tag{9}$$

will be adopted, with α some constant to be defined. A substitution in (8) gives

$$\frac{\partial}{\partial t}(\alpha\mathbf{B}) = -\nabla\left(\frac{p + B^2/8\pi}{q}\right) + (\nu\alpha)\nabla^2\mathbf{B} + \left(\frac{1}{4\pi q} - \alpha^2\right)\mathbf{B}\cdot\nabla\mathbf{B} \tag{10}$$

For a steady-state equilibrium of a medium with finite resistivity and viscosity, equations (3) and (10) give respectively

$$\nabla^2\mathbf{B} = 0 \tag{11}$$

and

$$(\nu\alpha)\nabla^2\mathbf{B} + \left(\frac{1}{4\pi q} - \alpha^2\right)\mathbf{B}\cdot\nabla\mathbf{B} = 0 \tag{12}$$

supplemented by

$$\frac{p + B^2/8\pi}{q} = \text{const.} \tag{13}$$

It is clear now that this system is meaningful for either

$$\mathbf{B}\cdot\nabla\mathbf{B} = 0 \tag{14}$$

or

$$\frac{1}{4\pi q} - \alpha^2 = 0\ . \tag{15}$$

The first condition, upon defining the tangent vector to the field lines by

$$\boldsymbol{\tau} = \mathbf{B}/B \tag{16}$$

leads to

$$(\boldsymbol{\tau}\cdot\nabla B)\boldsymbol{\tau} + B\kappa\mathbf{N} = 0 \tag{17}$$

where $\mathbf{N}$ is the first normal, κ the curvature and use has been made of the identity

$$\boldsymbol{\tau}\cdot\nabla\boldsymbol{\tau} = \kappa\mathbf{N} \tag{18}$$

Thus, condition (13) is the uninteresting case of a constant rectilinear field. Condition (15) determines the constant α uniquely to be

$$\alpha = \frac{1}{4\pi q} \tag{19}$$

so that [cf.(9)]

$$\mathbf{u} = \frac{\mathbf{B}}{\sqrt{4\pi q}} \tag{20}$$

But this is the local Alfvén velocity of the plasma. Thus, the conclusion can be drawn that: In a viscous, incompressible, electrically conducting fluid with finite resistivity, a time independent equilibrium state exists with a flow parallel to the magnetic field. And further, the velocity of the flow coincides with the local Alfvén velocity. It is noted that although the finite resistivity plays a fundamental role in defining the governing equations, it does not however appear in the solution in a direct way.

We proceed now to the solution of the axisymmetric case of (11) in toroidal coordinates. Details on the systems of coordinates and the operators to be used can be found in Evangelidis (1987). If (ρ,θ,ϕ) are

the minor radius, poloidal and toroidal angles respectively, and b the major radius, the components of equation (11) can be written

$$\nabla^2 B^{\hat{\rho}} - \frac{B^{\hat{\rho}}}{\rho^2} - \frac{2}{\rho^2}\frac{\partial B^{\hat{\theta}}}{\partial\theta} - \frac{\cos^2\theta}{(b+\rho\cos\theta)^2}B^{\hat{\rho}} + \frac{\sin\theta}{b+\rho\cos\theta}\left(\frac{\cos\theta}{b+\rho\cos\theta} + \frac{1}{\rho}\right)B^{\hat{\theta}} = 0 \quad (21)$$

$$\nabla^2 B^{\hat{\theta}} - \frac{B^{\hat{\theta}}}{\rho^2} + \frac{2}{\rho^2}\frac{\partial B^{\hat{\rho}}}{\partial\theta} + \frac{\sin\theta}{b+\rho\cos\theta}\left(\frac{\cos\theta}{b+\rho\cos\theta} - \frac{1}{\rho}\right)B^{\hat{\rho}} - \frac{\sin^2\theta}{(b+\rho\cos\theta)^2}B^{\hat{\theta}} = 0 \quad (22)$$

$$\nabla^2 B^{\hat{\phi}} - \frac{B^{\hat{\phi}}}{(b+\rho\cos\theta)^2} = 0 \quad (23)$$

The expressions $\nabla^2 \underline{B}^{\hat{i}}$ are the usual Laplacian operator

$$\nabla^2\psi = \frac{\partial^2\psi}{\partial\rho^2} + \frac{1}{\rho^2}\frac{\partial^2\psi}{\partial\theta^2} + \left(\frac{1}{\rho} + \frac{\cos\theta}{b+\rho\cos\theta}\right)\frac{\partial\psi}{\partial\rho} - \frac{\sin\theta}{b+\rho\cos\theta}\frac{\partial\psi}{\rho\partial\theta}\,. \quad (24)$$

The $B^{\hat{\phi}}$- component is already decoupled, a fact directly accountable for by the condition of axisymmetry. Its solution can be verified to be

$$B^{\hat{\phi}} = A(b+\rho\cos\theta) + \frac{C}{b+\rho\cos\theta} \quad (25)$$

with A,C, some constants. The system of equations (21) and (22) can be decoupled upon making the transformations

$$B^{\hat{\rho}} = \sin\theta\cdot G(\rho,\theta) \quad (26)$$

$$B^{\hat{\theta}} = \cos\theta\cdot G(\rho,\theta) \quad (27)$$

so that the solution of the initial system is reduced to the solution of

$$\nabla^2 G = 0 \quad (28)$$

It is noticed that Laplace's equation has no analytic solution in the trigonometric representation (ρ,θ,ϕ). However, an analytic solution exists in the hyperbolic representation (ϑ,ω,ϕ), to which one goes upon using the transformations (cf. Morse and Feshbach, p.666; or for more details Evangelidis 1987, p. 9)

$$b+\rho\cos\theta = R_o\frac{\mathrm{Sinh}\vartheta}{\mathrm{Cosh}\vartheta - \cos\omega} \quad (29)$$

$$\rho\sin\theta = R_o\frac{\sin\omega}{\mathrm{Cosh}\vartheta - \cos\omega} \quad (30)$$

Thus equation (28) becomes

$$(\mathrm{Cosh}\vartheta-\cos\omega)^2\left(\frac{\partial^2 G}{\partial\vartheta^2} + \frac{\partial^2 G}{\partial\omega^2}\right) + (\mathrm{Cosh}\vartheta-\cos\omega)\left(\frac{1-\mathrm{Cosh}\vartheta\cos\omega}{\mathrm{Sinh}\vartheta}\frac{\partial G}{\partial\vartheta} - \sin\omega\frac{\partial G}{\partial\omega}\right) = 0 \quad (31)$$

Making then the substitution

$$G = \sqrt{\mathrm{Cosh}\vartheta - \cos\omega}\cdot f(\vartheta,\omega) \quad (32)$$

(31) becomes

$$\frac{d^2 f}{d\vartheta^2} + \mathrm{Coth}\vartheta\frac{df}{d\vartheta} + \frac{\partial^2 f}{\partial\omega^2} + \frac{1}{4}f = 0 \quad (33)$$

which can be further Fourier-analyzed to give the "radial equation"

$$\frac{d^2 f_n}{d\vartheta^2} + \mathrm{Coth}\vartheta \frac{df_n}{d\vartheta} - (n^2 - \frac{1}{4}) f_n = 0 \tag{34}$$

This is a special case of Gegenbauer's equation, whose solution for n=integer is Legendre's polynomials of the second kind $Q_{n-1/2}(\mathrm{Cosh}\vartheta)$ appropriate for the interior solution. Hence

$$G(\vartheta,\omega) = \sqrt{\mathrm{Cosh}\vartheta - \cos\omega} \sum_{n=0} A_n \cos(n\omega)\, Q_{n-1/2}(\mathrm{Cosh}\vartheta), \tag{35}$$

and the sought for solution is

$$\hat{B}^{\rho} = \sin\theta \cdot \sqrt{\mathrm{Cosh}\vartheta - \cos\omega} \sum_{n=0} A_n \cos(n\omega)\, Q_{n-1/2}(\mathrm{Cosh}\vartheta) \tag{36}$$

$$\hat{B}^{\theta} = \cos\theta \cdot \sqrt{\mathrm{Cosh}\vartheta - \cos\omega} \sum_{n=0} A_n \cos(n\omega)\, Q_{n-1/2}(\mathrm{Cosh}\vartheta) \tag{37}$$

Finally it is noted that the angle ω is related to θ by

$$\sin\omega = \mathrm{Sh}\vartheta \frac{\rho\sin\theta}{b + \rho\cos\theta} \tag{38}$$

In order to determine the coefficients A_n, it is observed that the energy

$$|B_o(\omega)|^2 \equiv [(\hat{B}^{\rho})^2 + (\hat{B}^{\theta})^2]/8\pi \tag{39}$$

deposited at the limiter at $\vartheta = \vartheta_o$ can be Fourier analysed, so that

$$|B_o(\omega)| = \frac{I_o}{2} + \sum_{m=1} I_l(\vartheta_o)\cos(m\omega) \sqrt{\frac{\mathrm{Cosh}\vartheta - \cos\omega}{8\pi}} \sum_{n=0} A_n \cos(n\omega)\, Q_{n-1/2}(\mathrm{Cosh}\vartheta) \tag{40}$$

Upon using then the identity $(\mathrm{Cosh}\vartheta_o - \cos\omega)^{-1/2} = \frac{\sqrt{2}}{\pi} \sum_{l=0} Q_{l-1/2}(\mathrm{Cosh}\vartheta_o)$ (41)

the coefficients A_n are found to be

$$A_n = \frac{\sqrt{16\pi}}{\pi^2\, Q_{n-1/2}} \sum_{l=0} Q_{l-1/2} \int_0^{2\pi} B_o(\omega) \cos(l\omega)\cos(n\omega)\, d\omega \tag{42}$$

As an example we give the first two coefficients A_o, A_1, in terms of the measured quantities I_m. They are

$$A_o = \sqrt{\frac{16}{\pi}} \{ I_o(\vartheta_o) + \frac{1}{Q_{-1/2}} \sum_{m=1}^{m=\mathrm{Max}(m)} Q_{m-1/2} \cdot I_m(\vartheta_o) \} \tag{43}$$

$$A_1 = \sqrt{\frac{4}{\pi}} \{ I_o(\vartheta_o) + \frac{Q_{-1/2}}{Q_{1/2}} \cdot I_1(\vartheta_o) + \frac{1}{Q_{1/2}} \sum_{l=0}^{\infty} [Q_{l-1/2} \sum_{m=1}^{m=\mathrm{Max}(m)} I_m(\vartheta_o) \cdot \delta_{m-l=1}] \} \tag{44}$$

References

Evangelidis, E. A. On the Theory of a Line Current on a Toroidal Configuration. 1987, Atomic Energy Co., PER-160, ISBN 0 86960 851 7.

Evangelidis, E. A.- Neethling, J.D. 1986, Phys.Fluids, **29**, 2914.

McCool, S. C. et al. 1988, Electron Thermal Confinement Studies with Applied Resonant Fields on TEXT. Submitted to "Nuclear Fusion" (Preprint)

Takamura, S-Okuda, T. 1988, Plasma Physics and Controlled Fusion, **30**, 615

A complete set of resistive compressible ballooning equations for 2-D flow equilibria

K.Grassie and M.Krech
Max-Planck-Institut für Plasmaphysik, Euratom Associaton
D-8046 Garching bei München, Fed. Rep. of Germany

Abstract: Based on the linearized compressible resistive MHD equations we derive a system of five equations describing the time dependent behaviour of ballooning modes in equilibria with sheared flow. The subsequent ordering scheme is based on a two scale expansion, where the fast varying scale is prescribed by an appropriately chosen eikonal.

1. Introduction: Recently considerable effort has been taken to study the stability behaviour of ballooning modes for MHD flow equilibria. In Refs. 1,2 the ideal MHD equations are investigated, where the equilibrium flow consists of a component parallel to the magnetic field and a rigid toroidal rotation. This ideal limit allows a stability analysis in terms of a single quantity ξ, the Lagrangian displacement vector, which is well known from the energy principle. In their analysis Chun and Hameiri [2] find periodic bursts in the time dependence of the perturbed flow velocity due to a parametric resonance in their equation. Similar conclusions are reached by Cooper [3], who studies the resistive but incompressible case in the framework of the WKB-method [4,5], where periodic bursts in the perturbed flow velocity as a function of time are found numerically. Now, looking at investigations of stability of resistive ballooning modes for static MHD equilibria [6,7], the governing equations are derived in a certain ordering scheme, which is directly applied to the linearized MHD equations. In the following section we will follow this line and derive a set of five ballooning equations for MHD flow equilibria, i.e. containing resistivity as well as compressibility effects.

2. The ballooning equations: We start from the usual linearized MHD equations.
Momentum balance :

$$(1)\quad \rho\frac{\partial\tilde{\mathbf{v}}}{\partial t} = -\rho(\tilde{\mathbf{v}}\cdot\nabla)\mathbf{V} - \rho(\mathbf{V}\cdot\nabla)\tilde{\mathbf{v}} - \tilde{\rho}(\mathbf{V}\cdot\nabla)\mathbf{V} - \nabla\tilde{p} + (\nabla\times\tilde{\mathbf{b}})\times\mathbf{B} + (\nabla\times\mathbf{B})\times\tilde{\mathbf{b}}.$$

Continuity equation :

$$(2)\qquad \frac{\partial\tilde{\rho}}{\partial t} = -\mathbf{V}\cdot\nabla\tilde{\rho} - \tilde{\mathbf{v}}\cdot\nabla\rho - \tilde{\rho}\nabla\cdot\mathbf{V} - \rho\nabla\cdot\tilde{\mathbf{v}}.$$

Energy balance :

(3) $$\frac{\partial \widetilde{p}}{\partial t} = -\mathbf{V}\cdot\nabla\widetilde{p} - \widetilde{\mathbf{v}}\cdot\nabla p - \Gamma\widetilde{p}\nabla\cdot\mathbf{V} - \Gamma p\nabla\cdot\widetilde{\mathbf{v}}.$$

Maxwell's equations:

(4) $$\frac{\partial \widetilde{\mathbf{b}}}{\partial t} = \nabla\times(\widetilde{\mathbf{v}}\times\mathbf{B}) + \nabla\times(\mathbf{V}\times\widetilde{\mathbf{b}}) - \eta\nabla\times(\nabla\times\widetilde{\mathbf{b}})$$

(5) $$\nabla\cdot\widetilde{\mathbf{b}} = 0$$

All perturbations are indicated by twidles. To consistently introduce our ordering scheme, we specify two distinct scales denoted by $x_{fast} = x_\perp, x_{slow} = x_\parallel$ and t_{fast}, t_{slow} for rapid and slow variation of quantities in space and time, respectively. The scales are distinguished by the 'bookkeeping' parameter ε and our requirements on derivatives

$$\nabla_\perp\widetilde{a} = O(\varepsilon^{-1}), \quad \nabla_\parallel\widetilde{a} = O(1), \quad \nabla_\perp A = O(1), \quad \nabla_\parallel A = O(1)$$

(6) $$\frac{\partial\widetilde{a}}{\partial t}|_{fast} = O(\varepsilon^{-1}), \quad \frac{\partial\widetilde{a}}{\partial t}|_{slow} = O(1)$$

of perturbations and equilibrium quantities, as well as

(7) $$\eta = O(\varepsilon^2)$$

for the resistivity. The symbols $\nabla_\perp$ and $\nabla_\parallel$ denote derivatives perpendicular and parallel to the equilibrium magnetic field, respectively. All perturbations are now expanded asymptotically in powers of ε, e.g.

(8) $$\widetilde{a}(x_\perp, x_\parallel, t_{fast}, t_{slow}) = \widetilde{a}_0(x_\perp, x_\parallel, t_{fast}, t_{slow}) + \varepsilon\widetilde{a}_1(x_\perp, x_\parallel, t_{fast}, t_{slow}) + \ldots$$

The scales are separated by means of an eikonal ansatz of the form

(9) $$\widetilde{a}_i = a_i(x_\perp, x_\parallel, t_{fast}, t_{slow}) exp\frac{i}{\varepsilon}S(x_\perp, t_{fast}), \quad i = 0, 1, \ldots$$

Equations (1)-(5) are now consistently solved to order ε^{-1}, if the eikonal satisfies

(10) $$\frac{\partial S}{\partial t}|_{fast} + \mathbf{V}\cdot\nabla_\perp S = 0$$

and the constraints from momentum balance

$$\frac{1}{\varepsilon}\nabla S(p_0 + \mathbf{B}\cdot\mathbf{b}_0) = 0. \tag{11}$$

From the continuity equation ,energy balance and Maxwell's equations we obtain :

$$\frac{1}{\varepsilon}\nabla S\cdot\mathbf{v}_0 = 0, \qquad \frac{1}{\varepsilon}\nabla S\cdot\mathbf{b}_0 = 0 \quad . \tag{12}$$

These constraints are equivalent to the following representations of the perturbations

$$\mathbf{v}_0 = \frac{v_\parallel}{B^2}\mathbf{B} + v_\perp\frac{\mathbf{B}\times\nabla S}{B^2} \quad , \quad \mathbf{b}_0 = -\frac{p_0}{B^2}\mathbf{B} + b_\perp\frac{\mathbf{B}\times\nabla S}{(\nabla S)^2} \tag{13}$$

Physically this ordering scheme implies effectively an incompressible motion on the fast time scale. After some algebra we obtain for the momentum balance equations :

$$\begin{aligned}\rho\frac{\partial v_\parallel}{\partial t} &= -\rho(\mathbf{V}\cdot\nabla_\parallel)v_\parallel + \rho v_\parallel\frac{\mathbf{B}}{B^2}\cdot[(\mathbf{V}\cdot\nabla)\mathbf{B} - (\mathbf{B}\cdot\nabla)\mathbf{V}]\\ &+ \rho\frac{v_\perp}{B^2}[(\mathbf{B}\times\nabla S)\cdot(\mathbf{V}\cdot\nabla)\mathbf{B} - \mathbf{B}\cdot[(\mathbf{B}\times\nabla S)\cdot\nabla]\mathbf{V}]\\ &- \rho_0\mathbf{B}\cdot(\mathbf{V}\cdot\nabla)\mathbf{V} - \mathbf{B}\cdot\nabla p_0 + b_\perp\frac{B^2}{(\nabla S)^2}(\nabla\times\mathbf{B})\cdot\nabla S\end{aligned} \tag{14}$$

$$\begin{aligned}\rho(\nabla S)^2\frac{\partial v_\perp}{\partial t} &= 2\rho v_\perp\nabla S\cdot(\nabla S\cdot\nabla)\mathbf{V} - \rho(\nabla S)^2(\mathbf{V}\cdot\nabla_\parallel)v_\perp\\ &+\rho v_\perp\frac{(\nabla S)^2}{B^2}\mathbf{B}\cdot[(\mathbf{V}\cdot\nabla)\mathbf{B} + (\mathbf{B}\cdot\nabla)\mathbf{V}]\\ -\rho v_\perp(\nabla S)^2\nabla\cdot\mathbf{V} &- \rho_0(\mathbf{B}\times\nabla S)\cdot(\mathbf{V}\cdot\nabla)\mathbf{V} - 2p_0\boldsymbol{\kappa}\cdot(\mathbf{B}\times\nabla S) + B^2(\mathbf{B}\cdot\nabla)b_\perp\\ &-\rho v_\parallel\frac{(\mathbf{B}\times\nabla S)}{B^2}\cdot[(\mathbf{V}\cdot\nabla)\mathbf{B} + (\mathbf{B}\cdot\nabla)\mathbf{V}].\end{aligned} \tag{15}$$

From Faraday's law we obtain :

$$\frac{\partial b_\perp}{\partial t} = -2\frac{\nabla S\cdot(\nabla S\cdot\nabla)\mathbf{V}}{(\nabla S)^2}b_\perp - \frac{\mathbf{B}}{B^2}\cdot[(\mathbf{B}\cdot\nabla)\mathbf{V} + (\mathbf{V}\cdot\nabla)\mathbf{B}]b_\perp \tag{16}$$

$$+\frac{(\mathbf{B}\times\nabla S)}{B^2}\cdot[(\frac{\mathbf{B}}{B^2}\cdot\nabla)\mathbf{V}-(\mathbf{V}\cdot\nabla)\frac{\mathbf{B}}{B^2}]b_{\|}-(\mathbf{V}\cdot\nabla_{\|})b_{\perp}+\frac{(\nabla S)^2}{B^2}(\mathbf{B}\cdot\nabla)v_{\perp}-\eta n^2(\nabla S)^2 b_{\perp}$$

and from the continuity equation and energy balance :

$$\frac{\partial\rho_0}{\partial t}=-(\mathbf{V}\cdot\nabla_{\|})\rho_0-\mathbf{v}_0\cdot\nabla\rho-\rho_0\nabla\cdot\mathbf{V}-\rho\nabla_{\|}\cdot\mathbf{v}_0-\rho\nabla_{\perp}\cdot\mathbf{v}_1 \tag{17}$$

$$\frac{\partial p_0}{\partial t}=-(\mathbf{V}\cdot\nabla_{\|})p_0-\mathbf{v}_0\cdot\nabla p-\Gamma p_0\nabla\cdot\mathbf{V}-\Gamma p\nabla_{\|}\cdot\mathbf{v}_0-\Gamma p\nabla_{\perp}\cdot\mathbf{v}_1. \tag{18}$$

Note that the term $\propto \nabla_{\perp}\cdot\mathbf{v}_1$ in the last two equations is of the next to leading order in ε and has to be eliminated by the parallel component of Faraday's law :

$$B^2\nabla_{\perp}\cdot\mathbf{v}_1=\frac{\partial p_0}{\partial t}+\mathbf{B}\cdot(\mathbf{b}_0\cdot\nabla)\mathbf{V}-\mathbf{B}\cdot(\mathbf{V}\cdot\nabla_{\|})\mathbf{b}_0+p_0\nabla\cdot\mathbf{V}-\frac{1}{2}(\mathbf{v}_0\cdot\nabla)B^2+\eta n^2(\nabla S)^2 p_0 \tag{19}$$

3. Discussion: In the flowless case the system of equations (14)-(19) trivially reproduces the ordinary time dependent ballooning equations of Refs.(6,7). Furthermore we see from eq.(10) that the parametric resonance disappears in the case of parallel flow. In this limit the eikonal remains, as in the static case, constant in time.
One important feature of our ordering scheme is the appearance of slow time derivatives only. Since the system appears to be incompressible on the fast time scale, we do not have to consider effects of the fast magnetoacoustic wave in this ordering.
Numerical solutions of these equations will be presented in a forthcoming publication.

Acknowledgement: We thank K. Lackner for helpful discussions.

References

1. E. Hameiri and P. Laurence, J. Math. Phys. **25 (1984), 396.**
2. S.T. Chun and E. Hameiri, Courant Institute of Mathematical Sciences report, New York (1988).
3. W.A. Cooper, Centre de Recherches en Physique des Plasmas report, Lausanne (1988).
4. J.W. Connor, R.J. Hastie, and J.B. Taylor, Phys. Rev. Lett. **40 (1978), 396.**
5. R.L. Dewar and A.H. Glasser, Phys. Fluids **26 (1983), 3038.**
6. D. Correa-Restrepo, Z. Naturforschung **37a (1982), 848.**
7. H.P. Zehrfeld and K. Grassie, Nuclear Fusion **28 (1988), 891.**

STUDY OF CURVATURE INDUCED LOW FREQUENCY INSTABILITIES in a Toroidal Plasma

D.Bora, C.B.Dwivedi and P.K.Kaw

Institute for Plasma Research, Gandhinagar 382424, India.

ABSTRACT

Experimental and theoretical studies of low frequency curvature induced instabilities have been conducted in a basic toroidal magnetic field system called BETA. Coherent fluctuations in density and potential around 9 kHz are observed. At radially outer locations, the oscillation is identified as curvature induced Rayleigh-Taylor (R-T) instability. The instability is stabilized by applying a small shear to the toroidal field. The measured threshold values for shear stabilization are found to be higher than those predicted from collisionless plasma theory. A quantitative explanation for the increased shear fields required has been given in terms of a collisional plasma theory, which is worked out in some detail.

I. INTRODUCTION

It is well known that a magnetically confined plasma in a region with bad curvature is unstable to flute perturbations. This is due to the fact that the centrifugal force acting on the particles gives rise to the 'gravitational instability'. Several experiments with curved magnetic field lines have been conducted to study this instability[1-4]. However, in all these experiments the plasma is typically in contact with end plates. We report here on experiments on the curvature induced instability in a purely toroidal magnetised plasma column. In this configuration the field lines are endless (or very long even when field errors and/or shear fields are taken into account) and difficulties associated with end plates are minimised.

II. EXPERIMENTAL SET-UP AND RESULTS

The measurements are carried out in a toroidal basic plasma device BETA[5]. The major radius of the vacuum vessel is $R_o = 45$ cm while the minor radius is $a = 15$ cm. Argon plasma with a density $n_e \simeq 10^{11}$ cm^{-3} is produced at different pressures between 10^{-4} to 10^{-5} torr. The electron temperature is measured to be $T_e \simeq 5$ eV while the ion temperature (T_i) is measured as (0.7 ± 0.2) eV. The experiment has been conducted at low toroidal magnetic field (B_T) values (typically 200 gauss). At such magnetic field values, a crowbarred magnetic field duration of ~ 40 msec is obtained. A circular conducting aperture with a diameter of 20 cm defines the main plasma radial dimension.

The equilibrium plasma density (n) and the floating potential (V_f) profiles are measured in the radial direction with the help of electrostatic Langmuir probes (fig. 1). Low frequency fluctuations in density ($\tilde{n}$) and floating potential ($\tilde{V}_f$) are also measured during the experiment.

It is observed that beyond a critical field $B_T \sim 150$ gauss, the fluctuations appear suddenly (during the fluctuation measurement the field varies by less than 6%). As B_T is increased, higher harmonics of the basic frequency also appear and finally the fluctuations become turbulent. Radial profiles of $\tilde{n}$ and $\tilde{V}_f$ are plotted in fig. 2. Fluctuations in the ion saturation current and floating potential are simultaneously recorded at different radial and azimuthal positions. Cross correlation P_{12} between two signals $\tilde{n}$ from two azimuthal positions is shown in fig. 3. The coherence spectrum is also shown in the same figure. The fundamental frequency is measured as $\simeq 9$ kHz. The phase difference between $\tilde{n}$, $\tilde{V}_f$ signals at the two azimuthal locations has a value of 180°. The phase shift is same at the radially outer position ($r = 6$ cm). However, in contrast, the phase shift at the inner radial position ($r = -3$ cm) is measured to be less than 45°. To further identify the instability, we introduce a small shear to the toroidal field by applying a weak vertical magnetic field. The amplitude of the fluctuations as a function of the vertical field is shown in fig. 4. The instability is suppressed at all positions except $r = -3$ cm. Since the R-T instability is strongly suppressed by shear and gives 180° phase shift between $\tilde{n}$, $\tilde{\phi}$ we conclude that fluctuations at all locations other than $r \simeq -3$ cm are dominated by R.T. mode. Fluctuations in the vicinity of $r \simeq -3$ cm seem to be dominated by the density gradient drift waves. It is interesting to note that $r = -3$ cm is the location of the maximum density gradient in the good curvature region.

III. THEORETICAL CONSIDERATIONS

Experimentally it is observed that the vertical field required for shear stabilization of the R-T instability is larger than that predicted by collisionless theory. To explain this discrepancy, the dispersion relation for R-T instability in a collisional plasma (dominant collisional effect being the friction on the parallel electron motion) is derived on the basis of Braginskii two fluid equations. The dispersion relation in slab geometry, may be written[6]

$$\omega_i^2 + \omega_i\,[-(k_\perp g/\Omega_i + k_\perp C_i^2 k/\Omega_i) + i(m_i k_\parallel^2 \Omega_i^2/m_e k_\perp^2 \nu_e)(1 + k_\perp^2 C_e^2/\Omega_i \Omega_e)]$$

$$+ [k\,g - i(k_\parallel^2 m_i \Omega_i^2/m_e k_\perp^2 \nu_e)\{(k_\perp C_e^2 k/\Omega_e) + (k_\perp C_i^2 k/\Omega_i)\}] = 0 \qquad (1)$$

where $\omega_i = [\omega + (k_\perp k\, C_i^2/\Omega_i) + (k_\perp g_i/\Omega_i) + (k_\perp C E_o/B_o)]$, $C_{i,e}^2 = k_B T_{i,e}/m_{i,e}$, $\nu_e = \nu_{ei} + \nu_{en}$, $g = (C_i^2 + C_e^2 m_e/m_i)/R$, $g_i = C_i^2/R$, $k = -(1/n_o)(dn_o/dR)$, $r_L = C_i/\Omega_i$, ν_{ei} and ν_{en} are the electron-ion and electron neutral collision frequencies and other symbols have usual meanings. Eqn. (1) has been derived under the assumptions of quasi-neutrality, neglect of electron inertia and the conditions $\omega_i \ll \Omega_i$, $k_\perp r_L \ll 1$, $\nu_e \ll \Omega_e$. Fig. 5 shows a plot depicting the variation of the growth rate with the applied shear ('vertical') field and the background pressures. The vertical field needed for suppression of the R-T instability and its variation with background pressure are found to be in good agreement with experimental results.

Certain features of the experimental results, such as the existence of R.T. instability dominated fluctuations in the good curvature region ($r = -8$ cms) cannot be explained by the local slab approximation theory described above. We have set up the eigenvalue problem for R.T. modes in a plasma with equilibrium density variations $n_o(R,z) = n_{oo} \exp[-(R-R_o)^2/2L_n^2]$ but with modes defined by boundary conditions $\tilde{\phi} = 0$ on a circular conducting aperture of radius a, as in the experiment. The electron and ion continuity equations may be written as

$$-[\bar{\omega}_p + (ik_{\parallel}^2 C_e^2/\nu_e)](n_p/n_o) + (g_e/n_o\Omega_e)\,[(m+p)(n_{p+1} + n_{p-1})/\rho + (n_{p+1} - n_{p-1})/\rho$$
$$+ (n'_{p+1} - n'_{p-1})] + [C(m+p)/2B_oL_n^2 + ek_{\parallel}^2/m_e]\,\phi_p + \Phi_p = 0 \qquad (2)$$

and

$$-\bar{\omega}_p\,(n_p/n_o) - (e\omega_p/m_i\Omega_i^2)\,[\{\partial(\bar{\omega}_p\,\partial\phi_p/\partial\rho)/\partial\rho\}/\bar{\omega}_p + (\partial\phi_p/\partial\rho)/\rho$$
$$+ (m+p)^2\,\phi_p/\rho - \rho\Omega_i\phi_p/2\omega_p L_n^2] + \Phi_p = 0 \qquad (3)$$

where $g_e = m_eC_e^2/m_iR$, $\bar{\omega}_p = \omega - (m+p)\,CE_o/B_o\rho$, m,p denote poloidal mode numbers which couple to each other due to equilibrium θ variations.

$$\Phi_p = (a_oC/2B_o)\,[(m+p)(\phi_{p+1} + \phi_{p-1})/\rho + (\phi_{p+1} - \phi_{p-1})/\rho + (\phi'_{p+1} - \phi'_{p-1})]$$
$$+ (\rho C/4B_oL_n^2)[m+p)(\phi_{p+2} + \phi_{p-2})/\rho + 2(\phi_{p+2} - \phi_{p-2})/\rho + (\phi'_{p+2} - \phi'_{p-2})]$$

In the limit $(m+p) >> 1$, we recover the slab results as we should. The above difference-differential equations are being numerically solved after using an appropriate truncation procedure and results will be published separately. They show that R.T. fluctuations indeed have a finite amplitude in the good curvature region.

IV. CONCLUSIONS:

R.T. instability has been observed in purely toroidal magnetic field and stabilized with the help of weak shear in B_T. Experimentally observed shear requirement is well explained by a theory including parallel electron friction. A more realistic geometry calculation can qualitatively explain appearance of R-T fluctuations in good curvature region.

We thank G.Prasad for his assistance in numerical work.

REFERENCES:

1. N.D'Angelo et. al. Phys. Rev. Lett. 11, 525 (1963).
2. A.C.Kolb et al. Phys. Fluids, 8, 1005 (1965).
3. H.Sugai et al. Phys. Fluids, 20, 90 (1977).
4. A.Komori et al. Phys. Rev. Lett. 40, 768 (1978).
5. D.Bora et al. Phys. Lett. A. 49, 411 (1987).
6. F.F.Chen. Phys. Fluids, 8, 1323 (1965).

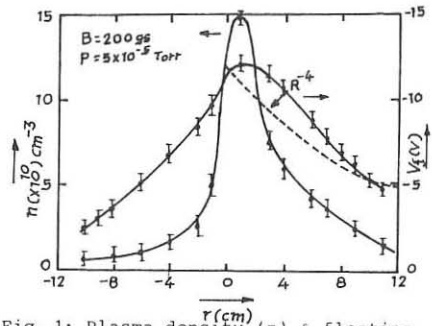

Fig. 1: Plasma density (n) & floating potential (V_f) as a function of minor radius (r).

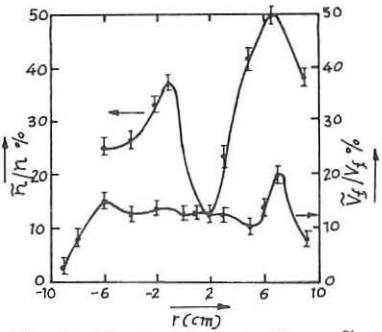

Fig. 2: Fluctuations in $\tilde{n}$ and $\tilde{V}_f$ as a function of r.

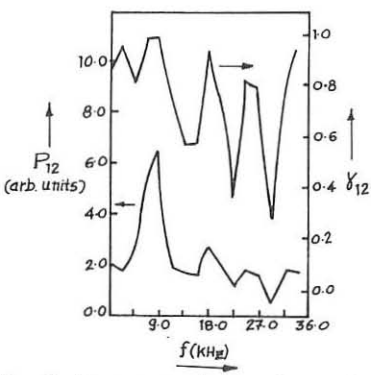

Fig. 3: Cross correlation P_{12} and corresponding coherence spectrum γ_{12}.

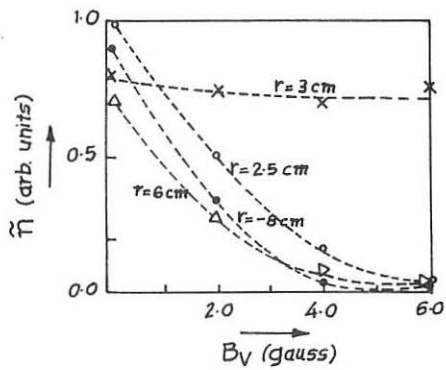

Fig. 4: Amplitude of $\tilde{n}$ as a function of B_v for various radial positions.

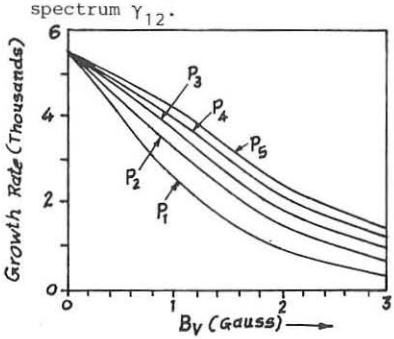

Fig. 5 : Collissional growth rate as a function of B_v for different pressures. $P_1 < P_2 < P_3 < P_4 < P_5$.

ADDITIONAL ADIABATIC HEATING OF PLASMA

Marin R. Mehandjiev

"BIOTECH" Science & Engineering Co., Varna, Bulgaria

A theoretical possibility of a plasma additional adiabatic heating up to temperatures needed for the begin of D-T thermonuclear fusion reaction, has been found on the base of the polyenergetic conjugation expression, developed in the Thermodynamics of Accumulation Processes /TAP/. TAP is a branch of the non-equilibrium thermodynamics. The thermodynamics of irreversible processes is another branch of the entire non-equilibrium thermodynamics. TAP deals with the phenomena associated with the introduction, conversion and accumulation of mass or energy or both in the affected, open or closed, systems. A general form of the polyenergetic conjugation relationship is:

$$T \prod_{r=1}^{j} P_r^{\pm\theta_r} \prod_{i=j+1}^{n} X_i^{\pm\theta_i} = \text{constant}; \; /r+i+1=n \geqslant 2; \; r \neq i/ \qquad 1$$

where: T - Kelvin temperature; P_r, X_i - intensity and capacity factors of n various elementary energy kinds; θ_r, θ_i - experimentally determined exponents. In practical cases n is rarely bigger than 2 or 3. The well known equations which associate the factors of adiabatic gas systems are particular cases of Eq.1; the latter has been proved also for factors as T and the surface area s of solid particles in adiabatic fluid systems. θ_i-value for s in such cases is $|0.04|$. A polyenergetic conjugation equation written for T and s , /n = 2/, has the following forms:

$$T.s^{0.04} = \text{constant} \; ; \quad T_1 s_1^{0.04} = T_2 s_2^{0.04} = \text{constant}, \qquad 2$$

where the symbols are indexed for two successive times: 1 and 2 respectively.

In the initial stage of a D-T thermonuclear fusion reaction, injections of 10^5- 10^6 $m^{-3}s^{-1}$ carbon dust particles with approximately 10^{-8} m diameter are necessary for a plas-

ma heated up to 6 keV and having 10^{17} m^{-3} deuterium and tritium ions. Assuming $s_2 = 10^{-6} s_1 \to 0$ in Eq.2, the effective plasma temperature T_2, due to the adiabatic disappearance of 3.10^{10} $m^2 s^{-1}$ surface area of dust particles, calculated by Eq.3:

$$T_2 = 6\left(\frac{1}{10^{-6}}\right)^{0.04} = 10.44 \text{ keV} \qquad 3$$

is 10.44 keV, which is considered sufficient for the begin of the fusion reaction.

Heat quantities needed for heating up to 4470 K and for evaporation of the dust particles, as well as for the ionization of the carbon atoms are, in the case of 10^6 m^{-3} particles, as follows: 1815.10^{16} $keV.g^{-1}$; 37441.10^{16} $keV.g^{-1}$ and 55220.10^{16} $keV.g^{-1}$ respectively, or 2.10^{-2} $keV.s^{-1}.ion^{-1}$ on the whole. That total heat can be ensured by the collisions between the plasma flux particles and the dust particles or carbon atoms. Assuming a realization of 0.1 s^{-1} collisions and 0.033 s^{-1} favorable collisions; using the constant value $k = 0.8625.10^{-7}$ $keV.K^{-1}$, an initial plasma temperature $T_1 = 6$ keV $= 4.64 \cdot 10^7$ K and, a negligible initial dust particles' temperature, we can calculate that the favorable collisions ensure an energy equal to:

$$1.32 \cdot 10^{-1} \text{ keV.s}^{-1}\text{.ion}^{-1} > 2.10^{-2} \text{ keV.s}^{-1}\text{.ion}^{-1}$$

The value of the slowing-down radiation power density is: $2.6 \cdot 10^{-1}$ $keV.m^{-3}.s^{-1}$ and therefore is also negligible.

Thus an additional adiabatic heating of the plasma in accordance with Eq.3, using injections of carbon dust particles in the plasma flux, can ensure a stabilized and controlable thermonuclear fusion process. As known, carbon powder with particles' diameter of about 10^{-9} m is produced and used in chemical experiments nowadays [1].

According to the Adenergetic Effect Rule of TAP each continuous constant impact can cause an instability of the affected system, due to acceleration phenomena [2]. Therefore, an absolutely constant dust quantity injection velocity $/g.s^{-1}/$ should be avoided. On the other side, the evaporation of the dust particles in the plasma volume should prevent the fragmentation of the plasma flux, observed in the thermonuclear fusion experiments. That fragmentation is, probably, a

result of the process' acceleration, regarding the adenergetic effect rule of TAP.

Conclusion.

A theoretical possibility of controlled thermonuclear fusion realization in limited plasma volumes and at moderate input plasma conditions is proposed on the base of regularities of the thermodynamics of accumulation processes. That possibility consists in injections of carbon dust particles of high purity and dispersity, or other similar particles, in the heated up to 6 keV D-T plasma flux.

References.

1. Astahov M.V., E.P. Solovieva and I.V. Frolova, Journ. of Phys. Chem. 57 /1983/ 5, 1252 /Russian/
2. Mehandjiev M.R., Metalloberfläche, 31 /1977/ 7, 303-308.

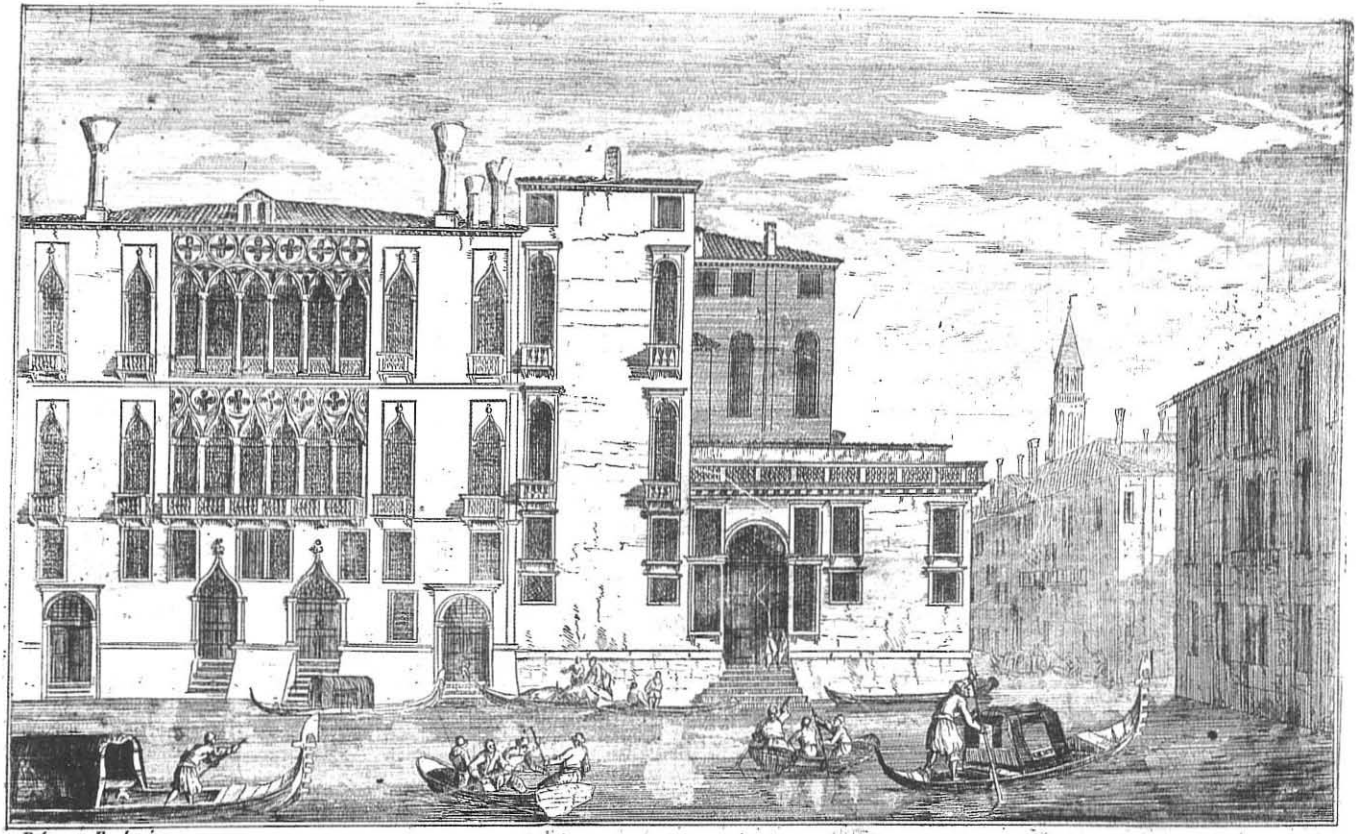

1 Palazzo Barbarigo

PALAZZO PISANI

A' S. Tomaso Sopra il Canal Grande

87.

Luca Carlevarijs del. et inc.

QUASILINEAR THEORY OF BUNEMAN'S INSTABILITY IN HOT ELECTRON PLASMA $T_e \gg T_i$

Sh. M. Khalil and B. F. Mohamed

Atomic Energy Authority, Nuclear Research Centre
Plasma Physics and Accelerators Dept
Cairo, Egypt

The development of Buneman kinetic instability in plasma with hot electrons and cold ions is investigated in the quasilinear approximation. It is supposed that the current in the plasma is determined by the relative motion of ions and electrons that appears, for instance, due to propagation of low frequency surface wave or big amplitude waves in plasma injection, θ-pinches and other devices.

We confine ourselves to the case of sufficiently high frequency and small scale plasma oscillations, so that unperturbed density n_0, temperature T and current velocity u are practically homogeneous and do not change during the development of instability. Thus the problem is reduced to the study of instability excited in a homogeneous plasma in which electrons move with respect to ions with a velocity exceeding the threshold velocity ($u > u_{cr}$).

It is known that, at great current velocities ($u \gg u_{cr}$), Buneman's instability takes place /1/, and it can be saturated under the conditions of plasma strong turbulence /2/. Accordingly, strong turbulent heating of the plasma may lead to rapid increase of u_{cr} up to a value u. Therefore, it is of great interest to investigate the instability at current velocities close to the instability threshold values, i.e. at $\Delta u = u - u_{cr} \ll u_{cr}$

We start using the collisionless, field-free Vlassov's kinetic equation

$$\frac{\partial f^\alpha}{\partial t} + \vec{v}\frac{\partial f^\alpha}{\partial \vec{r}} - \frac{e}{m}\vec{\nabla}\phi\frac{\partial f^\alpha}{\partial \vec{v}} = 0 \,. \tag{1}$$

As usually done in the quasilinear treatment we set $f^\alpha = f_0^\alpha + \tilde{f}^\alpha$ with $|f_0^\alpha(\vec{r},t)| \gg |\tilde{f}(\vec{r},\vec{v},t)|$, $\alpha = e, i$.

Hence we get

$$\frac{\partial f_0^\alpha}{\partial t} = \frac{e}{m}\frac{\partial}{\partial \vec{v}}\langle \nabla\phi\, \tilde{f}^\alpha \rangle \,, \tag{2}$$

$$\frac{\partial \tilde{f}^\alpha}{\partial t} = -\vec{v}\frac{\partial \tilde{f}^\alpha}{\partial \vec{r}} + \frac{e}{m}\vec{\nabla}\phi\frac{\partial f_0^\alpha}{\partial \vec{v}} + \frac{e}{m}\left[\vec{\nabla}\phi\frac{\partial \tilde{f}^\alpha}{\partial \vec{v}} - \frac{\partial}{\partial \vec{v}}\langle \vec{\nabla}\phi\, \tilde{f}^\alpha \rangle\right] , \tag{3}$$

where $\langle \cdots \rangle$ are averaging symbols over phases, and $\langle \tilde{f} \rangle = \langle \phi \rangle = 0$. Neglecting nonlinear terms on the right hand side of (3) and using Fourier transform

$$\{\tilde{f}^{\alpha}, \phi\} = \sum_{\varkappa} \{f^{\alpha}_{\varkappa}, \phi_{\varkappa}\} e^{i(\vec{k}\cdot\vec{r} - \omega t)}, \quad \varkappa \equiv \vec{k}, \omega$$

equation (3) becomes

$$(\omega - \vec{k}\vec{v}) f^{\alpha}_{\varkappa} = -\frac{e}{m} \phi_{\varkappa} \left(\vec{k} \frac{\partial f^{\alpha}_{0}}{\partial \vec{v}}\right) \tag{4}$$

Using Fourier transformation over velocity, we get

$$\left(k \frac{\partial}{\partial p} + i\omega\right) f^{\alpha}_{\varkappa}(\vec{p}) = \frac{e}{m} \phi_{\varkappa} \cdot (\vec{k}\vec{p}) f^{\alpha}_{0}(\vec{p}) \tag{5}$$

with the following solution:

$$f_{\varkappa}(\vec{p}) = \phi_{\varkappa} \cdot M_{\varkappa}(\vec{p}), \tag{6}$$

$$M_{\varkappa}(\vec{p}) = \frac{e}{mk} \exp\left(-i \frac{\omega(\vec{k}\vec{p})}{k^2}\right) \int_{\infty}^{(\vec{k}\vec{p})/k} d\vec{p}\, (\vec{k}\cdot\vec{p}) f^{\alpha}_{0}(\vec{p}) \exp\left(i \frac{\omega(\vec{k}\vec{p})}{k^2}\right) \tag{7}$$

Similarly we can obtain for (2)

$$\frac{\partial f^{\alpha}_{0}}{\partial t} = \frac{e}{m} \sum_{\varkappa} |\phi_{\varkappa}|^2 (\vec{k}\cdot\vec{p}) M_{\varkappa}(\vec{p}) \tag{8}$$

and from Poisson's equation we have

$$\phi_{\varkappa} = \frac{4\pi}{k^2} \sum_{\alpha} e_{\alpha} \int_{0}^{\infty} f^{\alpha}_{\varkappa}\, d\vec{v} \tag{9}$$

In the case of weak nonlinearity the background distribution function not a Maxwellian function. It is convinent to set

$$f^{\alpha}_{0}(\vec{p}) = f^{\alpha}_{m}(\vec{p}) + \delta f^{\alpha}_{0}(\vec{p}) \; ; \; f^{\alpha}_{m} = n_0 e^{-i\vec{p}\vec{u}_{\alpha} - \frac{1}{2} p^2 V_{T\alpha}^2}, \; V_{T\alpha} = (T_{\alpha}/m_{\alpha})^{1/2} \tag{10}$$

Denoting

$$\vec{p}' = p_{\parallel} \frac{\vec{k}}{k} + \frac{\vec{k} \times (\vec{p} \times \vec{k})}{k^2} = \vec{p}_{\parallel} + \vec{p}_{\perp},$$

and using (10) in (6), (8) we can obtain the the linear and quasilinear dielectric permeabilities describing the system as

$$\varepsilon^{\alpha}(\vec{k}, \omega) = 1 - \sum_{\alpha} \frac{\omega^2_{p\alpha}}{k^2} \int_{0}^{\infty} dp_{\parallel} \frac{(\vec{k}\cdot\vec{p}')}{k} e^{i \frac{\omega}{k^2} p_{\parallel}} f^{\alpha}_{m}, \tag{11}$$

$$\delta\varepsilon^{\alpha}(\vec{k}, \omega) = \sum_{\alpha} \frac{\omega^2_{p\alpha}}{k^2} \int_{0}^{\infty} dp_{\parallel} \frac{(\vec{k}\cdot\vec{p}')}{k} e^{i \frac{\omega}{k^2} p_{\parallel}} \delta f^{\alpha}_{0}, \tag{12}$$

where,

$$\delta f^{\alpha}_{0} = -\left(\frac{e_{\alpha} n_0}{m_{\alpha} V_{T\alpha}}\right)^2 \sum_{\varkappa'} (\vec{k}'\vec{p}) \left(\int_{0}^{t} I_{\varkappa'} dt'\right) W_p(z^{\alpha}_{\varkappa'}) e^{-i \frac{\omega(\vec{k}'\vec{p})}{k^2}} \tag{13}$$

with

$$W_p(z^{\alpha}_{\varkappa'}) = 2 \int_{(\vec{k}'\vec{p})V_{T\alpha}/\sqrt{2}k'}^{\infty} d\tau \cdot \tau \cdot \exp(-\tau^2 + 2i z^{\alpha}_{\varkappa'} \tau),$$

$$Z^{\alpha}_{\varkappa'} = \frac{\omega - \vec{k}'\vec{u}_\alpha}{\sqrt{2}\,k' V_{T\alpha}}, \quad I_{\varkappa} = |\phi_{\varkappa}|^2, \quad \omega_{p\alpha} = (4\pi e_\alpha^2 n_0 / m_\alpha)^{1/2}$$

Introducing $\sum_{\varkappa'} \to \int d\vec{k}'$

the quasilinear dielectric will take the form

$$\delta\varepsilon^{\alpha}(\vec{k},\omega) = -\frac{e_\alpha}{\sqrt{\pi}}\left(\frac{\omega_{p\alpha}}{k T_\alpha}\right)^2 Z^{\alpha}_{k} e^{-Z^{\alpha\,2}_{k}} \int \frac{k'^3}{\left(\frac{\omega}{k} - \frac{\omega'}{k'}\right)^3} dk' \int_0^t I_{k'} dt \qquad (14)$$

In our case $T_e \gg T_i$, and we can find that $|\delta\varepsilon^e / \delta\varepsilon^i| \ll 1$, i.e. the contribution of the electrons is very small in the dispersion equation and can be neglected.

The dispersion equation of the system will have the form

$$1 + \varepsilon^{\alpha}_{\ell} + \delta\varepsilon^{i} = 0 \qquad (15)$$

Using the value of $\delta\varepsilon^i$ from (14) in the dispersion equation (15), and making use of the results of the linear theory /3/, we can obtain the frequency and growth rate of the instability

$$\omega = \omega_\ell + \delta\omega, \qquad \gamma = \gamma_\ell + \delta\gamma \qquad (16)$$

$$\delta\omega = \frac{\omega_0 k_0^2 V_{Ti}^2}{2\omega_{pi}^2} \operatorname{Re}\delta\varepsilon^i, \qquad \delta\gamma = \frac{2k_0^2 V_{Ti}^2}{2\omega_{pi}^2} \operatorname{Im}\delta\varepsilon^i \qquad (17)$$

$$\gamma_\ell = \sqrt{\frac{\pi}{8}}\,\omega_0 \left(\frac{u_{cr}}{V_{Te}}\right)\left(\frac{T_i}{T_e}\right)\left(\frac{\Delta u}{u_{cr}} - \frac{\theta^2}{2} - \left(\frac{\Delta k}{k_0}\right)^2\right) \qquad (18)$$

$$\omega_\ell = \omega_0\left(\frac{T_i}{T_e}\right)\left[2X_1^2\left(\frac{\Delta u}{u_{cr}} - \frac{\theta^2}{2}\right) - \frac{3}{2}(1 - X_1^2)\left(\frac{\Delta k}{k_0}\right)^2\right], \quad X_1 = \frac{u_{cr}}{\sqrt{2}\,V_{Te}} \qquad (19)$$

ω_0, k_0, u_{cr} are the threshold(frequency, wave number, velocity) of the instability, θ is the angle between $\vec{k}$ and $\vec{u}$.

The equation describing the intensity of oscillations will have the form

$$\frac{\partial I_{\vec{k}}}{\partial t} = 2 I_{\vec{k}} (\gamma_\ell + \delta\gamma) \qquad (20)$$

At $T_e \gg T_i$, equations (14),(16) indicates that, under the condition $(\omega/k) > (\omega'/k')$, $\delta\varepsilon^e$ and hence $\delta\gamma$ is of negative value, and this showes that the quasilinear effect leads to the suppression of the Buneman's instability. On the other hand when $(\omega/k) < (\omega'/k')$, the instability is growing sharply. In the case of hot ion plasma $T_i \gg T_e$ /4/, the quasilinear effect leads to a gradual increase of the growth rate and to the transformation from a weak instability in the linear stage into strong one ($\gamma_k \simeq \omega_k$).

For isothermal plasma $T_i = T_e$ /5/, in the case when an external electric field is applied, it is found that for critical value of this field E_{cr}, the instability is amplified for $E < E_{cr}$ and a saturation of the instability at $E > E_{cr}$, in the quasilinear approximation.

The nonlinear stage of Buneman's instability in the proximity of its excitation threshold is studied in ref. /6/. It was proved that for such instability the nonlinear wave interaction is not essential, and the major effect, saturation of the instability, is when taking into account quasilinear approximation.

References.

/1/ Buneman, O., Phys. Rev. Lett., 1, 8 (1958).

/2/ Sizonenko, V.L., and Stepanov, K.N., Plasma Physics, 13, 1033 (1971).

/3/ Khalil, Sh.M., Sayed, Y.A., and Sayed, R.A., Arab J. Nuclear Sciences and Applications (accepted for publication, 16.11.1986). IC/86/186, INT. REP. - ICTP,Trieste-Italy (1986).

/4/ El-Naggar, I.A., Khalil, Sh.M., and Sizonenko, V.L., J. Plasma Physics, 20, 75 (1978).

/5/ Khalil, Sh. M., El-Naggar, I.A., and Sizonenko, V.L., Int. Congress on Waves and Instabilities in Plasmas, June 27-July 1, Palaiseau Cedex, France (1977).

/6/ Hussein, A.M., Khalil, Sh.M., and Sizonenko, V.L., Plasma Physics, 20, 545 (1978).

GYROKINETIC CYCLOTRON INSTABILITY OF ENERGETIC IONS IN TOKAMAK PLASMAS

R. O. Dendy and C. N. Lashmore-Davies
Culham Laboratory, Abingdon, Oxfordshire, OX14 3DB, England
(Euratom/UKAEA Fusion Association)

The stability of the fast wave in the presence of an energetic ion population is of interest in both beam-heated and thermonuclear fusion plasmas. Here, tokamak plasmas are modelled using a magnetic field $\underline{B} = B_o \underline{e}_z (1+x/L_B)$, the hot ion velocity distribution is represented by a drifted ring, and fast wave cyclotron resonance is examined within the framework of gyrokinetic theory. This enables the variation of magnetic field strength across the gyro-orbit to be included, giving a treatment of finite Larmor radius cyclotron resonance that differs qualitatively from a locally uniform approach.

We employ the arbitrary frequency gyrokinetic theory of Chen and Tsai[1,2], which provides an exact linear formulation of cyclotron resonance in general non-uniform magnetic fields. The relevance of this formalism to radio frequency plasma phenomena has been noted by Lee, Myra and Catto[3], but its full potential has not yet been exploited. Following Refs.1 and 2, we start with the linearized Vlasov equation in particle phase space $(\underline{x}, \underline{v})$:

$$[\partial/\partial t + \underline{v}.\underline{\nabla}_x + (q/mc)(\underline{v} \times \underline{B}).\underline{\nabla}_v]\delta f = -(q/mc)(c\delta\underline{E} + \underline{v} \times \delta\underline{B}).\underline{\nabla}_v F, \quad (1)$$

where δf and F are the perturbed and equilibrium distribution functions, and $\delta\underline{E}$, $\delta\underline{B}$ and $\underline{B}$ are the perturbed electric and magnetic fields and the equilibrium magnetic field respectively. The arbitrary frequency gyrokinetic equation[1,2], is obtained by transforming Eq.(1) to guiding centre phase space $(\underline{X}, \underline{V})$, where $\underline{X} = \underline{x} + \underline{v} \times \underline{e}_\parallel/\Omega$ and $\underline{V} = (\epsilon, \mu, \alpha)$. Here $\epsilon = v^2/2$, $\mu = v_\perp^2/2B$, $\underline{e}_\parallel = \underline{B}/B$, $\Omega = eB/mc$, α is the gyrophase angle defined by $\underline{v}_\perp = v_\perp(\underline{e}_1 \cos\alpha + \underline{e}_2 \sin\alpha)$, and $\underline{e}_\parallel$, $\underline{e}_1$ and $\underline{e}_2$ are local orthonormal vectors. We refer to Refs. 1 and 2 for the derivation of the high frequency gyrokinetic equation,

$$\langle L_g \rangle_\ell \langle \delta H_g \rangle_\ell \simeq i(q/m)[\omega \partial F_{go}/\partial\epsilon + (\ell\Omega/B)\partial F_{go}/\partial\mu]\langle \delta\psi_g \rangle_\ell \quad , \qquad (2)$$

where $\langle L_g \rangle_\ell = (\tilde{v}_\parallel \underline{e}_\parallel + \underline{v}_d).\underline{\nabla}_X - i(\omega - \ell\Omega + \ell\omega_\alpha)$, and the subscript g refers to guiding centre coordinates. Note that magnetic field inhomogeneity enters $\langle L_g \rangle_\ell$ explicitly, through the spatial dependence of Ω. The quantities $\tilde{v}_\parallel$ and ω_α are defined in Refs. 1 and 2 but are not required here, and $\underline{v}_d$ is the equilibrium drift (soon to be neglected) due to magnetic field inhomogeneity. The perturbed field amplitudes enter Eq.(8) through the quantity $\delta\psi_g = \delta\phi_g - \underline{v}.\delta\underline{A}_g/c$, where $\delta\phi$ and δA are the electromagnetic potentials and the Coulomb gauge is used. In obtaining Eq.(2), the perturbed quantities have been expanded as Fourier series in α, which enters through the guiding centre transformation. For example, $\langle \delta H_g \rangle_\ell = (2\pi)^{-1}\int_0^{2\pi} d\alpha \delta H_g(\underline{X}, \mu, \epsilon, \alpha)\exp(i\ell\alpha)$, where δH_g is proportional to the perturbed distribution function

δf [1,2]. We represent all perturbed quantities by eikonals of the form $\delta f = \delta f_{\underline{k}} \exp(i\underline{k}.\underline{x})$, where $\underline{k} = \underline{e}_x \cos\xi + \underline{e}_y \sin\xi$. The contribution to $\delta f_{\underline{k}}$ associated with the resonant value of ℓ is

$$(\delta f_{\underline{k}})_R = \frac{qL_B/\ell m}{(v_\perp \sin\alpha - \beta_\ell)} \left[\frac{(\omega - \ell\Omega)}{v_\parallel} \frac{\partial F_o}{\partial v_\parallel} + \frac{\ell\Omega}{v_\perp} \frac{\partial F_o}{\partial v_\perp}\right] \times$$
$$\sum_{p=-\infty}^{\infty} \exp[i(p-\ell)(\alpha-\xi)] J_p\left(\frac{k_\perp v_\perp}{\Omega}\right) \left\{J_\ell\left(\frac{k_\perp v_\perp}{\Omega}\right)\left[\delta\phi_{\underline{k}} - \frac{v_\parallel}{c}\delta A_{\underline{k}}\right] - \frac{v_\perp}{k_\perp} J'_\ell\left(\frac{k_\perp v_\perp}{\Omega}\right)\frac{\delta B_\parallel \underline{k}}{c}\right\}, \tag{3}$$

where $\beta_\ell = (L_B/\ell)[\omega - \ell\Omega(x)]$. The resonant contribution to the x-component of the perturbed current density is

$$(\delta J_{x\underline{k}})_R = q\int(\delta f_{\underline{k}})_R v_\perp^2 \cos\alpha \, dv_\perp dv_\parallel d\alpha. \tag{4}$$

For the y-component, $\cos\alpha$ in Eq.(4) is replaced by $\sin\alpha$. In order to perform the integration in Eq.(4), it is necessary to specify the equilibrium hot ion velocity distribution F_o in Eq.(3). We choose a drifted ring distribution,

$$F_o = (n_o/2\pi v_\perp)\delta(v_\perp - v_{\perp o})\delta(v_\parallel - v_{\parallel o}) \ . \tag{5}$$

Combining Eqs. (3) and (5) with Eq.(4) and its equivalent for $(\delta J_{y\underline{k}})_R$, we obtain the resonant perpendicular current that arises from the perturbed hot ion distribution. For substitution into Poisson's and Maxwell's equations, we require the expressions

$$\begin{vmatrix} (\underline{k}.\delta\underline{J}_{\underline{k}})_R \\ (\underline{k}\times\delta\underline{J}_{\underline{k}})_R \end{vmatrix} = -\frac{n_o q^2 \Omega k_\perp L_B}{2\pi m v_{\perp o}} \sum_{p=-\infty}^{\infty} \int \frac{\partial g_p}{\partial v_\perp}\Bigg|_o \exp[i(p-\ell)(\alpha-\xi)] \begin{vmatrix} \cos(\alpha-\xi) \\ \sin(\alpha-\xi) \end{vmatrix} d\alpha. \tag{6}$$

Here $|_o$ denotes evaluation at $v_\perp = v_{\perp o}$ and $v_\parallel = v_{\parallel o}$, and

$$g_p = \frac{v_\perp J_p\left(\frac{k_\perp v_\perp}{\Omega}\right)}{(v_\perp \sin\alpha - \beta_\ell)} \left[J_\ell\left(\frac{k_\perp v_\perp}{\Omega}\right)\left(\delta\phi_{\underline{k}} - \frac{v_\parallel}{c}\delta A_\parallel \underline{k}\right) - \frac{v_\perp}{k_\perp} J'_\ell\left(\frac{k_\perp v_\perp}{\Omega}\right)\frac{\delta B_\parallel k}{c}\right]. \tag{7}$$

Note that α enters the gyrokinetic resonant denominator in the integrand in Eq.(6), through its appearance in Eq.(7). This is a consequence of magnetic field variation across the Larmor orbit. By combining Eq.(6) with standard expressions for the contributions to

$\underline{k}.\delta\underline{J}_k$ and $\underline{k} \times \delta\underline{J}_k$ from background ions, electrons, and non-resonant hot ion terms, the dispersion relation for the fast wave propagating across the inhomogeneous magnetic field can be obtained from Poisson's and Maxwell's equations.

This approach has enabled us to identify a new instability for the fast wave in the presence of the hot ion distribution Eq.(5), which exists in the limit of uniform magnetic field. We denote bulk ions and hot ions by subscripts a and b respectively, and assume a small hot ion population $\omega_{pb}^2 << \omega_{pa}^2$. The appearance of $\delta A_{\parallel k}$ in Eq.(7) is a new feature of our theory. Here, however, we take the limit $v_{\parallel o}/c << 1$, so that the term proportional to $\delta A_{\parallel k}$ in Eq.(7) is negligible. Eliminating the remaining field amplitudes $\delta\phi_{\underline{k}}$ and $\delta B_{\parallel k}$ between Poisson's and Maxwell's equations, we obtain the following dispersion relation for fast wave propagation perpendicular to the magnetic field, in the limit $L_B \to \infty$:

$$\omega^2 - c_A^2 k_\perp^2 = \frac{\Omega_a^2(\omega^2 - \Omega_a^2)}{\omega_{pa}^4(\omega - \ell\Omega_b)} \left[G_1 + \frac{G_2}{(\omega - \ell\omega_b)}\right]' . \tag{8}$$

Here, c_A is the Alfvén velocity and, writing $k_\perp v_{\perp o}/\Omega_b = \nu_o$,

$$G_1 = -\frac{\ell^3\Omega_b\omega_{pb}^2\omega_{pa}^2}{(\omega^2 - \Omega_a^2)} \left\{\frac{\Omega_b}{\Omega_a}[J_{\ell-1}^2(\nu_o) + J_{\ell+1}^2(\nu_o) - 2J_\ell^2(\nu_o)] + \left[\frac{\nu_o^2}{\ell^2} - 2 - \frac{c_A^2 k_\perp^2(\omega^2 - \Omega_a^2)}{\ell^2\Omega_b^2\Omega_a^2}\right]\frac{2J_\ell(\nu_o)J'_\ell(\nu_o)}{\nu_o}\right\} , \tag{9}$$

$$G_2 = -\ell^2\omega_{pb}^4\left[\left(1 - \frac{\ell^2}{\nu_o^2}\right)J_\ell^2(\nu_o) + J_\ell'^2(\nu_o)\right]^2 . \tag{10}$$

We now examine the stability of the fast wave near the cyclotron resonance of the hot ions. Setting $c_A k_\perp = \ell\Omega_b$, and solving Eq.(8) for $\omega = \ell\Omega_b + \delta\omega$, we obtain a cubic equation for $\delta\omega$. This has complex roots, corresponding to instability, provided

$$G_2^2 > \frac{4\Omega_a^2(\ell^2\Omega_b^2 - \Omega_a^2)}{54\ell\Omega_b\omega_{pa}^4} G_1^3 . \tag{11}$$

For $\ell\Omega_b > \Omega_a$, the inequality Eq.(11) is necessarily satisfied whenever G_1 is negative. By Eq.(9), G_1 is negative whenever $J_\ell(\nu_o) = 0$. This demonstrates the existence of an instability. Let us denote the nth zero of J_ℓ by $s_{\ell n}$, so that fast wave instability at the ℓth cyclotron harmonic resonance of the hot ions occurs whenever $\nu_o \simeq s_{\ell n}$. Then the growth rate is given by

$$\gamma_{\ell n} = \mathrm{Im}\ \delta\omega = \ell\Omega_b \frac{3^{1/2}}{4^{1/3}} \frac{\omega_{pb}}{\omega_{pa}} \frac{\Omega_a^{1/2}}{\Omega_b^{1/2}} J_{\ell-1}(s_{\ell n}) . \tag{12}$$

This is proportional to the square root of the hot ion density. We note that $\gamma_{\ell n}$ is proportional to $\ell J_{\ell-1}(s_{\ell n})$, which is a monotonically increasing function of ℓ. Also, the conditions $c_A k_\perp = \ell\Omega_b$ and $\nu_o \simeq s_{\ell n}$ yield

$$v_{\perp o}/c_A \simeq s_{\ell n}/\ell. \tag{13}$$

It follows that instability requires a super-Alfvénic perpendicular velocity $v_{\perp o}$, whose magnitude decreases with increasing resonant harmonic number ℓ. A more detailed analysis of the dependence of Eqs.(9) to (11) on ν_o would enable us to quantify the properties of the instability more exactly.

In conclusion, our gyrokinetic analysis has shown a new cyclotron instability for the fast wave, propagating perpendicular to a uniform magnetic field in the presence of a drifted ring hot ion population. The formalism required to extend this treatment to non-uniform magnetic fields, which is our next objective, is given by Eqs.(6) and (7). Gyrokinetic theory offers a means of extending the existing approach [5] to cyclotron instabilities driven by energetic particles, by including both magnetic field inhomogeneity and more realistic fusion product and beam distributions.

REFERENCES

[1] L. Chen and S.-T. Tsai, Phys. Fluids 26, 141 (1983).
[2] L. Chen and S.-T. Tsai, Plasma Phys. 25, 349 (1983).
[3] X. S. Lee, J. R. Myra and P. J. Catto, Phys. Fluids 26, 223 (1983)
[4] C. N. Lashmore-Davies and R. O. Dendy, Culham Preprint CLM-P850.
[5] K. N. Stepanov and A. B. Kitsenko, Sov. Phys. Tech. Phys. 6, 127 (1961).

A GALILEI-INVARIANT GYROKINETIC EQUATION FOR MAGNETOPLASMAS

Massimo Tessarotto

Dipartimento di Scienze Matematiche, Università degli Studi di Trieste
TRIESTE, Italy

ABSTRACT – This paper addresses the problem of derivation of a general nonlinear gyrokinetic equation for magnetoplasmas fulfilling the basic symmetry property of Galilei invarance.

INTRODUCTION

A common feature of all existing kinetic theories for magnetoplasmas immersed in a strong magnetic field $\underline{B}$, which exibits time and space variations weak in an appropriate sense, [2–11] is that they are derived from non-relativistic particle dynamics by an expansion in a small parameter ϵ – to be identified with the ratio between the particle Larmor radius and a characteristic macroscopic scale length L, i.e. $\epsilon = r_L/L$ – in a fashion analogous to the time-honoured Chew, Golberger and Low technique [1]. A basic aspect of such approaches [2–11], besides the aforementioned expansion technique, is the adoption of averaging with respect to the gyro-phase (φ), i.e. an azimuth in velocity space in a plane perpendicular to the magnetic field $\underline{B}$, yielding the so-called guiding center mechanics. Thus they produce an iterative scheme in which the expansion in ϵ is truncated at prescribed order in ϵ, yielding a closed set of equations.

A problem is, however, that such truncation leads usually to the loss of exact conservation laws and symmetries and, in particular to violation of the basic symmetry of Galilei invariance.

Various approaches have been proposed in order satisfy, at least in part, such requirements and, at the same time, furnish a rational basis for guiding center kinetic theories [7,9,11].

Thus Boozer [7], considering the particular case of time-independent fields, proposed an "ad hoc" modification of the drift kinetic equation, in such a way to make possible the fulfillment of approximate conservation laws (i.e., the gyrophase-average of the canonical momentum conjugate to an ignorable spatial coordinate in the case of exact spatial symmetries).

Instead, Littlejohn [9], while still retaining time-independent fields and disregarding kinetic theory, considered the problem in the framework of guiding center mechanics in the presence of large drift, showing that, by defining appropriate non canonical transformations, it is possible to preserve at least some conservation theorems and, at the same time, include higher-order terms.

Finally, a third independent approach due to Bernstein and Catto [11], developed in the framework of the so-called gyrokinetic theory, was able to reproduce and extend the results of Littlejohn, adopting a conceptually simpler approach, based on a gyrokinetic change of variables due to Catto [6]. Their theory apart simplicity has the merit of yielding, for a particular set of phase-space coordinates, a (gyro-) kinetic equation which is authomatically accurate through first order with respect to a Larmor radius expansion without the need of recurring to an iterative scheme.

However, common feature of such guiding center kinetic theories is that they do not fulfill an exact property of Galilei invariance. The violation of such a basic

symmetry property, on the other hand, might lead to unpredictable results, especially when dealing with a nonlinear guiding center kinetic theory. Purpose of this communication is to show how such a deficiency can be corrected and a Galilei invariant guiding center kinetic equation can be derived. The method adopted, which has recently been proposed by the author [12], is based on an extension of an algorithm previously developed by Catto [6] and by Bernstein and Catto [11], allowing the derivation of a gyrokinetic equation in terms of the respective guiding center drift orbits.

GALILEI-INVARIANT GYROKINETICS

It has been questioned by Wimmel [10] whether Galilei invariance can be preserved at all in a guiding center theory, suggesting that some formal restrictions might actually exist inhibiting the existence of an optimized, i.e. Galilei invariant guiding center theory. However, it is not hard to find out the origin of the difficulties met by customary guiding-center theories [12]. Here we intend to point out a solution to this wellknown problem, showing that a Galilei invariant gyrokinetic equation can be formulated, by introducing a suitable set of velocity-space coordinates.

Galilei invariance is, of course, espressed by the condition that for an isolated mechanical system the equations of motion are invariant with respect to the (special) Galilei transformation:

(1) $\underline{r} \to \underline{r}' = \underline{r} + \underline{V}_0 t$

with $\underline{V}_0$ an arbitrary constant (non-relativistic) velocity, which induces the velocity transformation:

(2) $\underline{v} \to \underline{v}' = \underline{v} + \underline{V}_0$

Hence, for a magnetoplasma immersed in an electromagnetic field $\{\underline{E},\underline{B}\}$, it is understood that the transformation (1) is a rigid transformation applied not only to the mechanical system forming the plasma but also to the (external) sources generating the electromagnetic field, i.e. $\underline{E}$ and $\underline{B}$ transform under (2) as:

(3) $\underline{E} \to \underline{E}' = \underline{E} - \frac{\underline{V}_0}{c} x \underline{B}$, and $\underline{B} \to \underline{B}' = \underline{B}$

while they are invariant with respect to a rigid traslation in the previous sense.

Let us now recall that in previous guiding-center theories [see for example Refs. 9,11] the gyrophase φ was defined according to Eq.(9), identifying the reference velocity $\underline{U}(\underline{r},t)$ with the electric drift velocity $\underline{U}_E = c\underline{E}x\underline{B}/B^2$. Accordingly φ, by itself, is not invariant with respect to the velocity transformation (2). Introducing, in addition, as customary, the decomposition:

(4) $\underline{v} = u\underline{b} + \underline{w} + \underline{U}$

where

(5) $u = \underline{b}.(\underline{v} - \underline{U})$

(6) $w = \left[(\underline{v} - \underline{U})^2 - u^2 \right]^{1/2}$

we find that u and w are similarly non invariant.

It is possible to notice that the basic difficulty met by previous guiding-center theories is essentially related to such a type of choice for the velocity-space coordinates as well as to the truncation procedure used in the perturbative expansion

in terms of the small parameter ϵ. We observe, in fact, that the kinetic (Fokker-Planck) equation expressed in terms of the previous velocity-space variables is, of course, still Galilei invariant as its gyro-phase average. However, upon introducing a perturbative expansion with respect to the small parameter ϵ, and a truncation to some prescribed order in ϵ, Galilei invariance may be lost due to the fact that the some of the terms assuring preservation of Galilei invariance (and appearing in the transformed variables corresponding to φ, u, w) are usually neglected, being considered of higher order in ϵ.

Such a problem would evidently not appear if the velocity-space coordinates (φ, u, w) could be suitably chosen in such a way to be already invariant with respect to the velocity transformation (2).

Here we intend to show that this problem can be solved in an simple way. In particular we find that an invariant gyrophase can be obtained by redefining appropriately the reference velocity $\underline{U}(\underline{r},t)$ in Eq.(9), i.e. by setting:

$$(7) \qquad \underline{U}(\underline{r},t) = \underline{U}_E - \underline{U}_B(\underline{r},t)\cdot\underline{bb}$$

with $\underline{U}_E = \frac{c}{B^2}\underline{E}\times\underline{B}$ the electric drift and $\underline{U}_B(\underline{r},t)$ the baricentric velocity of the fluid element:

$$(8) \qquad \underline{U}_B(\underline{r},t) = \frac{\Sigma_s M_s N_s^{-1}\int d^3v\,\underline{v}f_s(\underline{r},\underline{v},t)}{\Sigma_s M_s}$$

Denoting here with a prime the quantities in the moving frame, in fact by definition one gets:

$$(9) \qquad \underline{U}'_E = \frac{c}{B'^2}\underline{E}'\times\underline{B}' = \underline{U}_E + \underline{V}_0\cdot(\underline{\underline{I}}-\underline{bb})$$

$$(10) \qquad \underline{U}'_B = \underline{U}_B + \underline{V}_0$$

and therefore il follows that $\underline{U}' = \underline{U} + \underline{V}_0$ and $\underline{v}' - \underline{U}' = \underline{v} - \underline{U}$. By redefining accordingly also the velocity-space coordinates u and w (see Eqs.(4)-(6)), we obtain a set of velocity-space coordinates (u, w, φ) which are invariant with respect to the velocity transformation (2). As can readily be seen they advance in time through the following set equations of motion:

$$(11) \qquad \dot{u} = \underline{b}\cdot\left(\frac{Ze}{M}\underline{E} - \frac{1}{2}w^2\nabla\ln B - \frac{d}{d\tau}\underline{V}\right) + \underline{w}\cdot\left[\frac{d}{d\tau}\underline{b} - (\nabla\underline{U})\cdot\underline{b}\right] + w^2\frac{\partial}{\partial\varphi}\underline{\underline{F}}:\nabla\underline{b}$$

$$(12) \qquad \begin{aligned}\dot{\varphi} = &-\Omega + \underline{e}_1\cdot\frac{d}{d\tau}\underline{e}_2 - \frac{1}{2}(\underline{\underline{I}}-\underline{bb}):(\nabla\underline{V})\times\underline{b} + \frac{1}{w^2}\underline{w}\times\underline{b}\cdot\left[\frac{d}{d\tau}\underline{V} - \frac{Ze}{Mc}\underline{U}_B\times\underline{B} + \right.\\ &\left. + w^2\underline{b}\times\nabla\underline{e}_1\cdot\underline{e}_2\right] - \frac{\partial}{\partial\varphi}\underline{\underline{F}}:(\nabla\underline{U})\times\underline{b} + u\underline{\underline{F}}:\nabla\underline{b}\end{aligned}$$

$$(13) \qquad \dot{w} = -\frac{1}{2}w(\underline{\underline{I}}-\underline{bb}):\nabla\underline{V} - \frac{1}{w}\underline{w}\cdot\left[\frac{d}{d\tau}\underline{V} - \frac{Ze}{Mc}\underline{U}_B\times\underline{B}\right] - \frac{\partial}{\partial\varphi}w\underline{\underline{F}}:(\nabla\underline{U})$$

where $\frac{d}{d\tau} = \frac{\partial}{\partial t} + (u\underline{b}+\underline{U})\cdot\nabla$ and $\underline{\underline{F}} = \frac{1}{4}\left[\frac{2}{w^2}\underline{w}\underline{w} - \underline{\underline{I}}\right]\times\underline{b}$.-

In conclusion, using such a set of invariant velocity-space coordinates, we find that a Galilei-invariant guiding-center Mechanics can be constructed. In particular, we state here that in terms of them a gyrokinetic equation which exactly preserves Galilei invariance can actually be recovered.

While the details of this derivation shall be reported elsewhere [13], here it sufficies to point out that a procedure analogous to that of Bernstein and Catto

[11] can be conveniently used, which is based on the introduction of a set of so-called gyrokinetic variables $\vec{\xi}'=(\underline{r}',u',w',\varphi')$ related to $\vec{\xi}=(\underline{r},u,w,\varphi)$ through the transformation

$$(14)\quad \vec{\xi}'=\vec{\xi}+\int\frac{d\varphi}{\Omega}\left(\frac{d}{dt}\vec{\xi}-\left\langle\frac{d}{dt}\vec{\xi}\right\rangle\right)$$

where $\Omega = ZeB/Mc$ is the Larmor frequency, the φ-integrals are evaluated keeping $\vec{\xi}$ constant, the brackets "< >" denote the φ-average ($\langle A\rangle=\frac{1}{2\pi}\oint_0^{2\pi}d\varphi A$) and the integration limits are chosen in such a way that $\langle\vec{\xi}'\rangle=\langle\vec{\xi}\rangle$. By introducing furthermore the gyrokinetic gyroaverage:

$$(15)\quad \langle\!\langle Q\rangle\!\rangle=(2\pi)^{-1}\oint d\varphi' Q(\underline{r}',u',w',\varphi',t)$$

(to be performed keeping $\underline{r}'$, u', w' and t constant), a gyrokinetic equation correct through first order in ϵ can then be simply obtained, following a a method analogous to that employed by Bernstein and Catto [11]. In fact, taking the gyroaverage, in the previous sense, of the Fokker-Planck kinetic equation, one obtains, neglecting corrections of higher order in ϵ a *gyrokinetic equation* of the form:

$$(16)\quad \frac{\partial}{\partial t}\langle\!\langle f\rangle\!\rangle+\langle\!\langle \underline{t}'\rangle\!\rangle.\nabla'\langle\!\langle f\rangle\!\rangle+\langle\!\langle \dot{u}'\rangle\!\rangle\frac{\partial}{\partial u},\langle\!\langle f\rangle\!\rangle+\langle\!\langle \dot{w}'\rangle\!\rangle\frac{\partial}{\partial w},\langle\!\langle f=\langle\!\langle C\rangle\!\rangle$$

where the gyrokinetic averages $\langle\!\langle \underline{t}'\rangle\!\rangle$, $\langle\!\langle \dot{u}'\rangle\!\rangle$ and $\langle\!\langle \dot{w}'\rangle\!\rangle$ can be determined upon inversion of the transformation (14), differentiation with respect to time and gyro averaging in terms of (15).

ACKNOWLEDGMENTS

The author is indebted to Prof. Ira B. Bernstein (Yale University, New Haven, Conn., USA) and Dr. Peter J. Catto (Lodestar Research Corp., Boulder, Colo., USA) for clarifying discussions. Work performed in the framework of the MPI 40% Research Program "Modelli e problemi non lineari in Fisica Matematica" of the Italian "Ministero della Pubblica Istruzione".

REFERENCES

1 - G.F.Chew, M.L.Goldberger, F.E.Low, Proc.Roy.Soc.(London), **A236**, 112 (1956).
2 - T.G.Northrop, The adiabatic motion of charged particles, Interscience, 1963.
3 - P.H.Rutherford, E.A.Frieman, Phys.Fluids, **11**, 569 (1968)
4 - J.B.Taylor, R.J.Hasties, Plasma Phys., **10**, 479 (1968)
5 - T.G.Northrop, J.A.Rome, Phys.Fluids, **21**, 384 (1978)
6 - P.J.Catto, Plasma Phys. **20**, 719 (1978).
7 - A.H.Boozer, Phys.Fluids, **29**, 904 (1980).
8 - T.M.Antonsen, B.Lane, Phys.Fluids, **23**, 1205 (1980).
9 - R.G.Littlejohn, Phys.Fluids, **24**, 1730 (1981).
10 - H.K.Wimmel, Z.Naturforsch., **37A**, 985 (1982).
11 - I.B.Bernstein, P.J.Catto, Phys.Fluids, **28**, 1342 (1985).
12 - 6 - M.Tessarotto, Proc. 16th International Symposium on Rarefied Gas Dynamics (July 10-16, 1988, Pasadena, California, USA).
13 - M.Tessarotto, to appear.

WHISTLER AND CYCLOTRON MASER INSTABILITY: NON-RELATIVISTIC, WEAKLY AND FULLY RELATIVISTIC ANALYSIS

M. Bornatici[a,b] and U. Ruffina[b]

[a] Physics Department, University of Ferrara, Ferrara, Italy

[b] Physics Department "A. Volta", University of Pavia, Pavia, Italy

A numerical analysis of the dispersion relation of the right-hand mode is performed for a loss-cone velocity distribution and propagation along the magnetic field. The relevant one-dimensional integral to be dealt with is expressed in terms of a function that is simply related to the conventional plasma dispersion function Z in the weakly relativistic approximation. A comparative study of the fully and weakly relativistic solution relevant to the eletron-cyclotron maser mode as well as of the weakly relativistic and non-relativistic solution for the whistler mode is carried out.

Introduction. Hot electron plasmas formed by electron cyclotron heating in magnetic mirror configurations are characterized by equilibria which can be expressed analytically as a superposition of loss-cone type distribution functions[1,2]. Such anisotropic velocity distributions are susceptible to instabilities of both the whistler[1-3] and the electron-cyclotron maser mode[1,3-8], the latter occurring in the regime where the relativistic corrections to the wave dispersion are significant[7]. In general the (relativistic) dispersion relation relevant to the study of these instabilities has to be solved numerically by performing a two-dimensional integral, which may be reduced to a one-dimensional integral in the limit of temperature isotropy ($T_{\parallel} = T_{\perp}$). Furthermore, the stability analysis is carried out for ω complex and k real, the emphasis being on the instability temporal growth rates which, for the case of the maser instability and arbitrary propagation, are evaluated within the weakly relativistic approximation[5-7], the fully relativistic calculation being limited to propagation along the dc magnetic field and the specific case of $k_{\parallel} = 0$ for which the instability growth rate is maximum[1,3,4].

Here we consider the right-hand mode, propagating parallel to the magnetic field, for which the fully relativistic dispersion relation for a (relativistic) loss-cone distribution (with $T_{\parallel} = T_{\perp}$) can be written in terms of a function that, in the weakly relativistic approximation, is simply related to the conventional (non-relativistic) plasma dispersion function Z. The dispersion relation thus obtained is studied numerically for either ω or k complex, and the accuracy for the weakly relativistic approximation

for the fast mode and the non-relativistic approximation for the slow mode (whistler) is discussed.

Fully relativistic dispersion relation for a loss-cone distribution. For propagation along the magnetic field $\underline{B}_o = \hat{\underline{z}}\,|\underline{B}_o|$, the dispersion relation of the right-hand circularly polarized mode is $N_{\parallel}^2 = (\varepsilon_{xx} + i\varepsilon_{xy})_{N_\perp=0}$, where $N_{\parallel}$ ($N_\perp$) is the parallel (perpendicular) refractive index and ε_{ij} are the ij-elements of the dielectric tensor. For a relativistic loss-cone distribution function one obtains

$$N_{\parallel}^2 = 1 - \left(\frac{\omega_p}{\omega}\right)^2 a_{\ell+2}(\mu)\left\{-\frac{\ell}{a_{\ell+1}(\mu)} + \mu\left[(\ell+1)\,\tilde{F}_{\ell+5/2} - \frac{\omega_c}{\omega}\,\ell\,\tilde{F}_{\ell+3/2}\right]\right\} \qquad (1)$$

where ℓ is the loss-cone index ($\ell=0$ corresponds to the relativistic Maxwellian), $a_q(\mu) = (\pi/2\,\mu)^{\frac{1}{2}}\, e^{-\mu}/K_q(\mu)$ ($=1$, to lowest order in $\mu^{-1} \equiv (mc^2/T)^{-1}$), and the fully relativistic plasma dispersion function $\tilde{F}_q \equiv \tilde{F}_q(\omega/\omega_c,\ \mu,\ N_{\parallel}^2)$ is

$$\tilde{F}_q \equiv -i\int_0^\infty d\tau \frac{e^{\mu(1-i\frac{\omega_c}{\omega}\tau)}}{[(1-i\tau)^2 + N_{\parallel}^2\tau^2]^{q/2}} \left(\frac{2\tilde{z}}{\pi}\right)^{\frac{1}{2}} K_{q-\frac{1}{2}}(\tilde{z}) \qquad (2a)$$

with $\tilde{z} \equiv \mu[(1-i\tau)^2 + N_{\parallel}^2\tau^2]^{\frac{1}{2}}$. By making use of the asymptotic expansion of the Bessel function $K_{q-\frac{1}{2}}$, one can express $\tilde{F}_q$ as

$$\tilde{F}_q = \sum_{k=0}^{n-1} \frac{\Gamma(q+k)}{k!\,\Gamma(q-k)} \frac{1}{(2\mu)^k} F_q + O\left(\frac{1}{\mu^n}\right) \qquad (2b)$$

with $n = 1,2,\ldots$, and

$$F_q \equiv -i\int_0^\infty d\tau \frac{e^{\mu\left[1-\left([1-i\tau]^2+N_{\parallel}^2\tau^2\right)^{\frac{1}{2}} - i\frac{\omega_c}{\omega}\tau\right]}}{[(1-i\tau)^2 + N_{\parallel}^2\tau^2]^{q/2}} \qquad (2c)$$

Note that i) dispersion relation (1) with (2a) is obtained by following the same procedure as the derivation of the second of Trubnikov's formulae for the dielectric tensor fo a relativistic Maxwellian[9]; ii) in the limit $N_{\parallel}^2 \to 0$, the $\tilde{F}_q$-function (2) is the same as the one entering the dispersion relation of the extraordinary mode for perpendicular propagation[8]; iii) in the non-relativistic limit, $a_q(\mu) \to 1$, and

$$\tilde{F}_q \to -\frac{1}{|N_{\parallel}|\sqrt{2\mu}}\, Z(\zeta) \quad , \quad \zeta \equiv \frac{\omega-\omega_c}{\omega}\,\frac{(\mu/2)^{\frac{1}{2}}}{N_{\parallel}} \qquad (3a)$$

($Z(\zeta)$ is the familiar (non-relativistic) plasma dispersion function) so that the dispersion relation (1) reduces to

$$N_{\parallel}^2 = 1 + \left(\frac{\omega_p}{\omega}\right)^2\left\{\ell + \left(\frac{\mu}{2}\right)^{\frac{1}{2}}\frac{1}{|N_{\parallel}|}\left[1 + \left(1 - \frac{\omega_c}{\omega}\right)\ell\right] Z(\zeta)\right\} \qquad (3b)$$

(The effect of the temperature anisotropy associated with a bi-Maxwellian

distribution is accounted for in (3b) by simply replacing ℓ with with $[(\ell+1)\ T_\perp/T_\parallel - 1]$ and μ with $mc^2/T_\parallel$)[2]; iv) in the weakly-relativistic limit, $a_q(\mu) \to 1$, and

$$\tilde{F}_q \to W_q\left[\mu(1-\omega_c/\omega),\ N_\parallel^2\right] \equiv -i\int_0^\infty d\tau\ \frac{i\mu(1-\frac{\omega_c}{\omega})\tau - \frac{\mu N_\parallel^2}{2(1-i\tau)}\tau^2}{(1-i\tau)^q} \qquad (4)$$

the W_q-function being related to the Z-function[10,11]; vi) in the cold limit, $\tilde{F}_q \to \mu(1-\omega_c/\omega)^{-1}$ and (1) yields the well-known (cold) result $N_\parallel^2 = 1-(\omega p/\omega)^2 \cdot (1-\omega_c/\omega)^{-1}$.

Numerical analysis and discussion. The dispersion relation (1) is solved numerically and the solution corresponding to instability is shown in Fig.s 1 and 2 for the whistler (slow) mode, for which $N_\parallel > 1$ and $\omega < \omega_c$, and in Fig.s 3 and 4 for the electron-cyclotron maser mode, that is the relativistic part of the fast ($N_\parallel < 1$) mode at $\omega \lesssim \omega_c$. More specifically, for the whistler mode, the dispersion relation is solved in the weakly-relativistic approximation (4) as well as in the non-relativistic approximation (3b). As it appears from Fig.s 1 and 2, with respect to the non-relativistic solution, the relativistic effects significantly reduce the instability growth rates, the corresponding instability range being somewhat shifted to lower frequencies, cf. Fig.1, and wave numbers, cf. Fig. 2. As for the real part of either the wave number or the frequency, this deviates only slightly from the cold values (the dotted curves). As for the cyclotron maser mode, the solution of the dispersion relation (1) at the cutoff, i.e., for $N_\parallel = 0$, is shown in Fig.s 3 and 4 along with the corresponding solution in the weakly-relativistic approximation (4). It appears that the weakly relativistic approximation is quite accurate for $T \lesssim 50$ keV, tending to overestimate the growth rate for $T > 50$ keV; also, $\mathrm{Re}\,\omega$ strongly deviates from the cold value (dotted curve in Fig.3).

Acknowledgements. This work was supported by the Ministero della Pubblica Istruzione of Italy.

References

1. G.E. Guest and R.L. Miller, Nucl. Fusion 28, 419 (1988)
2. C. Litwin and R.N. Sudan, Phys. Fluids 29, 3760 (1986)
3. K.T. Tsang, Phys. Fluids 27, 1659 (1984)
4. Y.Y. Lau and K.R. Chu, Phys. Rev. Lett. 50, 243 (1983)
5. D. Le Queau, R. Pellat and A. Roux, Phys. Fluids 27, 247 (1984)
6. H.K. Wong, C.S. Wu and J.D. Gaffey Jr., Phys. Fluids 28, 2751 (1985)
7. P.L. Pritchett, Phys. Fluids 29, 2919 (1986)
8. M. Bornatici and U. Ruffina, Plasma Phys. Contr.Fusion 30, 113 (1988)
9. M. Bornatici, R. Cano, O. De Barbieri and F. Engelmann, Nucl. Fusion 23, 1153 (1983)
10. V. Krivenski and A. Orefice, J. Plasma Phys. 30, 125 (1983)
11. I.P. Shkarofsky, J. Plasma Phys. 35, 319 (1986)

Figure Captions

Fig. 1 The real part of the wave number ($Rek_{\parallel}$) and the spatial growth rate ($Imk_{\parallel}$) of the whistler mode as a function of frequency, for $(\omega_p/\omega_c)^2=1$, T=10keV, and different values of the loss-cone index ℓ. Weakly-relativistic solution: ——, $Rek_{\parallel}$; — -- —, $Imk_{\parallel}$; non-relativistic solution: — — —, $Rek_{\parallel}$; ----, $Imk_{\parallel}$. Cold solution (dotted curve)

Fig. 2 The real part of the frequency ($Re\omega$) and the temporal growth rate ($Im\omega$) of the whistler mode as a function of the wave number, for the same parameters as in Fig. 1.

Fig. 3 The real part of the frequency and the growth rate of the absolute cyclotron maser instability as a function of $(\omega_p/\omega_c)^2$, for loss-cone index ℓ= 1 and different values of the temperature. Fully-relativistic solution: ———, $Re\omega$; — -- —, $Im\omega$; Weakly-relativistic solution: — — —, $Re\omega$; -----, $Im\omega$. Cold solution (dotted curve).

Fig. 4 The same as in Fig. 3 as a function of the temperature, for $(\omega_p/\omega_c)^2$= 0.3 and 0.5.

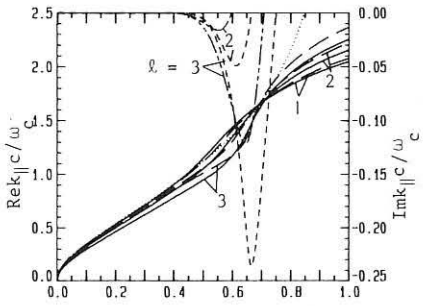

Fig. 1 ω/ω_c

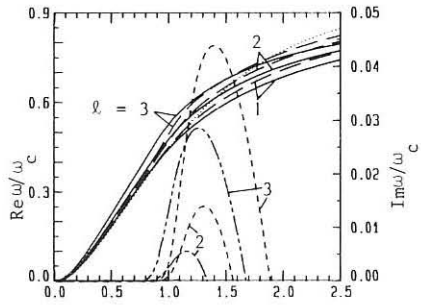

Fig. 2 $k_{\parallel}c/\omega_c$

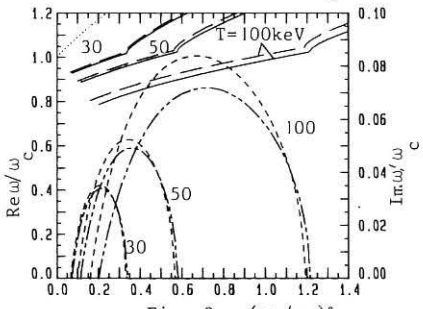

Fig. 3 $(\omega_p/\omega_c)^2$

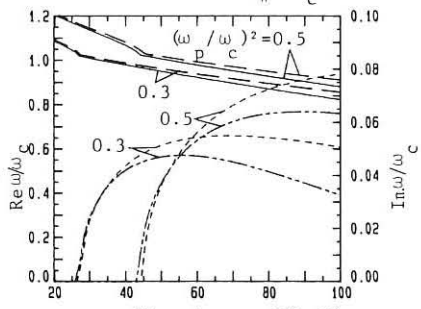

Fig. 4 T(keV)

COLD PLASMA ELECTROMAGNETIC RADIAL MODES WHICH PROPAGATE WITH THE LIGHT VELOCITY ALONG A MAGNETIZED PLASMA COLUMN

J.A.C. Cabral and S. Kuhn*

Centro de Electrodinâmica, Instituto Superior Técnico,
1096 Lisboa Codex - Portugal

*Institut fur Theoretische Physik, Universität Innsbruck,
Technikerstrasse 25, Innsbruck - Austria

In a recent publication the experimental observation of a new electromagnetic mode was reported [1]. This mode has the following characteristics: (a)- it propagates with almost the light velocity along a strongly inhomogeneous plasma column; (b)- it can only be excited when its frequency f_o is close to f_{ce}; (c)- its phase velocity is almost independent of the local value of f_{pe}; (d)- its E- and H- field amplitudes decay exponentially with r; (e)- the radial damping rate increases with B; (f)- it is almost circularly polarized. A simplified theoretical description (plane geometry) of this e.m. mode, consistent with all the relevant experimental observations, was presented in [2].

In this paper we consider that the pure standing waves observed in [1] belong to an axially bounded system in which $k_z \sim k_o$ ($v_{ph} \sim c$). The cold plasma dispersion equation

$$p^4+[k_z^2(K_{/\!/}/K_\perp+1)-k_o^2(K_{/\!/}+K_rK_l/K_\perp)]p^2+(K_{/\!/}/K_\perp)(k_o^2K_r-k_z^2)(k_o^2K_l-k_z^2)=0 \quad (1)$$

can be solved for p as a function of w, w_{pe}, w_{ce}, given k_z, with $k_o=w/c$, $k_y=0$ and $B_o=B_o a_z$ and the usual definitions for the dielectric tensor components:

$$K_{/\!/} = 1 - w_{pe}^2/w^2 \quad (2)$$

$$K_r = 1 - w_{pe}^2/(w(w-w_{ce})) \quad (3)$$

$$K_l = 1 - w_{pe}^2/(w(w+w_{ce})) \quad (4)$$

$$K_\perp = (K_r+K_l)/2 \quad (5)$$

$$K_x = j(K_r-k_l)/2 \quad (6)$$

Since $v_{ph} \sim c$ we solved equation (1), forcing k_z to be k_o, and the frequency dependence of the p values is presented in Fig.1 (f_{ce}=600 MHz) for five values of f_{pe} (a-150, b-300, c-450, d-600 and f-750 MHz). One of these branches has, for $f_{pe} < f_o < 1.5\, f_{ce}$, a pure imaginary transverse wavenumber, p_1. The other mode has a wavenumber p_2 which is either real ($f_{pe} < f_o < f_{uh}$) or pure imaginary ($f_o > f_{uh}$). This second dispersion branch shows a resonance for $f=f_{uh}$. As was pointed out in [2] the experimental results are qualitatively described by branch p_1.

Equation (1) can also be solved as a function of f_{pe} for a given

value of f_o. Results are presented in Fig.2, where we can see that, for three values of f_o around f_{ce} (a-550, b-600 and c-650 MHz) branch p_1 can

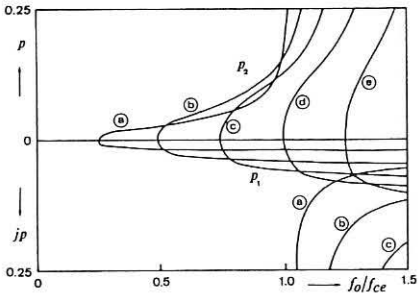

Fig.1

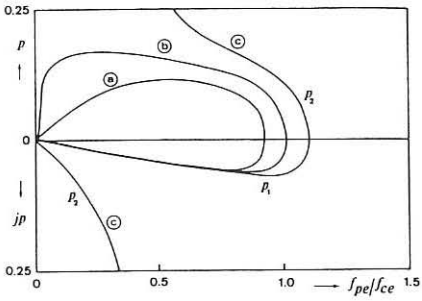

Fig.2

exist in plasmas with $0<f_{pe}<f_o$. The other branch, p_2, has a real wavenumber in the entire region where $f_{pe}<f_o$ only when $f_o<f_{ce}$. When $f_o>f_{ce}$ real propagation is only possible between $f_{pe}=f_o$ and the value of f_{pe} which leads to the upper hybrid resonance. For plasmas of lower density this second dispersion branch also becomes radially evanescent.

With knowledge of k_z and of the values of p_1 and p_2 we can calculate the relative electromagnetic field amplitudes. Following the formalism established by Allis, Buchsbaum and Bers [3], assuming radial symmetry (m=0) and wave dependence of the form $\exp(j(wt-k_z z))$, we derived expressions for the six field components:

$$E_z = 1 \tag{7}$$

$$E_r = -p_1(1-k_o^2 p_2^2 K_\perp/Q_r Q_1)/k_z \tag{8}$$

$$E_\phi = -p_1(1-Q_\perp p_2^2/Q_r Q_1)K_\perp/K_X k_z \tag{9}$$

$$H_z = -(Q_\perp K_{//}-p_1^2 K_\perp)/w\mu_o k_z K_X \tag{10}$$

$$H_r = -p_1(Q_\perp p_2^2/Q_r Q_1-1)K_\perp/K_X w\mu_o \tag{11}$$

$$H_\phi = p_1 p_2^2 k_o^2 K_\perp/Q_r Q_1 w\mu_o \tag{12}$$

with

$$Q_\alpha = (k_o^2 K_\alpha - k_z^2). \tag{13}$$

Fig.3 shows the frequency dependence of the transverse E-field components ($E_z=1$) for both dispersion branches. For the radially evanescent branch (p_1) E_{r1} and $E_{\phi 1}$ are in quadrature and they have similar amplitudes. The other dispersion branch, (p_2), shows the upper hybrid resonance in which the E-field is almost radial ($E_{r2}\to\infty$, $E_{z2}=1$ and $E_{\phi 2}=0$).

Fig.4 shows the calculated magnetic field components. We verify that for mode p_1 the H-field has almost the same behaviour as the E-field. The wave has transverse fields in quadrature of similar amplitudes. For branch p_2 the magnetic field, at the upper hybrid resonance, is reduced to its

longitudinal component ($H_{\phi 2}=H_{r2}=0$).

For $f_o=f_{pe}$, the magnetic field vanishes, as well as the two transverse E-field components. The wave is therefore pure electrostatic, with only a longitudinal E-field.

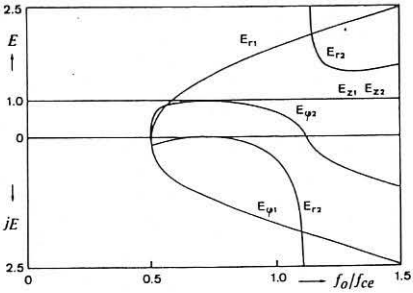

Fig.3

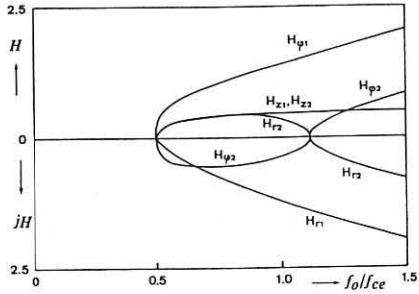

Fig.4

We plotted in Fig.5 the polarization ratios $P'_{re}=E_r/E_z$ and $P_{\phi e}=E_\phi/E_z$, and in Fig.6 the corresponding values for $P_{rh}=H_r/H_z$ and $P_{\phi h}=H_\phi/H_z$.

Fig.5 shows that mode p_1 has the two components of the transverse E-field of almost identical amplitude. For $f_o=f_{ce}$ the waves are circularly

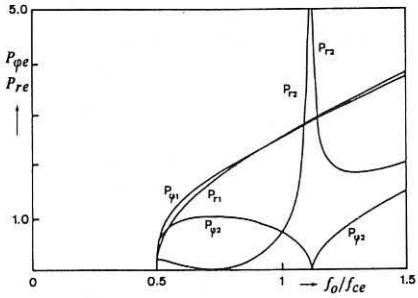

Fig.5

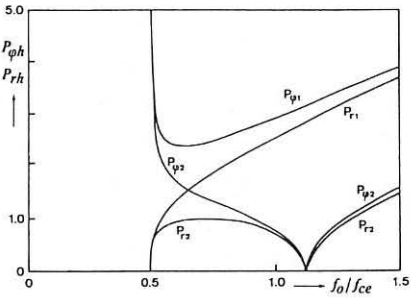

Fig.6

polarized. The other mode p_2 shows that, at the upper hybrid frequency, the E-field is almost purely radial and that there is a certain frequency for which this mode has $E_{\phi 2}=E_{z2}$ and $E_{r2}=0$. Fig.6 shows that mode p_1 has a magnetic field that is always eliptically polarized, although for $f_o \geq f_{ce}$ the two transverse H-fields have similar amplitudes. Mode p_2 has also eliptical polarization. From Figs.5 and 6 we see that, for the radially evanescent mode p_1, near the cyclotron frequency, both the E- and H-transverse fields are larger than the longitudinal fields. Also the larger field components are E_r and H_ϕ. These results agree with the experimental observations reported in [1].

In the experiments we observed that v_{ph} was comprised between 0.8c and c. We now show that the conclusions presented above remain valid for other values of v_{ph}. In Fig.7 we present p_1 and p_2 for three values of

v_{ph}/c (a-0.8, b-0,9 and c-1.0). We see that the radial evanescent mode always exists showing an increase of p_1 when v_{ph} decreases.

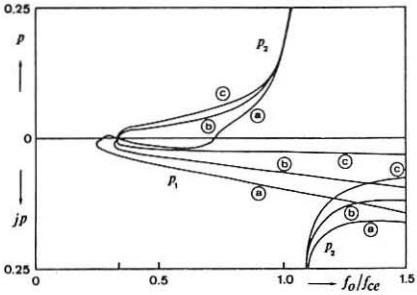

Fig.7

We plotted in Figs.8 and 9 the frequency dependence of the E- and H-field components for v_{ph}=0.9c. We recognize the two radial modes formerly described and we see that their behaviour is qualitatively the same. Comparing this case with the former one (v_{ph}=c) we see an increase in the absolute values of both p_1 and p_2 and the possibility of propagation for $f_0 < f_{pe}$. Further we verify that the two longitudinal H-field components, H_{z1} and H_{z2}, are now separated (in Fig.4 they were practically coincident) and that there is a frequency for which $E_{\phi 2}=0$, $H_{\phi 2}=0$ and $E_{r2}=E_{z2}$.

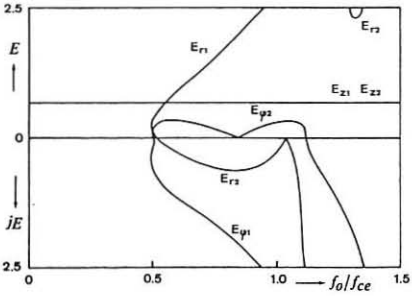

Fig.8

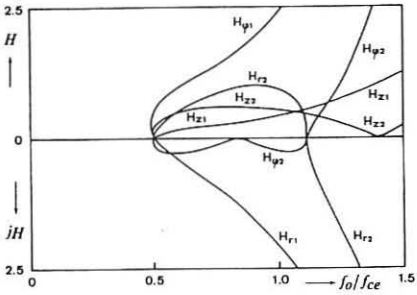

Fig.9

In conclusion, our analysis of the radial modes of a cold plasma cylindrical column shows that the preliminary results presented in [2] (plane geometry) were qualitatively correct. Both analysis have shown that the E-field (H-field) is circularly (eliptically) polarized. To fit the experimental radial profiles the e.m. fields of the first mode (p_1) must follow Hankel function dependences on the radius, of the type K_0 (K_1) for their axial (transverse) components. It is our intention to look for the excitation of the second radial mode (p_2) in our rf-plasma experiment.

References:

[1]- J.A. da Costa Cabral - XVIII Int. Conference on Phenomena in Ionized Gases, Swansea (1987) Vol.2, p.286.

[2]- J.A. da Costa Cabral - ibid, p.288.

[3]- Allis, W.P., Buchsbaum, S.J. and Bers, A. - (1962) - "Waves in Anisotropic Plasmas" M.I.T. Press, Cambridge, Mass.,p.232.

MODELING OF NON-MAXWELLIAN DISTRIBUTION FUNCTIONS BASED ON X-RAY AND EC EMISSION.

F. Castejón, C. Alejaldre, J. C. Girado, V. Krivenski and V. Tribaldos
Asociacion EURATOM / CIEMAT para Fusión
28040 Madrid, SPAIN

INTRODUCTION

X-ray and EC-emission are powerful diagnostics capable of yielding valuable information on the actual electronic distribution functions of fusion experiments. In this paper, we present the different X-ray bremsstrahlung spectra obtained using several analytic models for the electron distribution function of a tokamak plasma. An "experimental" X-ray emission, obtained from a distribution function calculated by a Fokker-Planck code, is used to fit the free parameters of the models. Finally the same method is used to model a bi-maxwellian model based on its EC emission.

X-RAY EMISSION

The X-ray emission intensity for photons of energy E=hν and scattrering angle, Θ, is given by [1]:

$$I(E, \Theta) = \int_{u_{min}}^{+\infty} du\ u^2 \int_0^{2\pi} d\varphi \int_0^{\pi} d\theta \sin\theta \frac{u\ c}{\gamma} f(u, \theta) \frac{d\sigma(E, u, \Theta)}{dE\ d\Theta} \qquad (1)$$

Where u=p/mc is the normalized electron momentum, f is the electron distribution function and $\frac{d\sigma(E, u, \Theta)}{dE\ d\Theta}$ is the relativistic bremsstrahlung cross section. This cross section is calculated taking into account e-i and e-e bremstrahlung. The former contributes about 10% to the emission for the energies considered. Both cross sections are calculated following the relativistic Born approximation and corrected by Elwert's factors to take into account Coulomb screening.

The geometrical feature of the bremsstrahlung is plotted in figure 1. To emphasize the differences among the models, we have considered local emission from a point in the plasma with given characteristics of density, temperature.

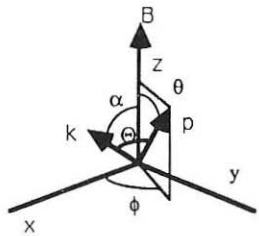

Figure 1

In this reference frame the angle between the outgoing photon and the incoming electron momenta is:

$$\Theta = \cos^{-1}\left(\frac{\vec{k}\cdot\vec{p}}{k\ p}\right) =$$

$$= \cos^{-1}(\sin\alpha\sin\theta\sin\varphi + \cos\alpha\cos\theta)$$

Where the angle α is fixed by the detector position.

We have used three analytical distribution function models. The first one is a drifted maxwellian added to a bulk maxwellian:

$$f(u_{\|}, u_{\perp}) = (1-\eta)f_b(u) + \eta f_t(u_{\|}, u_{\perp}) \qquad \textbf{(2)}$$

$$f_b(u) = \frac{\mu}{4\pi K_2(\mu)}\exp(-\gamma\mu) \quad ; \quad \mu = \frac{mc^2}{T}$$

$$f_t(u_{\|}, u_{\perp}) = \left(\frac{\mu_t}{2\pi}\right)^{3/2}\exp\left\{-\frac{\mu}{2}\left[u_{\perp}^2 + (u_{\|}-u_0)^2\right]\right\}; \quad \mu_t = \frac{mc^2}{T_t}$$

This function is plotted in figure 2 for u_0=3pth, tail temperature T_t=20 Kev and population η=.01

The second model is a plain tail distribution function [2]:

$$f_t(u_{\|}, u_{\perp}) = C \times \begin{cases} \exp(-\mu\gamma)\ ;\ u_{\|} < u_1 \\ \exp\left(-\mu\sqrt{1+u_{\perp}^2+u_1^2}\right);\ u_1 \le u_{\|} \le u_2 \\ \exp\left(-\mu\sqrt{1+u_{\perp}^2+(u_{\|}-u_2+u_1)^2}\right);\ u_{\|} > u_2 \end{cases} \qquad \textbf{(3)}$$

$$C = \frac{C_m}{1 + 2\pi C_m(u_2-u_1)\dfrac{e^{-\mu\sqrt{1+u_1^2}}}{\mu}\left[\dfrac{1}{\mu} + \sqrt{1+u_1^2}\right]} \quad ; C_m = \frac{\mu}{4\pi K_2(\mu)}$$

See figure 3

And the third model is [3]:

$$f_t(u_\parallel, u_\perp) = N \exp(-\mu\tilde{\gamma})\ ;\ \tilde{\gamma} = \sqrt{1 + a(u_\parallel)u_\perp^2 + b(u_\parallel)u_\parallel^2} \qquad (4)$$

This model gives additional freedom in the election of the functions a and b. In this work we have chosen two step functions for a and b see figure 4 . Figure 5 shows the "experimental" X-ray emission of a tokomak in the lower hybrid regime. It hasbeen obtained using the electron distribution function derived from a Fokker-Plank code . We then choose the free parameters of the different analytical models to fit the results obtained with this calculated function [4]

$$b(u_\parallel) = \begin{cases} \left(\dfrac{T}{T_B}\right)^2 ; u_\parallel < u_1 \\ 1 ; u_1 \le u_\parallel \le u_2 \\ \left(\dfrac{T}{T_F}\right)^2 ; u_\parallel > u_2 \end{cases} \quad ; \quad a(u_\parallel) = 1$$

Figure 6 shows the bremsstrahlung X-ray spectra for these functions and an angle α=90^0.

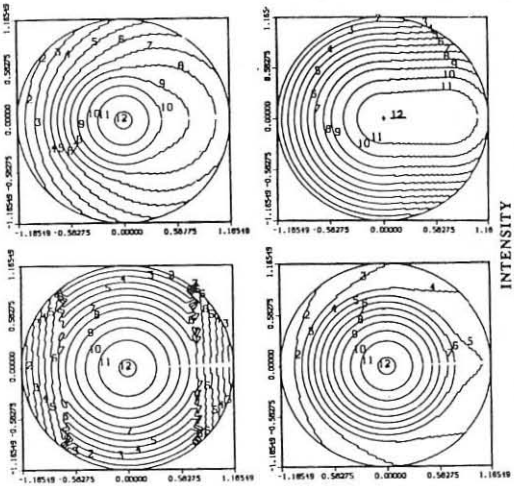

Figures 2,3,4,5

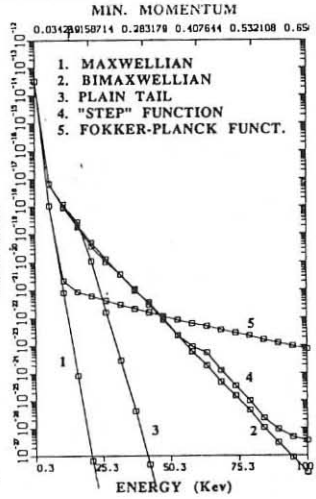

Figure 6

ECE

Following ref [5],the expression for the power radiated in the spectral range $d\omega$, in the solid angle $d\Sigma$, by the elementary area $d\sigma$ is given by

$$\frac{dP_j}{d\Sigma d\omega d\sigma} = \int_{x_o}^{x_1} dx\ \beta_j(n_\parallel, x)\ e^{-2\int_x^{x_1} k'_{\perp j} dx'}$$

where $\beta(x,n_\parallel)$ is the emissivity and $k_\perp$ is theimaginary part of the perpendicular component of the wave vector for the mode considered j.The integral is extended to cover the region where the wave can be absorbed or emitted.We present the results for the following plasma parameters and profiles.

$$N_o(x) = N_o(0)\left[1-\left(\frac{x}{70}\right)^2\right], \quad N_o(0) = 5\times 10^{19}\,m^{-3}$$

$$T_{eb}(x) = T_{eb}(0)\left[1-\left(\frac{x}{70}\right)^2\right]^2, \quad T_{eb}(0) = 3\,KeV$$

$$B_t(x) = \frac{B_t(0)}{1+\frac{x}{225}}, \qquad B_t(0) = 4.5\,Teslas$$

A given plasma current can be modelled with a bimaxwellian distribution function with a given tail population, with different pairs of temperatures and drifts . Each one reproducing the global current value but giving a quite different EC emission and therefore yielding insight on the actual electron distribution function.

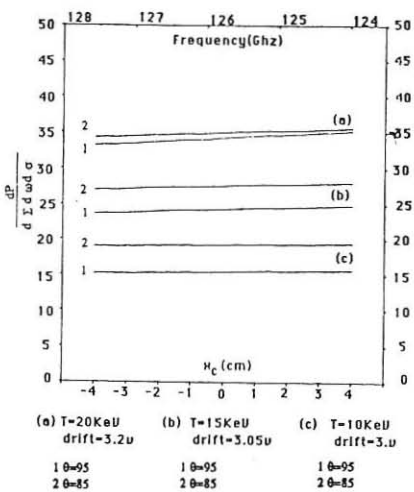

FIG.7. Ec. 1 versus f and ω for η=.01 and several values of T_t and drift

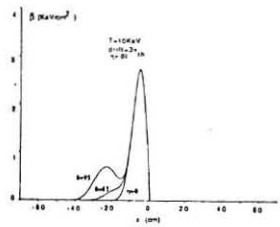

FIG.8. Emissivity β versus position for $\omega=\omega_c(0)$

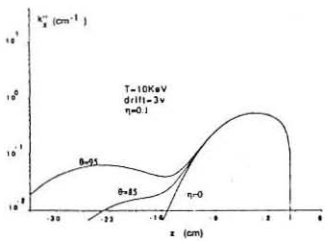

FIG.9. $k_\perp''$ versus position for $\omega=\omega_c(0)$ and the same cases as above

[1] Stevens et al, Nuc. Fusion **25**, 1529 (1985)

[2] Parail et al. Nuc. Fusion **18**, 303 (1978)

[3] Fidone. Private communication

[4] Krivenski et al. Phys. Fluids **30**, 438 (1978)

[5] Fidone et al. Phys. Fluids **23** (1980)

CALCULATION OF ALPHA TRANSPORT PHENOMENA SOLVING A MODIFIED FOKKER-PLANCK-EQUATION

G. Kamelander

Austrian Research Center Seibersdorf
A-2444 Seibersdorf, Austria

INTRODUCTION

Progress in the confinement of hot plasmas in TOKAMAK and STELLERATOR experiments on serveral places in the world has stimulated research in the physics of ignited D-T-plasmas. Especially the role of the 3.5-MeV-alpha particles emerging from D-T-reactions as a heating source and - after slowing down - as an impurity is of high interest. Furthermore it is well known that hot alpha particle populations could trigger plasma instabilities. Therefore selfconsistent alpha particle transport calculations are of importance for the next generation of fusion machines with magnetic confinement. In the following a method to calculate the alpha particle deposition rates to the plasma is presented solving a FOKKER-PLANCK-equation with a source term accounting for transport. Neoclassic transport laws are used to test the feasibility of the method.

THEORY

The proposed method to calculate the alpha particle distribution function $F_\alpha(x,E,t)$ in a high temperature plasma consists of a generalization of Refs.[1] and [2] starting with the kinetic equation

$$\frac{\partial F_\alpha}{\partial t} + \frac{\partial}{\partial E}(LF_\alpha) - \frac{\partial^2}{\partial E^2}(DF_\alpha) = Q_\alpha \cdot \delta(E-E_\alpha) + Q_{in}. \qquad (1)$$

L and D are the FOKKER-PLANCK-coefficients [3]. Q_α represents the fusion alpha source and Q_{in} the inner source due to transport. Refs. [1] and [2] dealing with neoclassic transport approximate F_α by a sum of Maxwellian distributions $m(x,T_k)$

$$F_M(x,\alpha) = \sum_k n_k \cdot m(x,T_k). \qquad (2)$$

In this case to any n_k and T_k a particle flux Γ_k and a heat flux q_k can be attributed. Γ_k and q_k have been calculated by the neoclassic formulae from Ref. [4] and setting

$$Q_{in}(x,E) = -\mathrm{div}\left(\Sigma\Gamma_k m_k\right) - \mathrm{div}\left(\Sigma m_k q_k \frac{s_k - E}{s_k{}^2 - b_k}\right) \qquad (3)$$

where s_k and b_k are the zero-th and the first energy moment of m_k. Performing the zero-th and the first energy moment of equ.(1) it may easily be demonstrated that this equation conserves the particle number and the energy. The formalism proposed by Refs.[1] and [2] has been somewhat improved and transformed to toroidal flux surface geometry by Refs.[5] and [6] using Ref.[7]. This computer code has been written to calculate the alpha energy deposition rate and to be linked with a dynamic plasma transport code [8]. The method used by Refs. [1,2,3] suffers from the ambiguity of the ansatz (2) respectively from the incompleteness of the Maxwell functions. The present paper proposes to use

$$Q_{in} = -\mathrm{div}(\Gamma_\alpha f_\alpha) - \mathrm{div}[q_\alpha(\gamma - \beta.E) f_\alpha] \qquad (4)$$

as a transport source. The coefficients γ and β are assumed to be solutions of

$$\gamma\int dE q_\alpha(E) f_\alpha(E) dE - \beta\int dE q_\alpha . E . f_\alpha(E) = 0 \qquad (5a)$$

$$\gamma\int dE q_\alpha(E) E . f_\alpha(E) - \beta\int dE q_\alpha(E) E^2 . f_\alpha(E) = \int dE \Gamma_\alpha . f_\alpha(E) . E . dE \qquad (5b)$$

In this case particle- and energy balance are fulfilled. f_α is the normalized distribution function

$$f_\alpha(E) = F_\alpha(E) / \int dE F_\alpha(E)$$

It is supposed that $\Gamma_\alpha(E, T_e, T_i . n_i, n_e \ldots)$ and $q_\alpha(E, T_e, T_i, n_i, n_e, \ldots)$ are known.

RESULTS

Equ. (1) together with equ. (4) can be solved by iterations. The alpha energy deposition rate to the electrons and ions

$$W_{\alpha e} = \int L_e F_\alpha dE, \quad W_{\alpha e} = \int L_i F_\alpha dE$$

are source terms for the plasma energy balance. Starting with a plasma with parabolic density and temperature distributions (T_{axis} = 7000 ev, T_{edge} = 1500 ev, $N_{e,axis}$ = 1,3E+14, $n_{e,edge}$ = 0,6E+13) using the neoclassic transport model [4] and switching on the fusion source at t = 0 we obtain distribution functions exhibiting inversions as shown in figure 1. Figure 2 shows the deposition rate to the plasma for several times.

CONCLUSION

It is demonstrated that the method works well. The neo-classical model is a background of alpha particle transport. An extension of the method to more realistic transport models seems possible. The inversion of the distribution function could give rise to thermonuclear instabilities.

REFERENCES

[1] D.F.DÜCHS, D.PFIRSCH, Proc.5th IAEA-Conference, Tokyo, IAEA-C N-33, 1974

[2] D.PFIRSCH, EUR FU/XII/476/80

[3] B.A.TRUBNIKOV, Reviews of Plasmaphysics, Vol.1 (1965)

[4] J.W.CONNOR, Plasma Physics, Vol.15 (1973), 765

[5] G.KAMELANDER, JET-IR-88-13

[6] G.KAMELANDER, JET-IR-88-15

[7] F.L.HINTON, R.D.HAZELTINE, Reviews of Modern Physics, Vol. 48, No.2, Part I, April 1976

[8] G.CENACCI, A.TARONI, JET-IR, 1988

Fig. 1: Alpha Particle Distribution for FE (E,ρ)

t - time after switch on the fusion source

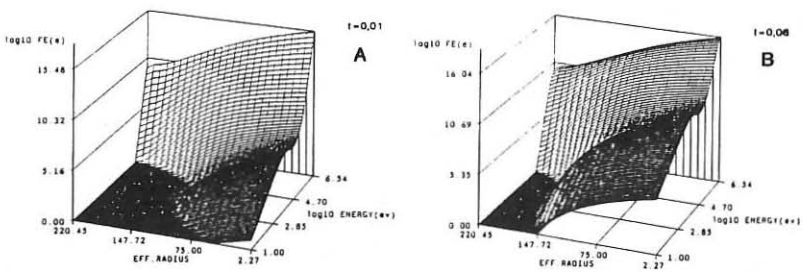

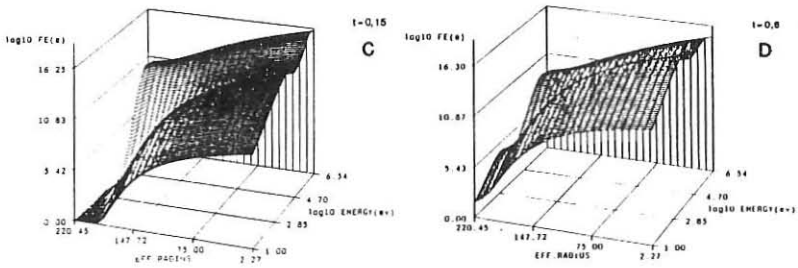

Fig. 2: Alpha Power Deposition Rate

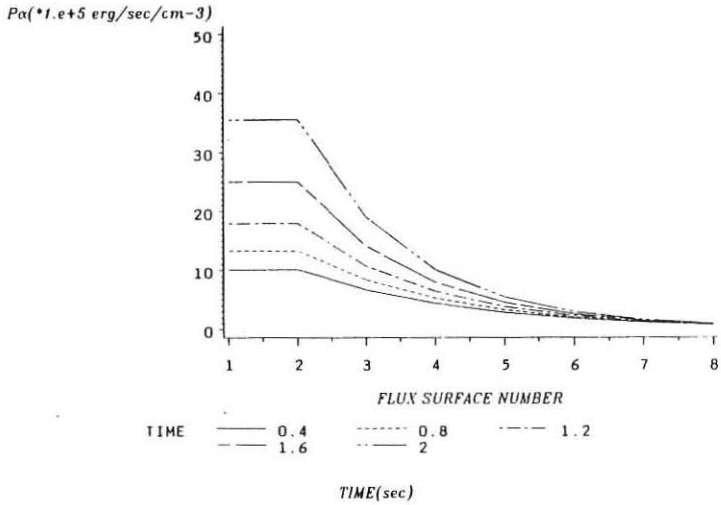

ABLATION OF A SOLID HYDROGEN DISC UNDER THE IMPACT OF PLASMA ELECTRONS IN A UNIFORM MAGNETIC FIELD

F.L. Tang

EURATOM fellow, on leave of absence from the Institute of Mechanics, Academia Sinica, Beijing, People's Republic of China

C.T. Chang

EURATOM-Risø Association, Risø National Laboratory, Roskilde, Denmark

In order to study the effect of the geometry of the expansion process on the ablation rate of a pellet, an ablation of a thin disc in a uniformly magnetized plasma shall be considered. The results are applicable for cases where the effect of pellet curvature could be neglected.

As a first example, the magnetic field lines are taken to be normal to the disc surface. The basic physical phenomena of a plane ablation is similar to that of a spherical ablation, which is caused mainly by the impact of plasma electrons. For simplification, plasma electrons are considered to have monoenergetic distribution with energy $E = 2\,T_e$ and energy flux $q = n_e \times \sqrt{T_e/2\pi m_e} \times E$ [1], where T_e, n_e and m_e are temperature, density and mass of electrons, respectively.

Assuming the ablatant is a nondissipative ideal gas, using the conservation laws of mass, momentum, and energy, and the equation of state, the velocity, u and temperature, T of the ablatant can be derived explicitly, they are

$$\frac{du}{dx} = -\frac{(\gamma-1)q\Lambda}{mu^2-\gamma T} \tag{1}$$

$$\frac{dT}{dx} = \frac{(mu^2-T)(\gamma-1)q\Lambda}{u(mu^2-\gamma T)} \tag{2}$$

where γ is the ratio of the specific heats, $m = m_{H_2}$, is the mass of the ablatant, $\Lambda[(E)]$ [2] is the cross section for the attenuation of the energy flux of the incoming electrons.

Eq. (1) indicates that when a continued expansion of $du/dx > 0$ is required, the flow must be subsonic the whole way. In addition, Eq. (2) further shows that a continued heating of the ablatant is only possible when $u \leq \sqrt{T/m}$.

As the flow of ablatant is subsonic all the way, the ablation of the pellet depends not only strongly on the undisturbed conditions of the plasma state but also is influenced greatly by the ablatant state at the pellet surface. This feature differs greatly from that of a spherical or cylindrical expansion.

By choosing proper state of the ablatant at the pellet surface, T_v and n_v, the integration is initiated at the pellet surface and proceed outward until the following conditions at the downstream location, X, are satisfied:

1. Energy and energy flux of plasma electrons reach their undisturbed values, $q \rightarrow q_o$ and $E \rightarrow E_o$;
2. Temperature of ablatant T_F must be less than or equal to the temperature of plasma electrons T_{eo};
3. Local Mach number should be lass than $\sqrt{1/\gamma}$;
4. X must be in a reasonable range.

Subscript o denotes the corresponding parameters of undisturbed plasma electrons, subscript F denotes that of ablatant in the downstream.

In Fig. 1 the variation of dimensionless parameters of ablatant and E/E_o, q/q_o of plasma electrons vs. distance x is shown.

For $0.5 < T_{eo} < 5$ keV and $5\times10^{13} < n_{eo} < 5\times10^{14}$ cm^{-3}, from numerical computation we obtain the scaling law of the mass ablation flux

$$g^* \cdot n^*v \cdot T^*v \cdot x/n_{eo} = 0.382\times10^{-26} T_{eo}^{3.15} \tag{3}$$

where with the exception of the temperature given in unit of eV, all other parameters are in c.g.s units. g^*, n^*v, T^*v are the dimensionless mass ablation flux, density and temperature at the pellet surface respectively, and

$$g^* = g/\rho_s a_s, \quad n^*_v = n_v/n_s, \quad T^*v = Tv/Ts,$$

the subscript s denotes corresponding parameters of solid hydrogen. Ts is the surface temperature of the disc, in computation here, we take Ts = 10 K, and $a_s = \sqrt{\gamma Ts/m}$. The scaling law (3) is shown in Fig. 2.

When state of undisturbed plasma electrons are in the range mentioned above, the limitations of X, T^*v and n^*v are the following:

$$X > 0.5 \text{ cm}, \quad 0.5 < T^*v < 10, \quad 0.5 < n^*v < 10$$

From subsonic flow theory it is well known that the mass flux is determined by the pressures at both the upstream and downstream of the flow. Naturally, owing to the subsonic character of the plane expansion, the mass ablation flux g depends not only on the pressure of electrons $p_{eo} = n_{eo}\cdot T_{eo}$, which is related to the ablatant pressure $p_F = n_F\cdot T_F$ at the downstream, but also on the pressure of ablatant $p_v = n_v \cdot T_v$ at the pellet surface. This can be seen more clearly by rewritten Eq. (3) in the following way

$$g = 0.181\times10^{-3} \times (p_{eo}/p_v)\times(T_{eo}^{2.15}/X) \tag{4}$$

It can be shown that $T_{eo}^{2.15}$ is related to the total specific energy given by the electrons during the ablating period. $T_{eo}^{2.15}/X$ can then be taken as the average linear intensity of the total specific energy. Thus, the higher $T_{eo}^{2.15}/X$, the larger g.

When magnetic field is parallel to the pellet surface, it can be proved that $q_y = q_z = q_x$, q_x is the energy flux of plasma electrons for the case when magnetic field lines are normal to the pellet surface. The scaling law of the mass ablation flux therefore remains the same. For monoenergetic plasma electrons, and the magnetic field intensity within the interval of fusion interest

$$10 < B < 10^2 \text{ KG}$$

the influence of drift velocity of electrons can be neglected.

A comparison of the mass ablation fluxes among plane, spherical and cylindrical expansions at the same plasma state might be of interest. Thus at the given plasma condition of $T_{eo} = 1$ keV and $n_{eo} = 1.0 \times 10^{14}$ cm^{-3}, the mass ablation flux g of the thin disc is 0.78 $gm/cm^2/sec$. The mass ablation flux g, $gm/cm^2/sec$, of a cylindrical and that of a spherical pellet of the following radii are given below

Expansion form	$r_p = 0.1$ cm	$r_p = 0.01$ cm
spherical	23.69	109.79
cylindrical	0.87	4.01

From the above results, we observe that for a cylindrical pellet of radius, $r_p = 0.1$ cm, the ablation of the ends at most is of the same order of magnitude as that of a plane disc.

The above conclusion, however, is based on the assumption that $T_s = 10$ K ($\sim 10^{-3}$ eV), if T_s is taken to be comparable to the sublimation energy of 10^{-2} eV, the mass ablation flux of a disc pellet will be reduced by approximately an order of magnitude further.

References:

[1] Parks, P.B. and Turnbull, R.J. Phys Fluids (1978) 21, 1735.
[2] Chang, C.T. Risø Report (1982), Risø-R-460.

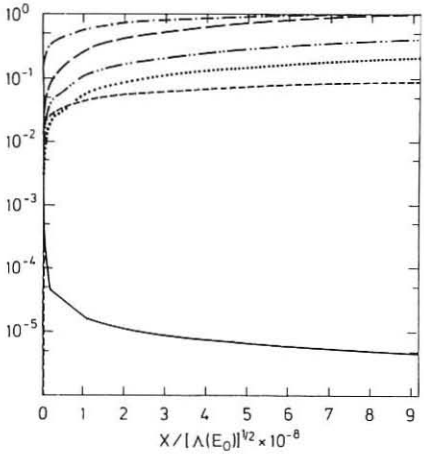

Fig. 1. Dimensionless electron energy E/E_o, electron energy flux q/q_o, flow velocity v/a_s, temperature T/T_s, density ρ/ρ_s and Mach number M of ablatant versus distance x.

Legend:
- —·— E/E_o
- — — — q/q_o
- —··—··— $v/a_s \times 10^{-2}$
- ..... $T/T_s \times 10^{-6}$
- — — — — — M
- ——— ρ/ρ_s

$T_{eo} = 800$ eV
$n_{eo} = 1.0 \times 10^{14}\ cm^{-3}$
$g/\rho_s a_s = 1.9 \times 10^{-4}$

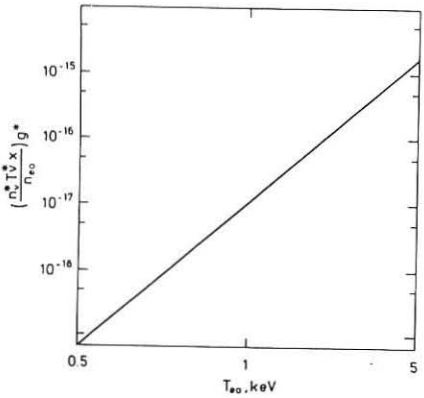

Fig. 2. Scaling law of

$$\left(\frac{n_v^* T_v^* X}{n_{eo}}\right) g^*$$

versus plasma electron temperature T_{eo} (for plasma electron density n_{eo}, $5 \times 10^{14} \geq neo \geq 5 \times 10^{13}\ cm^{-3}$).

ABLATION OF A CYLINDRICAL HYDROGEN PELLET IN A MAGNETIZED PLASMA

Paolo Villoresi

Euratom-CNR Association, Instituto Gas Ionizzato
Padova, Italy

C. T. Chang

Euratom-Risø Association, Risø National Laboratory
Roskilde, Denmark

In view of the fact that most pellets used in present injection experiments are actually cylinders. The influence of the expansion geometry on the pellet ablation rate is examined in this paper. As an approximation, we consider the ablation of a long cylinder (length $l > d$, diameter) with its axis normal to the field lines of a uniform magnetic field. Neglecting the ablation of the ends, the expansion of the ablated cloud can be viewed as cylindrically symmetrical and is described by the following system of equations:

$$p = \rho T/m \tag{1}$$

$$\frac{1}{r}\frac{d}{dr}(\rho u r) = 0 \tag{2}$$

$$\rho u \frac{du}{dr} + \frac{dp}{dr} = 0 \tag{3}$$

$$\frac{1}{r}\frac{d}{dr}\left[\rho u r\left(\frac{\gamma}{\gamma-1}\frac{T}{m} + \frac{u^2}{2}\right)\right] = Q \tag{4}$$

where Q is the volumetric heat source,i.e. the energy delivered per unit volume per second to the ablatant. We assume further that Q is due to the slowing down of plasma electrons in an ablated cloud consisting of a molecular hydrogen gas. To be able to use the available stopping power information, we shall replace the plasma electrons by an equivalent beam with the same energy flux and particle flux as that of the plasma electons having a Maxwellian distribution of n_e and T_e, thus the energy E of the equivalent beam, $E_0 = 2\,T_e$ [1]. The dynamics of the ablating cloud thus is completly described by taking $Q = dq/dr$ where

$$\frac{dq}{dr} = \frac{\rho}{m}\Lambda(E)q \tag{5}$$

$$\frac{dE}{dr} = 2\frac{\rho}{m}L(E) \tag{6}$$

where $\Lambda(E)$ is the cross section for the energy flux attenuation and $L(E)$ is the loss function of the incident electrons in a molecular hydrogen gas; their explicit expressions are given in reference [2].

It can be shown that the system of equations, Eqs. (1)-(4). has a singularity at the sonic radius, r_*. Thus, the kinetic energy of the flow can be written explicitly as

$$\frac{d\left(\frac{u^2}{2}\right)}{dr} = \frac{\frac{\gamma T}{m} - (\gamma-1)2\pi rQ/G}{1 - \frac{\gamma T}{mu^2}} \tag{7}$$

where G is the mass ablation rate per unit length of the cylinder. The singular behavior of the system of equations describing the hydrodynamics of the expanding cloud, however, is inhibited through a delicate balance between the heating and the expansion process at r_*.

By normalizing all the variables with respect to their corresponding values at r_*, the system of equations is solved as an initial value problem by first evaluating the derivatives of all the variables at r_*. In particular, the definitiveness of du'/dr' requires that

$$G = 2\pi(\gamma-1)r_* q_* \lambda_* / u_*^2 \tag{8}$$

where variables with the * notation denote those at the sonic radius, r_* and those with the ' notation denote the normalized ones, e.g. $u' = u/u_*$, $r' = r/r^*$, etc., and

$$\lambda_* = \rho_* \Lambda_* r_* / m \tag{9}$$

The mass conservation at r_* gives

$$G = 2\pi r_* \rho_* u_* \tag{10}$$

Using Eq.(9), and after the elimination of u_* between Eqs. (8) and (10), we obtain the ablated mass flux, $g_c = G/2\pi r_p$ as

$$g_c = \frac{\lambda_*}{2\pi}\left|\frac{\gamma-1}{\hat{r}\tilde{q}}\right|^{1/3} r_p^{-2/3} q_o^{1/3}\left(\frac{m}{\Lambda_*}\right)^{2/3} \tag{11}$$

In the above equation, we have introduced $\hat{r} = r_p/r_*$ and $q = q_0/q_*$ where q_0 is the ambient electron energy flux and r_p is the pellet radius. Recalling that $\Lambda_* = \Lambda(E_0/\tilde{E})$, the four numerical constants $\hat{r}$, $\tilde{q}$, Λ_* and E_* are to be determined from the appropriate boundary conditions at the pellet surface and the ablated cloud boundary. Comparing Eq.(11) with the corresponding one of a spherical pellet,

$$g_s = \frac{\lambda_*}{\hat{r}}\left|\frac{\gamma-1}{2\hat{r}\tilde{q}}\right|^{1/3} r_p^{-2/3} q_o^{1/3}\left(\frac{m}{\Lambda_*}\right)^{2/3} \tag{12}$$

we observe that the ablated mass flux scales similarly with respect to the pellet radius, r_p and the plasma state T_e and n_e in both cases.

Asymptotic solutions: -- The system of equations admitts an asymptotic solution, thus explicitly

$$\tilde{v}' = \left(\frac{3\tilde{\Lambda}'\tilde{q}'}{2\gamma-1}\right)^{1/3} r'^{1/3}, \quad \tilde{T}' = \frac{2}{\gamma}\left(\frac{3\tilde{\Lambda}'\tilde{q}'}{2\gamma-1}\right)^{2/3} r'^{2/3},$$

$$\tilde{\rho}' = \left(\frac{3\tilde{\Lambda}'\tilde{q}'}{2\gamma-1}\right)^{-1/3} r'^{-4/3}, \quad \tilde{M}^2 = \frac{2}{\gamma} \tag{13}$$

Comparing these expressions with the corresponding ones of a spherical pellet, we observe that the only differences are the density and Mach number of the ablated flow.

Computational Results: -- The system of equations, Eqs.(1)-(6), are solved numerically in a similar fashion as that of a spherical pellet, [1]. Thus, from a given E_0 ($=2\ T_e$), we first guess a E_* and then select a Λ_* to initiat the integration at r_*, and proceed inward using the boundary condition at the pellet surface

$$\hat{q}\left(\equiv \frac{q_p}{q_*}\right) \leq 10^{-3}, \quad \hat{T}\left(\equiv \frac{T_v}{T_*}\right) < \hat{q} \tag{14}$$

to locate the pellet position with respect to the sonic radius, $\hat{r}$ $(= r_p/r_*)$; the integration is then continued outward from r_* until the conditions at the cloud boundary

$$E' \to \tilde{E}\left(\equiv \frac{E_0}{E_*}\right), \quad q' \to \tilde{q}\left(\equiv \frac{q_0}{q_*}\right) \tag{15}$$

are satisfied. An example of the variation of the ablatant state as well as the energy and the energy flux of the incident electrons in the ablated cloud, obtained this manner, is shown in Fig.1. The scaling of the ablated mass flux is shown in Fig.2. For comparison, the ablation flux of a spherical pellet is given by the dashed line.
Comparing two pellets of the same radius, we observe that the ablation rate of a cylindrical pellet is approximately an order of magnitude lower than that of a spherical pellet.

References:

[1]. Parks,P.B. and Turnbull, R.J. (1978) Phys. Fluids 21, 1735.
[2]. Chang, C. T., Risoe Report (1982), Risoe-R-460.

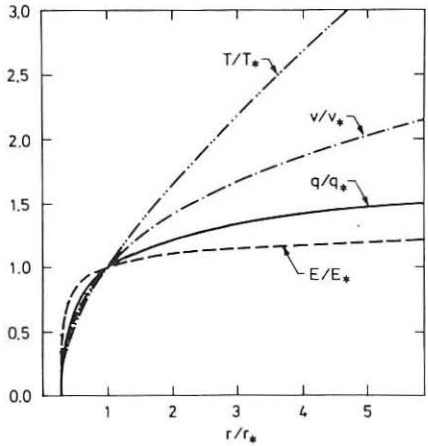

Fig. 1. Variation of the normalized ablatant state and the attenuation of plasma electron energy E/E_* and energy flux q/q_* with respect to the normalized cloud radius, r/r_*. (T_{eo} = 676 ev).

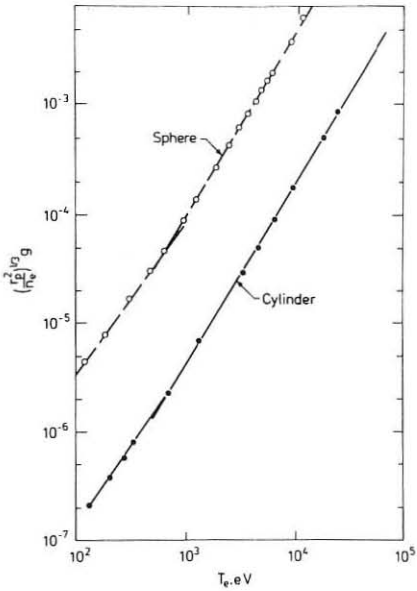

Fig. 2. Scaling of the mass ablation flux, g, with respect to the pellet radius, r_p, and the plasma electron density n_e and temperature, T_e. All parameters except T_e are in c.g.s. units.

OPTIMAL WAVE SPECTRUM FOR ELECTRON ACCELERATION BY TURBULENT WAVES

P.Deeskow and K.Elsässer

Institut für Theoretische Physik, Ruhr-Universität
D-4630 Bochum 1, West Germany

1. Introduction

The stochastic acceleration of charged particles by electrostatic or electromagnetic waves is well known in space and in laboratory plasmas. In the past it has been studied with respect to heating aspects, the relation between heating rate and diffusion coefficient, trapping effects and the validity of quasilinear theory [1]. Here we try to estimate wave spectra which are most favourable for stochastic electron acceleration. We use a model that is suitable for acceleration in Langmuir or lower hybrid waves. Therefore our results apply to the production of suprathermal electrons in solar flares as well as to plasma heating experiments. For a complete discussion of the material presented here see [2].

2. Estimation of optimal spectra

As a first approach one neglects the self consistent interaction between particles and waves and considers a onedimensional system of finite length L. Then it is sufficient to study the motion of charged particles in an external longitudinal electric field E(x,t). E(x,t) derives from a potential $\Phi(x,t)$,

$$E(x,t) = -\frac{\partial\Phi}{\partial x} = \sum_{m=1}^{\infty} k_m \Phi_m \sin(k_m x-\omega(k_m)t+\varphi_m) \qquad (1)$$

where $k_m=2\pi m/L$. $\omega = \omega(k)$ denotes the dispersion relation. To describe electron acceleration in Langmuir or lower hybrid waves we choose $\omega = \omega_{pe}$ or $\omega = \omega_{LH} = \omega_{pi}(1+\omega_{pe}^2/\Omega_e^2)^{-1/2}$ with ω_{pe}, ω_{pi} electron and ion plasma frequency, Ω_e electron gyrofrequency and ω_{LH} lower hybrid frequency. By

supposing a constant ω we have restricted the following calculations to sufficiently small wave vectors, say $k\lambda_D \leq 0.2$.

This system is described by a Hamiltonian $H = H_0 + H_1$ with a periodic perturbation H_1

$$H = H_0 + H_1 = \frac{p^2}{2m} - e\cdot\sum_{m=1}^{\infty} \Phi_m \cos(k_m x - \omega t + \varphi_m), \tag{2}$$

so that the well known theory of Hamiltonian stochasticity becomes applicable. We now expect stochastic acceleration only in those parts of phase space where resonances overlap. The usual Chirikov reasoning predicts marginal overlap of neighbouring resonances for a perturbation spectrum Φ_m^* fulfilling

$$\frac{4}{\Gamma}\cdot\sqrt{e m_e \Phi_m^*} \geq m_e \cdot \min(|v_m - v_{m-1}|, |v_m - v_{m+1}|) \tag{3}$$

where we set the stochasticity parameter $\Gamma \approx 1$. Taking into account that in our model the resonant velocities are given by $v_m = \omega(k_m)/k_m = \omega L/2\pi m$ and supposing that $m \gg 1$ this leads us to a critical spectrum

$$\Phi_m^* = \frac{\Gamma^2 \pi^2}{4}\cdot\frac{m_e \omega^2}{e L^2}\cdot\frac{1}{k_m^4} =: \frac{\varepsilon^*}{k_m^4} \tag{4}$$

We now demonstrate that this critical spectrum is also most favourable for particle acceleration.

For an arbitrary spectrum Φ_m stochasticity arises only in the neighbourhood of those resonances v_m with $\Phi_m > \phi_m^*$. For power law spectra $\Phi_m^{(\eta)} = \varepsilon/k_m^{\eta}$ this condition is fulfilled if $v_m > (\varepsilon^*/\varepsilon)^{1/(\eta-4)}$ for $\eta > 4$ or $v_m < (\varepsilon^*/\varepsilon)^{1/(\eta-4)}$ for $\eta < 4$. That means a spectrum Φ_m which is flatter than Φ_m^* can accelerate particles only up to a highest velocity, while a steeper spectrum accelerates all particles above a lower boundary. Therefore sufficiently steep spectra are more favourable for particle acceleration than flat ones. Suppose now that there are nonvanishing modes Φ_m only in a wave vector interval $[k_{min}, k_{max}]$. Stochastic acceleration across the corresponding velocity interval $[v_{min} = \omega/k_{max}, v_{max} = \omega/k_{min}]$ is possible only if all resonances in $[v_{min}, v_{max}]$ overlap. This requires a wave with a power law spectrum to have an energy density w_{st} of at least

$$W_{st} = \frac{e^2}{16\pi^2\varepsilon_0}\cdot L^2 n^2 \cdot f(\eta, v_{min}, v_{max}) \tag{5}$$

with

$$f(\eta, v_{min}, v_{max}) = \begin{cases} \dfrac{\Gamma^2}{16(3-2\eta)}\cdot\left[\dfrac{v_{max}}{v_0}\right]\cdot\left\{\left[\dfrac{v_{min}}{v_{max}}\right]^{2\eta-3} - 1\right\}, & \eta<4 \\ \dfrac{\Gamma^2}{16(2\eta-3)}\cdot\left[\dfrac{v_{min}}{v_0}\right]\cdot\left\{\left[\dfrac{v_{max}}{v_{min}}\right]^{2\eta-3} - 1\right\}, & \eta>4 \end{cases}$$

where n denotes the electron density and $v_0 = L\omega_{pe}/2\pi$. $f(\eta)$ is minimal for $\eta=4$. That means that the critical spectrum requires minimal energy density to accelerate a particle across a given interval of resonances. In this sense Φ_m^* is the optimal spectrum for particle acceleration.

We have performed numerical calculations to verify these predictions [2]. The trajectories of an ensemble of particles in a longitudinal electrostatic field (1) have been followed to determine the region of stochasticity in phase space. We found the extent of this area to be in good agreement with our careful evaluation of Chirikov's overlap reasoning. Additionally it should be pointed out that the more elaborate criterion for the onset of stochasticity due to Greene leads to different conclusions. Greene stated that -without any dependence on the Fourier amplitude of the perturbation- the most noble KAM - surface is the last to be destroyed. Thus the extent of stochasticity in phase space should not depend on the wave spectrum. Our numerical results show that this is not correct in general and therefore confirm the conjecture that the Chirikov criterion has the wider scope.

3. Quasilinear diffusion

For a longitudinal electrostatic wave with a power law spectrum $\Phi_m = \varepsilon/k_m^\eta$ the quasilinear diffusion equation is

$$\frac{\partial f}{\partial t}(v,t) = \frac{\partial}{\partial v}\left[D(v)\frac{\partial f}{\partial v}(v,t)\right] \quad , \quad D(v) = \frac{\pi}{2}\cdot\varepsilon^2 v^{2\eta-3} \quad , \tag{6}$$

where we have normalized t to ω_{pe}^{-1}, v to $L\omega_{pe}/2\pi$ and Φ to $L^2 en/4\pi^2\varepsilon_0$. With appropriate boundary conditions ($f(v_{min},t)$=const. and $f(v,t) \longrightarrow 0$ for

$v \longrightarrow \infty$) and for $\eta > 5/2$ (6) has a stationary solution $f(v) \sim v^{-2\eta+4}$, which corresponds to the well known suprathermal tails of the distribution function arising in connection with the electron acceleration in Langmuir turbulence. The typical time scale τ_R for the formation of such a suprathermal tail can be estimated using the analytic solution of (6). It is for $\eta > 5/2$

$$\tau_R = \frac{2}{\pi\varepsilon^2(\eta-5/2)^2 v_{min}^{2\eta-5}\chi_{1\nu}^2} \approx \frac{1}{\pi\varepsilon^2 v_{min}^{2\eta-5}} \cdot \frac{128}{\pi^2(10\eta-23)^2}, \qquad (7)$$

where v_{min} denotes the lowest resonant velocity and $\chi_{1\nu}$ is the first zero of the ν-th order Bessel function with $\nu = |4-2\eta|/|2\eta-5|$, $J_\nu(\chi_{1\nu})=0$. Obviously the relaxation time decreases with increasing η. In a plasma with $L/\lambda_D \approx 10^4$, $\omega_{pe} \approx 10^{12} s^{-1}$ and $v_{min} \approx 5 v_{th}$ the critical spectrum Φ_m^* leads to $\tau_R \approx 7 \cdot 10^{-4}$ s that means to a time scale for electron tail formation which is comparable to the collision time.

4. Conclusions

We have shown the Chirikov criterion to be a valuable tool to estimate wave spectra which are optimal for stochastic particle acceleration. For a simple model describing acceleration in Langmuir or lower hybrid waves we found spectra with power law form $\sim k^{-\eta}$, $\eta \geq 4$ to be most favourable for electron acceleration. The time scale for suprathermal tail formation could be estimated to be of the order of the collision time or smaller. Further investigations will apply this method to more complicated situations. Especially we will estimate the optimal spectra for ion cyclotron heating.

[1] S.P.Gary, D.Montgomery, Phys. Fluids **11**, 2733 (1968); R.W.Flynn, Phys. Fluids **14**, 956 (1971); K.N.Graham, J.A.Fejer, Phys. Fluids **19**, 1054 (1976); F.Doveil, D.Gresillon, Phys. Fluids **25**, 1396 (1982); O.Ishihara, A.Hirose, Com. Plasma Phys. Contr. Fusion **8**, 229 (1983)

[2] P.Deeskow, Ph.D. thesis, Ruhr-Universität Bochum 1989, West Germany.

QUASILINEAR ENERGY TRANSPORT IN A STOCHASTIC MAGNETIC FIELD DERIVED FROM MOMENTUM EQUATIONS

W. Feneberg

IPP Garching, EURATOM-Association, D-8046 Garching, Fed. Rep. of Germany

Introduction.

In this paper transport in a stochastic magnetc field is studied on the basis of a fluid theory. The Kadomtsev-Pogutse approach [1, 2] has been extended to take account of solving beside an energy equation also an equation for the heat flux consistent with Grad's 13-moment method.

It is an advantae of the macroscopic equations that collisions can be considered exactly within the complete Fokker-Planck operator while kinetic calculations usually work with the Krook [3, 4] or a similar simplified collision model [5] .

The presentation here is restricted only on the case of a steady-state perturbation field. But the model has been also investigated for a fluctuating field perturbation.

The resonance width for enhanced transport comes out to be very small in the case of a steady-state ergodic magnetic field when applied such to ergodize the bulk region of the plasma. It is found that transport occurs only in the range

$$0 \leq |(m - nq)| \leq \left(\frac{\lambda_e}{Rq}\right)^{-1} \left(\frac{m\omega^*}{\nu}\right)^{1/2} \tag{1}$$

Here m and n are the poloidal and toroidal mode numbers. ν is the electron-ion collision frequency, $\omega^* = (T_e/eBr)d\ell nn_e/dr$ is the diamagnetic drift frequency of the elctrons, and λ_e is the electron mean free path.

The geometry of the system is idealized and represented by a periodic cylinder of radius r and periodicity length $2\pi R$. Using realistic tokamak parameters characterizing the ASDEX plasma near the separatrix under H-mode conditions we have $0 \leq |(m - nq)| \leq 3 \cdot 10^{-2}$. From this follows that large transport in a steady-state stochastic magnetic field can only occur in a situation with a dense mode spectrum. This result, which is also in complete agreement with that as derived from the drift kinetic theory [4] has been found on the basis of the so-called linear approximation and is in contradiction with test particle models [5, 6] which start with the calculation of the magnetic field topology. Further below the range of validity of the linear theory will be considered and it will be shown that it depends only on the strength of the perturbation field.

In order to find larger anomalous transport one needs field fluctuations in the range of the electron-ion collision frequency which is also the time scale for establishing a Maxwellian distribution with constant temperature along the magnetic field lines.

Transport Equations

The electron temperature distribution $T_e(r,\Theta,\varphi,t)$ and the electron heat flux $\vec{S}_e(r,\Theta,\varphi,t)$ are assumed to be governed by the following approximate form of the 13-moment balance equations

$$\frac{3}{2}n_e\frac{\partial T_e}{\partial t} + div\vec{S}_e = S(r,\Theta,\varphi,t) \tag{2}$$

$$\frac{\partial \vec{S}_e}{\partial t} + \frac{5P_e}{2m_e}\nabla T_e + \frac{e}{m_e}[\vec{S}_e \times \vec{B}] = -\vec{S}_e\nu\alpha \tag{3}$$

with $\alpha \approx 1.87$

Here, e, m_e, n_e and p_e are the elctron charge, mass, density and pressure. The source term S will be taken into account for the case of Ohmic heating $S = \sigma E^2$ with $E = U/2\pi R$ the induced electric field and the conductivity σ which is described with the self-consistent temperature T_e. For simplicity we neglect density perturbations, the convective contributions to the energy balance and the electric current arising within the equation of the heat flux. The presence of a heat flux causes a deviation Φ from the Maxwellian f_M given by

$$\Phi = \frac{m_e}{T_e}(n_e m_e)^{-1}\vec{S}_e\varsigma\left(\frac{1}{5}\varsigma^2 - 1\right) \tag{4}$$

where $\vec{\varsigma} = \vec{u}/v_e$ is the random walk velocity normalized with the electron thermal speed v_e.

The model equations (2) and (3) can be used in the range $\Phi \ll 1$. In order to examine this condition to be the only one to exist, a temperature perturbation with arbitrary mode numbers m and n was assumed for the case of a configuration with closed magnetic surfaces (that is in absence of a helical perturbation field) and the decay due to heat conductivity parallel to field lines was studied. The result of the simple calculation shows that each non-resonant temperature perturbation $(m - nq) = 0$ decays on the time scale of the elctron-ion collision time independent of the mean free path. For this time being much longer than the transit time the model can also be used in the region of long mean free path.

We consider cylindrical flux surfaces perturbed by a weak stochastic magnetic field with radial component b_r, which we expand as

$$b_r = \sum b_{\omega,m,n} exp(i(\omega t + m\Theta - n\phi)) \tag{5}$$

The temperature $T_e = T_{0e}(r) + T_1$ and heat flux $\vec{S}_e = \vec{S}_{0e}(r) + \vec{S}_1$ are similarly expanded with $< T_1 >=< \vec{S}_1 >= 0$.

Averaging the energy equation (2) over the unperturbed circular magnetic surfaces and the time gives for $S_{0e}(r)$ to satisfy the equation

$$\frac{1}{r}\frac{d}{dr}S_{0e,r} =< \sigma E^2 > \tag{6}$$

Only the often-discussed case of a steady-state perturbation field will be presented here in the following. From eq.(3) the expression of the radial heat flux is found to be

$$S_{e,r} = -\chi_{\|} b_r(\vec{b}\nabla T_e) - \chi_{\perp}\frac{\partial T_e}{\partial r} + \frac{5p_e}{2eBr}\frac{\partial T_e}{\partial \Theta} - \frac{5p_e}{2eBR} f_p \frac{\partial T}{\partial \phi} \tag{7}$$

Here $\chi_{\|}$ is the classical parallel heat conductivity and $\chi_{\perp} = \chi_{\|}(\nu^2/\omega_e^2)$ with ω_e the electron gyrofrequency. $\vec{b} = \vec{B}/B$ is the unit vector of the magnetic field $\vec{B}$ which will be decomposed into $\vec{B} = \vec{B}_0 + \vec{B}_1$ and $\vec{B}_1$ is the perturbation field. $f_p = B_\Theta/B_\varphi$.

The average radial heat flux $S_{0e,r} =< S_{e,r} >$ can be found after linearizing eq.(2) and (3) in terms of $\vec{B}_1$ and T_1. In calculating T_1 from b_r we neglect in eqs.(2) and (3) the contribution of $\chi_{\perp}$ being smaller in the order of ν/ω_e than the contribution of the $\nabla T \times \vec{B}$ drift. The Kadomtsev-Pogutse model does not contain this drift and therefore the neglection of the non-linear terms is not justified there [2] . A simple calculation shows that

$$T_{m,n} = b_{m,n} T_e' \frac{(ik_{\|} + Ak_{\|} + A(n/R)f_p^2)}{(k_{\|}^2 - (im/r)A(d\ell n n_e/dr) - B)} \tag{8}$$

The following abbreviations have been used: $A = T_e/eBv_e\lambda_e$ and $B = 3\alpha e^2E^2/5T_e^2$ and $k_{\|} = (m - nq)/Rq$, with q the safety factor. The temperature entering on the right side of eq.(8) is always T_{e0}. Discussing eq. (8) the source term B will be neglected. This is a very good approximation for realistic tokamak parameters. One has to distinguish between two different regions characterized by the value of $k_{\|}$: In the so-called resonance region $k_{\|}^2 \ll |D|$ with $D = m/rA(d\ell n n_e/dr)$ the solution for $T_{m,n}$ can be represented with

$$T_{m,n} \approx ib_{m,n} T_e' f_p^2 nr/Rm(d\ell n n_e/dr) \tag{9}$$

an expression, which is independent from the mean free path λ_e. Inserting this into eq. (7), it is shown that the average radial heat flux $S_{0e,r}$ is enhanced very much with the parallel heat conductivity $\chi_{\|}$ resulting in a formula for the diffusion coefficient similar to that of Rosenbluth-Rechester [6] but with an enhancement factor λ_e/Rq agreeing with the one obtained earlier on the basis of the drift kinetic theory (see eq. (8)) of ref.[4]). Outside the resonant region where $k_{\|}^2 \gg |D|$ we can expand the solution for $T_{m,n}$ using an ordering parameter $\gamma = D/k_{\|}^2 \ll 1$.

The zero order solution $T_{m,n} = ib_{m,n}T_{e,o}'k_{\|}^{-1}$ is that of $\vec{b}\nabla T_e = 0$ and gives no contribution to the parallel transport.
The lowest order of $\vec{b}\nabla T_e$ is therefore proportional to γ which scales like λ_e^{-1} cancelling λ_e arising in $\chi_{\|}$. The parallel transport comes out to be independent from the collision time but is very small as compared to the formula of Rosenbluth-Rechester with a factor v_D/v_e where v_D is the electron drift velocity.

To estimate the validity of the linear theory we have to consider two different regions: In the region of parallel transport $k_{\|} \approx 0$ the deviation from the Maxwell

distribution has to be small. Using eq.(4) together with (8) we find for $k_{\|} = 0$ the condition to hold

$$\lambda_e b_r \frac{\partial}{\partial r}(\ell n T_{e0}) < 0.1 \tag{10}$$

Outside the resonance region the non-linear terms arising within the expression of the parallel heat flux should be small leading to the condition $\frac{\partial T_{e,1}}{\partial r} \ll T'_{e0}$ with $T_{e,1}$ given from $\vec{b}\nabla T = 0$. From this follows a condition for the perturbation field easy to fulfill in realistic cases with $b_r \leq 10^{-4}$.

References

[1] Kadomtsev B.B. and Pogutse O.P., Proc. 7th Int. Conf. Innsbruck, 1978;

[2] Thyagaraja A. and Haas F.A., Physica Scripta, Vol. 31, 83 – 86, 1985;

[3] Shaing K.C., ORNL/P-87/3477;

[4] Feneberg W., Hellberg M.A., EPS Dubrovnik (Cavtat), 1988;

[5] Haas F.A. and Thyagaraja A., Plasma Physics and Contr. Fusion, Vol. 29, 2, 1987;

[6] Rechester A.B. and Rosenbluth M.N., Phys. Rev. Lett. **40**,38, 1978;

[7] Rebut P.H., Brusati M., Hugon M., Lallia P., IAEA Kyoto. 1986, CN-47/E-III-4.

FOURIER LAW VIOLATIONS AND HEAT-CURRENT TRANSFER IN PLASMA

A.A.Filyukov

Keldysh Institute of Applied Mathematics, Academy of Sciences
U S S R

In the problems of astrophysics and high, temperature plasma physics the intensity of electron heat transfer achieves in some cases the limiting level admissible by the conservation laws. In such cases the applicability of the Fourier law is restricted by the condition that the free range and electron collision time are small in comparison with the relative scales of changes in macroscopic quantities. The use of higher moments of kinetic approximation is needed in such cases.

For these aims the hyperbolic equation has been proposed recently for the description of intensive electron heat transfer. This equation takes into account the process of heat flux relaxation [1,2]. It may be derived formally from the Boltzman equation by Grad's "13 moments" method [3]. This approach may be considered as an effective account for the time delay connected with the inertia of electrons and the finiteness of electron velocity. It leads to the natural account of flux limit for large values of temperature gradient [4].

In contrust to the Fourier law where the heat flux is collinear to the temperature gradient at any moment , in the hyperbolic approximation the connection between these quantities is defined by the sum, including in addition the heat flux rate multiplied by the characteristic time τ of the heat flux relaxation.

$$q + \tau \cdot \dot{q} + \varkappa \cdot \mathrm{grad}\ T = 0$$

A natural question arises concerning the physical interpretation of relaxation contribution to the heat flux vector. Exactly this contribution defines the finiteness of the propagation velocity in contrast to the Fourier law where this physical demand is violated.

In the nonuniform plasma with temperature gradients not only the heat fluxes emerge, but the electron current also arises. It occures due to the Maxwell velocity distribution alteration caused by temperature gradients, and as a consequence the electron flow appears. By analogy with this the existence of

electric field in plasma, which displaces the velocity distribution as a whole , leads to the heat flux emergence.

Electron currents due to temperature gradients result in the charge redistribution and electric fields arise generating reverse currents. In the steady case these currents compensate the initial ones and the stationary charge distribution defines the so called selfconsistent field. The latter has such direction that it reduces the heat flux.

The interaction of simultaneous nonequilibrium processes, that means heat and electron flows, may be described by the phenomenological laws of nonequilibrium thermodynamics,

$$j = (1/\eta)\ E + \alpha\ \nabla\ T;$$

$$q = -\beta\ E - \varkappa\ \nabla\ T;$$

where the role of thermodynamic fluxes is played by the flows of electrons and heat. Meanwhile the thermodynamic forces are the quantities proportional to the gradients of potential and temperature.

If E^* is the selfconsistent field that terminates electron current in the steady state then

$$E^* = -\ \eta\ \alpha\ \nabla\ T,$$

and the heat flow reduces to the value $q = -\varkappa\ (1 - \beta\eta\alpha/\varkappa)\ \nabla\ T$ due to the selfconsistent field action. One may treat this effect as an effective reduction of conductivity coefficient. In accordance with Spitzer and Harm calculations [5] the reduction factor $(1 - \beta\eta\alpha/\varkappa)$ is near 0.4.

It is important to note that according to the form of phenomenological equations the heat flux and electron current represent the linear combination of the same forces. The simultaneous existence of two nonequilibrium processes results in violations of both the Fourier law and the Ohm law in their ordinary form. The Fourier form dependence rehabilitates only by the current compensation due to selfconsistent field. At the absence of such a compensation, immidiately with the current appearence the Fourier relation is violated. Just the same situation occurs in nonstationary case when one takes into account the flux relaxation according to the Maxwell-Cattaneo [6,7] relation. Such an analogy gives the grounds for physical interpretation of heat flux relaxation in the terms of nonsteady current effects excited by the rapid change of temperature gradients. Keeping in mind the inertia of electrons, such rapid changes cause disagreement between compensation field and temperature gradient vector. Nonsteady currents arise, they tend to distribute the charges in order to reconstruct the selfconsistent field. The nonsteady currents noncorrelated with the instant temperature gradient vector are the reason to

appearence of some nonlinear thermoelectric effects, the latter having the significant influence on the heat transfer process. Below these effects are listed.

First it is the heat release in the domain of current flow due to the Joule heating proportional to the square current density.

Second it is the heat release or absorption due to the Thomson effect, the sign of which depends on the mutual orientation of the current and temperature gradient vector.

Third it is the heat transfer to the given point with electron currents carrying entropy of transfer from the adjoining domains, the latter being colder or hotter in comparison to the given point; this phenomenon is defined by the Peltier effect and it can lead both to warming and cooling.

Finally, the last fourth effect is defined by energy consumption connected with the work for distributing charges in the internal plasma fields, for instance, the consumption for the selfconsistent field reconstruction.

As the steady state is approached the current relaxes to zero and all the above mentioned effects vanish. On the contrary in the strong nonstationary case all these thermoelectric phenomena prevail over the custom diffusive heat transfer. They define quite different type of physical behaviour resembling the propagation of wave perturbations.

Running of the nonsteady currents is accompanied by the change of internal energy due to dissipative processes as well as the potential energy connected with charge distribution in the internal field $E = -\operatorname{grad} \varphi$.

The global change of internal energy U per unit volume due to the heat and current conductivity is defined by the equation

$$\rho\partial U/\partial t = -\operatorname{div} q + (j,E) - \varphi\cdot\operatorname{div} j \equiv -\operatorname{div} (q + \varphi\cdot j),$$

which testifies the necessity of unified treatment for heat and current transfer in plasma.

If the Gibbs–Dugem equation is taken as a ground for the change of specific entropy S due to internal energy U and particle number N alteration at the given chemical μ and electric φ potentials

$$T\, dS = dU - (\mu - F\cdot\varphi)\, dN$$

(F is the Faraday constant) with account for energy and charge conservation laws in the following form

$$\rho\partial U/\partial t = -\operatorname{div} (q + \varphi\cdot j); \qquad \rho\partial FN/\partial t = \operatorname{div} j$$

as well as for Coulomb law in the form of Poisson equation

$$\operatorname{div} \operatorname{grad} \varphi = 4\pi\cdot\rho_e = -\rho\cdot F\cdot N\ ,$$

then after some substitutions one may obtain

$$T \cdot \rho \cdot \partial S/\partial t = -\mathrm{div}\ q - j \cdot \mathrm{grad}\ \varphi - (\mu/F) \cdot \mathrm{div}\ j\ .$$

The use of identity

$$T \cdot \mathrm{div}\ \{ [\ q + (\mu/F) \cdot j\ ] / T \} \equiv \mathrm{div}\ q + (\mu/F) \cdot \mathrm{div}\ j -$$

$$-[q + (\mu/F) \cdot j] \cdot \mathrm{grad}\ T\ /\ T + j \cdot \mathrm{grad}\ (\mu/F),$$

leads to the following form of entropy balance equation

$$\rho \partial S/\partial t + \mathrm{div}\ \{ [q + (\mu/F) \cdot j]/\ T \} = \sigma$$

with $Q/T \equiv [q + (\mu/F) \cdot j]/T$ as a vector of the entropy flux and σ as an entropy production in two equivalent forms

$$T \cdot \sigma = (q + (\mu/F) \cdot j\ ,\ -\mathrm{grad}\ T\ /\ T) + (j\ ,\ E + \mathrm{grad}\ (\mu/F));$$

$$T \cdot \sigma = (q\ ,\ -\mathrm{grad}\ T/T) + (j\ ,\ E + T \cdot \mathrm{grad}(\mu/FT));$$

the latter confurms that the generalized heat flux Q corresponds to the thermodynamic force $-\mathrm{grad}\ T/T$ or the current flux j corresponds to the thermodynamic force $E + T\ \mathrm{grad}\ (\mu/FT)$.

The substitution of so defined phenomenological relations in the energy conservation equation gives the possibility to write down explicitly expressions for the above mentioned nonlinear thermoelectric effects responsible for relaxation properties in hyperbolic equation of heat-current transfer.

REFERENCES

1. Choi S.,Wilhelm H. Phys.Rev. 1976,A 14,1825
2. Moses G.,Duderstadt J. Phys.Fluids 1977,20,762
3. Grad H. Commun.Pure Appl.Math. 1949,2,331
4. Fechner W.B.,Mayer F.J. Phys.Fluids 1984,27,6,1538
5. Spitzer L.,Harm R. Phys.Rev. 1953,89,977
6. Cattaneo, Atti.Sem.Mat.Fis.Univ.Modena 1948,3,83
7. Maxwell J.C. Phil.Trans.Roy.Soc.Lond.1867,157,49

FULLY TOROIDAL FLUID MODEL FOR LOW FREQUENCY MODES IN MAGNETIZED PLASMAS

J. Nilsson, M. Liljeström and J. Weiland

Institute for Electromagnetic Field Theory, Chalmers University of Technology and EURATOM-NFR Association
S-412 96 Göteborg, Sweden.

Although less accurate than a full kinetic description, fluid models of plasmas have been widely used in the literature. This is mainly due to their relative simplicity but also because they give more explicit results where parameter scalings can be directly seen, while kinetic methods give results in terms of integrals that usually have to be evaluated numerically. Although also more complete fluid models usually requre the help of computers in order to obtain quantitatively accurate results, the computing time is significantly reduced. This is particularly important for nonlinear turbulence calculations where kinetic models cannot be used for more realistic geometries. We will here investigate the accuracy of a two fluid description which applies for arbitrary ω_0/ω[2,4]. The model includes all the curvature effects in the Braghinskii energy eqs.

We will here take the limiting case $\omega \gg k_\parallel C_s$ where the parallel ion motion can be neglected. This assumption considerably simplifies the description at the same time as it includes some of the most important modes in tokamaks. We also neglect resistive and vixcous effects. The localization of the particles in the perpendicular plane is thus provided by the magnetic field. In this approximation the only contribution to the heat flow comes through the diamagnetic (Roghi-Leduc) heat flow $\vec{q}_*$ given by

$$\vec{q}_* = \frac{5}{2}\frac{P}{m\Omega_c}(\hat{e}_\parallel \times \nabla T) \qquad (1)$$

This is the diamagnetic heat flow derivde by Braghinskii [1] using a collision dominated model. The form (1) of $\vec{q}_*$ is, however, more general since $\vec{q}_*$ for physical reasons has to cancel other convective diamagnetic effects in the energy equation [3]. After this cancellation only compressibility effects of $\vec{q}_*$ remain. This effect turns out to be quite important in general, e.g. providing an additional pressure driving force for the MHD ballooning mode branch but giving a stabilizing effect on η_i modes.

We use the perturbed equations of continuity and energy for ions in the form [4].

$$\frac{\partial n_i}{\partial t} + \vec{v}_E\cdot\nabla n_i + n_i\,\nabla\cdot\vec{v}_E + \nabla\cdot(n\vec{v}_{*i}) + \nabla\cdot(n\vec{v}_{\pi i}) + \nabla\cdot(n\vec{v}_{pi}) = 0 \qquad (2)$$

$$\frac{3}{2}\,n\left(\frac{\partial}{\partial t} + \vec{v}\cdot\right)T + p\nabla\cdot\vec{v} = -\nabla\cdot\vec{q}_* \qquad (3)$$

to find the ion density response

$$\frac{\delta n_i}{n_i} = \frac{e\phi}{T_e}\,\frac{\left[\omega_{*e} + \tau\omega_{Di} - k^2\rho^2(\omega - \omega_{*i}(1+\eta_i))\right]\left[\omega - \frac{5}{3}\omega_{Di}\right] + \tau\left(\frac{2}{3} - \eta_i\right)\omega_{*i}\omega_{Di}}{\omega^2 - \frac{10}{3}\omega\omega_{Di} + \frac{5}{3}\omega_{Di}^2} \qquad (4)$$

which explicitly shows the correct limit $-\frac{e\phi}{T_i}$ for $\frac{\omega_{Di}}{\omega} \to \infty$.

The kinetic ion density response as obtained from a gyrokinetic equation can be written [5]:

$$\frac{\delta n_i}{n} = \frac{e\phi}{T_i}\left\{-1 + \int \frac{\left\{\omega - \omega_{*i}\left[1 + \eta_i\left(\frac{m_i v^2}{2T_i} - \frac{3}{2}\right)\right]\right\} J_o^2(\xi) f_{Mi}}{\omega - \omega_{Di}(v_\parallel^2 + v_\perp^2/2)/v_{th_i}^2}\, d^3v\right\} \qquad (5)$$

where $\xi = \frac{k_\perp v}{\omega_{ci}}$, J_o is a Bessel function and f_{Mi} is a Maxwellian distribution function.

The integration over velocity space can be performed to a rather large extent. With $k^2\rho^2 \ll 1$ the result is

$$\begin{aligned}\frac{\delta n_i}{n_i} = \frac{e\phi}{T_i}\Big\{&-1 + 2i\frac{\eta_i}{\varepsilon_n}\sqrt{\pi\alpha}\,e^{-\alpha}\left(\mathrm{erf}(-i\sqrt{\alpha}) - 1\right) - \\ &- \pi\left\{\alpha - \frac{1}{\varepsilon_n}\left[1 + \eta_i(2\alpha - 1)\right]\right\}e^{-2\alpha}\left(\mathrm{erf}(-i\sqrt{\alpha}) - 1\right)^2 + \\ &+ 2k^2\rho^2\Big[\left(\alpha - \frac{1}{\varepsilon_n}\right)\pi e^{-2\alpha}\left[(1+\alpha)\left(\mathrm{erf}(-i\sqrt{\alpha}) - 1\right)^2 - 2\,\mathrm{erf}(-i\sqrt{\alpha})\right] + 2 + \\ &+ 4\frac{\eta_i}{\varepsilon_n}e^{-\alpha}(\alpha - 3) - 2i\sqrt{\pi\alpha}\,e^{-\alpha}\left(\mathrm{erf}(-i\sqrt{\alpha}) + 2\alpha - \frac{2}{\varepsilon_n}\right)\Big]\Big\}\end{aligned} \qquad (6)$$

where $\alpha = \frac{\omega}{\omega_{Di}} > 0$ in the ion diamagnetic direction.

When $\omega \sim \omega_{*i} \ll \omega_{Di}$ it is possible to expand our density responses. For the kinetic model this expansion gives

$$\frac{\delta n_i}{n_i} = \frac{e\phi}{T_i}\left\{-1 + \pi\left[(1-\eta_i)\frac{\omega_{*i}}{\omega_{Di}} - \frac{\omega}{\omega_{Di}}\right]\right\} \qquad (7)$$

whereas the fluid model gives

$$\frac{\delta n_i}{n} = \frac{e\phi}{T_i}\left[-1 + \left(\frac{7}{5} - \frac{3}{5}\eta_i\right)\frac{\omega_{*i}}{\omega_{D_i}} - \frac{7}{5}\frac{\omega}{\omega_{D_i}}\right] \qquad (8)$$

which is qualitatively the same result as (7).

When ω is in the diamagnetic electron direction the fluid and kinetic responses are not possible to separate fig. 1[6]

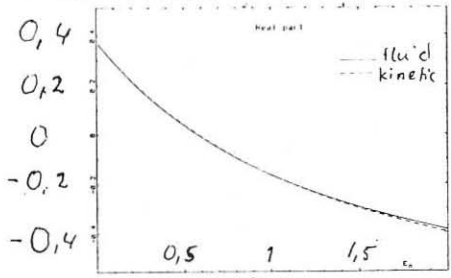

Fig. 1. The ratio $f = \frac{\delta n}{n} / \frac{e\phi}{T_e}$ as a function of $\varepsilon_n = 2L_n/L_B$ for propagation in the electron drift direction, $\omega_r = 2\omega_{*e}$, $\gamma = \omega_{*e}$, $\eta_i = 3$ and $k\rho_s = 0.1$

Using the condition of quasineutrality with adiabatic electrons we may form density responses which give us η_i tresholds as a function of ε_n For $k^2\rho^2 = 0$ the fluid eqs. give

$$\eta_{ith} = \frac{1}{2}\left(\frac{4}{3} - \tau\right) + \frac{1}{4}\varepsilon_n\left(\tau + \frac{40}{9\tau}\right) + \frac{\tau}{4\varepsilon_n} \qquad (9)$$

while the kinetic model gives

$$\eta_{itr} = \varepsilon_n \frac{\left(\alpha - \frac{1}{\varepsilon_n}\right) e^{-\alpha}\sqrt{\frac{\pi}{\alpha}}\, erf(-i\sqrt{\alpha})}{e^{-\alpha}\sqrt{\frac{\pi}{\alpha}}\, erf(-i\sqrt{\alpha})(2\alpha - 1) + i} \qquad (10)$$

where ω satisfies

$$\left(1 + \frac{1}{\tau}\right)\left[1 + \left(\frac{1}{\sqrt{\alpha}} - 2\sqrt{\alpha}\right) i\sqrt{\pi}\, e^{-\alpha} erf(-i\sqrt{\alpha})\right] +$$
$$+ \left(\alpha - \frac{1}{\varepsilon_n}\right) e^{-2\alpha}\pi\left(1 - erf^2(-i\sqrt{\pi})\right) = 0 \qquad (11)$$

As seen in fig. 2.[6] the agreement is extremely good for $\tau = 1$.

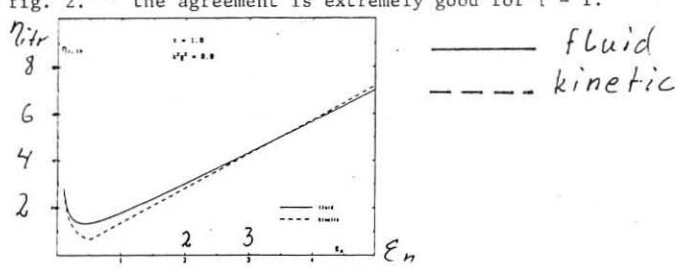

Fig. 2 a) The stability threshold in η_i for toroidal η_i modes as a function of $\varepsilon_n=2L_n/L_B$ for the fluid and fully kinetic models. The temperature ratio is $\tau=1$ and FLR effects are absent.

For $\varepsilon_n \gg 1$ both the fluid and the kinetic thresholds are of the general form

$$\eta_{i\,thr} = g(\tau)\,\varepsilon_n \qquad (12)$$

where for the fluid model

$$g(\tau) = g_f(\tau) = \varepsilon_n\left(\frac{\tau}{4} + \frac{10}{9\tau}\right)$$

The agreement with kinetic theory is good for $\tau \lesssim 4$. For large τ, however, the kinetic g approaches 1 as

$$g_k(\tau) \rightarrow 1 + \frac{1}{2\tau} \qquad (\tau \rightarrow \infty)$$

In this limit, however, the eigenfrequency is given by

$$\omega \approx \frac{\frac{1}{2}\omega_{Di}}{1-\left(1+\frac{1}{\tau}\right)^{-1/2}} \longrightarrow -\omega_{De} \text{ when } \tau \rightarrow \infty$$

This means that $\alpha \gg 1$ and the fluid limit should apply. Thus although the exact thresholds differ strongly in this limit the kinetic and fluid thresholds is very small.

The conclusion to be drawn from these results is that the present fully toroidal fluid model appears to be a good description for toroidal fluid instabilities.

References

1. S.I. Braghinskii in Reviews of Plasma Physics (Ed. M.A. Leontovich) Vol I, Consultants Bureau, New York, 205 (1965).
2. P. Andersson and J. Weiland, Phys. Fluids 31, 359 (1988).
3. S.I. Tsai, F.W. Perkins and T.H. Stix, Phys. Fluids 13, 2108 (1970).
4. A. Jarmén, P. Andersson and J. Weiland, Nucl. Fusion 27, 941 (1987).
5. W.M. Tang, J.W. Connor and R.J. Hastie, Nucl. Fusion 20, 1439 (1980).
6. J. Nilsson, M. Liljeström and J. Weiland Preprint CTH-IEFT/PP-1988-14, Chalmers University of Technology, Göteborg 1988 (Submitted to Phys. Fluids).

TRANSPORT DUE TO FULLY TOROIDAL COLLISIONLESS DRIFT WAVES INCLUDING TRAPPED ELECTRON EFFECTS.

J. Weiland, A. Jarmen and H. Nordman

Institute for Electromagnetic Field Theory, Chalmers
University of Technology and EURATOM-NFR Association
S-412 96 Göteborg, Sweden.

A fully toroidal fluid model (not expanded in L_n/L_B) for ion temperature gradient driven drift modes(η_i modes) has been extended to include effects of electron trapping. As a result a new collisionless trapped electron mode has been found. The electron and ion thermal conductivities are comparable and particle or heat pinch effects with a tendency to equilibrate L_n and L_T have been found.

In recent large tokamak experiments improved confinement regimes for both peaked and flat density profiles have been found. As it turns out both these trends may be consistent with energy transport due to η_i modes. It has, however, not yet been explained why the particle flux may be inward[1] or why the temperature profile peakes immediately after the peaking of the peaking of the density profile in connection with pellet fuelling.[2] In the present paper we attempt to explain these two effects as due to the influence of collisionless electron trapping on the toroidal η_i mode.

We use the fully toroidal fluid model of Ref 4 for both ions and trapped electrons.

$$\frac{\partial n_j}{\partial t} + \vec{v}_E \cdot \nabla n_j + n_j \nabla \cdot \vec{v}_E + \nabla\cdot(n_j \vec{v}_{*j}) + \nabla\cdot(n_j \vec{v}_{\pi j}) + \nabla\cdot(n_j \vec{v}_{pj}) = 0 \qquad (1)$$

$$\frac{3}{2} n_j\left(\frac{\partial}{\partial t} + \vec{v}_j\cdot\nabla\right)T_j + p_j \nabla\cdot\vec{v}_j = -\nabla\cdot\vec{q}_{*j} \qquad (2)$$

where j is the particle index for ions and trapped electrons and q is the diamagnetic heat flow given by

$$\vec{q}_{*j} = \frac{5}{2}\frac{p_j}{m_j \Omega_{cj}}(\vec{e}_\parallel \times \nabla T_j)$$

The other notations are conventional i.e. v_E is the ExB drift, v is the diamagnetic drift and v_p is the polarisation drift. The stress tensor drift v_π has been included only in order to retain the lowest order finite Larmor radius (FLR) effect. The drifts v_p and v_π have been neglected for the trapped electrons and the temperature perturbations enter into (1a) through $\nabla(nv_j)=(1/T_j)v_{Dj}.\nabla\delta p_j$ where v_{Dj} is the magnetic drift. For the trapped electrons this will be the bounce averaged drift. Parallel ion motion has been neglected under the assumption $k^2\rho^2>0.1$. The free electrons are assumed to be Boltzmann distributed.

The system (1)-(3) leads to the linear dispersion relation

$$\frac{\omega_{*e}}{N_i}\left[\omega(1-\varepsilon_n)-\left(\frac{7}{3}-\eta_i-\frac{5}{3}\varepsilon_n\right)\omega_{Di}-k^2\rho_s^2(\omega-\omega_{*i}(1+\eta_i))\left(\frac{\omega}{\omega_{*e}}+\frac{5}{3\tau}\varepsilon_n\right)\right]=$$

$$=f_t\frac{\omega_{*e}}{N_e}\left[\omega(1-\varepsilon_n)-\left(\frac{7}{3}-\eta_e-\frac{5}{3}\varepsilon_n\right)\omega_{De}\right]+1-f_t \tag{4}$$

where $\varepsilon_n = 2L_n/L_B$ and

$$N_j=\omega^2-\frac{10}{3}\omega\omega_{Dj}+\frac{5}{3}\omega_{Dj}^2$$

The dispersion relation (4) is of fourth degree in ω. It is characterized by a symmetry between the ion part, devided by N_i and the trapped electron part devided by N_e, for $f_t=1$ and $k^2\rho_s^2=0$. In the limit $f_t=0$ it turns into the dispersion relation for η_i modes of ref 4. For typical realistic parameter values it has one unstable branch with $N_i<N_e$ (η_i branch) propagating in the ion drift direction and one unstable branch with $N_e<N_i$ (trapped electron branch) propagating in the electron drift direction. This leads us to suggest that the latter is the mode propagating in the electron drift direction observed in ref 3. We may derive quasilinear diffusion coefficients for the system (1)-(3) in the same way as done in Ref 4 with the saturation level estimated by

$$\frac{e\phi}{T_e}=\frac{\gamma}{\omega_{*e}}\frac{1}{k_xL_n}$$

The result may be written in the form:

$$\chi_i=\frac{1}{\eta_i}\left[\eta_i-\frac{2}{3}-(1-f_t)\frac{10}{9\tau}\varepsilon_n-\frac{2}{3}f_t\Delta_i\right]\frac{\gamma^3/k_x^2}{\left(\omega_r-\frac{5}{3}\omega_{Di}\right)^2+\gamma^2}$$

$$\chi_e=f_t\frac{1}{\eta_e}\left(\eta_e-\frac{2}{3}-\frac{2}{3}\Delta_e\right)\frac{\gamma^3/k_x^2}{\left(\omega_r-\frac{5}{3}\omega_{De}\right)^2+\gamma^2}$$

$$D=f_t\Delta_n\frac{\gamma^3/k_x^2}{\omega_{*e}^2}$$

where $\omega = \omega_r + i\gamma$, $\tau = T_e/T_i$ and Δ_i are fourth degree expressions in ω and ε_n given in Ref 4. In the limit $f_t=0$, χ_i turns into the result given in ref 4. In the present system the pinch effects may dominate so that one or two of the diffusion coefficients may become negative.
In Fig 1 we show a diagram with stability boundaries and signs of the diffusion coefficients as a function of $\eta = \eta_i = \eta_e$ and ε_n. We note that the pinch effects always tend to equilibrate L_n and L_T. Such trends are also present in the magnitudes of the diffusion coefficients when all are positive.

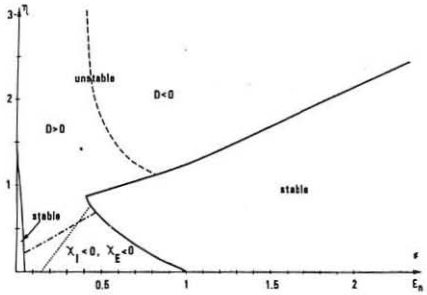

Fig 1. Stability boundaries in $\eta=\eta_i=\eta_e$ and signs of transport coefficients as a function of $\varepsilon_n=2L_n/L_T$ for $\tau=1$, $f_t=0.5$ and $k^2\rho^2=0.1$. In the region below the dotted line $\chi_e<0$ and below the dashed dotted line $\chi_i<0$.

In Fig 2 we show the variation of the diffusion coefficients as a function of ε_n for $\eta=0.1$ where heat pinch effects are present.

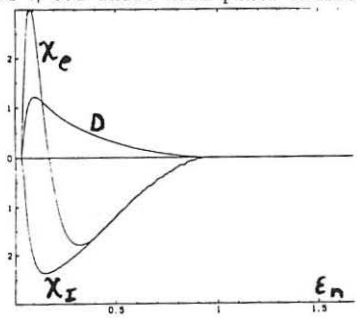

Fig 2 The scaling of diffusivity with ε_n for $\eta_e=\eta_i=0.1$, $k^2\rho^2=0.1$, $\tau=1$ and $f_t=0.5$.

The coupling between particle and energy diffusion is in agreement with experimental observations. The particle pinch effect seems to be present in most present day tokamaks while the heat pinch effect occurs only under rather extreme conditions.

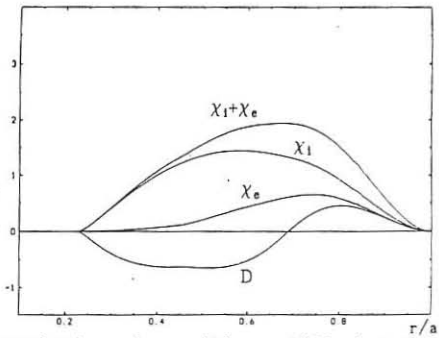

Fig 3. Radial variation of quasilinear diffusion coefficients for the TEXTOR profile with N=1.91 in ref 6 with τ=1, $k^2\rho^2$=0.1 and $f_t = 2\varepsilon/(1+\varepsilon)$ where ε=r/R.

References:

1. B. Coppi and N. Sharky, Nuclear Fusion 21, 1363 (1981).
2. B. Coppi, Phys Lett. A128, 193 (1988).
3. A.J. Wootton, M.E. Austin, R.D. Bengtson et. al. Plasma Phys. and Contr. Fusion 30, 1479 (1988).
4. H. Nordman and J. Weiland, Preprint CTH-IEFT/PP-1988-12, Chalmers University of Technology, Göteborg, Sweden 1988.(To be published in Nuclear Fusion).
5. J. Weiland, A. Jarmen and H. Nordman Preprint CTH-IEFT/PP-1988-22, Chalmers University of technology, Göteborg 1988.
6. A. Rogister, G. Hasselberg, F. Waelbroeck and J. Weiland, Nuclear Fusion 28, 1053 (1988).

ON CONVECTIVE FLUCTUATIONS IN A THREE-COMPONENT PLASMA IN A CURVED MAGNETIC FIELD

A.G.Sitenko, P.P.Sosenko

Institute for Theoretical Physics, Academy of Science of the Ukrainian SSR, Kiev - 130, the Ukrainian SSR (USSR)

1. Introduction. The theory of nonlinear interaction of low-frequency waves and fluctuations in a two-component plasma in a homogeneous magnetic field /1-5/ predicts a nonlinear dynamics of low-frequency motions and stationary spectra of low-frequency fluctuations with nonlinear effects taken into account, as well as an anomalous plasma transport due to these fluctuations. Meanwhile, the laboratory, geophysical and astrophysical studies reveal the importance of low-frequency nonlinear phenomena in many-component plasmas in a curved magnetic field /6-10/.

The present paper establishes the possibility of nonlinear convective waves in a three-component plasma in a curved magnetic field, suggests reduced equations appropriate for description of such waves and predicts the stationary spectrum of flute (interchange) fluctuations, as well as the possibility of critical fluctuations. The existence of a nonlinear mechanism generating large-scale electrostatic fields in the form of a double cascade of waves is demonstrated.

2. Reduced nonlinear equations for the convective oscillations. Let us consider the case of a three-component plasma in crossed magnetic $\vec{B}_o$ and gravity $\vec{g}$ fields, which are assumed to be homogeneous. (The gravity field is introduced to model the magnetic field curvature /11/). Plasma inhomogeneity is assumed to be in the direction of a gravity field, along the x-axes. We start from the transport equations /1-3/

$$\partial_t n_a + \vec{\nabla}(n_a \vec{v}_a) = 0, \quad a = e, i, \tag{1}$$

$$\vec{v}_{\perp a} = (c/B)(\vec{u}_a \times \vec{b} + (1/f_{Ba})(\partial_t + \vec{v}_{\perp a}\cdot\vec{\nabla})\vec{u}_{\perp a}), \tag{2}$$

$$\vec{u} = \vec{E} + m\vec{g}/q - (\vec{\nabla} p + \vec{\nabla}\cdot\pi)/qn .$$

(Here n, $\vec{v}$, $\vec{E} = -\vec{\nabla}\varphi$, p, are, respectively, a density, an electric field strength, a pressure, a viscosity tensor, q and m are the charge and the mass of a particle, c is a light velocity, f_B is a gyrofrequency, $\vec{b} = \vec{B}/B$, index e (i) refers to electrons (ions)). Eq.(2) takes into account the low-frequency and flute character of plasma motion. The third component (a hot one which represents either electrons or ions)is

described in the adiabatic approximation /2-5,8,9,12/

$$n_h = n_{ho}(1 - q_h\varphi/T_h), \tag{3}$$

where n_{ho} is an unperturbed density, T_h is a temperature, the potential φ is governed by the Poisson equation

$$\Delta\varphi = -4\pi\,(\sum_a q_a n_a + q_h n_h)\ . \tag{4}$$

Eqs.(1)-(4) yield a system of reduced equations for the potential and density ($\delta n_e = n_e - n_{eo}$) perturbations (the frame is chosen so as to have the electrons at rest in an unperturbed state): $(\partial_t(1-\rho^2\Delta) + \nu\rho^2\Delta + \vec{v}_d\cdot\vec{\nabla} + (1-\rho^2\Delta)\vec{v}_g\cdot\vec{\nabla})\varphi -$

$$-\rho^2\vec{v}_E\cdot\vec{\nabla}\Delta\varphi + (c/B)\vec{b}\times\vec{\nabla}\ln a\cdot\vec{\nabla}\varphi^2 - 4\pi q_e a^2\vec{v}_g\cdot\vec{\nabla}\delta n_e = 0, \tag{5}$$

$$(\partial_t + \vec{v}_E\cdot\vec{\nabla})\delta n_e + \vec{v}_E\cdot\vec{\nabla} n_{eo} = 0, \tag{6}$$

where the following notations are used: $\vec{v}_g = \vec{g}\times\vec{b}(1/f_{Bi} - 1/f_{Be})$, $\vec{v}_E = (c/B)\vec{b}\times\vec{\nabla}\varphi$, $a^2 = T_h/4\pi q_h^2 n_{ho}$, $\rho^2 = a^2(1+\alpha)$, $\alpha = 4\pi n_{io} m_i c^2/B^2$, ν is the ion viscosity coefficient, v_d is the diamagnetic drift velocity for the hot component. Eqs.(5) and (6) imply that the wavelength of the oscillations is much less than the inhomogeneity scale of the unperturbed density and temperature, as well as small density perturbations /1/: $|\varphi| \gg |\delta n_a T_a/q_a n_{ao}|$. In the case of weakly nonlinear motions the solution of Eq.(6) for the density perturbation can be cast in the form of expansion in increasing powers of the electric field strength. Introducing this expansion into Eq.(5), we derive a closed nonlinear equation for the space-time Fourier component φ_K for the potential ($E_K = -ik\varphi_K$, $K = \vec{k}, f$):

$$\varepsilon(K)E_K + \sum_{1+2=K} \varkappa^{(2)}(1,2)E_1E_2 + \ldots = 0, \tag{7}$$

where $\varepsilon(K)$ is a dielectric permittivity, $\varkappa^{(2)}$ is a second order nonlinear electric susceptibility. The similarities between the electrostatic mode under consideration and the magnetic electron mode /13,14/ are obvious.

3. Linear waves and fluctuations. The eigen-frequency of plasma oscillations follows from the zero of the dielectric permittivity: $f_k = f_k^{\pm} = (1/2)(f_g + f_h)(1 \pm (1 - 4\,f_g f_h/(f_g + f_h)^2)^{1/2})$. In the case of a nonequilibrium unperturbed plasma state (unfavorable curvature) the waves with the frequency $f^+(f^-)$ have a positive (negative) energy. In the case of favorable curvature both branches are characterized with positive energies.

In order to take into account the fluctuations, a random source s is to be introduced into the right-hand side of Eq.(7), with a quadratic spectral correlation function for the source being determined within the context of the theory of hydrodynamic fluctuations /16/. Then, the spectral distribution of electric field strength fluctuations is as follows $\langle E^2\rangle_K = \langle s^2\rangle_K/|\varepsilon(K)|^2$. The Landau-Lifshitz approach yields $\langle s^2\rangle_K = (8\pi T_i/(f - f_g))\mathrm{Im}\,\varepsilon$. Then, $\langle E^2\rangle_K = (8\pi T_i/(f - f_g))\mathrm{Im}(1/\varepsilon^*)$. The latter relation has the form of a fluctuation-dissipation

relation /18/, nevertheless it is appropriate for a description of fluctuations in the nonequilibrium state too. The integration of this spectrum over the frequency results in the following expression for the fluctuation intensity:

$$I_{\vec{k}} = \sum_f \langle E^2 \rangle_K = \frac{4\pi T_i \gamma}{1+\rho^2 k^2}\left(\frac{(f_1+i|\gamma_1|)^2}{|\gamma_1|\,((f_1-f_2+i|\gamma_1|)^2+\gamma_2^2} + (1 \rightleftarrows 2)\right),$$

where $f_1-i\gamma_1$ and $f_2-i\gamma_2$ are the roots of the linear dispersion equation with regard for the dissipation. When $\gamma \ll |f^+-f^-|$, the latter equation simplifies to

$$I_k = I^{eq}(|f^+|+|f^-|)/(|f^+-f^-|),\quad I^{eq} = 4\pi T_i a^2 k^2/(1+\rho^2 k^2),$$

i.e. $I_k = I^{eq}$ in the case of favorable curvature. In the unfavorable curvature case the fluctuation intensity increases substantially as $f^+ \to f^-$ (critical fluctuations). But the simplified equation for the intensity is unjustified in that region. When $\gamma \sim |f^+-f^-|$, the general equation yields ($\gamma \ll |f^+|$)

$$I_k = I^{eq}(|f^+|/2\gamma)^{1/2} \gg I^{eq},\quad f^+ = (f_h+f_g)/2$$

i.e. the level of fluctuations in nonequilibrium plasma is much above the fluctuation level in the equilibrium state. When $\gamma \gg |f^+|$, the fluctuation level is the same for both cases of favorable and unfavorable curvatures, and it equals to I_k^{eq}.

4. <u>Decay instability</u>. Let us consider the nonlinear interaction of convective waves in the stability domain, with viscosity being disregarded. The decay instability /17/ takes place, if the condition, $Q = s_2 s_3 V(\vec{k}_1,-\vec{k}_3)V^*(\vec{k}_1,-\vec{k}_2) > 0$, is satisfied ($\vec{k}_1 = \vec{k}_2 + \vec{k}_3$).

The nonlinear electric susceptibility possesses symmetry properties which reflect the nonlinear interaction conservation laws. We use them to transform the decay instability criterion, $(s_2\hat{f}_2)(s_3\hat{f}_3)(f_{g1}/\hat{f}_1 - f_{g3}/\hat{f}_3)(f_{g2}/\hat{f}_2 - f_{g1}/\hat{f}_1) > 0$.

In what follows the condition, $|f_h| \gg |f_g|$, is assumed to hold.

For the interaction of waves with the same sign of the energy, the instability condition (along with the monotonic dependence of the quantity $f_g/\hat{f}$ upon the wavenumber) implies that the pump wave is to have an intermediate value of the wavenumber, and nonlinear interaction causes a simaltaneous excitation of waves with large and small wavenumbers, i.e. a double cascade of waves takes place in the wavevector space.

The decay instability criterion can be put into the form $k_{2y}(k_{1y}-k_{2y}) > 0$, if the sign of the energy is the same for all three waves, i.e. nonlinear interaction causes a spectral cascade of waves towards the small values of $|k_y|$, which may result in an emergence of structures elongated in the direction normal to the inhomogeneity gradient and in a formation of zonal particle flows in this direction. Then, it is possible to suggest the turbulent transport due to low-frequency

convective oscillations to be maximal in the same direction (in the case of toroidal configuration of the confining magnetic field this phenomenon implies that plasma parameters are rapidly equalized in the poloidal direction).

If the waves from different branches interact, for instance f_1^+, f_2^+ and f_3^-, then the instability criterion can be reduced to the form, $k_2 > k_1$, implying $|f_2^+| < |f_1^+|$ ($|f_2^+| > |f_1^+|$) for the case of favorable (unfavorable) curvature, i.e. an up-conversion phenomenon is possible in a nonequilibrium plasma due to the nonlinear interaction of positive energy and negative energy waves.

It is to be noted that the double cascade of waves accompanied by plasma motion anisotropy is a typical feature of the weak nonlinear interaction of low-frequency waves, and it is the form of plasma self-organization /5/.

1. Sitenko A.G., Sosenko P.P. Fizica Plasmy 11 (1985) 957.
2. Sitenko A.G., Sosenko P.P. Ibid. 12 (1986) 63.
3. Sitenko A.G., Sosenko P.P. Ibid. 13 (1987) 456.
4. Sitenko A.G., Sosenko P.P. Problems of Theoretical Physics.-Kiev: Naukova Dumka, 1986. P.225-237.
5. Sitenko A.G., Sosenko P.P. 1987 ICPP inv.papers 1(1987)486
6. Sanuki H., Chen F.F. Phys.Fluids 28 (1985) 3567.
7. Pavlenko V.P., Sanuki H. J.Phys.Soc.Japan 57 (1988) 516.
8. Bharuthram R., Yu M.Y. Phys.Rev. A36 (1987) 1753.
9. Bharuthram R., Yu M.Y. Phys.Lett. A122 (1987) 488.
10. Furth H.P. Phys.Fluids 28 (1985) 1595.
11. Ruhadze A.A., Silin V.P. Usp.Fiz.Nauk 96 (1968) 87.
12. Hasegawa A., Mima K. Phys.Fluids 21 (1978) 87.
13. Nycander J., Pavlenko V.P. Ibid. 30 (1987) 1367.
14. Sitenko A.G., Sosenko P.P. SPIG'88 Contr.papers (1988) 569
16. Landau L.D., Lifshitz E.M. Zh.Eksp.Teor.Fiz. 32 (1957) 618
17. Oraevsky V.N., Sagdeev R.Z. Zh.Tech.Fiz. 32 (1962) 1291.
18. Sitenko A.G. Fluctuations and non-linear wave interactions in plasmas.-Oxford: Pergamon Press, 1982.- 262p.

DRIFT-CYCLOTRON TURBULENCE AND ANOMALOUS TRANSPORT IN INHOMOGENEOUS PLASMA

Michailenko V.S., Stepanov K.N.

Institute of Physics and Technology, the Ukrainian SSR Academy of Sciences, 310108 Kharkov, USSR

Abstract. Drift-cyclotron instability saturation of the plasma with the density and temperature inhomogeneities has been studied. Basic mechanisms of the instability saturation and the turbulence level are established. The anomalous particle and heat fluxes are determined.

The drift cyclotron instability (DCI) is known to develop in the inhomogeneous plasma immersed in the magnetic field [1], its frequency and growth rate being

$$\omega(\vec{k}) \approx n\omega_{ci}\left(1+(\sqrt{2\pi}\,k_\perp\rho_i)^{-1}\right) = n\omega_{ci} + \delta\omega(\vec{k}), \quad (T_e > T_i), \qquad (1)$$

$$\gamma(\vec{k}) \approx -\frac{T_i}{T_e}\frac{n\omega_{ci}}{k_\perp\rho_i}\left[z_e - z_e^*\left(1-\frac{1}{2}\eta_e - z_e^2\eta_e\right)\right]\exp\left(-\frac{\omega^2}{2k_\parallel^2 v_{Te}^2}\right), \qquad (2)$$

where $\rho_\alpha = v_{T\alpha}/\omega_{c\alpha}$, $z_e = \omega/\sqrt{2}k_\parallel v_{Te} \sim 1$, $z_e^* = \omega_e^*/\sqrt{2}k_\parallel v_{Te} \sim 1$, $\omega_e^* = k_y T_e x_e/m_e\omega_{ce}$, $x_A = d\ln A(x)/dx \sim L_A^{-1}$, $\eta_\alpha = d\ln T_\alpha/d\ln n_\alpha$. DCI is excited by resonant electrons with the parallel velocity $v_\parallel = \omega_e^*/k_\parallel \lesssim v_{Te}$.

The turbulence level and anomalous diffusion coefficient estimates due to the drift-cyclotron parametric turbulence in the plasma with the homogeneous temperature were obtained earlier [2]. (The first attempt to analyze the nonlinear stage of DCI was made by A.B.Michailovsky [3] who pointed out that the basic DCI saturation mechanism in the stimulated scattering of oscillation off ions whereas the decay effects are negligible). The present report deals with the dynamics of the drift-cyclotron turbulence which is establishing for the plasma with the inhomogeneous density and temperature, and the particle and heat fluxes are determined.

Accounting for the stimulated scattering of ion cyclotron waves off bare ions the process of establishing the drift-cyclotron turbulence is governed by the equation for the spectral intensity of oscillations $I(\vec{k})$

$$\frac{1}{2}\frac{\partial I(\vec{k},t)}{\partial t} = \left[\gamma(\vec{k}) + \sum_{n_1}\left(\frac{\partial \mathrm{Re}\,\varepsilon_i}{\partial\omega(\vec{k})}\right)^{-1}\int d\vec{k}_1\, \mathrm{Im}\, U_i(\vec{k},\vec{k}_1)\, I(\vec{k}_1)\right] I(\vec{k}), \qquad (3)$$

$$\mathcal{J}m\, U_i(\vec{k},\vec{k}_1) = \mathcal{J}m\, U_i^{(h)}(\vec{k},\vec{k}_1) + \mathcal{J}m\, U_i^{(inh)}(\vec{k},\vec{k}_1),$$

where

$$\mathcal{J}m\, U_i^{(h)} \approx -\frac{\sqrt{2}}{\pi}\frac{e_i^2 k_\perp k_{1\perp}\rho_i^2}{k^2\lambda_{Di}^2 T_i^2}\frac{\omega_{ci}^3(n-n_1)}{(\delta\omega(\vec{k}))^2}\,\delta(\delta\omega(\vec{k})-\delta\omega_1(\vec{k}_1)), \qquad (4)$$

$$\mathcal{J}m\, U_i^{(inh)} \approx \frac{\sqrt{2}}{\pi}\frac{e_i^2 k_\perp k_{1\perp}\rho_i^2}{k^2\lambda_{Di}^2 T_i}\frac{\omega_{ci}\varkappa_{n_i}}{\delta\omega(\vec{k})}(k_y-k_{1y})(1-\eta_i)\,\delta(\delta\omega(\vec{k})-\delta\omega_1(\vec{k}_1)). \qquad (5)$$

As in the case $\nabla T_{e,i}=0$ [2] on the first stage of DCI nonlinear evolution determined by $\mathcal{J}m\, U_i^{(h)}$, the energy transfer to the low frequency range occurs. As a result on the oscillation density level

$$\frac{W}{n_i T_i} \sim \frac{T_i}{T_e}\left(\frac{T_e}{T_i}\frac{\rho_i}{L_A}\right)^4, \qquad (6)$$

where $L_A = L_{n_i}$ at $\eta_e < 1$ and $L_A = L_{T_i}$ at $\eta_e > 1$, the ion cyclotron waves with $\omega = n\omega_{ci}$ ($n \geqslant 2$) are supressed and the only branch with $\omega \approx \omega_{ci}$ survives. Due to this circumstance the matrix element $\mathcal{J}m\, U_i^{(h)}$ vanishes because now $n = n_1$ for interacting waves. The consequent DCI evolution is governed by the matrix element $\mathcal{J}m\, U_i^{(inh)}$.

The DCI saturation process develops differently depending on the values of η_i and η_e magnitudes. In cases $\eta_i < 1$, $\eta_e < 1$ and $\eta_i > 1$, $\eta_e > 1$ the stimulated scattering of ion cyclotron waves off bare ions leads to the energy transfer over the wavenumber spectrum in the linear damping region, the DCI saturation levels W becoming equal to

$$\frac{W}{n_i T_i} \sim \left(\frac{T_e}{T_i}\frac{\rho_i}{L_{ne}}\right)^4, \quad \eta_e < 1,\ \eta_i < 1, \qquad (7)$$

$$\frac{W}{n_i T_i} \sim \frac{L_{Ti}}{L_{Te}}\left(\frac{T_e}{T_i}\frac{\rho_i}{L_{Te}}\right)^4, \quad \eta_e > 1,\ \eta_i > 1. \qquad (8)$$

In the estimate [2] for W the factor $(T_e/T_i)^2$ is missing as compared with (7).

In cases $\eta_e > 1$, $\eta_i < 1$ or $\eta_e < 1$, $\eta_i > 1$ the energy tranfer occurs in the region of maximum $\eta_{|k_y|}$ under the condition of $k_\perp$ conservation for all interacting ion cyclotron waves i.e. in this case $k_y \to k_\perp$, $k_x \to 0$. Now $\mathcal{J}m\, U_i^{(inh)} \to 0$ and the saturation level is determined by the strong turbulence level, based e.g. on the account of cyclotron resonance nonlinear broadening (see [2]). In this case the DCI saturation levels are:

$$\frac{W}{n_i T_i} \sim \left(\frac{T_e}{T_i}\frac{\rho_i}{L_{ne}}\right)^4, \quad \eta_e < 1,\ \eta_i > 1, \qquad (9)$$

$$\frac{W}{n_i T_i} \sim \left(\frac{T_e}{T_i}\frac{\rho_i}{L_{Te}}\right)^4, \quad \eta_e > 1, \ \eta_i < 1. \qquad (10)$$

Note that the level (7) obtained in the case $\eta_e < 1$, $\eta_i < 1$, also happens to be the order of the DCI saturation level establishing as a result of ion cyclotron resonance nonlinear broadening. The broadening is negligible for $\eta_e > 1$, $\eta_i > 1$ when $L_{Ti} < L_{Te}$ but it is dominant in the opposite case when $L_{Ti} > L_{Te}$. In the latter case the DCI saturation level is determined by the estimate (10).

The electron heat flux Q_e across the magnetic field is due to electron scattering off ion cyclotron oscillations and it is determined from the quasilinear kinetic equation for electrons

$$Q_e = \pi\frac{e^2}{m_e^2}\int d\vec{k}\, I(\vec{k})\int d\vec{v}\,\frac{m_e v_\perp^2}{2}\frac{k_y}{\omega_{ce}} J_0^2\left(\frac{k_\perp v_\perp}{|\omega_{ce}|}\right)\left(k_\parallel\frac{\partial F_e}{\partial v_\parallel} + k_y\frac{\partial F_e}{\partial x}\right)\delta(\omega(\vec{k}) - k_\parallel v_\parallel) \sim \frac{W}{\rho_i}\frac{cT_i}{eB_0} \qquad (11)$$

in which the levels W are determined by the estimates (7)-(10). Hence, the temperature conductivity coefficient χ_e may be obtained conventially

$$\chi_e = \frac{Q_e}{\partial P_e/\partial x} \sim D_B\frac{W}{n_i T_i}\frac{T_i}{T_e}\frac{L_{Te}}{\rho_i} \qquad (P_e = n_e T_e) \qquad (12)$$

where $D_B = cT_e/eB_0$. Similar expression in which L_{Te} is changed for L_{ne} has been obtained for diffusion coefficients for electrons and ions. The diffusional flow appears to be ambipolar [2].

This transport appears to be weaker than the transport due to long wavelength drift turbulence that may develop in long devices with $L_\parallel > 10a$ [1]. In short traps $L_\parallel < 10a$ and $L_\parallel/\rho_i > (m_i/m_e)^{1/2}$ the transport is determined by the drift-cyclotron turbulence considered.

References

1. Michailovsky A.B. Theory of Plasma Instabilities (Consultant Bureau, New York, 1974), vol.2.
2. Michailenko V.S., Stepanov K.N. Fizika plasmy (1986), v.12, p.1461-1468 (In Russian).
3. Michailovsky A.B. Doklady AN SSSR (1964), v.158, p.1-68 (In Russian).

Hinc ex F.F. Discalceatorum Templo, illinc ex S. Simeone Minore usque ad Fullonium. XI

SECOND HARMONIC GENERATION IN INHOMOGENEOUS ANISOTROPIC PLASMA DUE TO BEAM-PLASMA INTERACTION

Sh. M. Khalil and R. N. El-Sherif

Atomic Energy Authority
Nuclear Research Centre
Plasma Physics and Accelerators Dept.
Cairo - Egypt

Investigation of beam-plasma interaction presents a great interest for development of new methods in amplification and generation of electromagnetic waves, acceleration of charged particles in plasma, high-frequency heating of plasma and so on.

In the present work, we shall study the nonlinear interaction of a homogeneous beam of electrons of an arbitrary density with an inhomogeneous plasma layer. When the beam density is small as compared with the plasma density and beam Langmuir frequency is small as compared with the wave frequency, the wave phase velocity is close to the beam velocity. In this case, nonlinear interaction associated with the plasma can be neglected as compared with that associated with the beam.

For simplicity, we consider the case of one-dimensional electrostatic oscillations when the direction of beam propagation, plasma density gradient and wave electric field coincide with the x-axis. An external static magnetic field H_0 perpendicular to both beam and plasma is also considered.

The initial set of equations describing the oscillations has the form:

$$\frac{\partial V_s}{\partial t} + V_s \frac{\partial V_s}{\partial x} = -\frac{e}{m} E - \Omega V_s \quad , \quad \Omega = \frac{eH_0}{mc} \tag{1}$$

$$\frac{\partial N_s}{\partial t} + \frac{\partial}{\partial x}(N_s V_s) = 0 \tag{2}$$

$$\frac{\partial E}{\partial x} = -4\pi e \sum_s N_s \tag{3}$$

S indicates the electrons type ($S = b$ for beam, $S = p$ for plasma). The velocity and density of both beam and plasma can be represented as:

$$V_b = u + v_b^{(1)} + v_b^{(2)} \quad , \quad N_b = n_b^{(0)} + n_b^{(1)} + n_b^{(2)}$$

$$V_p = 0 + v_p^{(1)} + v_p^{(2)} \quad , \quad N_p = n_p^{(0)} + n_p^{(1)} + n_p^{(2)}$$

the symbol (0) denotes the unperturbed quantities, (1) denotes

the perturbed values with frequency ω (grounded waves associated with an electric field E_1), and (2) denotes the perturbed values with frequency 2ω (generated waves associated with electric field E_2).

Above values satisfy the relations

$$\frac{\partial u}{\partial t} = \frac{\partial u}{\partial x} = \frac{\partial n_b^{(0)}}{\partial t} = \frac{\partial n_b^{(0)}}{\partial x} = 0 \ , \quad u > 0 \ , \quad n_b^{(0)} \gg |n_b^{(1)}| \ ,$$

$$u \gg |v_b^{(1)}| \ , \quad |v_p^{(1)} \frac{\partial}{\partial x}| < |\frac{\partial}{\partial t}|$$

From equations (1), (2) we can obtain the perturbations with frequency (grounded waves), in velocity and density of the beam and plasma as

$$v_b^{(1)} = -\frac{e}{mu} e^{i\frac{\omega'}{u}x} \int E_1(x) e^{-i\frac{\omega'}{u}x} dx \ , \tag{4}$$

$$n_b^{(1)} = \frac{e n_b^{(0)}}{m u^2} e^{i\frac{\omega}{u}x} \int e^{-i\frac{\omega}{u}x} \left[\frac{\partial}{\partial x} \left(e^{i\frac{\omega'}{u}x} \int e^{-i\frac{\omega'}{u}x'} E_1(x') dx' \right) \right] dx \tag{5}$$

$$v_p^{(1)} = -\frac{ie}{m\omega'} E_1(x) \ , \quad n_p^{(1)} = -\frac{e}{m\omega\omega'} \frac{\partial}{\partial x} \left(n_p^{(0)} E_1(x) \right) \tag{6}$$

where, $\omega' = \omega + i\Omega$ includes the effect of the external magnetic field.

From Poisson's equation (3), we have $\partial E_1/\partial x = -4\pi e(n_b^{(1)} + n_p^{(1)})$, and using the values $n_b^{(1)}$, $n_p^{(1)}$ we can obtain the following differential equation:

$$\left(u\frac{\partial}{\partial x} - i\omega\right)\left(u\frac{\partial}{\partial x} - i\omega'\right)\left[\epsilon(x) E_1(x)\right] + \omega_b^2 E_1(x) = C_1 \ , \tag{7}$$

$$\epsilon(x) = 1 - \frac{\omega_p^2}{\omega\omega'} \ , \qquad \omega_s^2 = \frac{4\pi e^2 n_s^{(0)}}{m}$$

C_1 is integration constant which can put equal to zero when we consider that in the region of medium's homogeneity the oscillations with infinite wavelengths are absent.

Let us set $\omega + \omega' = 2\omega_g$, and under the condition $\omega + \omega' \ll \Omega$ we can rewrite equation (7) in the form:

$$\left(u\frac{\partial}{\partial x} - i\omega_g\right)^2 \left[\epsilon(x) E_1(x)\right] + \omega_b^2 E_1(x) = 0 \ , \quad \omega\omega' \simeq \omega_g^2 \tag{8}$$

Writting the field of the grounded waves in the form

$$E_1(x) = F_1(x) / \epsilon(x) \, e^{i\frac{\omega_g}{u}x}$$

equation (8) becomes

$$\frac{\partial^2 F_1(x)}{\partial x^2} + \frac{K^2}{\epsilon^2} F_1(x) = 0 \ , \quad K^2 = \frac{\omega_b^2}{u^2} \ . \tag{9}$$

In similar way we can get the perturbations- with frequency 2ω - in the velocity and density of the beam and plasma as:

$$v_b^{(2)} = -\frac{1}{u} e^{i\frac{\omega''}{u}x} \int \left(\frac{eE_2}{m} + v_b^{(1)} \frac{\partial v_b^{(1)}}{\partial x} \right) e^{-i\frac{\omega''}{u}x} dx \ , \tag{10}$$

$$n_b^{(2)} = -\frac{1}{u} e^{i\frac{2\omega}{u}x} \int e^{-i\frac{2\omega}{u}x} \left[n_b^{(0)} \frac{\partial v_b^{(2)}}{\partial x} + \frac{\partial}{\partial x}\left(n_b^{(1)} v_b^{(1)} \right) \right] dx \ , \tag{11}$$

$$v_p^{(2)} = -\frac{ieE_2}{m\omega''} + \frac{ie^2 E_1}{m\omega'^2\omega''} \frac{\partial E_1}{\partial x} , \tag{12}$$

$$n_p^{(2)} = \frac{\partial}{\partial x} \left[-\frac{e n_p^{(0)} E_2}{2m\omega\omega''} + \frac{e^2 n_p^{(0)} (\omega+\omega'')}{2m^2\omega^2\omega'^2\omega''} E_1 \frac{\partial E_1}{\partial x} + \frac{e^2 n_p^{(0)} E_1^2}{2m^2\omega^2\omega'^2} \frac{\partial n_p^{(0)}}{\partial x} \right] ,$$

$$\omega'' = 2\omega + i\Omega . \tag{13}$$

The differential equation describing the field of the generated waves for an arbitrary dependence of $n_p^{(0)}$ on x can be obtained as:

$$\frac{\partial^2 F_2}{\partial x^2} + \frac{k^2}{\epsilon'} F_2 = R(x) \ , \tag{14}$$

$$\epsilon' = 1 - \frac{\omega_p^2}{2\omega\omega''} \ , \quad E_2(x) = \frac{F_2(x)}{\epsilon'} e^{i\frac{\omega_h}{u}x} \ , \quad 2\omega_h = 2\omega + \omega'' ,$$

$$R(x) = \left\{ -8\pi e \frac{\omega_h}{u} - 4\pi e \frac{\partial}{\partial x} + 8\pi e \left(\frac{\omega_h}{u}\right)^2 \int dx'' \right\} \cdot \left\{ \frac{\partial}{\partial x} \left[\frac{e^2 n_p^{(0)} (\omega+\omega'')}{2m^2\omega^2\omega'^2\omega''} \cdot E_1 \frac{\partial E_1}{\partial x} + \frac{e^2 n_p^{(0)}}{2m^2\omega^2\omega'^2} E_1^2 \frac{\partial n_p^{(0)}}{\partial x} \right] + \frac{1}{u} e^{i\frac{2\omega}{u}x} \int e^{-i\frac{2\omega}{u}x} \left[\frac{n_b^{(0)} v_b^{(1)}}{u} \frac{\partial v_b^{(1)}}{\partial x} - \frac{\partial}{\partial x}\left(n_b^{(1)} v_b^{(1)} \right) + \frac{i n_b^{(0)} \omega''}{u^2} e^{i\frac{\omega''}{u}x} \int e^{-i\frac{\omega''}{u}x} v_b^{(1)} \frac{\partial}{\partial x} v_b^{(1)} dx' \right] dx \right\} \tag{15}$$

Let us find the solution of (14), i.e., the fields associated with waves of frequency 2ω. We consider the case of plasma layer of width a such that: $n_p^{(0)} = 0$ in regions $x<0$ and $x>a$, and $n_p^{(0)}(x)$ is arbitrary continous function of in region $0 \leq x \leq a$.

In the region $x<0$, we have: $\omega_p = 0$, $R = R_b = R(n_p^{(0)} = 0)$, $\epsilon' = 1$, and we can obtain the following solution:

$$F_2(x) = \frac{1}{2ik} e^{ikx} \int_0^x R_b e^{-ikx} dx + C_2 e^{ikx} - \frac{1}{2ik} e^{-ikx} \int_0^x R_b e^{ikx} + C_3 e^{-ikx} , \quad x<0 \tag{16}$$

where, C_2 and C_3 are integration constants, and since we are looking for the solutions of the generated waves, the terms $C_2 e^{ikx}$, $C_3 e^{-ikx}$ - which describes grounded waves - must be taken to be zero.

In a similar way we can obtain a solution in the region

$$F_2(x) = \frac{1}{2ik} e^{ik(x-a)} \int_a^x R_b e^{-ik(x-a)} dx - \frac{1}{2ik} e^{-ik(x-a)} \int_a^x R_b e^{-ik(x-a)} dx , \quad x>a \tag{17}$$

To solve equation (14) in the region of inhomogeneous medium ($0 \leq x \leq a$), we make use of the condition

$$ka \ll 1, \quad \sqrt{\epsilon(x \geq a)}, \sqrt{\epsilon'(x > a)}$$

which enables us to use the method of successive approximation. Accordingly, we can derive the following solution:

$$F_2(x) = \int_0^x dx' \int_0^{x'} dx'' R - k^2 \int_0^x dx' \int_0^{x'} \frac{dx''}{\epsilon'} \int_0^{x''} dx''' R +$$
$$+ C_4 \left(x - k^2 \int_0^x dx' \int_0^{x'} dx'' \frac{x''}{\epsilon'} \right) + C_5 \left(1 - k^2 \int_0^x dx' \int_0^{x'} \frac{dx''}{\epsilon'} \right) \qquad (18)$$

C_4 and C_5 are the integration constants which can be determined from the condition of continuity of the functions $F_2(x)$ and $\partial F_2(x)/\partial x$ at $x = 0, a$ and in terms of the amplitudes of the ground waves as:

$$C_4 = \frac{2}{mku^2}\left(K_+ A^2 - K_- B^2\right) \quad ,$$

$$C_5 = \frac{-ie}{mk^2u^2}\left(K_+ A^2 + K_- B^2 + \frac{2\omega}{u} AB\right), \quad K_\pm = \frac{\omega''}{u} \pm k$$

The amplitudes A, B define the solution of equation (9) in the region $x \leq 0$ as:

$$F_1(x) = A e^{ikx} + B e^{-ikx}, \qquad x \leq 0, \ \epsilon = 1 \qquad (19)$$

It seems from (15) and (18) that the presence of external magnetic field my lead to sharp increase in the amplitude of generated waves at 2ω in the plasma layer.

As seen, the amplitudes of the exponentially growing oscillations at twice the frequency is expressed through the amplitudes of the beam Langmuir oscillations (A, B) in the region where is no plasma present. Thus, once there are Langmuir oscillations in the beam, even in the presence of external magnetic field, their frequency being equal to ω in the laboratory frame, and the oscillations with frequency 2ω are always generated at the inlet of the beam into the plasma when the beam in the plasma is unstable in relation to the excitation of oscillations with frequency 2ω. This lead to the conclusion that far enough from the plasma boundary inwards, the external magnetic field may increase the amplitude of grounded waves, but still the electric field of waves with double frequency would be stronger than that of basic frequency.

A PERCOLATION MODEL FOR THE TRANSPORT IN THE DRIFT MODE POTENTIAL STRUCTURE

F.Spineanu, M.Vlad

Central Institute of Physics,Măgurele,Bucharest,P.O.Box MG-7,Romania

The electrostatic drift wave instabilities are belived to play the most important role in the anomalously large heat and particle transport in tokamaks. Formally, the origin of the transport is the phase relation between the electron density perturbation and the collective electric field and is determined by the dissipative part of the electron propagator /1/.

In the case of a stationary drift mode, the transport exhibits some specific features leading to a nonuniform distribution of the density in the structure determined by the wave potential. This problem has been recently investigated using the method of multiple space scales /2/ and, alternatively, considering the transport of a passive component (heat) in the convective background /3/. However, a certain fraction of particle density contributing to the enhanced transport has been ignored in these studies. These are the particles performing large jumps along the separatrices of the quasiperiodic stationary potential distribution. A jump allows the particle to leave a cell of the potential (in which it performs usual $\vec{E}x\vec{B}$ oscillations) and to stick to another, neighbour potential cell. The cause of the jump may be simply the collisions or the periodic opening up of the potential lines when two or more drift waves are present /4/. This effect was observed in the numerical simulations for the first time in Ref. /4/ and it was found that the contribution of this fraction of anomalous trajectories to the determination of an "over all" diffusion coefficient was rather high (for some conditions, 764 particles from 2000 performed large jumps). However, we consider that this contribution is not of diffusive type and must be treated separately, with a different method.

In principle, it is possible to have a chain of "favourable" events i.e. succesive jumps along the separatrices of the stationary potential distribution which can permit a particle to reach regions situated far from the plane taken as origin. The importance of this source of anomalous transport depends on the number of particles performing $\vec{E}x\vec{B}$ motion in a narrow region along the separatrices and on the probability of the event consisting in the succesive jumps.

In the present paper we propose a possible description of this transport, based on the analogy with the percolation on a 2-dimensional

lattice. In an idealised form, the stationary drift mode electrostatic potential distribution in a plane orthogonal to $\vec{B}$ is represented as a 2-dimensional periodic structure with the separatrices being the bonds of a Z^2 lattice. We also simplify the problem assigning the probability p to the event that a particle at a site leaves and 1-p to the event that the particle remains. A measure of the penetration of the particles is given by the correlation length $\xi(p)$, with which the probability P_p that the length of a path exceeds a given value n, is bounded as follows /5/:

$$C_1 \exp(-n/\xi(p))/n \leqslant P_p \leqslant C_2 \exp(-n/\xi(p))n$$

where C_1 and C_2 are constants. The unit of length is $k_\perp^{-1}$, with the typical scaling : $k_\perp \rho_s \sim 0.1$, $\rho_s = m_i T_e / e^2 B^2$. Numerical simulations /5/ give small correlation length at small p which imply very low probabilities that particles escape beyond the drift mode layer.

It is known that the probability $\theta(p)$ of leaving to infinity (i.e. the particle is lost) exhibits a threshold at $p=p_c$. For 2-dimensional percolation this value is $p_c=1/2$. It is interesting to note that in the frame of this analogy, this contribution to the transport is connected to a threshold condition for the local rate of the process which determines the jumps (i.e. collisions or opening up of potential lines), which clearly distinguishes it from usual transport mechanisms.

In the vicinity of the threshold there are estimates based on characteristic exponents which allows to write :

$$\theta(p) \sim (p-p_c)^{\beta} \qquad 1 > \beta > 0 \quad \text{and} \quad \xi(p) \sim (p-p_c)^{-\nu} \qquad 1 < \nu$$

The loss of particles Φ ($cm^{-3}s^{-1}$) results from multiplying $\theta(p)$ with the fraction of density which can perform large jumps. For the collision induced percolation, p scales as $n_e T_e^{-3/2}$, but the (higher) particle density around the separatrices of the vortices introduces the dependence of Φ from the field amplitude E /2,3/. For the case treated in Ref. /4/, the probability p is determined by the rate of the process of opening up of the potential lines. Here, the scaling of θ near p_c with critical exponent $\beta < 1$ explains the slow dependence on E of the diffusion, observed in numerical simulations. We note that Φ does not depend directly on the gradient of the density.

These qualitative results were confirmed by the method of functional integration which can take into account the effect of these anomalous trajectories /6/.

/1/ W.Horton,in Basic Plasma Physics vol.2,Eds.A.A.Galeev and R.N.Sudan North-Holland,Amsterdam,1984
/2/ M.V.Osipenko,O.P.Pogutze,N.V.Chudin,Fizika Plazmi 13(1987)953
/3/ M.N.Rosenbluth,H.L.Berk,I.Doxas,W.Horton,Report IFS 261,1987
/4/ R.G.Kleva,J.F.Drake,Phys. Fluids 27(1984)1686
/5/ H.Kesten,The Annals of Probability 15(1987)1231
/6/ F.Spineanu,M.Vlad,Phys. Lett. A 133(1988)319

Study of Sawtooth Oscillation in Tokamaks

Li, Weiqiang
(Univ. of Sci. & Tech. of China, Hefei, China)

Sawtooth oscillation has been studied by many authors since its discovery by S.Von Goeler[1] in 1974. B.B.Kadomtsev's[2] resistive reconnection tearing mode theory seems consistent with the experiment observation and is accepted as a normal explanation of sawtooth. However, recent experiment evidences from large tokamaks[3-13] clearly turn out that resistive mode may not be the cause of sawtooth. Therefore research on mechanism of sawtooth is needed for further understanding.

In considering physical mechanism of sawtooth crash, several basic questions should be kept in mind:

1. What kind of instability drives sawtooth crash?
2. What is mechanism of sawtooth crash process?
3. How can the crash have a form of relaxation process?
4. How can sawtooth be suppressed by additional heating?
5. What is double sawtooth or compound sawtooth?
6. What does m=1 oscillation mean?

From the point of view of fast sawtooth crash time scale, one can easily relate it to ideal m=1 mode. M.N.Bussac[14] had calculated ideal m=1 mode in toroidal geometry with circular section. Recently M.F.F.Nave and J.A.Wesson[15] modified the model using a flat center current profile assumption $|1-q(0)| \ll 1$. $\beta_p \approx 0$ is achieved with $q(0) \approx 1$. The mode is pressure driven and is not consistent with experiment observation[16]. Other kind of theories[17,18] are developed recently concerning sawtooth, but problems are still quite unclear. A recent computer simulation reveals a possible mechanism of sawtooth[19]. A.Y.Aydemir has calculated ideal m=1 mode in a weak shearing toroidal system. He concludes that if $|1-q(0)| \ll 1$ and $q(0) > 1$, then m/n=1/1 mode is unstable even for $\beta=0$.

Internal ideal MHD mode has two driving forces: pressure gradient driven internal interchange mode and current driven internal kink mode. Actually, before Bussac, A.A.Ware[20] had considered ideal MHD mode in a toroidal tokamak. At plasma center, dp/dr=0, $\Lambda = -3/4$. We still have a weak shearing assumption, $k_{\parallel} \sim O(r^3/R^3)$, Ignoring mode coupling. Choosing a single mode perturbation:

$$\xi = \xi_r \exp[i(m\theta - n\varphi)]$$

and

$$k_{\parallel} B = (m/r) B_\theta - (n/R) B_t$$

energy principle gives:

$$\delta W = \int d\tau/2 \left\{ (k_{\parallel} B)^2 \left[(m^2-1)\xi_r^2 + r^2 \left(\frac{\partial}{\partial r}\xi_r\right)^2 \right] / m^2 + \right.$$
$$+ 2\xi_r^2 (k_{\parallel} B) B_\theta r / m R_c^2 \left[2\Lambda^2 + 7\Lambda + 9 - 3 n^2/m^2 \right] +$$
$$+ 2\xi_r^2 B_\theta^2 / (r B_t^2) \cdot \frac{dp}{dr} \left[1 - \frac{\omega^2}{t} \right]$$

Let $A=2\Lambda^2+7\Lambda+9-3n^2/m^2=1.875$ (Note: the factor before n/m is 2 obtained by Ware, rather than 3 here. However it does not change the physics involved).

The first term is definitely positive and could be minimized by flat current profile assumption or $|k_{\parallel}B|<<1$ and eigen-function choosing of displacement. Instabilities are determined by other two terms. Necessary condition for current driven local internal kink 1/1 mode instability is $k_{\parallel}B<0$, that is: $1-q<0$. With $q<1$, ideal kink mode is stable. Since $dp/dr<0$, pressure gradient interchange mode is unstable if $q<1$. With $q>1$, interchange mode is stable.

Considering $q(0)<1$ case, for unstable interchange mode, we need: $|\delta Wp|>|\delta Wj|$, or: $\beta p>\beta pcrit=A/4=0.5$. Pressure gradient has to be large enough for interchange mode unstable under $q(0)<1$. This is similar to that obtained by Bussac[14], where $\beta pcrit=0.3$. For the same reason, pressure driven instability could not response to sawtooth oscillation.

Now we discuss in case of $q(0)>1$. Only kink term is unstable here, and pressure term could be ignored. Comparing shearing energy with kink mode energy, plasma is locally unstable in region of $(1, 1+\Delta qc)$. Δqc is estimated by: $|\delta Wb|<|\delta Wj|$. That is: $\Delta qc=3.75\, r_c^2/R_c^2$. With $r_c/R_c=0.05$, we have $\Delta qc=0.01$. Although unstable region is very narrow in q-representation, it does cover wide region of central plasma. Thus, central plasma will suffer instability of ideal m=1 mode in region of $r<r$, and $q(r)=1+\Delta qc$.

Ideal MHD sawtooth model describes sawtooth process in this way. At the beginning of sawtooth, plasma is stable anywhere. $q(0)>1+\Delta qc$. With Ohmic heating, $q(0)$ decreases and finally falls into the unstable region $(1, 1+\Delta qc)$. Then $m/n=1/1$ ideal kink mode grows quickly and disturbs center plasma ($r<r_c$). At non-linear stage, center hot plasma is pushed out and replaced by outer cold plasma. Such a process has a mode of m=1, but soon becomes m=0 because of large conductivity along magnetic surfaces. Therefore, variation of temperature has a sawtooth behavior when the process repeats.

Note the dependence of δW on r that $\delta W=0$ at r=0. Center plasma is always in an arbitrary equilibrium state and is stabilized by inertial. At the beginning of sawtooth rising phase, although center plasma falls into region of $(1, 1+\Delta qc)$, it contributes little mode energy. When outer region is unstable, perturbation is localized by steady center plasma through shearing effect. Such disturbation is regarded as precursor m=1 oscillation. At the time of crash, mode energy grows large enough to disturb center plasma to move together with the outer. $|d\xi_r/dr|$ decreases and mode energy increases. This positive feedback process makes mode energy grow more rapidly. As long as plasma at center axes is disturbed, crash occurs. One could never see precursor oscillation at the axes. The marginal stable plasma center happen to be the cause of relaxing sawtooth crash.

At the time of crash, only kink term is important. Crash time could be estimated using energy principal, which gives:

$$t=\sqrt{2/k\Delta q}\; R_0^2/r_c C_f$$

Put in JET parameters: $t_c=1.8\times10^{-4}(\Delta q)^{1/2}$ (s). Choosing $\Delta q=0.005$,

we have t_c = 25 μs. This is consistent with experiment. And estimated t_c do not vary significantly as tokamak size changing.

Now, we are trying to interpret other sawtooth characteristic which could not be understand by other model.

1. Sawtooth crash with additional heating: If we suddenly change the profile of q at the center so that q(0)<1, center plasma would be stable again, leaving a very localized unstable region outside center. Sawtooth crash could be suppressed in this way. Actually there are many methods to change q value. Additional heating, no matter ICRH, ECRH, NBI, would raise plasma parameter obviously. There are two mechanism which could result decrease of q. One is diamagnetic effect to cut toroidal field Bt. It can result in variation of q by: $\Delta q = -0.5\Delta\beta$. Putting in JET parameter gives Δq=0.002. Although it is smaller than Δqc, taking account of marginal stable center plasma, Δqc may be reduced to 0.002. The other is bootstrap current. It is estimated in JET[8] that bootstrap current will increase from 50kA to over 100kA during monster period. It makes q decrease of 1.0-2.5%. Part of current diffuses into center and together with diamagnetic effect, sawtooth could be suppressed. q value can be decreased directly during LHCD. Therefore sawtooth could also be suppressed during current driving phase.

2. Double sawtooth or compound sawtooth: At large devices, outer perturbation could be very large but leave center plasma at the axes undisturbed. If local perturbation outside is large enough, energy transport would be increased greatly. Partial crash thus occurs locally there. After partial crash, residual displacement of surfaces would return to its original position. This result a damping m=1 oscillation.

3. Helical coil experiment: When the plasma is perturbed by imposed helical current, magnetic island may be produced at the resonant surface. In our model, q>1 anywhere during sawtooth period, no q=1 surface exists in plasma. Therefore m/n=1/1 helical current would have no effect on sawtooth. However, m/n=3/2 helical current would cause a island at q=1.5 surface. Extra energy transport makes temperature profile be sharper at the center, and amplitude of sawtooth larger. In the case of monster sawtooth, q(0) 1 at the center as assumed, m/n=1/1 current would disturb the plasma seriously. This is to be verified by experiment.

4. Further experiment suggestion: We have several other methods to attain q(0)<1 simply by adjusting discharge parameters. One is to increase current suddenly during sawtooth period. The other is, more simply, to cut toroidal field. When the field is modulated by 1% long period sawtooth, q(0) is modulated. Sawtooth can thus be suppressed even at small tokamaks.

5. m=1 oscillation during sawtooth: The precursor m=1 oscillation is a ideal MHD mode. The amplitude of oscillation is nonlinearly saturated before crash. Growth rate of saturated level is not the growth rate of m=1 ideal mode, but related to Ohmic heating power.

In conclusion, we have developed a theoretic model of

sawtooth oscillation based on ideal m=1 internal kink mode. Only flat current profile is assumed and this assumption is consistent with process of sawtooth activity in plasma center. Sawtooth crash instability region is locallized in (1, $1+\Delta q_c$), but not $q<1$. Sawtooth oscillation is found possible to be eliminated from discharges. Many phenomena associated with sawtooth are explained based on the model.

The author would give his thanks to Prof. Z.L.Xiang; Prof. B.R.Shi; Prof. L.Wong and Prof. C.X.Yu for their help in the work.

REFERENCES:

[1] Von Goeler,S., Stodiek,W., Sauthoff,N., Phys. Rev. Letts. 33 (1974) 1201.
[2] Kadomtsev,B.B., Sov. J. Plasma Phys. 1 (1975) 389.
[3] a) Pfeiffer,W., Marcus,F.B., Armentrout,C.J., Jahns,G.L., Petrie,T.W., Stockdale,R.E., Nucl. Fusion 25 (1985) 655.
b) Pfeiffer,W., Nucl. Fusion 25 (1985) 673.
[4] Campbell,D.J., Gill,R.D., Gowers,C.W., Wesson, J.A., et al., Nucl. Fusion 26 (1986) 1085.
[5] Taylor,G., Efthimion,P.C., Arunasalam,V., Goldston,R.J., Grek,B., et al., Nucl. Fusion 26 (1986) 339.
[6] Parail,V.V., Pereverzev,G.V., Sov. J. Plasma Phys. 6 (1980) 14.
[7] Snips,J.A., Gentle,K.W., Nucl. Fusion 26 (1986) 1507.
[8] a) Huo,Y.P., in Proceedings of Huangshan summer school on plasma physics, 1988, China.
b) Todd,T,N., in Proceedings of Huangshan summer school on plasma physics, 1988, China.
[9] Campbell,D,J., Start,D,F.H., Wesson,J.A., et al., JET-P(87)20.
[10] Sillen,R.M.J., Piekaar,H.W., Oyevaar,T., Gorbunov,E.P., Bagdasarov,A.A., Vasin,N.L., Nucl. Fusion 26 (1986) 303.
[11] Chu,T.K., Bell,R., Bernabei,S., Cavallo,A., Guharay,S., et al., Nucl. Fusion 26 (1986) 666.
[12] a) Soldner,F.X., McCormick,K., Eckhartt,D., Kornherr,M., Leuterer,F., et al., Phys. Rev. Letts. 57 (1986) 1137.
b) McCormick, K., Soldner,F.X., Eckhartt,D., Leuterer,F., Murmann,H., et al., Phys. Rev. Letts. 58 (1987) 491.
[13] Knowlton,S., Porkolab,M., Takase,Y., Nucl. Fusion 28 (1988) 99.
[14] Bussac,M.N., Pellat,R., Edery,D., Soule,J.L., Phys. Rev. Letts. 35 (1975) 1638.
[15] Nave,M.F.F., Wesson,J.A., Nucl. Fusion 28 (1988) 297.
[16] Wesson,J.A., Plasma Phys. & Contr. Fusion 28 (1986) 243.
[17] Park,W., Monticello,D.A., Chu,T.K., Phys. Fluids 30 (1987) 285.
[18] Ramos,J.J., Phys. Rev. Letts. 60 (1988) 523.
[19] Aydemir,A.Y., Phys. Rev. Letts. 59 (1987) 649.
[20] a) Ware,A.A., Haas,F.A., Phys. Fluids 9 (1966) 956.
b) Ware,A.A., Phys. Rev. Letts. 26 (1971) 1304.

H

DIAGNOSTICS

H

DETERMINATION OF POLOIDAL VELOCITY PROFILES IN THE TJ-I TOKAMAK FROM LINE ASYMMETRY AND SHIFT MEASUREMENTS

B. Zurro and TJ-I Group
Asociación **EURATOM/CIEMAT**. E-28040 Madrid. Spain

One important issue in tokamak plasma confinement is to understand the role of radial electric fields on the particle transport. Although they can be calculated from the standard neoclassical theory, perturbative experiments (1) and measurements in actual plasmas (2) have revealed the difficulties encountered for it to understand the observed effects. From the experimental point of view the difficulties are not lesser, on the one hand the only available direct method is the heavy ion beam probe which is not a routinely diagnostic. On the other hand measurements of spectral line shifts, for determining poloidal plasma rotation and subsequently deduce electric fields, are not direct one and suffer from inaccuracies due to the limited applicability of extremely high resolution techniques in fusion plasmas. In this work this problem has been approached by a new method based on using conventional high resolution techniques combined with numerical code and searching for a more sensitive feature than the spectral line shift for performing the comparison between model and experimental data. A code for predicting spectral line shapes oriented to determine poloidal rotation profiles in the TJ-I tokamak has been developed. Its performances and limitations to account for the actual spectral line shapes are discussed.

Impurity and hydrogen line shape measurements are performed in the TJ-I ohmically heated tokamak (R_0 =30 cm, a =10 cm, $B_T < 1.5$ T and $I_P < 60$ kA) by using a 1 m monochromator provided with spatial and temporal resolution capabilities. The line shape is scanned within 1 to 4 ms by means of a rotating refractor plate which is synchronized to the tokamak discharge lasting typically between 20 - 30 ms. The refractor plate delivers a signal valid as a relative wavelength marker. The line shape, which appears like a pulse, presents a delay with respect to the former reference which is proportional to the spectral shift. The optical system line of sight is chosen by a rotatable mirror electronically positioned. This mirror can be replaced by a fast rotating polygonal prism to obtain line integrated emission profiles.

The tokamak was operated for this experiment with hydrogen, and besides the H_β near UV and visible lines of oxygen and carbon were selected for this study.

We have developed a code for unfolding the information contained in the spectral line shape. The actual measured shape depends on the temperature and rotation profiles so as the magnetic field structure due to the Zeeman effect. In order to get local information from line integrated measurements the code takes into account all these effects and instead of trying to unfold each process separately, we compare the resulting line shape deduced by the numerical code with the experimental one. The plasma has been modeled by a set of non concentric flux contours which shape is given by the following parametric equations, covering most cases of practical interest,

$$Z(\rho) = \varepsilon(\rho)\, \rho \sin\theta$$
$$R(\rho) = R_0(\rho) + a\rho \cos[\theta + \delta(\rho) \sin\theta]$$

where ρ is the normalized minor radius ($0 \le \rho \le 1$), ε is the ellipticity ($\varepsilon = b/a$), a is the minor radius in the midplane, b is the maximum displacement along the Z axis, θ is the polar angle ($0 \le \theta \le 2\pi$), R_0 is the major radius of the flux surface, δ is the triangularity ($\delta = c/a$), and c is the triangularity shift of the major radius along the midplane.

The plasma is partitioned into a discrete set of shells, typically 50, within each of them the ion temperature, emissivity and rotation velocity of the sensed particles are assumed to be constant. Analytical profiles are used for these parameters and the plasma is allowed to rotate as a non rigid body as suggested by the experimental data. For a fixed observational geometry, the code performs the average along the selected optical pixel of a set of shifted (according to its local rotation velocity), broadened gaussian (according to the local ion temperature) splitted by the local magnetic field due to the Zeeman effect. The intensities and wavelengths of the splitted components are calculated (3) under the assumption of LS coupling. The resulting simulated line is analyzed and characterized by the same method and parameters (shift, apparent temperature and line bisector) as used to study the actually measured spectral line. Construction of the bisectors of the spectral lines involves drawing horizontal-line segments from each measured point on the left half of the profile to interpolated points on the right hand of the profile; the midpoints of these segments comprise the measured bisector. The code allows to overcome the limitation of measuring along a chord to deduce local ion temperature and shift values, and at the same time the line bisector has a precise physical meaning. The model allows to distinguish between line asymmetries due to non rigid rotation of the plasma from those caused by other mechanism even if they can not be identify by the present model. The particle convection should be included, since in some cases its velocity field can compete with plasma rotation velocities. This effect will be later evident on analizing hydrogen lines asymmetries.

We have measured the shift of the OV 2781 Å, in third order, along different plasma chords by using a shot to shot technique running a set of good reproducible tokamak discharges. The results obtained are plotted in Fig. 1, in which the line shift in mÅ is represented versus the chord radius for three different toroidal fields 1.5 T (the most complete sequence), 1 and 0.8 T. The main conclusions derived from these data are as follows: the plasma rotate poloidally in the electron diamagnetic drift direction with a velocity decreasing as the toroidal field is reduced and reversing its sign for the lowest toroidal field. In the best documented case (1.5 T) its absolute value is significant higher than v_{de}. These data are consistent with a negative potential plasma core for 1.5 - 1 T and positive for 0.8 T. This observed trend of poloidal velocity with toroidal field contrast with the observation made in the FT-1 by diagnostic pellet injection (4), in which the poloidal velocity diminished on rising the toroidal field. However, the present TJ-I observation is consistent with the increasing of particle confinement with toroidal field measured by the laser blow-off technique (5).

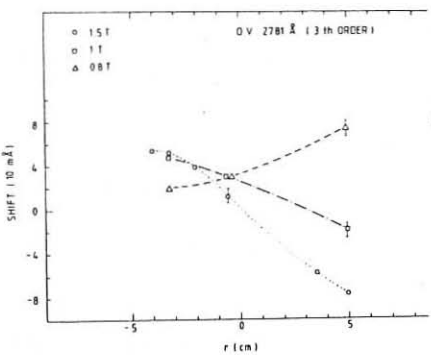

Fig. 1. Plot of line shift versus chord radius for three different toroidal fields.

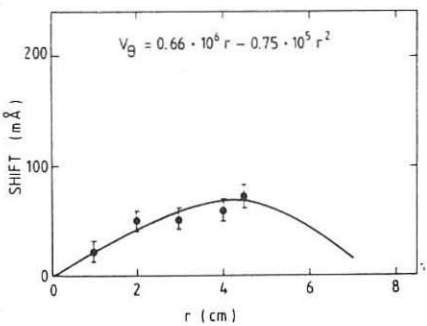

Fig. 2. Comparison of the symmetrized shift profile with the numerical code results to deduce the shown v_θ profile.

Although we do not have line shift data at the plasma edge, the symmetrized shift data, plotted in Fig. 2, are in better agreement with a plasma rotating non like a rigid body. The poloidal rotation profile has been chosen to match not only the measured shifts but also the asymmetry of the line (bisector) measured along a chord of radius 4 cm, which is depicted in Fig. 3. The OV emissivity profile used in the analysis code was chosen to match the line integrated emission profile measured by a polygonal rotating mirror.

Our present analysis based on the matching by the code of the line asymmetry, measured through the median line bisector, yields an inversion of the poloidal velocity profile at the plasma edge, which is not surprising because it has also been observed in other tokamak (2).

We have also studied the H_β line asymmetry by measuring its bisector along a fixed chord for different puffing levels. Fig. 4 depicts the systematic behaviour of H_β bisector varying the plasma density. However, the first attempt to get information about the rotation profile, mainly at the edge, by studying this asymmetry as a function of the chord radius had failed because it seems that other mechanism besides rotation contribute significantly to the asymmetry. The fact that cold and fast atomic hydrogen are not tied to the magnetic field could be a difficult point to analyze with a model that ignore the toroidal angle.

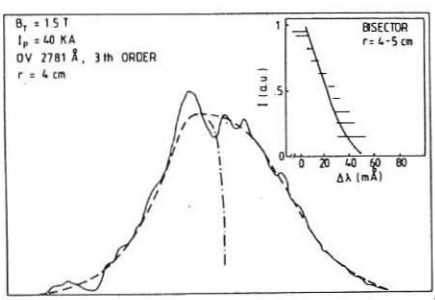

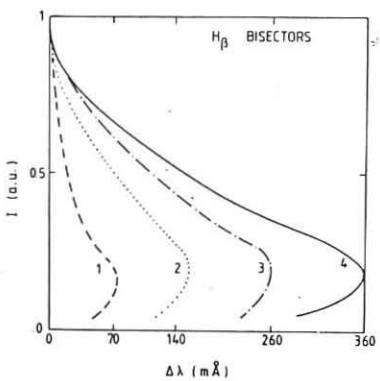

Fig. 3. Smoothed OV line profile; expanded view depict the experimental (band) and simulated (line) bisectors.

Fig. 4. Variation of H_β line bisector, measured along fixed chord, at different plasma densities.

REFERENCES

(1) L. Oren, L. Keller, F. Schwirzke, S. Talmadge and R. J. Taylor J. Nucl. Mater. **111&112**, 34 (1982).

(2) V. I. Bugarya et al. Nuclear Fusion **25**, 1707 (1986).

(3) I. I. Sobelman, L. A. Vainshtein and E. A. Yukov *Excitation of Atoms and Broadening of Spectral Lines*. Springer-Verlag. Berlin (1981),

(4) D. G. Bulyginskij et al. in Proc. IAEA Conf. , paper CN-44/F-II-4 (198).

(5) B. Zurró, C. Pardo and F. Mompeán, Plasma Phys. Controll. Fusion **30**, 1767 (1988).

ABSOLUTE NEUTRON YIELD DETERMINATION FOR ASDEX USING In ACTIVATION AND MONTE CARLO CALCULATIONS

R. Bätzner, K. Hübner, L. Ingrosso
Institut für Angewandte Physik, Universität Heidelberg, D-6900 Heidelberg
S. Bosch, H. Rapp, B. Wolle
Max-Planck-Institut für Plasmaphysik, EURATOM Association, D-8046 Garching
C. van Calker
Institut für Experimentalphysik, Universität Düsseldorf, D-4000 Düsseldorf
B. V. Robouch
Ass. EURATOM-ENEA sulla Fusione, Centro Ricerche Energie Frascati, I-00044 Frascati
J. Kucinski
Institute for Nuclear Studies, Swierk
J. S. Brzosko
Stevens Institute of Technology, Hoboken, NJ 07030, USA
Neutronics/Photonics R&D, Jersey City, NJ 07305, USA

The absolute neutron rate of a fusion plasma is usually measured with counter arrays calibrated in situ at low neutron rates with an appropriate neutron source inside the vessel. In actual fact, however, these counters are used up to the much higher rates produced by plasma discharges. It is thus of great importance that the calibration be independently checked at high neutron yields. This can be done by a yield determination using activation methods or nuclear emulsions. Results from activation measurements are available a few hours after the discharge, but they have a poor energy resolution. The advantage of emulsions is their good energy resolution, but it usually takes weeks till the results are available. - Our intention is to combine both methods on ASDEX.

Application of both methods, activation and emulsions, to tokamaks requires solution of three problems. Firstly, one has to measure either the absolute value of the number of activated nucleids N_{In} in the In sample or of the number of tracks N_p in the emulsion. Secondly, one has to determine the response of the detector, i.e. the relation between N_{In} or N_p and the neutron fluence Φ at the position of the detector. Thirdly, one has to know the relation between this neutron fluence Φ and the neutron yield Y of the discharge. The last two problems could be solved together by calibration with a strong neutron source in situ or by a numerical simulation. Such in situ calibration is not possible on ASDEX, and so we have to use Monte Carlo simulations.

Activation measurements

For the activation measurements the reaction $^{115}In(n,n')^{115}In^m$ and the subsequent γ emission of $^{115}In^m$ at 335 keV is used. The number of γ-ray emissions per disintegration is $r_\gamma = 0.459$ and the decay time $1/\lambda = 23319.72$ s [1].

Our In samples are disk-shaped with a diameter of 5 cm and thickness of 0.3 cm. They were placed inside a Cd box with a wall thickness of 0.1 cm located in front of a large quartz window and exposed over series of n discharges. In order to account for the decay of $^{115}In^m$ during the shots of one series, a reduced yield of the series is calculated as

$$Y_{red} = \Sigma_i\, Y_i \exp\{-\lambda(t_n - t_i)\}, \qquad i = 1,\ldots,n,$$

where t_i are the instants of the different shots and Y_i their neutron yields as determined by the counter array. This procedure is justified because we find a linear relation between the results of the counters and the yield.

The γ emission was measured with a Ge counter over a time interval Δt = 1000 s starting at t_c. The counter efficiency, i.e. the number of counts per γ decay, was determined by means of an absolutely calibrated source of the same size as the In samples but with a much smaller thickness of only 0.03 cm. The efficiency therefore had to be corrected for geometric effects due to the thickness of the samples and the γ absorption in the In. The final result at 335 keV is

$$\varepsilon = Z / N_\gamma = 0.048 \text{ counts/decay} \pm 10\%.$$

The activity of the sample at t_n in the γ-line considered is calculated from the measured number N_γ of γ decays by

$$A_0 = N_\gamma \lambda \exp\{\lambda(t_c - t_n)\} / \{1 - \exp(-\lambda \Delta t)\}.$$

Fig. 1 gives the reduced neutron yield per discharge Y_{red}/n determined with the different counters as a function of the activity per discharge and per gramme of the sample $A_0/n\,M$ in Bq/g. M is the mass of the sample. We get the linear relation $Y_{red} = 2.2\times10^{13}\ A_o/M$.

With the errors of all calibrations involved being taken into account, our final experimental result for the relation between the In activity and the total neutron yield is

$$A_0/M\,Y = 4.6\times10^{-14}\ \text{Bq/g}\,Y \pm 15\%.$$

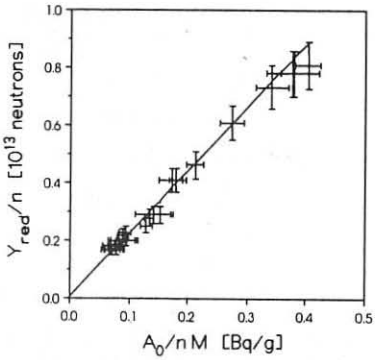

Fig. 1: Reduced neutron yield per discharge versus activity per discharge and per gramme of the sample.

Monte Carlo calculations

The relation of the neutron fluence Φ at the position of the In sample and the total neutron yield Y of the discharge is to be determined in three steps. Firstly, one has to calculate the fluence factor $f_{obs} = \Phi_0/Y$ from the observed part of the plasma volume and its corresponding neutron fluence $\Phi_0 = \int\{Y(\mathbf{r})/4\pi s(\mathbf{r})^2\}d\mathbf{r}$ at the detector position. Here $Y(\mathbf{r})$ is the local source strength and $s(\mathbf{r})$ is the distance between the point of emission and the detector.

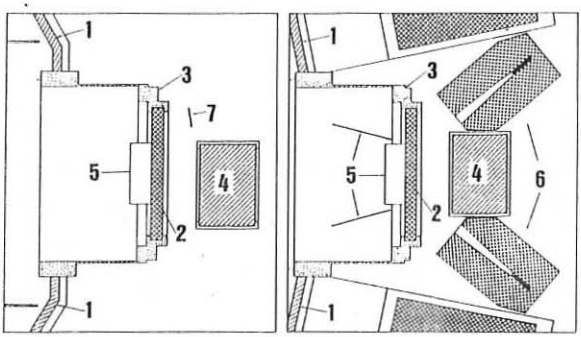

1: vessel,
2: quartz window,
3: flange,
4: lens (BK7, Al casing, (light scattering system)
5: shields and shutters for protection of quartz
6: nuclear emulsion collimators (PE)
7: In sample with Cd box

Fig. 2: Detail of the computer model of ASDEX near the position of the In sample, vertical (left) and horizontal (right) cut through the centre of the quartz window.

Secondly, one has to take into account the fluence attenuation factor F_{abs} for the neutron absorption between the plasma and detector. Thirdly, one has to determine the fluence enhancement factor F_{col} caused by the background of scattered neutrons. So we have $\Phi = \Phi_0 F_{abs} F_{col}$ and the absolute neutron yield is given by $Y = \Phi / f_{obs} F_{abs} F_{col}$.
For ASDEX all three factors are simultaneously determined by neutron migration calculations using the VINIA software [2]. The results of these calculations are used as input for the 3DMCSC-RWR software which simulates the response of the In sample to the incoming neutron fluence and gives the activation of the sample as output.

As ASDEX provides no observation port for the neutron diagnostics, the In sample was exposed in front of the large quartz window for the Thomson light scattering system, as shown schematically in Fig. 2. It is this the same position which we are using for emulsion measurements and allows thus for a comparison of activation and emulsion measurements. At this position we find from the Monte Carlo calculation for the neutron fluence

$$f_{obs} = 1.75 \times 10^{-6}\,\text{neutr./cm}^2\,Y \pm 2\%, \quad F_{abs} = 0.28 \pm 2.5\%,$$
$$F_{col} = 4.5 \pm 24\%, \quad \Phi/Y = 2.2 \times 10^{-6}\,\text{neutr./cm}^2\,Y \pm 19\%.$$

Since the fluence enhancement factor for this position is so large, the most sensitive point in the calculation of the activation is the contribution of the scattered fluence. However, the strong drecrease of the In activation cross-section below 2 MeV (Fig. 3) somewhat reduces the relative contribution of the scattered fluence to the activation.

The detecting points inside the In sample, i.e. the points where the activation reaction takes place, were already randomly selected in the Monte Carlo simulation of the neutron migration through the ASDEX device. The neutron absorption inside the In sample is taken into account in calculating the number of activated nuclei N_a. From this number an effective activation cross-section $\langle\sigma\rangle$ could be deduced by means of the relation $N_a = N_{In}\Phi\langle\sigma\rangle$, where N_{In} is the total number of ^{115}In nuclei in the sample. Furthermore, the activity A of the sample is calculated by $A = r_\gamma \lambda N_a$. - The numerical results for fluence, activation and $\langle\sigma\rangle$ are given in Table 1.

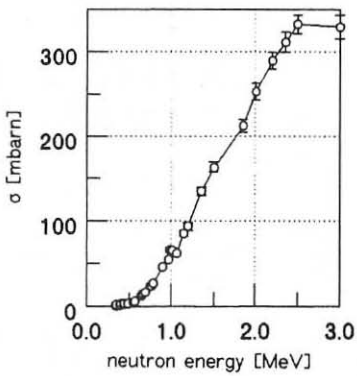

Fig. 3: The $^{115}In(n,n')^{115}In^m$ reaction cross-section [1].

Discussion of results

The scattered neutron background contributes 78% to the neutron fluence, 52% being above 2.1 MeV and 26% below. The scattered fluence causes 72% of the activation, only 10% of which comes from the background below 2.1 MeV. - Within their error bars the numerical and experimental results for the activity per emitted neutron agree very well. In the past we measured the neutron energy spectrum at the position of the In samples by means of nuclear emulsion [3]. This will allow us to check the Monte-Carlo calculations in detail. Furthermore, the determination of Φ from the emulsion measurements suffers much less from the scattered background. Here we will use only the energy region above 2.3 MeV where we have $F_{col} = 1.57 \pm 4\%$ and $\Phi/Y = 7.7 \times 10^{-7}$ neutr./cm^2 Y ± 3.5%. The combination of In activation, nuclear emulsion and Monte Carlo simulation is expected to offer a possibility of checking the counter calibration in situ at high neutron rates.

The effective activation cross-section essentially depends on the scattered neutron spectrum as is obviously seen from the results in Table 1. Our overall result of ‹σ› = 252 mbarn agrees well with the value given by Gentilini et l. [4]; they found ‹σ› = 266 mbarn for a plasma focus device using the neutron energy spectrum measured with nuclear emulsions. In their work on PLT Zankl et al. [5] used ‹σ› = 343 mbarn, i.e. the value for 2.5 MeV, but they expected a correction of 15 to 40% due to scattered fluence.

The main problem in Monte Carlo simulations are the large contributions to the scattered background coming from parts of the device which are very close to the detector; they introduce large error bars in the result. Therefore a new technique is now being used to improve the statistical fluctuations. In our case the most critical contributors are the quartz window and its flange (see Table 2). It is obvious that the contribution of the scattered fluence to the activation could not be reduced by means of shields or collimators, because the main sources are in front of the In sample and a shield would essentially contribute to the scattered background. An improvement is expected to be obtained by exposing the In inside the vessel at a distance of about 10 cm from the plasma edge. Preliminary results for this position are also given in Table 1. There the contribution of the scattered fluence to the activity now coming mainly from the vessel will be less than 30%, while the total activity is enhanced by a factor 6, thus essentially improving the statistics.

Table 1: Numerical results

	direct neutrons	scattered neutrons 0.3...2.1 MeV	scattered neutrons 2.1...3.0 MeV	total	
outside the vessel (position 7 in Fig. 2)					
Φ/Y	4.91 ± 1.5%	5.68 ± 25%	11.46 ± 61%	22.04 ± 48%	10^{-7} neutr./cm^2 Y
A/MY	15.23 ± 4%	5.53 ± 25%	33.38 ± 61%	54.13 ± 48%	10^{-15} Bq/g Y
‹σ›	316	99	295	252	mbarn
inside the vessel (10 cm from plasma edge)					
Φ/Y	45.0 ± 8%	18.2 ± 46%	13.6 ± 17%	76.8 ± 13%	10^{-7} neutr./cm^2 Y
A/MY	142.8 ± 9%	14.1 ± 46%	40.7 ± 18%	197.6 ± 14%	10^{-15} Bq/g Y

Table 2: Contributors to the scattered neutron fluence and corresponding activity

	scattered fluence [10^{-7} neutr./cm^{2}Y] 0.3 ... 2.1 MeV	2.1 ... 3.0 MeV	activity [10^{-15} Bq/g Y] 0.3 ... 2.1 MeV	2.1 ... 3.0 MeV
quartz	1.24 ± 40%	7.20 ± 77%	0.96 ± 40%	21.56 ± 77%
port *	2.08 ± 43%	2.80 ± 48%	2.41 ± 43%	7.96 ± 48%
core, coils	1.23 ± 31%	0.63 ± 28%	0.98 ± 31%	1.62 ± 28%
vessel	0.43 ± 16%	0.49 ± 10%	0.58 ± 17%	1.41 ± 11%
divertor	0.27 ± 10%	0.26 ± 9%	0.27 ± 11%	0.77 ± 10%
collimators	0.26 ± 10%	0.0	0.16 ± 11%	0.0
rest**	0.11 ± 19%	0.02 ± 31%	0.18 ± 20%	0.06 ± 31%

*parts 3, 4, and 5 from Fig. 2, ** Tokamak hall, air, diagnostics

References

[1] D.C. Santry, J.P. Butler, Can.J.Phys. 54, 757 (1976)

[2] K. Hübner, et al., 14th Europ. Conf. on Controlled Fusion and Plasma Physics, Madrid 1987, part 3, pp 1298-1301, and Report IPP III/122, August 1987

[3] K. Hübner, et al., 15th Europ. Conf. on Controlled Fusion and Plasma Physics, Dubrovnik 1988, part 1, pp 11-14

[4] A. Gentilini, et al., Nuclear Instruments and Methods 172, 541 (1980)

[5] G. Zankl, et al., Nuclear Instruments and Methods 185, 321 (1981)

PLASMA ROTATION EFFECTS ON NEUTRON PRODUCTION AND MEASUREMENT ON ASDEX

K. Hübner, R. Bätzner, H. Hinsch, L. Ingrosso, R. Mechler
Institut für Angewandte Physik, Universität Heidelberg, D-6900 Heidelberg

B. V. Robouch
Ass. EURATOM-ENEA sulla Fusione, Centro Ricerche Energie Frascati, I-00044 Frascati

B. Bomba, S. Bosch, H. Rapp, A. Kallenbach
Max-Planck-Institut für Plasmaphysik, EURATOM Association, D-8046 Garching

Three principal effects of plasma rotation on neutron production and measurement on ASDEX are discussed in this paper: firstly, the change of the neutron rate during D injection into D plasmas; secondly, the shift of the neutron energy spectra; and, thirdly, changes in the neutron absorption in quartz associated with the energy shift.

D injection into deuterium plasma

The dependence of the neutron rate Q during D injection on the plasma rotation velocity is investigated by means of our neutron rate interpretation and prediction code (NR code) [1]. For the ASDEX plasma parameters during D injection the neutron rate is dominated by beam-target reactions of the injected ions with the thermal plasma [1]. It is given by

$$Q_{inj} = \frac{n_D}{n_e} \int D(\mathbf{r}) \left[\int (n_e \tau_W / W) \, [\sigma v]_{inj} \, dW \right] d\mathbf{r} \, . \qquad (3)$$

Here $D(\mathbf{r})$ is the profile of the deposition rate of the injected ions and $(D\tau_W/W)$ their velocity distribution function resulting from the classical energy relaxation; n_D is the target deuteron density, n_e the electron density and τ_W the energy relaxation time; the energy relaxation parameter $n_e\tau_W$ is a function of W and T_e and is independent of the density; $[\sigma v]_{inj} = f(W,T_D)$ is the fusion reactivity for a deuteron with energy W in a target plasma with ion temperature T_D. Plasma rotation causes a reduction of the relative energy W and therefore a reduction of $[\sigma v]_{inj}$ and $n_e\tau_W$, but for the parameters of the ASDEX plasma an increase in $n_e\tau_W/W$. The effects of the plasma rotation on the fusion reactivity and fast ion distribution function thus partially compensate each other.

Fig. 1 shows the dependence of $[\sigma v]_{inj}$ on the rotation velocity for the injection energy W_{inj} = 45 keV used on ASDEX

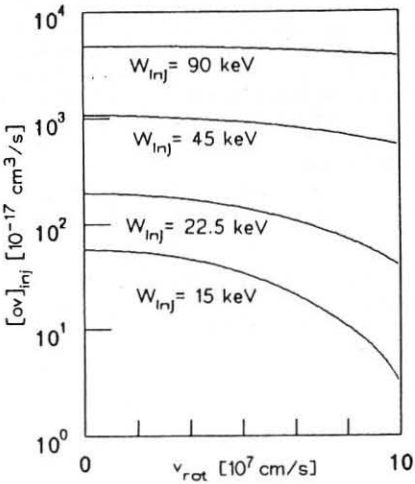

Fig. 1: Fusion reactivity as a function of the rotation velocity.

and for one-half and one-third of this energy, because the neutral beam always contains ions with these three energies. Furthermore, as an example of higher injection energies the curve for W_{inj} = 90 keV is given. Since $[\sigma v]_{inj} = f(W)$ rises faster for low W than for higher values, and the influence of the rotation on the reactivity is more pronounced at low injection energies.

As an example we consider ASDEX discharge #24896 at 1.25 s with an injection power P_{inj} = 2.8 MW, T_e = 1.7 keV, and T_D = 2.0 keV. For the same plasma parameters but with H injection the rotation velocity determined by CXRS measurements was $v_{rot} = 2.2\times10^7$ cm/s. As v_{rot} is proportinal to the square root of the mass of the injected ions [2], we expect $v_{rot} = 3.1\times10^7$ cm/s for D injection. Table 1 gives the neutron rate for the three species of the beam calculated with and without allowance for this plasma rotation. As the neutron production is dominated by the ions with the largest injection energy, the overall effect is a reduction of less than 4% in the neutron rate. The measured neutron rate is 3.3×10^{13} neutr./s, but its error is essentially larger than the rotation effect.

Table 1: Neutron rates for ASDEX discharge #24896

injection energy	45.0	22.5	15.0	keV
neutron rate, without rotation	2.78×10^{13}	3.70×10^{12}	4.24×10^{11}	neutr./s
neutron rate, with rotation	2.68×10^{13}	3.41×10^{12}	3.61×10^{11}	neutr./s
decrease in neutron rate	3.6	7.8	14.9	%

The plasma rotation velocity increases with the injection power and is inversely proportional to the plasma density [2]. For illustration Fig. 2 shows the dependence of the neutron rate for the 45 keV species as a function on $v_{rot}(0)$. As the relative energy W decreases quadratically with v_{rot}, the effect of rotation on the neutron rate appreciably increases with v_{rot}. According to these results we would expect for high injection powers.and low plasma densities an observable effect of plasma rotation on the neutron rate.

Obviously, the neutron rate will depend on the rotation velocity profile. But assuming

$$v_{rot}(r) = v_{rot}(0)\{1 - (r/a)^{\alpha}\}^{\beta}$$

(a = normalization radius), we find for variations of α and β between 0.1 and 2 only an effect of at most 2.5% on the neutron rate.

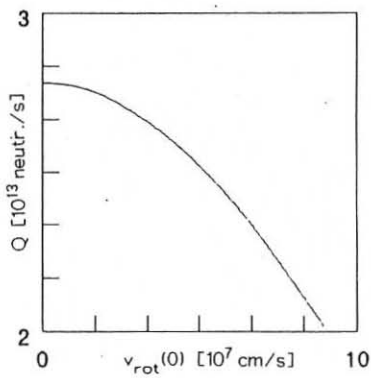

Fig. 2: Neutron rate as a function of rotation velocity.

Shift of the neutron energy spectra (H injection)

The shift of the neutron energy spectra is well known. It could be observed by means of tangentially orientated measurements of the spectra. In the past [3] we simultaneously measured spectra with nuclear emulsions while observing the plasma in the forward and backward directions with respect to the direction of injection (Fig. 3). For tangential measurements the resulting energy shift is determined by integration along the lines of sight over different rotation velocities as well as over different angles of neutron emission with respect to the direction of rotation.

As it is very complicated to calculate the resulting spectral fluence at the position of the detector by analytical methods, we are using a reduced output of the VINIA-3DAMC software in which we consider only the emission and absorption, but not the scattering of neutrons in the ASDEX facility. The plasma data necessary for the input are taken from measurements on typical plasma discharges with H injection in deuterium plasmas with a plasma current of 380 kA. The neutron emission profile is calculated from these data with the NR code. For the rotation velocity profile we are using a = 42 cm, α = 2.0, β = 0.9 [4].

The resulting line shift is obviously expected to be determined mainly by $v_{rot}(0)$. $T_D(0)$ and the profile parameters of Q, v_{rot}, and T_D will be of minor importance. This is confirmed by the numerical results. Fig. 4 gives the calculated relative energy shift ΔE (circles) between the two tangential spectra as a function of $v_{rot}(0)$. Variation of $T_D(0)$ between 1 and 5 keV only resulted in changes of the line shift smaller than the energy resolution of the calculations, presently taken as 10 keV. The influences of the velocity profile are still under investigation. For comparison in Fig. 4 the values of the total line shift are shown which would result from exact tangential observation of the central rotation velocity alone (dotted line).

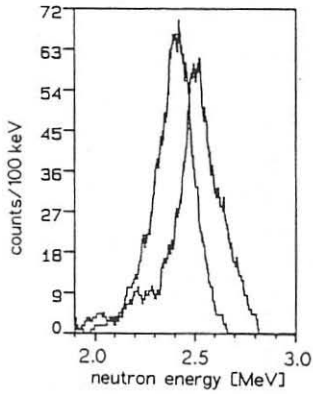

Fig. 3: Measured neutron energy spectra.

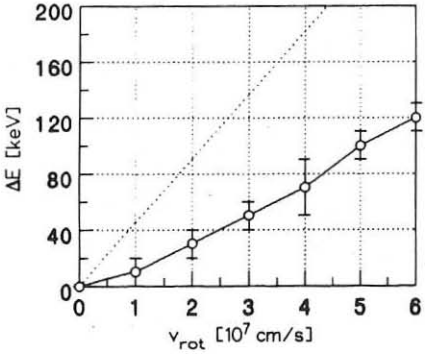

Fig. 4: Line shift as a function of the central rotation velocity.

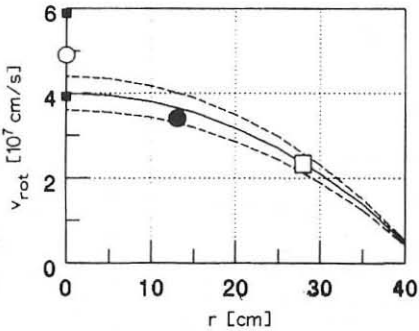

Fig. 5: Measured rotation velocities (P_{Inj} = 3.6 MW).

From Fig. 3 the measured line shift is found to be ΔE = 95 ± 10 keV.The injection power for these measurements was 3.6 MW. This value yields in Fig. 4 a central rotation velocity of $v_{rot}(0) = 4.9\times10^7$ cm/s ± 20%. This is essentially higher than the value deduced earlier [3], because we have now taken into account the integration over the different angles of neutron emission. In Fig. 5 we compare our results from the neutron energy spectra with CXRS measurements and mode frequency determination; they agree very well.

Absorption effects in quartz

We measured the neutron spectra through a quartz window. Owing to the strong increase of the neutron cross-section of oxygen at 2.45 MeV (Fig. 6) the absorption for the two spectra in the quartz is different and thus the ratio of the observed neutron fluences in the two directions mentioned becomes a function of the rotation velocity. This ratio was also calculated with the VINIA software. The results are given in Fig. 7 together with the value determined from the neutron spectra in Fig. 3. The agreement is good, thus this effect may offer a new possibility for measuring the rotation velocity.

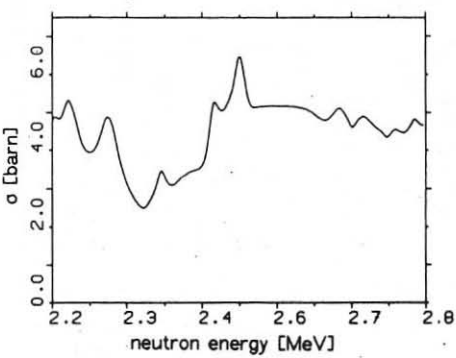

Fig. 6: Cross-section for neutron scattering in quartz.

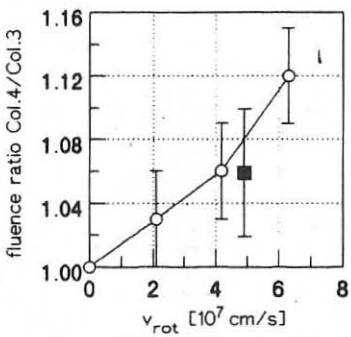

Fig. 7: Ratio of tangentially observed neutron fluence versus central rotation velocity.

References

[1] K. Hübner, et al., 15th Europ. Conf. on Controlled Fusion and Plasma Physics, Dubrovnik 1988, part 3, pp 1191-1194

[2] W. M. Stacey, et al., Nuclear Fusion, 26, 293-302 (1986)

[3] K. Hübner, et al., 14th Europ. Conf. on Controlled Fusion and Plasma Physics, Madrid 1987, part 3, pp 1294-1297

[4] D. E. Roberts, et al., 15th Europ. Conf. on Controlled Fusion and Plasma Physics, Dubrovnik 1988, part 1, pp 15-18

PARAMETER STUDIES OF NEUTRON PRODUCTION DURING ADDITIONAL HEATING IN ASDEX

K. Hübner, S. Lutz
Institut für Angewandte Physik, Universität Heidelberg, D-6900 Heidelberg
J. Kucinski
Institute for Nuclear Studies, PL-05400 Swierk
B. Bomba, S. Bosch, A. Eberhagen, H.-U. Fahrbach, O. Gehre, W. Herrmann, H. Murmann, H. Rapp, H. Röhr, K.-H. Steuer, O. Vollmer
Max-Planck-Institut für Plasmaphysik, EURATOM Association, D-8046 Garching

The neutron production in a deuterium plasma is determined solely by the ion distribution function. In the case of thermonuclear plasmas this distribution function is given by two simple plasma parameters, the ion density and the ion temperature. Unfortunately, neither is easy to measure and so they are not always available. Furthermore, in some situations we cannot expect a simple relation between the deuteron density and other plasma parameters. This situation complicates parameter studies for the neutron production in tokamaks and it is thus sometimes impossible to find clear correlations between the neutron rate and other experimental parameters such as the heating power, electron density, and plasma current.

Thermonuclear neutron production

The total neutron rate Q of a thermonuclear plasma is given by the volume integral

$$Q = \frac{1}{2} \int n_D^2(\mathbf{r})\, [\sigma v]_{\mathbf{r}}\, d\mathbf{r} = \frac{1}{2}\, n_D^2(0)\, [\sigma v]_0 \int f_D^2(\mathbf{r})\, f_{[\sigma v]}(\mathbf{r})\, d\mathbf{r}. \qquad (1)$$

Here $n_D(\mathbf{r}) = n_D(0)\, f_D(\mathbf{r})$ and $[\sigma v] = [\sigma v]_0 f_{[\sigma v]}(\mathbf{r})$ are the local profiles of the deuteron density and reactivity. The profile function of the neutron rate is $f_Q(\mathbf{r}) = f_D^2(\mathbf{r}) f_{[\sigma v]}(\mathbf{r})$. The profile functions for the deuteron density and temperature have not been measured, but in ASDEX we have very flat profiles for Z_{eff} and so we can use the measured density profile function of the electrons for the ions as well. Furthermore, the same temperature profile function can be expected for electrons and ions with the heating methods considered here, namely minority ICRH and H injection [1].

We are using our NR code [2] to determine the deuteron density from the measured neutron rate Q. First we consider the ratio

$$Q^* = Q \Big/ \frac{1}{2}\, n_D^2(0) = [\sigma v]_0 \int f_Q(\mathbf{r})\, d\mathbf{r} = [\sigma v]_0\, \frac{V}{Q(0)/\langle Q \rangle}\,, \qquad (2)$$

where V is the plasma volume and $Q(0)/\langle Q \rangle$ the peaking factor of the neutron emission profile. The ratio Q^* is only a function of this peaking factor and the central deuteron temperature, which determines the central reactivity.

Figs. 1, 2 and 3 give Q^* as a function of the deuteron temperature for minority ICRH and H injection L-mode and H-mode discharges in deuterium plasmas. For H injection the deuteron temperature was determined from CX measurements. For ICRH this was

only possible for some dicharges but from these we found $T_D = T_e$ for the parameter region used in Fig. 1. L-mode results are given for a single set of plasma current I_p = 380 kA and toroidal magnetic field B_{tor} = 2.2 T. H-mode results are given for two different currents and fields, and ICRH results for all currents and magnetic fields used in the minority heating experiments.

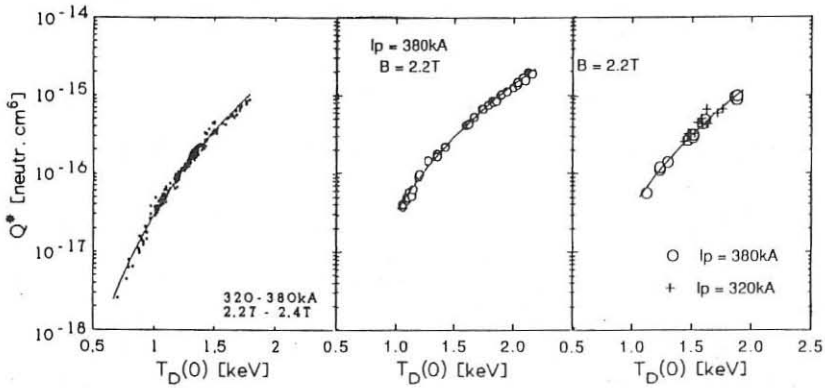

Figs. 1 to 3: $Q^* = Q \Big/ \frac{1}{2} n_D^2(0)$ as a function of the deuteron temperature,
1) minority ICRH, 2) H injection, L-mode, 3) H injection, H-mode.

For fixed temperature the influences of the current and magnetic field on Q are only due to the influences on Q(0)/‹Q›. In order to show this more clearly, in Figs. 4 to 6 Q(0)/‹Q› is given on a linear scale as a function of the deuteron temperature. Q(0)/‹Q› ranges between 10 and 18 and is thus essentially larger than the peaking factors for the density and temperature profiles owing to the quadratic dependence of Q on n_D and the strong

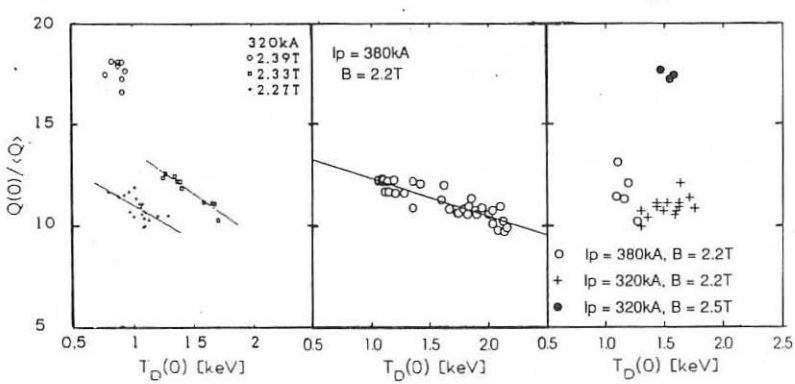

Figs. 4 to 6: Q(0)/‹Q› as a function of the deuteron temperature,
4) minority ICRH, 5) H injection, L-mode, 6) H injection, H-mode.

temperature dependence of [σv]. Furthermore, Q(0)/‹Q› decreases with increasing ion temperature because the reactivity [σv] rises faster for the lower temperatures in the outer regions of the profiles than for the maximum temperature in the centre.

At present, our data base is not sufficient to derive scaling laws for Q(0)/‹Q› with I_p and B_{tor}, but Figs. 4 and 6 show a clear increase of Q(0)/‹Q› with B_{tor} for fixed I_p. There also seems to be an increase with I_p for fixed B_{tor}. Owing to eq. 2 an increasing peaking factor for the neutron rate results in a decrease of Q^*. - For comparable currents and fields Q(0)/‹Q› and hence Q^* are the same for minority ICRH and H injection.

If the ion temperature is known, the measured neutron rate Q offers the most direct way of determining the deuteron density; it is given by $n_D(0) = \sqrt{2Q/Q^*}$. This expression directly demonstrates the problems of this procedure; errors in the determination of T_D will essentially affect the results for n_D. For ICRH our results for n_D are in general too high. This may by caused by a systematic error in the ion temperature or by non-thermonuclear effects and needs further investigation. The results for H injection are more reasonable. We restrict the discussion here to the L-mode case with the single current and field set used above. Fig. 7 gives n_D as a function of T_D. A decrease of n_D with increasing temperature is expected because the plasma is heated by H injection, but it may be overestimated owing to the problems mentioned. Nevertheless n_D decreases and T_D increases as the heating power per mean electron density $P_{inj}/\langle n_e \rangle$ (Fig. 8), and so the results do not seem to be affected too much by errors in temperature determination.

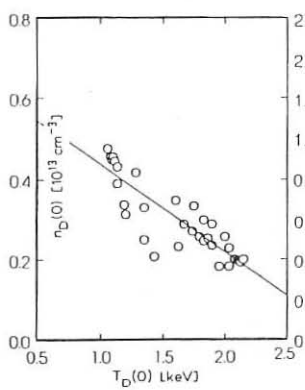

Fig. 7: n_D as a function of the ion temperature.

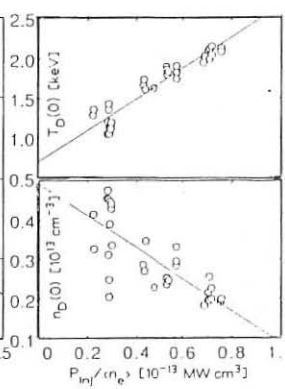

Fig. 8: n_D and T_D as a function of $P_{inj}/\langle n_e \rangle$.

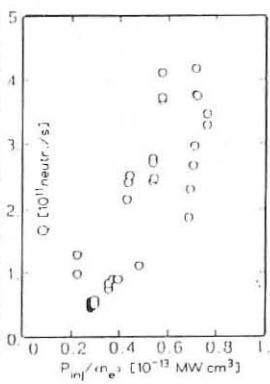

Fig. 9: Q as a function of $P_{inj}/\langle n_e \rangle$

Finally, we want to demonstrate in Fig. 9 that the large scattering of the values for n_D and T_D in Figs. 7 and 8 results in widely spread values if one tries to scale the measured neutron rate Q with the heating power. As Fig. 9 gives the results for a fixed current and field set, it is obvious that one cannot expect to find scaling laws of the measured Q with the direct parameters of the discharge, such as the heating power, current, magnetic field, and electron density.

Neutron production during D injection

There are always two contributions to the neutron rate during D injection in deuterium plasmas, the thermonuclear production and the beam-target production. As the target temperatures in ASDEX are mostly below 3 keV, the thermal contribution only amounts to a few per cent [2] and is therefore neglected in the following considerations. The beam-target neutron rate is given by

$$Q_{inj} = \frac{n_D}{n_e} \int D(\mathbf{r}) \left[\int (n_e \tau_W / W) \, [\sigma v]_{inj} \, dW \right] d\mathbf{r} . \qquad (3)$$

The deposition rate profile $D(\mathbf{r})$ gives the radial distribution of the injected ions. It is directly proportional to the injected power absorbed. $(D\tau_W/W)$ is their velocity distribution function resulting from the classical energy relaxation. n_D is the target deuteron density, n_e the electron density, and τ_W the energy relaxation time. $[\sigma v]_{inj} = f(W, T_D)$ is the fusion reactivity for monoenergetic deuterons with energy W in a target plasma with ion temperature T_D. The energy relaxation parameter $n_e \tau_W$ is mainly a function of the electron temperature T_e. Thus Q_{inj} is mainly a function of the injection power and the electron and ion temperatures.

For D injection we find from CX measurements $T_D = 1.2\,T_e$. In the parameter region considered here we have approximately $n_e \tau_W \sim T_e$. It is therefore sufficient to discuss Q_{inj} as a function of the product $P_{inj} T_e$, as shown in Fig. 10. For the L-mode discharges we are in the region where T_e saturates and becomes independent of the injection power and plasma density. Therefore, Q_{inj} is proportional to $P_{inj} T_e$. For the H-mode discharges T_e still depends on P_{inj}, and so Q_{inj} in Fig. 10 becomes larger for H-mode discharges than the extrapolated values for L-mode discharges.

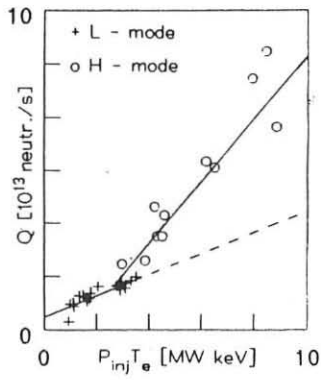

Fig. 10: Neutron rate during D injection as a function of $P_{inj} T_e$.

The peaking factor $Q(0)/\langle Q \rangle$ for the neutron rate for D-injection is also dominated by the beam-target reactions and therefore it shows behaviour completely different to that for H injection. The small thermonuclear contribution has $Q_{therm}(0)/\langle Q_{therm} \rangle \approx 10$ as for H injection. The peaking factors of the deposition profile and density are of the same order, namely $D(0)/\langle D \rangle \approx n(0)/\langle n \rangle \approx 2...3$. The fusion reactivity $[\sigma v]_{inj}$ is a linear function of T_D for the parameter region considered and we thus have $Q_{D-inj}(0)/\langle Q_{D-inj} \rangle \approx 5$ for D injection.

References

[1] F. Wagner, et al., Report IPP III/86, March 1983

[2] K. Hübner, et al., 15th Europ. Conf. on Controlled Fusion and Plasma Physics, Dubrovnik 1988, part 3, pp 1191-1194

CENTRAL MASS FEEDBACK CONTROL USING THE DISCRETE ALFVEN WAVE SPECTRUM

Th. Dudok de Wit, A.A. Howling, J.B. Lister, Ph. Marmillod

Centre de Recherches en Physique des Plasmas
Association Euratom - Confédération Suisse
EPFL, Lausanne (Switzerland)

Introduction Discrete Alfvén Waves (DAW) in TCA plasmas have been well documented both experimentally and theoretically [1]. Their dispersion relation depends on several important internal plasma parameters, such as the *central effective mass*, for which no other measurement technique has yet been developed.

By frequency tracking a single DAW during a current flat-top, we obtained a real-time estimate of the central effective mass. Using this measurement, we have been able to feedback control both the effective mass and the electron density of the plasma.

Theoretical background The shear Alfvén wave dispersion relation is given by :

$$\omega^2(r) = \left(\frac{B_o^2}{\mu_o\,\rho(r)}\right)\frac{\left(n+\frac{m}{q(r)}\right)^2}{R_o^2}\left(1-\frac{\omega^2(r)}{\omega_{ci}^2}\right) \qquad 1)$$

where n, m are respectively the toroidal and poloidal wavenumbers, $\rho(r) = n_e(r)\,A_{eff}(r)\,m_p$ the mass density and m_p the proton mass.

Since we have $\omega_{DAW} \approx \min\omega(r) \approx \omega(r=0)$ and assuming $\omega^2 \ll \omega^2_{ci}$, this becomes :

$$\omega^2_{DAW} \sim \frac{\left(n+\frac{m}{q(0)}\right)^2}{A_{eff}(0)\,n_e(0)} \qquad 2)$$

Some common values for A_{eff} are 1 for hydrogen, 2 for deuterium and most fully stripped impurities, 3 for tritium only.

Results from a 1-D simulation code fully confirm 2). However, particular attention must be paid to several parameters that may modify the approximate form of the DAW dispersion relation and which do not appear explicitly here, such as: a) the plasma current and its profile (other than q(0)); b) the density profile (other than $n_e(0)$); c) the position of the magnetic axis.

Experimental setup The diagnostic uses a small double-bar antenna situated on the outer equatorial midplane mounted on a rotating flange which allows it to be tilted with respect to the magnetic field lines. This antenna is fed by a 100W amplifier which provides an oscillatory current up to 15 A via a wideband matching circuit in the 1-6

MHz range. The system (fig. 2) has been designed to operate ultimately together with the high power Alfvén wave heating of TCA.

The plasma response to the excitation is detected by an RF pickup coil which gives the toroidal wavefield component b_ϕ, both in amplitude and in phase. Alfvén resonances are easily identified by amplitude peaks and phase rotations of 360°. Since the phase changes rapidly during a resonance, a phase-locked loop can be used to track a peak [2]. Earlier results [3,4] have proven this method to be sufficiently accurate to track a DAW with a bandwidth up to 10 kHz.

Once we know the DAW frequency and the mode numbers (n,m), the effective mass, or rather its inverse, can be computed in real time using a set of analog multipliers. For real-time calculations, the central electron density is approximated by taking the line-averaged density signal and multiplying it by a constant. This may introduce a small error when sudden gas puffs temporarily broaden the density profile, but this could ultimately be compensated.

Next, we feedback control both the plasma effective mass and the electron density. A 2-input, 2-output feedback loop (fig. 3) compares the analog signals 1/Aeff and $\bar{n}_e$ with two values programmed by the operator. The resulting errors ε are crosscoupled and the outputs act separately on both the hydrogen and deuterium gas valves.

<u>Temporal evolution of the effective mass</u> We tested the mass control system by running it with several different target values. It works well provided that the target density can be reached smoothly. Reasonable ranges are $\bar{n}_{e19}>1.5$ and $A_{eff}=1.2–2$. An absolute calibration of A_{eff} was carried out in a deuterium conditioned vessel, in which case the effective mass the least sensitive to impurity concentrations, and thus as close as possible to 2. Subsequently, all experiments were run during the current flat-top (I_p=130 kA, q(a)=3.1, (n,m)=(–2,–1) or (–1,–1)). The error on the measured effective mass for a single shot is estimated to be less than 3%.

We studied the temporal evolution of A_{eff} by puffing hydrogen into deuterium plasmas. The values of A_{eff} and $\bar{n}_e$ may be used to estimate the gas recycling rate at the centre of the plasma. Fig. 1 presents a shot with mass control, during which both A_{eff} and $\bar{n}_e$ evolve asymptotically towards the preset target values. The offset errors and the relatively low convergence time ($\tau \approx 7$ ms) can be reduced by optimizing the PI control circuits.

<u>Conclusion</u> We report the first attempt to estimate and control the plasma central effective mass by tracking the frequency of a global Alfvén eigenmode. The control system is easy to use, although several internal plasma parameters must be taken into account. Since deuterium and tritium have different effective masses, the diagnostic also offers a way to measure D-T mixtures in next generation tokamaks.

Acknowledgements : We are grateful for the continuous support of the TCA team in carrying out this study, which was partly funded by the Fonds National Suisse de la Recherche Scientifique.

References

[1] G.A. COLLINS *et al.*(1986), Phys.fluids **29**, 2260

[2] Equipe TFR (1977), Proc. of the Sixth Int. Conf. on Plasma Physics and Controlled Nuclear Fusion Research, IAEA, Berchtesgaden, **III**, 39

[3] G.A. COLLINS *et al.*(1987), Plasma Phys. Contr. Fusion **29**, 323

[4] G.A. COLLINS *et al* (1987), Plasma Phys. Contr. Fusion **29**, 1631.

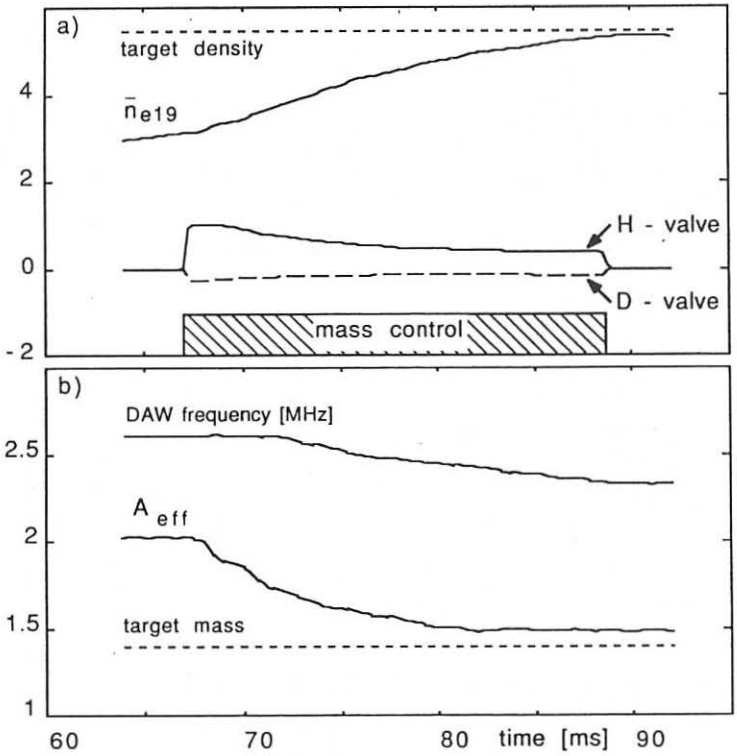

Figure 1 Shot with both density and mass control working between t=67 and 89 ms. Tha plasma initially contains only deuterium. In a), the hydrogen gas input is approximately proportional to the valve signal, whereas the deuterium valve remains closed. The target density and effective mass are reached respectively with an error of 3% and 7% (#28351, 130kA).

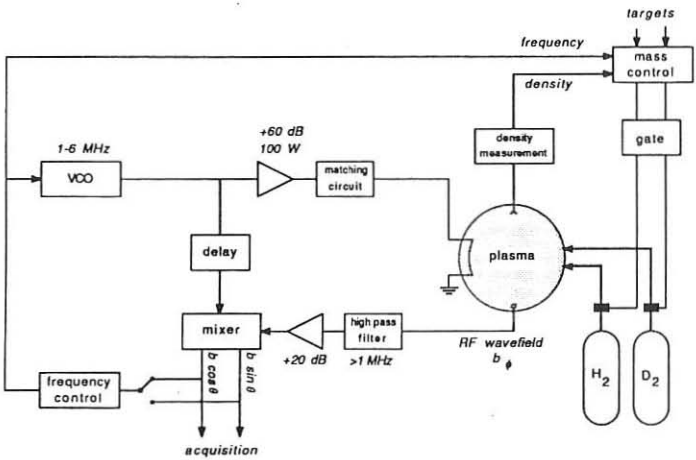

Figure 2 : The frequency tracking and mass control circuits

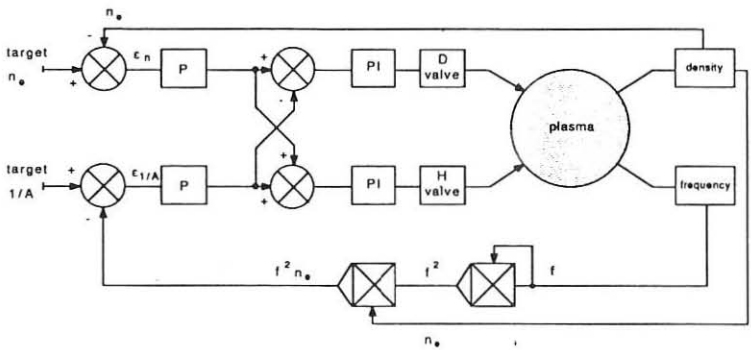

Figure 3 : Mass control schematic layout

ION TEMPERATURE MEASUREMENTS OF H-, D- AND He-PLASMAS IN THE TCA TOKAMAK BY COLLECTIVE THOMSON SCATTERING OF D_2O LASER RADIATION

R. Behn, D. Dicken*, J. Hackmann*, S.A. Salito and M.R. Siegrist

Centre de Recherches en Physique des Plasmas
Association Euratom - Confédération Suisse
Ecole Polytechnique Fédérale de Lausanne
21, Av. des Bains CH-1007 Lausanne, Switzerland

*Permanent address: Institut für Laser- und Plasmaphysik, Universität Düsseldorf, F.R.G.

Development of collective Thomson scattering as a method to measure the ion temperature of a tokamak plasma has been successful and encouraging results have been obtained during experiments on TCA in H-, D- and He-plasmas. Using a laser source in the far-infrared spectral region allows scattering angles close to 90°, which results in excellent spatial resolution. The system installed on the TCA tokamak comprises an optically pumped D_2O laser emitting 0.5 J in a 1.4 μs pulse on its Raman transition at 385 μm. A heterodyne receiver with a Schottky barrier diode mixer has been chosen to detect the scattered radiation and analyze its spectral distribution in 12 channels of 80 MHz. Recent improvements of the mixer and 1st IF-amplifier yielded a system NEP of $2.2 \cdot 10^{-19}$ W/Hz. As a consequence we have obtained results which allow for the first time to evaluate the ion temperature T_i in a single laser shot.

Under the conditions of the scattering experiment on TCA the presence of impurity ions and the magnetic field were shown to have a noticeable influence on the shape of the spectrum. Fig.1 shows calculated spectra for parameters typical for a H-plasma in TCA. An example of a measured spectrum in hydrogen is presented in Fig.2. A value of $T_i = 330$ eV is found, using a standard curve fitting routine with the ion temperature T_i as the only free parameter. In order to determine the precision of a T_i measurement that can be obtained by our present set-up, a series of experiments under reproducible plasma conditions have been carried out in H-, D- and He-plasmas. The results are listed in Table I . A statistical analysis yields a standard deviation of 80 to 100 eV which corresponds to a relative error of about 25% . However, it should be mentioned that uncertainties in the other plasma parameters (especially Z_{eff}) provided as input to the fitting routine will lead to systematic errors. As long as the errors in T_e and N_e are less than 10% their influence on the evaluation of T_i is negligible.

During our first experiments a scattering geometry has been chosen where the difference wave vector $k = k_s - k_i$ is almost perpendicular to the vector of the total magnetic field $B = B_t + B_p$. Under these conditions a strong enhancement of the scattered intensity towards the centre of the spectrum is observed in agreement with the theoretical predictions. Although this influence can be taken into account by the fitting routine, the combined effect of the magnetic field and the impurity ions makes the interpretation of the spectra difficult, especially when the impurity content and Z_{eff} are not precisely known.

Therefore a second series of experiments has been carried out in a He-plasma after the geometry of the scattering experiment had been changed to avoid an orientation of k perpendicular to B (angle between $\underline{k}$ and $\underline{B}$: 86°). In He, as long as $T_e > T_i$, theory predicts a noticeable enhancement of the scattered intensity at a frequency corresponding to the ion-acoustic resonance. Under these conditions uncertainties in Z_{eff} do not strongly affect the shape of the spectrum in the region of interest and the evaluation of T_i is more precise. Fig. 3 shows a typical spectrum for a He- plasma in TCA; the fitting routine yields $T_i = 260$ eV.

The spectrum clearly shows the ion-acoustic feature in agreement with the theoretical model. As in the case of H- and D-plasmas we find a significant difference between T_e and T_i, which at present is not yet fully understood. The T_i-values from collective Thomson scattering are also systematically lower than those measured by a neutral particle analyzer (NPA). These observations will be subject to further investigations.

So far the experiments have demonstrated that collective Thomson scattering is a valuable method to measure the ion temperature of a tokamak plasma. The measured spectra are consistent with theoretical predictions assuming density fluctuations at the thermal level. The influence of the magnetic field can be avoided by a suitable choice of the scattering geometry. In the presence of light impurity ions (e.g. O and C) additional information about Z_{eff} is required to obtain optimum precision of a T_i measurement.

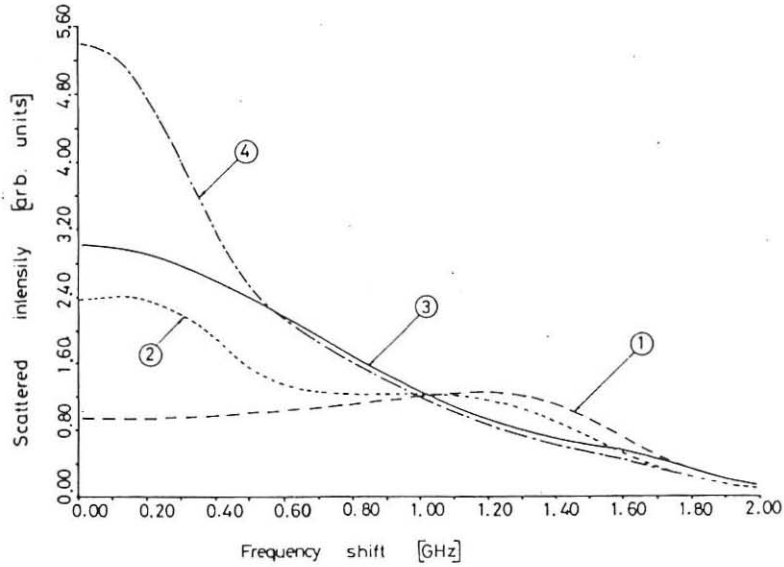

Fig. 1: **Calculated spectra for a H-plasma**
The 4 cases show the influence of the magnetic field and the impurity ions
Case 1: Basic spectrum (no magnetic field no impurities)
Case 2: Impurities included (Z_{eff}=2.5)
Case 3: Magnetic field included (B_t=1.5T, orientation 1° from normal)
Case 4: impurities and magnetic field included
Plasma parameters: $N_e=5.5*10^{19}m^{-3}$, T_e=680eV, Z_{eff}=2.5, B_t=1.5T

Table I Summary of T_i measurements

These results have been obtained during series of tokamak shots with reproducible plasma parameters. The standard deviation and the corresponding relative error value give an indication of the uncertainty of the measurement. However, it has been assumed that the other plasma parameters (N_e, T_e, Z_{eff} and β), required by the fitting procedure to evaluate T_i, are exact.

	H-Plasma	D-Plasma	He-Plasma
Ne	$5.5*10^{19}m^{-3}$	$5.3*10^{19}m^{-3}$	$5.0*10^{19}m^{-3}$
Te	680 eV	830 eV	600 eV
Zeff	2.5	2.5	2.7
Ti(fit)	250 eV	310 eV	380 eV
	320	450	430
	440	320	370
	230	460	410
	260	220	470
	370	300	260
	460	480	470
	300	490	270
	320	450	400
mean	330 (±30) eV	390 (±30) eV	390 (±25) eV
stand. dev.	80 eV	100 eV	80 eV
rel. error	25%	26%	20%

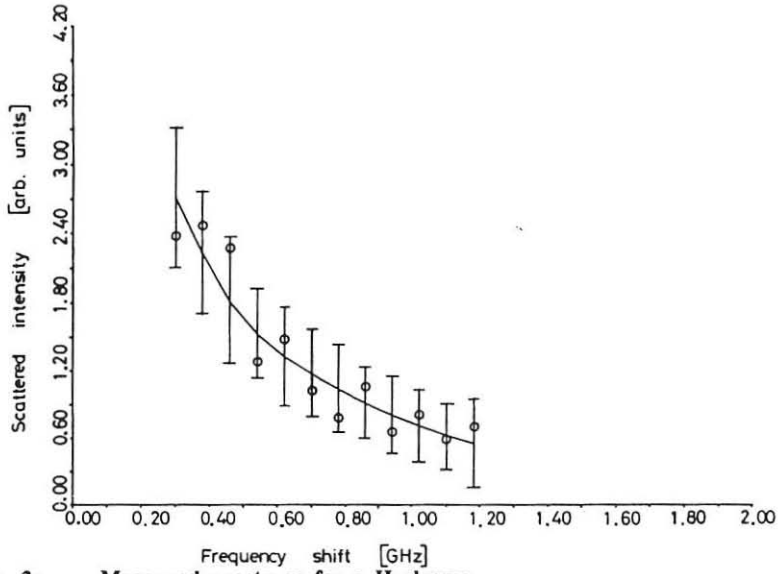

Fig. 2: **Measured spectrum for a H-plasma**
The spectrum is obtained from a single laser shot. The plasma parameters are:
$N_e = 7.9*10^{19}m^{-3}$, T_e=590 eV, Z_{eff}=2.5, B_t=1.5 T, angle $(\underline{k},\underline{B})=89^o$.
The fitting procedures yields an ion temperature of T_i=330 eV.

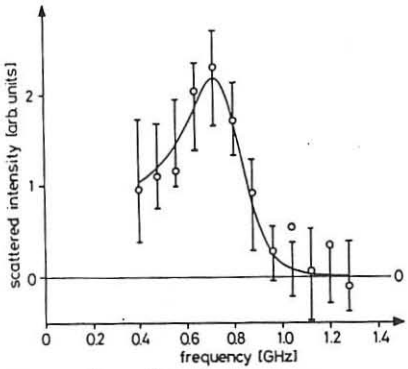

Fig. 3: **Measured spectrum for a He-plasma**
The spectrum is obtained from a single laser shot. The plasma parameters are:
$N_e=8*10^{19}m^{-3}$, T_e=620 eV, Z_{eff}=4.2, angle $((\underline{k},\underline{B})=86^o$.
The fitting procedures yields an ion temperature of T_i=260 eV.

HIGH RESOLUTION SPECTROSCOPY ON THE FRASCATI TOKAMAK FT

R. Bartiromo, F. Bombarda

Associazione EURATOM-ENEA sulla Fusione, C. R. E. Frascati,
C.P. 65 - 00044 - Frascati, Rome, Italy

The bent crystal spectrometer installed on the Frascati tokamak FT is a high resolution ($\lambda/\Delta\lambda \simeq 20000$) instrument of the Johann type [1]. Over the last period of operation it was fitted with a crystal (quartz 213) suitable for observing the high ionization stages of chromium.

H-LIKE SPECTRUM

We believe it is the first time that the Cr XXIV resonance spectrum has been observed in high resolution. As usual, the interest in this measure is doublefold: on one hand, it is possible to test the accuracy of calculated atomic data and, on the other hand, to actually diagnose the plasma. In this paper, we only relate the observations more relevant to fusion plasma diagnostic.

The spectrum between 2.085 and 2.120 Å was recorded over a series of discharges at 8 T of magnetic field, 300÷350 kA of plasma current, 3.0±10% of electron temperature and an average density of 3 to 7 10^{13} cm^{-3}. Due to the limited spectral range available, it was necessary to set the instrument in four different positions and then join the various sections via software. The result is shown in Fig. 1. the experimental points can be compared with a simulated theoretical spectrum obtained by using the wavelengths and satellite intensity factors calculated by J. Dubau and his group for all the transitions with n=2,3,4,5 (private communication); similar results are obtained with data from other authors [2,3]. Except for a small discrepancy in the position of line T, the experimental data can be fitted well with a spectrum relative to

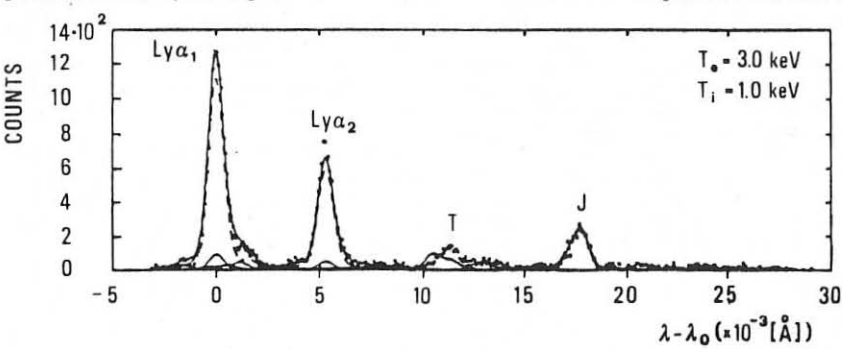

Fig. 1 - Spectrum of Cr XXIV

an electron temperature T_e=3.0 keV, with the absolute intensity normalized on the Ly α_1 peak. The relative importance of including the high n transitions blended with the resonance lines was evident in another set of observations on discharges at different T_e, where the measured intensity ratio I(T)/I(Lyα_2) could be made to agree with the theoretical curve only if the contribution of the high n satellites were included in the calculation.

SUPRATHERMAL ELECTRON EFFECTS

The intensity ratio R between a dielectronic recombination satellite line and the optically allowed resonance line is a function of T_e only, but it can also provide a means of detecting the presence of suprathermal tails in the electron distribution function. This possibility was first suggested by the authors et al. in [4], following the observation on FT of strong deviations of the measured intensity ratio of the n=3 satellite line d_{13} to the w line of He-like Cr in low density discharges, and it was more thoroughly investigated and experimentally exploited in a set of observations on the Fe XXV spectrum [5]. In the following, we report some recent results again with Cr XXIII. The physical principles of this measure rely on the fact that a dielectronic satellite is excited through a resonant mechanism only by electrons with kinetic energy comprised in a narrow band of the distribution function. The resonance line, on the contrary, is excited by impact with all the electrons with an energy greater than the transition energy E_0. If a high energy tail is present, the intensity of the resonance line will be enhanced and, therefore, R will be lower with respect to its thermal value. For a more quantitative analysis, it was pointed out in [5] that the excitation rate coefficient of the optically allowed line remains fairly constant for impact electron kinetic energies greater than about 3 times E_0, due to relativistic effects. It is, therefore, easy to deduce the fractional density $n_{s.t.}$

$$n_{st} = \left(\frac{1}{R_{exp}} - \frac{1}{R_{th}(T_e)} \right) \cdot \frac{C_{sat}(T_e)}{<\sigma v>}$$

where R_{exp} is the experimentally measured line ratio, $R_{th}(T_e)$ is the expected value relative to the bulk plasma temperature, $C_{sat}(T_e)$ is the effective exitation coefficient of the satellite line or lines considered, and $<\sigma v>$ is the high energy average value of the excitation rate of the w line (2.2 10^{-11} $cm^3 \cdot sec^{-1}$ for Cr XXIII). In Fig. 2 the suprathermal electron fractional density is plotted vs the relative deviation of R, for different temperatures. It can be observed that at higher temperatures, the method is decreasingly sensitive, but also less critically dependent on T_e, which, it is worth stressing here, must be independently measured.

The present experiment is intended for studying the effects of the 8 GHz LH wave on the electron distribution function. The power level was too low (~150 kW) to produce any important heating effect of the bulk plasma, but enough to induce an observable distortion of the ECE emission spectra. Discharges at 6 and 8 T, I_p=350÷450 kA were produced with density as the varying parameter, ranging from 0.4 to 2.0 10^{14} cm^{-3}. In general, it was possible to use the 2nd harmonic to measure T_e at the plasma center, and the signal at 1.6 ω_{ce} as a monitor of the occurence of suprathermal tails. The experimental ratio of the n=3 satellites to the w line was measured as described in [5]. The agreement between the ECE and the line ratio measured temperature has been checked as being reasonably good for thermal discharges.

The results can be summarised as follows: At 8 T there are no detectable signs of distortion in the distribution spectrum from the line ratio for $n_e \geq \sim 9 \times 10^{13}$ cm^{-3}, even when the ECE spectrum is strongly affected; this could be interpreted as an off-center

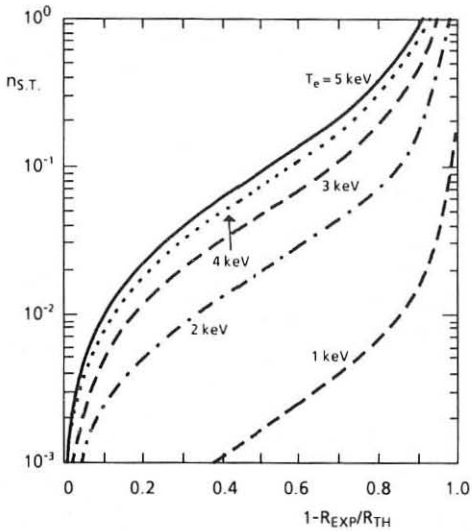

Fig. 2 - Suprathermal electrons fractional density as a function of the relative deviation of the experimental line ratio R

localization of the tails (the emission region of Cr XXIII is only ~1/3 of the minor radius around the center), but also as being due to an insufficient sensitivity of the method, at least for the higher temperature cases. At lower density, 1 to 8%, or more, of suprathermal electrons were measured, but at 6 T the effects were marginally observable. At very low density (~$5 \cdot 10^{13}$ cm^{-3}), the whole discharge could enter the slideaway regime, more or less independently of the RF. A quantitative analysis was in this case difficult to carry out due to uncertainties on the measured T_e.

SPACE RESOLVED MEASUREMENTS

The cylindrically bent crystal spectrometer is characterized by a sensibly higher throughput than a flat crystal instrument. The spectrally resolved image line, however, gives no information on the spatial distribution of the emitting source, due to the astigmatic imaging of the reflected rays in the plane perpendicular to the diffraction plane. In order to obtain a space resolved image along the poloidal section of the tokamak, two horizontal slits could be used, although at the expenses of luminosity. A preliminary measurement of the T_i and emission profiles has been performed placing the first slit (5×120 mm) in a such position as to have the widest possible view of the plasma for the given dimensions of the detector (10 cm) and the Mylar window separating the high vacuum of the machine from the rough vacuum of the instrument, and a second slit in front of the detector, determining a space resolution of ~1.5 cm in the plasma. Twenty-five discharges with almost identical parameters (B_T=6 T, I_p=350 kA, n_e=1.4 10^{14}) were needed to obtain a measurement along eight different chords across the plasma section. The normalized T_i profile in Fig. 3 looks relatively peaked compared to the emission profile, which could be partially explained with the slightly

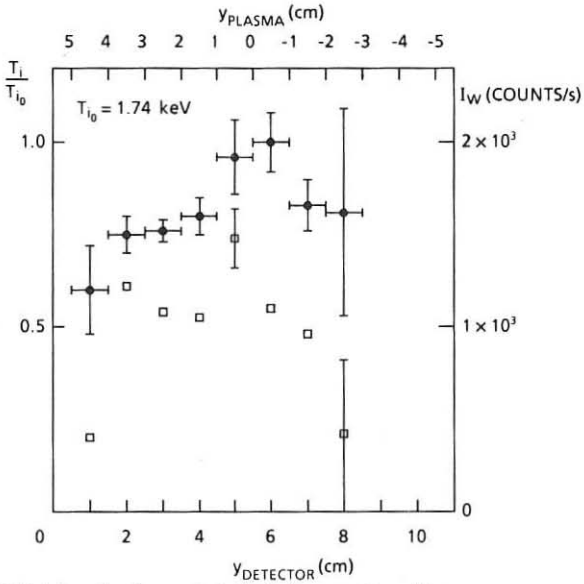

Fig. 3 - Normalized T_i (dots) and w line emissivity I_w (squares) profiles

varying condition of the discharges during the day, while the sharp drop in the intensity rate should be a profile effect combined with the Mylar window vignetting.

REFERENCES

[1] R. Bartiromo, R. Giannella, M.L. Apicella, F. Bombarda, S. Mantovani, G. Pizzicaroli: Nucl. Instrum. & Meth. **225**, 378 (1984)

[2] K.R. Karim, C.P. Bhalla: Phys. Rev. A **378**, 4744 (1986)

[3] L.A. Vainshstein, U.I. Safronova: At. Data and Nucl. Data Tables **21**, 49 (1978)

[4] M.L. Apicella, R. Bartiromo, F. Bombarda, R. Giannella: Phys. Letts. **98A**, 174 (1983)

[5] R. Bartiromo, F. Bombarda, R. Giannella: Phys. Rev. A **32**, 531 (1985)

COLLECTIVE SCATTERING FROM 60 GHZ ECRF WAVES AT RTP

S.K. Kim, C.A.J. Hugenholtz, A.J.H. Donné, W.A. Peebles*, N.C. Luhmann, Jr*

FOM-Institute for Plasma Physics 'Rijnhuizen', Association EURATOM-FOM
P.O.Box 1207, 3430 BE Nieuwegein, The Netherlands

*University of California, Los Angeles, CA, USA

Introduction

Electron cyclotron resonance heating (ECRH) experiments with three 60 GHz, 200 kW gyrotrons will be performed on the Rijnhuizen Tokamak Project (RTP). RTP tokamak has a major radius of 72 cm, minor radius of 17 cm, and $B_T \leq 22$ kG (to be increased eventually to 28 kG), $n_e \leq 1 \times 10^{20}$ m^{-3}, $I_p \leq 200$ kA. Various heating schemes will be investigated, including X-mode inside launch with adjustable launch angle and O-mode outside perpendicular launch. Research topics include electron heat transport during modulated ECRH and profile control via localized heating. For such investigations, it is crucial to understand the ECR heating process. In this paper, we will discuss the feasibility of collective Thomson-scattering measurement of various (fully or partially) electrostatic waves involved in ECRH, e.g., X-mode and mode-converted electron Bernstein waves with $\omega/2\pi \approx 60$ GHz, utilizing radiation sources in the infrared (IR) or far-infrared (FIR) region. The information thus obtained will help understand the physics mechanism(s) of the heating process with ECRF waves.

Collective scattering

Collective scattering monitors basically electron-density fluctuations. Hence its application to the measurements of coherent plasma waves is limited to those involving such fluctuations, i.e., (fully or partially) *electrostatic* waves. For ECRH, such scattering measurement will be useful primarily for X-mode heating schemes. Figure 1 shows the schematic of the dispersion curve of X-wave and the electrostatic Bernstein wave in the vicinity of $\omega = \omega_{ce}$ and $\omega = \omega_{UH}$, where ω_{ce} is the cyclotron frequency and ω_{UH} is the upper-hybrid frequency, after Puri [1]. Mode conversion of the slow X-mode at the upper hybrid resonance layer into an electrostatic Bernstein mode is depicted. This process is relevant to the inside launched X-mode heating and the outside obliquely launched O-mode heating with high density target plasma [2]. From the figure, for an observation window located at $\omega \approx \omega_{ce}$, one expects two relatively distinct waves: small k (long wavelength) X-mode with $k \approx k_{vac} \approx 12$ cm^{-1} and large k (short wavelength) electron Bernstein mode with $k \approx \rho_e^{-1} \approx 100 \sim 1000$ cm^{-1} resultant from mode-conversion of the X-mode. For X-modes, the scattering is in the collective regime, i.e., $\alpha = (k\lambda_D)^{-1} >> 1$ where Debye length $\lambda_D \sim$ 0.003cm for typical RTP parameters. For Bernstein waves, the scattering is marginally collective, i.e., $\alpha \approx 1$. This poses both as a difficulty and as a challenge for an accurate interpretation of measurement results from Bernstein waves. As ω approaches ω_{UH}, which, for a fixed wave frequency of ω, is equivalent to translating the scattering volume outward from cyclotron layer to upper-hybrid layer, wavenumbers of the two modes will converge. For Bragg scattering ($k_o \approx k_s >> k_w$), the scattering angle is given by $\sin\theta_s = (k_w/2k_o)$, where k_o, k_s, and k_w are the wavenumbers of the probe radiation, the scattered and the scatterer wave, respectively. The wavelength range suitable for achieving reasonable collective scattering angle thus falls within the infrared (IR) and far-infrared (FIR) region ($k_o \approx$ 50~7000 cm^{-1}).

However, the high wave frequency of 60 GHz renders simple homodyne measurement unattractive due to the resultant high intermediate frequency (IF). Therefore, a separate local oscillator (LO) at a different frequency is desirable so that a manageable IF can be produced.

Scattering at large k_w

For large-k_w electron Bernstein modes, we will employ two CO_2 lasers whose output frequencies are different by ~60GHz. Large wavenumber of IR radiation (λ=10.6 μm, k_o= 5900 cm^{-1}) permits a manageable scattering angle of ~2° up to ~5° for k_w = 1000 cm^{-1}. For small-k X-modes, the system can be configured as a far-forward scattering ($\theta_s \approx 0$) system, where a high-dispersion grating can be used if necesary to separate the down-shifted scattered radiation from the probe beam. To achieve the necessary frequency separation between LO and probe beam, each laser will operate at one of two adjacent CO_2 laser lines from the p-branch in either 9 μm or 10 μm band, which have a frequency difference in the vicinity of 60 GHz. Specifically, 10P38-10P36, and 9P36-9P34 have difference frequencies of 60.23 GHz and 60.28 GHz, respectively [3]. Thus the beat frequency between the scattered radiation and the LO will be in the range of ~500 MHz. Fast IR detectors, such as Ge:Cu photoconductors counterdoped with Sb and HgCdTe photovoltaic detectors, are available for IF of up to a few GHz, with a noise equivalent power (NEP) of ~10^{-19} Watt/Hz. This amounts to a minimum detectable power of ~10^{-10} Watt for an IF bandwidth of 1 GHz.

For an estimation of the measurability of the ECRF waves through IR scattering, a comparison with similar measurements [4] might be useful. For example, in ICRF heated Microtor discharges ($P_{RF}/P_{OH} \approx 0.1$~$0.5$), typically $\tilde{n}_e$ of ~10^{16} m^{-3} (~ 0.1% of background density) was observed in association with mode-converted ion-Bernstein waves. In addition, the fluctuation level was found to increase as $P_{RF}$was increased. If we take this fluctuation level as the lowerbound for RTP ($P_{RF}/P_{OH} \geq 1.0$ at similar densities), then the collective scattering power $P_s = 0.25\ P_o(r_e \lambda \tilde{n}_e L_v)^2$, where the probe beam power P_o=100 Watt with λ=10.6 μm, a scattering volume length L_v=0.5 cm, and r_e is the electron radius, will be in the range of ~10^{-10} Watt. This figure is comparable to the expected minimum detectable power. Actual minimum scattered power level should be comparable to this, since the weaker density dependence (~$\tilde{n}$) of non-collective scattering power (α<<1) will be matched by higher density fluctuation level for large k electron Bernstein waves than that of ion waves for the same RF field strength ($\tilde{n}$~kE). Therefore reasonable S/N values are expected . This measurement requires the CO_2 lasers to operate at stable output frequency with respect to each other and to have no higher transverse spatial mode other than TEM_{oo} during the tokamak discharge. For the low-power CO_2 laser for LO, the nominal stability is 20 kHz per 100 ms and a similar value is expected for the high power laser. As an alternative for LO generation, possibilities of employing the technique of CO_2 laser sideband generation via microwaves [5] will be investigated. This technique is well-established both in IR and FIR region for application in high-resolution Doppler-free molecular spectroscopy. It basically is a process of mixing the IR (or FIR) radiation with the output of a (tunable) microwave source on a nonlinear crystal such as CdTe or GaAs.

Scattering at small k_w

For measurement of small-k X-mode, an FIR scattering scheme will be employed [6]. The system is based on a heterodyne receiver system at 185 GHz, with a 245 GHz (k= 51 cm^{-1}) far-infrared laser output radiation as the probe and a multiplied solid-state Gunn oscillator at ~185 GHz as the LO. Scattered FIR radiation whose frequency is down-shifted from 245 GHz to 185 GHz, is mixed with the LO on a low-noise GaAs Schottky diode

mixer, to generate IF signals. One advantage of this FIR scattering scheme is that the plasma microturbulence can be measured simultaneously with the same collection optics. This is due to the fact that the frequency of FIR radiation scattered from microturbulence remains much closer to the probe frequency, which can therefore be separated from ECRF wave signal via an frequency-selective quasi-optical diplexer. Such information of microturbulence will help investigate simultaneously the ECRH effect on the turbulent transport. In a similar manner to IR scattering, the expected scattered power level from ECRF waves can be shown to be in $\geq 10^{-8}$ Watt range, for $P_o = 10$ mW at wavelength of 1.2 mm and L_v of 3 cm. Mixers operating in the 170-260 GHz range with double-sideband NEP of 10^{-20} watt/Hz are available, resulting in a minimum detectable power level of $\sim 10^{-11}$ Watt with an IF bandwidth of 1 GHz. In this scheme, however, careful interpretation of the scattering geometry is necessary, since the wavenumbers of the probe and the scattered radiation are different and thus the scattering is not in the Bragg regime. In addition, enhanced harmonic ECE during ECRH observed in many tokamaks might have to be carefully discriminated against the scattered signal (3rd harmonic ECE falls in the vicinity of 185 GHz). These difficulties are absent for IR (λ=10.6 μm, k_o= 5900 cm^{-1}) scattering, since $f_o \approx 28$ THz $>> f_{ce}$ and thus $k_o = k_s$ (Bragg scattering).

Ray path and experimental set-up

Unlike the low frequency ICRF waves, the ECRF waves behave more like rays. This means one should choose carefully the site of the scattering volume to intersect with the ECRF waves, especially along the toroidal direction. Consequently wave activity is more likely to be observed when the measurement is made at a closer position to the ECRH port. For RTP, two port positions are available, one separated from ECH port by less than 10° and another by 60° toroidally. Figure 3 shows results from TORAY ray-tracing code for RTP parameters, simulating an X-mode inside launch at an angle of 45° with respect to the major radius, which corresponds to a situation where the waves can travel the farthest toroidally. Note that the ray stops midway, past the plasma center, when it encounters the upper-hybrid resonance layer. However, the unabsorbed X-mode power reaching the upper hybrid layer is almost completely mode converted into electron Bernstein waves propagating backward, which are damped subsequently as they approach the cyclotron resonance layer. This is indicated schematically in the figure since TORAY does not calculate mode-conversion processes. Even though the ray for mode-converted Bernstein waves gives an impression of an almost parallel propagation as the wave approaches the cyclotron resonance layer, the wavenumber composition is still such that $k_\perp$ becomes more and more dominant over $k_{||}$ [2]. Therefore, the scattering will be confined almost within the poloidal cross section, unlike the expectations in ref.[6] where the possibility of a parallel scattering was discussed.

References

1] Puri S. et al. (1973), J. Plasma Physics **9**, 89.
2] Maekawa T. et al. (1979), Phys. Lett. **69A**, 414.
3] Bradley L.C. et al. (1986), IEEE J. Quantun Electronics **QE-22**, 234.
4] Lee P.S.C. et al. (1982), Phys. Rev. Lett. **49**, 205;
Surko C.M. et al. (1972), Phys. Rev. Lett. **29**, 81.
5] Magerl G. (1982), IEEE J. Quantum Electronics **QE-18,** 1214.
6] Peebles W.A. et al. (1986), Rev. Sci. Instrum. **57**, 1980.

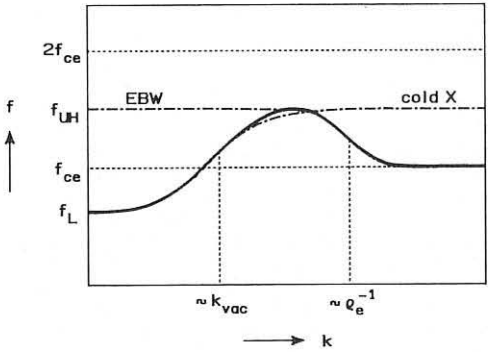

Figure 1 Schematic of the extraordinary wave dispersion in the vicinity of ω_{ce}(after [1]). ω_{pe} = 1.5 ω_{ce}.

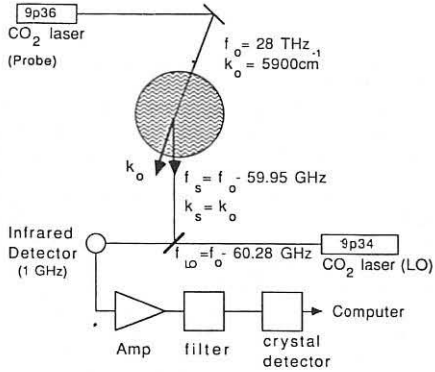

Figure 2 Schematic of the collective IR scattering system.

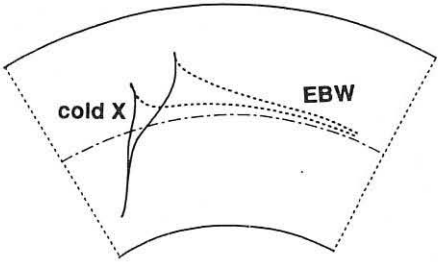

Figure 3 Toroidal projection of X-mode rays (solid line) for RTP calculated from TORAY code, launched from inside at 45° from the major radius and from the meridian plane, with beam divergence (FWHM) ≈ 10°. B_T = 22 kG, I_p=200 kA, n_{eo}=6x10^{19} m^{-3}. Rays for the mode-converted electron Bernstein waves (broken line) are added schematically, originating at the upper-hybrid layer where cold X-mode stops (after [2]).

DENSITY FLUCTUATION MEASUREMENTS IN THE TORTUR TOKAMAK

G.J.J. Remkes, C.J. Barth, B. de Groot, S.K. Kim,
H. de Kluiver, H.A. van der Laan and A.J.H. Donné

FOM-Institute for Plasma Physics, 'Rijnhuizen', Association EURATOM-FOM,
P.O. Box 1207, 3430 BE Nieuwegein, The Netherlands.

Introduction

In the TORTUR tokamak (R = 0.46 m, a = 0.085 m, $B_T < 2.9$ T, $Z_{eff} < 2$) plasmas are produced by currents up to 55 kA during about 40 ms. By the application of elevated loop voltages, a stationary weakly turbulent state is brought about with an enhanced dissipation, due to low-frequency electromagnetic turbulence [1]. In this way, relatively high values of the electron and ion temperatures (up to 1 keV) are obtained at high plasma densities ($< 10^{20}$ m^{-3}). Despite the weakly turbulent state of the plasma, the energy confinement time (< 2.5 ms) follows closely the values from currently used scaling laws. A typical TORTUR shot is shown in Fig. 1.

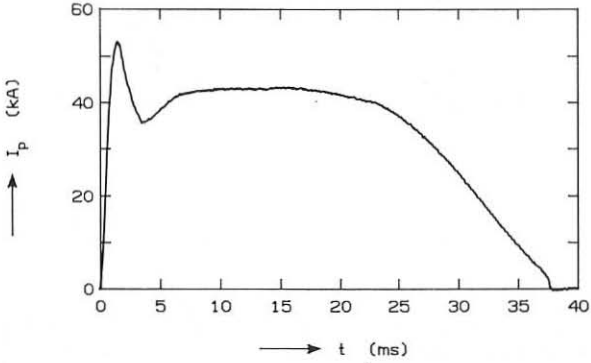

FIG. 1. Plasma current as a function of time for a typical TORTUR shot.

Fluctuations due to plasma turbulence in TORTUR have been studied previously by means of collective scattering of 4 mm waves in a wide frequency range extending from 10 kHz up to 100 MHz [2,3].

Experimental set-up

The present set-up can measure collective scattering of 2 mm waves for a range of scattering angles (4°-40° and 80°-110°) and in the same frequency domain as used in the 4 mm scattering set-up. A schematic drawing of the 2 mm scattering device is given in Fig. 2. A part of the microwave power from a 65 mW klystron source is branched off by a beam splitter and is fed directly to the local oscillator input of a double-balanced mixer (homodyne detection). The other part of the microwave power is shaped into a gaussian beam which is focussed onto the centre of the plasma. This is performed by means of an oversized waveguide antenna, two lenses and a gold-coated mirror. The receiving system is identical to the beam launching system. By means of changing the angle and the position of the two mirrors it is possible to tune the device to various **k**-values (restricted to the poloidal plane). The scattering vectors are nearly parallel to the equatorial plane pointing in- or outwards. The finite dimensions of the scattering volume implies that measurements performed at the plasma edge are mainly sensitive to fluctuations propagating in the radial direction, whereas measurements near the plasma centre yield both radially and azimuthally propagating fluctuations.

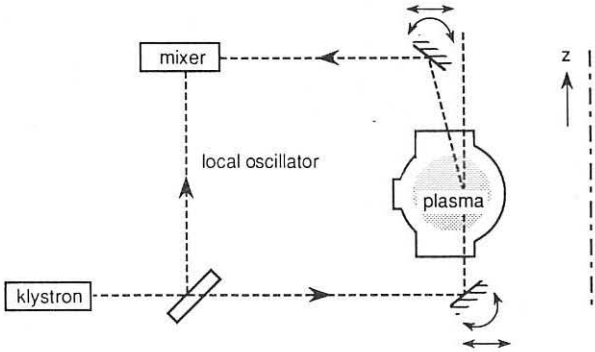

Fig. 2. Schematic drawing of the collective scattering set-up.

The range of k-values is 2 - 20 cm^{-1}. The device allows also measurements at larger k-values, but here the spectral density is thought to be small. The one-dimensional k-resolution is typically 2 cm^{-1}, dependent on the scattering angle. The spatial resolution is about 1 cm.

The mixer output is preamplified and divided in a low, an intermediate and a high frequency domain from 10 - 10^3 kHz, 0.25 - 4 MHz and 0.7 - 100 MHz respectively. The signals are further amplified with adjustable amplification factors and real time recorded. The recordings start simultaneously during the shot and cover time slices of 4, 1 and 0.3 ms for the low, the intermediate and the high frequency domain, respectively. Fast Fourier Transform techniques are applied on the signals to obtain three separate frequency spectra. These can be combined to yield the complete spectrum from 10 - 10^5 kHz.

Results

In Fig.3, the spectral scattered power (P_k), observed at the plasma centre, is shown as a function of frequency (f). Curve A and B are observed at k-values of 5 and 15 cm^{-1}, resp. From curve A it is seen that for f > 100 kHz and k=5 cm^{-1} the spectral power is proportional to f^{-4}. Curve C represents the noise level.

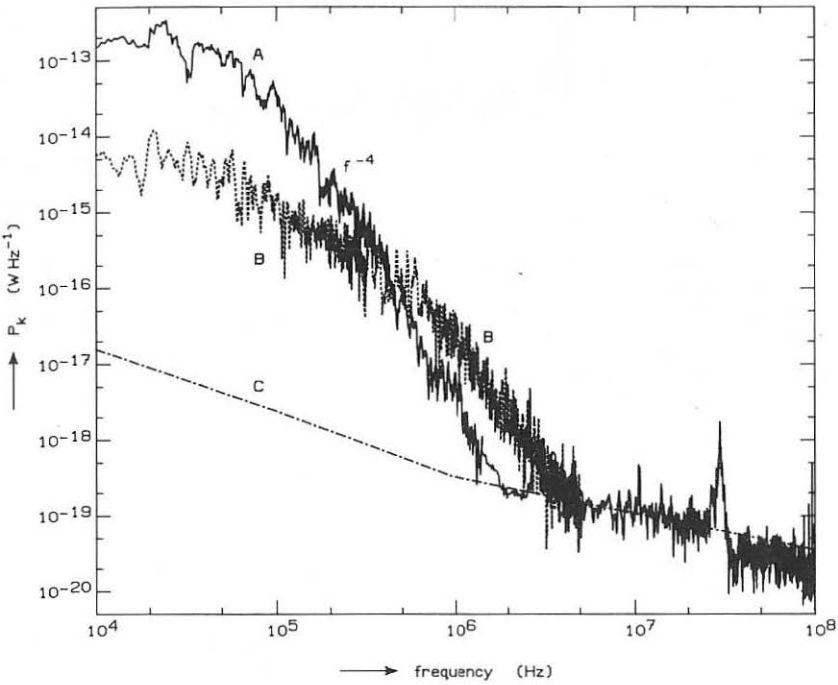

Fig. 3. The complete spectrum of the mixer output, due to density fluctuations in the plasma centre. Curve A and B are observed at k-values of 5 and 15 cm^{-1}, resp. Curve C represents the noise level.

The total scattered power present in three frequency bands, roughly corresponding to the formerly mentioned domains, could be obtained by means of band filters and rectifiers. The time evolution of these three signals has been recorded for the full discharge duration. In Fig. 4 the power present in the frequency band 0.7 - 3 MHz is shown as a function of time. The spike in the beginning of the curve corresponds to the predischarge. This shows that the plasma behaviour is different for the predischarge and the plateau st: ge.

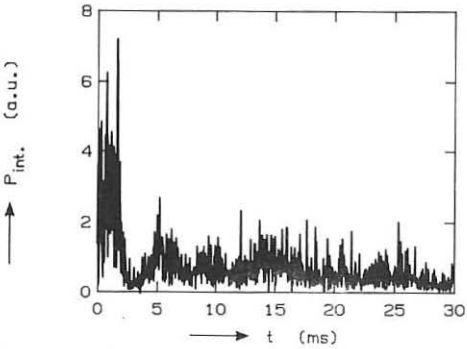

Fig. 4. The scattered power integrated in the frequency band 0.7 - 3 MHz during the TORTUR discharge.

In many shots, a strong correlation between the signals obtained from collective scattering and from the poloidal and toroidal pick-up coils has been observed, as is demonstrated in Figs 5a and 5b. The fourier transforms of these signals have been compared. Narrow spikes of 30 kHz with higher harmonics are present in the spectra of the scattered signal and of the pick-up coils. These frequencies can be ascribed to MHD-modes with m=2 and n=1. This effect is not likely to be due to 'Bragg scattering'.

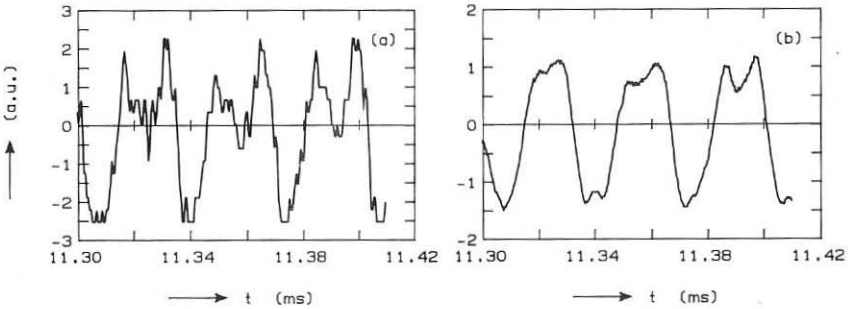

Fig. 5. The signals from (a) collective scatterring at the plasma centre at $k = 7.5\ cm^{-1}$ and (b) from a poloidal pick-up coil, as a function of time.

Acknowledgement

This work was performed under the Euratom-FOM association agreement with financial support from NWO and Euratom.

References

[1] Haas F.A. *et al.* (1987) Plasma Phys. Controlled Fusion **29**, 145.
[2] De Kluiver H.*et al.*, (1988) Plasma Phys. Controlled Fusion **30,** 699
[3] Donné A.J.H. *et al.* (1987) Europhys. Conf. Abstr. (Madrid) **11D**, 245.

THE OBSERVATION OF NON-THERMAL FEATURES BY TANGENTIAL THOMSON SCATTERING AT THE TORTUR TOKAMAK

A.C.A.P. van Lammeren, C.J. Barth, A.J.H. Donné, Q.C. van Est and G.C.H.M. Verhaag

FOM Institute for Plasma Physics, "Rijnhuizen", Association EURATOM-FOM,
P.O. Box 1207, 3430 BE Nieuwegein, The Netherlands.

Introduction

Tangential Thomson scattering at TORTUR plasmas was set-up to determine the local current density j_φ. From a feasibility test it was expected that j_φ could be measured in a single laser pulse with an accuracy of 20% [1] at $n_e = 5 \times 10^{19}$ m^{-3}. Similar measurements were performed by Alladio and Martone [2] adding several shots to determine j_φ. Our experiment is the first that measures a complete tangential spectrum by a single laser pulse.

Experimental set-up

In the TORTUR tokamak [3] (R = 0.46 m, a = 0.085 m, B_T = 2.9 T) hydrogen plasmas are produced by plasma currents up to 55 kA during about 40 ms (see Fig. 1). At densities of 5×10^{19} m^{-3} plasma temperatures up to about 800 eV are attained. Plasmas with relatively high values of poloidal beta are obtained during the mildly current-driven turbulent heating which occurs immediately after initial plasma formation, and are maintained during the plateau stage. Thomson scattering over 90° is applied to measure the local electron temperature, T_e, and density, n_e, at two radial positions, r = 5 and 60 mm, respectively. At r = 5 mm the scattering spectrum can be observed both radially as well as tangentially (see Fig. 2a). All observations are performed with the same high-transmission 20-channel polychromator which covers a spectral range of 600 to 800 nm [4]. The radial measurement of T_e and n_e can be performed with an accuracy of 1 %, which allows for the recording of non-thermal features in the electron velocity distribution. These phenomena can also be observed in the tangential direction although its collection efficiency is five times smaller. Adequate correction for plasma light is possible since it is sampled just before and after the laser pulse. During the plateau stage of the plasma these samples are equal within the statistical error. The laser beam is directed vertically through the plasma (Fig. 2a), while the scattered light is collected in the horizontal plane. From Fig. 2b it becomes clear that the scattering vector, $\underline{k}$, is under 45° with the horizontal plane, since $\theta = \varphi = 90°$. It should be emphasized that the observed spectrum represents the projection of the electron velocity distribution on $\underline{k}$.

Results

An example of a single shot j_φ -measurement is given in Fig. 3 from which one gets $(1 \pm 0.2) \times 10^7$ A/m^2. The sign of the wavelength shift corresponds to the actual current direction. Assuming Spitzer resistivity with $Z_{eff} = 2$ [5], T_e = 446 eV, $n_e = 5.87 \times 10^{19}$ m^{-3} and V_l = 5 V one finds $j_\varphi = 8.3 \times 10^6$ A/m^2, corresponding to q_o = 1.2. Earlier observations in the radial direction at TORTUR [1, 3] revealed the existence of distortions of the scattered spectrum. The present recordings confirm these radial spectra (Fig. 4a, b). Moreover, similar spectra are observed in the tangential direction (Fig. 4c, d). During the build-up phase of the plasma the non-thermal features on the radial spectra are stronger than

during the plateau (Fig. 4b). The amplitude and wavelength shift of these non-thermal features are influenced by plasma conditions, such as direction of the toroidal magnetic field, ion mass and T_e.

Discussion

Possible explanations for these kind of distortions were given by several authors who reported similar effects measured in the radial direction. Strong dips in the spectra of the L-2 stellerator were ascribed to trapped electrons [6]. Since observations in TORTUR were performed at the plasma centre the trapped electrons should be of no significance. At ALCATOR [7] and FT [8] the non-thermal features are explained by the existence of slide -away and suprathermal electrons resp.. Non-thermal spectra in THOR were ascribed to runaways [9]. The congruence between radial and tangential spectra in TORTUR demonstrates that the distortion of radial spectra can not be the projection of toroidal tail distributions. Furthermore the partial density of the observed non-thermal features ($\sim 0.05 \times n_e$) is much larger than the run-away density n_e-tail $\leq 1.4 \times 10^{15}$ m^{-3} at t = 10 ms which is calculated from the run-away production rate according to Knoepfel and Spong [10]. Our first explanation is to ascribe these features to the existence of magneto-sonic waves, such as the Alfvén wave, since the distortions are strongest at a wavelength shift which corresponds well to the Alfvén velocity [3,4]. This picture is supported by the presence of distinct frequency peaks near 3 MHz in the density fluctuation spectra, as recorded by collective scattering [3], but in contradiction to the found mass dependence. From the dispersion relation one expects stronger growth rates for these waves in the direction parallel to B_T than perpendicular to B_T. Preliminary data acquisition indicates that the amplitude of the distortions in the tangential direction is larger than in the radial one and thus supports the given explanation. Further study and data-analysis is required to verify the hypothesis that the velocity distribution function is disturbed quasi-stationary by the presence of magneto-sonic waves.

Conclusion

Tangential and radial Thomson scattering at TORTUR plasmas demonstrate that the velocity distribution of mildly turbulent plasmas is non-Maxwellian, which is of great importance for transport computations. At $T_e \leq 500$ eV the current density can be determined with an accuracy of 20% by a single laser pulse.

Acknowledgement

This work was performed under the Euratom-FOM association agreement with financial support from NWO and Euratom.

References

[1] Barth C.J. (1989) "Determination of the local current density by means of tangential Thomson scattering: experimental set-up, feasibility test and preliminary observations", submitted to Rev. Sci. Instrum..
[2] Alladio F. and Martone M. (1977) Phys. lett. **60A**, 39.
[3] De Kluiver H. et al. (1988) Plasma. Phys. and Contr. Fus. **30**, 699.
[4] Barth C.J. (1984) Appl. Opt. **27**, 2981.
[5] Lopes Cardozo N.J. (1985) Rijnhuizen Report 85-160.
[6] Blokh M.A. and Larinova N.F. (1981) Sov. J. Plasma Phys. **7**, 31.
[7] Pieroni L. and Segre S.E. (1975) Phys. Rev. Lett. **34**, 928.
[8] Bartiromo R. et al. (1979) Proc. Ninth Eur. Conf., Oxford, 47.
[9] Tartari U. (1984) "Thomson-scattering measurements and non-thermal regimes in the THOR plasma", FP.-84/20.
[10] Knoepfel H. and Spong D.A. (1979) Nucl. Fusion **17**, 785

Fig. 1: Typical plasma current.

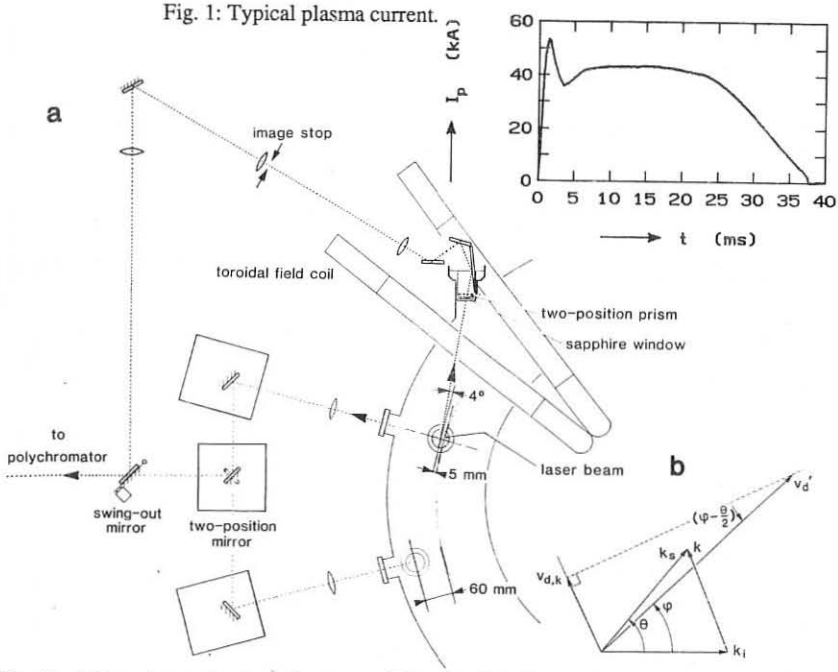

Fig. 2: a) Experimental set-up for tangential and radial Thomson scattering, b) scattering geometry.

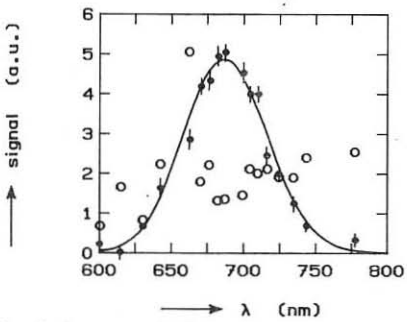

Fig. 3: A scattered spectrum from tangential observation, t = 10 ms, $\Delta\lambda_d = -2.5 \pm 0.5$ nm, $n_e = (5.87 \pm 0.16) \times 10^{19}$ m^{-3}, $T_e = 446 \pm 11$ eV. The dots represent the scattered and the open circles the plasma light.

Fig. 4: (next page) Scattered spectra and relative deviations, δ, with respect to the fit, corrected for relativistic effects. a) radial direction, t = 10 ms, $T_e = 406$ eV, $n_e = 6.27 \times 10^{19}$ m^{-3}, b) radial direction, t = 4 ms, $T_e = 575$ eV, $n_e = 6.80 \times 10^{19}$ m^{-3}, c) tangential direction, t = 18 ms, $T_e = 551$ eV, $n_e = 5.29 \times 10^{19}$ m^{-3}, d) tangential direction, t = 18 ms, $T_e = 568$ eV, $n_e = 3.94 \times 10^{19}$ m^{-3}.

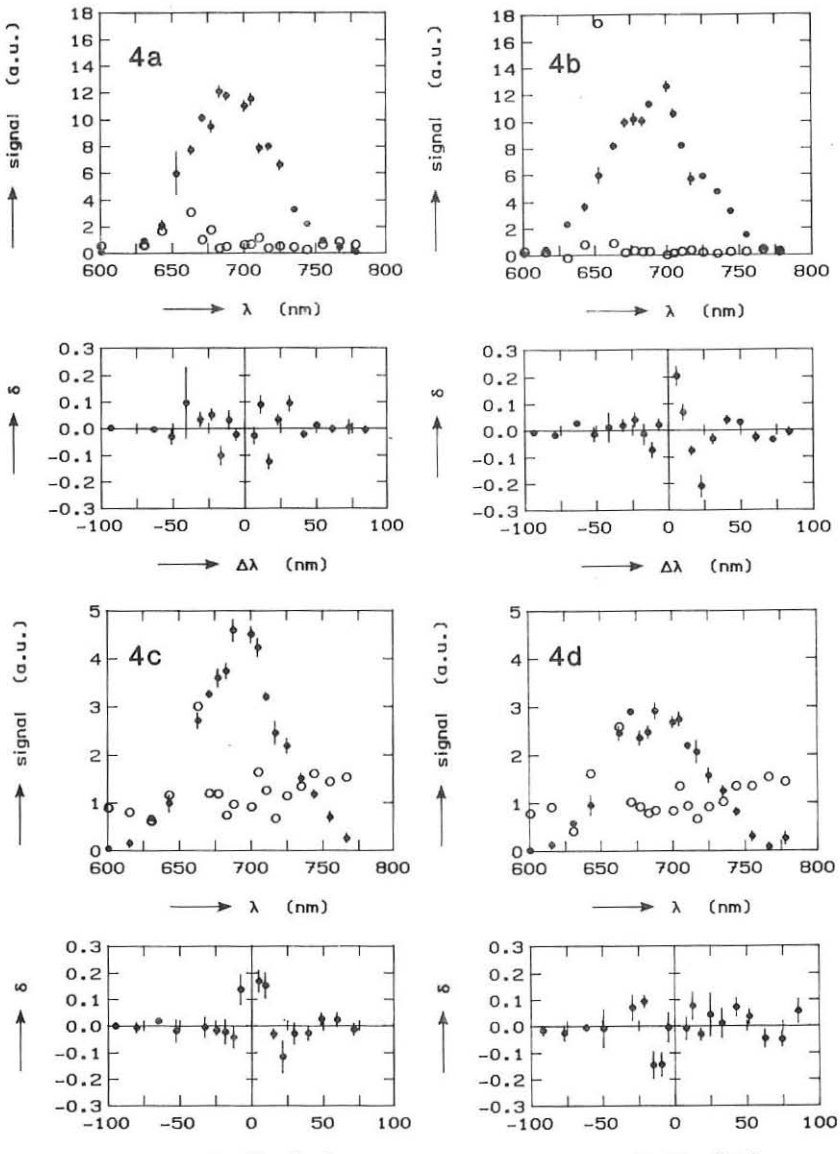
4a
4b
4c
4d
signal (a.u.)
λ (nm)
δ
Δλ (nm)

A TIME-OF-FLIGHT SPECTROMETER FOR DETECTION OF LOW ENERGETIC HYDROGEN ATOMS

W. van Toledo, A.R. de Bree, R. van Buuren, H. de Kluiver and A.J.H. Donné

FOM Institute for Plasma Physics, 'Rijnhuizen', Association EURATOM-FOM, P.O. Box 1207, 3430 BE Nieuwegein, The Netherlands

Low energetic neutral hydrogen atoms that are released from wall and limiters of a tokamak as well as Franck-Condon neutrals may undergo charge exchange with plasma ions. The resulting fast neutrals are not confined to the magnetic field and thus contribute to energy losses, including those due to impurity radiation when the fast atoms sputter impurity ions from the wall. These processes determine the particle and energy transport from the plasma center and quantities as the sputtering coefficient, the reflection coefficient of the wall and the diffusivity of H or D in the wall material play a decisive role here. By detecting especially the cold neutrals from the boundary layer one gains information on the hydrogen or deuterium recycling and hence on the energy balance of the plasma. This paper shall be concerned with a time-of-flight method, that requires direct detection of hydrogen atoms and is able to detect hydrogen or deuterium atoms with an energy down to 10 eV.

The poor detection sensitivity of detectors like channeltrons, channelplates, etc. for low energetic neutrals requires conversion of the atoms into charged particles that must be accelerated towards the detector. The method ordinarily used is that of the Daly detector [1,2]. Its main disadvantage is that the emission coefficient varies two orders of magnitude in the energy range from 10 to 200 eV and drops sharply below 20 eV, that is in the energy region in which we are interested.To overcome this disadvantage a new detection method was proposed [3], drawing upon a suggestion made by Massmann et al. [4]. The method is based on conversion of hydrogen atoms from the plasma into H^- ions on a cesiated tungsten (110) surface. Because of the low work function of the surface the affinity level of the hydrogen atoms is easily populated by an electron from the surface.

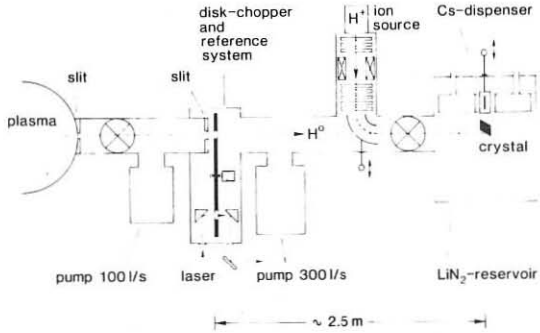

Fig. 1. Schematic overview of the time-of-flight spectrometer

The time-of-flight spectrometer (see Fig. 1) consists of a chopper disk with 16 equally spaced slits and running at 400 Hz, a flight tube and a detector housing. The open time varies from 6 to 10 μs and the duration of a spectrum from 150 to 250 μs. The various differential pumping sections are necessary to overcome the pressure fall from the torus (1 x 10^{-3} Torr) to the vacuum chamber (1 x 10^{-9} Torr). After passage through the tube the neutrals will hit the cesiated surface in the vacuum chamber (see Fig. 2). The cesium is contained in a socalled dispenser and is evaporated at a constant rate when current is applied through the dispenser. The generated H^- ions are detected by a channeltron which had to be mounted in a box to prevent it from being covered with cesium during or shortly after the dispenser activation period. Cesium is known to react violently with lead-glass (the main component of the channeltrons). The effect would be a strongly reduced pulse height of the channeltron output. When the cesiation is finished the dispenser is pulled into a cavity in a LN_2 cooling trap situated above the tungsten target. In that position redundant cesium is trapped on the cooled surface.The dispenser is moved back in front of the crystal whenever cesiating of the surface is required. By the time the dispenser has been withdrawn, a shutter that covers the entrance of the box is opened, so that H^- ions reflecting from the cesiated surface can be detected. To this end a positive bias voltage of 1000 V is applied to the channeltron. Unfortunately, this bias voltage stimulates cold electronic emission from metallic parts outside the box that have been partially covered with cesium. These electrons are equally attracted by the field towards the channeltron and are a cause of severe noise during the first minute after cesiating. Placing grids at the entrance of the box could not prevent penetration of the field. A razor-blade dump was designed to prevent saturation of the channeltron due to excessive exposure to plasma light, which is led to the dump whereas the H^- ions are bent to the channeltron.

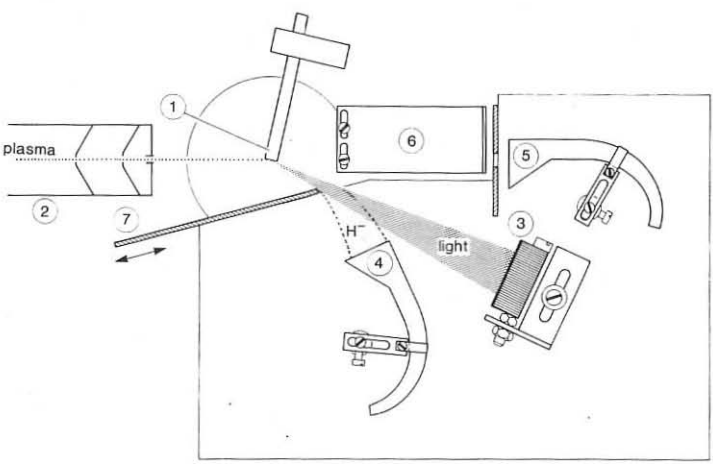

Fig. 2. The scattering chamber: 1. tungsten surface; 2. collimator; 3. razor-blade light dump; 4,5. channeltrons; 6,7 moveable shutters

Positive hydrogen ions (H_2^+) from the source mounted on the flight tube (see Fig. 1) have been made incident on the surface for calibration purposes. We were compelled to work with H_2^+ instead of H^+ ions because of the small H^+ production of the ion source which would have made calibration cumbersome, especially at low energies. The dissociation of the incident ions near the surface has been taken into account. All incident ions are neutralized before reflecting from the surface, while the H^- formation process takes place after reflection. For this reason the neutralization of the positive ions does not interfere with the H^- formation process. This means that positive ions can be used for calibration purposes and that the results are valid for measurements with neutral atoms. This idea has been confirmed in work by Van Wunnik et al.[5].

Each efficiency value was obtained by determining the difference in the number of reflected particles from an activated and not activated surface and by dividing the outcome by the number of incident ions. The latter value is obtained by pulling downward the platform on which the surface and surface holder are mounted, together with a second shutter that protects a negatively biased channeltron (see Fig. 2) which detects the incoming positive beam. The two channeltrons are identical. All data have been corrected for noise in the channeltron output due to cold electronic emission and cesium.

The efficiency and consequently the detection sensitivity is maximum for a cesium coverage of about half a monolayer (= 3.3 x 10^{14} atoms/cm^2). With this cesium coverage the conversion efficiencies were measured before using Faraday cups to show the feasibility of the proposed technique . The best results were found to occur when the neutral beam makes an angle of 78° with the surface normal (see Fig. 3, triangles).The calibration has been discussed in detail in Ref.[3]. The conversion efficiencies are exponentially dependent on v^{-1}, perpendicular to the surface normal, which has been predicted from theoretical considerations [6].

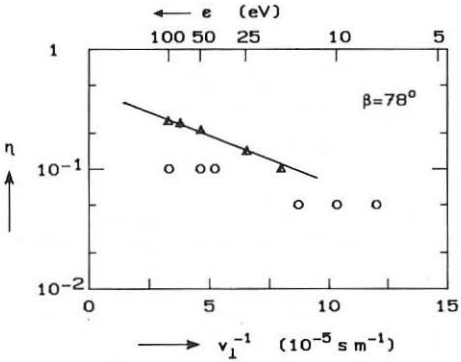

Fig. 3. The conversion efficiency as a function of energy and the reciprocal normal incident velocity per nucleon. Circles obtained with channeltrons, triangles with Faraday cups.

The found conversion efficiencies are smaller than those obtained by Faraday cups (see Fig. 3). One of the possible causes is that we are not able to monitor how the efficiency varies with cesium coverage unlike the calibration done with Faraday cups. As a result the cesium coverage might not have been half a monolayer. The optimum cesium coverage had to be found by adjusting the dispenser activation time and the dispenser current. The values were stored in a memory to assure the same coverage throughout the whole calibration.The accuracy of the data is in the order of 20%. The data below 20 eV are less accurate because the dissociation energy of H_2^+ ions is in the order of the incident velocity per nucleon.

Very good vacuum conditions are required to prevent contamination of the surface. Under such conditions it is not necessary, as was originally intended, to perform a new surface activation between each two discharges. Only after half an hour of operation we saw a considerable decline of the efficiency, provided that the surface has been cleaned thoroughly before covering it with cesium. This is done by flashing the surface once at 2000° C before each activation. The time-of-flight spectrum in Fig. 4 extends to approximately 60 μs and is the product of adding 52 subsequent spectra obtained within one single plasma shot, taking a chopper open time indicator as reference signal. This has been done for statistical reasons. The small number of slits in the chopper disk and consequently the long duration of a single spectrum allows for a clear distinction between plasma signal and background. The latter consists of noise from cesium and cesium-induced electronic emission, and X-rays from the plasma. The spectrum in Fig. 4 is corrected for this background signal.

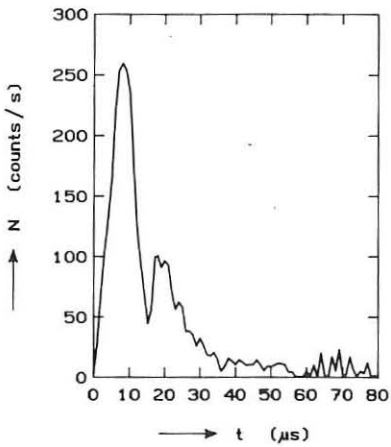

Fig.4. Time-of-flight spectrum

The X-ray induced background has been minimized by constructing the chopper disk out of 1 mm thick stainless steel. Only during the open time X-rays could reach the detector, but measurements done with a 2 μm macrofoil placed between surface and plasma did not bring forward any significant signal. The corresponding energy-resolved spectrum has to be corrected for the conversion efficiency (as measured with channeltrons) and the attenuation of the neutral flux due to residual gas in the TOF tube.

Acknowledgement
This work was performed under the Euratom-FOM association agreement with financial support from NWO and Euratom.

References

[1] Verbeek H. (1986) J. Phys. E: Sci. Instrum. **19**, 964
[2] Brocken H.J.B. and De Kluiver H. (1983) Plasma Phys. **25**, 317
[3] Van Toledo W. *et al.* (1986) Physics Letters A **119**, 126
[4] Massmann P. *et al.* (1979) Nucl. Instrum. Methods **165**, 531
[5] Van Wunnik J.N.M. *et al.* (1983) Surf. Sci. **131**, 17
[6] Geerlings J.J.C. *et al.* (1985) Surf. Sci. **157**, 151

DIRECT OBSERVATION OF HIGH FREQUENCY TURBULENCE DURING INJECTION OF HIGH-CURRENT RELATIVISTIC ELECTRON BEAM INTO PLASMA

I.V.Kandaurov, E.P.Kruglyakov, M.V.Losev, A.L.Sanin, L.N.Vyacheslavov
Institute of Nuclear Physics Siberian Division of the USSR Academy of Sciences, 630090 Novosibirsk, USSR

In the experiments on high-current relativistic electron beam (REB) interaction with a plasma for a study of the possibility of its heating owing to collective processes a key question is a type of oscillations excited by the beam in a plasma. At present, a great deal of the data obtained evidences that the beam excites in a plasma electron Langmuir oscillations at a frequency ω_{pe}. The energy of these oscillations is then transmitted to plasma electrons [1]. However, so far none of the experiments enabled a direct observation of the occurence of electron Langmuir turbulence. In the present paper an attempt is made of direct discovering and studying of HF plasma turbulence by the laser scattering method. The experiments were carried out on the GOL-M device [2] under the following beam and plasma parameters.

REB: energy of electrons, E=0,5 MeV, beam current $I_b \lesssim$ $\lesssim$ 90 kA, electron beam density, $n_b \simeq 10^{12} \div 5 \cdot 10^{12}$ cm^{-3}, beam duration, $\tau_b \simeq 100$ ns.

Plasma: density, $n_e = 2 \cdot 10^{15}$ cm^{-3}, plasma column length, L= =750 cm, magnetic field strength, $B_o \lesssim 5$ T.

It is known that homodyne laser methods can be used for studying the low frequency turbulence. When an electron Langmuir turbulence is excited in a plasma these methods are not suitable (for a plasma density shown above the frequency of a plasma oscillations should be equal to $\omega_{pe}/2\pi \simeq 4 \cdot 10^{11}$ Hz). Therefore, the system for observation of the laser radiation scattered by HF plasma oscillations was based on a classical scheme and consisted of three main parts: a laser, a spectral

instrument and detector. A system consisting of a pulse CO_2 single-transverse mode laser and the triple-passed amplifier provided a source of radiation. The selection of a necessary transition was performed by using a diffraction grating (150 lines/mm) in the laser resonator. To facilitate the formation of a transverse space discharge in the amplifier the triethyl-amine ($p \simeq 1$ Tor) was added to the CO_2, N_2 mixture (total pressure is of the order of 0.5 atm), similar to that proposed in Ref. [3]. The laser system described could be operated within the range of 9-11 μm providing a pulse energy of 10 J. The laser pulse duration could be changed from 0.07 up to 2 μs. The spectral instrument was built on the base of a grazing incidence scheme with double reflections from the surface of diffraction grating (5x10 cm^2). The use of a lens with a focal distance of 30 cm provided a linear dispersion of 10 GHz/mm. Liquid helium-cooled SiB photoconductors were used as detectors. For an area 2x2 mm^2 and a bandwidth of amplifiers 10 MHz the detector sensitivity threshold was 10^{-6} W.

To study the energy distribution of the Langmuir oscillations over wave vectors $\vec{K}$ the optical scheme should provide the registration of the scattered radiation in a wide range of angles α with respect to the direction of laser beam propagation up to $\alpha \simeq \frac{\omega_{pe}}{\omega_L}$ (here ω_L is the frequency of laser radiation incident on a plasma). For the wave length of the laser radiation $\lambda \sim 10\,\mu$m and plasma density $n_e = 2 \cdot 10^{15}$ cm^{-3} this observation angle should be equal to $\alpha \simeq 10^{-2}$ rad. Under these conditions a considerable portion of laser radiation with non-shifted frequency together with the scattered by a plasma radiation reaches the spectral instrument. An extraction of a useful signal may only be possible if a spectral instrument of a super-high contrast is available. This problem has been successfully solved with the use of radiation of a CO_2 laser operated on R14 transition ($\lambda = 10{,}29\,\mu$m) and an absorbtion cell (total length of the

cell is 40 cm) filled with ammonia under a pressure of up to 0.25 atm. Since ammonia has a single absorption line well coinciding with the R14 laser line, this gas filter provided the suppression of laser radiation with non-shifted frequency by a factor of 10^{12}-10^{13}.

In the preliminary experiments with detection of the scattered radiation the following experiment geometry was used. The laser beam crossed the plasma column perpendicularly to the direction of REB propagation. The total solid angle of detection system of scattered radiation was $\Omega \simeq 3 \cdot 10^{-4}$ sterad. In the cross section formed by REB and laser beam propagation directions the scattered radiation was detected in the following range of angles: $2 \cdot 10^{-3} < \alpha < 2 \cdot 10^{-2}$. In our case, it corresponded to laser scattering by Langmuir oscillations with wave vectors $\vec{K}$ under 33°-82° with respect to direction of the REB propagation. As to the value $|\vec{K}|$ it could vary within the range: $\frac{\omega_{pe}}{c} < |\vec{K}| < 1{,}8 \frac{\omega_{pe}}{c}$

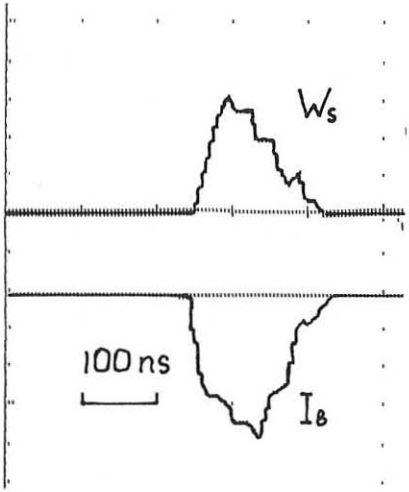

The time behaviour of a scattered radiation signal, W_s, in the vicinity of the frequency $\omega \simeq \omega_L + \omega_{pe}$ (upper trace) and of the REB current, J_b (lower trace). Current density, j_b=5,5 kA/cm^2. J_b=65 kA. Magnetic field strength, B_o= =2,5 T. Plasma density, n_e= =$2 \cdot 10^{15}$ cm^{-3}.

In the figure presented here a signal is shown of laser radiation scattered by plasma. This signal is shifted with respect to the frequency of initial laser radiation by value of ω_{pe}. For the case shown in the figure the duration of the laser pulse is much larger than that for the scattering signal. In the figure below the REB current pulse is shown. One can see that the durations of the signals are approximately the same. Preliminary results make it possible to come the following conclusions.

1. The scattered radiation is observed in the vicinity of frequency $\omega_L + \omega_{pe}$. This fact confirms the excitation of Langmuir turbulence in a plasma.
2. The scattered radiation power exceeds the equilibrium level by over 6 orders of magnetude.
3. The scattered radiation duration corresponds approximately to the duration of the REB current exciting oscillations, as it should be in the case of the Langmuir turbulence excitation.

REFERENCES

1. Breizman B.N., Ryutov D.D. Nuclear Fusion, 1974, v.14, p.873.
2. Burmasov V.S., Vyacheslavov L.V., Kandaurov I.V. et al., Voprosy Atomnoi Nauki i Tekhniki (seriya Termoyaderniy Sintez), 1987, N 2, p.31.
3. Apollonov V.V., Vaskovsky Yu.M., Zhavoronkov M.I., Kvantovaya electronika, 1985, v.12, N 1, p.5.

INTERFEROMETRY AND REFLECTOMETRY DIAGNOSTICS FOR RFX

A.Buffa, P.Innocente, S.Martini, M.Moresco, E.Spada, E.Zilli

Istituto Gas Ionizzati del C.N.R., Associazione EURATOM-ENEA-CNR
Corso Stati Uniti,4 Padova, Italy

Abstract A multichord CO_2 interferometer, a reflectometer and a 6-chord FIR interferometer-polarimeter are being designed for RFX, the new large RFP machine under construction at Padua. The motivations in favour of the use of these diagnostics on RFX are discussed. The main features of the apparatuses are presented and some specific problems and original technical solutions are highlighted.

1. INTRODUCTION The availability of detailed measurements of the density behaviour in space and time and of as much as possible information on the internal magnetic field profile is considered of crucial importance [1] for RFX (a=0.5 m, R=2m, I=2MA). To achieve this goal, a CO_2 interferometer, a microwave reflectometer and an FIR interferometer-polarimeter are being developed.

2. THE CO_2 INTERFEROMETER The main interferometer for density profile measurements will be a multichord two-colour (CO_2 laser λ=10.6 μm, CO laser λ=5.3 μm) system similar to that developed [2] for the ETA-BETA II RFP. The CO_2 interferometer has been chosen mainly for two reasons: it allows to have many chords, hence a good profile reconstruction, despite the limited access available and it does not suffer from refraction even in very high density gradient plasmas, such as those which might be produced by pellet injection.

The choice of building a vibration compensation system at λ=5.3 μm instead of using shorter wavelengths [3,4], gives several advantages [2] in terms of vibration tracking capability, misalignment immunity, required surface quality and accuracy of the optics.

The initial set-up of the interferometer will entail 8 chord spanning the two arms of a granite C-frame (fig.1), and an upgrade to 16 is included in the design, although it will have to utilize also mirrors mounted inside the vacuum vessel (see fig.1). The expected sensitivity is $\leq 10^{18}$ m^{-2}, i.e. $\leq 5 \cdot 10^{17}$ m^{-3}. The design include a real time demodulation system capable of tracking vibrations with a maximum speed of ~50 mm/s and amplitude of ~3 mm, which could be used for density/profile feedback.

3. THE MICROWAVE REFLECTOMETER The millimeter wave wide-band reflectometry is also particularly attractive for RFX because of its ability to operate through only one access of limited cross-section and to work well in presence of density gradients. This tecnique has been successfully used on several Tokamaks, both with ordinary (O) and extraordinary (X) wave propagation, to measure the spatial and temporal behaviour of the electron density or, when operated at a fixed frequency, of the density fluctuations.

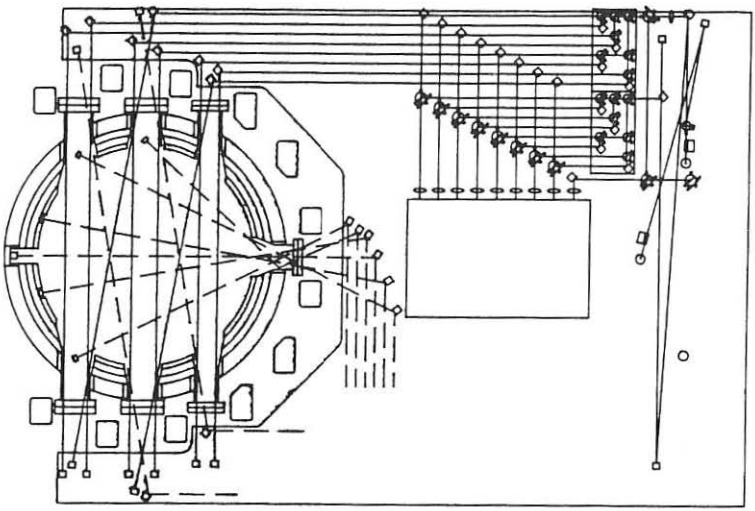

Fig.1 The granite C-frame, the vacuum vessel and the scheme of the 8-chord set-up of the multichord CO_2 interferometer. The dashed lines show the position of the chords for a possible upgrade of the diagnostic.

One of the main doubts about the feasibility of this measurement is connected to the mode mixing between the O and X waves, which can be significant in RFX because of both the large magnetic shear and the long optical path. It has already been shown [4] that (O-wave) reflectometry is still possible in RFX, notwithstanding the presence of important mode mixing, provided the wave is launched (and received) by a set of single T-R antenna with the correct polarization (parallel to the magnetic field at plasma edge). On the other hand, the magnetic field pitch at the edge is not fixed. Typically variations of the order of ±2° during the current flat-top phase of a shot and ±10° between shots with different field programming can be expected.

To evaluate the sensitivity of the diagnostic to an incorrect polarization of the launched wave a numerical simulation of a reflectometry experiment has been performed. A monochromatic wave is launched with a given angle (ϕ) between the polarization vector and the edge magnetic field in a plasma with a given density profile; the reflected signal (amplitude an phase) is calculated by means of a ray-tracing code (RAY-RFP) [5] which takes into account propagation of both O and X (local) modes. The component of the electric field seen by the antenna is then mixed with the local oscillator (homodyne); the frequency of the wave is swept in the appropriate range in order to obtain the interferences fringes. Density profile is then reconstructed from the position (in the frequency domain) of the interference minima. In Fig.2 both the primitive and the reconstructed density profiles are shown for ϕ=0°, 20°, 45°. It appears that a conservative value for the allowed polarization error is ±20°, which is well within the estimated operating range.

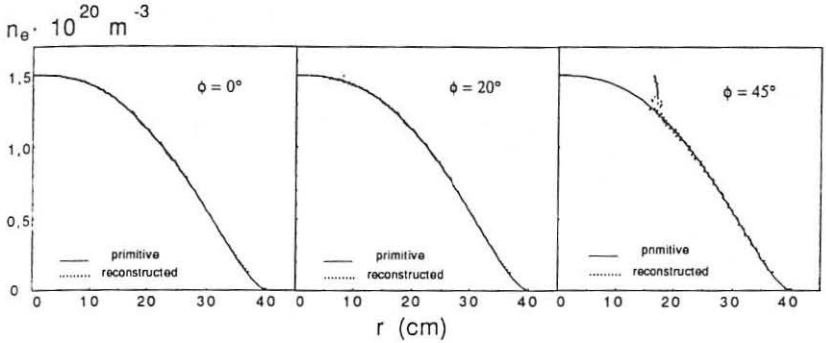

Fig.2 Results of the numerical simulation of the reflectometry experiment for three values of the mismatching angle ϕ. BFM magnetic field and parabolic density profiles have been assumed.

Design criteria have been established for an homodyne reflectometer able to sweep the 22-110 GHz band in about 1 msec covering the density range $6 \cdot 10^{18} \div 1.5 \cdot 10^{20}$ m^{-3}; fundamental waveguide propagation has been preferred for a better control of phase characteristics of the microwave circuit. The frequency interval will be divided into 4/5 bands, depending on the type of sources (BWO or solid state).

The access port is a Φ=96 mm circular pipe. To establish the number of antenna systems it may accomodate with reasonable insertion losses, the round trip losses have been evaluated by means of a modified version of the RAY-RFP code: they resulted typically 24 dB for an array of 4 identical conical horns (Φ=36mm) and 28 dB for 7 horns (Φ=28 mm). In the latter case two or three antennas could be available, for instance, for launching the extraordinary mode wave in order to gather information on the magnetic field profile.

4. THE FIR INTERFEROMETER-POLARIMETER A 6-chord 119 μm (CH_3OH) FIR interferometer-polarimeter is being developed, which will use the CO_2 pumped twin-cavity scheme to produce a frequency shift $\Delta f \cong 1$MHz for hetherodyne detection by Schottky diodes.

Although no more than 6 chords are allowed by the available viewing ports, the system will provide very useful information on the poloidal magnetic field profile. Indeed, two μ&p model [7] RFP profiles, e.g. those shown in fig.3(a), which have the same value of F and θ but different values of α, θ_0 and β_θ, produce quite different Faraday rotation profiles, as shown in fig. 3(b). In other words the two profiles should be distinguished even by a 10% accurate estimate of the Faraday rotation angle, whereas nothing could be obtained from external magnetic field measurements only.

On the other hand the Faraday rotation measurement is easier in a RFP than in a tokamak because of the lower B_ϕ values, which induce much less ellipticity in the polarization of the beams [8]. In fig.4 Faraday rotation angles Ψ, expected for a typical RFP profile with I=1MA and $n_0=10^{20}$ m^{-3}, are compared with the ellipticity ε. It can be seen that the ratio

$|\varepsilon/\Psi|$ is $\leq 5\cdot 10^{-4}$. Since $|\varepsilon/\Psi|$ scales as λ^3 n_0 B^2, even for the worst case which can be expected in RFX, i.e. I=2MA and $n_0=5\cdot 10^{20}$ m^{-3}, the ratio $|\varepsilon/\Psi|$ is $\leq 10^{-2}$ and therefore only a negligible 10^{-4} change is induced [9] in the Faraday rotation angle.

The FIR system will anyway also provide accurate density measurement in the range $5\cdot 10^{17} \div 5\cdot 10^{20}$ m^{-3}, which, together with the CO_2 interferometer and the reflectometer data, will allow to study the propagation of density fluctuations or localized perturbation (such as those produced by pellet injection) and to gain insight in the particle transport.

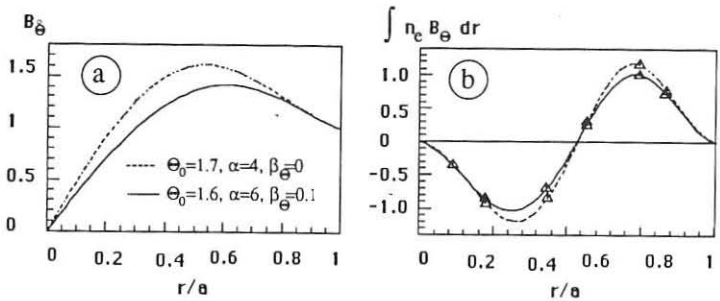

Fig.3 Two different μ&p model magnetic field profiles (a) with the same value of F and θ and the corresponding Faraday rotation profiles (b). Parabolic density and temperature (when β≠0) profiles have been assumed. The triangles indicate the position of the FIR measuring chords.

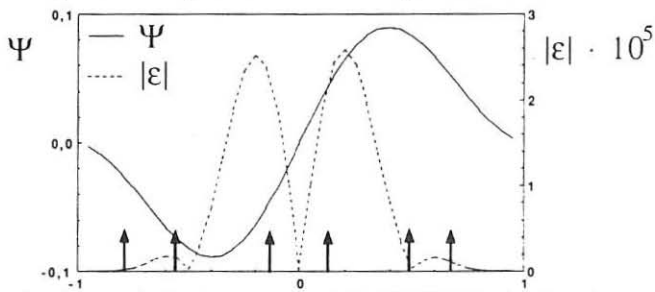

Fig.4 Comparison between the Faraday rotation angle and ellipticity induced in the polarization of the 119 μm FIR beams by a 1MA RFX plasma with I=1MA and $n_0=10^{20}$ m^{-3}. The arrows indicate the position of the measuring chords.

REFERENCES

[1] Trilateral Workshop to Promote Int. Cooperat. on RFP Res., IGI Rep. 87/03 Nov. 1987.
[2] Innocente, P., Martini,S., Rev. Sci. Instr. **59**, (1988) 1571.
[3] T. Carlstrom, et al., Bull. Am. Phys.Soc. **31**, 1534 (1986) .
[4] C.W. Gowers e C. Lamb, J. Phys. E, **15**, 343 (1982).
[5] M. Brambilla, and M. Moresco, Plasma Phys. 29, 381 (1987).
[6] M. Brambilla, and M. Moresco, Report IPP 5/11 Garching bei Munchen (1986).
[7] S.Ortolani, *Course on Mirror Based and Field Rev. Appr.to Magn.Fus.*, Varenna 1983, Vol. II (1984) 513.
[8] S.E. Segre, Plasma Phys. **20**, 295 (1978).
[9] H.Soltwisch, Report Jül - 1638, Jülich (1980).

SPECTROSCOPIC DIAGNOSTIC FOR THE REVERSED FIELD PINCH EXPERIMENT RFX.

Carraro,L., Puiatti,M.E., Scarin,P., Valisa,M.

Istituto Gas Ionizzati del C.N.R., Associazione EURATOM-ENEA-CNR
Corso Stati Uniti,4 - Padova, Italy

RFX is a new reversed field pinch experiment under construction at Padova, with typical plasma parameters $I_\Phi = 1 \div 2$MA, $T_e = 300 \div 600$eV, $n_e = 0.5 \div 1 \times 10^{20} m^{-3}$, $\tau_E = 2 \div 10$ms [1]. The internal wall will be entirely covered by graphite tiles, to protect the liner and avoid heavy impurities contamination. In this scenario, the main impurities will be carbon from the internal armour graphite tiles and desorbed oxygen. In the electron temperature and density range of RFX, the most populated ionization stages will be the He- and H-like ones. Fig.1 shows an example of the time evolution of carbon and oxygen ions, as obtained from a zero-dimensional model in which the electron temperature and plasma current time behaviour are also calculated [2]; this example corresponds to a flat-top temperature of 370eV, with $I/N = 2 \times 10^{-14}$ Am. A metal contamination has also been considered. Fig.2 shows the time behaviour of nickel ions (nickel is the main component of the liner) with the same temperature and density evolution: in this case, the Ne-like NiXIX is the dominant ion . As for the He-like and H-like ions of light impurities, also NiXIX and the neighbouring ions emit essentially in the XUV range ($\lambda \leq 300$Å), which is therefore the crucial range for RFX spectroscopic diagnostic.

The radial distribution of light impurity ions has been studied by means of a one-dimensional transport code, in which the ion diffusion equations are solved [3]. Fig.3 shows an example of carbon and oxygen distributions at two times; here the impurities are supposed to enter from the wall in the first 50 ms, and to spread with a diffusion coefficient 10 times the classical one. Parabolic temperature and density profiles are assumed. Also in these conditions, after the discharge setting-up(about 20-30msec) most of the impurities are in high charge ionization stages; ions with lower charge are present only in an external layer of about 5cm.

Following these considerations, two spectrographs cover the XUV region of the spectrum: the first one is a low resolution flat-field grazing incidence [FFGI] ($\alpha = 71^0$) [4] and has the main objective of providing for each discharge a survey of the impurity emission over the whole range $100 \div 1100$Å (see table I, where all the spectroscopic instruments are listed with the corresponding wavelenght range). The second is a 2m extreme grazing incidence spectrograph [EGI] ($\alpha = 89^0$) [5] for high resolution spectroscopy in the range $10 \div 340$Å (with a 600g/mm grating), equipped with two MCP detectors , to cover simultaneously two wavelenght ranges. The extreme grazing incidence spectrometer will be absolutely calibrated: in the range $10 \div 114$Å against an absolute photon counter at the K_α lines of elements between Mg and Be, produced by a low-power X-rays source [6]. This calibration can be extended at longer wavelenghts by the

branching ratio technique, using carbon, oxygen and helium lines [7,8]. In this way the EGI spectrometer yields absolute intensities of impurity resonance lines, from which ion populations may be calculated by a collisional-radiative model. A further aim is the determination of the electron temperature from line intensity ratio of resonance and intercombination lines of He-like ions [9] . The extreme grazing incidence spectrometer calibration may be transferred to the flat-field instrument in their overlapping range (100-700Å with a 300g/mm grating on the EGI); the flat-field spectrometer calibration may be extended at higher wavelenghts by branching ratio, using helium and hydrogen line pairs.

A spectroscopic diagnostic at longer wavelenght is also important, not only to cover the remaining emission spectrum, but also to study line profiles. In RFX the whole spectral region between 1200 and 8000Å will be observed with one high resolution spectrometer, a vacuum Czerny-Turner (focal lenght 1.3m and f-number 12) [VCT] , with one detector , consisting in a MCP intensifier coupled to a photodiode array (PDA). The photocathode will be for one half (semi-circle) a CsTe type and for one half a trialkali (S-20) type; the window is a plano-plano MgF_2 plate. The phosphor is P11, to allow a high time resolution. Indeed the PDA is characterized by a very fast read-out time (0.25ms for 1025 pixels), with time sequencing and data acquisition accomplished by standard Camac modules. This fast read-out time is necessary to study the impurity time behaviour in RFX: infact, as shown in fig.1, the characteristic times of the ionization evolution are less than the minimum integration time of a standard PDA (16ms). The VCT spectrometer will be absolutely calibrated by a MgF_2 windowed deuterium lamp in the range 1200-3700Å , and by a tungsten lamp at longer wavelenghts. By these three absolutely calibrated spectrometers (FFGI, EGI, VCT) the electron temperature from line intensity ratio for ions from He-like to B-like may be measured (table II). The ion temperature may also be obtained from Doppler broadening for ions between He-like to B-like using the VCT spectrometer. In particular, this will allow the study, in terms of temperature and radiation, of the edge region of the plasma, where the lower charged ions are localized.

In the UV-visible range plasma emission will be measured along 9 chords, to obtain a spatial resolution of emitted lines and continuum emission: this allows the study of the impurity diffusion in the plasma and the experimental evaluation of the plasma effective charge profile. For each chord, the light is collected by a telescope and transferred by a fused silica 600μm core optical fiber 18m long to a Czerny-Turner monochromator (focal lenght=0.65m, f-number=5) [CT], where, after dispersion, is detected by a photomultiplier. This instrument is optically designed to avoid cross-talk of the different fibers if they are vertically placed on the entrance slit at an axis-to-axis distance of 1.5mm between adjacent fibers. At the same time, for each chord another fiber carries the light to a changeable interference filter (10Å bandwidth) [IF], to measure continuum radiation (with the possibility to verify simultaneously with the spectrometer that the spectral interval is line-free) and to monitor the emission of pre-selected lines. The CT instrument may be used also as a spectrograph with a photodiode array as detector on a single chord; in this configuration, in order to reduce the scattered light and measure weak lines, the instrument has an optional filter stage (double pre-dispersing monochromator with spherical gratings in subtractive configuration). This system works in the range 2500-8000Å, where the emission is essentially due to low charge ions, localized (after the setting-up) in the external plasma region: this permits the study of the edge region and of plasma-wall interactions.

[1] Giubbilei,M., et al.,this conference
[2]Antoni,V.,et al.,12th Int.Conf.on Plasma Phys. and Contr. Nucl. Fus. Res., Nice(France)1988(to be published)
[3] Carraro ,L.,et al., 15th Europ. Conf. on Contr. Fus. and Plasma Heating, Dubrovnik, 1988, vol 12B, partII, p.561
[4]Fonck,R.J., et al., Applied Optics, 21, (1982) 2115
[5]Schowb,J.L., et al., Rev Sci. Instrum. 58(9) (1987)1601
[6]Terry,J.L., et al., PFC/CP-86-11 (1986)
[7] Gabriel, A.H., Jordan,C., "Cases studies in Atomic Collision Physics", North Holland (1972)266
[8]Ortolani,S, et al., Plasma Physics 27 (1985)69
[9] TFR group, DoyleJ.G. and Schwob,J.L., Jour. Phys.B: At. Mol. Phys. 15 (1982)813

TABLE I : spectroscopic instruments with corresponding spectral range

INSTRUMENT	SPECTRAL RANGE
EGI	10-340Å
FFGI	100-1100Å
VCT	1200-8000Å
CT	2500-8000Å
IF	visible

TABLE II: couples of lines for electron temperature measurements

ION	λ(Å)		Spectrometer
OVII	21.8	21.6	EGI
CV	40.73	40.27	EGI
OVI	150.1	1031.9	EGI, FFGI
CIV	312.4	1550.8	EGI, VCT
OV	172.2	629.8	EGI
CIII	386.2	977.0	EGI, FFGI
OIV	238.5	790.2	EGI, FFGI
CII	687.3	1335.3	EGI, VCT

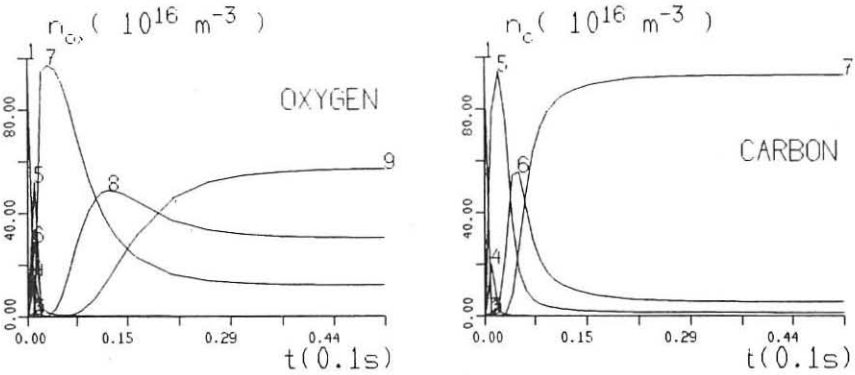

Fig.1: Time evolution of oxygen and carbon ion populations

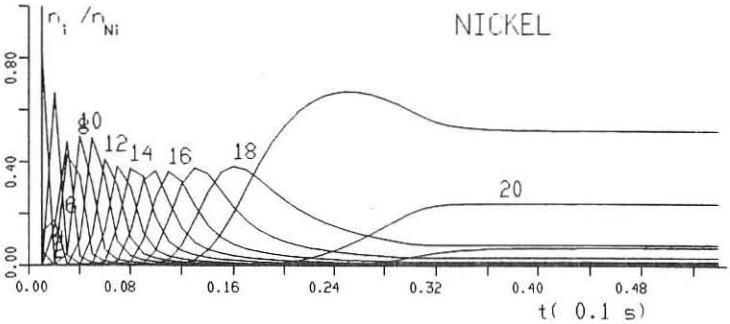

Fig.2 Time evolution of normalized nickel ion populations

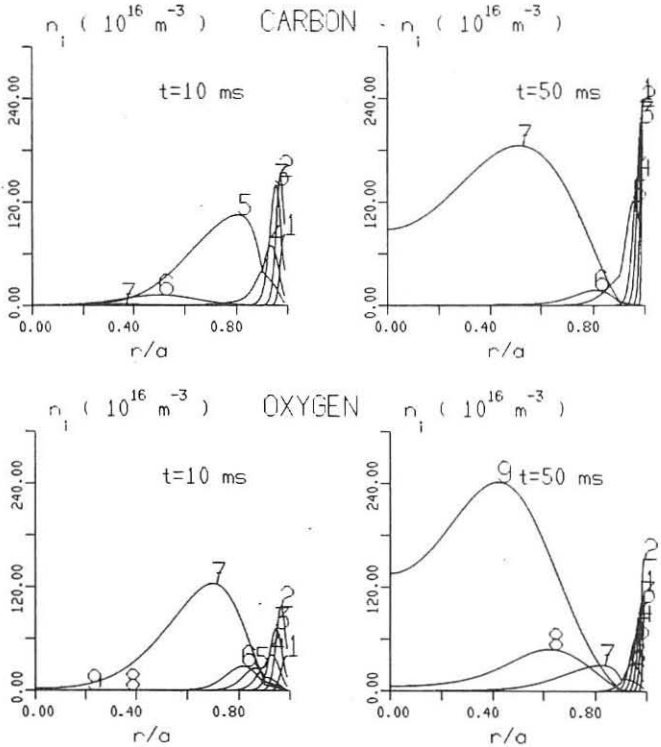

Fig.3: Radial distributions of carbon and oxygen ion populations

COLLECTIVE SCATTERING OF ELECTROMAGNETIC WAVES IN THE PRESENCE OF SUPRATHERMAL ELECTRONS

M. Lontano, U. Tartari

Istituto di Fisica del Plasma, EURATOM/ENEA/CNR Association
Milano, Italy

Introduction

The availability in the near future of high power ($P > 200$ kW), high frequency ($f > 100$ GHz) gyrotrons, besides heating and current drive experiments in new operational regimes (e.g. at high plasma densities), will allow measurements of spectra of electromagnetic (EM) waves scattered on collective plasma density fluctuations, in conditions where very severe requirements on the observation geometry would be imposed if laser sources were to be used. Collective Thomson scattering (CTS) allows to investigate the plasma response to those additional heating methods which release most of the input power to the electron population (ECRH/1/, LHH in the electron regime/2/), possibly creating non equilibrium electron distributions.

Here we present a preliminary investigation of the effects of suprathermal electrons on the CTS spectrum. Pines and Bohm /3/ and Perkins and Salpeter /4/ have pointed out that, in an unmagnetized plasma, the presence of high energy electrons leads to the excitation of oscillations at the plasma resonance above the thermal level. We have studied the spectrum of density fluctuations of a non thermal, magnetized plasma, focussing the attention to the high frequency resonant electron feature for $k\lambda_{De} < 1$. The high frequency spectrum of the scattered radiation is analyzed within the classical approximation for the collisionless wave damping; the effects of a relativistic treatment, of the Coulomb collisions and of anisotropic distribution functions are also briefly discussed.

Suprathermal effects in a collisionless magnetized plasma

It is well known /5/ that, given an incident wave with frequency ω_i and wavevector $\underline{k}_i$, the power scattered from the electrons in the frequency range $d\omega_s$ and in the solid angle $d\Omega$ is proportional to the spectral density function $S(\underline{k}_s - \underline{k}_i, \omega_s - \omega_i)$ defined in terms of the power spectrum of the density fluctuations:

$$S(\underline{k},\omega) = \lim_{\Gamma \to 0} \frac{2\Gamma}{V} \left\langle \frac{|\tilde{n}_e(\underline{k},\omega)|^2}{n_o} \right\rangle \qquad (1)$$

where $\underline{k}_s$ and ω_s are the wavevector and the frequency of the scattered radiation, V is the scattering volume, the angular brackets denote the

ensemble average on the initial particle positions and the measurement is performed in a time $T \sim 1/\Gamma$.

In the frequency interval $\omega \gtrsim \omega_{pe}, \omega_{Be}$ (the electron plasma and cyclotron frequencies, respectively) ion motion can be neglected and the spectral function (1) takes the form/6,7/:

$$S(\underline{k}, \omega) \simeq -\frac{2}{\alpha^2 \omega} \mathrm{Im}(1/\varepsilon_L) \cdot T_{fl}/T_o, \tag{2}$$

where $\alpha = 1/k\lambda_{De}$ is the Salpeter parameter, ε_L is the dielectric permittivity for longitudinal waves and T_o is the plasma temperature; T_{fl} will be defined and discussed later.

Around the plasma resonance $\omega \approx \omega_o(\underline{k})$, where $\mathrm{Re}\,\varepsilon_L(\omega_o) = 0$, we have

$$\mathrm{Im}(1/\varepsilon_L) \simeq -\frac{\pi}{\varepsilon'_{RO}} \mathcal{J}(\omega, \underline{k}) \tag{3}$$

with $\mathcal{J}(\omega, \underline{k}) = \frac{1}{\pi} \frac{|\Gamma|}{(\omega - \omega_o)^2 + \Gamma^2}$, $\Gamma = -\frac{\mathrm{Im}\,\varepsilon_L}{\varepsilon'_{RO}}$, $\varepsilon'_{RO} = \frac{\partial \mathrm{Re}\,\varepsilon_L}{\partial \omega_o}$.

Furthermore, in a thermal plasma $T_{fl} = T_o$. Eqs.(2) and (3) show that for an equilibrium plasma the scattered spectrum is peaked around the upper hybrid frequency $\omega_o \simeq \omega_{UH}$, the line shape being a Lorentzian whose width at half height is the collisionless damping coefficient Γ.

For an arbitrary electron distribution function $f_e(\underline{v})$ (normalized to unity), the "fluctuation temperature" T_{fl} can be defined as follows:

$$\frac{T_{fl}}{m_e} \equiv -\frac{\int d^3v\, \eta(\omega, \underline{k}, \underline{v})\, f_e(\underline{v})}{\int d^3v\, \eta(\omega, \underline{k}, \underline{v})\, \hat{\mathcal{L}}\, f_e(\underline{v})}, \tag{4}$$

where $\eta(\omega, \underline{k}, \underline{v}) \propto \sum_{\ell} \delta(\omega - k_{\parallel} v_{\parallel} - l\,\omega_{Be})\, J_{\ell}^2(b_e)$ (5)

is the emissivity for longitudinal waves, $b_e = k_{\perp} v_{\perp}/\omega_{Be}$, $\omega_{Be} > 0$ and

$$\hat{\mathcal{L}} \equiv \frac{k_{\parallel} v_{\parallel}}{\omega} \left[\frac{1}{v_{\parallel}} \frac{\partial}{\partial v_{\parallel}} - \frac{1}{v_{\perp}} \frac{\partial}{\partial v_{\perp}} \right] + \frac{1}{v_{\perp}} \frac{\partial}{\partial v_{\perp}}. \tag{6}$$

In order to study the spectral density function in the presence of suprathermals, we model the electron distribution function with the sum of two Maxwellians:

$$f_e(\underline{v}) = (1 - \epsilon)\, g_o(v^2) + \epsilon\, g_1(v^2) \tag{7}$$

where $g_a(v^2) = \frac{1}{\pi^{3/2} v_{Ta}^3} \exp(-v^2/v_{Ta})$, $v_{Ta} = (2T_a/m_e)^{1/2}$ and $a = 0,1$ for thermal and non thermal electrons, respectively; furthermore we consider $\epsilon = n_1/n_o$ and $\Lambda^{-1} = T_o/T_1$ as small parameters.

To simplify the analysis we assume that $\omega^2_{pe}/\omega^2_{Be} \lesssim 1$, as it is the case in most practical situations, so that only the $l = 1$ term contributes in eq.(5) and in the computation of the collisionless damping; in other words we restrict ourselves to the frequency range: $\omega_{Be} \lesssim \omega \sim \omega_{UH} << 2\omega_{Be}$. From the standard linear theory the damping coefficient turns to be exponentially small, provided $k_{\parallel}$ is not too large, and we can replace in eq.(3) $\lim_{\Gamma \to 0} \mathcal{F}(\omega, \underline{k}) = \delta[\omega - \omega_o(\underline{k})]$ and obtain

$$\mathrm{Im}(1/\varepsilon_L) \simeq -\frac{\pi}{2}\frac{\omega_{pe}^2}{\omega_o}\cdot\delta(\omega-\omega_o),$$

which doesn't depend on the presence of suprathermal electrons. Observing that for a thermal plasma the spectral density function is /5/:

$$S_{th}(\underline{k},\omega) = \pi\frac{1}{\alpha^2}\frac{\omega_{pe}^2}{\omega_o^2}\delta(\omega-\omega_o),$$

we can rewrite eq.(2) in the form

$$S(\underline{k},\omega) = S_{th}(\underline{k},\omega)\cdot\frac{T_{fl}}{T_o}\bigg|_{\omega=\omega_o} \tag{8}$$

where the effect of the energetic electrons is all included in the factor T_{fl}/T_o. Using eqs.(4 ÷ 7), in the non relativistic limit we then obtain:

$$\frac{T_{fl}}{T_o} \simeq \frac{(1-\epsilon)e^{-z_{ol}^2}e^{-\beta}I_1(\beta) + \frac{\epsilon}{\Lambda^{1/2}}e^{-z_{1l}^2}e^{-\beta\Lambda}I_1(\beta\Lambda)}{(1-\epsilon)e^{-z_{ol}^2}e^{-\beta}I_1(\beta) + \frac{\epsilon}{\Lambda^{3/2}}e^{-z_{1l}^2}e^{-\beta\Lambda}I_1(\beta\Lambda)}, \tag{9}$$

where $\beta = \frac{k_\perp^2}{k^2}\frac{1}{\alpha^2}\frac{\omega_{pe}^2}{\omega_{Be}^2}$, $z_{al} = (\omega - \omega_{Be})/k_{\parallel}v_{Ta}$ and I_1 is the Bessel function of imaginary argument. For not too small $k_{\parallel}$ values the suprathermal contributions are negligible and $T_{fl}/T_o \approx 1$. When $k_{\parallel} \to 0$, due to the factor $\Lambda \gg 1$ in the exponents the thermal contributions become exponentially small while the suprathermal terms remain finite; in this case we obtain:

$$T_{fl}/T_o \simeq \Lambda = T_1/T_o, \tag{10}$$

so that we have the significant result that the enhancement of the CTS signal over the thermal level turns to be directly proportional to the average energy of the suprathermals and independent of their fraction. Only the width of the $k_{\parallel}$ interval around $k_{\parallel} = 0$ where this enhancement manifests itself does depend on ϵ, approaching zero for $\epsilon \to 0$.

Limits of the model

We have considered three possible effects which could modify the picture outlined in the previous section:

a)**relativistic treatment of wave-particle interaction**; if in eq.(5) the argument of the δ-function is replaced with the relativistic expression $\gamma - N_{\parallel}u_{\parallel} - lY$,, where $\underline{u} = \underline{p}/mc$, $\gamma = (1 + u^2)^{1/2}$, $Y = \omega_{Be}/\omega$,

$N_{\parallel} = ck_{\parallel}/\omega$, the damping coefficient $\Gamma \neq 0$ only if $N_{\parallel} > N_{cr} = (1 - Y^2)^{1/2}$, being $Y < 1$ since $\omega_{UH} > \omega_{Be}$; for $N_{\parallel} > N_{cr}$ the resonant electrons are mainly located in the suprathermal range of energies in the plane $u_{\parallel}$,$u_{\perp}$ so that again a relation similar to eq.(5) is expected to hold.

b)**Coulomb collisions**; as we have seen when $k_{\parallel} \to 0$ both in the classical and in the relativistic treatments (if $Y < 1$) $\Gamma \to 0$ and the collisional spreading of the resonant line should be considered; in the $k_{\parallel}$ range where eq.(10) holds, the classical theory shows that for $\epsilon \gtrsim 10^{-3}$ no appreciable change in the general picture is introduced by a "global" collisional frequency $\nu_c/\omega_{Be} \lesssim 10^{-5}$.

c)**anisotropic distribution function**; a relevant question concerns the sensitivity of the result (10) to the anisotropy of the suprathermal distribution; for example, assuming a two temperature Maxwellian it is easily shown that, in the non relativistic approximation, eq.(10) becomes:

$$\frac{T_{fl}}{T_o} = \frac{T_1}{T_o} \; \frac{3R}{R+2} \; \frac{1}{1-Y(1-R)} \tag{11}$$

where $R = T_{\parallel}/T_{\perp}$ and $3T_1/2 = T_{\parallel}/2 + T_{\perp}$; eq.(11) shows that for $0.25 < R < 4$ no appreciable changes in T_{fl}/T_o are introduced due to the anisotropy.

Conclusions

We have analyzed the high frequency CTS spectra relevant to a magnetized plasma in the presence of a small suprathermal electron population, which can simulate the effect of an external electron heating. When the scattering plane is almost perpendicular to the magnetic field, the electron feature at the upper hybrid resonance is very sensitive to the presence of energetic electrons in the scattering volume, the scattered power in the resonant line being enhanced by the ratio between the average suprathermal energy and the bulk temperature, independently of the fraction of suprathermal electrons. This peculiarity allows one to obtain useful informations on the spatial distribution of the energy of the suprathermals and, if combined with ECE measurements, on their density distribution.

References

/1/ R.E. Slusher, C.M. Surko, Phys. Fluids, 23, 472 (1980);

/2/ R.E. Slusher et al., Phys. Fluids, 25, 457 (1982);

/3/ D. Pines, D. Bohm, Phys. Rev., 85, 338 (1952);

/4/ F. Perkins, E.E. Salpeter, Phys. Rev., 139A, 55 (1965);

/5/ J. Sheffield, **Plasma Scattering of Electromagnetic Radiation**, Academic Press, New York (1975), Ch. VIII;

/6/ G. Bekefi, **Radiation Processes in Plasmas**, Wiley, New York (1966), Sect. 4.6;

/7/ A.G. Sitenko, **Electromagnetic Fluctuations in Plasma**, Academic Press, New York (1967), Ch. V.

SPACE- AND TIME-RESOLVED DIAGNOSTIC OF LINE EMISSION FROM THE SEPARATRIX REGION IN JET X-POINT PLASMAS

P Chabert*, C Breton*, C DeMichelis*, B Denne, R Giannella, N Gottardi, G Magyar, M Mattioli*, J Ramette*, and B Saoutic*

JET Joint Undertaking, Abingdon, Oxon., OX14 3EA, UK
* EURATOM-CEA Association, Cadarache 13108 St Paul lez Durance, FRANCE

1. INTRODUCTION The SPEX GISMO VUV spectrometer installed on JET has appeared to be appropriate to study the impurities radiation during X-point operation [1]. Preliminary results have been obtained with 2 of the 3 spectrometers. They concern mainly the light impurities emission, C III, O VI in the vicinity of the X-point during the transition from L to H mode. The results are reported for both single X and double X discharges and future prospects are assessed.

2. INSTRUMENTATION As described in more detail in ref.[1] the diagnostic is made up of 3 spectrometers, 2 viewing in the horizontal direction, one viewing vertically. Each of them scans the plasma by means of a rotating mirror providing typically one angular profile in 10 msec every 100 msec. Furthermore, each mirror can be stopped at any predetermined position so as to obtain time evolution along fixed chords. The light is diffracted by a grazing incidence grating, and 3 wavelength can be monitored simultaneously. The 2 UV detectors cover the wavelength range from 100 A to 2500 A. The auxiliary slit of the spectrometers defines a spatial resolution of a few cm in the X-point region.

A poloidal cross-section of the JET machine and the port of the diagnostic can be seen in Fig.1, together with the mirrors of the horizontal spectrometers. The spectrometers are referred as UH (upper horizontal), LH (lower horizontal) and scan respectively the lower and upper halves of the plasma.

The plot of the poloidal magnetic surfaces for a typical single X-point discharge shows that the X-point corresponds to a mirror angle between 12 and 14°.

3. RESULTS Figure 2 shows the time evolution of the C III line integrated signal observed by UH and LH at an angle of 14°. The formation of the X-point give rise to a strong signal at the top of the plasma while the corresponding signal at the bottom decreases. This is consistent with the bolometer data.

The H-mode transition causes a sudden fall in the carbon signal for both UH and LH.

Figure 3 is an example of fast fluctuation commonly observed on O VI signal, along the line-of-sight between 10° and 14°, after the injection of neutral beam. As they are correlated with the spikes observed on Dα and poloidal coils, they are considered to be due to ELM instabilities [2]. The sudden drop in the frequency at the L-H transition preceeds the termination of the ELMS, as observed previously [3].

Figure 4(a) shows a typical example of the angular profile evolution of O VI emission in single null discharges. The X-point establishment phase shows clearly a rise in the emission at 14°. The resulting profile is quite consistent with what is commonly observed by bolometry [4]. The start of NBI can cause ELM fluctuations to occur for a short time, changing the profile in an artificial way, the period of the fluctuations being smaller than the scanning time.

The profile eventually stabilises to the one shown in dotted line in Fig.4(b) which is quite similar to those before NBI. The L-H transition (as seen by the drop in D_α) shows a shrinking of the profile, with the appearance of a new peak apparently located on the inner side of the X-point which last until the end of the H-mode. Without the vertical line it is not possible to know the direction in which the maximum of radiation has moved.

Figure 4(a) has to be compared with fig.5 (L mode case) where the neutral beam injection causes a sudden burst of O VI radiation. (The small bumps observed are due to ELM fluctuations and are not spatial variations for the reasons given above.)

Figure 6 shows the time behaviour of O VI emission profile in double null H-mode discharge for the upper and lower spectrometers. It should be noted that the profiles are narrower than in the single null case. The H-mode causes a slight decrease in both the upper and lower signals.

4. CONCLUSION AND FUTURE PLANS A preliminary study of the impurities radiation from the X-point region during H-mode discharges has been undertaken. Further investigations, carried out in 1989 will require the implementation of the vertical line, to localise more accurately the bright region near the X-point, as well as an absolute calibration of the detector so as to give an estimate of the radiated power.

REFERENCES

[1] K H Behringer et al., Course and Workshop on basic and advanced diagnostic techniques for fusions plasma, Varenna 1986, Vol.1, p.305.
[2] P Cripwell et al., This conference.
[3] A Hubbard et al., Proc. 15th EPS Dubrovnik, May 1988.
[4] H J Jaeckel et al., Proc. 14th EPS Madrid, June 1987.

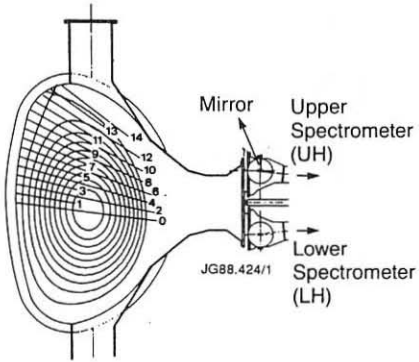

Fig.1: JET vacuum vessel octant 6 showing 2 rotating mirrors of the horizontal spectrometers. Also shown are several lines-of-sight for various angles of the lower mirror together with a typical poloidal flux plot in upper single X-point discharge.

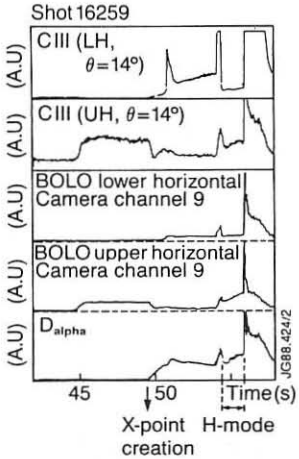

Fig.2: Time evolution of C III line integrated intensity (λ=977 Å) together with bolometer and Dα signals in upper single null H-mode. The chords of the bolometers correspond roughly to those of the spectrometers. (NBI at 54 sec)

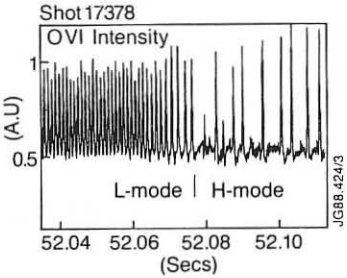

Fig.3: Edge fluctuations on O VI signal (λ=1032 Å) during an L-H transition, in upper single null discharge. Signal viewed by LH with θ=12°.

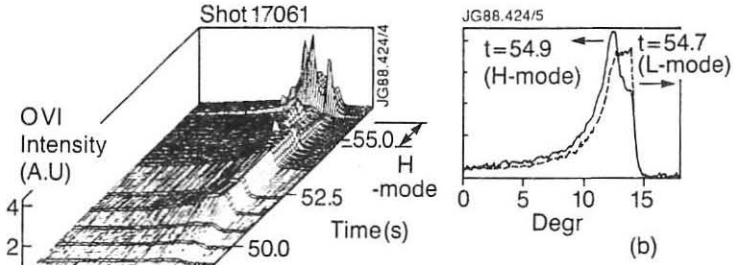

Fig.4: a) time evolution of the angular profile of O VI line integrated intensity (λ=1032 Å) seen by LH. H-mode in upper single X-point. I_p=3 MA, B_T=2.2T, NBI power = 12 MW, NBI starts at 54.5 sec.

b) detail of the L-H transition.

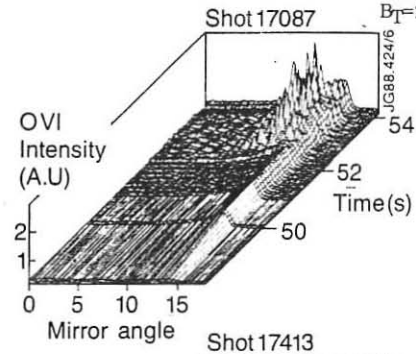

Fig.5: Same parameters as fig.4 for an L-mode in upper single X-point. I_p=3 MA, B_T=2.2T, NBI power = 8 MW, NBI starts at 52 sec.

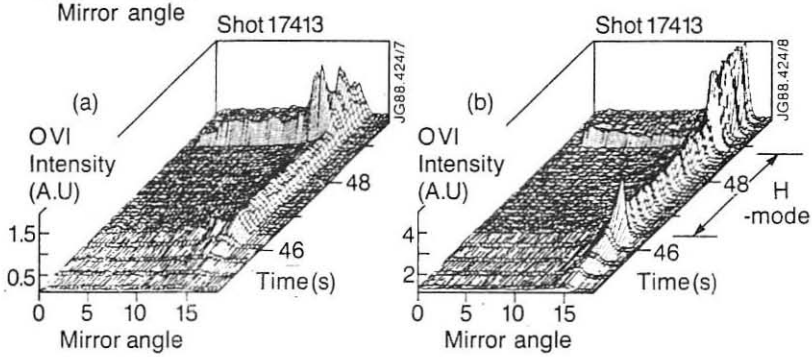

Fig.6: Time evolution of O VI intensity profile in double X-point H-mode. NBI power = 6 MW, NBI starts at 46 sec.
a) LH b) UH.

PHYSICS ASPECTS OF A THOMSON SCATTERING DIAGNOSTIC FOR FAST ION AND ALPHA PARTICLE VELOCITY DISTRIBUTIONS IN JET

T P Hughes*, D A Boyd**, A E Costley, J A Hoekzema,
S R P Smith+ and E Westerhof++

JET Joint Undertaking, Abingdon, Oxon, OX14 3EA, UK
* Permanent address: University of Essex, Colchester, CO4 3SQ, UK
**Permanent address: University of Maryland, College Park, Maryland 20742, USA
+ University of Essex, Colchester, CO4 3SQ, UK
++ FOM-Instituut voor Plasmafysica, Rijnhuizen, The Netherlands

1. INTRODUCTION

A diagnostic system to measure the velocity and spatial distributions of fast ions in JET is being designed, based on collective scattering of microwaves from a high power (up to 1 MW), modulated, long pulse (up to CW) gyrotron. Several of the simplifying assumptions usually made for scattering in the visible or infrared will not be valid. Following a brief description of the diagnostic, we discuss aspects of the relevant physics and present some results of detailed calculations.

2. THE DIAGNOSTIC SYSTEM

For incident radiation with frequency ω_I and wave vector $\underline{k}_I$ the scattered radiation with ω_S and $\underline{k}_S$ at an angle θ to $\underline{k}_I$ is due to density fluctuations with $\omega = \omega_S - \omega_I$ and $\underline{k} = \underline{k}_S - \underline{k}_I$. If $\alpha \equiv 1/|\underline{k}|\ \lambda_D \gtrsim 1$, the shielding electrons moving with each ion scatter collectively and the scattered spectrum contains features dependent on the ion velocity distributions. The spectral function S is the sum of contributions from all particle species, including contributions from the various thermal plasma ions, from DT reaction product alpha particles slowing down from their birth energy of 3.5 MeV and from fast ion populations created by neutral beam injection or RF heating. The ion velocities along $\underline{k}$ are mapped on to the frequency shift of the scattered radiation: $\Delta\nu_i = \underline{k}\cdot\underline{v}_i/2\pi$.

The gyrotron frequency is selected to minimize noise due to electron cyclotron emission while ensuring access to the plasma centre. There is a minimum in the ECE spectrum between ν_{ce} and $2\nu_{ce}$, near 140 GHz at B = 3.4 T. At this frequency the plasma is accessible for 'O' mode radiation up to the cut-off density of $2.4 \times 10^{20}\ m^{-3}$.

To measure the expected alpha particle contribution to the scattered spectrum under JET conditions we need $\alpha \gtrsim 2$. For JET plasmas this requires $\theta \lesssim 60°$. If θ is reduced the signal-to-noise ratio improves but the spatial resolution deteriorates: the optimum will probably be in the range $20° \lesssim \theta \lesssim 40°$. To simplify interpretation the angle ϕ between $\underline{k}$ and $\underline{B}$ will normally be restricted to $\phi < 80°$, to avoid severe magnetic field effects.

Modulated radiation from the gyrotron is injected via a steerable mirror. Scattered radiation is collected in the similar, steerable antenna pattern of the receiver. The antennas will be located symmetrically about the horizontal midplane of the torus (for details see Costley et al, JET-R(88)08, 1988).

3 EFFECTS OF REFRACTION

The refractive index of the plasma, μ, is given by the Appleton-Hartree formula. In the proposed system the injected beam will be 'O' mode and the scattered 'O' mode will be detected. Refraction can be substantial: typically, $0.7 < \mu('O') < 1$ in JET.

The refractive index has an important direct effect on the scattered spectrum, because $\underline{k} = \underline{k}_S - \underline{k}_I = \frac{\omega_I}{c} \mu_I \hat{\underline{k}}_I - \frac{\omega_S}{c} \mu_S \hat{\underline{k}}_S$, so the frequency shift corresponding to a given ion velocity depends on μ_I and μ_S.

Refraction also modifies the paths of the incident and scattered beams. We have used a modified TORAY code (Kritz et al, PPPL-1980, 1983) as follows: (a) for given position and orientation of the injector, follow the central ray into the plasma and find the point P of intersection with a specified plane (eg. the horizontal mid-plane). (b) for given position of the receiver, find by iteration the orientation which brings the central ray of its antenna pattern to P. (c) find $\underline{k}_I$, $\underline{k}_S$, $\underline{B}$, n_e, T_e at $\underline{P}$, remembering that the ray direction is not in general the same as $\underline{k}$.

The diagnostic will use focused, near-Gaussian beams with $w_0 \sim 3$ cm. We have devised an approximate method of calculating the behaviour of simple Gaussian beams based on the fact that the hyperboloid which defines the beam may be generated from a set of straight lines. We take several generators spaced around the axis of each beam and we follow them through the plasma. Figure 1 shows the intersections with three horizontal planes. The generators do not accurately represent the direction of propagation, but the patterns they create are well centred on the axes of the beams and indicate the shape of the scattering volume.

Effects of density fluctuations on the patterns are being studied.

4. THE SCATTERING CROSS-SECTION

It will be shown elsewhere that for similar incident and scattered antenna patterns with Gaussian radius w, the scattered power detectable by a heterodyne receiver in a resolving bandwidth $\Delta\nu$ Hz is

$$P_S = P_I \, n_e \, \Delta\nu \, r_0^2 \, \lambda_S^2 \, S(\underline{k},\omega) \; G/(\pi^{1/2} w \sin\theta_r) \qquad (1)$$

where G is a function of the incident and scattered polarization vectors, the dielectric tensors and the scattering geometry, and $r_0^2 = 7.94 \times 10^{-30} m^2$. 'O' to 'X' scattering can be strong just above the upper hybrid frequency but is unlikely to affect the detection of 'O' to 'O' scattering.

5. SIGNAL-TO-NOISE RATIO

The noise power received by a heterodyne detector in bandwidth $\Delta\nu$ Hz may be characterised by an effective temperature T_N(eV):

$$P_N = 1.6 \times 10^{-19} \, T_N \, \Delta\nu \; W \qquad (2)$$

For JET plasmas a typical value for T_N at 140 GHz is about 500 eV. This is expected to be the main source of statistical noise.

Although the gyrotron beam path never takes it near a zone where it approaches the rest mass cyclotron resonance, in hot JET plasmas there is still some significant cyclotron absorption. The absorbed power will cause increased electron cyclotron emission; as this extra emission is in phase with the modulated gyrotron power it will not be distinguishable from the scattered signal. The cyclotron resonance condition for the second harmonic (the significant resonance in this case) is

$k - k_{\parallel} \beta_{\parallel} - 2k_{co} (1-\beta^2)^{1/2} = 0$, where k is the free space wavenumber of the gyrotron radiation, $k_{\parallel}$ is its component parallel to the magnetic field, k_{co} the wavenumber associated with the rest mass cyclotron frequency, β the velocity of the resonant electrons normalized to c and $\beta_{\parallel}$ its component parallel to the magnetic field. This condition determines the surface in velocity space on which the gyrotron power is absorbed (see Figure 2). The same equation with slightly different parameters stipulates the condition for cyclotron emission to be detected by a receiver channel. The differences arise because the receiver is tuned to a frequency different

from the gyrotron and its antenna points in a different direction which produces a different Doppler shift. For these resonance curves see the figure. At the intersection of the two curves are those few electrons which both absorb gyrotron power and emit power which can be detected by the receiver. Calculations suggest that the extra modulated power received as a result of this process is negligible.

With phase sensitive detection and an integrating time τ, the final signal-to-noise ratio of the system is

$$s/n = (P_S/P_N)\ (1 + \tau\Delta\nu)^{1/2}/(1 + P_S/P_N) = (P_S/P_N)\ (\tau\Delta\nu)^{1/2} \qquad (3)$$

for $P_S/P_N \ll 1$ and $\tau\Delta\nu \gg 1$. Then from (1), (2) and (3) with ν_S = 140 GHz

$$\frac{s}{n} = 3.4 \times 10^{11}\ SG\ \frac{(n_e/10^{19}m^{-3})\,(P_{inc}/300kW)\,(\tau/200ms)^{1/2}(\Delta\nu/100MHz)^{1/2}}{(w/3cm)\,(T_N/500eV)\,(\sin\theta/\sin 20°)} \qquad (4)$$

6. CALCULATIONS FOR TYPICAL JET PLASMAS

In the pre-DT phase fast ions will be created by ion cyclotron heating of minority ions with RF power, and also by neutron beam injection.

ICRF Heating. We have assumed that ICRH on ^{3}He minority ions in a deuterium plasma (+ 10% hydrogen) absorbs half the 25 MW of available RF power and creates anisotropic Maxwellian minority velocity distributions with $T_\perp$ and $T_\parallel$ perpendicular and parallel to B. It is assumed that θ = 20°, and ϕ = 60°, with B = 3.4 T. The effective minority temperature is taken to be $T_{m_{eff}} = T_\perp \sin^2\phi + T_\parallel \cos^2\phi$.

The plasma conditions assumed for Figures 3(a) and (b) are:

	$n_e(10^{19}m^{-3})$	T_e(keV)	T_i(keV)	$n_{min}(10^{17}m^{-3})$	$T_{m_{eff}}$(keV)
a	2	10	10	14	3,010
b	10	5	5	10	282

Best-fit Maxwellians for the wings have been added, together with the spectra with no RF heating (all ions at T_i). The Maxwellian half-intensity widths are within 5% of the expected values after allowing for the refractive index effects. Signal-to-noise ratios are given for the channel widths shown (1/5 of half intensity half width). Satisfactory measurements of $T_{m_{eff}}$ should be possible.

Neutral Beam Injection. In Figure 3(c) it is assumed that a beam of 140 keV deuterons is injected into a deuterium (+ 10% hydrogen) plasma. The fast particles slow down classically with an isotropic distribution function $f(v) \propto 1/(v_c^3 + v^3)$ where $v_c \sim 0.1\ v_{e(thermal)}$. The calculated scattered spectrum is shown for θ = 20°, ϕ = 0, with $n_e = 2 \times 10^{19}\ m^{-3}$, T_e = 10 keV, T_i = 30 keV, $n_{fast} = 2 \times 10^{18}\ m^{-3}$. The background curve is calculated with all deuterons at T_i. It is clear that it will not be possible to deduce reliable information about the fast deuterons.

The feasibility of measuring the alpha particle distribution in the DT phase of JET has already been discussed (Costley et al, 1988). More detailed calculations allowing for refractive effects confirm that it should be possible to measure velocity distributions of the expected alpha populations in the energy range 0.5 to 3.5 MeV. A calculated scattering spectrum is shown in Figure 3(d), with predicted signal-to-noise ratios.

7. CONCLUSION

The diagnostic should provide valuable information about the velocity distributions of alpha particles and fast RF-heated minority ions in JET.

ACKNOWLEDGMENTS - To E Corbett, J G Cordey and T Hellsten for their help.

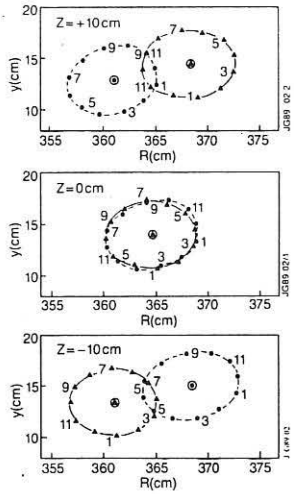

FIGURE 1

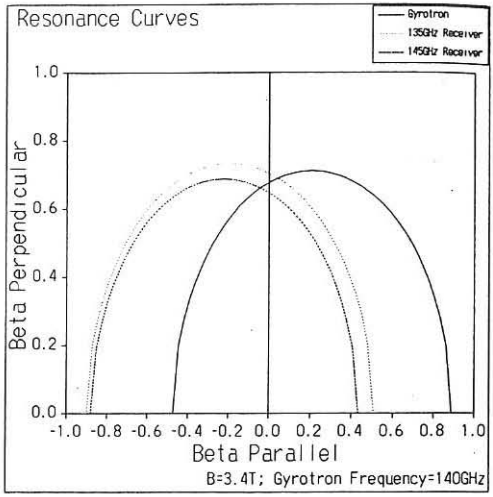

FIGURE 2

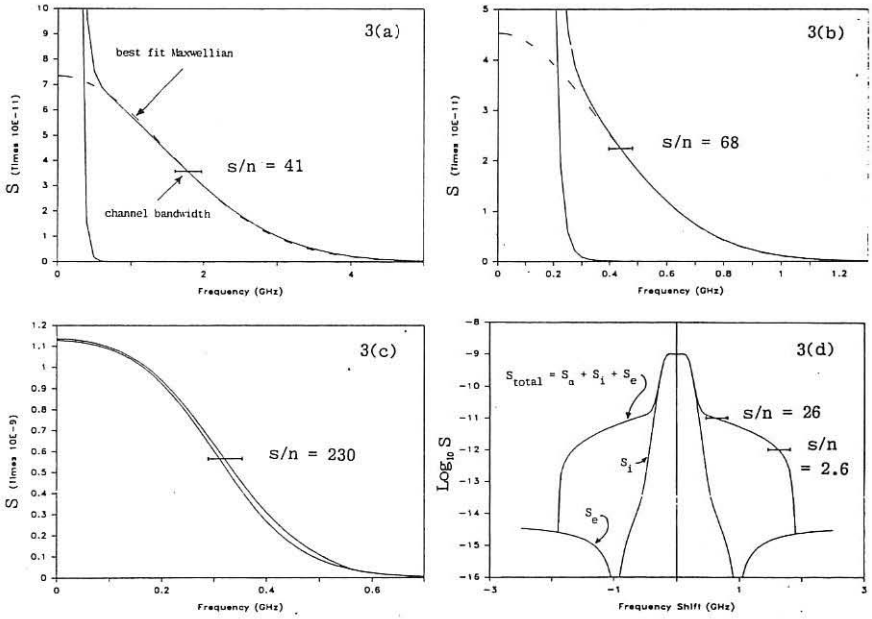

FIGURE 3

SPUTTERING MEASUREMENTS ON JET USING A MULTICHANNEL VISIBLE SPECTROMETER

M F Stamp, M J Forrest*, P D Morgan, and H P Summers

JET Joint Undertaking, Abingdon, Oxon., OX14 3EA, UK
* UKAEA Association, Culham Laboratory, Abingdon, Oxon., OX14 3DB, UK

1. INTRODUCTION

A multichannel visible spectrometer has been used on JET to simultaneously observe the emission from D, H, He, C and O atoms and ions in the proximity of a belt limiter. The absolute intensity of the line emission, along with a Langmuir probe measurement of the edge electron temperature and an atomic physics model, allows us to calculate the influxes of these species.

Under steady-state conditions the influxes of D and He are the same as the effluxes, so the ratio of impurity to fuel fluxes, eg. carbon to deuterium, is the apparent sputtering yield of deuterium on carbon in the tokamak environment.

The measured flux ratio Γ_C/Γ_D is also indicative of the central carbon impurity concentration in JET, because the limiters are the main source of impurities. For similar particle transport, $\Gamma_C/\Gamma_D = n_C(o)/n_D(o)$, so for a 10% flux ratio, $n_C/n_e = 6.6\%$, $Z_{eff} = 3$.

2. INSTRUMENTATION

Visible light, emitted by atoms and ions in front of the JET belt limiter is collected by a telescope and focused onto one end of a 1mm dia quartz optic fibre. Aperture matching optics focus the other end of the optic fibre onto the entrance slit of a 1-m Czerny-Turner monochromator that has been modified to accept an intensified linear diode array on its focal plane.

The active area of the detector is 25mm, covering approximately 20nm for a typical reciprocal linear dispersion of 0.8nm/mm. The spectrometer is equipped with a 600 ℓ/mm ruled grating of blaze wavelength 1.25μm. Spectral lines of D_γ, O II and C IV are seen in the third order of diffraction, and D_α, He I and C II in the second order of diffraction, when the spectrometer is set to a wavelength of 1.2μm (fig.1).

3. DATA INTERPRETATION

We use the standard interpretation [1-3], where the observed line intensities are proportional to the influxes of the observed ions:

$$\text{Particle Influx} \quad , \quad \Gamma = 4\pi \left(\frac{S}{XB}\right) I$$

where I is the measured intensity of a line of excitation rate X and branching ratio B, and S is the ionisation rate for that ion (atom).

It is important to note that the ratio S/XB is essentially density independent for JET electron edge densities, and varies approximately linearly with electron temperature for most low Z impurity lines [4]. (For D_α, this ratio is essentially constant for $20 < T_e < 1000$ eV and $n_e < 5\times10^{18}$ m^{-3}).

4. RESULTS

The carbon influx has been measured in JET deuterium and helium discharges, over a range of electron density, plasma current and additional heating power.

Figure 2 shows the carbon flux as a function of line-average electron density for two sets of consecutive 3 MA discharges, one in helium and the other deuterium. The flux is constant or slowly falling with density, and is higher in helium discharges. This is in contrast to the deuterium and helium fluxes, which increase with density squared and linearly with density, respectively [4].

The apparent sputtering yield ($\Gamma_C/\Gamma_{D,He}$) is shown in fig.3. For He plasmas this has a minimum of ~ 7% ($T_e(a)$ ~ 20 eV) and for D plasmas, ~ 4.5% ($T_e(a)$ ~ 30 eV). These low values are close to those expected from physical sputtering, including self-sputtering, of room temperature graphite [5]. At surface temperatures above 1000°C, radiation-enhanced sublimation should become important and may dramatically increase the sputtering yield [6]. The carbon self-sputtering yield also increases above 1000°C. Figure 3 shows that at low density and high edge electron temperature the sputtering yield is over 50% in the helium discharges, and nearly 20% for the deuterium, though higher values have been observed in other lower density deuterium plasmas. However, observation of the belt limiters with a CCD camera [7] showed that in the D plasmas the limiter temperature was less than 1000°C, and in the helium plasmas there were some 'hot-spots' with a maximum temperature of 700-750°C.

Figure 4 shows Z_{eff} plotted against the measured flux ratio for the previous deuterium data. The dashed curve assumes $\Gamma_C/\Gamma_D = n_C(o)/n_D(o)$. The general agreement is very good, suggesting that the main impurity is carbon, and that the transport of deuterium and carbon is similar.

Figure 5 shows the carbon flux plotted against the total input power to the plasma, for several plasma currents and additional heating powers. The data at different plasma currents are for similar shaped plasmas (though the 5 MA discharges were only 3 cm from the inner wall) that were nominally 'balanced' on the upper and lower belt limiters. The toroidal fields were different such that q~9 for I_p = 2 MA, q~5 for I_p = 3-4 MA and q~3.5 for I_p = 5 MA. Most of the additional heating was ICRH, but data points for upto 8 MW of NBI are included. The radiated power fraction was approximately constant at 0.4 (± 0.1).

Figure 5 clearly shows that the carbon influx is proportional to the total input power, and although the gradient is different for different plasma currents, it is within the error bars of the absolute measurements and the uncertainty with which the top-bottom belt limiters were 'equally' loaded.

In contrast the deuterium flux is independent of the additional heating, being approximately proportional to the line-average electron density squared.

5. SUMMARY

Simultaneous measurement of C, He, D lines emitted in front of the JET belt limiter allows an evaluation of the particle fluxes, and of the carbon sputtering yield.

At high electron density the sputtering yield is ~4% for D on carbon and ~7% for He on carbon, in agreement with physical sputtering calculations. At low electron density the sputtering yields can be very high (>50%), consistent with very high Z_{eff} values (>5), and this cannot be explained by sputtering calculations for the measured limiter temperatures of <800°C.

Such large experimental sputtering yields suggest that the carbon self-sputtering yield is higher than reported in ion-beam experiments [5], perhaps because of non-normal angle of incidence.

The carbon influx from the limiter seems to depend only on the input power to the plasma, whether it be ohmic, ICRF or NBI, at a measured rate of $\sim 6\times10^{20}$ atoms/s/MW. Consequently, the 'cleanest' plasmas are obtained at high electron densities when the deuterium (or helium) influxes are largest. Conversely, operation in D at low density, and with He conditioning (in order to reduce the recycling and the deuterium influx) will produce carbon dominated plasmas.

6. REFERENCES

[1] M F Stamp et al., Proc. 12th European Conf. on Controlled Fusion and Plasma Physics, Budapest, Vol.9F, Part II (1985), p.539.
[2] W Engelhardt, Proc. of Course on Diagnostics for Fusion Reactor Conditions, Villa Monastero, Varenna, Vol.1, (1982) p.11, (Report EUR 8351-I EN).
[3] A Pospieszczyk et al., J. Nucl. Mat. 145-147 (1987), p.574.
[4] M F Stamp, K H Behringer, M J Forrest, P D Morgan, and H P Summers, J. Nucl. Mat. 162-164 (1989), in press.
[5] J Roth, J Bohdansby and W Ottenberger, Report IPP 9/26 (1979).
[6] J Roth, J. Nucl. Mat. 145-147 (1987) p.87.
[7] D D R Summers, private communication.

Fig.1 Survey spectrum from the limiter viewing OMA spectrometer, showing lines of D, He, O and C.

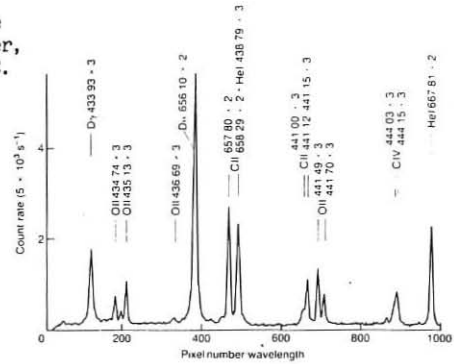

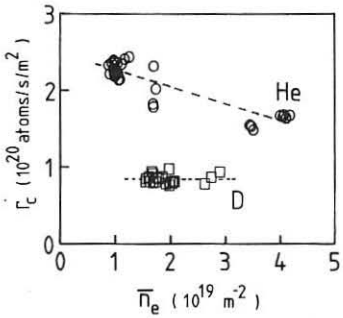

Fig.2 The variation of carbon influx with line-average density in ohmic 3 MA He and D discharges.

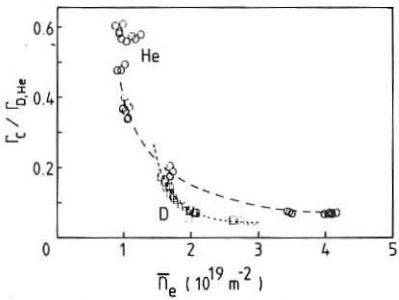

Fig.3 The variation of carbon sputtering yield with line-average density in ohmic 3 MA He and D plasmas.

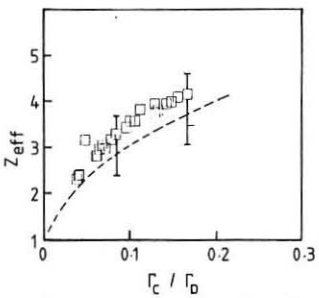

Fig.4 Z_{eff}(bremsstrahlung) vs carbon sputtering yield. The dashed line assumes i) $\Gamma_C/\Gamma_D = n_C(0)/n_D(0)$ and ii) carbon is the only impurity.

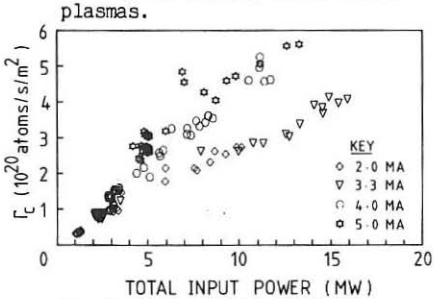

Fig.5 The variation of carbon influx with total input power for several plasma currents. The radiated power fraction is approximately constant.

BROADBAND MICROWAVE REFLECTOMETRY ON ASDEX

M.E. Manso, F. Serra, J. Barroso, J. Comprido, C. Teixeira, A. Monteiro F. Nunes and A. Silva *; J. Neves, J. Pereira, A. Almeida S. Ramos and L. Cupido**; A. Cardoso, C. Costa and A. Garrett***

* Instituto Superior Técnico, 1096 Lisboa Codex, Portugal
** Universidade de Aveiro, Portugal
*** Laboratório Nacional de Engenharia Civil, Lisboa, Portugal

INTRODUCTION

A reflectometric system has been developed to measure density profiles and density fluctuations on the ASDEX tokamak, using O-mode operation /1/. The system has been constructed and installed. The first results have been obtained with the three frequency bands. Here we present a description of the experimental system and we report on the obtention of preliminary density profiles.

REFLECTOMETRIC SYSTEM

The reflectometric system consists in three reflectometers, in the ranges 18-26.5 GHz, 26.5-40 GHz and 40-60 GHz (respectively standard K, Ka and U bands), so electron densities from 0.4 to $4.5 \times 10^{13} cm^{-3}$ can be measured. A probing wave is launched into the plasma and is reflected at the cutoff layer x_c, where the wave frequency equals the local plasma frequency; x_c is determined from the phase change the wave undergoes after propagation and reflection in the plasma. Each reflectometer has two measuring channels corresponding to antennas in inner and outer positions, placed in the equatorial plane, in the same poloidal cross section of the machine. The system has been constructed and implemented on ASDEX /2/; presently only the outer channels are installed.

The reflectometers for the K and Ka bands use YIG oscillators; special drivers have been developed and fast frequency sweeping operation (2ms) has been achieved. Work is under progress in order to decrease the sweeping time to 500 μs. A BWO is used for the U band, that can be operated from 100 μs. The reflectometers are of one type antenna and uses focused hog-horn antennas (beam width: 20°, 10° and 5°). Raytracing calculations, taking into account the topology of the refractive index surfaces of the ASDEX plasma, show that the width of the incident beams that is reflected back to the antennas is of the order of 1° /3/. The signals reflected from the plasma are probed through directional couplers that are placed inside the machine, in order to avoid contributions of the incident signals, coming from reflections at the microwave windows. The reference signals are obtained from pins placed at the end of the antennas feeding waveguides. The transmission line for the U-band includes oversized waveguides so losses can be minimized; the estimated transmission line losses for the three frequency bands are 23, 29 and 34 dB, (respectively K, Ka and U bands).

The configuration of the system used for density profile measurements

is presented in Fig.1. The detection system is homodynic and uses sensitive Schottky diodes. Filters (70 dB/oct) and amplifiers (bandwith 1MHz) have been developed in order to minimize the effect of spurious reflections and density fluctuations in the detected signals. The oscillators and the detection system are placed close to the tokamak, and both the operation of the oscillators and the characteristics of the filters and amplifiers are remotely controlled.

The control and data acquisition system is based on a PC (AT) computer and Camac Modules. Specific hardware has been studied in order to improve the performance of the system, namely to decrease the time needed to generate the waveforms for the sweep operation of the oscillators. The signals are sampled with a 1 MHz/10 bits Waveform analyser (Camac Module 8210). Sampling rate is adjustable from 1 μs-1 ms. A total number of 1024 points is acquired per sweep for each reflectometer, and so a sampling rate of 2 μs is obtained for the actual density profiles measurements (2ms). The beat frequencies observed in the three reflectometers are measured with an accuracy of 2%, 5% and 10% (K, Ka and U bands). With the actual memory capacity of the system (32 K) the data corresponding to a maximum of eight profiles can be acquired; a delay of 500ms (to transfer the data to the PC) is required before the next set of measurements can be made. So during one shot, and for a typical measuring time of 3 s, some 40 profiles can be obtained, either distributed along the shot or in groups of eight every 516 ms.

TESTING OF THE SYSTEM

Several tests have been performed both at the laboratory and at ASDEX. The tests done at the laboratory aimed mainly at the characterization of the most critical components to be used in the system, namely detectors, oscillators, flexible waveguides, microwave windows and DC breaks. A prototype reflectometer, where the fusion plasma was simulated by a movable vibrating mirror, has been used to determine the sensivity of the system and to study the influence of the fluctuations on the measured profiles. A prototype antenna (Ka band) was tested and its radiation pattern was measured. The experimental results agree with predictions based on numerical calculations, having into account the geometry of the hog-horns antennas.

The set-up on ASDEX was tested, and the phase and attenuation due to the transmission line and aerial were determined for the three reflectometers. The system was calibrated, by using a mirror placed inside the tokamak vessel. The reference pins have narrow band characteristics and were adjusted so that reflectometric "fringes" could be obtained in the whole frequency bands. Measurements showed that: (1) no significative cross-talk between antennas occurs; (2) reflections from the tokamak walls are not important.

DENSITY PROFILE MEASUREMENTS

Density profiles are obtained with broad band frequency operation. The mixing of the reference and plasma signals produces "fringes", that exhibit the phase variation $\Phi(f)$ due to the propagation of the probing

waves, in the path between the pin and the plasma reflecting layers.

The wave equation is solved by using a WKB solution in the propagating region, and by assuming a linear density profile in the reflecting layer where the WKB solution is not valid and the exact solution of the wave equation has to be found. The following integral equation results from that analysis:

$$a - x_c(f) = \frac{c}{2\pi^2} \int_0^F \frac{d\Phi}{df} (F^2 - f^2)^{-1/2} \, df \qquad (1)$$

where a is the minor plasma radius (a=40 cm).

Therefore, by inverting the reflectometric phase information $d\Phi/df$, the localization of the several layers (and so the density profile) can be obtained from (1).

The theoretical spatial resolution of the system is defined as the error in the localization of the cutoff layer, due to the use of the aproximate WKB solution /4/. For a typical density profile of the ASDEX plasma, corresponding to $\bar{n}_e \sim 3\times10^{13}$ cm^{-3}, a spacial resolution between 1.1 - 1.3 cm is foreseen.

The first reflectometric measurements on ASDEX aimed at: (1) the testing of the experimental system, namely the behaviour of detectors, oscillators and control, in a tokamak environement; (2) the selection of adequated amplification and filtering (both electronic and numerical) of the detected signals; (3) the testing of the data processing; (4) the obtention of a reliable density profile.

Good signal-to-noise ratios were obtained in the three reflectometers, in several experimental conditions; the signals were electronicaly filtered and amplified. In Fig.2-a a K-band reflectometric signal is shown. Numerical filtering (based on a non-recursive band pass filter with finite impulse reponse (FIR) and zero phase delay), was applied to the recorded signal of Fig.2-a, and provided a more flexible and selective filtering process (Fig.2-b). The data evaluation is based on the number of the minimums of the fringes, corresponding to phase variations of 2π. The phase information $\Phi(f)$, is inverted using numerical interpolation methods, as proposed by /4/, and recently tested for typical ASDEX profiles /5/. A one-point direct interpolation method was aplied to the phase information corresponding to the signal shown in Fig.2, and the density values were obtained (points (+) in Fig.3). The experimental results show good agreement with density information obtained from the 16-channel (Nd-YAG) laser scattering diagnostic (full line in Fig.3).

Work is under progress to obtain a complete density profile based on the results of the three reflectometers.

REFERENCES

/1/ - M. Manso, F. Serra et al., Proc. "15th Europ. Conf. on Controlled Fusion and Plasma Heating", Dubrovnik, 12B, 1127, (1988).
/2/ - The transmission line was designed in collaboration with Dr. Siller (IPP) and was constructed as well as the antennae by IPP. The collaboration with IPP is headed by Dr. Soldner.
/3/ - C. Teixeira, Priv. Comunic., (1988); raytracing calculations have been done using a numerical code developed at CEN Cadarache.
/4/ - F. Simonet and C. Passeron, Priv. Comunic., TS 66.87.03, (1987).
/5/ - A. Monteiro and A. Silva, Internal Report CEL-01/88, (1988).

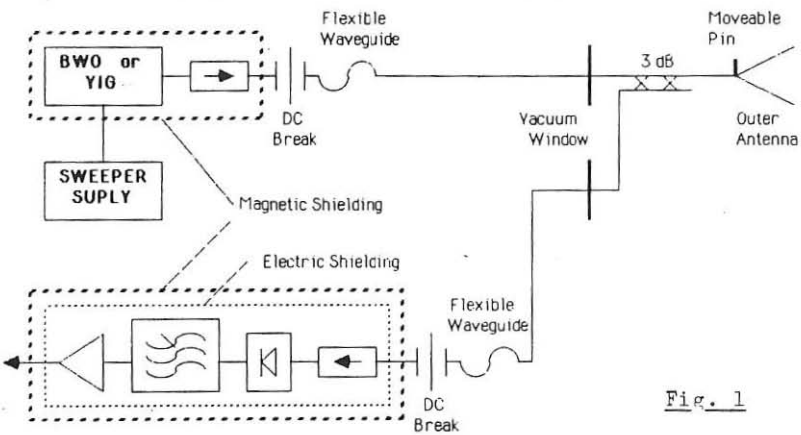

Fig. 1

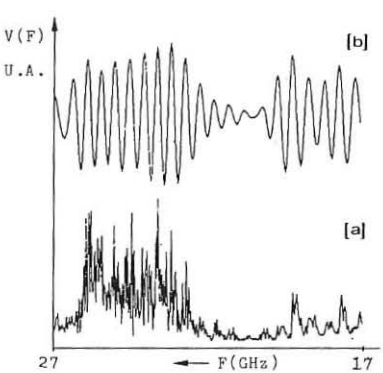

Fig. 2

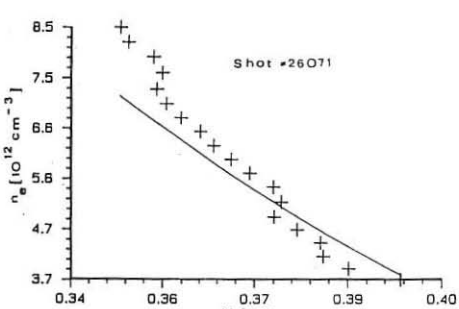

Fig. 3

SCATTERING EFFECTS OF SMALL-SCALE DENSITY FLUCTUATIONS ON REFLECTOMETRIC MEASUREMENTS IN A TOKAMAK PLASMA

J.P. Garcia, M.E. Manso, J.T. Mendonça[+] and F.M. Serra

Instituto Superior Técnico, 1096 Lisboa Codex, Portugal
[+]JET Joint Undertaking, Abingdon, Oxfordshire, England

1. Introduction

When a wave propagates in a non homogeneous fluctuating plasma part of the incident energy is scattered due to the nonlinear interaction between the wave and the oscillating modes perturbing the plasma. The possibility of enhanced scattering at the cutoff layer , where reflection of the incident wave occurs, has been recently suggested as the basis of a reflectometric experiment to determine the spatial location of small scale fluctuations in a fusion plasma /1/.

Here we report on the development of a theoretical model to evaluate the flux of energy scattered by fluctuations, in order to give insight about the interpretation of measurements using a microwave reflectometry diagnostic in a tokamak. The scattered field is obtained through the resolution of a (non-homogeneous) wave propagation equation where the source term is related with the nonlinear current due to the interaction between the incident wave and local fluctuations.

We use a slab model for the plasma, and an ordinary (O) wave propagating along the density gradient is considered. The amplitude of the scattered wave at the border of the plasma is estimated. In order to know the contributions to the energy scattered both from the propagation region and the reflecting layer, an approach was used where perturbations are modelled by spatial step functions at several layers. The main contribution to the scattered power comes from the cutoff region, where the electric field amplitude swells as compared with the incident value. Considering the reflectometric system recently installed on the ASDEX tokamak /2/, and using typical density profiles, expected values of the 'swelling factor' have been numerically evaluated. The role of incoherent scattering due to drift wave activity is discussed as well as the coherent scattering due to fluctuations induced by lower hybrid (LH) waves.

2. Theoretical Model

We consider a two dimensional slab geometry (Fig. 1) , and a normally incident monochromatic O-mode wave ($\omega_o, \bar{K}o$). When no density fluctuations are present, the fields satisfy the homogeneous wave equation

$$\frac{\partial^2 E_z}{\partial x^2} + \frac{\omega_o^2}{c^2} \varepsilon_{zz}(x)\, E_z = 0 \qquad (1)$$

where (cold plasma approximation): $\varepsilon_{zz}(x) = 1 - \omega^2 p_e(x)/\omega_o^2$.

Reflection occurs at a plasma layer, x=xc, where ω_0 equals the plasma frequency $\omega pe(xc)$.

When density fluctuations exist in the plasma, the interaction between the (incident and reflected) waves (ω_0, $\bar{K}o$) and the density fluctuations with Fourier component (Ω, $\bar{K}$) originates scattered waves with frequencies $\omega_s = \omega_0 \pm \Omega$ and directions $\bar{K}s = \bar{K}o \pm \bar{K}$.

For density fluctuations characterized by a spatial scale length greater than the incident wavelength (large-scale fluctuations) , the methods of geometric optics may be used in the propagation region, and in the reflecting layer a small scattering occurs mainly along the direction of the reflected rays; on the contrary, for small-scale perturbations the scattering effects on the coherent wave energy must be taken into account.

The wave equation for the scattered field can be written

$$\frac{\partial^2 E_z^s}{\partial x^2} + \frac{\omega_s^2}{c^2} \varepsilon_{zz}(x) E_z^s = I_z \tag{2}$$

where the source term associated with the nonlinear current component Jz is

$$I_z = - j\omega_s \mu J_z \tag{3}$$

Assuming that the internal fluctuations of the plasma are only of electrostatic nature ($\delta B=0$) and that the current terms resulting from By can be neglected compared to those from Ez, we obtain

$$J_z = - j \frac{e^2}{m_e} \frac{\delta_n}{\omega_o} \left[E_z - j \frac{\Omega}{\omega_s} \frac{K_{2x}}{K_2^2} \frac{\partial E_z}{\partial x} \right] \tag{4}$$

As a first approximation we can consider Ez as the solution of equation (1). The fields scattered backwards at x=a will be given by

$$E_z^s (a) = - \frac{E_z^-}{W} \int_a^b E_z^+ I_z \, dx \tag{5}$$

where W represents the wronskian . Outside the integral Ez can be replaced by its WKB approximation. We will now consider the average backwards scattered power for both coherent and non-coherent fluctuations.

(i) Coherent density fluctuations

In this case we get, at the plasma boundary, a scattered plane wave in the directions

$$K_{sx} = \left[\left(\frac{\omega_s}{c}\right)^2 - K_y^2 \right]^{1/2} , \quad K_{sy} = \pm K_y \tag{6}$$

with an associated Poynting vector

$$\vec{S}(a, \omega_s, \vec{K}_s) = \frac{1}{2 Z_o} \frac{\vec{K}_s}{K_s} \left[E_z^s (a, \omega_s, \vec{K}_s) \right]^2 \tag{7}$$

The relation between the scattered and the incident power is the effective scattering area:

$$\sigma_s = \left[E_z^s (\omega_s, \vec{K}_s) \right]^2 / \left[E_z^+ (\omega_o, \vec{K}_o) \right]^2 \tag{8}$$

This approach might be adequate to study the role of fluctuations induced by LH (coherent) waves injected in the plasma.

(ii) Incoherent fluctuations

The non-coherent behaviour means that for each Ω there is a spectrum of possible $\bar{k}$ values. This is the case of drift wave induced fluctuations, existing in the density gradient region of a tokamak.

The ensemble average of the Poynting vector is

$$< \vec{S}(a) > = \lim_{T \to \infty} \frac{1}{2T} \int_{-\infty}^{+\infty} \frac{d\omega_s \, dK_{sy}}{(2\pi)^2} \frac{1}{Z_o} \frac{\vec{K}_s}{K_s} < | E^s(a, \omega_s, K_{sy}) |^2 > \qquad (9)$$

3. Results

Numerical calculations were done, considering the slab model approximation for a toroidal section of a tokamak plasma. A simple model using Dirac functions to simulate very localized density fluctuations was used, in order to give insight about the relative contributions of the various regions of the plasma to the scattered field. Adopting a linear approximation for the gradient region of a typical ASDEX density profile and using only a Ky component for the fluctuations, we represent in Figs. 2 and 3, respectively, the behaviour of the square of the electric field (E^2) and of the contributions of the fluctuation (depending on its location along the plasma) to the scattered power (S):

$$E^2 \propto A_i^2(x) \qquad (10) \quad , \quad S(a) \propto |x| \, J_{1/3}^2 \left(\tfrac{2}{3} |x|^{3/2}\right) A_i^2(x) \qquad (11)$$

with Ai, $J_{1/3}$ representing Airy functions, and $x = \left[\frac{K_o^2 \, (dn_e/dx) xc}{n_e(x_c)} \right]^{1/3} (x - x_c)$.

The model can be improved considering that the instability in the plasma has a finite extent. If a step function is used with width Δx being of the order of the correlation length of the wavenumbers $\bar{K}$ (semi-coherent situation) we obtain

$$< S(a) > \propto \int_{\Delta x} Q(\Omega, \vec{K}) \, |x| \, J_{1/3}^2 \left(\tfrac{2}{3} |x|^{3/2} \right) A_i^2(x) \, dx \qquad (12)$$

where $Q(\Omega, \vec{K})$ is the spectral density of the fluctuations. The plasma layers within Δx behave like independent radiators and their contributions add together. Fig. 4 shows the contributions for the scattered field of a step function $\Delta x = 1$ cm, depending on its localization between a and xc. When the incident frequency increases the cutoff is displaced towards the plasma center; the propagation region increases too, so its contribution to the scattered power becomes greater and might be comparable to the one from the reflecting layer.

A simple way to analyze the case of drift wave fluctuations is to consider two step functions, one covering the propagation zone (modeling fluctuations in the whole region) and the other centered at the cutoff. The swelling factor (SF), defined as the ratio of the scattered powers coming from both regions, was calculated accordingly to the broadband (18-60 GHz) reflectometric system for ASDEX; values of SF(fo=40GHz) ~ 2 , and SF(fo=26.5GHz) ~ 6, show that the main contribution comes from the reflecting layer, if we exclude the worst case of the cutoff more inside the plasma (where SF(fo=60GHz)~ 1, Xc ~ 13 cm). In addition,we must stress that the values from the propagation region are overestimated, as we are simply adding all local contributions and assuming fluctuations

everywhere. Reflectometry seems therefore a good diagnostic to localize this type of instabilities. A more accurate model should consider the structure of the fluctuations wavenumbers along the wave direction and this study is currently under progress.

References

/1/ Simonet, F., 14th Europ. Conf. on Controlled Fusion and Plasma Physics, Madrid, III-1305 (1987).
/2/ Manso, M.E., et al. This Conference.

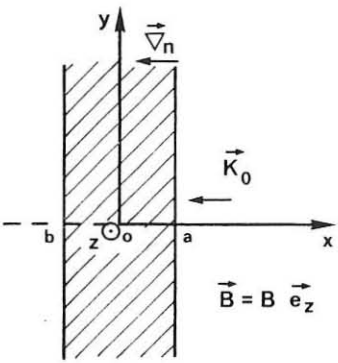

Fig.1 - Plasma slab geometry.

Fig.2 - Square of the electric field (normalized to the maximum value), for fo=60 GHz, Xc=12.5cm. A linear density profile for ASDEX is used: $ne(X)=6.5x10^{13}\ (1-X/a)\ cm^{-3}$. a=40cm, roughly corresponding to the average density $\bar{n}e \sim 3x10^{13}\ cm^{-3}$.

Fig.3 - Scattered power (normalized), for a Dirac type perturbation at different X, between a and Xc (fo and profile as for Fig.2).

Fig.4 - Same as Fig.3, for step functions with ΔX= 1cm.

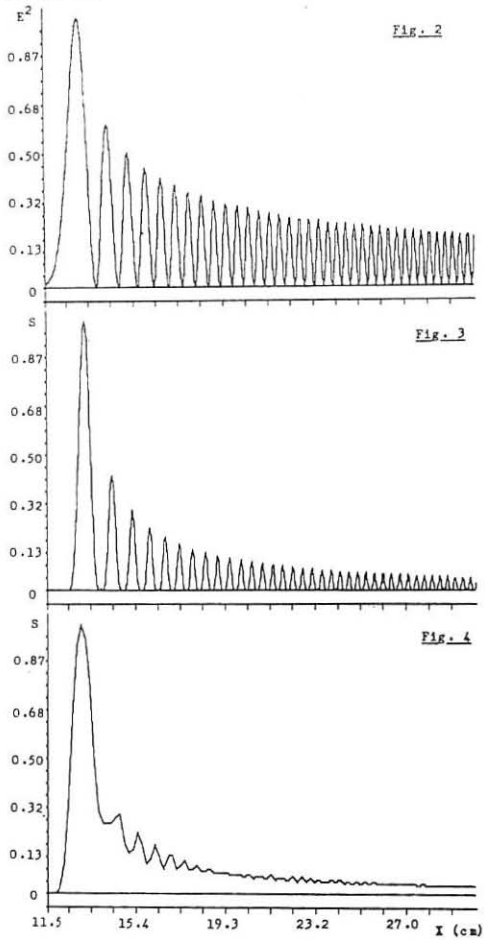

DETERMINATION OF ION TEMPERATURES IN MAGNETISED PLASMAS BY MEANS OF A ROTATING DOUBLE PROBE

K. Höthker, W. Bieger* and H.J. Belitz

Institut für Plasmaphysik,Kernforschungsanlage Jülich GmbH,
Association EURATOM-KFA, Postfach 1913, D 5170 Jülich/FRG
*Fachhochschule Aachen, Abt. Jülich, Ginsterweg 1,
D 5170 Jülich/FRG

Electrical probes are widely used in magnetised plasmas such as the scrape-off layer of tokamaks to determine the electron temperature and density. A principal difficulty for the interpretation of probe signals in such plasmas is due to the fact that the flow of the particles to the probe pin is anisotropic and often turbulent.

A well known approach aiming at an theoretical understanding of probe signals in magnetised plasmas has been put forward in ref. /1/ and is known as ´Bohm diffusion´. However, the effect of finite Larmor radii can also determine the electrical current as collected by a probe perpendicular to the magnetic field.

In this paper we present measurements in the scape-off layer of the tokamak TEXTOR where the conditions are such that the contribution of the diffusion to this current is insignificant and the effect of finite ion Larmor radii prevails. We demonstrate that it is then possible to determine the ion temperature by comparing the saturation currents as measured by means of an electrical double probe with the flux as calculated by the Monte-Carlo method.

Experimental set-up

Parameters of the tokamak TEXTOR and details of the design of the probe were described in more detail in ref. /2/. The diameter and the length of the cylindrical probe pins are 5 mm. The axis of the probe was perpendicular to the magnetic field direction and the probe was rotated during a tokamak discharge with a frequency of ca. 2 Hz, cf. fig. 1.

Results

Rotating the probe during a discharge we measure a probe characteristic every 2.5 ms. In fig. 2 a detail of such a measurement taken 5 mm inside the limiter shadow is shown. The two envelopes of the curve give the time dependence of the ion saturation current to each of the probe pins. The value of the electron temperature is 17 eV, the density 1.3*E12 cm-3 and the magnetic field strength 1.6 T.

The probe pins generate flux tubes along the magnetic field. As the angle α, cf. fig 1, decreases the flux tubes approach one another, at α=30 degrees the flux tubes as defined by the geometrical cross section of the probe pins start to overlap and at α=0 they coincide.

First of all we conclude from the symmetry of the probe signal at $\alpha=0$ that the plasma is not streaming at the position of the probe for the present plasma conditions.
Secondly we observe that the ion saturation current starts to decrease already for values of the angle α, for which the flux tubes as determined by the geometrical cross section of the probe pins do not yet overlap and
finally we notice that the ion saturation current does not decrease for $\alpha=0$ to half of that value which is measured when the flux tubes do not overlap. If the Bohm diffusion coefficient ($D=0.7\ m^2/s$) is assumed to give an upper limit to the cross field diffusion it can be calculated from the measured parameters that the contribution of cross field diffusion to the incomplete screening of one probe pin by the other for $\alpha=0$ is insignificant.

We assume therefore that the incomplete screening of the probe pins is due to the finite Larmor radii of the ions.
We have tried to simulate the experimental situation by means of single particle Monte-Carlo calculations in the six-dimensional phase space and to deduce the value of the ion temperature by a best fit of the calculations to the measured ion saturation current profile. For the measurements shown in fig. 2 this procedure leads to an ion temperature of T_i = 120 eV.

In fig. 3 we show the normalised ion flux to a probe pin as a function of the angle α from these calculations for different normalised ion temperatures.The dimensions are those of our probe: D=5mm, A=10mm and length of the probe pins L=5mm.

In fig. 4 we have drawn the normalised ion flux to a probe pin for $\alpha=0$ as a function of the normalised ion temperature. We notice that the precision of the measurement depends on the ratio of value of the ion gyro radius to the probe pin diameter.

The precision of the ion temperature measurement can also be effected if the mean ion mass is not well known, if the axis of the probe is not well aligned perpendicular to the magnetic field direction and if the single particle model of the Monte-Carlo calculations does not apply to the actual plasma conditions.
We will present results and the discussion of these conditions which limit the applicability and precision of the T_i measurement in a more detailed publication. As far as the justification of the single particle model is concerned we mention here: The ions are collisionless as far as binary collisions are concerned. The electrical field of the sheath in front of the pins changes the orbits of the particles entering into the sheath. For the geometry of our probe in the magnetic field the ExB field in the sheath adds a drift parallel to the pin axis to the undisturbed particle orbits leading to a reduced flux to the probing pin. Because our Monte-Carlo calculations neglect this effect we determine a lower limit to the ion temperature. If the electron temperature is small compared to the ion temperature we expect that the effect of the sheath of the "shadow casting" pin on the flux as collected by the probing pin can be ignored.

Finally we have tried to estimate the significance of the sheath criterium of Bohm for the precision of the ion temperature measurement. To this end we have simulated in the Monte-Carlo calculations the flow of the ions along the magnetic field lines by using Maxwell distributions drifting with velocities $v \leq c_s$ from both sides to the probe pins, c_s being the ion sound speed. The neglect of the Bohm criterium would lead to an overestimate of the ion temperature.

/1/ D. Bohm, I. Mott-Smith and H. S. W. Massey in 'The Characteristics of Electrical Discharges in Magnetic Fields, ed. A.Gurthie and R. K. Wakerling, New York 1949

/2/ K. Höthker, W. Bieger and R. van Nieuwenhove, Rev. Sci. Instr. 56(1987)1046

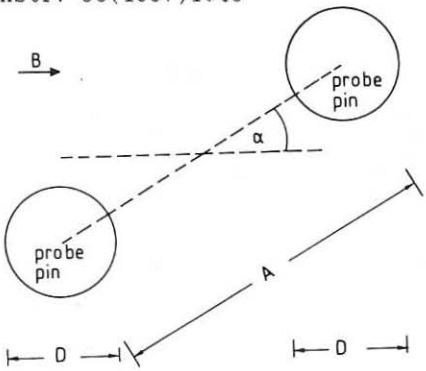

Fig 1 Probe pin configuration in the magnetic field

Fig 2 Comparison of normalised ion saturation current as function of angle α with Monte-Carlo calculations

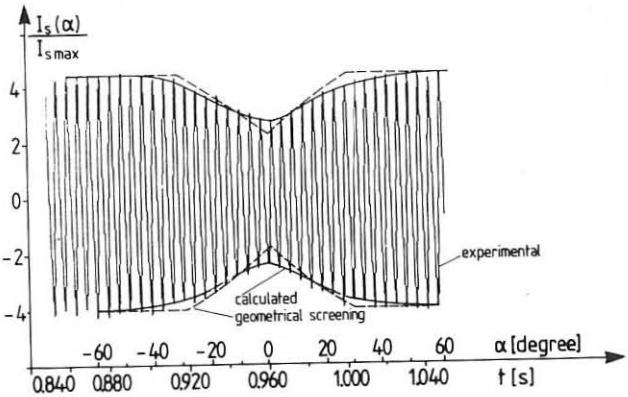

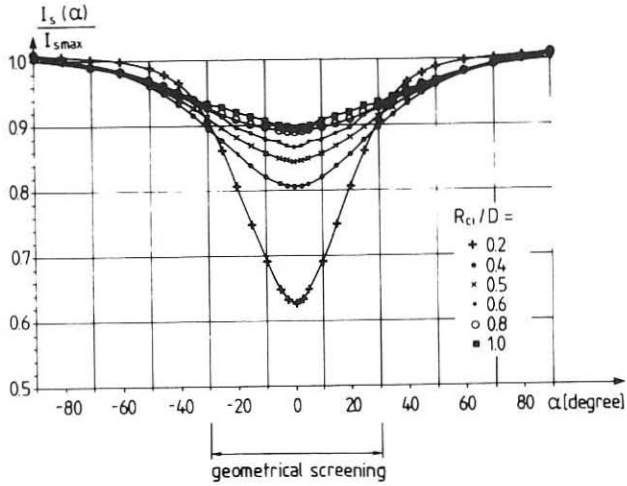

Fig 3 Measured probe current as function of the angle α during a TEXTOR discharge and best fit from Monte-Carlo calculations

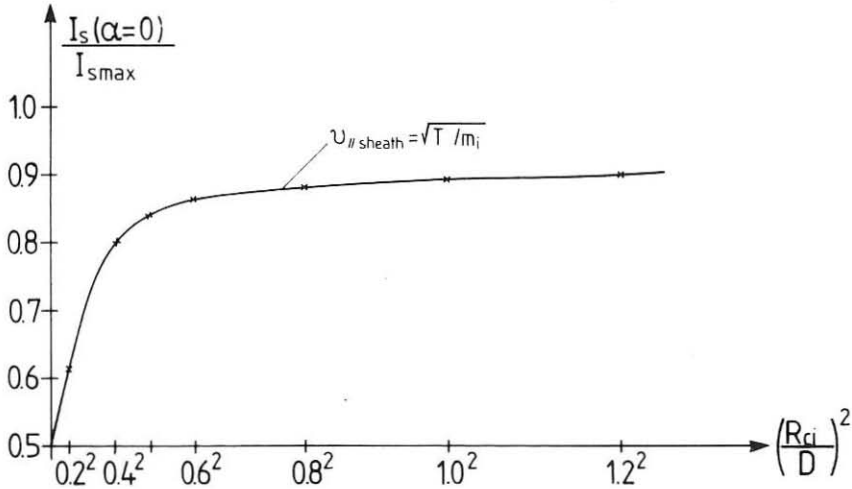

Fig 4 Normalised ion flux to a probe pin for α=0 as a function of the normalised ion temperature from Monte-Carlo calculations

PLASMA PARAMETER MEASUREMENTS WITH THE VARIABLE ENERGY ANALYZER AND THE μ-ANALYZER

by

Edbertho Leal-Quiros, and Mark A. Prelas
Fusion Research Laboratory
Nuclear Engineering Dept.
University of Missouri-Columbia
Columbia, MO 65211

Abstract

A novel diagnostic that allows measurement of $\beta_\perp$ and the magnetic moment μ is described as well as some results with the variable energy analyzer.

The μ-Analyzer consists of a Directional Energy Analyzer (miniature) and a Magnetic Hall in the same case. The Directional Energy Analyzer measures the ion temperature in the direction perpendicular to the magnetic field and the hall probe measures the magnetic field. The μ-Analyzer has a relatively small diameter of 6 mm. This allows the measurement of the ion temperature and the magnetic field in the same spatial region at the same time, therefore $\beta_\perp$ and μ (the first adiabatic invariant) can be found. From the above parameters, the local larmor radius can also be calculated.

The variable energy analyzer is a retarded potential gridded energy analyzer in which geometrical parameters can be dynamically controlled externally. This analyzer has accurately measured ion temperatures of 0.125 eV. It has been found that geometrical parameters can affect temperature measurements leading to errors as large as a factor of 10. Additionally, the optimum geometrical parameters are specific to plasma parameters. Thus a fixed geometry gridded energy analyzer would have errors in measurement which vary with plasma parameters.

Introduction

The μ-Analyzer is a new concept in detectors with the capability of measuring, simultaneously, the $\beta_\perp$-parameter, the first adiabatic invariant μ, (magnetic moment) of a magnetic confinement device and also calculate the Larmor radius.

The μ-Analyzer consists of a miniature directional energy analyzer [1] and a small Hall probe in the same detector case (Fig. 1).

With the retarded field directional energy analyzer, it is possible to find the perpendicular kinetic energy, $W_\perp$, to the magnetic field. And with the small Hall probe, the localized magnetic field can be measured.

From the analysis of the data simultaneously taken in time and space, it is possible to find μ and $\beta_\perp$ of the system. These are very important quantities, along with some other parameters, to aid in the determination of the stability of the magnetic confinement device using the MHD stability criterium.[2]

In addition to the above, a direct measurement of the Larmor radius of each region is also possible with the μ-Analyzer.

The μ-Analyzer can be used in tokamaks, stellerators, reverse-field pinches, Spheromaks, Cusps, and in Mirrors as a tool to measure μ or $\beta_\perp$ directly.

We report here results from initial measurements of a plasma generated in the **M**odified **M**issouri **M**agnetic **M**irror e**X**periment (M^4X) with the μ-Analyzer.

The variable energy analyzer was described by Leal-Quiros and Prelas in Reference 3. This analyzer was able to measure temperatures as low as 0.125 eV (limited only by the plasma source). The variable energy analyzer is a retarded potential gridded energy analyzer with external dynamic control of its geometrical parameters.

We report here further studies which indicate that the resolution of retarded potential gridded energy analyzers is dependent upon aperture diameter, separation distance between the grids, separation distance between the Faraday cup and the grids, grid mesh, and plasma parameters. This last discovery indicates that a static gridded energy analyzer measuring dynamic plasma parameters would experience variable errors in measurement.

Table 1. Results from M^4X Cusp Configuration Holding Coil Current at 420 Amps and Varying μ-Wave Power.

P(kW)	$W_\perp$(eV)	n (10^{14}) m^{-3}	B_r (10^{-2}) Tesla	μ (10^{-18}) A-m^2	$\beta_\perp$ (10^{-3})	r_L(10^{-2}) m
3	3.25	1.625	11.5	2.26	5.03	0.1596
2.5	3.35	1.675	9.5	2.82	7.489	0.1362
2	3.367	1.683	8.5	3.168	9.362	0.1176
1.5	4.5	2.25	8	4.499	12.2	0.1530
1	3.63	1.815	8	3.6288	10.98	0.1684
0.5	3.25	1.6286	8	2.035	10.38	0.1595

Results from the μ-Analyzer

Measurements of the plasma generated by the M^4X device have been made using the μ-analyzer. Two experiments were performed: The first experiment held the current to the magnetic coils constant and varied the μ-wave power; The second experiment held the μ-wave power constant and varied the coil current. With the μ-analyzer, it was possible to obtain several plasma parameters in the same region simultaneously {e.g. ion energy in the perpendicular

direction ($W_\perp$), plasma density (n), local radial field strength (B_r), magnetic moment (μ), plasma beta ($\beta_\perp$), and Larmor radius (r_L)}. As can be seen in Tables 1 and 2, the ion energy in the cusp was only a few eV. The cusp was able to maintain high values of local plasma beta, ranging from 0.5 to 7.6 %.

Table 2. Results from M^4X Cusp Configuration Holding μ-Wave Power at 2.4 kW and Varying Coil Current.

I (A)	$W_\perp$(eV)	n (10^{14}) m^{-3}	B_r (10^{-2}) Tesla	μ (10^{-18}) A-m^2	$\beta_\perp$ (10^{-3})	r_L(10^{-2}) m
610	2.235	2.18	3.2	11.17	76.1	0.4672
550	1.96	2.33	3.8	8.25	50.6	0.3684
530	1.268	2.89	5.1	3.977	22.5	0.2208
480	2.663	1.997	9.7	4.392	9.04	0.16823
420	2.34	2.132	11.5	3.392	6.03	0.133
340	1.445	2.71	12.1	1.9	4.27	0.0993

It should be noted in Table 1, that the local magnetic field measurement changes as μ-wave power is increased even though the coil current remains constant. This result is attributed to the formation of hot electron rings which form a magnetic well in the plasma. The higher readings are taken at the edge of the well and are a result of field lines being forced out of the well because of the plasma's diamagnetic properties.

Results from the Variable Energy Analyzer

A variable energy analyzer has been built and tested by the authors [3]. Some of the observations that the authors made were left out of Reference 3, and will be discussed here. Results clearly show that the optimum grid separation distance is not the minimum distance, as is currently believed, and is also highly dependent upon the aperture diameter, the grid mesh, the separation distance between the grids and the Faraday cup, and is even dependent upon the plasma conditions. This latter conclusion indicates that an ion energy analyzer with static geometrical parameters will not have constant errors if plasma parameters change. If a third grid is used in the analyzer for screening out secondary electrons, then the separation distance between it and the middle grid also has an optimum.

We have found that there is a synergistic relationship between all of the geometrical parameters of the analyzer and the plasma parameters. A conventionally designed static energy analyzer used with a low temperature plasma would likely measure temperatures 2 to 10 times higher than the true temperature.

Conclusion

Two new plasma diagnostics have been designed; the μ-Analyzer and the variable energy analyzer.

The μ-Analyzer allows measurement, simultaneously of the ion temperature and the magnetic field at the same spot at the same time. The μ-Analyzer is a very important tool for studies of the magnetic confinement in plasma devices that are used in fusion research, like tokamaks, stellerators, cusps, tandem mirrors, reverse pinch mirrors, etc.

The μ-Analyzer has, in a localized point, the ability to find the $\beta_{\perp}$-parameter and μ, the diamagnetic moment (first adiabatic invariant) of the plasma and calculate the Larmor radius.

The μ-detector will be helpful in analyzing the plasma produced in M^4X in order to determine the magnetic confinement properties in the Cusp mode as well as the mirror. The μ-Analyzer will also fill the lack of this kind of diagnostic tool for fusion research experiments.[4]

The variable energy analyzer has demonstrated high resolution and accurate measurement of low temperature plasmas (< 1 eV). It was found that retarded potential gridded energy analyzers measure temperatures higher than the true temperature and that through dynamic optimization of geometrical parameters, an accurate measurement can be made. Static ion energy analyzers using conventional designs would likely measure 2 to 10 times the true plasma temperature in a sub-eV plasma.

References

1. R.L. Stenzel, R. Williams, R. Agiiero, K. Kitazaki, A. Ling, T. McDonald, and J. Spitzer, *Rev. Sci Instrum.*, **53**(7), Jul 1982.
2. N.A. Krall and A.W. Trivelpiece, Principles of Plasma Physics, McGraw Hill, 1973.
3. E. Leal-Quiros and M. A. Prelas, *IEEE Trans. Plasma Sci.*, **16** (6), 661, Dec.1988.
4. E. Sindoni and C. Wharton, "Diagnostics for Fusion Experiments".Pergamon press,1979.

OPTICAL MIXING AND MODE CONVERSION AS A CURRENT DENSITY DIAGNOSTIC IN A TOKAMAK PLASMA

Th. PIERRE and G. LECLERT

LPMI, Université de NANCY I BP 239 54506 VANDOEUVRE CEDEX FRANCE

Optical mixing has been of great interest for the past ten years, particularly in view of the development of local non-perturbative measurements in plasmas. The nonlinear mixing of two microwave beams in a magnetoplasma is here studied experimentally; such a method could be of interest as a local diagnostic for the current density in a tokamak.

This paper reports on the first experimental observation of an electron plasma wave excited by nonlinear mixing in a magnetoplasma. From the propagation properties of the excited wave, the direction of the magnetic field can be deduced. The two waves are launched perpendicularly to the magnetic field, the frequency and wavevector of the excited wave being defined as: $\omega = \omega_1 - \omega_2$, $\vec{k} = \vec{k}_1 - \vec{k}_2$, were the subscripts 1,2 are related to the incident extraordinary waves. The excited wavevector is here chosen lying along the magnetic field direction. The theoretical estimation of the coupling efficiency can be obtained from the calculation of the excited electric field, derived from the nonlinear current induced by the beating of the incident wave. This current expresses as:

$$\vec{J}_{nl} = e(n_0 \mu(\vec{v} x \vec{B}) + (m/e)\vec{v}\nabla\vec{v}) + n\vec{v})$$

where $n, \vec{v}, \vec{B}$ are the first order density , velocity and magnetic field respectively. In our case, the main component of the current lies along the magnetic field and expresses as:

$$J_{nl} = \frac{A_1 A_2 \varepsilon_0 e \omega_{pe}^2}{2\ m\ \omega_1 \omega_2\ \omega} (k_1 + k_2) \sin\Phi$$

where A_1 and A_2 are the amplitudes of the electric field of each pump wave, and Φ is the half angle between the beams. The electric field is then deduced, involving the dispersion tensor of the magnetoplasma. The power flux escaping from the interaction region is estimated, and the efficiency of the process is defined as the ratio of the excited power flux to the geometric mean of the incident power fluxes. In the case corresponding to the experiment in the laboratory plasma, choosing f_p=0.7 GHz and f_c=0.9 GHz as the plasma and cyclotron frequencies, with an incident flux of 1W/cm^2, and an interaction length of 4 cm, the efficiency is of the order of 10^{-11}. This very low level implies a very sensitive detection system for the excited wave.

Another interesting parameter for the experiment is the resonance width, which is calculated using the group velocity and the interaction length.

If we choose a plasma frequency lower than the cyclotron frequency, i.e. the case of most tokamak plasmas, the whistler mode can be excited by the nonlinear coupling, using a difference frequency slightly lower than the plasma frequency, and an excited wavevector quasi-parallel to the magnetic field direction. The excited wave can then travel down the density gradient until it reaches the plasma layer, where it can be converted into the electromagnetic ordinary mode, which can escape from the plasma and be detected outside, if the efficiency of the process is sufficient. The variations in the orientation of the orientation of the excited wavevector will then induce the variations of the detected signal outside the plasma, and the local direction of the magnetic field will then be obtained.

The experiment is carried out in a magnetized multipolar plasma device, producing a plasma column (1 m in length and 30 cm in diameter) immersed in a solenoid with a field strength lower than 900 gauss. The electron density goes up to $2.10^{11} cm^{3}$ and the electron temperature is raughly 3 eV. The micowave beams are delivered by an E.I.O. (30W) and a B.W.O. (10W) at frequencies around 70 GHz. The angle between the beams is 18 degrees, and they are focussed on the axis of the column, defining an excited wavevector of 455 m^{-1}. The detection of the wave excited by the nonlinear interaction is performed using a UHF probe moving in the interaction region . The received signal is amplified, filtered and a synchronous detection is performed, after a heterodyne detection. The probe signal is then recorded versus the electron density.

The microwave optics can be rotated around an axis perpendicular to the magnetic field, allowing to set an angle between the excited wavevector and the magnetic field. This arrangement is seen on figure 1.

A typical record is depicted in figure 2, showing that the detected level is of the order of 1.5 10^{-15}watt, roughly in accordance with the expected level. The resonance width is also in agreement with the theory. The level of the excited wave decrease rapidly outside of the interaction region.

The angle between the excited wavevector and the magnetic field is then varied, and the evolution of the detected level is recorded. The detection being always performed inside the interaction region, the angular position corresponding to the maximum level is obtained with an accuracy of 3 degrees. This result is quite encouraging, considering the poor caracteristics of the microwave optics used.

The conversion process is analysed with an antenna located outside the plasma and receiving only the ordinary electromagnetic mode. The corresponding record is shown in figure 3, where the level on a linear scale is reported versus the rotation angle of the microwave optics. An accura-

cy of roughly 5 degrees is obtained for the determination of the local orientation of the magnetic field. This larger value, compared to the *in situ* measurement is due to a rather long interaction region across the density gradient.

These experimental results allow to elaborate a diagnostic scheme for the determination of the current density in a tokamak plasma. The excited wave could be the oblique resonance of the whistler mode whose conversion into the O-mode inside the plasma layer could be used in order to obtain the poloidal magnetic field intensity inside the interaction region.

The choice for the sources for the incident waves will partly determine the angular accuracy of the proposed diagnostic. Infrared lasers could be used for a local measurement, but the large wave number associated to the sources would lead to a long interaction region. Microwaves at very short wavelengths (e.g. gyrotrons at 200 GHz) would presumably be more adequate, but refractive effects will then occur, leading to a rather difficult localisation of the interaction region.

In any case, the efficiency of the coupling will be greater with microwave sources than with laser sources. The overall efficiency of the method, including the conversion process, will depend on several parameters, including in particular the damping of the excited wave along the density gradient, which will determine the incoming power flux into the plasma layer.

An angular accuracy of a fraction of degree would be necessary for the exact determination of the current density along the minor radius of the tokamak.

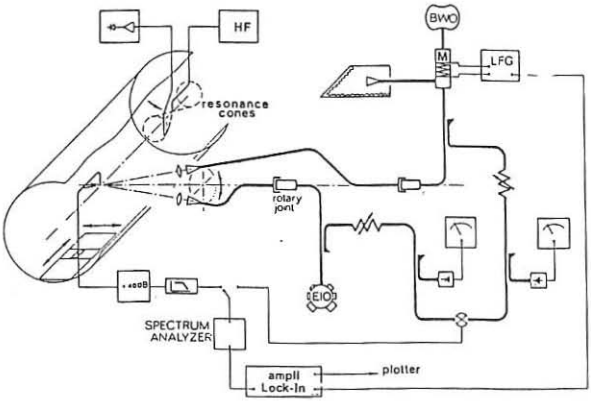

Figure 1

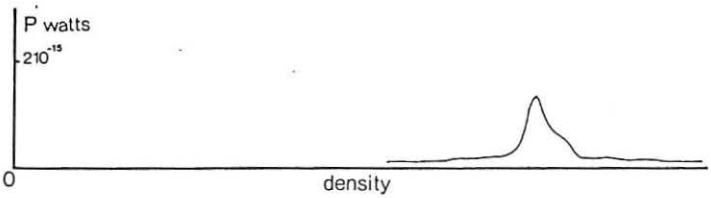

Figure 2

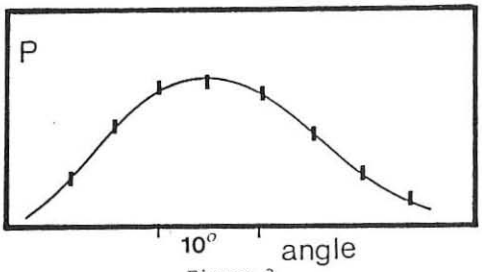

Figure 3

ION TEMPERATURE IN SOC AND IOC DISCHARGES IN ASDEX

H.U. Fahrbach, W. Herrmann, H.M. Mayer

IPP Garching, EURATOM Association, D-8046 Garching, Fed. Rep. of Germany

Abstract. Active and passive charge exchange measurements were made to investigate the behaviour of the central ion temperature and the temperature profile for SOC and IOC discharges in ASDEX. Both methods show an increase in the central ion temperature during transition from SOC to IOC. Both methods also show a wider temperature profile for ions than for electrons. Peaking of the ion temperature profile during IOC cannot be definitely concluded from the measurements.

The applied Ti-diagnostics. Passive and active beam charge exchange diagnostics were used simultaneously. The main advantage of the passive analysis is its continuous applicability during the discharge. The active system in principle allows space-resolved measurements but normally in the pulsed beam mode only.

The earlier difficulties in interpreting the passive signal at higher densities have been widely overcome. As long as the line density $\bar{n}_e$ is below about $3 \cdot 10^{19}\ m^{-3}$ the central ion temperature T_{io} can be derived direct from the passive signal. At higher densities the outer parts of the plasma deform the neutral flux spectrum and T_{io} is generally underestimated. The amount underestimated was calculated by simulations with the AURORA Monte Carlo code[1], taking into account the neutral density due to recombination[2], which is important at elevated densities. A set of correction factors was obtained for line densities of up to $8 \cdot 10^{19}\ m^{-3}$. These allow the "central" ion temperature in the line of sight of the analyzer to be determined with an estimated error of probably less than 10 %. Owing to the continuous availability of the electron density and temperature profiles from the YAG laser scattering a good basis for this correction procedure is given at ASDEX. For the ion temperature profile an estimate from the raw data and other information is made.

In Fig. 1 the underestimate obtained with the AURORA code for a large variety of ohmic discharges is shown as a function of the mean neutral energy $\langle E_{cx} \rangle$, normalized to T_{io}. Because the n_e and T_e profiles are well known the uncertainty of the correction for a distinct discharge is much smaller than the band in the figure indicates. At neutral energies higher than $7 \times T_{io}$ the resulting correction $(T_{io,cx}/T_{io})^{-1}$ is lower than 20 % even for high density and low temperature. Towards lower energies the correction and its dependence on the profiles increases. Figure 2 shows that for a given type of profile the underestimate can be uniquely determined over a wide range of temperatures T_{io}. In all our measurements the neutral fluxes were sufficiently high to permit evaluation at energies higher than about $5 \times T_{io}$ and to keep the correction to less than 35 %.

The active diagnostic takes into account beam penetration, charge exchange and absorption of the neutrals on the way to the analyzer. The accuracy of these calculations depends mainly on the accuracy of the density measurement (YAG laser). The temperature evaluation procedure is improved in several respects, the most important being that the statistical weight of the measuring points is taken into account. Not included hitherto, however, are effects resulting from the beam halo. For the high densities concerned in this paper the active system is at the limit of its applicability and the error for the central temperature might be as large as ± 15 %.

SOC-IOC discharges. Since ASDEX was remodelled for long-pulse heating and the slits between the main chamber and divertor were reduced, at mean densities higher than $3 \cdot 10^{19}\ m^{-3}$ a new ohmic confinement regime, the IOC regime, has been detected[3,4]. It has peaked density profiles and improved confinement and can be induced and sustained by reduced gas puffing. The hitherto usual regime has flat density profiles and a saturated confinement time at large densities and is called the SOC regime.

Figure 3 shows the temporal behaviour of various physical quantities in a series of discharges with two SOC-IOC transitions. The line density $\bar{n}_e$ was used for controlling the plasma density. During the first density flat-top the plasma stays in the linear confinement regime. Then the first strong gas puffing increases the density and the saturated regime is reached. During the second density flat-top there is a transition from SOC to IOC. With the density increase towards the third plateau the plasma switches back to the SOC discharge but recovers to IOC during the plateau. The central electron and ion temperatures are strongly modulated during these transitions. The values are clearly higher during IOC and lower during the SOC phase. From the figure the amplitude might appear to be lower in the active T_i measurements than in the passive ones. The complete set of data, including discharge series, which are not shown here, proves that this difference has to be contributed to statistics, and that there is no systematic difference in the central ion temperatures gained with the active and passive methods (see Fig. 4). The time dependences of the central electron and ion temperatures are very similar. The gap between the two is smaller during IOC than during SOC. This would be consistent with the assumption of reduced anomalous ion transport during IOC[5].

Figure 3 also gives information on the profiles in the form of peaking factors (central value divided by the volume-averaged value). Strong anomalous transport as would be caused by η_i-modes could lead to a less peaked profile during SOC. The ion temperature profiles were measured in a series of shots with different analyzer sightlines in the plasma. As Fig. 3 shows, the changes in the peaking factor of T_i are within the error bars and a possible peaking of the T_i profile during transition to IOC is less than 10 %. The gradual peaking of the T_i profile during the IOC, which is indicated in the passive data and approximately follows the density peaking is at the detection limit and is not confirmed by the other experimental series.

The T_i profiles are consistently broader than T_e profiles and show higher ion than electron temperature at the edge. This behaviour is reproduced in many other profile measurements on ASDEX. Figure 4 shows the ranges of active and passive ion temperature profiles found during SOC and IOC. In the central plasma region the ranges overlap well, but in the outer plasma regions the passive ion temperatures are

systematically higher than the active ones. The difference may be due to the fact that ripple-banana trapped fast ions influence the passive measurement[6], which especially measures the fast ion tail in contrast to the active system, which can use each part of the spectrum.

Future improvements. In the passive diagnostic the trapped particles can be avoided during the next measuring period by toroidal inclination of the analyzer. The necessary correction factors can be determined more accurately by iteratively using the obtained profile in the simulation runs. For the active system the application of He beams[7] may reduce possible halo effects and the disturbance, especially of the central measurement, produced by the three energy components of the hydrogen beam.

Summary. The accuracy of passive charge exchange ion temperature measurements at high plasma densities has been improved by plasma simulation calculations with the AURORA Monte Carlo code. The central ion temperatures from active and passive measurements agree within the error bars. The profiles from the passive method are wider than those from the active method. The difference may be due to ripple-banana-trapped fast ions. During transition from SOC to IOC the central ion temperature increases by around 40 % and the ratio T_i/T_e from 75 % to 90 %. This is consistent with lower anomalous transport during IOC than during SOC. Generally, the ion temperature profiles are distinctly wider than the electron temperature profiles obtained with the YAG laser.

References.

[1] M.H. Hughes, D.E. Post, J. Comp. Phys. **28**, (1978) 43.

[2] R.J. Goldston, Plasma Physics **20**, (1978) 1199.

[3] E.R. Müller et al., 15th Europ. Conf. on Contr. Fus. and Plasma Heating, Dubrovnik, 1988, **12B**, 19.

[4] F.X. Söldner et al. Phys. Rev. Lett. **61**, (1988) 1105.

[5] O. Gruber et al., Plasma Physics and Controlled Fusion, **30**, (1988) 1611.

[6] E.L. Berezovskij et al., Nucl. Fusion **23**, (1983), 1575.

[7] W. Herrmann, IEA Large Tokamak Workshop on Ion Temperature Measurements, Princeton (USA), 1987.

Figure Captions.

Fig. 1: Results of the AURORA code simulations for a large variety of plasma parameters, which covers well the ohmic operational range of ASDEX. $T_{io,cx}/T_{io}$ is the underestimate of ion temperature when determined direct from the slope of the passive CX spectrum. $\langle E_{cx}\rangle/T_{io}$ is the mean energy of CX flux used for evaluation and normalized to T_{io}. (A, B, ... = 1, 2 ... points).

Fig. 2: Similar to Fig. 1, but all plasma parameters fixed to the values during the IOC phase, except T_{eo} and T_{io}, which are varied.

Fig. 3: Time evolution of temperatures and density in discharges with SOC-IOC transitions.

Fig. 4: CX ion temperature profiles during the SOC and IOC phases.

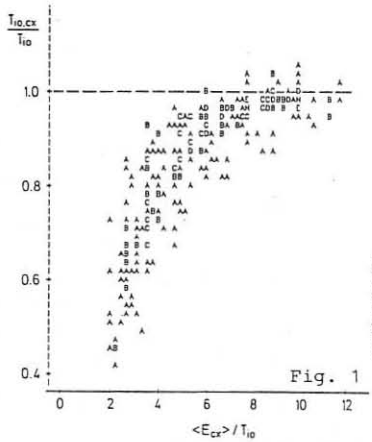

Fig. 1

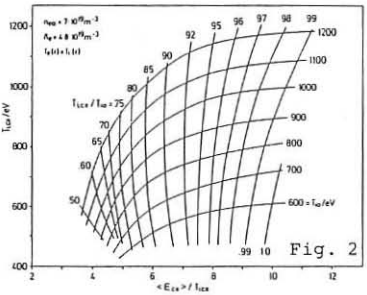

Fig. 2

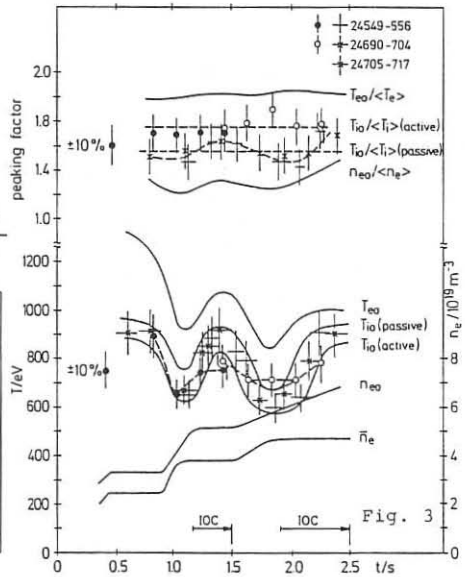

Fig. 3

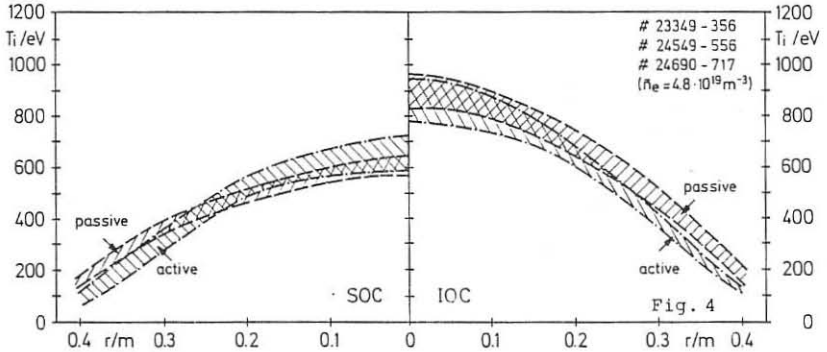

Fig. 4

DETERMINATION OF THE POLOIDAL FIELD AND SHAFRANOV SHIFT IN TOROIDAL PLASMAS BY MEANS OF MOLECULAR HYDROGEN BEAMS.

W. Herrmann

IPP Garching, EURATOM Association, D-8046 Garching, Fed. Rep. of Germany

The local q-value is one of the important parameters for the stability and transport behaviour of plasma. Its determination requires knowledge of the toroidal and poloidal components of the magnetic field and of the minor radius of the flux surface. (For references for q-measurements see [3].) In many cases the toroidal field is known well enough, whereas the minor radius is less well known owing to different shifts and possible changes in the plasma configuration, and the poloidal field is often not known at all. This paper describes a method of directly evaluating the local ratio of the poloidal and the toroidal fields and the Shafranov shift, if the field geometry is known.

The method. A molecular hydrogen beam is radially injected into a toroidal field geometry with negligible ripple. Its energy is assumed to be 30 keV in the context of this paper. Part of the molecules are ionized in a first collision at time a and are dissociated after some rotation in a second collision at time b. During rotation in the field the radially injected particles gain axial velocity v_z as a result of interaction with the poloidal field (in a locally straigth geometry with cylindrical coordinates the z-component corresponds to the toroidal component and the poloidal field is split into a radial and an azimuthal component, see Fig. 1):

$$v_z = \int_a^b \dot{v}_z dt = \int_a^b \frac{q}{m}(v_r B_\vartheta - v_\vartheta B_r) dt.$$

This equation may be written in the following way:

$$\alpha \approx \frac{v_z}{v_o} = \int_a^b \frac{B_{pol}}{B_z} \cdot (\frac{v_r}{v_o} \cdot A - \frac{v_\vartheta}{v_o} \cdot B) \cdot \omega_z \, dt = \int_\gamma^\delta \frac{B_{pol}}{B_z} \cdot \frac{v_{pol}}{v_o} \cdot F(r, \vartheta, \psi) \cdot d\psi.$$

Here $F(r, \vartheta, \psi) = A(r, \vartheta) \cdot sin(\psi - \vartheta) - B(r, \vartheta) \cdot cos(\psi - \vartheta)$ is a pure geometrical factor, q and m are the charge and mass of the particle, ω_z the Larmor frequency in the toroidal field, v_o the total and v_{pol} the poloidal velocity of the molecular ion. γ, δ and ψ are phase angles in the frame of the toroidal Larmor orbit. As long as v_z is small and the field can be replaced by the field of the guiding centre, v_z only depends on the field geometry, here assumed to be known, and the unknown ratio of the poloidal and toroidal fields.

In many cases areas in the plasma can be indicated where the radial component of the poloidal field is negligible. One then has A=1 and B=0. In any case, as long as the

field geometry is known the axial velocity can be calculated as a function of the ratio of the poloidal and toroidal fields. A neutral particle analyzer with spatial resolution in the toroidal direction can measure this axial (toroidal) velocity, determining the toroidal angle of the neutral product of the dissociated molecule. From comparison of the measured and calculated angles one obtains the field ratio at the crossing point of the molecular beam and the line of sight of the analyzer.

Production and penetration of molecular beams. Production of molecular ions in hydrogen sources is well known and can be optimized. With low pressure in the neutralizer[1)], the number of full-energy neutral molecules may be larger than 25 % of the half-energy atoms (which may disturb the measurement) and larger than 20 % of the accelerated molecular ions at 30 kV. The penetration is mainly determined by charge exchange, which is very similar for 30 keV molecules and 15 keV atoms[2)]. As the neutrals after dissociation are emitted into a limited space in a small energy range, the beam intensity or the penetration can be much lower than for the usual active charge exchange diagnostic, where the particles are emitted into full space and a wide range of energies. This means that the method is applicable at larger $\int n \; d \; l$ than active charge exchange.

Dissociation of the molecule. After the charge exchange (or ionization) process the molecule will be dissociated rather fast. In a 1 keV plasma and for a 30 keV molecule the plasma density for a dissociation e-folding time equal to a Larmor period in a 2 T field is about 5×10^{13} cm^{-3}. Although the axial velocity slightly changes with increasing number of turns of the molecule for a given observation line, this will not affect the measurement, because the short lifetime of the ionized molecule ensures that the atomic hydrogen is emitted during the first turns.

Influence of the atomic beam particles. Atomic hydrogen with half-energy may undergo double charge exchange in the plasma and hit the analyzer with the same energy as the atoms emitted from dissociation. If the second charge exchange occurs during the first turns of the ion, these atoms do not disturb but add to the signal. The charge exchange process of the beam ions even with the neutral particles of the beam is, however, much less probable than dissociation of the molecule. With (high) neutral beam densities of 10^9 cm^{-3} the lifetime of an ion for charge exchange is at least 7 ms or 1.0×10^5 turns. As the drift time of a 15 keV proton to the plasma edge (40 cm) in the gradient of the toroidal field is of the order of 100 μs, only about 1 % of the protons have a chance of charge exchange during this time and actually the proton will have left the beam area in the line of sight of the analyzer ($\approx$2 cm) in 5 μs. As the number of molecules was estimated at about 25 % of the protons with corresponding energy, the direct double charge exchange proton contribution to the signal will be much less than 5 %. The contribution of the trapped protons originating from outside the analyzed area is even smaller. Although their number is 20 times as large (40 cm beam path compared with 2 cm of analyzed beam area), the neutral density outside the beam is much smaller and only a small fraction of the trapped ions (about 5 %) makes a charge exchange collision when crossing the field of view of the analyzer.

Model calculations for ASDEX geometry. In ASDEX (see Fig. 1) a diagnostic beam can be radially injected from below 30° from the vertical axis in the poloidal direction. An analyzer can observe the beam through a horizontal port. For this geometry model calculations were made to relate the toroidal angle of the escaping atoms

to the field ratio, averaged over the path of the ionized molecule. The equations of motion were solved in local Cartesian geometry with a ripple-free toroidal field and a poloidal field, linearly increasing with the radius of the Shafranov-shifted circular flux surfaces and inversely proportionally to the major plasma radius. Figure 2 shows the toroidal angle α as a function of the geometrical minor radius of ionization of the molecule. According to the toroidal field directions in ASDEX the molecule rotates about three-quarters of a turn till dissociation with a velocity in direction of the analyzer. The Shafranov shift in this case is 5 cm. The angular width of the curve is due to a possible maladjustment of the beam of ± 1 cm in the radial direction when crossing the horizontal midplane. Figure 3 shows α for different Shafranov shifts and at the same time gives the value $\bar{\beta}$ defined as the arctangent of the average ratio of the poloidal and toroidal fields in degres. A 10 % error in determining the Shafranov shift leads to an error in measuring β of less than 0.1°.

Proposal for the measurement of the Shafranov shift and the poloidal field. If the beam scans across the plasma and the analyzer observes the atomic flux in the toroidal midplane (with perpendicular flux surfaces), not only can the poloidal field be measured over a large part of the plasma cross-section but also the Shafranov shift. Figure 4 displays the toroidal angle α as a function of the radial position of the measuring volume in the midplane. α crosses zero at the position of the Shafranov shift. As the analyzer can be calibrated in situ for zero plasma current by observing the double charge exchange protons in a gas-filled chamber with toroidal field, the shift can be determined absolutely. The width of the curves gives the spread of the observed angle by observing the area about 1 cm above and below the midplane.

Effects of divergence and Frank-Condon effect. A systematic shift of the beam or analyzer can be detected and corrected by the in situ calibration. However, the divergence of the beam, and here especially the toroidal divergence, adds directly to the observed angle. The beam divergence should therefore be reduced to about $\pm 0.5°$ by suitable diaphragms. Also the widths of the beam should be reduced to a few cm. The unavoidable Frank-Condon effect, which contributes a mean energy of 4.5 eV to the atom, leads to an angular spread of $\pm 1°$ and a mean value in the toroidal direction of 0.64°. These symmetric angular spreads reduce the requirements for the angular resolution of the analyzer. A resolution of even more than 0.2° will allow the maximum of the angular distribution to be determined with an accuracy of about 0.2°.

Discrimination of the signal against charge exchange background. Although the molecular content of the total beam may reach only 10 %, the beam induced charge exchange signal at the energy of the dissociated neutral atom will be much smaller than the signal to be measured, because of the wide energy and angle spread of the charge exchange neutrals. In any case the passive and the actively induced background can be subtracted, when a pulsed beam is used and if the observation includes angles, where the signal to be measured is expected to be zero.

The measuring device. The analyzer could work with electrostatic deflection without mass analysis. Diaphragms reduce the observation angle along the beam, and the beam itself limits the observation in the toroidal direction. Stripping of the 15 keV neutral atoms in the analyzer could be done in a foil. Detection can be performed via channel plates that view a toroidal angle of about $-2°$ to $+8°$ and are divided into a number of subsections depending on the desired angular resolution.

Summary. The toroidal angle of the energetic atoms resulting from dissociation of an injected and ionized hydrogen molecule can be measured and related to the local value of the poloidal and toroidal field ratio. From these measurements the Shafranov shift and the local values of q can be determined. For ASDEX q=1 at r=0.1 m leads to a mean angle of about 3.5°. q-values in this range might therefore be determined with an accuracy of better than 10 %. The time resolution is expected to be of the order of 1 ms. This measurement may therefore give additional information about the redistribution of currents during sawteeth or internal disruptions.

Acknowledgements. The author is indebted to H.M. Mayer, who drew his attention to this subject, to S. v. Göler, who contributed some aspects of his earlier considerations for PDX, and to H.-U. Fahrbach and K. Lackner for helpful discussions.

References.

[1] J. Kim, H.H. Haselton, ORNL/TM-6302, July 1978.

[2] R.L. Freemann, E.M. Jones, Culham Laboratory Report CLM-R137, (1974).

[3] H. Weisen et al., LRP 353/88, Lausanne, 1988.

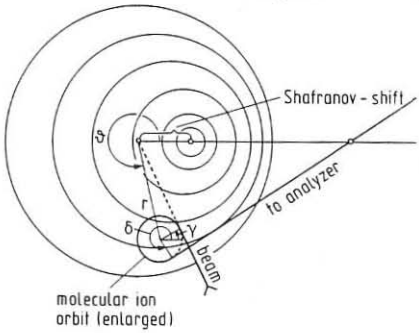

Fig. 1

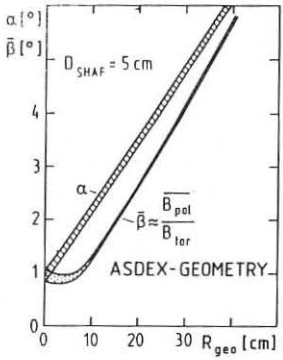

Fig. 2

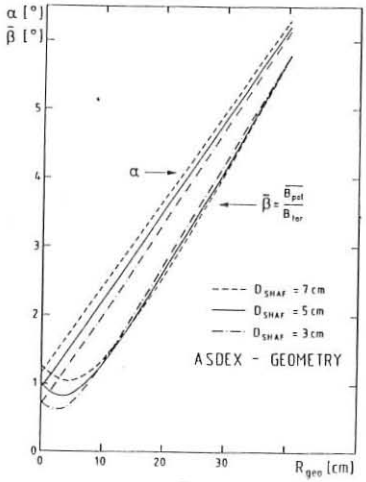

Fig 3

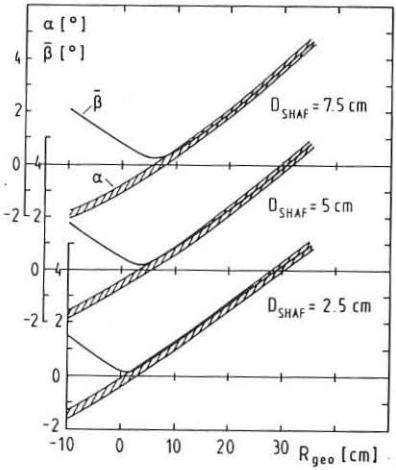

Fig. 4

Non-Doppler Broadening Mechanisms of CXRS-Emission Profiles and their Contributions to Ion Temperature Measurements

J. V. HOFMANN, G. FUSSMANN

Max-Planck-Institut für Plasmaphysik
D-8046 Garching, West Germany

We discuss various broadening mechanisms on emission profiles in the UV and visible range resulting from charge exchange recombination (CXR) reactions. In particular, broadening contributions from fine structure splitting, Zeeman - and Stark effects are calculated for Kr^{25+} and O^{7+} ions to deduce ion temperatures in ASDEX.

1. Introduction

During the last years charge exchange recombination spectroscopy has been developed to a very successful diagnostic tool in tokamak devices where high energy neutral injectors are applied for additional heating. Especially the UV and visible range experienced a renaissance because of apparative advantages and the possibility to substantiate fully stripped ions in the plasma core providing important information on the plasma ion temperature, plasma rotation velocity and impurity concentrations. The charge exchange reaction

$$\begin{aligned} H^0_{(beam)} + X^{Z+}_{(impurity)} &\rightarrow H^+ + X^{(Z-1)+}(n,l)^* \\ &\rightarrow H^+ + X^{(Z-1)+}(n',l')^* + h\nu \end{aligned}$$

leads to photon emission in the UV and visible range which is most suitable for ion temperature measurement based on the Doppler broadening of the profiles. The emission results from $\Delta n = 1$, $\Delta l = 1$ transitions of highly excited Rydberg states (n',l')*. In this context we do not consider possible - but generally small - deviations between the temperatures of background and impurity ions [1] but concentrate on atomic physics aspects. Specifically contributions from fine structure splitting of the generally unresolved l-levels of a transition, the Zeeman splitting in the magnetic field of the tokamak and the translational Stark effect due to the $\vec{v} \times \vec{B}$ field of the ions may have a non negligible influence on the total broadening depending on the investigated impurity and the observed transition.

We elucidate these effects by refering to H-like $^8O^{7+}$ and Na-like $^{36}Kr^{25+}$ which are sufficiently different in mass and charge. The visible transitions of these two ions and their population structures have been carefully analysed in ASDEX [2,3].

2. Fine Structure Contributions

We first calculate the intensities of all $\Delta l = \pm 1$ transitions within an observed $\Delta n = 1$ emission line. An example is shown in *Fig.* 1 where these intensities are plotted as a function of wavelength λ for the measured Kr^{25+} transition n = 17-16 ($\lambda =$

302.11 nm). As expected, the emission is dominated by the $\Delta l = -1$ transitions (labeld ○) originating from the highest l-states. The $\Delta l = +1$ transitions are much smaller in intensity (see logarithmic insert). The fine structure for H-like O^{7+} is obtained from the well-known relation

$$E_{nj} = E_n^0 + \Delta E_{nj} = E_n^0 \left(1 + \frac{(Z\alpha)^2}{n}\left(\frac{1}{j+1/2} - \frac{3}{4n}\right)\right)$$

with $E_n^0 = -(Z\alpha)^2 \cdot mc^2/(2n^2)$, $\alpha = e^2/(4\pi\epsilon_0 \cdot \hbar c)$, $j = l \pm 1/2$. For the lower j-levels of Kr^{25+} which, however, contribute very little to the total intensity this formula cannot be used. The numerical calculations are based on a code by Summers [4].

Next we assign to each transition a Doppler profile and obtain by superposition the total emission profile shown in *Fig.* 2 (labeled as ○). To this profile we fit a single Gaussian to deduce a fit temperature. According to our measurements we choose Poisson statistics for the weight of the datapoints. The resulting fit, which is very close to the data in the core region, is the solid curve in *Fig.* 2. However, as can can be seen, some deviations remain in the wings of the profile.

Applying this procedure for several temperatures as input (T = 0.5-6 keV), our calculations yield a linear dependence between true and fit temperatures with a slope very close to 1 but with a positive off-set for the fit temperature. For the n = 17-16 transition of Kr^{25+} this off-set is as large as $T_{fit} - T_{true} = 1.7$ keV. This clearly demonstrates the importance of the additional fine structure broadening in this case. In the case of the O^{7+} n = 10-9 (λ = 606.83 nm) transition this contribution is markedly reduced to 0.16 keV.

3. Zeeman- and Stark-Effect

The contributions according to Zeeman splitting and translational Strak effect are estimated for ASDEX conditions ($B = 2$ T) for the observed $\Delta n = 1$ transitions (Kr^{25+} : n=23-22,...16-15, O^{7+} : n=10-9,...8-7,). Strictly speaking we have to consider the anomal Zeeman effect for each unresolved fine structure transition which leads to a vasting number of components. However, for high orbital momenta l and $j = l \pm 1/2$ (one electron outside closed shells) the Landé g-factor, $g = 1 + (j(j+1) + s(s+1) - l(l+1))/(2j(j+1))$, is always close to 1. In this case the anomal Zeeman effect can be approximated by the normal Zeeman effect yielding triplets with a total energy splitting of $\Delta E = 2 \cdot \mu_B \cdot B$ where μ_B is Bohr's magneton. To a first estimate we take this splitting into account by assuming an additional equvalent Gaussian broadening (typically $\Delta E = 2.3 \cdot 10^{-4}$ eV). After performing the corresponding convolution with the Doppler profile we find a rather small effect on the fit temperature of order 1-3 % for both Kr^{25+} and O^{8+}.

The translational Stark effect is estimated for $B = 2$ T and $T_i = 2$ keV, leading to a characteristic electric fieldstrength of $\mathcal{E} = \sqrt{2E/m} \cdot B = 3.0 \cdot 10^5$ V/m for oxygen. In this case we have to consider a splitting of the degenerate j-levels ($j = l \pm 1/2$) given by

$$\Delta E_S(eV) = \frac{3}{2} \cdot \frac{\mathcal{E}}{\mathcal{E}_0} \cdot E_0 \cdot \frac{n}{2Z} \cdot \frac{\sqrt{n^2 - (j+1/2)^2}}{j \cdot (j+1)}$$
$$= 3.971 \cdot 10^{-11} \cdot \mathcal{E}(V/m) \cdot \frac{n}{Z} \cdot \frac{\sqrt{n^2 - (j+1/2)^2}}{j \cdot (j+1)}$$

where $E_0 = 2 \cdot hc/e \cdot Ry = 27.2$ eV and $\mathcal{E}_0 = e/(4\pi\epsilon_0 \cdot a_0^2) = 5.142 \cdot 10^{11}$ V/m. This yields for example a splitting of the O^{7+} $n = 10$, $l = 8$, $j = 17/2$ level of $\Delta E_S(O^{7+}) = 8.039 \cdot 10^{-7}$ eV which is only 0.75 % of the fine structure splitting. The splitting increases for the lower j levels and reaches for $j = 1/2$ about 7 % of the fine structure. Conversely, for the highest j component ($j = 19/2$) the Stark splitting is exactly zero since this level is not degenerate. Since the main contribution to our investigated lines originates from the highest l- and j- states we conclude that the Stark effect can indeed be neglected.

4. Results

In *Figs.* 3, 4 the several contributions to the ion temperature for the visible krypton and oxygen transitions are plotted. The numerically determined fit temperature (FIT) is asumed to be the sum of the various contributions namely Doppler (D), fine structure (FS), Zeeman (B) and apparative broadening (A). Apart from the FS contribution, all other terms are known independently. The FS term is thus obtained from $T_{FIT} = T_D + T_{FS} + T_B + T_A$. Clearly Doppler broadening dominates in all cases but for the medium Z ion Kr^{25+} the contribution of the fine structure is already 24 % of the fit temperature.

A direct comparison of ion temperatures from different ionic spezies has not jet be performed. Taking the various broadening contributions into account we compare doppler temperatures for O^{7+} and Kr^{25+} with those deduced from neutron flux measurements. For O^{7+} we find an agreement within the error bars (2.7 $\pm$ 0.3 keV). In the case of Kr^{25+} however the determined Doppler temperatures (4 keV) are systematically to high by more than 30 %. A possible explanation for this difference could be an underestimation of the fine structure splitting of the lower j-levels. The different scalings of the additional broadening terms with wavelength (see *Figs.* 3, 4) together with our observations on ASDEX suggest the O^{7+}, n = 10-9 (λ = 606.83 nm) transition as best suited for ion temperature measurements using CXRS in cases where intensity problems are of minor importance. On the other hand the Kr^{25+} lines may be more suited for rotation measurements because of a more favourable relation between lineshift and broadening.

REFERENCES

[1] . Fussmann, *Effects on doppler profiles in beamheated plasmas*, JET-R(87)12 (1987)

[2] J. V. Hofmann, G. Fussmann, G. Janeschitz, *Charge Exchange Spectroscopy (CXRS) of Highly Ionised Ions in ASDEX*, in *DPG - Frühjahrstagung (Düsseldorf, FRG, Feb 29 - Mar 4, 1988)*, IPP III/134, April 1988

[3] J. V. Hofmann, *Spectroskopische Analyse von Umladungsprosessen hochionisierter Rydberg-Atome am Experiment ASDEX*, Thesis, Technische Universität München, Nov. 22, 1988

[4] J. Spence, H. P. Summers, *The recombination and level populations of ions: III. The role of charge exchange from neutral hydrogen*, J. Phys. B, Vol 19, 3749-3776 (1986)

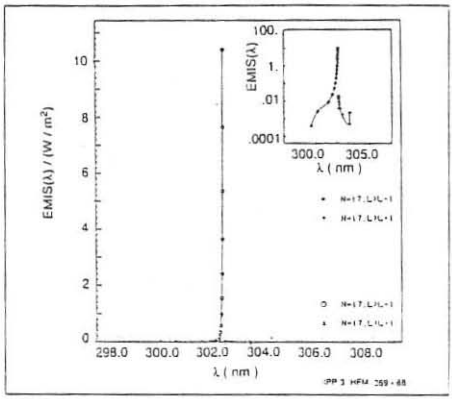

Fig. 1: Contributions of the fine structure components for the $^{36}Kr^{25+}$ n = 17-16 (λ = 302.11 nm) transition. The $\Delta l = -1$ transitions are labeled $\circ$, the $\Delta l = +1$ transitions, only to be seen in the logarithmic insert, are labeled $\triangle$.

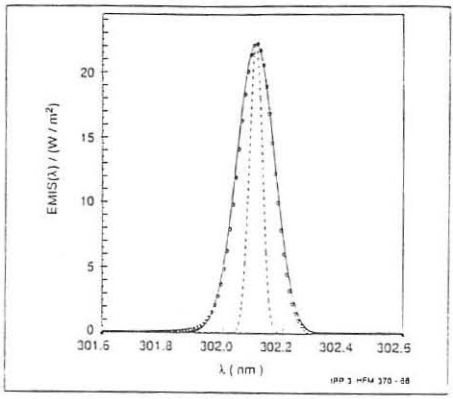

Fig. 2: Complete line profile of the Kr^{25+} n = 17-16 transition shown in *Fig.* 1 including all Doppler broadened fine structure components (dotted curve). The fitted single Gaussian (solid line) and the apparative profile (dashed line) are also shown.

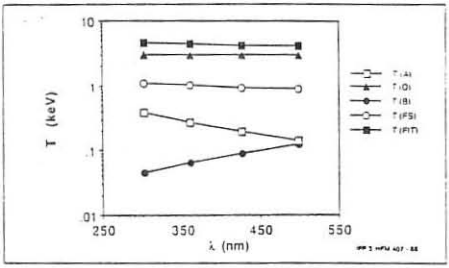

Fig. 3: Contributions to the ion temperature for Kr^{25+} including effects of: apparative profile (A), Doppler broadening (D), Zeeman effekt (B), fine structure (FS) and fit temperature (FIT).

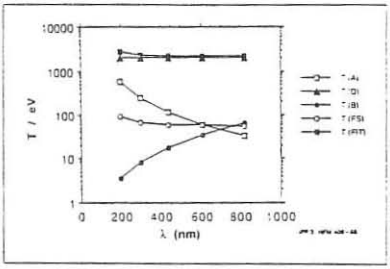

Fig. 4: Contributions to the ion temperature in case of O^{7+} analog to *Fig.* 3.

Impurity concentrations and their contribution to Z_{eff} in ASDEX

G. Janeschitz, L. B. Ran*, G. Fussmann, K. H. Steuer
and the ASDEX team

Max Planck Institut für Plasmaphysik, ERATOM Association
D-8046 Garching

Introduction:

We report on a new method to obtain immediately after the discharge timedependent central impurity concentrations of the four most important impurity species (C,O,Fe,Cu) found in ASDEX, from VUV spectroscopy (SPRED). Up to now impurity densities have been obtained at the earliest, one day after machine operation from the comparison of absolutely measured line intensities (Cu XIX, Fe XVI, O VI, C IV)(Fig.1) with the corresponding intensities calculated by a time dependent transport code (ZEDIFF)/1/. Besides the time delay, this method suffered from the fact, that only a few discharges could be looked at due to the complexity of the input data file and the time consuming calculations performed on the CRAY computer. Following a procedure developed at JET/2/ to obtain concentrations of metallic impurities directly by a fit- function, which connects measured line intensities with the corresponding central impurity densities, using measured ne and Te profiles, we introduced a similar method on ASDEX. This enables us to obtain the time dependent central concentrations of the four dominating impurities as well as Z_{eff}(VUV) immediately after each discharge.

Parameterization procedure:

In order to calculate the dependence of line intensities of various ion species on electron temperature and density an extended scan over the accessible parameter range at ASDEX was performed with our impurity transport code ZEDIFF. This scan was made for 2 different confinement scenarious:

1.) ohmic confinement where the electron density and temperature profiles were taken from an ohmic standard discharge (n_e= 2.8.10^{13} cm^{-3}) and the impurity transport was defined by an anomalous diffusion coefficient of D(r) = constant = 5000 cm^2s^{-1} for C and O, D(r) = 4000 cm^2s^{-1} for Fe and Cu, and an inward drift velocity v_{in}= 230 cm s^{-1} at the plasma edge (with a linear decay towards the plasma center).

2.) NBI heated L-mode confinement where the density and temperature profiles are obtained from a standard L- plasma (1.5 MW NBI- heating, n_e= 3.5.10^{13} cm^{-3}) and the impurity transport is defined by D(r) = constant = 9000 cm^2s^{-1} and v_{in}= 230 cm s^{-1} at the plasma edge. As described in /1/ the changed ionisation equilibrium due to charge exchange recombination from beam neutrals is also taken into account by the code.

The electron density and temperature profiles are obtained from the ASDEX Thomson scattering diagnostic timedependently.

In our parameter scan the central density was changed from 1.10^{13} cm^{-3} to 8.10^{13} cm^{-3} in steps of 1.10^{13} cm^{-3} by keeping the shape of the profile constant. For each density the central electron temperature was varied from 500 eV to 2500

* Southwestern Institute of Physics P.O. Box 15, Leshan, Sichuan, P.R. of China

eV in steps of 500 eV, again keeping the temperature profile shape constant. These calculations were performed for the above mentioned four main impurity species Cu, Fe, O, C. For each species the most prominent line intensities between 10 nm and 110 nm (Cu XIX _ 27.4 nm, Fe XVI _ 33.6 nm, O VI _ 103.2 nm, C III _ 31.2 nm, C IV _ 38.4 nm) were calculated considering a central impurity density of $n_Z(0)=10^{10}\ cm^{-3}$. We thus obtain the line intensities I^Z as a function of ne(0) and Te(0). By applying an exponential fit- ansatz this dependence can be written as:

$$I^Z = a0 * n_e(0)^{\alpha} * T_e(0)^{\beta} \quad (1)$$

taking the logarithm of eqation (1) we obtain a system of linear equations, which allows us to calculate the coefficients a0, α and β by using a linear regression fit. In fig. 1a the O VI line intensity (103.2 nm) calculated by the impurity transport code for various electron- densities and temperatures (trangles) is compared with the O VI intensity obtained from the fit formula (solid line). Fig. 1b displays the same comparison for the Cu XIX line intensity (27.3 nm). As to be seen the agreement between the fit formula and the transport code is quite satisfactory.

Central impurity concentrations and Z_{eff}:

In order to determine the central impurity densities for a special discharge, we have to compare the intensities calculated by the fit formula with the absolutly measured ones obtained from the VUV SPRED spectrometer.

$$n_Z(0) = (I^Z_{SPRED} / I^Z_{calc.}) * 10^{10}\ cm^{-3} \quad (2)$$

These calculations are made for all four main impurity species time dependently on a regular basis imedeately after each discharge. In addition their contributions to the central Z_{eff} resulting in the total $Z_{eff}(0,t)$ can be calculated by introducing an average charge state (in the plasma center) for each ion species:

$$Z_{eff}(0) = \sum n_Z(0) * Z^2 / n_e(0); \quad \text{where:}(Z_C = 6;\ Z_O = 8;\ Z_{Fe} = 22;\ Z_{Cu} = 24) \quad (3)$$

This simple approach for the average charge state in the plasma center is justified by the fact that in the main part of our parameter space these numbers are correct, while at the two extreme ends the situation is as follows: At high density and low temperature the metallic concentration is very low and does practically not contribute to Z_{eff}. The light impurities, which then solely define Z_{eff}, are also under these conditions totally stripped in the central plasma. On the other hand, in low density, high temperature discharges the metallic contribution to Z_{eff} is more important, which is also true for additional heating. In these cases the above listed charge states again agree rather well with the experimental ones. Moreover, small devations (+-2) in the charge states of the metallic impurities do not have a significant effect on Z_{eff} which is largely dominated by the two light impurities.

Experimental results:

The above described method has been applied to all discharges of the last experimental campain. However, the results obtained are only correct for the two parameterized confinement regimes (OH, L), thus we are not able to assess impurity concentrations for the high confinement plasmas (H-mode, pellet, counter NI) observed in ASDEX. Due to the limited space we can only present the impurity concentrations and their contribution to Z_{eff} for a few representative discharges under carbonized wall condition.

- During **ohmic heating** several density scans have been performed covering almost the whole parameterized density and temperature range. The dependence of the central concentration of O and C on $n_e(0)$ is displayed in Fig.2a. In this case we observe an almost inverse linear dependence of the light impurity

concentration on the electron density. This dependence is more pronounced for carbon than for oxygen, resulting in twice as much carbon (4%) compared to oxygen (2%) at low densities ($2*10^{13}cm^{-3}$). The metallic impurity concentration on the other hand (Fig. 2b), shows almost no dependence on $n_e(0)$ above $3.5*10^{13}$ cm^{-3} but increase nearly exponentially towards lower densities. This behaviour reflects the retention capability of the ASDEX divertor for target plate produced materials /3/. We have to point out that practically 100% of the Cu influx and approximately 30 to 50% of the Fe influx is produced in the non carbonized divertor chambers/4/. Thus the Cu contribution to Z_{eff} at low densities ($2*10^{13}$ cm^{-3}) becomes as important as the contribution of oxygen or carbon.

Fig.2c shows the n_e- dependence of the contribution of the different impurity species to Z_{eff} and the dilution of deuterons. Further, the spectroscopic- Z_{eff} is compared with the bremsstrahlung- Z_{eff}. The over all agreement between these two quantities is rather good, except for low densities where the spectroscopic Z_{eff} is always higher than the bremstrahlung- Z_{eff}. This systematic deviation can be partly explained by the worse fit quality in this range (Fig. 1). In addition however, the uncertainity in determining n_e at the position of the radiating shells of C IV and O VI is increasing when these shells are shifted outwards towards stronger density gradients due to the higher temperatures at low n_e.

- During neutral **beam heating** with two different beam species (H^0, D^0) and during combined **beam- (1.2 MW) and ICRF- heating (2 MW)** the above described method proved to be a powerful tool for automatic impurity evaluation also under **L- mode** conditions. Fig. 3a shows the time dependence of the Z_{eff} contributions and the D^+ dilution for a beam heated (1.2 MW) L- mode discharge. There is a first heating period (0.8 - 1.7 sec) of 1.0 MW with H^0 beams and a second one (2.0 - 2.9 sec) of 1.2 MW with D^0 beams. During the first period the moderate increase of Z_{eff} (1.7 to 2.2) is mainly caused by an increase of carbon as well as Cu and Fe. This behaviour coroborates the observed enhancement of wall erosion during neutral beam heating. In the D^0 heating period Z_{eff} increases to a value higher than 3, with a contribution of all four impurities (Fig.3a). In agreement with previous results/3/ the D^0 beams seem to cause much higher wall erosion especially in the divertor region compared to the H^0 beams. The dilution of D^+ in the second heating period turns out to be already 35%, mainly due to the relatively high concentration of light impurities (C+O=2.9%).

In addition to pure NI- heating 2.0 MW ICRH heating was applied to the above discharges during 0.9 to 2.7 seconds (Fig.3b). Three time intervals can be distinguished: During the first one (H^0+ICRH) Z_{eff} nearly reaches 3 due to a strong increase of C and Fe wheras O and Cu show only a slight increase compared to the pure NI case. This behaviour is consistent with previous conclusions/5/, according to which ICRF enhances the wall erosion in the main chamber due to accelerated ions in the scrape off layer. In the second interval (1.7 - 2.0 sec) of pure ICRF heating Z_{eff} is reduced to 2.4 mainly by the reduction of Cu and Fe. In the third interval (D^0+ICRH) Z_{eff} rises up to 4 due to a pronounced increase of the metals. This enhancement of the metallic fluxes can be explained by a deteriorated absorption condition for the ICRF waves (H^+- second harmonic heating) because of a too low H^+ concentration (< 20%) in case of D^0 beam heating of the deuterium background plasma. Such effects of impurity enhancement under bad coupling conditions have been found already in previous investigations/5/.

References:
/1/ G. Janeschitz, IPP- Report 1989 to be published
/2/ K. Behringer, privat communication
/3/ G. Janeschitz et al., Proc. of the 8th PSI-conference, Jülich 1988, to be published in Nucl. Materials 1989
/4/ J. Roth and G. Janeschitz paper submitted to Nucl. Fusion
/5/ G. Janeschitz G. Fussmann, J. M. Noterdame et al., Proc. of the 13th EPS- conference Schliersee 1986, Vol1, p. 407

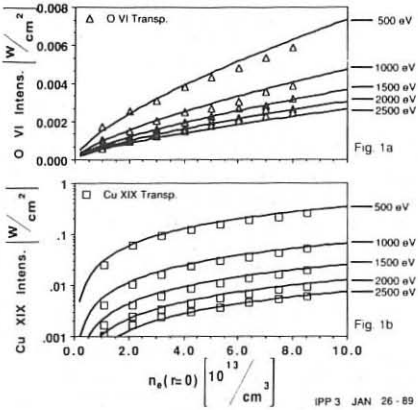

Fig. 1: Calculated line intensities (integrated along a central chord) for oxygen (1a) and copper (1b) as a function of central n_e and T_e in ASDEX. Code results are presented by Δ (O VI, 103.2 nm) and ◻ (Cu XIX, 27.3 nm), solid lines according to the fitting formula eq.(1).

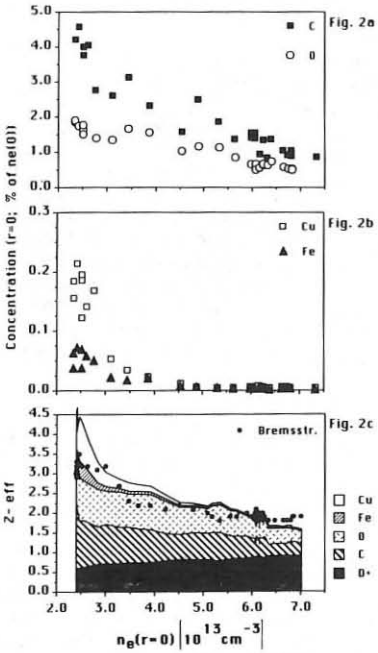

Fig. 2: Central concentrations of light impurities (2a) and metals (2b) vs. ne(0) for a ohmic ASDEX discharge. The various contributions to Z_{eff} and the comparison with bremsstrahlung- Z_{eff} is shown in (2c).

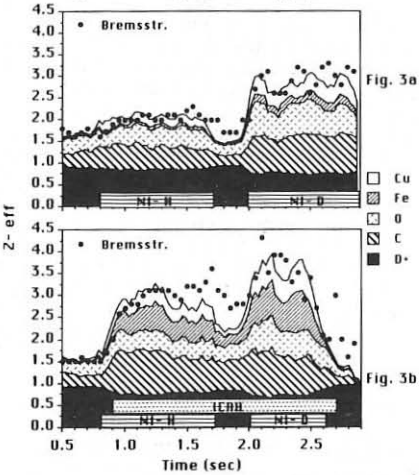

Fig. 3: Z_{eff} variations in case of auxiliary heating. (3a): H^0 and D^0 beams, (3b): H^0 and D^0 beams combined with 2MW ICRH. The contributions of the four main impurities and the deuteron dilution (D^+) are indicated. Z_{eff} according to bremsstrahlung is also shown for comparison.

EXCITATION OF MODE ACTIVITY IN TOKAMAKS

G. Lisitano

Max-Planck-Institut für Plasmaphysik,
EURATOM Association, Garching, FRG

A correlation study between m = 2, $\dot{B}_p$ mode activity and perturbations of the density gradients in the plasma interior shows a rotational transform coupling mechanism between an m = 1, n = 1, helically displaced plasma core and an m = 2 perturbation of the current surrounding it.

Schlieren measurement of the density gradient perturbations

A detailed schlieren study of the perturbations of the density gradients in the plasma interior is carried out during a single, typical cycle of an almost steady-state train of m = 2, $\dot{B}_p$ oscillations in ASDEX. On an enlarged time scale, Fig. 1 shows the schlieren signals provided by five λ = 2 mm pencil beams exploring a poloidal plane at distances d = 0 cm, ±10 cm and ±20 cm from the midplane of the tokamak /1/. The amplitude ΔA of the schlieren signals is dependent on the density gradient /1/ and is self-calibrated with respect to the unperturbed amplitude A. The following study is limited to a typical two-hump fluctuation cycle, like one of those labeled 1 and 5 in Fig. 1. During these cycles, the density gradients at d = ±10 cm vary from $\nabla N = 0.45 \times 10^{12}$ cm^{-4} for the maximum schlieren amplitude $\Delta A/A = 0.91$ up to $\nabla N = 2.8 \times 10^{12}$ cm^{-4} for the minimum value $\Delta A/A = 0.41$. Note in Fig. 1 that the fluctuating schlieren signals are 180° out of phase on opposite channels, at d = ±10 cm. They clearly establish the poloidal excursion of a macroscopically large variation of the density profile during each MHD perturbation cycle. The two passages of the large density gradient through the midplane of the machine, at $\theta = 0°$ and $\theta = 180°$ are clearly manifested in Fig. 1 by the rapid variations of the density gradient on opposite channels at d = ±10 cm.

This behaviour and the individual gradients derived from Fig. 1 were used to construct, as shown in Fig 2(a), the variations of the density profile during one fluctuation cycle. The density perturbations of Fig. 2(a) consist of a highly peaked, almost triangular central density profile which is radially displaced and rotates poloidally. This observed behaviour of the perturbation was used as a model in a numerical simulation experiment where the deviation of the schlieren rays and the schlieren experimental facilities were simulated as in real space /1/. With the density distribution of Fig. 2(a), a peak density $n_o = 6.3 \times 10^{13}$ cm^{-3} and a radial displacement $\rho/a = 0.16$ of the peak, it was possible to reproduce, as shown in Fig. 2(b), the schlieren waveforms of representative cycles 1 and 5 of Fig. 1. The high sensitivity of the schlieren signals is demonstrated by the two hump waveforms on opposite channels at d = ±10 cm. They indicate the four passages of the density peak through the schlieren chords during one perturbation period and become sensitively deformed or vanish for a slight variation from the above ascertained values of the density perturbation parameters. It should be noted in this regard that the observed schlieren signals of Fig. 1 cannot originate from density perturbations caused by magnetic islands. A steplike /2/ local flattening of a parabolic density profile would in fact only deflect very few rays of the schlieren ray fan /1/, thus producing a negligible variation of the schlieren signals as compared with the observed signals of Fig. 1. No variation of the schlieren signal amplitude should in addition occur for the central schlieren channel at d = 0 cm.

The signals were recorded during an L-phase of deuterium injection into a deuterium plasma with NI = 4 MW, I_p = .32 MA, $\langle n_e \rangle = 3 \times 10^{13}$ cm^{-3} and q(a) = 3.3.

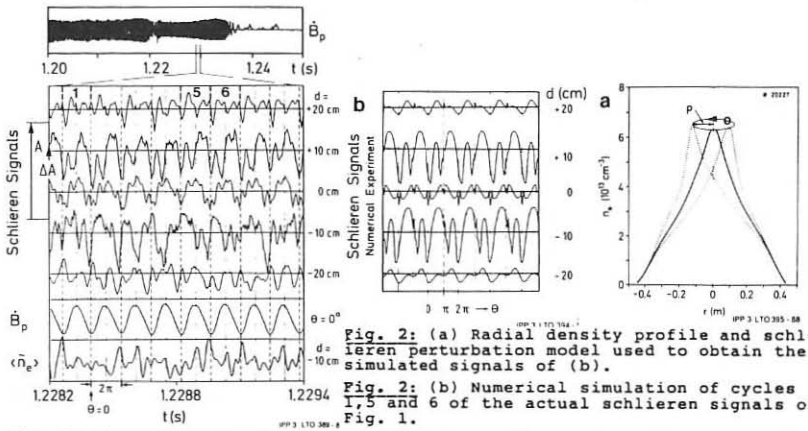

Fig. 2: (a) Radial density profile and schlieren perturbation model used to obtain the simulated signals of (b).

Fig. 2: (b) Numerical simulation of cycles 1,5 and 6 of the actual schlieren signals of Fig. 1.

Fig. 1: Characteristic two-hump schlieren wave forms at d = ±10 cm, indicating an m=1-like density distribution structure in the plasma interior. The last trace demonstrates the poor correlation of the simultaneously detected line-integrated density signals to the corresponding schlieren signals. The unperturbed amplitude A of the schlieren signals is shown for the channel at d = +10 cm only.

A decrease of the mean value of the density /1,3/ from 4.1×10^{13} cm^{-3} to 3×10^{13} cm^{-3} is observed on transition from the H to the L-phase of the discharge. At the transition, the observed onset of almost steady state m = 2, $\dot{B}_p$ oscillations shown in Fig. 1, upper trace /3/, is associated with the measured peaking and helical displacement of the density profile shown in Fig. 2(a).

Mode coupling structure of the m=1 and m = 2 perturbations

As the observed perturbation model of Fig. 2(a) is well correlated with $\dot{B}_p$ fluctuations, the model is first compared with the external B_p field perturbation contour derived from the simultaneously detected Mirnov oscillations. The latter are shown in Fig. 3 in accordance with the poloidal angle θ at which they were detected. The first trace of Fig. 3 also shows the schlieren signals of the chord d = +10 cm of Fig. 1. The schlieren signals estabilish the period T of a complete poloidal excursion of the helically displaced plasma core. The poloidal phase distribution of the Mirnov oscillations at a given instant is shown in Fig. 3, left. The total poloidal phase variation of 4π clearly identifies the m = 2 mode number of the oscillations. Such an m = 2 mode is also identified in Fig. 3 by the two travelling waves B and C, obtained by joining points of equal phase /4/.

A straight-line approximation of the travelling-wave path of Fig. 3 allows straightforward calculation /4/ of the poloidal B_p field distribution $B_p = B_{max} \cos m(\theta + \pi/2)$, which induces the Mirnov oscillations $e(\theta) = vB_p(\theta) = (\omega/m) r B_{max} \cos(\omega t + m(\theta + \pi/2))$ at the r = const. radial position of the coils. In the above expression, the time t = 0 corresponds to the passage of the plasma peak through the midplane, at $\theta = 0^0$, as indicated by dashed lines in Fig. 3 and Fig. 1. With equal amplitude of the Mirnov oscillations being assumed, the poloidal field exhibits the m = 2 variations indicated

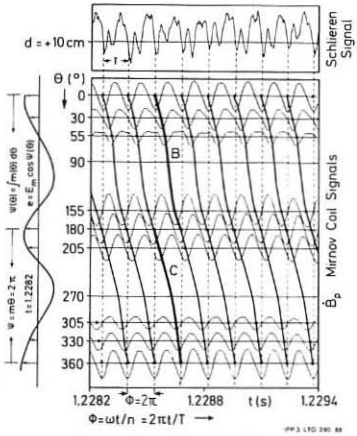

Fig. 3: Schlieren signal at d=+10 cm, first trace, and simultaneously detected Mirnov oscillations, shown in accordance with the poloidal angle θ at which they were detected.

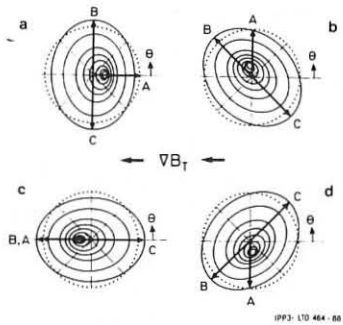

Fig. 4: B_p field contour and angular position of the radially displaced plasma peak, vector A, and of the two travelling waves of Fig. 3, vectors B and C, at four instants t/T = 0, 1/4, 1/2 and 3/4. The dotted circles indicate the r = const. position of the Mirnov coils. Note the non-resonant rotational transform coupling between the driver m = 1 helical displacement of the current core, vector A, and the m = 2 current perturbation, vectors B and C.

in Fig. 4 (a),(b),(c),(d) by the last, external traces. Figure 4 also shows the angular position of the plasma peak, vector A, and that of the two travelling waves, vectors B and C, at four instants t/T = 0, 1/4, 1/2 and 3/4.

The poloidal distribution of the B_p field, which is produced by the radially displaced plasma core, can now be sketched throughout the plasma interior by assuming identical current and density distributions for the perturbation model of Fig. 2(a). Besides being justified by the following study of the poloidal field distribution, this assumption is also dictated by the typical current character of the observed helical displacement of the highly constrained density profile. On this assumption, Fig. 2(a) provides the B_p field strength on a chord perpendicular to the machine midplane and crossing the centre of the plasma . On the basis of this field profile and of the position of the plasma peak, the poloidal contour of the B_p field perturbation in the plasma interior is extended, as shown in Fig. 4, to that of the measured B_p field external to the plasma. To provide a clear representation in Fig. 4, the m = 2 ellipticity of the perturbed external B_p field contour has been exaggerated. Considering that $\tilde{B}_p/B_p$ is only a few per cent, the dominant features in Fig. 4 are the m=1 helical displacement of the central current profile and its rotational transform coupling to the light m=2 perturbation of the current surrounding it.

A comparison with the theoretical perturbation model

Owing to the limited space and time resolution of available diagnostics the measured radial displacement of the profile, shown in Fig. 2(a), would not be observed by means of conventional measurements. These large variations of the profile, observed during one perturbation cycle, do not allow, however, an understanding of the Mirnov oscillations on the basis of theoreti-

cal current perturbations on $q = m$ resonant and centred equilibrium flux surfaces. The observed helical displacement of the current core suggests, on the other hand, an $m = 2$ current perturbation mechanism based on ∇B_T-drift forces acting on the poloidal excursion of the current. Figure 4 shows in fact an $m = 2$ redistribution of the current which, being always directed towards $-\nabla B_T$, is subjected to a continuous rotational-transform, angular-delay θ/m with respect to the poloidal excursion θ of the highly peaked and helically displaced central current profile. Accordingly, the $m = 2$ shape of the B_p field and its angular position (see Fig. 4) are determined by, respectively, the "$m = 2$" symmetry of the ∇B_T field on both sides of the machine midplane and by the position of the plasma peak, vector A, with respect to ∇B_T. Note that the observed $n = 1$ helicity of the $m = 2$ perturbation is established by that of the driver current core helix, which, in turn, is governed by the sole condition of a complete $n = 1$ toroidal cycle.

As mentioned, the experimentally observed helical displacement of the current core is in disagreement with the theoretical assumption of selectively located perturbations on resonant $q = m$ field lines. However, the observed non-resonant B_p field perturbations, caused by ∇B_T, provide a modulation of the poloidal phase of the Mirnov oscillations, $\psi(\theta) = \int m(\theta)d\theta$, identical to that caused by the theoretical $q(\theta) = m(\theta)$ pitch angle variations of the resonant field lines. In the expression for the poloidal periodicity, $m(\theta) = m(1+(r/R_0)\cos\theta)^{-1}$, the radius r no longer localizes the theoretical $q = m$ resonant flux surfaces. Instead it localizes the $m = 2$ regions at $\rho < r < a$, where the slight ∇B_T current perturbations that are enlarged sketched in Fig. 4, are driven by the dominant $m = 1$ helical displacement of the central current profile. On the assumption of Mirnov oscillations of equal amplitude, no off-centre correction /5/ are necessary for $m(\theta)$.

It should be noted, finally, that the observed density decrease /1,3/ and profile peaking during the steady-state $m = 1$ and $m = 2$ mode activity are very probably caused by an excess of neutral gas influx. No data are, however, available as yet for describing the kinetics /6/ of the large increment of neutral gas that is known to be associated with the additional-heating pulse. Despite the lack of data on this subject, the excess of neutral gas influx suggests that a considerable amount of atomic processes involving the neutrals /6/ may occur in an internal region of high plasma density. The enhanced resistivity, which displaces the location of the unbalanced $J \times B = \nabla p$ equilibrium flux surfaces, may excite there the observed helical displacement of the current core, probably via Hall effects on the current ring which is highly constrained by the excess of neutral gas influx. The instantaneous current profiles and the projections of their magnetic surfaces on each poloidal plane rotate toroidally unperturbed, however. This may produce dynamic equilibrium conditions for the helically twisted and toroidally rotating magnetic flux surfaces. In disagreement with theoretical predictions, the observed $m = 1$ and $m = 2$ perturbations shown in Fig. 4 are nevertheless tightly coupled to each other by a rotational transform mechanism independent of magnetic field line helicities.

References

/1/ G. Lisitano, Rev. Sci. Instrum. 58, 249 (1987); G. Lisitano, Proc. 14th Europ. Conf. Contr. Fus. and Plasma Physics, Madrid, Vol. III, 1334 (1987).
/2/ A. Sykes and J.A. Wesson, Phys. Rev. Lett. 44, 1215 (1980).
/3/ O. Klüber et al., 13th Europ. Conf. Contr. Fus. and Plasma Physics, Schliersee, Vol. I, 136 (1986).
/4/ E. Levi, Electromechanical Power Conversion (Mc Graw-Hill, New York, 1966) pp. 226-231.
/5/ V.G. Merezhkin, Sov. J. Plasma Phys. 4, 152 (1978).
/6/ M. Tendler and D. Heifetz, Fusion Technol. 11, 289 (1987).

RADIATION-SHIELDED DOUBLE CRYSTAL X-RAY MONOCHROMATOR FOR JET

R. Barnsley, U. Schumacher[1], E. Källne[2], H.W. Morsi, G. Rupprecht[3]

JET Joint Undertaking, Abingdon, Oxon OX14 3EA, UK
[1] MPI für Plasmaphysik, Ass. EURATOM-IPP, D-8046 Garching, Fed. Rep. of Germany
[2]Fysik 1, Kungl. Tekniska Högskolan, S-10044 Stockholm, Schweden
[3] Now at Eur. Southern Observatory (ESO), D-8046 Garching, Fed. Rep. of Germany

Abstract

A double crystal X-ray monochromator for absolute wavelength and intensity measurements with very effective shielding of its detector against neutrons and hard X-rays was brought into operation at JET. Fast wavelength scans were taken of impurity line radiation in the wavelength region from about 0.1 nm to 2.3 nm, and monochromatic as well as spectral line scans, for different operational modes of JET.

1. Introduction

Soft X-ray plasma spectroscopy is a well established technique which provides a range of diagnostic information relating to the concentration, transport and temperature of impurity ions [1,2]. A high temperature plasma, producing a significant rate of DT fusion reactions, as anticipated in the latter phases of JET operation (active phase) will produce high fluxes of neutrons and γ-rays. The need to provide good shielding of the detector while covering a wide spectral range, places severe constraints on the design of an active phase crystal spectrometer. This required the development of a new high precision crystal-drive mechanism, and special techniques to evaluate the suitability of crystal diffraction properties over a larger surface area [3,4]. Shielding is achieved by placing the instrument outside the JET torus hall and by using two crystals in the parallel (non-dispersive) mode. For this device input and output beams are fixed for all wavelengths, allowing a labyrinth radiation shield to be built around the optical path between the small penetration in the JET biological shield and the detector (Fig. 1).

2. The active phase double crystal monochromator

The crystals are mounted via rotary tables to linear displacement tables, and their trajectories necessary to maintain the Bragg condition are controlled by a fast digital servo system [3]. It is necessary that the crystals be kept parallel to well within their diffraction profiles, which is achieved by the control system to about 6 arc sec. in the full Bragg angle range from 26° to 60°. The resolving power is $\lambda/\Delta\lambda = (1/\Delta\Theta) \cdot tan\Theta$ where the angular width $\Delta\Theta$ is defined mainly by remotely interchangeable coarse $(1/\Delta\Theta = 600)$ and fine $(1/\Delta\Theta = 5000)$ gridded collimators. The sight-line contains a

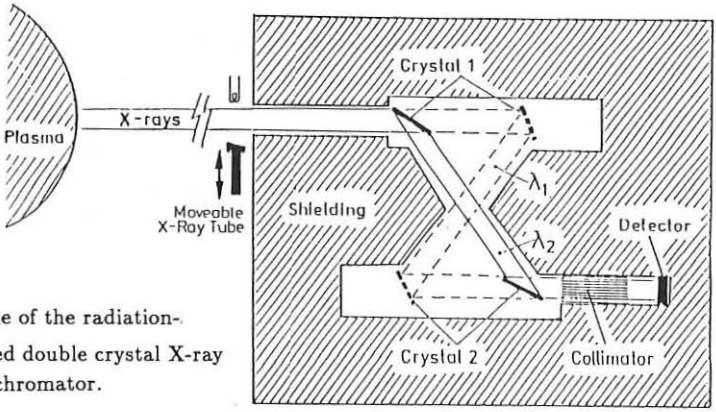

Fig. 1 Scheme of the radiation-shielded double crystal X-ray monochromator.

remotely deployable calibration source which, together with the high resolution angle encoders and the fine collimator, allows absolute wavelength calibration and Doppler line-profile and line-shift measurements.

Absolute intensity measurements are performed using the throughput relation: $N = IF_c\chi\Delta\Theta R_{cc}P_{cc}\eta/\omega$, where N is the counts integrated in a spectral line of intensity I (photons $m^{-2}s^{-1}sr^{-1}$), F_c the projected crystal area, χ the acceptance angle perpendicular to the plane of dispersion, $\Delta\Theta$ the collimator acceptance angle, R_{cc}, P_{cc} the double crystal integrated and peak reflectivities, respectively, ω the crystal rotational velocity and η the combined efficiency of detector and windows. The luminosity of the system is typically about $10^{-9}sr \cdot m^2$.

The detector is a multiwire gas proportional counter (MWPC) with thin polymer window for which the gas pressure, high voltage, and pulse height window can be controlled automatically to suit the observed wavelength range. This gives a high quantum detection efficiency (QDE) and allows background rejection and selection of the desired diffraction order by pulse height analysis. The 48 anodes are connected into 8 groups, each with its own signal processing chain, which allows signal-plus-background count rates of $\sim 10^7 s^{-1}$ without serious pile-up. All instrument and vacuum system functions can be controlled automatically by the JET control and data acquisition system (CODAS).

3. Examples for the operational modes of the active phase double crystal monochromator

The double crystal monochromator can be operated in different modes: Broad band spectra can be taken covering the Bragg angle range from about 26° to 60° in a time of about one second. With crystals like Topaz(303), LiF(220), Gypsum, TℓAP and KAP, as applied so far, the wavelength range from about 0.12 nm to about 2.3 nm was covered. An example of such a broad-band spectrum taken with TℓAP crystals is given in Fig. 2, showing some Ne-like Ni lines and some members of the oxygen Lyman

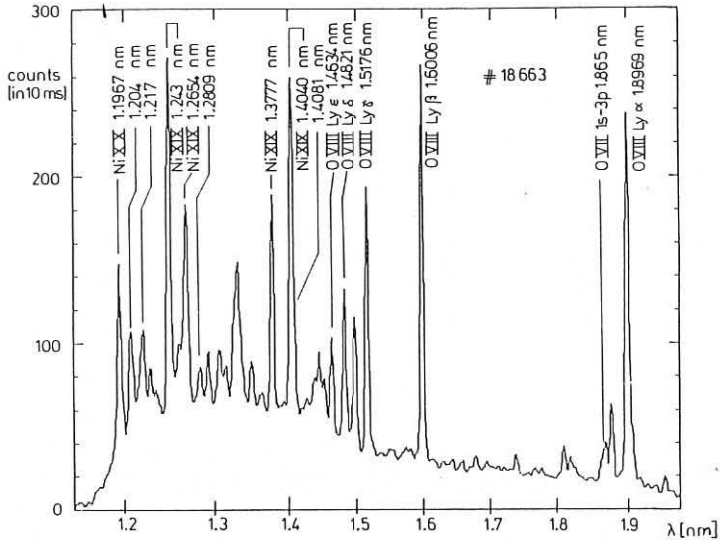

Fig. 2 Broad band spectrum obtained using TℓAP crystals covering the wavelength range from 1.13 nm to 1.95 nm with Ne-like Ni lines and the Lyman series of oxygen

series. Since the absorption in the thin foil (which separates the monochromator from the torus vacuum) increases with wavelength the count rate ratios do not directly reflect the line intensity ratios. Another mode is the repetitive scan of a smaller wavelength interval. An example of a line scan is given in Fig. 3. It is a scan of the profile of a certain spectral line performed many times throughout the discharge in order to follow the time behaviour of the line width and its intensity. This figure shows that the sensitivity of the monochromator is good enough to reveal the different behaviour of O and Ni. Fig. 4 gives as an example for the fourth operational mode, the monochromatic time behaviour of the Fe XXV line obtained from laser ablation of Fe into the JET discharge [5].

Acknowledgements

The authors are grateful to Drs. C. Andelfinger, W. Engelhardt, R. Giannella and H. Röhr for many fruitful discussions and to P. Abel, J. Fink, J. Keul, R. Lobel, J. Ryan, H. Schäfer, H.-B. Schilling, G. Schmitt, G. Snelling and B. Viaccoz for continuous support during construction and commissioning of the device.

References

/1/ E. Källne et al., Physica Scripta **31**, 551 (1985)
and J. de Physique **48**, C9/335 (1987)
/2/ R. Barnsley et al., Rev. Sci. Instrum. **57**, 2159 (1986)

/3/ C. Andelfinger et al., MPI für Plasmaphysik, Garching, Report IPP 1/226 (1984)
/4/ U. Schumacher, Nucl. Instr. and Meth. **A 251**, 564 (1986) and **A 259**, 538 (1987)
/5/ N. Hawkes, Z. Wang et al., this conference

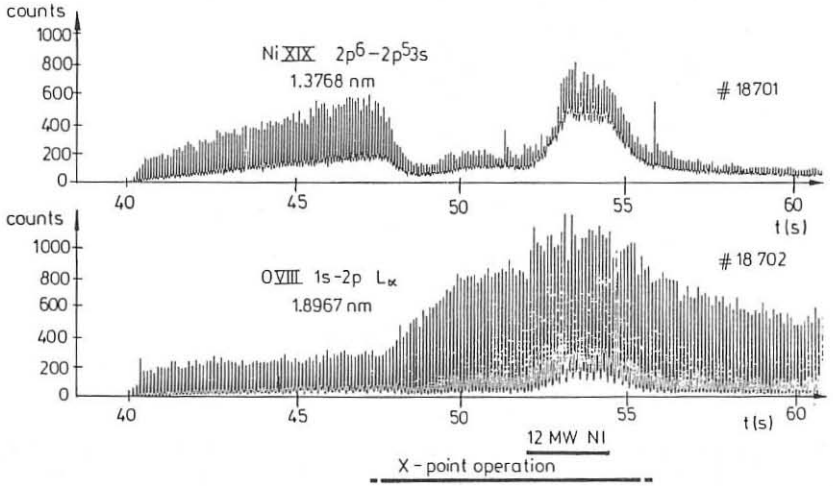

Fig. 3 Line scans for Ne-like Ni (above) and Oxygen Lyman α throughout two consecutive discharges at JET

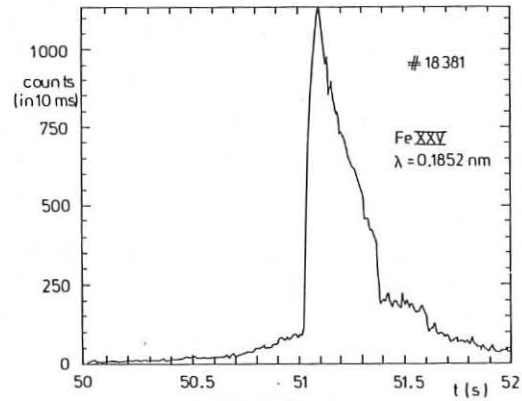

Fig. 4 Time behaviour of He-like Fe line from laser ablation of Fe.

PELLET ABLATION IN THE REVERSED FIELD PINCH AND TOKAMAK: A COMPARISON

G. A. Wurden*†, K. Büchl, T. E. Cayton*, R. S. Lang
W. Sandmann, and P. G. Weber*

Max Planck Institut für Plasmaphysik, Association EURATOM-IPP
D-8046 Garching, FRG

Introduction: While modelling of pellet ablation in plasmas using the neutral shielding cloud generated by the pellet gives general agreement with tokamak experiments,[1-3] many details are still not well understood. In particular, issues of ablation rate fluctuations, asymmetric cloud formation, pellet deflection, and self consistent effects of nonthermal energy and particle fluxes on the pellet (especially in auxiliary heated plasmas) require further consideration.

We compare the ablation of deuterium pellets with similar sizes and velocities in the ZT-40M reversed field pinch and ASDEX tokamak. While the two experiments have radically different plasmas, their effect on pellets is examined to illuminate similarities and differences in the pellet ablation physics. Photographs obtained both with still cameras and a fast gated-CCD video camera allow measurements of pellet cloud features, including intensity, curvature, velocity changes, cloud shape and striations. The shape of the pellet cloud and its light emission yield clues to processes in both the ablation layer and thermonuclear plasma.[4,5] Symmetry of the cloud is affected by the direction of the electron drift and magnetic field lines.[6] Gross track features, ranging from narrow, smooth and uniform, to broad and highly striated are noted, along with the corresponding plasma conditions that produce these features.

ZT-40M RFP: Injection of Deuterium pellets ($\sim 5\times10^{19} D^o$ atoms/pellet) at velocities of 400-600 m/sec into the ZT-40M reversed field pinch at Los Alamos[7] gives deep penetration and large $\Delta n/n$ refuelling. Typical pre-pellet plasma parameters are $I_\phi \sim$ 120-250 kA, $\bar{n}_e \sim$ 1.5-3$\times10^{13}$cm^{-3}, $T_e(0) \sim$ 150-300 eV, and global $\tau_E \sim$ 150-400 μsec. However, enhanced ablation in the outer plasma regions, stronger from the electron drift side than the ion side, results in extreme trajectory curvature.[8] A small population of energetic electrons ($\sim$ 1-10 keV) directed along magnetic field lines from the electron drift direction, would be sufficient to account for the observed motions assuming that asymmetric ablation rates (of order 30-100%) cause rocket-like acceleration of the pellet.

Images of the pellet taken every 100 μsec, with 5 μsec exposures, show the pellet cloud is brightest in the plasma edge region, with intensity decreasing through the plasma core.[9] Lineouts of these images show bright centrally peaked emission clouds with typical FWHM dimensions of $\sim$ 1.5 cm. A weak comet-like tail is often visible. The track gets narrower over the course of the pellet lifetime ($\sim$600-800 μsec). The pellet trajectory curvature is generally reproducible, although succesive pellets may be shielded by the first, and have less deflection.[8] Highly deflected pellets undergo significant velocity changes. Depending on the relative direction of the pellet velocity and electron drift (magnetic field direction), the pellets are observed to speed up, or slow down in the plasma. In extreme cases the pellet may be stopped, or even have its trajectory turned around in the plasma! In the plasma edge region, where the magnetic field is nearly poloidal, the deflection is poloidal, whereas in the plasma core region (with a principally toroidal field), the deflections are more toroidal.

ASDEX Tokamak: A variety of pellet sizes are possible in ASDEX,[10] typically 4×10^{19} ("small") but ranging to $1.4\times10^{20} D^o$ atoms/pellet ("large"), with a typical pellet velocity (for the centrifuge injector) of 570 m/sec. The plasma volume of 5.2 m^3 is about 5× larger than ZT-40M, and for ohmic conditions, a typical plasma is $I_\phi \sim$ 320-450 kA, $\bar{n}_e \simeq 1.5\text{-}4\times10^{13}\text{cm}^{-3}$, $T_e(0) \simeq 1.0\text{-}1.5$ keV, and global $\tau_E \sim 60\text{-}80$ msec.

We have recently installed the gated-CCD camera on ASDEX, and used it to obtain time resolved images of the pellet clouds. In situ pellet velocity remains close to that from the gun, although significant toroidal velocities can occur in the later part of the pellet lifetime. Velocity measurements are complicated by uncertainties in the pellet location within the dynamically evolving pellet cloud. Figure 1 shows a CCD photo (a), looking down on the pellet track from an angle of 75-45 degrees to the vertical, and corresponding densitometer lineouts, as well as the wide-angle spatially integrated D_α time history (b), of the pellet ablation. The darker central region in each bright cloud, with dimensions of 2 cm diameter, seen in the lineouts of Figure 1(b), is difficult to explain based on self absorption alone. Also, bumps or protrusions of the cloud, in the direction of pellet motion, suggest that the light emission is dynamically evolving, and is "left behind" as the pellet moves on. Precise location of the pellet is made difficult by the changing shapes of the light emitting region. Cross field dimensions of the cloud are $\sim 1\ cm$ radius, while along the toroidal field dimension, the elongated FWHM diameter is 5-7 cm, as seen in these 2μsec exposures. Collapse of the old emission region surrounding the pellet is strongly suggested by time resolved photos on ASDEX, and has also been reported in TEXT.[11] This darker central region near the pellet is not seen in experiments where the luminous region remains "spherical", as was always the case in ZT-40M, where the pellet tracks were uniformly smooth, and striations were the rare exception rather than the rule. This may have also been the case in ORMAK.[6]

An assortment of time-integrated ASDEX pellet photos are shown in Figure 2. The plasma separatrix is at r$\simeq$ 40 cm, although the pellet light emission first begins at r= 42-41 cm, near the bottom of each picture. The field of view extends radially from r= 44 cm to r=0 cm, and a reference picture with ruled 10 cm marks is shown for calibration. Two pellets from a multi-pellet sequence in the same ohmic discharge (#21143) are shown Fig. 2(a) and (b). The first is at 1.0 seconds and the fourth at 1.3 sec with a higher density of $\bar{n}_e = 4.6\times10^{13}\text{cm}^{-3}$. For lower electron densities, and/or higher T_e, the toroidal extent of the cloud is larger. Pellet trajectories are straighter, or curve in the ion drift direction with the application of significant Neutral Injection, as shown in Fig.2(c), shot #23216 with a "large" pellet, I_ϕ=385 kA, B_ϕ=2.21 T and 2.6 MW of co-beams. One of the largest toroidal deflections seen for pellets in ASDEX is shown in Fig. 2(d), where the 7th and 8th pellet (30 msec apart) in a 380 kA weak NI shot #21559 (0.35 MW co-beams) can be seen turning nearly 90°.

A transition between a relatively smooth ablation track, and an oscillating, or striated track, is commonly observed in the edge region, and can be seen in Fig. 2(a) (if the reproduction is good enough!). Durst[11] has associated this transition from smooth to non-symmetric (and oscillating) light emission with the q=2 layer in the TEXT tokamak. We see no correlation with the smooth/oscillating track boundary to the q value. In particular, beams force the oscillations to begin even closer to the plasma boundary than the usual 5-6 cm depth in ohmic discharges, for the same q at the edge. Also, ohmic discharges with q=1.95 at the plasma edge, still have a well defined smooth track zone, before the striations begin.

Discussion: The time development of the pellet ablation rate is dependent on the type of plasma conditions that are encountered. It is striking to compare the typical

ohmic tokamak pellet ablation time history, with that of a pellet ablating in the ohmic reversed field pinch. Usually in the tokamak discharge, the pellet ablates at first slowly, then ever more rapidly, with a sharp falloff in time as the pellet is consumed. In contrast, the RFP pellet time history is nearly the opposite....that is, the pellet light emission is strongest near the edge of the plasma, and then decreases as it nears the center. Tokamak discharges with large runaway content, or even neutral beam heating, also show enhanced edge ablation.[1,12] Unlike runaways in tokamaks, the energetic electrons in the RFP are evidently not of high enough energy to cause bulk heating of the pellet (and hence its explosive demise), and instead the pellet remains intact.

Striations are a common feature in the tokamak, and even stellarator discharges.[6,1,13] However, uniform, smooth bending tracks can also occur in tokamaks when pellets are fired early during the current rise phase.[5] A model of a neutral cloud being alternately formed, and then left behind as the pellet edges out of the dense cloud shielding influence, lends itself naturally to an oscillatory explanation of the pellet ablation rate. An instability in the neutral shielding cloud can evidently be triggered by as yet unspecified plasma conditions. The association of a dip in the light intensity in the ablatant cloud, with the presence of the instability, remains to be tested. Plasmas/pellets without striations may hold the key to the instability trigger conditions. We note, that for sufficiently short energy confinement time (ie, the tokamak edge, or todays RFP plasmas) compared to the time the pellet spends in these regions, smooth ablation of the pellet should be expected, since the energy will "fill in" locally faster than being depleted by the pellet. This may explain why in ZT-40M, striations were almost never visible, since the pellet cloud basically sampled the entire plasma energy flux during its lifetime, due to the short global energy confinement time of the pinch. Also, conditions which bypass the neutral shielding cloud (ie, energetic fluxes of particles), should also have smoother pellet ablatant tracks.

This work is supported by the U. S. DOE and the EURATOM Association.

* Los Alamos National Laboratory, Los Alamos, NM 87545, USA
† Present address: IPP, Garching, FRG

[1]S. L. Milora, Journal of Fusion Energy **1**, 15 (1981).

[2]M. Kaufmann, K. Lackner, L. Lengyel, and W. Schneider, Nuclear Fusion **26**, 171 (1986).

[3]W. A. Houlberg, S. L. Milora, and S. E. Attenberger, Nuclear Fusion **28**, 595 (1988).

[4]D. H. McNeill, G. J. Greene, and D. D. Schuresko, Phys. Rev. Lett. **55**, 1398 (1985).

[5]TFR Group, Nuclear Fusion **27**, 1975 (1987).

[6]C. A. Foster, R. J. Colchin, S. L. Milora, K. Kim, and R. J. Turnbill, Nuclear Fusion **17**, 1067 (1977).

[7]G. A. Wurden, P. G. Weber, R. G. Watt, et al., Nuclear Fusion **27**, 857 (1987).

[8]G. A. Wurden, P. G. Weber, R. G. Watt, C. P. Munson, T. E. Cayton, and K. Büchl, in *Int. School of Plasma Physics, Course and Workshop on Physics of Mirrors, RFPs and Compact Tori*, edited by S. Ortolani and E. Sindoni, Vol. 1, p. 411 (Societa Italiana Di Fisica, Varenna, Italy, 1987).

[9]G. A. Wurden, P. G. Weber, C. P. Munson, et al., in *IAEA Tech. Com. Meeting on Pellet Injection and Toroidal Confinement*, p. (Gut Ising, Bavaria, FRG, 1988) [Oct. 24-26, 1988].

[10]W. Amenda and R. S. Lang, J. Phys. E: Sci. Instr. **19**, 970 (1986).

[11]R. D. Durst, Technical Report FRCR 302, University of Texas (1988) [Ph.D. Thesis].

[12]K. Büchl, G. C. Vlases, W. Sandmann, and R. Lang, Nuclear Fusion **27**, 1939 (1987).

[13]K. P. Büchl, WVIIA Team, NI Team, and ECRH Team, Technical Report IPP 1/238, (1986).

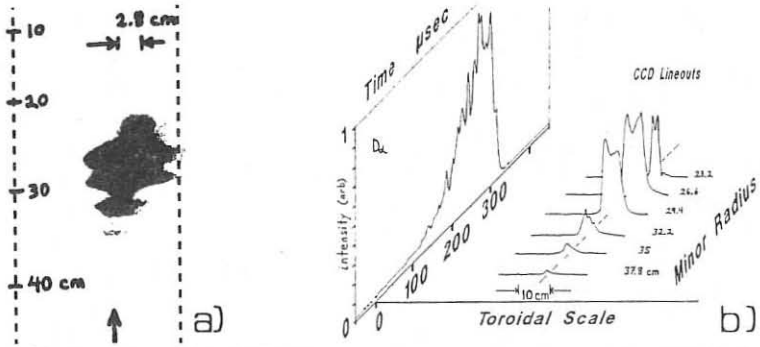

Figure 1: Deuterium pellet ($4x10^{19}$ D^o atoms) at 570 m/sec, ablating in an I_ϕ = 380 kA diverted ASDEX ohmic shot #26082. (a) Multiply-gated CCD picture (2μsec exposure every 50μsec). (b) Lineouts of the elongated (along field lines) cigar-shaped emission clouds show diminished emission in the central region of the brightest clouds, and $D_\alpha$emission on the dual time/penetration depth axis.

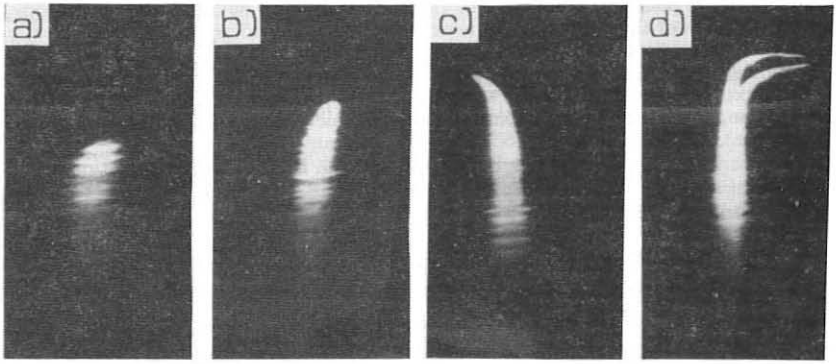

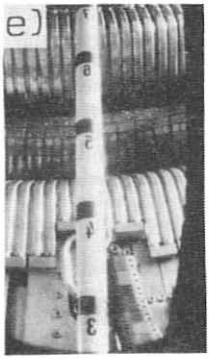

Figure 2: Top-view, time integrated ASDEX pellet photos. (a) Ohmic I_ϕ=350 kA, B_ϕ=2.49 T, $\bar{n}_e$=$3.4x10^{13}cm^{-3}$, "small" pellets, (a) first pellet and (b) fourth pellet. The striation (oscillation) frequency is about 75 kHz. (c) 2.6 MW Neutral injection, curvature in ion drift direction. (d) Strongest pellet curvature seen in ASDEX. (e) Reference photo, with radial calibration rod, marks every 10 cm. The diameter of the rod is 28.5 mm. The r=40 cm position is at the inner edge of the black mark, just above the inverted "3" on the rod. Due to lenses, the photos are inverted left-right, so the plasma current and toroidal field directions appear as if oriented from right to left, and drifting electrons impact the pellet cloud preferentially from the left side. The horizontal curved arc is light from the lower divertor throat.

BROADBAND MICROWAVE REFLECTOMETRY ON WENDELSTEIN VII-AS STELLARATOR

J. SANCHEZ *, E. ANABITARTE*, A. P. NAVARRO

Asociación EURATOM /CIEMAT 28040 Madrid, Spain

H. J. HARTFUSS

Max-Planck Institut für Plasmaphysik
Association EURATOM-IPP, D - 8046 Garching , FRG

* Present adress : MPI für Plasmaphysik, Garching

Microwave reflectometry has been applied recently to tokamaks (1,2,3,4) as a diagnostic tool to obtain information on electron density profiles and electron density fluctuations.

Density fluctuations are expected to play an important role in the anomalous transport that degrades confinement in tokamaks (5). This kind of transport also plays a dominant role in the plasma edge region of stellarator machines.

Fixed frequency reflectometry gains information on the movements of the reflecting layer, this is a k integrated measurement of the density fluctuation. Being mainly sensitive to low k perturbations , reflectometry shows good spatial resolution. In this way reflectometry appears as a complementary technique to the classical scattering experiments.

The absolute magnitude of the density fluctuations can be evaluated using the density gradient if the absolute value of the reflecting layer displacement is known. This implies a coherent measurement of the phase shift between the launched and reflected waves.

As it is shown later this kind of detection needs a special receiver which is under construction.

The first approach is single homodyne detection , that gives qualitative information on fluctuations and can be used to measure the density profile by sweeping the probing frequency.

EXPERIMENTAL SETUP

In this paper we describe the system installed and operating in WENDELSTEIN VII - AS stellarator (R = 2 m , a = 0.2 m , m = 5).

The system is based on two independent reflectometers looking to the plasma from the inner and outer side. The antennas are located in the equatorial

position of a poloidal plane with triangular plasma cross section (see fig . 1).

The specific B field geometry for this plane allows the use of extraordinary mode in both reflectometers , with a theoretical spatial resolution better than 5 mm in the radial direction. This is important for plasma edge studies, where ordinary mode reflectometers cannot operate.

For the standard value in W-VII-AS, B = 2.5 T, the system operates in the W microwave band : 75 - 110 GHz.

A single antenna reflectometer is installed at the outer side , where the machine has a port 28 mm diameter and direct straight access to the plasma. In the inner side a larger port is used. We have choosen a two antennas reflectometer to avoid the effect of parasitic references on the more complex line which is necessary due to the difficult access trough this port.

EXPERIMENTS AT B = 1.25 T

Although the standard field will be 2.5 T, initial operation with Helium and Deuterium has been performed at 1.25 T with 70 GHz second harmonic ECRH and densities $1.5 - 2.0 \times 10^{19}\ m^{-3}$.

Under these conditions the relevant cutoff frequencies lie in the V-band: 50 - 75 GHz . The vacuum window and low pass filtering to protect the diode from the gyrotron radiation restrict the useful range to 53-59 GHz.

Fixed frequency experiments have been carried out in this range with the single antenna system. Figure 2 shows two typical signals from OH (fig. 2 a) and ECRH discharges (fig. 2 b) . When the launched wave reaches the cut-off layer in the plasma, in both cases, a good correlation with the line integrated density is observed.

Density fluctuations were detected with this system. Reflectometer signals stored with a sampling rate of 500 kHz have been Fourier analyzed. A broad-band spectrum was found, with a maximun around 10 kHz and decaying with the frequency f as $f^{-\alpha}(\alpha=0.6\text{-}1.1)$.

In figure 3 the fluctuation spectrum for an incident frequency of 55.6 GHz is shown. In this case the radial density profile was trapezium shaped and the wave was reflected in the gradient region near the top.The density at the center of the discharge was about $2.3\ 10^{19}\ m^{-3}$.

The amplitude of the spectrum decays to 30% of maximun value at 100 kHz . This behaviour is important when considering density profile measurements by swept reflectometry because perturbations coming from fluctuations can then be avoided choosing the relevant beat signal above 150-200 kHz.

Similar results in the fluctuation spectrum have been obtained on NBI discharges.

HETERODYNE RECEIVER

To gain information on the amplitude of the fluctuations we need coherent phase detection.

Dual sin/cos detection has been tested in the experiment. The adjustment of the phase shifted paths was not difficult for a given frequency but a higher signal to noise ratio than that achieved in the experiment is necessary to be able to discriminate the phase behaviour.

Another way for coherent detection is the introduction of a high frequency carrier, the signal at the receiver will be: $V = A \sin(\omega t + \Phi(t))$ instead of $V = A \sin(\Phi(t))$, where $\Phi(t)$ gives the phase delay between the launched and reflected waves.

The carrier ω must be much higher than the highest spectral components of $\Phi(t)$. As we observed in the homodyne experiments 300 kHz can be a suitable upper limit for the spectrum of $\Phi(t)$.

The most stable way to introduce the carrier is the heterodyne technique. The system (see fig. 4) is being constructed.

RF and LO1 oscillators can be syncronously varied during the discharge . The mixing scheme allows for relative frequency shifts between both signals (6).

The IF system has been designed to be used in scattering and fast interferometry experiments by using different front ends. With several local oscillators this system converts the first IF signal (4 - 8 GHz) down to a final frequency low enough (10 MHz) to be handled by the phase detection system .

Phase detection will be done by standard sin/cos units working at this low frequency or by zero-crossing techniques.

A filter bank as a fast tool for qualitative analysis will also be used.

REFERENCES

1 Simonet F 1985 Rev. Sci. Instr. 56 664
2 Hubbard A E, Costley A E and Gowers C W 1987 J. Phys. E: Sci. Instr. 20 423
3 Anabitarte E et al. 1988 J. Phys. D:Appl. Phys. 21 1384
4 Liewer P C 1985 Nuclear Fusion 25 543
5 Senties J M et al . In this conference
6 Doane J L 1980 Rev. Sci. Instr. 51 317

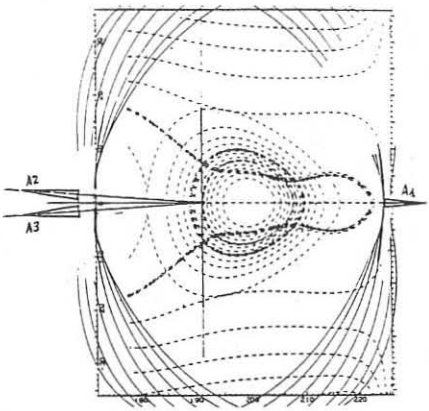

Fig. 1 Position of the antennas showing plasma density and B field contours.

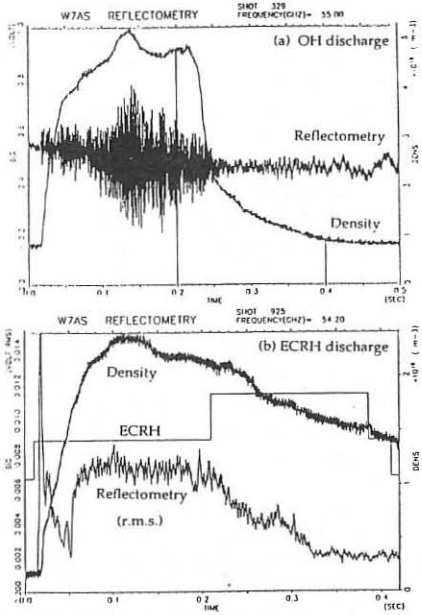

Fig. 2 Comparison of reflectometry and mean density signals

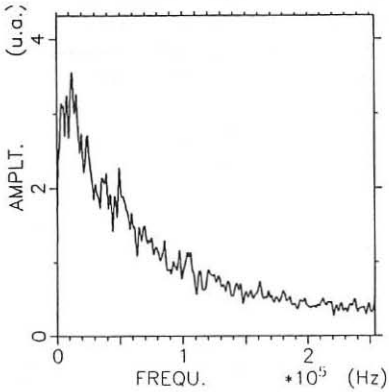

Fig. 3 Fixed frequency reflectometry spectrum

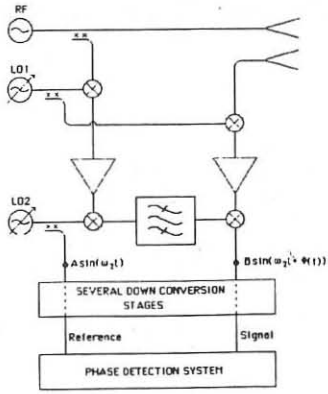

Fig. 4 Heterodyne receiver

STARK SPLITTING OF BALMER TRANSITIONS AS A METHOD FOR MEASURING MAGNETIC FIELDS IN A RFP PLASMA

P G Carolan

(UKAEA/Euratom Fusion Association)
Culham Laboratory, Abingdon, Oxon, OX14 3DB, UK

Introduction The departure of the magnetic field distributions in Reversed Field Pinch experiments from the ideal Taylor configurations [1] has a significant influence on the plasma resistance, transport and ion heating [2]. Whereas there are several possible techniques (e.g. [3-5]) for measuring magnetic fields in TOKAMAKS, this is not the case for RFP plasmas, primarily because of the smaller magnetic fields. Here we evaluate the diagnostic potential to an RFP of the induced Stark effect, as highlighted by recent observations of neutral beam atoms in the JET plasma [6]. These atoms are subject to varying Lorentzian electric fields as they traverse the plasma magnetic fields.

Neutral beam features and Balmer-alpha line intensity A plan view of the geometry used in the analysis is illustrated in FIG 1. Here we consider the neutral beam and viewing directions to be in the equatorial plane. As the beam traverses the plasma it will be attenuated by charge exchange and ionisation collisions with the plasma ions. Increased beam attenuation not only reduces the beam shine-through but it also reduces the line excitation rate ($\propto$ neutral density). These conflicting attributes may be resolved by adjusting the beam power, atom energy and the beam orientation with respect to the plasma. In FIG 2 are shown the calculated results of such a case where a neutral beam power of $\sim$100kW is used, with 40keV deuterium energy. The torus dimensions are: R/a = 2.0m/0.5m; the beam inclination angle, ξ_b, is 50° and the density distribution is of the form: $n_e(r) = 5\times10^{19}\ \{1-(\frac{r}{a})^3\}m^{-3}$. The cross-sections used are $\sigma_{CX} = 0.6\times10^{-19}m^2$ and $\sigma_{EX} = 1.2\times10^{-19}m^2$ for the n = 3 excitation rate. The optical/spectrometer characteristics assumed are: f/10 spectrometer, 4% quantum efficiency, 1% optical transmission (allowing for the use of fibre optics), spectrometer slit area = $2.5\times10^{-7}m^2$, 5cm effective diameter of the neutral beam and 1msec spectrum collection time. We can observe that the beam power is almost completely attenuated by the plasma and that the spectrometer should detect in excess of 10^4 photo electrons from most positions in the plasma diameter.

Stark splitting of the Balmer-alpha transition In the presence of background Balmer lines, discrimination is required to detect clearly those originating from the neutral beam. The easiest means of accomplishing this is from off-transverse viewing of the neutral beam to

avail of Doppler shifting of the detected spectrum. However, Doppler effects can smear the Stark spectrum due to finite beam divergence and light collection cone angles. It is worth noting that the beam velocity is unimportant in these considerations as it affects equally the competing Doppler and Stark effects. What matter are the magnetic field, the beam and optics geometry, and the atomic transition involved. The effects of finite beam divergence and light collection cones are included in the calculations where the respective angular cones are segmented into elements of apex and azimuthal angles. Each element in the beam yields a particular Stark spectrum which suffers a range of Doppler shifts when detected in the elements of the detection geometry. Composite spectra are formed by summing from all the elements in both systems. A fixed collection port size is used so the Doppler smearing decreases with increasing distance along the beam for the geometry selected. The spectral intensities are normalised to have unity integrated area from all the channels (500 in these cases). The degree of Stark splitting and the line component intensities are calculated from ref [7] and assuming full statistical mixing. Here we assume an ideal Bessel Function Model [1], for the RFP magnetic field configuration, with I_ϕ = 2MA and θ = 1.35 ($B_\phi(0)$ = 1.8T, $B_\phi(a)$ = -0.25T and $B_\theta(a)$ = 0.8T). Typical Lorentzian electric fields in the beam are ~2MV/m. A beam half cone angle of 0.01° (beam divergence ~0.35 mrad) is used and a 1cm radius collection port is positioned at X_c = -3.0m and Z_c = 0.5m ($X_b = R_o + a$; $Y_b = Y_c = 0$, cf FIG 1). A typical calculated spectrum is shown in FIG 3 where the Stark features are clearly resolved.

Diagnostic potential There are several features to the emitted spectra which may be exploited for making localised magnetic field measurements. Here we evaluate the diagnostic potential by comparing the changes wrought on these features by a 10% alteration to the magnetic field (the poloidal field is considered here). If a measurable effect is produced the technique would be of value where the equivalent accuracy of 10% in the determination of magnetic fields in RFPs is desirable. In the examples below, the 'standard plasma' is that referred to earlier and the calculations are made for the range of plasma positions where there is an appreciable line intensity (cf FIG 2). The differences in the Lorentzian electric fields, from that of the 'standard plasma', are shown in FIG 4. Except close to the axis, the changes from ~2% to 10% in the electric field should be measurable from the degree of Stark splitting. Similarly, the changes in the ratio of π to σ line intensities, as shown in FIG 5, offer much the same sensitivity although the analysis would be complicated by the degree of statistical mixing of the energy levels [6] which is density dependent. Finally, we show in FIG 6 the corresponding differences in the orientation of the Lorentzian electric field vector as seen from the axis of the collection optics directed to the various positions along the neutral beam. The orientation can be determined experimentally by spectrally selecting the π components and measuring the

orientation of the plane polarised light. Although experimentally difficult, changes in orientation of 1° can be measured by existing techniques using, for example, small half-shadow angle polarisers. Combining measurements of the Lorentzian electric field magnitude, which is proportional to the total magnetic field strength, and its orientation, both the toroidal and poloidal fields may be determined.

Conclusions In this feasibility study we find that the Lorentzian electric fields as seen by a neutral beam (100kW, 20keV/AMU) in a RFP can cause Stark splitting of Balmer transitions in excess of the Doppler smearing arising from the finite collection optics and the beam divergence. From observations of the various Stark spectral features, multipositional measurements of the magnetic fields may be made to an accuracy of about 10%.

Acknowledgements Fruitful discussions with N J Peacock, H P Summers, JB Taylor and M von Hellermann are kindly appreciated.

References

[1] Taylor J B, Phys. Rev. Lett. 33, 1139 (1974)
[2] Alper B et al, Plasma Phys. and Contr. Fus., 30, 843 (1988)
[3] Forrest M J, Carolan P G and Peacock N J, Nature, 271, 718 (1978)
[4] McCormick K and Olivain J, Rev. Phys. Appl. 13, 85 (1978)
[5] Soltwisch H et al, Plasma Phys. & Contr. Fus. 26, 23 (1984)
[6] Boileau A, et al 'Observations of Motional Stark features in the Balmer Spectrum in the JET Plasma', submitted to J. Phys. B (1989).
[7] Condon E U and Shortley G H, 'The Theory of Atomic Spectra' Cambridge University Press (1935).

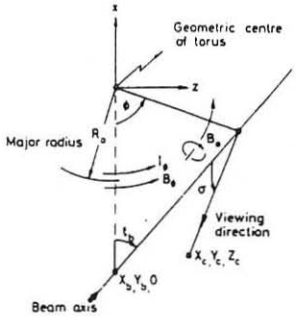

FIG 1 Plan view of neutral beam and viewing axis orientation with respect to the torus geometry.

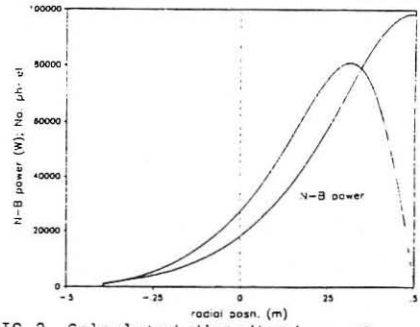

FIG 2 Calculated distributions of the neutral beam power and the detected photo electrons for 40keV deuterium beam, $n_e = 5\times10^{19}(1-(\frac{r}{a})^3)\ m^{-3}$ and detector characteristics described in the text.

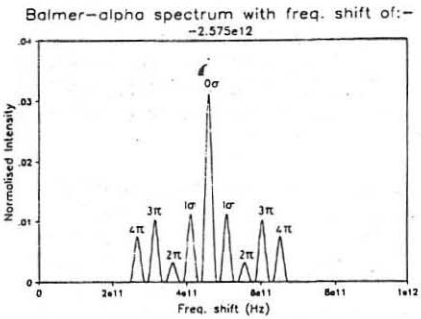

FIG 3 Typical calculated Stark Balmer-alpha spectrum at r = -0.22m. The spectral broadening arises from the range of Doppler shifts due to the finite beam divergence and the aperture of the collection optics

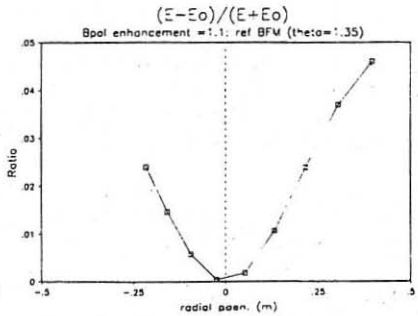

FIG 4 Normalised difference, $(|E|-|E_0|)/(|E|+|E_0|)$, of the Lorentzian electric field from the 'standard plasma' (giving an electric field $|E_0|$) and that where the poloidal field is increased by 10%.

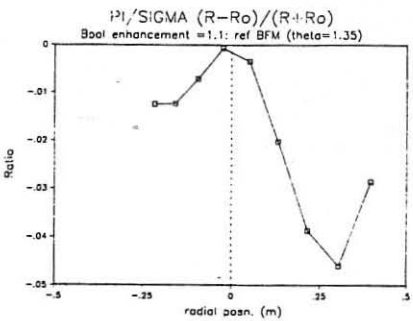

FIG 5 Normalised difference in the π to σ line intensity ratios between the 'standard' (giving the ratio $R_0 = I_\pi/I_\sigma$) and 10% enhanced poloidal field cases.

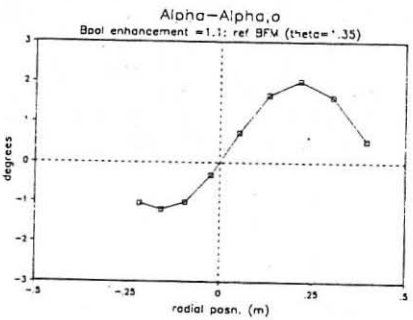

FIG 6 Difference in Lorentzian electric field direction, as seen from the collection optics, between the 'standard' and 10% enhanced poloidal field cases.

I

BASIC COLLISIONLESS PLASMA PHYSICS

I

DRIFT WAVE LAUNCHING IN A LINEAR QUADRUPOLE

G.Y. Tessema, J.A. Elliott and M.G. Rusbridge

Dept of Pure and Applied Physics, UMIST,
Manchester M60 1QD, UK

1. Introduction

The UMIST linear quadrupole is a steady-state device in which Hydrogen plasma is continuously injected axially, at one end, from an external duoplasmatron source. The system has been described by Phillips et al (1978) and Daly and Elliott (1982). A cross-section of the magnetic field configuration is shown in Fig.(1). The system manifests a range of plasma micro-instabilities, and of these the drift waves particularly have been studied in some detail (Carter et al (1981). They occur in the shared-flux region, between the separatrix and the critical surface. We report here that we have succeeded in launching drift waves from probes. We present the evidence for their firm identification as true drift waves, and a model for the launching process. We also present initial evidence that we can launch drift-ballooning modes, which are not spontaneously present. Finally, we will discuss proposed applications of the launching technique to the study of drift waves.

Drift waves must have a small component of the wave vector $\underline{k}$ along the magnetic field direction. In the quadrupole, therefore, since the field lines are closed, the parallel component forms a standing wave around the field line, while the wave propagates along the axial direction. Observed spontaneous drift waves manifest symmetry about the horizontal plane, with nodes at the field maxima. The converse symmetry, with nodes at the field minima, is not observed, but is referred to as the drift-ballooning mode. The anti-nodes would appear at the point of maximum destabilising curvature. Such modes are theoretically predicted (Hastie and Taylor, 1971), but with low growth rate.

2. The wave-launching system

The observed frequency of the drift waves is between 40 and 60 kHz, and the wavelength along the direction of propagation is about 60 mm. A launching system has been constructed using four flag probes each 30 x 20 mm, aligned with the long dimension along the machine axis, and the short dimension parallel to the field. The flags thus are one half-wavelength in size, giving maximum radiation efficiency. The flags are arranged symmetrically around a flux tube, and are driven with the desired symmetry matching the drift mode being launched: if the left pair are driven in anti-phase with the right pair, the normal drift mode is excited. If upper and lower pairs are in anti-phase, the ballooning mode is launched. The system draws no net current from the plasma; current is passed from one pair to the other through the plasma by means of an isolating transformer. In the experiments described, the voltage applied between the flags was sinusoidal, and 20 V peak-to-peak.

The launched waves were detected using small cylindrical Langmuir probes, 1 mm in diameter and 1 mm in length, and biassed to -60 V. Several combinations

were used. A single probe is sufficient to measure the frequency spectrum; two probes, with variable separation along the axial direction, were used to measure the axial correlation, and hence the wavelength. For studies of the drift-ballooning mode, two detecting probes were used, both at the same axial position, separated by 100 mm along a field line, phased so that the ballooning symmetry could be positively selected.

3. Experimental results

A typical power spectrum is shown in Fig.(2). The launching symmetry was that of the normal drift wave, with opposite sides in antiphase. The broad peak at about 50 kHz is the intrinsic drift instability. The other broad peak at low frequency is a flute-like mode which has generally been identified with the 'shallow-well flute mode' of Hastie and Taylor (1971). The very narrow peak at 30 kHz is the launched wave, with amplitude comparable to the intrinsic drift waves.

Correlation measurements made across the machine and 150 mm downstream of the launcher show clearly that opposite sides are in antiphase, as expected for the drift wave.

The conclusive identification of the launched wave as a drift wave is provided by measurements of the dispersion curve, $\omega(k)$. This is shown in Fig.(3). The measurements are shown superimposed on the dispersion data for the intrinsic drive waves obtained by the correlation-phase velocity method (Conway and Elliott 1987, Briggs et al 1949). There is a very satisfying agreement between the intrinsic and launched wave measurements. In addition, we have shown that the launched wave propagates in the electron diamagnetic drift direction, and that there is no propagation in the opposite direction, a necessary condition for identification as a drift wave.

The drift ballooning mode is also being investigated, and preliminary results show that it can be launched, and that the phase velocity is roughly half that of the normal mode. This result is unexpected, since Carter et al (1981) present theoretical calculations of the dispersion curve suggesting that the phase velocity should be greater for the drift-ballooning mode, basically because trapped particle effects are absent. Further work is needed to confirm the results.

4. The launching mechanism

Measurements of the plasma impedance to current flow have been made (Ashraf and Rusbridge, 1988). These show that when current is injected and extracted by probes on opposite sides of the quadrupole, and on the same flux tube, as in the launching experiments, the current does not simply flow along the flux tube physically connecting the probes, but first flows radially to fill an expanded flux tube. It is the radial flow across the magnetic field that drives the plasma oscillation: the transverse current is carried by the polarisation drift mechanism and the j x B force causes the local plasma to oscillate rotationally around the flux tube linking the two flag probes Fig.(4). Since the flag is one half wavelength in dimension, the displacements of the plasma at the two ends of the flag are phase matched to that required by a drift wave with that wavelength. In addition, the potential variation imposed by the flag probe phase matches that required for a drift wave. The phase matching is correct only for a wave travelling in the downstream direction.

In further confirmation of this model, we find experimentally that small probes much smaller than a wavelength in dimension, launch very inefficiently, and indeed for a given flag probe, efficiency falls off as the launching frequency rises above or falls below the matching frequency. However, there may be other possible coupling mechanisms: one puzzling observation is that if the flag probes are rotated to lie in the transverse plane, parallel to B, and with a negligibly small longitudinal dimension, the launching efficiency actually increases. We suspect that in this case the radial oscillation of the plasma along the downstream face of the flag dominates; also, the current channel will probably be very much larger than the flag thickness.

5 Decay rate measurements

The spatial decay constant has been determined as a function of frequency from the correlation measurements as a function of z. These values can be transformed into temporal decay coefficients using appropriate values of the wave velocity. The results are shown in Fig.(5). The decay constant has a minimum value at frequencies where the drift waves are spontaneously generated. At these frequencies, the waves are decaying not to zero but to some limiting amplitude where mode losses just balance the energy input. Earlier measurements of the growth rate of the spontaneous waves (Carter et al 1981), however, do not show a maximum within the band, so the interpretation of this result is not clear.

6 The future programme

The ability to generate drift waves of specific frequency opens up many avenues of study. The original purpose of these studies was to facilitate the control of drift instabilities by feedback control: we are now in a position to launch into the plasma sufficient wave power to phase cancel the intrinsic broad-band spectrum of instabilities. In principle this should prevent plasma loss due to these instabilities, and thereby giving information about the energy pathway in which the drift instability plays a part. Non-linear coupling between modes can also be investigated, by stabilising a narrow band of the fluctuations and observing the effect on other modes. Non-linear interactions may also be studied by launching two modes simultaneously and measuring the degree of frequency mixing: such work will be complementary to the studies of Greb and Rusbridge (1988) using bi-spectra of the intrinsic fluctuations.

References

M. Ashraf and M.G. Rusbridge, Plas. Phys. and Cont. Fus. 29, 969, 1987
B.H. Briggs, G.J. Phillips and D.H. Shinn, Proc. Phys. Soc. 63, 106, 1949
P.S. Carter, D.N. Edwards, P.R. Mossack, M.G. Rusbridge and R.J. Hastie, Plas. Phys. 23, 819, 1981
G.D. Conway, and J.A. Elliott, Plas. Phys. and Cont. Fus. 29, 807, 1987
E.J. Daly and J.A. Elliott, Plas. Phys. 24, 923, 1982
U. Greb and M.G. Rusbridge, Plas. Phys. and Cont. Fus. 30, 537, 1988
R.J. Hastie and J.B. Taylor, Plas. Phys. 13, 265, 1971
K. Phillips, M.G. Rusbridge and K.M. Young, Plas. Phys. 20, 653, 1978

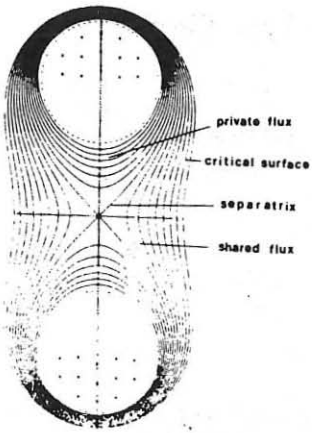

Fig. 1 The Quadrupole magnetic field

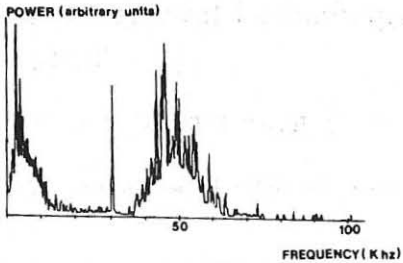

Fig. 2 A typical power spectrum, showing intrinsic fluctuations and a narrow peak of launched wave power.

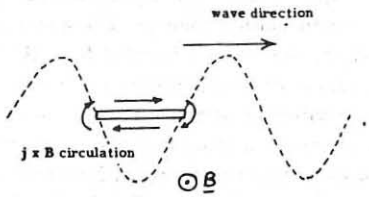

Fig. 4 The wave launching mechanism: plasma oscillates rotationally around the driving flux-tube, driven by the j x B force. The diagram shows the relationships at a maximum in the drift wave cycle.

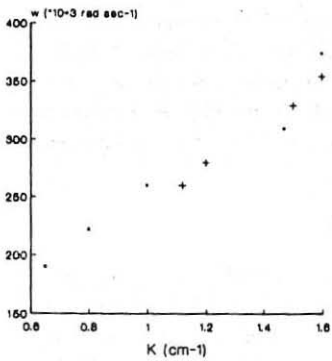

Fig. 3 Experimental dispersion data $\omega(k)$ for intrinsic drift waves (crosses) and launched waves (dots).

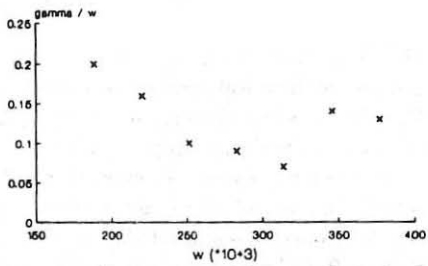

Fig. 5 The relative decay constant γ/ω for the launched waves.

Experimental Investigations of Flute Type Electrostatic Turbulence.

T. Huld+, S. Iizuka*, H. L. Pécseli+ and J. Juul Rasmussen+.

+Assoc. EURATOM-Risø National Laboratory, Phys. Dept., Risø, P.O.Box 49, DK-4000 Roskilde, Denmark.

*Faculty of Engineering, Yokohama National University, Yokohama 240, Japan.

Abstract

Low frequency flute type electrostatic fluctuations are investigated experimentally in a magnetized plasma column. The fluctuations are generated by the Kelvin-Helmholtz instability due to an azimuthal $\mathbf{E}_0 \times \mathbf{B}_0/B_0^2$ velocity shear at the edge of the column. Correlation measurements demonstrate a coupling between this instability and gradient drift instabilities located at the radial position with the strongest density gradient. Cross correlation measurements of density and potential fluctuations demonstrate that the instability saturates by shifting the phase between these two quantities to a value differing from the one predicted by a linearized analysis. The turbulent fluctuations give rise to an anomalous plasma flux across the magnetic field lines. This flux is estimated by measurements of density and velocity correlations, where the randomly varying velocity is identified with the fluctuating $\tilde{\mathbf{E}} \times \mathbf{B}_0/B_0^2$ velocity. An explicit value for the effective bulk plasma diffusion coefficient is obtained from the measurements.

Measurements

The experiment was conducted in a cesium plasma produced in a single-ended Q-machine, with typical parameters being $n_0 = 10^9 cm^{-3}$, $T_i \approx T_e = 0.2eV$ and $B_0 = 0.4T$. The plasma column is composed of two parts. First, a central core terminated by the hot plate of the device. Surrounding this core we have a residual or scrape-off plasma layer, where the density decreases rapidly in the radial direction while the DC-electric potential increases from the negative plasma potential characterizing the core and reaching the ground potential of the stainless steel vacuum vessel. The strongly sheared $\mathbf{E}_0(\mathbf{r}) \times \mathbf{B}_0/B_0^2$ rotation of the residual plasma layer gives rise to a Kelvin-Helmholtz instability causing an enhanced level of $\mathbf{B}_0$-field aligned, flute-type, electrostatic fluctuations [1,2]. Typical radial variations of the frequency spectrum are shown in fig. 1. We found that fluctuations in the central core are characterized by the approximate

relation $e\tilde{\phi}/T_e \approx \tilde{n}/n_0$ and have a peak rms-level where the density gradient is largest. These features are consistent with drift-wave type fluctuations. In the residual plasma we find on the other hand a high level of broadband turbulence with $e\tilde{\phi}/T_e \gg \tilde{n}/n_0$, as expected for flute-type fluctuations. We explicitly verified the B_0-field aligned property of the fluctuations by two-probe measurements and by varying the length of the plasma column.

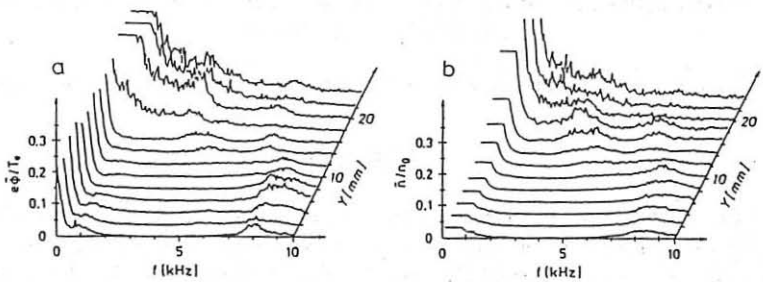

Figure 1.

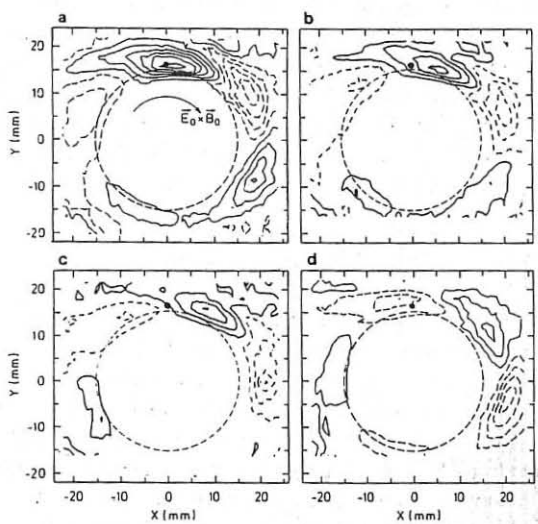

Figure 2.

The characteristic azimuthal velocity of propagation, associated with the broad band turbulence, was determined by cross-correlation measurements for different time

delays τ as shown in fig. 2; a) $\tau = 0$, b) $\tau = 25\mu s$, c) $\tau = 50\mu s$, d) $\tau = 100\mu s$. We found that this velocity was close to the azimuthal $\mathbf{E}_0 \times \mathbf{B}_0/B_0^2$ velocity deduced by averaging the radial electric field over the thickness of the residual plasma layer. Correlation techniques were used also to investigate the phase relations between density and potential fluctuations. By this procedure we also demonstrated a weak correlation between the drift wave fluctuations in the central plasma and the flute turbulence in the residual plasma.

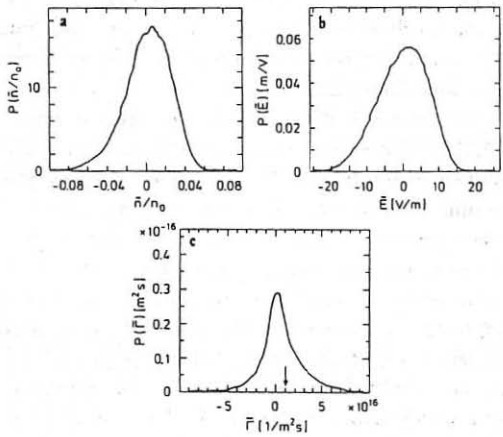

Figure 3.

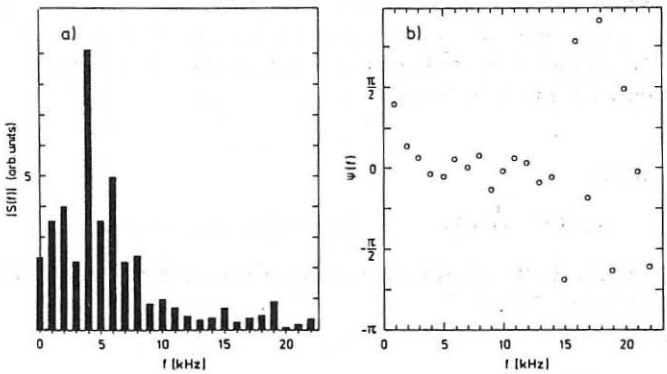

Figure 4.

In order to investigate a possible relation between the turbulent fluctuations and an enhanced, anomalous, radial transport we measured the average radial plasma flux $\langle \tilde{n}\tilde{v}_r \rangle$. Since the fluctuations are characterized by frequencies well below the ion cyclotron frequency, we identify $\tilde{v}_r = \tilde{E}/B_0$, where $\tilde{E}$ here denotes the azimuthal component of the fluctuating electric field. This component is measured by the fluctuating potential difference between two closely spaced Langmuir probes, while the fluctuations in plasma density are monitored by the fluctuations in saturation current to a third Langmuir probe [2]. Probability densities for the amplitudes of $\tilde{n}$, $\tilde{E}$ and the product $\tilde{n}\tilde{E} \equiv \tilde{\Gamma}$ are shown in fig. 3. An arrow indicates the average value $\langle \tilde{n}\tilde{E} \rangle \neq 0$, which corresponds to a net plasma flux *out* of the plasma column. A diffusion coefficient can be determined with a value several orders of magnitude larger than classical, collisional diffusion but somewhat below the value given by the traditional Bohm formula. The auto-correlation functions for $\tilde{n}$, $\tilde{E}$ and $\tilde{\Gamma}$ were measured together with the cross-correlation function $\langle \tilde{n}(t)\tilde{E}(t+\tau) \rangle$. The phase relations between $\tilde{n}$ and $\tilde{E}$ for various frequencies was determined by Fourier transform of the latter quantity, giving the complex cross-power spectrum which is written as $S(f = \omega/2\pi) = |S(f)|e^{i\Psi(f)}$. The two quantities $|S(f)|$ and $\Psi(f)$ are shown in fig. 4. The phase spectrum $\Psi(f)$ indicates that for high frequencies there is a phase difference of approximately 0 between $\tilde{n}$ and $\tilde{E}$ with our convention of notation. At the lowest frequencies, where much of the energy is condensed according to $|S(f)|$, we have on the other hand a phase difference closer to $\pi/2$. The high frequency (i.e. short wavelength) modes in $|S(f)|$ shown in fig. 4 are close to the density–electrical field phase relation of 0 which gives linear instability. The low frequency, long wavelength components, on the other hand have a phase relation corresponding to the saturated stage. The phase spectrum $\Psi(f)$ thus invites an interpretation where energy is being fed into high mode numbers by the instability with the energy cascading to lower mode numbers which are driven into saturation. For these modes energy can be ultimately dissipated by e.g. friction with the end plates of the device. The cascade of energy towards long wavelengths seems a generic feature of two-dimensional, i.e. flute type, turbulence.

References

[1] Kent, G.I., Jen, N.C. and Chen, F.F. (1969) Phys.Fluids **12**,2140

[2] Huld, T., Iizuka, S., Pécseli, H.L., and Rasmussen, J.J. (1988) Plasma Physics and Controlled Fusion, **30**,1297

THEORY OF WEAKLY NONLINEAR OSCILLATIONS IN THE PIERCE DIODE WITH EXTERNAL–CIRCUIT ELEMENTS

M. Hörhager and S. Kuhn

Bounded Plasma Systems Group, Institute for Theoretical Physics,
University of Innsbruck, A–6020 Innsbruck, Austria

Introduction and Summary. The dynamical evolution of a realistic bounded plasma system is, by definition, governed by the simultaneous and self–consistent interaction of the plasma, its material boundaries, and the external circuit. Being dissipative, bounded plasma systems will in practice most often be encountered in some well–defined nonlinear attractor state. While d.c. equilibria (fixed–point attractors) of various kinds often are relatively straightforward to calculate and hence have been treated extensively in the literature, the theory of oscillatory and chaotic attractors (periodic and non–periodic oscillations, respectively) in bounded plasma systems is still in its early beginnings and hence needs systematic development starting out from the very fundamentals.

In the present paper, a theory of weakly nonlinear steady–state oscillations is presented for one of the simplest and most fundamental bounded plasma systems, namely the uniform classical Pierce diode[1–3] extended by nontrivial external–circuit elements[4–7], cf. Fig. 1. The theory is applicable in parameter regimes where linear stability analysis predicts just one unstable eigenmode which is oscillatory and whose growth rate is sufficiently small for all perturbations to be approximately representable as Fourier series in time with just a small number N of harmonics ($N \geq 3$).

Numerical results are presented for the "three–harmonic approximation", in which, by definition, the fourth and higher harmonics are neglected. The dependence of the nonlinear fundamental frequency on the normalized system length is given, in some appropriate parameter range, for the short–circuit case. A slight discrepancy is found with Godfrey's[3] results, which, however, were obtained by purely numerical integration of the basic equations in integral form. Also shown are spatial velocity profiles.

To our knowledge, this is the first analytic treatment of self–consistent, steady–state nonlinear oscillations in a bounded plasma system.

Model and Basic Equations. In the "classical" Pierce Diode [1–3], a cold electron beam propagates without collisions between an emitter located at $x = 0$ and a collector located at $x = l$. The electrons (mass m, charge $-e$) leave the emitter with constant density n_0 and velocity v_0, and are absorbed when hitting either electrode. The ions are assumed to be immobile and to provide a uniform neutralizing background with density n_0. Being externally shorted, the two electrodes are constantly kept at the same potential. We furthermore assume that the dc state about which the oscillations occur is characterized by uniform electron density n_0 and, hence, zero electric field inside the diode gap. The various phenomena occurring in the classical Pierce diode are conveniently parametrized in terms of the normalized system length

$$\alpha = \omega_p l / v_0 , \tag{1}$$

where $\omega_p = \sqrt{n_0 e^2/(\epsilon_0 m)}$ is the electron plasma frequency.

For the more general "extended" Pierce diode considered here (Fig. 1), the basic

equations are

$$\frac{\partial n}{\partial t} + \frac{\partial}{\partial x}(nv) = 0 \qquad (2) \qquad (\frac{\partial}{\partial t} + v\frac{\partial}{\partial x})v = -\frac{e}{m}E \qquad (3)$$

$$\frac{\partial E}{\partial x} = \frac{e}{\epsilon_o}(n_o - n) \qquad (4) \qquad \epsilon_o\frac{\partial E}{\partial t} + j_P = J \qquad (5)$$

$$V(l,t) - V(0,t) = -\int_0^l dx\, E(x,t) = L\frac{dI}{dt} + RI + \frac{Q}{C} + U_B \qquad (6)$$

with $n(x,t)$ the electron density, $v(x,t)$ the electron velocity, $E(x,t)$ the electrostatic field; $j_P(x,t) = -env$ the plasma current density, $J(t) = I(t)/A$ the external–circuit current density (with $I(t)$ the total external–circuit current and A the electrode area); R, C and L the external–circuit resistance, capacitance, and inductance, respectively, and $Q(t)$ the electric charge sitting on the right–hand plate of the capacitor C. The battery voltage $U_B = -\bar{I}R$ serves to compensate the dc potential drop across the resistance R. The electrostatic potential $V(x,t)$ is defined by $E = -\partial V/\partial x$ and $V(0,t) = 0$. Equations (2)–(6) are the continuity, momentum, Poisson, total–current conservation, and external–circuit equations, respectively. They are complemented by the "standard" electron boundary conditions

$$n(0,t) = n_o \qquad (7) \qquad v(0,t) = v_o\,. \qquad (8)$$

Note that (5) is not an independent equation but follows by appropriate combination of (2)–(4).

Nonlinear Fourier Analysis. We now decompose any physical quantity u as

$$u(x,t) = \bar{u} + \tilde{u}(x,t), \qquad (9)$$

with $\bar{u}$ the constant equilibrium value and $\tilde{u}(x,t)$ the perturbation. The equilibrium quantities are given by $\bar{n} = n_o$, $\bar{v} = v_o$, $\bar{E} = 0$, $\bar{J} = -e\bar{n}\bar{v}$, and $\bar{Q} = 0$, the last equality following from the large inductance L_c, which bridges the capacitance C dc–wise. Then, upon inserting (9) into (2)–(8), the equations for the perturbations follow as

$$\frac{\partial\tilde{n}}{\partial t} + \frac{\partial}{\partial x}(\bar{n}\tilde{v}+\tilde{n}\bar{v}+\tilde{n}\tilde{v}) = 0 \qquad (10) \qquad \left[\frac{\partial}{\partial t} + (\bar{v}+\tilde{v})\frac{\partial}{\partial x}\right]\tilde{v} = -\frac{e}{m}\tilde{E} \qquad (11)$$

$$\frac{\partial\tilde{E}}{\partial x} = -\frac{e}{\epsilon_o}\tilde{n} \qquad (12) \qquad \epsilon_o\frac{\partial}{\partial t}\tilde{E} - e[\bar{n}\tilde{v}+\tilde{n}\bar{v}+\tilde{n}\tilde{v}] = \tilde{J} \qquad (13)$$

$$-\int_0^l dx\, \tilde{E}(x,t) = A\left[L\frac{d\tilde{J}}{dt} + R\tilde{J} + \frac{1}{C}\int_0^t d\tau\, \tilde{J}(\tau)\right] + \frac{\tilde{Q}(0)}{C} \qquad (14)$$

$$\tilde{n}(0,t) = 0 \qquad (15) \qquad \tilde{v}(0,t) = 0\,. \qquad (16)$$

Using (11) and (12) to express $\tilde{E}$ and $\tilde{n}$ in terms of $\tilde{v}$, we obtain from (13)

$$\frac{\partial^2\tilde{v}}{\partial t^2} + 2\bar{v}\frac{\partial^2\tilde{v}}{\partial x\partial t} + \omega_p^2\tilde{v} + \bar{v}^2\frac{\partial^2\tilde{v}}{\partial x^2} + \frac{\partial\tilde{v}}{\partial x}\frac{\partial\tilde{v}}{\partial t} + 2\tilde{v}\frac{\partial^2\tilde{v}}{\partial x\partial t} + \tilde{v}\left[\frac{\partial\tilde{v}}{\partial x}\right]^2$$
$$+ 2\bar{v}\tilde{v}\frac{\partial^2\tilde{v}}{\partial x^2} + \tilde{v}\left[\frac{\partial\tilde{v}}{\partial x}\right]^2 + \tilde{v}^2\frac{\partial^2\tilde{v}}{\partial x^2} = -\frac{e}{m\epsilon_o}\tilde{J}\,, \qquad (17)$$

and a second relation between $\tilde{v}$ and $\tilde{J}$ follows from inserting (11) into (14):

$$-\int_0^l dx\, \tilde{E}(x,t) = \frac{m}{e}\left[\frac{\partial}{\partial t}\int_0^l dx\, \tilde{v}(x,t) + \bar{v}\tilde{v}(l,t) + \frac{1}{2}[\tilde{v}(l,t)]^2\right]$$

$$= A\left[L\frac{d\tilde{J}}{dt} + R\tilde{J} + \frac{1}{C}\int_0^t d\tau\, \tilde{J}(\tau)\right] + \frac{\tilde{Q}(0)}{C}. \tag{18}$$

Finally, using (11) and (12), (15) becomes a second boundary condition for $\tilde{v}$:

$$\tilde{n}(0,t) = \frac{m\epsilon_0}{e^2}\left[\frac{\partial^2\tilde{v}}{\partial x\partial t} + \bar{v}\frac{\partial^2\tilde{v}}{\partial x^2} + \left[\frac{\partial\tilde{v}}{\partial x}\right]^2\right]_{x=0} = 0\,. \tag{19}$$

Looking for steady–state oscillations periodic in time, we now expand any real perturbation $\tilde{u}$, and specifically $\tilde{J}$, in Fourier series of the form

$$\tilde{u}(x,t) = \sum_{n=-\infty}^{\infty}\hat{u}_n(x)e^{-in\omega t} \quad (20) \qquad \tilde{J}(t) = \sum_{n=-\infty}^{\infty}\hat{J}_n e^{-in\omega t} \tag{21}$$

where the time–averaged profile $\hat{u}_0(x)$ and the nonlinear fundamental frequency ω are real, $\hat{u}_n(x) = [\hat{u}_{-n}(x)]^*$ is the spatial profile of the n–th harmonic, and, specifically, $\hat{J}_0 = 0$. Inserting the Fourier series for $\tilde{v}$ and $\tilde{J}$ into (17), (16), (19) and (18), and collecting powers of $\exp(-i\omega t)$, we obtain the following relations:

$$\left\{(-in\omega)^2\hat{v}_n + \omega_p^2\hat{v}_n + 2\bar{v}(-in\omega)\frac{\partial\hat{v}_n}{\partial x} + \bar{v}^2\frac{\partial^2\hat{v}_n}{\partial x^2} + \sum_{m=-\infty}^{\infty}\left[-i(n+m)\omega\hat{v}_{n-m}\frac{\partial\hat{v}_m}{\partial x} + \bar{v}\frac{\partial\hat{v}_{n-m}}{\partial x}\frac{\partial\hat{v}_m}{\partial x}\right.\right.$$
$$\left.\left. + 2\bar{v}\hat{v}_{n-m}\frac{\partial^2\hat{v}_n}{\partial x^2}\right] + \sum_{m=-\infty}^{\infty}\sum_{l=-\infty}^{\infty}\hat{v}_{n-m-l}\left[\frac{\partial\hat{v}_m}{\partial x}\frac{\partial\hat{v}_l}{\partial x} + \hat{v}_m\frac{\partial^2\hat{v}_l}{\partial x^2}\right]\right\} = \frac{-e}{m\epsilon_0}\hat{J}_n\,, \tag{22}$$

$$\hat{v}_n(0) = 0 \quad (23) \qquad \left[-in\omega\frac{\partial\hat{v}_n}{\partial x} + \bar{v}\frac{\partial^2\hat{v}_n}{\partial x^2} + \sum_{m=-\infty}^{\infty}\frac{\partial\hat{v}_m}{\partial x}\frac{\partial\hat{v}_{n-m}}{\partial x}\right]_{x=0} = 0 \tag{24}$$

$$\frac{m}{e}\left[(-in\omega)\int_0^1 dx\,\hat{v}_n(x) + \bar{v}\hat{v}_n(1) + \frac{1}{2}\sum_{m=-\infty}^{\infty}\hat{v}_{n-m}(1)\,\hat{v}_m(1)\right]$$
$$= (1-\delta_{n0})A\left[(-in\omega)L + R + (-in\omega C)^{-1}\right]\hat{J}_n \tag{25}$$

Three–Harmonic Approximation. From now on we restrict ourselves to weak nonlinearities, so as to be able to apply nonlinear perturbation theory with just a small number N of harmonics, where the n+1st harmonic ist one order smaller than the n–th one and the time–averaged part of the perturbation is of second order.

In the general procedure for evaluating the "N–harmonic approximation", we first write down Eqs. (22)–(24) for each order n involved ($n = 1$ for $N = 1$ and $n = 1, 0, 2, 3, \ldots, N$ for $N \geq 2$) and solve these separately to obtain the n–th order velocity profiles, with ω and the current amplitudes as parameters. Inserting these profiles into the appropriate n–th order external–circuit equations (25), and requiring ω to be real, we arrive at the relation(s) from which to calculate ω and the current amplitudes.

In both the linear ($N = 1$) [1,3–5] and two–harmonic ($N = 2$) [7] approximations, the current amplitudes remain undetermined, and the admissible values of ω are the linear eigenfrequencies, i.e., the (generally complex) solutions $\omega = \omega_{lin}$ of the "characteristic equation"

$$D_{lin}(\omega) \equiv A\left[-i\omega L + R + \frac{1}{-i\omega C}\right] + \frac{v_0}{2\epsilon_0\omega(\omega^2-\omega_p^2)^2}\left[\omega_p(\omega-\omega_p)^2\exp\left[i\frac{\omega+\omega_p l}{v_0}\right]\right.$$
$$\left. - \omega_p(\omega+\omega_p)^2\exp\left[i\frac{\omega-\omega_p l}{v_0}\right] + 2\omega(\omega^2+\omega_p^2) - 2\omega(\omega^2-\omega_p^2)\left[1-i\omega\frac{l}{v_0}\right]\right] = 0\,. \tag{26}$$

The lowest approximation that renders both the fundamental frequency ω and the current amplitudes well–defined is the "three–harmonic approximation" ($N = 3$), for which the general procedure outlined above leads to the relation

$$\rho(\omega) \equiv D_{lin}(\omega)/f(\omega) = |\hat{J}_1|^2 \tag{27}$$

with $f(\omega)$ a complicated function given in [7]. Since we are still dealing with an approximation, we cannot expect ω and $\rho(\omega)$ to be exactly real simultaneously, so we require ω to be real and determine its value by (numerically) minimizing $\mathrm{Im}\rho(\omega)$. The frequency shift $\Delta\omega \equiv \omega - \omega_{1\mathrm{in}}$ is of second and $\Delta\hat{v}_1 \equiv \hat{v}_1 - \hat{v}_{1\mathrm{lin}}$ is of third order, while $\hat{v}_0(x)$ and $\hat{v}_2(x)$ are the same as in the two–harmonic approximation [7].

Numerical Results. To demonstrate our theory, we present some numerical results for the short–circuit Pierce diode ($L = 0$, $R = 0$, $1/C = 0$). Figure 2 shows both $\mathrm{Re}\omega_{1\mathrm{in}}$ and the nonlinear ω in the parameter range $2.86 \leq \alpha/\pi \leq 2.90$, also as given by Godfrey [3]. Our theory should work best for α/π just slightly below 2.897 (at which value the linear growth rate vanishes) and break down completely for $\alpha/\pi \leq 2.865$ (where a period–doubling cascade occurs and hence our ordering scheme is inappropriate). In the whole range shown, our linear and nonlinear frequencies are typically 1% less than Godfrey's, and we believe that, at least for ω near $\alpha = 2.897$ and for $\mathrm{Re}\omega_{1\mathrm{in}}$ over the entire α–range, our results are more accurate. In addition, Figs. 3(a) and 3(b) show the linear first–order velocity profile and its third–order correction, respectively, for the parameter value $\alpha/\pi = 2.88$. More results can be found in [7].

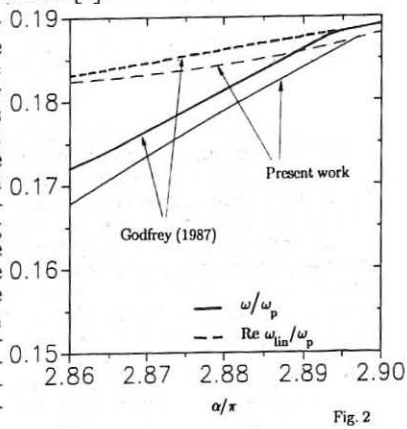

Fig. 2

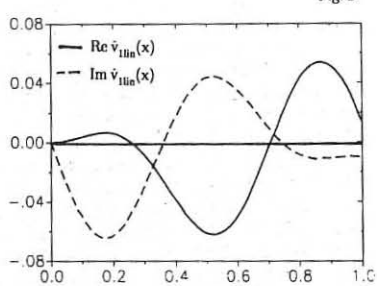

Fig. 3(a)

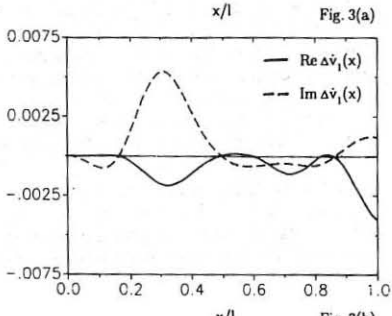

Fig. 3(b)

Acknowledgment. This work was supported in part by Austrian Research Fund contracts P5179 and P7005.

References

1. R. Pierce, J. Appl. Phys. **15**, 721 (1944).
2. T.L. Crystal and S. Kuhn, Phys. Fluids **28**, 2116 (1985).
3. B.B. Godfrey, Phys. Fluids **30**, 1553 (1987).
4. S. Kuhn, Phys. Fluids **27**, 1834 (1984).
5. S. Kuhn and M. Hörhager, J. Appl. Phys. **60**, 1952 (1986).
6. Wm.S. Lawson, PhD thesis (Electronics Res. Lab., U.C. Berkeley, CA, 1987).
7. M. Hörhager and S. Kuhn, to be published.

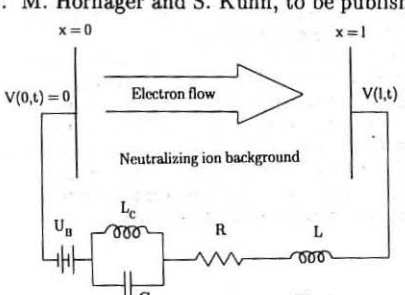

Fig. 1

BUILDUP OF ELECTRONS WITH HOT ELECTRON BEAM INJECTION INTO A HOMOGENEOUS MAGNETIC FIELD

V.A.Bashko, A.M.Krivoruchko, I.K.Tarasov

Kharkov Institute of Physics and Technology,
the Ukrainian SSR Academy of Sciences, 310108 Kharkov, USSR

The injection of the monoenergetic beam of electrons into the vacuum drift channel under the conditions when the beam current exceeds a certain threshold value involves a virtual cathode creation. The process of virtual cathode creation leads to an exchange of one-fluid movement of beam particles to three-fluid one corresponding to incident, reflected and passed through anticathode beam particles. For the monoenergetic beam case when the velocity spread $\Delta v \ll v_{dr}$ (v_{dr} is the beam drift velocity), the beam instability was predicted in theory and was observed in experiment in [1]. Meanwhile, the injection in the drift space of the "hot" beam having finite spread in velocities may be accompanied not only by the reflection of particles if their velocity $v < (2e\varphi/m)^{1/2}$ (where φ is the electrostatic potential dip value, e and m are the electron charge and mass, respectively), but also the mutual Coulomb scattering of incident and reflected electrons. The scattering process leads in its turn to appearance of viscosity forces and to trapping of a part of beam electrons into the effective potential well formed by electrostatic potential dip and the viscous force potential. The interaction of travelling and trapped particles may occur even at the stage preceding the virtual electrode formation and it may influence the process of its appearance and also the current flow through the drift space [2]. In this report there are described the experimental results on accumulation of electrons when electron beam propagates in vacuum and has a large spread in particle velocities $\Delta v \lesssim v_{dr}$ in the homogeneous longitudinal magnetic field when $\omega_{pe} \ll \omega_{He}$, where ω_{pe} is the electron Langmuir frequency of beam electrons, ω_{He} is the electron cyclotron frequency.

The experiments were performed in the device described in detail in 2 . The hollow electron beam (a =2cm diameter, $\Delta \simeq 1\div2$ thickness, 20÷50 eV energy) is injected into the drift space (tube of $L \simeq 150$ cm length and $2R$ =4cm diameter) which was limited from edges by entrance and exit plane grids. The tube is cut along the forming line into two equal parts with the angular dimension of 180° (π -electrodes). The constant homogeneous longitudinal magnetic field has

the intensity H =100 ÷ 1000 Oe. The working pressure is 10^{-6}Torr. In the experiments there were measured: the time averaged distribution function over longitudinal energies with electrostatic analysers; particle density in the drift space by measuring the frequency of the diocotron mode with the azimuthal number ℓ =1; the emission current of the electron gun cathode; the current I_{ent} on the drift space entrance; the current I_{ex} on its exit; the oscillations and currents on HF Langmuir probes; the currents on π -electrodes.

In the experiments performed, special attention was devoted to analyzing the ion background influence, the background having being formed by beam electrons ionizing the residual gas. In our experiments this influence of ion background with ionizing the residual gas by beam electrons was not essential. In Fig.1 there are depicted the dependence of the current passed through the drift space I_{ex} versus the current at the entrance I_{ent} when the voltage at the electron gun cathode is U =-50 V. Dependences 1 and 2 are measured automatically with the two-coordinate recorder with the large integration time. It is seen from Fig.1 that with I_{ent} increasing the movement along the curve 1 from the point 0 to point B is accoplished along its lower branch. When I_{ent} decreases, the movement along the curve from B to 0 is along its upper branch. Thus, curve 1 of Fig.1 exhibits a hysteresis on I_{ex} versus I_{ent} dependence which, however, is opposite in nature to the well-known similar hysteresis dependence for the monoenergetic beam [3,4] and the beam having a strong spread over longitudinal velocities [2] when they work in the stationary regime. Meanwhile, in curve 2 of Fig.2 the hysteresis in I_{ex} versus I_{ent} dependence is absent. Curve 2 differs from curve 1 in this Figure only in the delay time between two subsequent periodic current pulses. This time is 3.5 times larger in curve 2 as compared with curve 1. The different behaviour of curves 1 and 2 in Fig.1 points to the presence of the noticeable volume charge in the drift space even after switching off of the beam injection pulse. Indeed, only the presence of trapped electrons which drift comparatively long time in the magnetic field and the effect of which is essential 400 msec after the injection pulse ended may explain the reverse hysteresis on I_{ex} versus I_{ent} dependence,

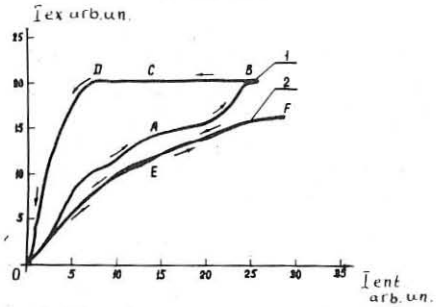

Fig.1. The dependence of the current I_{ex} versus I_{ent} for the pulsed beam: 1-pulse duration τ_{pul} =400 sec, time between the pulses t =800 sec; 2-τ_{pul}=400 sec t =2.8 sec.

curve 1 in Fig.2. When the beam of 400 μsec duration with 400 μsec pause between pulses is injected, the drift space has no time to free itself from the space charge accumulated during the previous current pulse. The time averaged distribution functions of incident, passing and reflected beams measured under these conditions has a spread in longitudinal velocities $\Delta v/v_{dr} \simeq 0.7 \div 0.8$. Fig.2 shows the oscillograms of: the negative voltage on the electron gun cathode; (ii) the current on one of the π -electrodes; and (iii) current on the same -electrode when on the other electrode a positive pulse of 0.3 msec duration and the amplitude 1 V is present. The oscillations registered with the -electrode correspond to the diocotron branch of charged plasma oscillations with the azimuthal wavenumber ℓ =1. It is easily seen from Fig.2 that the noticeable "tail" of oscillations exists during more than 1 msec after the beam injection pulse has been ended. It is also seen that the oscillation period increases with time and the times of growth and disruption of oscillations do not exceed their period as it follows from oscillogram 3 in Fig.2 where for dempnstration of this fact the positive pulse is given to one of π -electrodes. The pulse with 1 V amplitude totally damps the "tail" oscillations during the 0.3 msec period of its presence. Our experiments show that the diocotron mode of oscillations with =1 is excited as a rule also during the time of beam injection, the frequency of these oscillations being always higher than the "tail" oscillation frequency. The presence of diocotron oscillations points out that in the drift space apart from the beam electrons passing through it the electrons are present the lifetime of which is not less than the diocotron oscillation period to excite these oscillations at all. The presence of these "tails" in oscillograms in Fig.2 speaks to the lifetime of the part of electrons being considerably bigger than the period of the ℓ =1 diocotron mode. Using the relation of the drift frequency of rotation of the hollow beam in crossed own electrical and longitudinal magnetic field $\omega \simeq (b/2)(\omega_{pe}^2/2\omega_{He})$ ($b \simeq 0.5$, H =1 kOe for our experimental conditions) one may estimate the electron density n_e with the help of oscillograms of Fig.2. It amounts to $n_e \simeq 4.10^6 cm^{-3}$. The particle density of the injected beam is equal to $n_b = 2.10^7 cm^{-3}$. This estimate shows that the

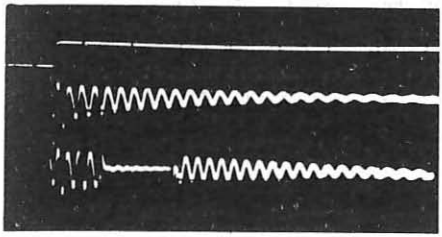

Fig.2. Oscillograms: 1-the negative voltage pulse at the electron gun cathode; 2-current on one of the π -electrodes; the same as in 2 but on the second π -electrode the positive pulse of o.3 msec duration and 1 V amplitude. 2 msec sweeps.

part of electrons drifting long time $\tau \sim 1 msec$ in the magnetic field is noticeable and amounts to n_e/n_b 0.2.

Thus we come to the conclusion that when electron beam with a large velocity spread is injected, the long lifetime electrons are accumulated in the drift space located in the magnetic field, the density of which being a noticeable fraction of the electron density of the injected beam. The obtained results on accumulation and confinement of electrons may be explained if the dissipative force of viscosity[5] is included in the balance of forces acting on a single electron along with the electrostatic force due to the dip of the electrostatic potential and the Lorentz force, this dissipative force occuring in the charged magnetized plasma due to electron-electron collisions between the travelling and the trapped particles in the presence of the drift velocity shear.

References

1. Bursian V.R., Pavlov V.I. Zhurnal Russkogo Fiziko-Khimicheskogo obshchestva, (1923) v.55, p.71 (In Russian).
2. Krivoruchko S.M., Tarasov I.K., Bashko V.A. Tezisy dokladov vsesojuzn.seminara "Plazmennaya electronika", Kharkov, 6-9 September (1988) p.180.
3. Krivoruchko S.M., Bashko V.A., Bakai A.S. ZhETF (1980) , v.80, p.579 (In Russian).
4. Nezlin M.V. Dinamika puchkov v plasme, Moscow, Energoatomizdat, (1982).
5. Miller R.B. An Introduction to the Physics of Intense Charged Particle Beams. Plenum Press, New York and London,1984
6. O'Neil T.M. Phys.Rev.Lett. (1985), v.55, p.943.

NON-LINEAR DIFFUSION OF CHARGED PARTICLES DUE TO STOCHASTIC ELECTROMAGNETIC FIELDS

A.M. Martins, J.T. Mendonça*, R. Balescu

Physical Statistique, Plasmas et Optique NL, Association Euratom-Etat Belge, CP 231, Campus Plaine ULB, Boulevard du Triomphe, 1050 Bruxelles, Belgium

* JET Joint Undertaking, Abingdon, Oxon, OX14 3EA, UK

1. INTRODUCTION

It is well known that the energy confinement times observed in tokamaks cannot be explained by the classical or neo-classical transport theory. The alternative explanations are based on the existence of various kinds of micro-instabilities, or on the stochastic destruction of the magnetic surfaces, due to the interaction of magnetic islands of different helicities.

In the absence of a well established theory of anomalous transport it is perhaps important to study in some detail the diffusion coefficient of single charged particles in the presence of electromagnetic fluctuation, because it can provide the physical grounds for more complete and self-consistent calculations.

In the present work we derive a general expression for the transverse diffusion coefficient of electrons and ions in a constant magnetic field and in the presence of space and time dependent electromagnetic fluctuation. We neglect macroscopic drifts due to inhomogeneity and field curvatures, but retain finite Larmor radius effects.

2. PERTURBED CYCLOTRON MOTION

Let us consider a particle, of charge q_α and mass m_α (where $\alpha = e,i$) moving in a constant magnetic field $\vec{B}_0 = B_0\hat{z}$, and submitted to the influence of electromagnetic field fluctuations, $\vec{E}(\vec{r},t)$ and $\vec{B}(\vec{r},t)$. The corresponding equation of motion can be written as:

$$[\frac{d}{dt} + \omega_{c\alpha}(1 + \beta_z(t)]\ \vec{v}(t) = -\omega_{c\alpha}\vec{\beta}_\perp(t)\Lambda\vec{v}(t) + \omega_{c\alpha}\vec{\epsilon}(t) \qquad (1)$$

where $\omega_{c\alpha} = q_\alpha B_0/m_\alpha$ in the cyclotron frequency, $\vec{\epsilon}(t) = \vec{E}(t)/B_0$ and β_z and $\beta_\perp$ are the parallel and perpendicular components of the normalized magnetic fluctuations,

$$\vec{B}(t)/B_0 = \vec{\beta}_\perp(t) + \beta_z(t)\hat{z}$$

Assuming that $|\beta_{z\perp}| << 1$, we can integrate eq. (1), using an iterative procedure [1].

The result is:

$$\vec{v}(t) = \sum_{n=0}^{\infty} U_r[*(-\omega_{c\alpha}\beta_\perp(t)\wedge U_r]^n[\vec{v}(t_0) + \omega_{c\alpha}\vec{\epsilon}(t)] \tag{2}$$

where we have used the renormalized cyclotron propagator $U_r(t,t_0)$, which obeys the equation:

$$[\frac{d}{dt} + \omega_{c\alpha}(1 + \beta_z(t)]\ U_r(t,t_0) = 0 \tag{3}$$

with $U_r(t_0,t_0) = 1$. The notation (*) appearing in eq. (2) means the convolution operation:

$$(A * B)_t = \int_0^t A(\tau)B(t-\tau)d\tau$$

In the following calculations we will use the first order approximation of eq. (2), which can be written as:

$$\vec{v}(t) = U_r(t,t_0)\vec{v}(t_0) + \omega_{c\alpha}\int_{t_0}^{t} dt_1 U_r(t,t_1)\vec{\epsilon}(t_1) - \omega_{c\alpha}\int_{t_0}^{t} dt_1 U_r(t,t_0)[\vec{\beta}_\perp(t_1)\wedge]U_r(t,t_0)\vec{v}(t_0) \tag{4}$$

3. TRANSVERSE DIFFUSION COEFFICIENT

For each initial particle position $\vec{r}_0 = \vec{r}(t=t_0)$, we have the following solution of the equation of motion:

$$\vec{r}(t) = \vec{r}_0 + \int_0^t dt'\vec{v}(t')$$

Defining the transverse component of the particle position by:

$$r_\perp(t) = x(t) + iy(t)$$

and integrating eq. (4) we obtain:

$$r_\perp(t) = r_{\perp_0} + \int_0^t dt' e^{-i\omega_{c\alpha}t'-i\gamma(t')} v_{\perp_0} + \omega_{c\alpha}\int_0^t dt'' \int_0^t dt' e^{-i\omega_{c\alpha}(t''-t')-i\gamma(t''-t')} h_\perp(t') \tag{5}$$

where $v_{\perp_0} = v_x(t_0) + iv_y(t_0)$ and:

$$\gamma(t) = \int_0^t dt' \; \beta_z(t')$$

$$h_\perp(t) = \epsilon_\perp(t) + iv_{z_0}\beta_\perp(t) \tag{6}$$

Let us assume now that the initial particle position, at $t = t_0$, is exactly known, $\vec{r}(t_0) = \langle \vec{r}(t_0) \rangle$, where $\langle\rangle$ means the stochastic average, and that the parallel fluctuations can be neglected. We can write:

$$\hat{r}_\perp(t) = r_\perp(t) - \langle r_\perp(t) \rangle = i \int_0^t dt' \; [e^{-i\omega_{c\alpha}(t-t')} - 1]h_\perp(t') \tag{7}$$

The transverse diffusion coefficient will be given by:

$$D_\perp(t) = \frac{d}{dt} \langle \hat{r}_\perp(t)\hat{r}_\perp{}^*(t) \rangle \tag{8}$$

Under the assumption of a stationary and homogeneous turbulence and modelizing the correlation of the field fluctuations by a step function characterized by a correlation time τ_c, we get:

$$D_\perp = \frac{4}{B_0{}^2} \int d\vec{k} \; H_{\perp k}(0)\Phi_\alpha(k,\tau_c) \tag{8}$$

where

$$\Phi_\alpha(k,\tau_c) = \frac{1}{k_\perp{}^2 D_\perp} \; [1 - \exp(-\tfrac{1}{2}k_\perp{}^2 D_\perp \tau_c] + \frac{k_\perp{}^2 D_\perp}{4\omega_{c\alpha}^2 + k_\perp{}^2 D_\perp{}^2} \cdot$$
$$[1 - (\cos(\omega_{c\alpha}\tau_c) - \frac{2\omega_{c\alpha}}{k_\perp{}^2 D_\perp} \sin(\omega_{c\alpha}\delta_c))\exp(-\tfrac{1}{2}k_\perp{}^2 D_\perp \tau_c)]$$

and

$$H_{\perp k}(t'-t'') = \frac{8\pi^3}{V} \langle h_{\perp k}(t')h_\perp{}^*(t'') \rangle$$

where V is the volume occupied by the system and $h_{\perp k}(t)$ is the space Fourier transform of $h_\perp(t)$.

4. QUASI-LINEAR AND NON-LINEAR REGIMES

Let us consider two important limiting cases. The first corresponds to the non-linear regime, where the non-linear exponential decay time $\tau_D = [k_\perp{}^2 D_\perp/2]^{-1}$ is much smaller than the correlation time τ_c. In this case, eq. (9) can be reduced to:

$$D_\perp = \frac{2}{B_0} \; [\int d\vec{k} \; \frac{H_{\perp k}(0)}{k_\perp{}^2}]^{1/2}[1 + \tfrac{1}{2}(\frac{m_\alpha}{q_\alpha})^2 \frac{1}{B_0{}^4} \int d\vec{k} \; k_\perp{}^2 H_{\perp k}(0)] \tag{10}$$

The first term of this expression shows the Bohm-like behaviour already obtained for the guiding-centre motion in the presence of electrostatic fluctuations [2]. The second term contains the corrections due to the finite Larmor radius.

In the opposite case of very long decay times $\tau_D \gg \tau_c$, we can derive from eq. (9):

$$D_{\perp} = \frac{2}{B_0^2} [\tau_c + \frac{1}{\omega_{c\alpha}} \sin(\omega_{c\alpha}\tau_c)] \int d\vec{k}\, H_{\perp k}(0) \qquad (11)$$

We recognise in the first term of this expression the well known quasi-linear diffusion coefficient. Again, the second term contains the contributions of the cyclotron motion.

5. CONCLUSIONS

The transverse diffusion coefficient of a charged particle in the presence of electromagnetic field fluctuations was derived taking into account the finite Larmor radius effects. This result contains, as particular cases, the quasi-linear and the non-linear Bohm-like diffusion coefficients.

As our expression contains the effects of the cyclotron orbits it seems adequate for comparing the anomalous transport of electrons and ions as a function of the scale lengths of the field fluctuations [3].

These results are now being generalized to take into account the contributions of the parallel field fluctuations and the drift effects in a tokamak geometry.

REFERENCES

[1] R. Balescu, "Equilibrium and Non-equilibrium Statistical Mechanics", Wyley-Interscience, NY (1975).
[2] J.B. Taylor and B McNamara, Phys. Fluids 14, 1492 (1971).
[3] M. Brusati et al, (1988) - submitted for publication.

ELECTRON-ACOUSTIC SOLITONS IN A TWO-ELECTRON TEMPERATURE PLASMA

S. Guha, C.B. Dwivedi and Meenu Asthana

Department of Physics, Ravishankar University,
Raipur 492010 (M.P.) INDIA

Introduction

A system of two electron temperature is observed in magnetosphere plasmas [Williams(1)], Solar Wind [Pledman et al (2)] and in laboratory plasmas [Jones et al(3)]. In such a system the existence of positive and negative ion-acoustic solitons have been shown experimentally and theoretically. However, the investigation of the existence of electron-acoustic soliton has not been done so far. Using the fluid model under the condition $C_h \gg \lambda \gg C_c$ analytical investigation of electron-acoustic solitary wave has been done. Both the Sagdeev potential formulation and reductive parturbation technique have been used. Finite thermal effects have also been incorporated for the sake of complete study of the solitary wave.

Sagdeev Potential Formulation

We assume that the hot electrons obey the Boltzmann relation and the dynamics of the cold electrons and ions are governed by the equation of motion and continuity. Using the Poisson's equation and normalising the variables as

$$\phi' = \frac{e\phi}{T_h}, \quad \rho^2 = \xi/\lambda_h^2, \quad \lambda_h^2 = T_h/4\pi n_{h0} e^2$$

$$x' = x/\lambda_h, \quad t' = \omega_{ph} t, \quad V'_{i(c)} = V'_{i(c)}/(T_h/m_e)^{1/2}$$

$$n'_h = n_h/n_{h0}, \quad n'_c = n_c/n_{c0}, \quad n'_i = n_i/n_{h0}$$

The Solitary wave comes out to be

$$\frac{1}{2}\left(\frac{d\phi'}{d\rho}\right)^2 + V(\phi') = 0 \qquad (1)$$

in a stationary frame.

Where $V(\phi')$ is the Sagdeev potential given by

$$V(\phi') = \frac{(\epsilon_n+1)}{\epsilon_n} \cdot I - \exp(\phi') - \epsilon_n^{-1} \cdot E + I.C.$$

and

$$I = -\frac{M^2\left(\frac{1}{\epsilon_n} + \frac{n_0}{n_{h0}} \cdot \frac{m_e}{m_i}\right)}{\left(\frac{1}{M^2}-1\right)^{-2}} \cdot \frac{m_i}{m_e} \left[\frac{\left(1 - \frac{2\phi'}{M^2} \cdot \frac{m_e}{m_i} \cdot \frac{\left(\frac{1}{M^2}-1\right)^{-2}}{\left(\frac{1}{\epsilon_n} + \frac{n_0}{n_{h0}} \cdot \frac{m_e}{m_i}\right)}\right)^{1/2}}{-\left(\frac{1}{M^2}-1\right)} - \frac{1/M^2}{\left(\frac{1}{M^2}-1\right)^2} \cdot \log\left\{ \frac{1}{M^2} - \left(\frac{1}{M^2}-1\right)\left(1 - \frac{2\phi'}{M^2} \cdot \frac{\left(\frac{1}{M^2}-1\right)^{-2}}{\left(\frac{1}{\epsilon_n} + \frac{n_0}{n_{h0}} \cdot \frac{m_e}{m_i}\right)}\right)^{1/2} \right\} \right]$$

$$E = \frac{M^2\left(\frac{1}{\epsilon_n} + \frac{n_0}{n_{h0}} \cdot \frac{m_e}{m_i}\right)}{\left(\frac{1}{M^2}-1\right)^{-2}} \left[\frac{\left(1 + \frac{2\phi'}{M^2} \cdot \frac{\left(\frac{1}{M^2}-1\right)^{-2}}{\left(\frac{1}{\epsilon_n} + \frac{n_0}{n_{h0}} \cdot \frac{m_e}{m_i}\right)}\right)^{1/2}}{-\left(\frac{1}{M^2}-1\right)} - \frac{1/M^2}{\left(\frac{1}{M^2}-1\right)^2} \log\left\{ \frac{1}{M^2} - \left(\frac{1}{M^2}-1\right)\left(1 + \frac{2\phi'}{M^2} \cdot \frac{\left(\frac{1}{M^2}-1\right)^{-2}}{\left(\frac{1}{\epsilon_n} + \frac{n_0}{n_{h0}} \cdot \frac{m_e}{m_i}\right)}\right)^{1/2} \right\} \right]$$

$$I.C. = \left[1 + \epsilon_n^{-1} \cdot \frac{M^2}{\left(\frac{1}{M^2}-1\right)^{-2}} \cdot \left(\frac{1}{\epsilon_n} + \frac{n_0}{n_{h0}} \cdot \frac{m_e}{m_i}\right) + \frac{\epsilon_n+1}{\epsilon_n} \cdot \frac{M^2}{\left(\frac{1}{M^2}-1\right)^{-2}} \cdot \frac{m_i}{m_e}\left(\frac{1}{\epsilon_n} + \frac{n_0}{n_{h0}} \cdot \frac{m_e}{m_i}\right) \right]$$

For small-amplitude case, the Solitary solution comes out to be

$$\phi' = \phi'_{max} \, \mathrm{Sech}^2 \sqrt{\frac{P}{2}} \cdot \rho \qquad (2)$$

where $\phi'_{max} = -P/Q$

$$P = \frac{1}{2}\left[1 - \frac{\epsilon_n^{-1}}{\frac{1}{M^4}\left(\frac{1}{M^2}-1\right)^2} \cdot \left(\frac{1}{\epsilon_n} + \frac{n_0}{n_{h0}} \cdot \frac{m_e}{m_i}\right)^{-1} \cdot \left\{1 + (\epsilon_n+1)\frac{m_e}{m_i}\right\}\right]$$

$$Q = \frac{1}{6}\left[1 - \frac{2\epsilon_n^{-1}}{M^6\left(\frac{1}{M^2}-1\right)^3} \cdot \left(\frac{1}{\epsilon_n} + \frac{n_0}{n_{h0}} \cdot \frac{m_e}{m_i}\right)^{-2} \left\{1 + (\epsilon_n+1)\left(\frac{m_e}{m_i}\right)^2\right\}\right]$$

In equation (2) when $n_{e0}/n_{h0} \equiv \frac{1}{\epsilon_n} = 0$, usual ion acoustic soliton of compressive nature is seen. Also if the cold electrons are present in traces such that $1/\epsilon_n \ll (m_e/m_i)^2$, the ion-acoustic wave still exists. However, when $1/\epsilon_n \gg m_e/m_i$, electron-acoustic soliton of rare factive nature is found to exist. In this case only electrons are perturbed and compressed to form negative soliton. The electron-acoustic soliton exists even when $1/\epsilon_n \simeq m_e/m_i$ wherein ions also participate in the wave propagation. Under this approximation electrons are more compressed than the ions, hence, negative potential exists.

K - dV equation

Introducing "Stretched" variables $\rho' = \epsilon^{1/2}(x' - qt)$, $\tau = \epsilon^{3/2} q t'$ and scaling parameter

$$\alpha = \frac{\epsilon\left[1 + (\epsilon_n+1)\cdot\left(\frac{m_e}{m_i}\right)^2\right]^{-1}}{\left[\frac{1}{\epsilon_n} \cdot \frac{(\epsilon_n+1)}{\epsilon_n} \cdot m_e/m_i\right]^{-2}} = \epsilon\alpha_1$$

and using reductive perturbation technique, one gets the K-dV equation for the small amplitude solitary wave as

$$\frac{\partial \phi'^{(1)}}{\partial \tau} - \frac{P}{Q} \cdot \phi'^{(1)} \cdot \frac{\partial \phi'^{(1)}}{\partial \rho'} + \frac{1}{Q} \cdot \frac{\partial^3 \phi'^{(1)}}{\partial \rho'^{(3)}} = 0. \qquad (3)$$

where

$$P = \alpha_1\left[1 + 3\epsilon_n^{-1} q^{-4}\left(\frac{1}{(1 - T_e/T_h\, q^{-2})^2} - \frac{(\epsilon_n+1)(m_e/m_i)^2}{\left(1 - q^{-2}\frac{m_e}{m_i} \cdot \frac{T_i}{T_h}\right)^2}\right)\right.$$

$$\left. - \epsilon_n^{-1} q^{-6}\left(\frac{T_e/T_h\left(1 - \frac{2}{\epsilon_n}\right)}{(1 - T_e/T_h \cdot q^{-2})^2} + \frac{T_i/T_h\left(1 + \frac{2}{\epsilon_n}\right)}{\left(1 - \frac{T_i}{T_h} \cdot q^{-2} \cdot \frac{m_e}{m_i}\right)^2}\right)\right]$$

and

$$Q = 2\epsilon_n^{-1} q^{-2}\left[\frac{1}{(1 - T_c/T_h \cdot q^{-2})} + \frac{(\epsilon_n+1)\cdot m_e/m_i}{(1 - q^{-2}\cdot\frac{T_i}{T_h}\cdot\frac{m_e}{m_i})}\right]$$

Equation (3) serves to model a weakly dispersive and weakly nonlinear solitary waves in a hot plasma. The nonlinear term in equation (3) arises from the combination of cold electrons and ion convection and flux, and the expansion of the Boltzmann distribution for hot electrons for $\phi \ll 1$. The dispersive term $1/Q\, \partial^3\phi^{1/2}/\partial\rho'^3$ arises from the duration from exact charge neutrality in Poisson's equation. Non linearities tend to steepen the wave whereas dispersion tends to spread it out. Therefore, it is possible to obtain a stationary solution if these two exactly balance each other. Such a solution is the "Solitary" wave solution given by equation (2).

The two-electron component plasma model present here may be useful in studying the behaviour of the magnetospheric and solar wind plasmas.

REFERENCES

WILLIAMS, D.J. Solar Terrestrial Physics (ed. E.R. Dyer), (1970), pp. 66-130 : Reidel.

FLEDMAN, W.C., ASBRIDGE, J.R., BAME, S.J., MONTGOMERY, M.D., and GARY, S.P., J. Geophys. Res. (1975) 80, 4181.

JONES; W.D., LEE, A., GLEMAN, S.M. and DOUCET, H.J. Phys. Rev. Lett. (1975) 35, 1349.

ON THE MAGNETIC FIELD EFFECT ON A PLANAR-SOLITON STABILITY

Hadžievski Lj., Škorić M.M.

The Boris Kidrič Institute of Nuclear Sciences, P.O.B. 522,
11001 Belgrade, Yugoslavia

Introduction

The stability of planar solitons is a problem which has attracted a certain interest on its own merits and, in particular, concerning the theory of strong Langmuir turbulence. Several papers have studied similar problems in a weakly magnetized plasma.[1-6] While in one dimension planar solitons are stable, as a rule, they become linearly unstable, in two and three dimensions, with respect to transverse perturbations. Moreover nonlinear stage of the instability often leads to a soliton collapse, a unique phenomenon of an intensive field growth followed by a rapid localization and subsequent wave dissipation.

In order to investigate the magnetic field effect on the linear stability of planar upper-hybrid (UH) solitons with respect to small transverse perturbations, we have performed a direct two-dimensional (2D) simulation[6] backed by an analytical study.

Basic equation

Basic equation describing the physics of nonlinear interactions of high-frequency upper-hybrid waves with low-frequency ion-sound motions, is given in a dimensionless form by[3]

$$\Delta(i\Psi_t + \Delta\Psi) - \sigma\Delta\,\Psi + \nabla(|\nabla\Psi|^2\,\nabla\Psi) = 0 \quad , \tag{1}$$

where Ψ is the slowly varying envelope of UH wave potential. Equation (1), valid in a weakly magnetized plasma ($\omega_{pe}^2 \ll \omega_{ce}^2$) is written in dimensionless units

$$t \to \frac{3}{2}\left(\frac{M}{m}\right)\omega_{pe}^{-1}t \ , \quad \vec{r} \to \frac{3}{2}\sqrt{\frac{M}{m}}\, r_d\vec{r} \ , \qquad \Psi \to \left(\frac{T_e}{e}\right)\sqrt{12}\,\Psi \ , \tag{2}$$

while σ stands for

$$\sigma = \frac{3}{4}\left(\frac{\omega_{ce}}{\omega_{pe}}\right)^2 \frac{M}{m} \ .$$

The only known stationary and localized, nonlinear solution of eq (1) in 2D (and 3D) is given [1,3] in a form of a planar soliton propagating along the ambient magnetic field (x - axis).

$$\frac{\partial}{\partial x}\Psi_s = \sqrt{2(1-V^2)}\lambda \text{ sech } \lambda(x-Vt)\exp i\left|(\lambda^2 - \frac{V^2}{4})t + \frac{Vx}{2}\right|, \tag{3}$$

where V is the soliton speed and λ is the soliton strength.

We numerically investigate the linear stability on the background of the standing soliton (V = 0) with respect to the initial transverse (y-axis) perturbation of the form

$$\delta\Psi_0 = 2\Psi_s \varepsilon \exp(-ik_\perp y) \quad , \quad \varepsilon \ll 1 \quad , \tag{4}$$

where $k_\perp$ is the transverse perturbation wave number and ε is the level of initial perturbation.

We look for an instability with the growth rate γ defined through

$$|\delta\Psi| = |\delta\Psi_0|\exp \gamma t \ . \tag{5}$$

Soliton stability

A certain amount of controversy has been following the problem of stability of planar solitons, steming from differences between various analytical results[1-2]. In our case, although general qualitative understanding of a stabilizing magnetic field effect on a UH soliton exists, disagreements, concerining the details of instability spectrum and critical values of parameters are present. Namely, in order to analytically simplify a complex nonlinear spectral problem, authors used various approximations often leading to different sometimes conflicting results[2].

To resolve some of these questions, in particular to single out the magnetic field effect, we solve equation (1) numerically in 2D by the spectral Fourier method with respect to space coordinates with periodic boundary conditions L_x, L_y. Nonlinear terms are computed by transforming back to real (x-y) space, while time integration is performed by an explicit method with a second order accuracy. A grid with 32x32 points and a time step of 0.001 have been typically used with a regular check on conserved integrals of (1); the plasmon number (N) and the Hamiltonian (H)[1]. As compared to Pereira et al.[4], we have decreased the perturbation level to $\varepsilon = 10^{-2}$ until γ has become independent on ε (see Ref.2). We have performed runs with different values of $k_\perp$ and σ: however in the range $k_\perp < 0.4$, grid resolution appears to be insufficient to correctly treat small $k_\perp$ region.

Results

We present the curves for the linear growth rate: as a function of the perturbation wavenumber $k_\perp$ (for σ=0;4;8;12) in Figure 1. and as a function of the ambient magnetic field σ(for $k_\perp$=0.52;0.74;0.90) in Figure 2. For an isotropic case (σ=0), the wavenumber dependance in Fig.1, shows a maximum at $k_{\perp m} \sim 0.5$ and a cut-off at $k_{\perp c} \sim 1.38$. Increasing the magnetic field (σ) shifts the cut-off to smaller $k_{\perp c}$, meaning that the spectral region of unstable wavenumbers becomes narrower. However, the maximum value of the growth rate weakly increases with σ.

Generaly taken, comparison between analytical predictions[1-5] and our numerical results, shows basically qualitative agreements. Not surprisingly, as approximate analytics normally rests on: an assumption of a smallnes of transverse as compared to longitudinal wave numbers, together with a perturbation theory expansion in small $k_\perp$. As seen on inspection (Figs. 1.-2.) both assumptions are poorly justified for finite $k_\perp$, in the region of the maximum growth up to the cut-off value. On the other hand, small $k_\perp$ region, treated analytically, is difficult to access by our direct simulation method. As an independent check of our curves (Figs 1-2) we find detailed agreements with more recent numerical results obtained by solving the spectral eigen value problem of the linearized version of the equation (1)[7]. However, the question of the small $k_\perp$ region behavior together with a more detailed analysis will be presented elsewhere.[7]

1. E.H.Kuznetsov, A.M.Rubenchik, V.E.Zakharov, Phys.Reports 142, 105 (1986)
2. M.J.Wardrop, D.ter Haar, Phys.Scripta 20, 493 (1979)
3. V.V.Krosnosel'skikh, V.I.Sotnikov, Fiz.Plazmy 3, 872 (1977)
4. N.R.Pereira, R.N.Sudan, J.Denavit, Phys.Fluids 20, 936 (1977)
5. H.L.Rowland, Phys.Fluids 28, 150 (1986)
6. Lj.Hadžievski, M.M.Škorić, Proc. XV EPS Conference on Contr.Fus. Plasma Heating, p.1287, Dubrovnik, (1988)
7. Lj.Hadžievski, A.M.Rubenchik, E.G.Shapiro, M.M.Škorić, S.G. Turitsin (to be published)

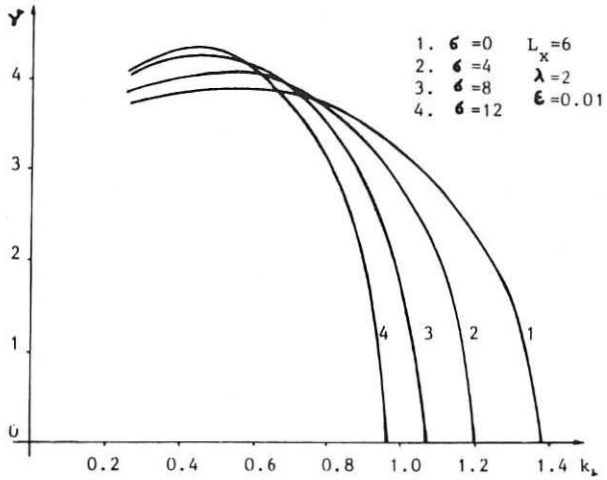
γ
4
3
2
1
0
0.2
0.4
0.6
0.8
1.0
1.2
1.4
k⊥
1. σ =0
2. σ =4
3. σ =8
4. σ =12
L_x =6
λ =2
ε =0.01
4
3
2
1

Fig.1

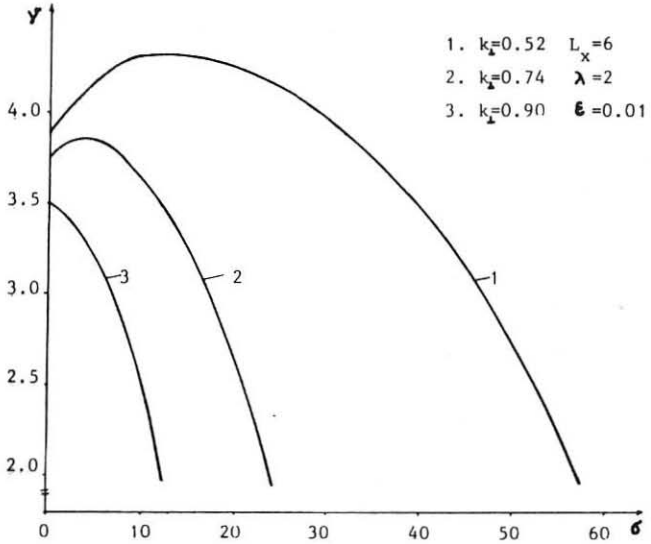
γ
4.0
3.5
3.0
2.5
2.0
0
10
20
30
40
50
60
σ
1. k⊥=0.52
2. k⊥=0.74
3. k⊥=0.90
L_x =6
λ =2
ε =0.01
3
2
1

Fig.2

GENERATION OF A PLASMA WAVE BY THE BEAT WAVE PROCESS USING 1 μm LASER BEAMS

M G Haines, A Dyson, A E Dangor, A K L Dymoke-Bradshaw, F Amiranoff*, G Mattheussent*, T Garvey**, T Ashfar-Rad***, C N Danson*** and R G Evans***

Imperial College, *Ecole Polytechnique, **CERN, ***Rutherford Appleton Laboratory.

Abstract: A relativistic plasma wave has been observed driven by two copropagating neodymium laser beams at 1.064 μm and 1.053 μm. This is inferred from an order of magnitude enhancement in the sideband amplitude of a copropagating 0.5 μm probe. The plasma wave amplitude is estimated to correspond to $\delta n/n \simeq 1\%$ giving a longitudinal electric field $E_p \simeq 10^7 \mathrm{Vcm}^{-1}$. The intensity of each pump beam is $I \simeq 2\mathrm{x}10^{14} \mathrm{Wcm}^{-2}$ and the interaction length measured by Moire deflectrometry is $\simeq$5mm. The low wave amplitude and its observed short lifetime of about 50ps at the peak of the pump beams suggest that the wave is heavily damped possibly by the modulational instability.

The need to probe smaller and smaller distances in matter has led to the requirement for large increases in particle accelerator energy. To accelerate a charged particle to relativistic velocities requires a longitudinal electric field and if a wave is used then the phase velocity must be close to c. The electric field in a plasma wave can be orders of magnitude greater than in a conventional accelerator. The beat wave mechanism (Tajima and Dawson 1979) is an interesting method of producing a relativistic plasma wave. This requires that two copropagating laser beams ω_0, ω_1 are focussed into a plasma with the laser beat frequency close to the plasma frequency so that $\omega_p = \omega_1 - \omega_0$. In the experiment reported here a neodymium glass laser was used to laser pump beams at 1.064 μm and 1.053 μm. Beat wave experiments have been performed using CO_2 laser pump beams (Clayton *et al* 1985; Ebrahim *et al* 1986) and have reported the generation of plasma waves with $\delta n/n \simeq 1-3\%$. However, the use of a neodymium laser gives a plasma wave of much higher phase velocity with $\gamma = 100$ as opposed to $\gamma = 10$ for the CO_2 lasers. Since the energy gain is $\propto \gamma^2$ the use of a neodymium laser is more relavent to particle acceleration.

The experimental arrangement is shown in Fig. 1. The laser pump beams were produced separately and followed separate air paths before being mixed under vacuum. This was done to prevent Raman scattering in air which considerably reduces the energy at the pump wavelengths. Each pump beam of $\simeq$50J in 200ps was focussed by a 2m lens (f/20) into the target chamber giving a peak irradiance of $\simeq 2\mathrm{x}10^{14} \mathrm{Wcm}^{-3}$. The main diagnostic monitored the sidebands formed on a separate copropagating green probe beam. This was focussed to the same spot as the pumps by a 3m lens (f/30). Precautions were taken to avoid sidebands formed on the green probe by CARS in quartz induced by the pump beams. To reduce the CARS sidebands sufficiently it was necessary to block the centre of the pump beams and all but the centre of the probe

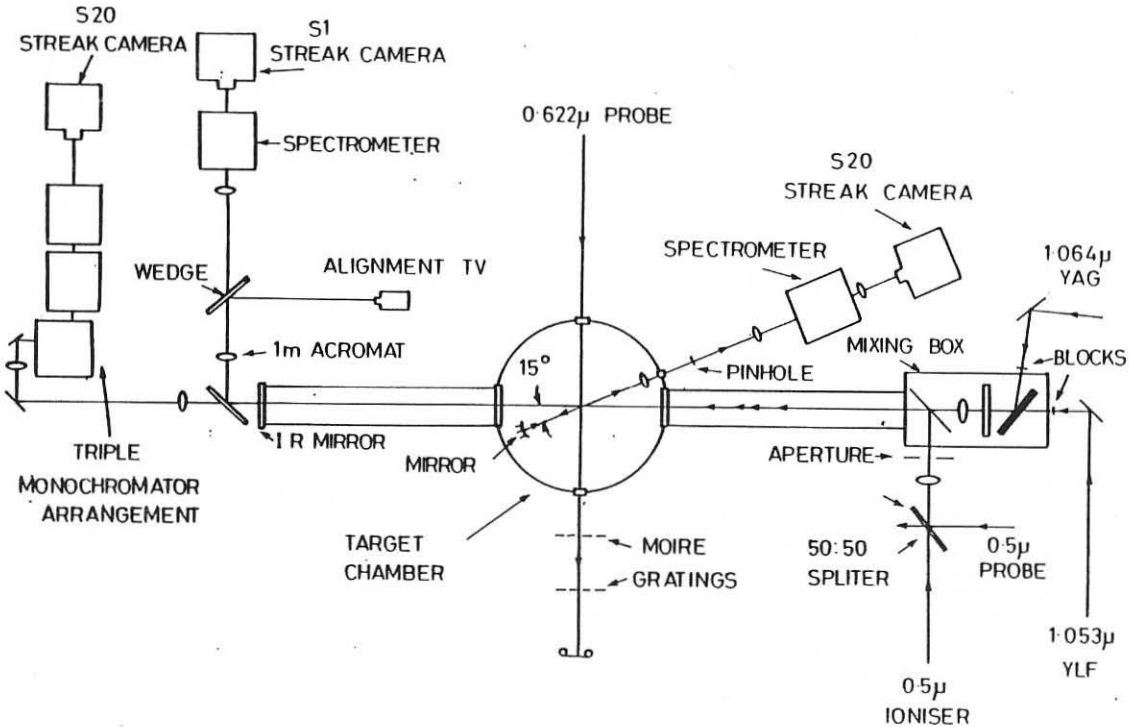

Fig. 1 *Schematic of the experimental arrangement.*

beam reducing it to f/100 so that the pumps and probe had no common path in quartz.

The probe light was monitored using a triple monochromator and Hadland 675 streak camera. Unfortunately it was only possible to view the spectrum on one side of the probe wavelength if sufficient rejection of the probe wavelength was to be obtained. A green ionising beam was used to generate a fully ionised plasma by multiphoton ionisation. The target chamber was filled with high purity hydrogen gas at pressures from 1−2torr. The pressure of the fill gas was measured to an accuracy of about 1mtorr and the temperature to about 0.5K. The pressure was varied from shot to shot so that the electron density was under, on and over resonance. Moire deflectrometry using a 0.622μm Raman shifted probe enabled the extent of the plasma to be determined. The probe beam was timed so that it crossed the axis of the pump beams withinabout 0.5μm after the pump beams. Using this diagnostic it was found that the pump beams generated a plasma by multiphoton ionisation so that a separate green ionising beam was not required. The Thomson scattered light from the green beams was monitored at 15^0 and 165^0 and showed that the ionising beam generated a fully ionised plasma.

The microdensitometer scans of the film data obtained at resonance and under resonance are shown in Fig. 2. The small residual sideband amplitude in the under resonance case is due to CARS. It is found that the anti−Stokes sideband amplitude at resonance is enhanced by about ten times over the under resonance case. Data shots over resonance show an enhancement of about four times. The Stokes sidebands were not monitored. The f/100 apperturing meant that only a high β plasma wave could be detected.

The maximum plasma wave amplitude is estimated from the relative sideband amplitude using

$$\frac{I_s}{I_o} = \left[\frac{\pi}{2} \frac{L_{eff}}{\lambda_o} \left[\frac{\omega_p}{\omega_o}\right]^2 \left[\frac{\delta n}{n}\right] \right]^2$$

Thus at resonance the ratio $I_s/I_o \simeq 10^{-5}$ and the interaction length $L_{eff} \simeq 5$mm give a wave amplitude of $\delta n/n \simeq 1\%$. The smaller sideband enhancement observed at over resonance densities is possibly due to some parts of the plasma being not fully ionised and so at resonant density. For fill pressures set under resonance no interaction is possible. The plasma wave exists only when the laser pump beams are most intense. The amplitude $\delta n/n \simeq 1\%$ and lifetime $\simeq$50ps are consistant with it being damped by the modulational instability (Pesme *et al* 1987). The fastest growth rate for this instablity is $\gamma \simeq (\delta n/n)\omega_p$ so that for $\delta n/n \simeq 1\%$ have $1/\gamma \simeq 5$ps. The plasma wave lifetime is longer than this as it has to grow to maximum amplitude.

We have observed an order of magnitude enhancement in the anti−Stokes sideband amplitude formed on a copropagating green probe beam when the plasma density is tuned to resonance. This is taken as tentative evidence of a beat wave induced plasma wave with amplitude $\delta n/n \simeq 1\%$. Only a preliminary data set has been obtained and the Stokes sideband was not monitored. It is intended to repeat the experiment and obtain a more complete data set.

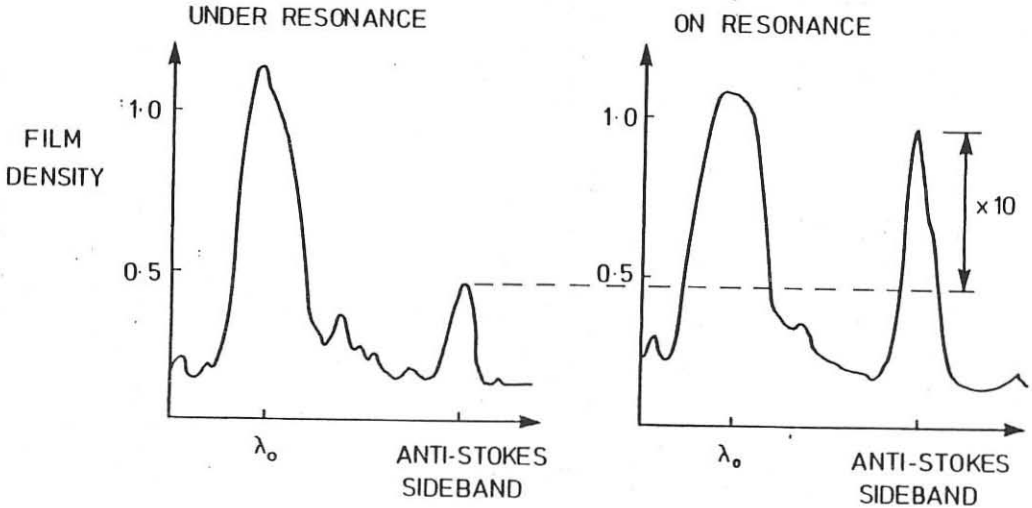

Microdensitometer traces of the data obtained under resonance and on resonance.

GENERATION OF ION BERNSTEIN WAVES BY OPTICAL MIXING: DETECTION OF THE COUPLING BY SPATIAL PHASE CONJUGATION

Thierry LEHNER
Laboratoire de physique des Milieux Ionisés, Laboratoire du C.N.R.S.,
Ecole Polytechnique, 91128 Palaiseau Cédex

ABSTRACT :

We have reported elsewhere[1] the first phase conjugation experiment in an unmagnetized plasma using microwaves. Here we concentrate on the theory and the experimental proposal for the generation of ion Berstein waves by optical mixing and their detection by spatial phase conjugation involving three or four waves mixing.

INTRODUCTION :

There has been recently a renewal of interest for plasma diagnosis using induced wave-wave interaction. We shall emphasize the use of phase conjugation as a diagnostic tool. The second order susceptibility $\Lambda^{(2)}$ for plasmas is never zero even in isotropic plasma thanks to the existence of longitudinal waves. The resonant coupling of two electromagnetic waves and a longitudinal wave is thus possible.However a very little number of experiments has been devoted to beat wave excitation in magnetized plasmas.Indeed for example only very recently the excitation of electron Bernstein waves by optical mixing has been reported[2].

We restrict to theory and experiment (under investigation) allowing the excitation of ion Bernstein waves by the optical mixing of two incoming electromagnetic waves. The presence of the coupling is detected by a method directly sensitive to the transfer of action between the pump waves. This transfer is computed by the Manley Rowe (MR) relations[3] valid for convective damping of the longitudinal resonance in an homogeneous plasma. The detection deals either with a direct absorption of power on one of the pump wave, or by launching a third wave 3 close in (k,ω) space of one pump wave 1. Wave 3 could be choosen parallel or antiparallel to wave 1,in each case wave 3 is scattered on the induced longitudinal resonance,and the outgoing wave is given by a three wave conjugation process with respect to second pump wave 2, either in transmission (TPC) or in reflexion (RPC).

1. THEORY

A. GENERATION OF THE DAUGHTER WAVE BY OPTICAL MIXING

Two electromagnetic waves supposed harmonic (k_1,ω_1), (k_2,ω_2) are incident on an infinite homogeneous plasma imbedded in a B_0 magnetic field. Their low frequency and wavenumbers beating $(k_1-k_2,\ \omega_1-\omega_2)$ creates a micro-anisotropy and inhomogeneity within the plasma in the k_1-k_2 direction. The phase gradient of this inhomogeneous term yields the ponderomotive force f_p, of second order in electric field E_1, E_2 . In a single particle model f_p derives from a full quadripotential (A_{12},Φ_{12}),where:

$$\Phi_{12} = -1/2 \langle \bar{r}_1.\bar{E}_2 + \bar{r}_2.\bar{E}_1 \rangle \quad \bar{A}_{12} = 1/2 \langle \bar{r}_1 \wedge \bar{B}_2 + \bar{r}_2 \wedge \bar{B}_1 \rangle \qquad (1$$

$r_i(E_i)$is the displacement of the particle in the pump fields (E_i,B_i) The brackets mean a temporal average over the high frequency (fast scale) : $T_i = 2\pi/\omega_i$ $(i = 1,2)$ as opposed to the slow scale $T_{12} = 2\pi/(\omega_1-\omega_2)$.The

first order velocity in E_i associated to r_i is given by the Lorentz equation of motion (to be solved in the dipolar approximation):

$$d\bar{v}_i/dt + \bar{\omega}_c \wedge \bar{v}_i = q/m\ (\bar{E}_i + \bar{v}_i \wedge \bar{B}_i)\ (2) \qquad i=1,2 \qquad \omega_c = qB_o/m$$

We suppose here that the pump frequencies ω_1, ω_2 are enough far from the gyrofrequency ω_c, if not time transit effects have to be considered[4,5].
One can also use a fluid model to write the density of ponderomotive force as (for electrons):

$$\bar{F}_e^{(2)} = \langle n \rangle \langle -m_e\ (\bar{V}_e^{(1)}.\bar{\nabla})\ \bar{V}_e^{(1)} + q_e(\bar{V}_e^{(1)} \wedge \bar{B}^{(1)}) + \partial/\partial t(n^{(1)}\bar{V}_e^{(1)})\rangle \quad (3)$$

This force is again taken at the beat frequency $\omega_1-\omega_2$, the density being $n=\langle n\rangle+n^{(1)}$. There is a second order current associated with this force: $j_e^{(2)}=\langle n\rangle q_e V_e^{(2)}$ with $m_e\ \partial V_e^{(2)}/\partial t + \omega_{ce} \wedge V_e = f_e^{(2)}$. One can show[6,7] that to connect the fluid model (force F_e) and the single particle model (force f_e) one has to substract the current of magnetization $j_m = \mathrm{Rot}\ M$, $M=\langle n\rangle\langle\mu\rangle$, $\langle\mu\rangle=q/2\langle r^{(1)} \wedge v^{(1)}\rangle$, from F_e. The single particule force is $\langle n\rangle f_e = F_e + m(\omega_{ce} \wedge V_L)$, with $V_L=\langle(r^{(1)}\cdot\nabla)V^{(1)}\rangle$. In this case on has a <u>potential</u> expression for $f_e = -\nabla\Phi_{12}$, with Φ given by (1) or also by

$$\Phi = m/2\langle(v^{(1)})^2\rangle + \langle\mu\rangle.B_o \qquad (4)$$

The current $j_e^{(2)}$ induces a second order polarization $P^{(2)}$ creating the longitudinal wave. From the general non linear equation, ε being the first order permittivity tensor :

$$\mathrm{Rot}\ (\mathrm{Rot}\ \bar{E}) - \bar{\bar{\varepsilon}}/c^2\ \partial^2\bar{E}/\partial t^2 = -\mu_o\ \partial^2\bar{P}/\partial t^2\ (5), \bar{P}=\chi^{(1)}\bar{E} + \bar{\bar{\chi}}^{(2)}:\overline{EE} + \bar{\bar{\chi}}^{(3)}\overline{EEE}\ (6)$$

$\chi^{(n)}$ being the nth order susceptibility, is deduced the non linear equation for the generation of the longitudinal waves using a multiple (two)time scale averaging[8] in real space. It is easier here to work in the Fourier space where the induced density of the L wave $n^{(2)}$ (or $E^{(2)}$ by Poisson equation) is given with the help of the longitudinal second order polarizability $\chi_L^{(2)}$ for an ion wave by[9]

$$n_i^{(2)}(\bar{k},\omega)\ /n_o = i\ \bar{\bar{\chi}}_{L,i}^{(2)}:((\bar{E}_1.\bar{E}_2^*)).\bar{k}\ n_o q_e\ (\varepsilon_o/\varepsilon_L(\bar{k},\omega)) \qquad (7)$$

$$\chi_{L,i}^{(2)} = \chi_e^{(1)*}\chi_i^{(1)})\chi_{o,L}^{(2)}/(1+\chi_e^{(1)}) \qquad (8)$$

$$\chi_{o,L}^{(2)} = -iq_e k/(2m_e\omega_1\omega_2) \qquad \varepsilon = 1 + \chi_e^{(1)} + \chi_i^{(1)}$$

$\chi^{(1)}$ is the first order susceptibility, and ε is the longitudinal dielectric constant. The coupling on longitudinal waves has been previously studied[10] and we can write also $n^{(2)}$ differently as

$$n_i^{(2)}(k,\omega)/n_o = \varepsilon_o k^2/q_i\ ((\chi_i^{(1)}\chi_e^{(1)}/\varepsilon_L)\ \Phi_{12,e} - \chi_i^{(1)}(1+\chi_e^{(1)})/\varepsilon_L\ \Phi_{12,i}) + \ldots$$
$$\ldots\ \bar{k}/\omega\ .(\bar{\sigma}_e(1+\chi_e^{(1)})/\varepsilon_L - q_e/q_i(\chi_i^{(1)}/\varepsilon_L)\bar{\sigma}_i) \quad (9)\ \sigma s = \langle n^{(1)}Vs^{(1)}\rangle\ s=e,i$$

The first and third terms in eq.(9) are just eq.(8), while other terms come from (negligible generally) ponderomotive potential applied on the ions directly. The last two terms are linked with $n^{(1)}$ the first order density perturbation possibly brought by pump waves. We make application of eq.(9) to ion Bernstein waves :we remind the existence of two extreme kind of

waves:the pure ion Bernstein waves (PIBW) for which there is no density fluctuations $n_e^{(2)} \simeq 0$ and $V_{\phi//}=\omega/k_{//} >> Vthe$,V_ϕ is the parallel wave phase velocity and Vthe the electron thermal velocity.Also exist the quasi-neutralized ion Bernstein waves (QNIBW) for wich $Vthe << \omega/k_{//}$,these waves exhibit zero group velocity points at maximum ω (Vg=0) in each of their harmonic $n\omega_{ci}$ bandpass,since the IBW are also caracterized by typical frequencies $\omega \simeq n\omega_{ci}$ and $k_\perp \rho_i \simeq 1$. We restrict now to high frequency pump $\omega_i >> \omega_{ce}$ and to pump waves propagating perpendicular to the B_o field (ordinary O or extraordinary X modes). Different coupling are possible like X+X->L,O+O->L and O+X->L.Here we give only the simple O+O->L case.For Maxwellian plasmas we get,Z being the Fried and Conte function

$$\Lambda s^{(1)}= k_{dj}^2/k_{de}^2 \Sigma_n \Gamma_n(\gamma)(1+\xi_{oj}Z(\xi_{nj})) \qquad \gamma=(k_\perp\rho_j)^2/2 \quad j=e,i$$

$$\xi_{nj}= (\omega-n\omega_{cj})/(k_{//}V_j),V_j^2 = 2k_bT_j/m_j,\Lambda_e^{(1)} \simeq (k_{de}^2/2k^2)Z'(\xi_{oe}),\Lambda^{(1)}_e \simeq 0 \text{ for PIBW}$$

and $\simeq k_{de}^2/k^2$ for QNIBW,$\Gamma_n(z)=\exp(-z)I_n(z)$,$I_n$ modified 1st kind Bessel function

In real space inverting the Fourier-Laplace transform in the case of spatial (convective damping) as opposed to Landau damping, the damping is $\nu_c = Vg_\perp/L$,L being the interaction length, we thus get at the max of the resonance ($Re(\varepsilon_L)=0$) in a given passband ,Q being the resonance quality factor

$$n_i^{(2)}/n_o=(V_1V_2/2Vthe^2)Q_i,\ Q_i \simeq k_{12}L\ 1/(k_{12}^2\rho_i^2)\ 1/(I'_n/I_n -1) \qquad (10)$$

$$n_i^{(2)}/n_o=(V_1V_2/2Vthe^2)Q_i,\ Q_i \simeq (k_{12}L)^2\ 1/(I''_n/I_n -2I'_n/I_n +1) \qquad (11)$$

Eq.(10) is for QNIBW and Vg#0,while eq.(11) is for Vg=0 (a double pole occurs in the k integration),generally one has $Q_i=(k_{12}L/2)(1/(2k_{12}\partial\varepsilon/\partial k_\perp)$. $\simeq kL/2$ implying the number of excited wavelengths λ within the interaction length L. This factor is also the geometrical gain factor in a phase conjugation process.Here polarizations E_1,E_2 are parallel normal to the plane (k_1,k_2) maximizing the coupling efficiency. One finds for the maximum of the power of the daughter wave at resonance for $Vg_\perp$#0

$$P_i^{(2)} =P_1P_2/P_* \ (12) \quad 1/P_* = \pi/2\ Z_i^2/P_o(c^4/Vthe^4)(\omega_{pe}^4/\omega_1^2\omega_2^2)\ \sigma_{12}L^2/\sigma_1\sigma_2 \ ..$$

$$... \ (\omega_1-\omega_2)/(k_{12}c)\ 1/(1+\Lambda_e^{(1)})^2\ 1/(\partial\varepsilon/\partial k_\perp) \qquad P_o = m_ec^3 / r_o$$

r_o being the electron classical radius. The generation of the longitudinal wave could be also computed starting from the Vlasov equation written to second order in E_1 and E_2, the system being closed by Poisson equation. Here the Fourier transform involves a convolution in Fourier space leading to $k=k_1-k_2$.From $f^{(2)}$ one gets $\Lambda^{(2)}$, $j^{(2)}$, $n^{(2)}$ as above.

B.PHASE CONJUGATION IN A PLASMA

The originality of plasmas as compared to usual neutral optical media reveals several features in phase conjugation processes which have been noticed elsewhere[1]

Three wave spatial conjugation: The Manley Rowe (MR) relations for action conservation can be derived directly on the three mode coupling equations which describe the interaction of the enveloppe (slow spatial and time scales) for the electric fields of the pump and daughter waves.These relations hold for a non dissipative medium and for an homogeneous plasma where a coherent phase relation between waves can exist throughout the whole pump waves interaction region. They read for $\omega_1>\omega_2$ $\Delta P_2/\omega_2 = P_i^{(2)}/(\omega_1-\omega_2) = - \Delta P_1/P_1$ (13) with $\Delta=\partial t+Vg.\partial_r$.One can

demonstrate[1] that $(\Delta E_1, E_2)$ and $(\Delta E_2, E_1)$ are phase conjugated by a three wave process, ΔE_i being the variation of the pump i during the interaction. Thus experimentally a direct absorption detection on one of the pump wave is a three wave spatial phase conjugation experiment allowing the detection of the whole action transfer between pump waves[1].

Four wave mixing: For the classical four wave phase conjugation, the existence of $\Lambda^{(2)}$ allows the expression of $\Lambda^{(3)}$ to be $\Lambda^{(3)}(1,2,3) = \Lambda_{nr}^{(3)}(1,2,3) + 2\Lambda^{(2)}_L(1,2)\Lambda^{(2)}(3,L)/\varepsilon_L(L)$ (14) $\Lambda_{nr}^{(3)}$ is the non resonant part of $\Lambda^{(3)}(\varepsilon_L=1)$, coming from a third order current $j_e^{(3)}=q_e n_o v_e^{(3)}$. One can show that the ratio of $\Lambda^{(3)}_r$ (second term of the rhs of (14)) to $\Lambda^{(3)}_{nr}$ is precisely $1/|\varepsilon_L|$, hence an important gain when a second order resonance with $Re(\varepsilon_L(L))=0$ is induced by the optical mixing.

For alow density plasma ($n_o=10^{10}-10^{14}$ cm^{-3}) an experiment with microwaves become possible whereas "usual" experiments are done at optical frequencies in crystals.

The term $\Lambda^{(3)}_r$ comes from a third order current $j_e^{(3)}=q_e n^{(2)} V_e^{(1)}$. This four wave mixing could be understood as a two stage three wave mixing : first the longitudinal wave is created by the two em pump waves giving $E_L^{(2)}$ and second (as an induced scattering process) the interaction of the probe wave 3 with the daughter wave L gives the scattered fourth wave 4. The equations are very similar to the coupled mode equations. $\Lambda^{(3)}$ could be computed by a fluid model or from Vlasov equation written to third order ($f^{(3)}$). We give relevant expressions for $\Lambda^{(3)}_r$ and P_4 the conjugated power for wave 4. At the maximum of the resonant excitation we have $1/\varepsilon_L$ replaced by $1/(\nu\partial\varepsilon/\partial\omega)$, with $\nu=\nu_c=Vg/L$ for spatial damping or $\nu=\nu_L$ for Landau damping (temporal damping). Situations, disregarded here, could also occur where collisional damping is dominant. For ion waves we have

$$\Lambda_i^{(3)} = \Lambda_{o,e}^{(3)}(k_{de}^2/k^2)(1+k_{de}^2/k^2)\,1/\varepsilon_L \qquad (15)$$

$$\Lambda_{o,e}^{(3)} = -q_e^2 k^2/(2\, m_e^2\, \omega_1\omega_2\omega_3\omega_4)$$

$$P_{4,i}/P_3 = |\kappa_i^{(3)}L|^2 = P_1P_2/P_o^2(k_4L)^2/|\varepsilon_L|^2)\omega_{pe}^4/(\omega_1\omega_2\omega_3\omega_4)\ \ldots$$
$$\ldots\ (4\pi)^2(c/Vthe)^4\ 1/(k_1k_3\ k_4\sigma_1\sigma_2)\ (k_{de}^4/k_{12}^2) \qquad (16)$$

Application for the experimental parameters: $n_o = 10^{10}$ cm^{-3}, $f_{pe} \simeq 1$GHz, $P_1 = P_2 = P_3 = 1$W, $k_bT_e \simeq 1$ev, $f_i \simeq 10$Ghz (i=1,2), $\theta_{12}=(k_1,k_2)\simeq 90°$, $k_{12}\simeq 2^{1/2}k_i$, $L \simeq 15$cms, $\sigma_i \simeq L^2$, $k_{de} \simeq 1.35\ 10^4\ m^{-1}$ $B_o \simeq 200G$, He^+ plasma, $T_i \simeq 0.2$ev, $\rho_i \simeq 2$mm, for example : $n_i^{(2)}/n_o \simeq 10^{-6}$ for a simple pole and $n_i^{(2)}/n_o \simeq 1.2\ 10^{-4}$ for a double pole around ω_{ci}, whereas $\kappa_i^{(3)}L \simeq 2\ 10^{-3}$ in the former case.

2. EXPERIMENT: an investigation is done about this coupling on IBW waves. The same device than for the excitation of longitudinal waves in an isotropic plasma has been modified to add a magnetic field B_o using two Helmholtz cooper coils put inside the device. The same double microwave bench in the X band frequency range will be used for the beat wave experiment.

references

1. T. Lehner, to appear in Physica Scripta (1989).
2. T. Pierre, Thèse d'état, (unpublished) Déc 1988, Nancy, France.
3. J.S. Manley, H.E. Rowe, Proc. IRE, 44, 904 (1956).
4. for ex: Lamb, Dimonte, Morales, Phys. of Fluids, 27, 1401 (1984).
5. D. Boucher, T. Lehner, to be published.
6. J.M. Alimi, P. Mora, R. Pellat, J de Physique, 48, 585 (1987).
7. T. Lehner, Thèse d'Etat, (unpublished), Sept. 1987, Paris VI, France.
8. Bogolioubov, Krylov, Mitropolsky, Asympotic Methods in non linear oscillations, (1948).
9. T. Lehner, Plasma Physics, 27, 1163 (1985).

XVI
FUSION
VENEZIA
1989

RESPONSIBLE AUTHOR
INDEX *

* (First author is listed when responsible author was not indicated)

XVI
FUSION
VENEZIA
1989

FULL AUTHOR
INDEX